

Alexander N. Pisarchik
Alexander E. Hramov

Multistability in Physical and Living Systems

Characterization and Applications



Springer

Springer Series in Synergetics

Series Editors

Henry D.I. Abarbanel, Institute for Nonlinear Science, University of California, San Diego, CA, USA

Dan Braha, New England Complex Systems Institute, Cambridge, MA, USA

Péter Érdi, Center for Complex Systems Studies, Kalamazoo College, USA
Hungarian Academy of Sciences, Budapest, Hungary

Karl J Friston, Institute of Cognitive Neuroscience, University College London, London, UK

Hermann Haken, Center of Synergetics, University of Stuttgart, Stuttgart, Germany

Viktor Jirsa, Centre National de la Recherche Scientifique (CNRS), Université de la Méditerranée, Marseille, France

Janusz Kacprzyk, Systems Research, Polish Academy of Sciences, Warsaw, Poland

Kunihiko Kaneko, Research Center for Complex Systems Biology, The University of Tokyo, Tokyo, Japan

Scott Kelso, Center for Complex Systems and Brain Sciences, Florida Atlantic University, Boca Raton, FL, USA

Jürgen Kurths, Nonlinear Dynamics Group, University of Potsdam, Potsdam, Germany

Ronaldo Menezes, Computer Science Department, University of Exeter, Exeter, UK

Andrzej Nowak, Department of Psychology, Warsaw University, Warsaw, Poland

Hassan Qudrat-Ullah, Decision Sciences, York University, Toronto, ON, Canada

Linda Reichl, Center for Complex Quantum Systems, University of Texas, Austin, TX, USA

Frank Schweitzer, System Design, ETH Zurich, Zurich, Switzerland

Didier Sornette, Entrepreneurial Risk, ETH Zurich, Zurich, Switzerland

Stefan Thurner, Section for Science of Complex Systems, Medical University of Vienna, Vienna, Austria

Editor-in-Chief

Peter Schuster, Theoretical Chemistry and Structural Biology, University of Vienna, Vienna, Austria

Springer Series in Synergetics
Founding Editor: H. Haken

The Springer Series in Synergetics was founded by Herman Haken in 1977. Since then, the series has evolved into a substantial reference library for the quantitative, theoretical and methodological foundations of the science of complex systems.

Through many enduring classic texts, such as Haken's *Synergetics and Information and Self-Organization*, Gardiner's *Handbook of Stochastic Methods*, Risken's *The Fokker Planck-Equation* or Haake's *Quantum Signatures of Chaos*, the series has made, and continues to make, important contributions to shaping the foundations of the field.

The series publishes monographs and graduate-level textbooks of broad and general interest, with a pronounced emphasis on the physico-mathematical approach.

More information about this series at <https://link.springer.com/bookseries/712>

Alexander N. Pisarchik · Alexander E. Hramov

Multistability in Physical and Living Systems

Characterization and Applications



Springer

Alexander N. Pisarchik 
Center for Biomedical Technology
Universidad Politécnica de Madrid
Pozuelo de Alarcón, Madrid, Spain

Innopolis University
Innopolis, Russia

Alexander E. Hramov 
Innopolis University
Innopolis, Russia

Immanuel Kant Baltic Federal University
Kaliningrad, Russia

ISSN 0172-7389
Springer Series in Synergetics
ISBN 978-3-030-98395-6
<https://doi.org/10.1007/978-3-030-98396-3>

ISSN 2198-333X (electronic)
ISBN 978-3-030-98396-3 (eBook)

© The Editor(s) (if applicable) and The Author(s), under exclusive license to Springer Nature Switzerland AG 2022

This work is subject to copyright. All rights are solely and exclusively licensed by the Publisher, whether the whole or part of the material is concerned, specifically the rights of translation, reprinting, reuse of illustrations, recitation, broadcasting, reproduction on microfilms or in any other physical way, and transmission or information storage and retrieval, electronic adaptation, computer software, or by similar or dissimilar methodology now known or hereafter developed.

The use of general descriptive names, registered names, trademarks, service marks, etc. in this publication does not imply, even in the absence of a specific statement, that such names are exempt from the relevant protective laws and regulations and therefore free for general use.

The publisher, the authors and the editors are safe to assume that the advice and information in this book are believed to be true and accurate at the date of publication. Neither the publisher nor the authors or the editors give a warranty, expressed or implied, with respect to the material contained herein or for any errors or omissions that may have been made. The publisher remains neutral with regard to jurisdictional claims in published maps and institutional affiliations.

This Springer imprint is published by the registered company Springer Nature Switzerland AG
The registered company address is: Gewerbestrasse 11, 6330 Cham, Switzerland

We dedicate this book to our families and friends, as well as to our colleagues who worked with us during many years.

Preface

Multistability is ubiquitous in nature. From a mathematical point of view, multistability is the coexistence of stable states (attractors) for the same set of system parameters. The emergence of a particular state depends on the initial conditions. In fact, multistability is a form of functional self-organization of matter, because this phenomenon endows a system with the ability of operating in either one of many regimes under the same conditions.

In our daily life, we constantly face the phenomenon of multistability. For the layman, not familiar with nonlinear dynamics, we can provide the following examples.

There is a common folk saying: If in the morning you get up with the wrong foot, then your day is doomed to be unsuccessful. Although this is a superstition, it reflects the essence of bistability, where the Left and Right foots play the role of initial conditions, on which the state of the person as a dynamical system strongly depends.

Another occult example can be found in astrology. Astrologers make forecasts based on the date and place, (when and where) a person was born, completely ignoring genetics and environment. They believe that your destiny is only determined by initial conditions. However, it is well known that all real systems, including our universe and humans, are not completely deterministic. Since a stochastic component is always present, we cannot ignore the influence of random processes, which can drastically change our life path, regardless of the initial conditions. In addition, external factors can also lead us astray if our condition is not stable enough.

However, seriously speaking, multistability does exist in nature and technology. It was found in climate, ecosystems (for example, the Amazon rainforest), brain, lasers, financial market, etc. Some of the coexisting attractors are undesirable and can lead to catastrophic events, such as extreme climatic changes, financial crisis, and equipment failures. The tragical examples are crashes of at least three military aircrafts in 1990s of the last century due to so-called “pilot-induced oscillation”, that was interpreted as a hidden attractor into which the aircrafts were attracted. To prevent such situations in the future, it is extremely important to know the structure

of coexisting states and their basins of attraction, as well as their stability under parameter changes. These concepts are considered in the book.

The study of multistability in dynamical systems is a fast-developing research topic with applications in almost all areas of science and engineering, ranging from mathematics to complex biological and social networks.

The book aims to provide a first approach to multistability for readers, who are interested in understanding its fundamental concepts and applications in several fields. This book will prove useful not only to researchers and engineers focusing on interdisciplinary studies, but also to graduate students and technicians. Both theoreticians and experimentalists will rely on it, in fields ranging from mathematics and laser physics to neuroscience and astronomy. The book is intended to fill a gap in the literature, to stimulate new discussions and bring some fundamental issues to a deeper level of understanding of the mechanisms underlying self-organization of matter and world complexity.

After introducing the reader to the basic concepts of multistability, the book illustrates how multistability arises in different systems and explains the main mechanisms of multistability emergence. A special attention is given to noise which can convert a multistable deterministic system to a monostable stochastic one. Furthermore, the most important applications of multistability in different areas of science, engineering and technology are given attention throughout this book, including electronic circuits, lasers, secure communication, and perception.

It should be noted that it is impossible to cover all aspects related to multistability in one book. In particular, the problems of synchronization and control of systems with coexisting attractors are not included in this book because they are well described in other monographs. For readers who are interested in these topics we refer to the book of Boccaletti et al. [1] and the comprehensive review in Physics Reports [2], respectively.

Madrid, Spain
Innopolis, Kaliningrad, Russia

Alexander N. Pisarchik
Alexander E. Hramov

References

1. Boccaletti S, Pisarchik AN, del Genio I, Amann A (2018) *Synchronization: From Coupled Systems to Complex Networks*. Cambridge University Press, Cambridge
2. Pisarchik AN, Feudel U (2014) Control of multistability. *Phys Rep* 540:167–218

Acknowledgements

The authors thank their colleagues for close cooperation. The results of joint research formed the basis of this book.

Alexander N. Pisarchik thanks his family, Liudmila, Zoya, Maria Anna, and Daria for the patient they showed during the long time of writing this book. He personally acknowledges his daughter Zoya for her help in proofreading the text.

Alexander E. Hramov expresses his sincere gratitude to his wife Marina for her constant support and inspiration. He also thanks his good colleague, Dr. Natalija Shusharina, who invited him to the Baltic Federal University (Kaliningrad) to complete Chap. 8 of this book.

Contents

1	What is Multistability	1
1.1	Historical Overview	1
1.2	Mathematical Basis	4
1.2.1	Main Definitions	4
1.2.2	Attractors and Basins of Attraction	9
1.2.3	Smooth and Fractal Basins	11
1.2.4	Wada Basins	14
1.2.5	Riddled Basins	15
1.3	Stability of Invariant Sets	17
1.3.1	Lyapunov Stability	17
1.3.2	Asymptotic Stability	18
1.3.3	Exponential Stability	18
1.3.4	Orbital Stability	19
1.3.5	Structural Stability	20
1.3.6	Linear Stability Analysis	20
1.4	Basin Stability	23
1.4.1	Resilience	24
1.4.2	Integral Stability	27
1.4.3	Final State Sensitivity	28
1.4.4	Survivability	28
1.4.5	Basin Catastrophe	30
1.4.6	Basin Integrity	32
1.5	System Complexity	35
1.5.1	Basin Entropy	35
1.5.2	Spectral Entropy	37
1.5.3	Sample Entropy	38
	References	39

2 Emergence of Multistability	45
2.1 Bifurcations Giving Rise to Multistability	45
2.1.1 Pitchfork Bifurcation	46
2.1.2 Saddle-Node Bifurcation	46
2.1.3 Andronov–Hopf Bifurcation	49
2.1.4 Neimark–Sacker Bifurcation	51
2.1.5 Multiple Limit Cycle Bifurcation	51
2.1.6 Infinite-Period Bifurcation	53
2.1.7 Inverse Gluing Bifurcation	54
2.1.8 Symmetry-Increasing Bifurcation	55
2.2 Mechanisms Leading to Multistability	56
2.2.1 Homoclinic Tangencies	57
2.2.2 Weak Dissipation	58
2.2.3 Clustering	61
2.2.4 Phase Multistability	63
2.2.5 Positive Feedback	68
2.2.6 Delayed Feedback	69
2.2.7 Periodic Forcing	71
2.2.8 Symmetry	73
2.2.9 Structural Multistability	75
2.3 Methods to Reveal Multistability	77
2.3.1 Varying Initial Conditions	78
2.3.2 Continuation Method	80
2.3.3 External Short Pulse	81
2.3.4 Stochastic Perturbation	82
2.3.5 Critical Velocity Surfaces	85
2.3.6 Complete Bifurcation Group	86
2.3.7 Quantifying Basins of Attraction	88
2.4 Methods for Detecting Hidden Attractors	90
2.4.1 Homotopy and Continuation Methods	91
2.4.2 Amplitude Control	95
2.4.3 Offset Boosting	96
2.4.4 Nested Double-Scroll Attractors	98
2.4.5 Final-State Machine	101
References	103
3 Manifestation of Multistability in Different Systems	111
3.1 Multistability in Discrete Systems	111
3.1.1 Hénon Map	111
3.1.2 Dissipative Standard Nontwist Map	113
3.2 Multistability in Continuous Systems	114
3.2.1 Duffing Oscillator	114
3.2.2 Rössler-Like Oscillator	117
3.2.3 Lorenz-Like System	118
3.2.4 Chua Oscillator	120

3.2.5	Jerk Systems	121
3.2.6	Fractional-Order systems	122
3.3	Multistability in Coupled Systems	123
3.3.1	Coupled Quadratic Maps	124
3.3.2	Coupled Hénon Maps	124
3.3.3	Coupled Duffing Oscillators	127
3.3.4	Coupled Rössler Oscillators	130
3.3.5	Coupled Lorenz Oscillators	131
3.4	Multistability in Neuronal Systems	132
3.4.1	Single Neuron	133
3.4.2	Coupled Neurons	136
3.5	Other Examples of Multistable Systems	139
3.5.1	Mechanical Systems	139
3.5.2	Micro- and Nanosystems	141
3.5.3	Thermochemical Systems	143
3.5.4	Climate	144
3.5.5	Ecology	149
3.5.6	Biosystems	152
3.5.7	Astrosystems	157
	References	159
4	Multistability in Lasers	167
4.1	Laser as a Nonlinear Dynamical System	167
4.1.1	History of Laser Dynamics	167
4.1.2	Dynamical Classification of Lasers	170
4.2	Multistability in Optical Systems	171
4.2.1	Optical Bistability	171
4.2.2	Spatial Multistability	173
4.2.3	Polarization Multistability	175
4.3	Multistability in CO ₂ Lasers	178
4.3.1	Loss-Modulated CO ₂ Laser	178
4.3.2	Targeting Attractors by Short Pulses	180
4.3.3	Bistability Induced by Resonant Perturbations	181
4.3.4	Bistability Induced by a Delayed Feedback	183
4.4	Multistability in Semiconductor Lasers	184
4.4.1	Semiconductor Laser with Delayed Feedback	185
4.4.2	Directly Modulated Semiconductor Laser	187
4.5	Multistability in Fiber Lasers	189
4.5.1	Loss-Modulated Fiber Laser	190
4.5.2	Pump-Modulated Fiber Laser	193
	References	195

5 Multistate Intermittency	199
5.1 Noise-Induced Escapes from Equilibria	199
5.1.1 Multiple Quasipotential	201
5.1.2 Escape From a Fixed Point with Smooth Basin Boundaries	202
5.1.3 Escape From a Chaotic Attractor with a Fractal Basin Boundary	205
5.2 Coherence Resonance in Multistable Systems	208
5.2.1 Stochastic Resonance in Multistable Systems	209
5.2.2 Deterministic Coherence Resonance in a Chaotic Bistable System	211
5.2.3 Logical Stochastic Resonance	214
5.3 Characterization of Noise-Induced Multistate Intermittency	217
5.3.1 Mean Residence Times	218
5.3.2 Structural Properties of Noise-Induced Multistate Intermittency	222
5.3.3 Entropy Measures of Multistate Intermittency	223
5.3.4 Wavelet Transform Method for Detection of Coexisting Regimes	224
5.4 Manifestation of Noise-Induced Multistate Intermittency	227
5.4.1 Stochastic Bistable Chua System	228
5.4.2 Anti-coherence Resonance in a Bistable Neural Network	229
5.4.3 Multistate Intermittency in Semiconductor Lasers	231
5.5 Noise-Induced Preference of Attractors	235
5.5.1 Attractor Probability Density and Optimal Basin Size	235
5.5.2 Experimental Evidence of Noise-Induced Preference of Attractors	238
5.5.3 Extreme Events in Multistable Systems	242
5.5.4 Preference of Attractors in a Network of Coupled Oscillators	244
5.6 Multistate Intermittency in Deterministic Systems	245
5.6.1 Multistate Intermittency Induced by Periodic Forcing	245
5.6.2 Modulational Intermittency in a Semiconductor Laser	247
References	249
6 Multistability in Complex Networks	255
6.1 Stability of Multistable Complex Networks	255
6.1.1 Single-Node Basin Stability	255
6.1.2 Multiple-Node Basin Stability	258
6.1.3 Resilience of Multistable Networks	259
6.1.4 Minimal Fatal Shock	261
6.1.5 Master Stability Function of Multistable Systems	263
6.2 Manifestation of Multistability in Different Networks	266
6.2.1 Network of Networks of Kuramoto Oscillators	266

6.2.2	Potential Landscape of a Network of Networks	269
6.2.3	Ring-Coupled Oscillators	272
6.2.4	Structural Multistability in Boolean Networks	274
6.2.5	Multistate Chimeras	277
6.3	Multistability in Neural Networks	280
6.3.1	Multistability in Small Neural Circuits	281
6.3.2	Spatial Phase Multistability	283
6.3.3	Multistability in Inhibitory Neural Networks	285
6.3.4	Multistability in Artificial Neural Networks	287
6.3.5	Functional Connectivity in Neural Networks	289
	References	292
7	Extreme Multistability	299
7.1	Extreme Multistability in Continuous-Time Systems	300
7.1.1	Game Dynamical Systems	300
7.1.2	Hamiltonian-Driven Dissipative Systems	300
7.1.3	Complex-Coupled Systems	302
7.1.4	Variable-Boostable Systems	304
7.1.5	Systems with Hyperbolic Cosine Nonlinearity	307
7.1.6	Systems with Time-Periodic Forcing	307
7.2	Extreme Multistability in Discrete-Time Systems	309
7.2.1	Two-Dimensional Chaotic Map	309
7.2.2	Area-Preserving Lozi Map	309
7.3	Extreme Multistability in Memristive Systems	310
7.3.1	Charge-Controlled Memristive Model	312
7.3.2	Flux-Controlled Memristive Model	314
7.4	Application of Extreme Multistability in Cryptography and Secure Communication	316
7.4.1	Chaotic Cryptography Based on Extreme Multistability	317
7.4.2	Secure Communication Based on Extreme Multistability	318
	References	323
8	Multistability in Perception	327
8.1	Multistability in Different Sensory Modalities	327
8.1.1	Perceptual Decision-Making	328
8.1.2	Visual Perception	330
8.1.3	Auditory Perception	333
8.1.4	Tactile Perception	336
8.1.5	Olfactory Perception	337
8.2	Bistable Perception Models	337
8.2.1	Brain Noise Estimation	338
8.2.2	Simple Energy Model	342
8.2.3	Fokker–Plank Equation Attractor Model	344
8.2.4	Oscillatory Model	347

8.2.5 Advanced Perception Model with Adaptation and Noise	349
8.3 Physiological Experiments with Ambiguous Stimuli	355
8.3.1 Behavioral Experiment with Ambiguous Stimuli for Brain Noise Estimation	355
8.3.2 EEG Experiments	360
8.3.3 MEG Experiments	367
8.4 Artificial Intelligence for Classification of Multistable Perceptual States	372
8.4.1 Recognition and Classification of Multistable Brain States Using Artificial Neuronal Networks	373
8.4.2 Detecting Human Uncertainty in Perception of Bistable Visual Stimuli Using Artificial Neural Networks	378
8.5 Brain-Computer Interfaces Based on Bistable Perception	384
8.5.1 Brain-Computer Interface for Monitoring and Controlling Alertness	384
8.5.2 Brain-to-Brain Interface for Enhancing Human Performance by Sharing Cognitive Load	389
References	391
9 Concluding Remarks	399
References	402
Index	405

Chapter 1

What is Multistability



Abstract This chapter introduces the reader to the history and main concepts of multistability or coexistence of attractors in dynamical systems. What is multistability? When was it first discovered? Where and why does it appear? What are the underlying mechanisms of this exciting phenomenon? How can it be revealed and mathematically described? The answers to these and other important questions are given in this chapter.

1.1 Historical Overview

Long ago, people noted that many things can be interpreted differently, depending on the current situation and previous experiences of each person. For example, there are many words and artworks which can have two or more different meanings. One of such ambiguous images is the Necker cube shown in Fig. 1.1 (left), which can be interpreted in two ways, as left-oriented or right-oriented one. Another example is the bust of Voltier, painted by Salvador Dali (Fig. 1.1 (right)), on which one can also distinguish human figures in the bust. Interpretation of these images remains unchanged for some time, and then a switch to another interpretation happens.

The coexistence of two different aspects is also known as *dualism* and can be found in philosophy, religion, physics, and mathematics. In philosophy, dualism is a concept used in theories in which two principles coexist; for instance, materialism and idealism or the so-called “mind-body dualism” by French philosopher René Descartes. In Occidental religion, this is known as *yin* and *yang*. In physics, there is the coexistence of classical and quantum mechanics or corpuscular and wave theories. In addition, *pluralism* is referred to as the coexistence of various views or stands in politics, philosophy, and religion.

In mathematics, the coexistence of different stable states is known as *multistability*. A dynamical system, starting from a particular initial condition, evolves into a stable state called *attractor*. In a multistable system, every initial condition leads to a certain attractive state.

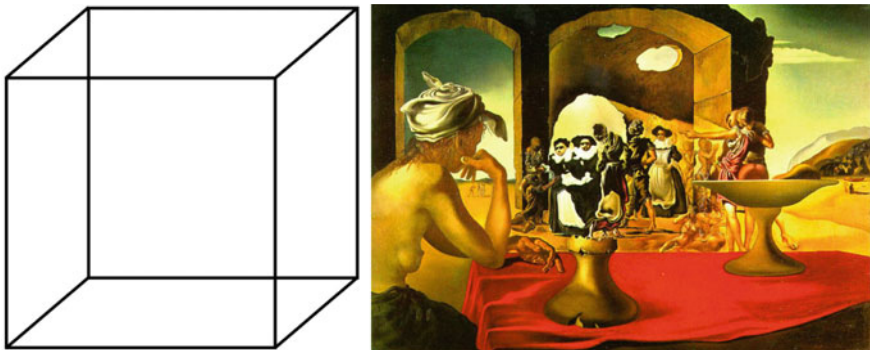


Fig. 1.1 Examples of ambiguous images. (Left) Necker cube that can be interpreted in two different ways, left-oriented or right-oriented. (Right) Bust of Voltier by Salvador Dalí

In the 19th century, French mathematician, physicist, and philosopher Henri Poincaré [1] introduced the notion of *homoclinic behavior* and suggested that this behavior can give rise to very rich dynamics. His ideas became basic for the mathematical theory of chaos and dynamical systems. He also introduced the important concept of bifurcation points. Indeed, mathematicians of the 20th century have proven that homoclinic tangency can lead to the coexistence of infinitely many strange attractors [2–10]. This mechanism for multistability is considered in Sect. 2.2.1.

The word “multistability” consists of two words, “multi” and “stability” meaning the coexistence of many stable states or attractors. The term “multistability” was first used by the American psychologist Fred Atteneave [11] (Fig. 1.2) with respect to perception of ambiguous images, such as the Necker cube (Fig. 1.1 (left)). However, the concept of multistability appeared in psychology as early as in the 16th century, when binocular rivalry was discovered.¹

Bistability is a particular case of multistability when only two stable states (attractors) coexist. Starting with German physicist Hermann von Helmholtz, some scientists thought that switches in bistability perception strongly relate to attention changes. Another school of thought, started by German physiologist Ewald Hering, conceptualized bistable perception in terms of a simple, mechanistic process that occurs more-or-less automatically.

While multistable visual perception has been studied since the 16th century, multistable auditory perception was discovered relatively recently by British–American psychologist Diana Deutsch [12], in the form of auditory illusions involving periodically oscillating tones.

For a long time, multistability was only known as a psychological paradox of perception, so-called *perceptual multistability*, illustrated in beautiful paintings by Salvador Dalí (Fig. 1.1 (right)), Octavio Ocampo, and other artists. Only in the 70s

¹ Binocular rivalry is a type of multistable visual phenomenon that occurs when different images are presented simultaneously to each eye. Since the brain cannot process two images at the same time, visual awareness switches randomly from one image to the other.

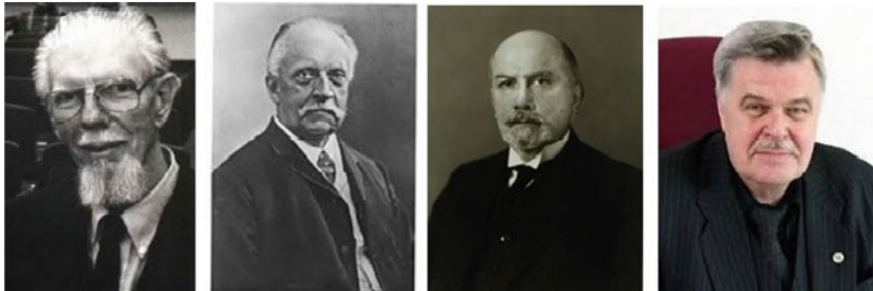


Fig. 1.2 Pioneers in studying multistability. (From left to right) Fred Atteneave (1919–1991), Hermann von Helmholtz (1821–1894), Ewald Hering (1834–1918), and Gennady Leonov (1947–2018)

of the last century, the first experimental evidence of bistability or the coexistence of two stable states was demonstrated by Gibbs and his colleagues [13] in an optical system. They found that transmission of the laser light through an active medium in a resonant cavity has a bistable property exhibiting a hysteresis cycle with respect to the incident intensity. They named this effect *optical bistability*. Later, Arecchi and co-workers [14] observed the coexistence of two stable periodic orbits in a loss-modulated CO₂ laser, and called this effect *generalized multistability* to distinguish it from the already known optical bistability, although from the viewpoint of nonlinear dynamics both effects represent the same phenomenon, namely, the coexistence of two attractors. One year later, Otsuka and Iwamura [15] reported on experimental observation of optical multistability in a semiconductor laser diode.

The extensive search for coexisting attractors allowed scientists to reveal multistability in many mathematical models and real systems, such as CO₂ [14], semiconductor [16], and fiber lasers [17, 18], lactose utilization networks [19], atoms [20], phosphorylation systems [21], bacteria evolution [22], electroencephalograms [23], neural networks [24], ice sheets [25], semiconductor superlattices [26], etc.

A significant contribution to the study of multistability made by Russian mathematician Gennady Leonov (Fig. 1.2) should be emphasized, who developed the theory of hidden attractors.² Since the basin of attraction of a hidden attractor is not connected with any equilibrium, the coexistence of hidden attractors cannot be found using standard computational procedures. Hidden chaotic attractors were discovered first in a Chua oscillator [27] and then in many other systems, such as Lorenz-like [28], Rabinovich [29], Glukhovsky–Dolzhansky [30], etc. (for comprehensive review see [31]).

The theory of multistability was also extensively developed by American mathematician Julien Clinton Sprott, who highlighted the universality of this phenomenon

² Hidden attractors are attractors which arise in systems without equilibria or with only one stable equilibrium.

[32–34] and explained how to obtain infinitely many coexisting attractors [35–37], the phenomenon called *uncertain destination dynamics* [38] or *extreme multistability* [39] will be considered in Chap. 7.

1.2 Mathematical Basis

1.2.1 Main Definitions

In order to explain multistability, as paradoxical as this may sound, we will first need to understand what is NOT multistability. As almost everyone recalls from their school years, the generic quadratic equation

$$ax^2 + bx + c = 0 \quad (1.1)$$

has two solutions

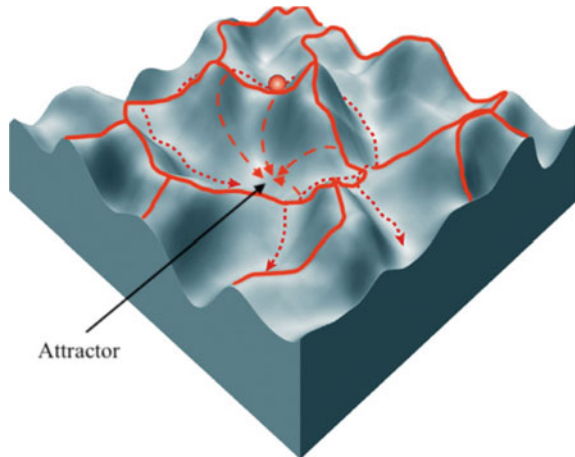
$$x_{1,2} = \frac{-b \pm \sqrt{b^2 - 4ac}}{2a}. \quad (1.2)$$

Thus, we see that the variable x given by nonlinear Eq. 1.1 takes two different values, x_1 and x_2 . In a similar way, a cubic equation has three solutions and an n -th order nonlinear equation has n solutions. This simple mathematical example illustrates the coexistence of various solutions of the same equation. However, we cannot talk about the stability of these solutions, because the quadratic Eq. 1.1 and other similar nonlinear equations are NOT dynamical systems. Nevertheless, this example will aid in the understanding of how coexisting stable states appear in a dynamical system.

Now we can proceed to explain what IS a dynamical system. Different from a nonlinear equation, such as Eq. 1.1, a dynamical system's state evolves with time. A straightforward example of a dynamical system is a ball rolling on a surface (Fig. 1.3). The actual state of the system is the ball's current position on the surface, while all conceivable states of the system can be represented by the entire surface or landscape on which the ball can roll. In the absence of any external disturbance but gravity itself, the ball, starting at any initial position, rolls downhill and naturally stops in the lowest point in one of the valleys, which we will call attracting state or simply an *attractor*, where the ball has a stable equilibrium. The valleys in the surface are domains of attraction for the ball's state. A set of states which direct the trajectory towards an attractor is called a *basin of attraction* of the attractor. The boundaries between the basins of attraction are known as unstable equilibria or *repellers*.

The behavior of dynamical systems is studied in the framework of *nonlinear dynamics* (see, for example, [40–45] and references therein). The ball's position on a surface represents the actual state of the dynamical system, and the ball's velocity is the system variable. Dynamical systems can be either *linear* (if the variable changes linearly with time) or *nonlinear* (if it does not).

Fig. 1.3 Basins of multiple attractors. The boundaries between coexisting attractors are shown by solid lines, and the trajectories towards the attracting point by dashed lines



The time evolution of a dynamical system can be presented in vector form as

$$\dot{\mathbf{x}}(t) = \mathbf{A}\mathbf{x}(t), \quad (1.3)$$

where $\mathbf{x} = (x_1, x_2, \dots, x_n)^T$ (T stands for transpose) is a state vector in the n -dimensional space of the system variables or *phase space*, \mathbf{A} is a constant matrix, and the dot indicates a time derivative, that is $\dot{\mathbf{x}}(t) = d\mathbf{x}(t)/dt$. Each point in the phase space represents a unique state of the system. In the case of a three-dimensional system, one can directly visualize the trajectory in three coordinates (x_1, x_2, x_3) , while for systems with $n > 3$, visualization of the orbit is only possible by means of projections of the phase space on planes (or hyper-planes) of two or three of the system's variables.

Linear dynamical systems have a single solution, and can be solved exactly. The solution of Eq. 1.3 can be found in an exponential form using a set of eigenvalues λ , given by the determinant

$$\det(\mathbf{A} - \lambda \mathbf{I}) = 0, \quad (1.4)$$

where \mathbf{I} is the identity matrix, and the eigenvectors \mathbf{v}_i satisfy the equation

$$\mathbf{A}\mathbf{v}_i = \lambda_i \mathbf{v}_i. \quad (1.5)$$

The eigenvalues λ represent powers of the exponential components of the solution, and the eigenvectors are their coefficients.

Linear systems exhibit very simple dynamics. The asymptotic solution of a bounded linear system, reached for $t \rightarrow \infty$, is a steady state only, i.e. a fixed equilibrium point that can be either stable or unstable. Therefore, linear dynamical systems are not able to describe many commonly observed behaviors, such as periodic oscillations, bifurcations, chaos, and multistability.

Strictly speaking, all natural processes are nonlinear; a linear dependence is just a mathematical approximation. A nonlinear dynamical system, which variables are nonlinearly related to each other, is described as follows

$$\begin{aligned}\dot{x}_1 &= F_1(x_1, x_2, \dots, x_n), \\ \dot{x}_2 &= F_2(x_1, x_2, \dots, x_n), \\ &\vdots \\ \dot{x}_n &= F_n(x_1, x_2, \dots, x_n),\end{aligned}\tag{1.6}$$

where F_i are functions that couple the variables among them. If at least one of these functions is nonlinear, the system in Eq. 1.6 is said to be nonlinear. In vector form, a nonlinear dynamical system is given as

$$\dot{\mathbf{x}}(t) = \mathbf{F}(\mathbf{x}(t)),\tag{1.7}$$

where $\mathbf{F} = (F_1, F_2, \dots, F_n)^T$ is a vector function: $\mathbb{R}^n \rightarrow \mathbb{R}^n$. The system described by Eq. 1.6 or Eq. 1.7 may have several states. The set of all possible states is referred to as \mathbf{X} . The state components x_i ($i = 1, \dots, n$) usually take real values only, i.e. $\mathbf{x}(t) \in \mathbb{R}^n$ and $\mathbf{X} \subset \mathbb{R}^n$.

Dynamical systems can be either autonomous or nonautonomous. In an autonomous system as in Eq. 1.7, the function \mathbf{F} is independent of time t , while in a nonautonomous system, time t is explicitly included in the function as

$$\dot{\mathbf{x}}(t) = \mathbf{F}(\mathbf{x}(t), t).\tag{1.8}$$

Nonlinear dynamical equations are difficult to solve analytically, and their dynamics can be very complex. Solutions are commonly searched by linearization, i.e., using linear equations. However, even rather simple nonlinear equations can exhibit a very sophisticated behavior, such as chaos or intermittency, and can only be solved numerically. For a given initial state $\mathbf{x}(0)$, the system's time evolution is governed by function \mathbf{F} , also known as *evolution operator* [46].

The system in Eq. 1.7 is called *deterministic* if at any given instant of time, its state can be represented by a point in the phase space. This differs from a *stochastic system*, which state under the influence of noise can only be defined with a certain probability.

Similar to nonlinear algebraic equations (like Eq. 1.1), nonlinear dynamical systems can have several solutions. A particular solution depends on the system parameters and initial conditions $\mathbf{x}(t_0)$ and can be either stable or unstable. The coexistence of several stable solutions (attractors) for a given set of system parameters is called *multistability*. Each attractor has its own basin of attraction defined by initial conditions.

The simplest case of multistability is the coexistence of only two stable states, that is *bistability*. An example can be seen on the left side of Fig. 1.4 where a ball moves

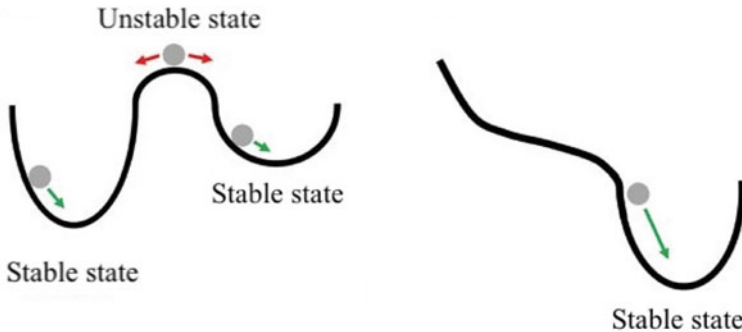


Fig. 1.4 The ball in (left) double-well and (right) single-well potentials, illustrating a bistable and a monostable dynamical system, respectively

in the double-well potential. This system has two stable states with their basins of attraction and an unstable equilibrium in between. The ball starting from a certain initial condition will reside in one of them. The left potential well is deeper than the right one, meaning that the left state is more stable than the right state, because it has smaller potential energy.

Now, the question is, how can we move the ball from one basin to the other? There are two ways to change the basin: either push the ball, or change the surface on which it lies. The first method requires the application of an external force to the ball (Fig. 1.4 (left)), while the second method needs a parameter change in order to modify the landscape (or basins of attraction) of the attractive states, so that the ball will change the basin (Fig. 1.4 (right)).

The potential function of a multistable system may have several local minima. For example, in Fig. 1.5 we plot the potential function

$$U(x) = \frac{b}{2}x^2 + \frac{c}{4}x^4 + \frac{d}{6}x^6 \quad (1.9)$$

which has three stable $(-x_2, x_0, x_2)$ and two unstable $(-x_1, x_1)$ fixed equilibria. Here, b , c , and d are the system parameters which define the positions of these points:

$$\begin{aligned} x_0 &= 0, \\ x_1 &= \sqrt{-\frac{c + \sqrt{c^2 - 4bd}}{2d}}, \\ x_2 &= \sqrt{-\frac{c - \sqrt{c^2 - 4bd}}{2d}}. \end{aligned} \quad (1.10)$$

In addition, dynamical systems are classified as conservative and dissipative. In a similar way, we will present an example of such systems with a ball on a surface. If

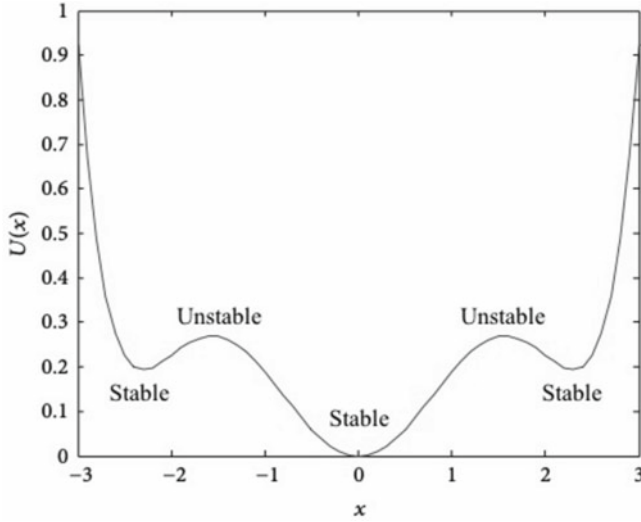


Fig. 1.5 Potential function Eq. 1.10 of a tristable system

the surface is completely flat, the ball will not move. Even if one pushed the ball in the absence of friction, it would roll along the surface with a constant velocity. Such a system is called *conservative*.

Thus, a *conservative system* is a system which maintains its total energy constant during time evolution, i.e. the function divergence is zero:

$$\nabla \cdot \mathbf{F} = \sum_{i=1}^n \frac{\partial \dot{x}_i}{\partial x_i} = 0.$$

Instead, a *dissipative system* constantly losses its energy due to friction or other processes, so that

$$\nabla \cdot \mathbf{F} = \sum_{i=1}^n \frac{\partial \dot{x}_i}{\partial x_i} < 0.$$

Starting from a set of initial conditions occupying volume V_0 in the n -dimensional phase space, the corresponding trajectories (on average) converge to invariant set $S \subset \mathbf{X}$ such that $\mathbf{x}(t_0) \in S$ implies $\mathbf{F}(\mathbf{x}(t_0)) \in S, \forall t \geq t_0$, satisfying the volume contraction, i.e., $\nabla \cdot \mathbf{F}(V_0) < 0$. Thus, an *invariant set* is a stable asymptotic state of a dynamical system or an attractor.

An example of a dissipative system can once again be illustrated with a ball, this time on a convex-concave surface, as shown in Fig. 1.3. The velocity of the ball on this surface will change in time until the ball falls at a lowest point in the valley, so that its energy will dissipate. It should be noted that all natural systems are dissipative; the concept of conservative systems is considered in quantum mechanics only.

1.2.2 Attractors and Basins of Attraction

The concept of *attractor* is very important in nonlinear dynamics. There are various formalizations of the attractor concept, which lead to different definitions of an attractor. The most commonly used definitions are the maximal attractor and the Milnor attractor.

The *maximal attractor* is defined as a closed set of phase-space points, $\mathcal{A} \subseteq \mathbf{X}$, which attracts nearby trajectories to converge onto it, and possesses the following properties [45]:

- (i) \mathcal{A} is a forward invariant set under \mathcal{A} , i.e., if $\mathbf{x}(t_0)) \in \mathcal{A}$ then $\mathbf{F}(\mathbf{x}(t_0)) \in \mathcal{A}, \forall t \geq t_0$.
- (ii) \mathcal{A} attracts an open set of initial conditions, i.e., there exists an open set U such that for all $\mathbf{x}(0) \in U$, $\mathbf{x}(0)$ enters \mathcal{A} as $t \rightarrow \infty$. In other words, the invariant set \mathcal{A} attracts trajectories starting inside U . The largest possible U for a particular attractor \mathcal{A} is called *basin of attraction* of attractor \mathcal{A} and denoted by $\mathcal{U}(\mathcal{A})$.
- (iii) \mathcal{A} is minimal, i.e., there is no proper filled subset of \mathcal{A} satisfying the properties (i) and (ii).

Thus, this definition requires the existence of some neighborhood of an attractor in phase space such that all initial conditions in this neighborhood generate orbits that limit on the attractor.

The above definition has two drawbacks. First, it is necessary to find an attracting area or basin of attraction. Secondly, if such area was chosen unsuccessfully, for instance, it contained an unstable fixed point, then the maximal attractor will contain points, which do not belong to the attractor.

The *Milnor attractor* is named after the American mathematician John Milnor [47], who defined an attractor as a set of phase-space points which is the limit set of orbits originating from a set of initial conditions of positive Lebesgue measure,³ preventing a point from being an attractor. The Milnor attractor means that if we randomly choose an initial condition with uniform probability density in a suitable sphere of initial condition space, there is a non-zero probability that the orbit from the chosen initial condition goes to the attractor.

It should be noted that structural properties of basins of attraction of the maximal and Milnor attractors are different. For example, the basin of the Milnor attractor may be riddled (see Sect. 1.2.5), while the basin of the maximal attractor not. The failure of the Milnor attractor to satisfy the first definition is because there are points arbitrarily close to an attractor with a riddled basin, such that these points generate orbits that go to another attractor. Therefore, the neighborhood mentioned above does not exist.

It is hard to picture this kind of interaction in real life, but maybe the funny example could be you returning home one night, planning to rest after a long day of work, but on the way home you suddenly receive a call from your friend saying

³ The Lebesgue measure, named after French mathematician Henri Lebesgue, is the standard way of assigning a measure to subsets of n -dimensional Euclidean space. For $n = 1, 2$, or 3 , it coincides with the standard measure of length, area, or volume.



Fig. 1.6 Types of attractor in dynamical systems. (Left) Fixed point, (middle) limit cycle, and (right) chaos. The arrows show the direction of the time evolution trajectories

he is celebrating his birthday in a pub, asking you to join him. You had completely forgotten! As he is a good friend, despite of having other plans, you decide to change your trajectory and end up waking the next morning in your friend's house, instead of your comfortable room.

Attractors are also classified according to their structure in phase space: shape (fixed point, limit cycle, quasiperiodic, chaotic), topology (spiral, double-scroll, symmetric), and phase-space position with respect to other equilibria (self-excited, hidden).

Some examples of attractors with different shape are illustrated in Fig. 1.6 with phase-space trajectories. A *fixed point* attractor is a single point in phase space (left picture). All trajectories initiated at different initial conditions are attracted to this point, unchanging over time. A *limit cycle* or a *periodic orbit* is a closed path (middle picture), i.e. all trajectories initiated outside and inside this orbit will end on it. Finally, a *chaotic attractor* is a subspace in which the trajectory are located in a restricted area of phase space or a bounded manifold, which often possesses a very sophisticated fractal structure (right picture).

Every attractors has its own *basin of attraction* defined as a set of all initial conditions in phase space, which trajectories will end on the attractor. The set of initial points leading the trajectories to infinity is called *basin of infinity attractor*. It is also possible for a dynamical system to have an infinite number of attractors; this makes the description of the system dynamics rather difficult. The coexistence of infinitely many attractors referred to as *extreme multistability* is considered in Chap. 7.

Depending on the relation between basins of attraction and equilibria, the attractors are classified into self-excited or hidden. While the basin of attraction of a self-excited attractor intersects an equilibrium, the basin of a hidden attractor does not. The coexistence of hidden and self-excited attractors is called *hidden multistability*. The properties of hidden attractors are described in Sect. 2.4.

The examples of phase portraits (or phase-space projections) of self-excited and hidden attractors are illustrated respectively in the left and right panels of Fig. 1.7.

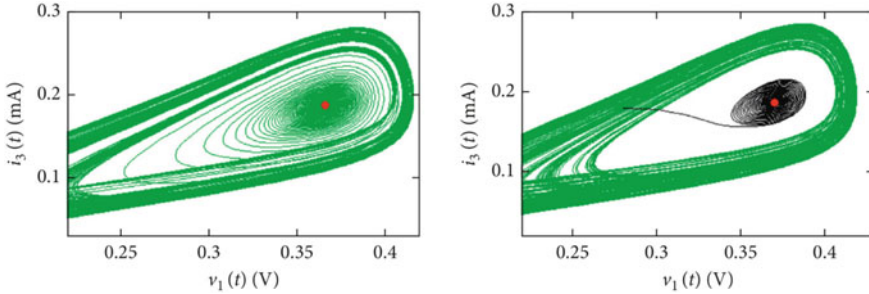


Fig. 1.7 Phase portraits of coexisting (left) self-excited and (right) hidden attractors (green lines) of the Chua system. The red dots at the spiral center represent (left) unstable and (right) stable non-zero equilibria. (Right) The black line is the trajectory attracted to the stable equilibrium

While the basin of attraction of the self-excited attractor overlaps the unstable equilibrium, the basin of attraction of the hidden attractor is not covered by the neighborhood of the stable equilibrium. Consequently, the self-excited and hidden attractors can be distinguished according to the intersection of their basins of attraction and the equilibrium neighborhood in the phase space.

1.2.3 Smooth and Fractal Basins

Basin boundaries can be either smooth or fractal. To illustrate these concepts, consider a particle with friction moving in the double-well potential $V(x)$ as shown in the upper panel of Fig. 1.8. Starting from almost any initial condition, the orbit will eventually be attracted to either of the two stable fixed points ($-x_0$ or x_0) [48]. An initial condition chosen in the dashed region eventually comes to the attractor x_0 , while any initial condition in the blank region tends to $-x_0$. The boundary separating these basins is the smooth curve passing through the origin $x = 0$. The initial conditions chosen on the boundary direct the trajectory to the unstable equilibrium at $x = 0$, i.e. the boundary is a stable manifold of the unstable point.

As distinct from the example shown in Fig. 1.8, the variety of systems have fractal basin boundaries [49]. To illustrate the fractal structure of basin boundaries, consider the Hénon map [50]

$$\begin{aligned} x_{n+1} &= 1 - \mu x_n^2 + y_n, \\ y_{n+1} &= -J x_n, \end{aligned} \tag{1.11}$$

where x_n and y_n are discrete variables, J is the Jacobian related to dissipation, and μ is the parameter. For $J = 0.9$ and $\mu = 1.05$ this map exhibits the coexistence of period-1 and period-3 attractors. Even for such a simple system, the basins of attraction have a fractal structure with very complex topology, as illustrated in Fig. 1.9.

Fig. 1.8 (Upper) Double-well potential $V(x)$ for a particle with friction moving in one dimension. Depending on the initial condition, the particle eventually arrives in one of two equilibrium points, $-x_0$ or x_0 . (Lower) Basins of attraction of the two fixed points in the position-velocity space. The boundary separating the basin of attraction of $-x_0$ (blank region) and the basin of attraction of x_0 (dashed region) is smooth

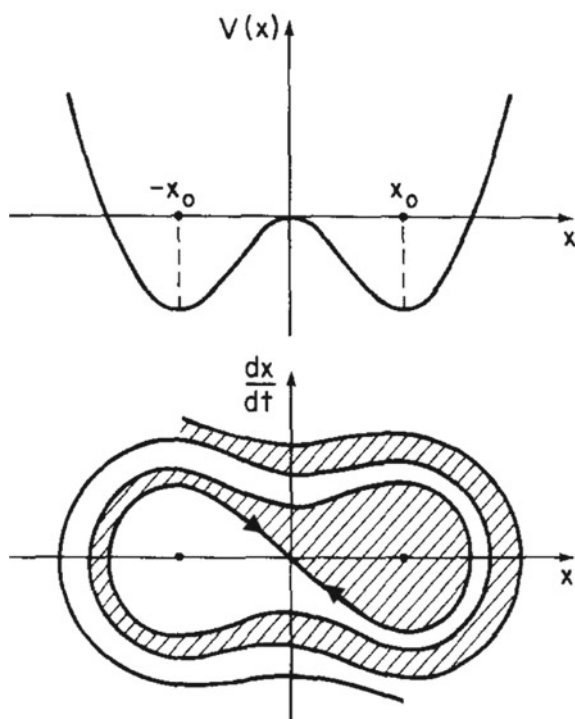
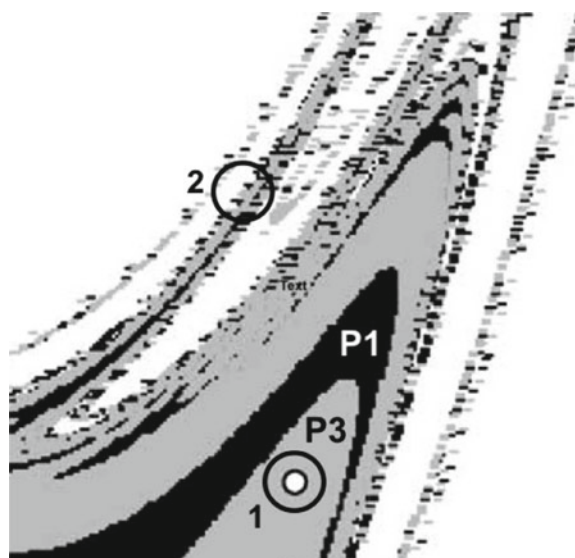


Fig. 1.9 Basins of period-1 (P_1) (black), period-3 (P_3) (grey), and infinity (white) attractors with fractal boundaries in the Hénon map given by Eq. 1.11. Circles 1 and 2 represent uncertainties in two initial conditions



Let us now consider two initial conditions in the centers of circles 1 and 2. Suppose that these initial conditions are measured with uncertainty ε equal to the radius of these circles. If the initial condition is selected inside circle 1, the phase-space trajectory definitely comes to the period-3 attractor because the circle does not touch the basin boundary. However, the initial condition selected inside circle 2 is uncertain since the trajectory may be attracted to either period-1 or period-3 states, or goes to infinity. Now, if we choose initial conditions randomly with uniform distribution, the fraction $f(\varepsilon)$ of initial conditions will be uncertain as to which state the trajectory is attracted. Many dissipative dynamical systems with fractal boundaries obey the power law [48]

$$f(\varepsilon) \sim \varepsilon^\alpha, \quad (1.12)$$

where α is the *uncertainty exponent* or *uncertainty dimension* which is related to basin boundary dimension d as [51]

$$\alpha = D - d, \quad (1.13)$$

where D is the phase space dimension. The uncertainty dimension of basins with smooth boundaries is $\alpha = 1$ and with fractal boundaries is $\alpha < 1$. The closer α is to zero, the more difficult it is to predict the final state of the system. For mixed basins with smooth and fractal boundaries, the uncertainty exponent for each boundary is still possible to calculate using a sophisticated procedure described by Grebogi et al. [52].

The *basin boundary dimension* can be represented in the form of *capacity dimension*

$$d = \lim_{\delta \rightarrow 0} \frac{\ln N(\delta)}{\ln(1/\delta)}, \quad (1.14)$$

where $N(\delta)$ is the minimum number of D -dimensional “cubes” of side δ required to completely cover the basin boundary. McDonald et al. [48] have proven that the uncertain fraction $f(\varepsilon)$ of a finite region of a D -dimensional phase space associated with initial condition error ε obeys the limit equation

$$\lim_{\varepsilon \rightarrow 0} \frac{\ln f(\varepsilon)}{\ln(1/\varepsilon)} = \alpha, \quad (1.15)$$

if and only if the basin boundary capacity dimension is equal to $d = D - \alpha$.

Thus, fractals are characterized by the following properties [53]:

- Detailed structure on an arbitrarily small scale.
- Local and global heterogeneity not described by conventional geometry.
- Some concept of self-similarity.
- The fractal dimension is larger than the topological dimension.
- Simple and possibly recursive definitions.

A thorough review of systems with fractal basin boundaries was carried out by Aguirre et al. [54].

1.2.4 Wada Basins

When three attractors coexist in phase space, their basins of attraction may have a *Wada property* named after Takeo Wada by his student Kunizō Yoneyama [55], who discovered an interesting geometry of boundaries between basins of three lakes or three disjoint open sets on the plane. In particular, he found out that for any point selected on the basin boundary of one of the lakes, the boundaries of the other two lakes also contained that point. However, this fractal property is rare in real-world systems.

The lakes of Wada are constructed as follows (Fig. 1.10). Imagine an island (white) in an ocean (red) with two lakes (blue and green) inside the island. First, we will dig a canal (red line) from the ocean at an equal distance between the ocean and lakes (see left panel). As a second step, we dig another canal (blue line) from the left lake so that every piece of land on the island is within the same distance from the first canal and the lakes (right panel). Next, a third canal is dug from the right lake so every piece of land on the island is within equal distance from water, and so on. After all canals are dug, every point of the island is a boundary point of both lakes and the ocean. This means that every boundary point can be reached by traveling through canals from each body of water, that is called *Wada property*. After an infinite number of steps, each boundary point belongs to all basins.

Later, it was found that the Wada property is not rare in the real world, and many dynamical systems possess this property [56, 57]. For instance, Wada basins were found in the forced damped pendulum [58], forced Duffing oscillator [59], hydrodynamical flows [60], tokamaks [61], ecological systems [62], etc. The example of Wada basins in a dissipative dynamical system is presented in Fig. 1.11.

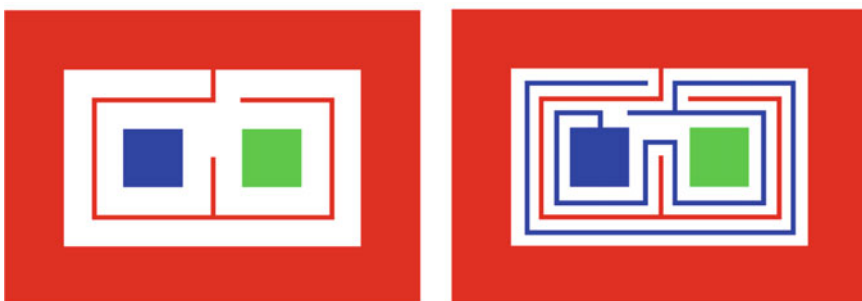
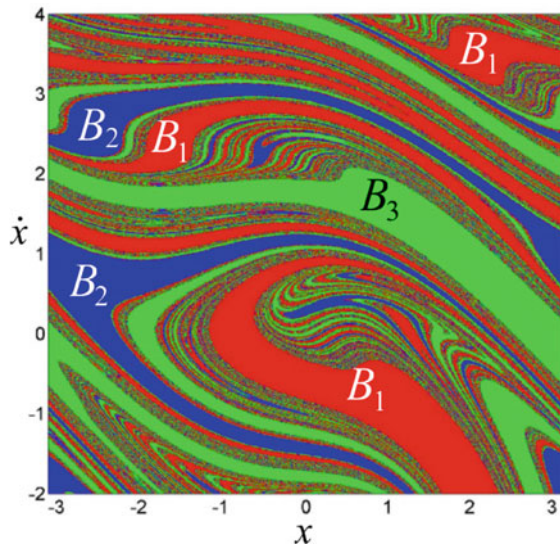


Fig. 1.10 Lakes of Wada. Configurations after (left) first and (right) second steps of canals digging. The blue and green squares are lakes on the white island surrounded by the red ocean

Fig. 1.11 Wada basins of attraction of three coexisting attractors: B_1 (red), B_2 (blue), and B_3 (green) of the forced damped pendulum $\ddot{x} + 0.2\dot{x} + \sin x = 1.66 \cos t$. Based on data from [63]



Thus, we say that a point on a basin boundary is a Wada point if every open neighborhood of this point has a nonempty intersection with at least three different basins. A basin boundary is a Wada basin boundary if all of its points are Wada points. This means that each point on the boundary belongs to all basins. Although the Wada boundary is always fractal, not all fractal boundaries have the Wada property. To possess the Wada property, a system must have at least three coexisting attractors, while for a fractal boundary the coexistence of only two attractors is sufficient.

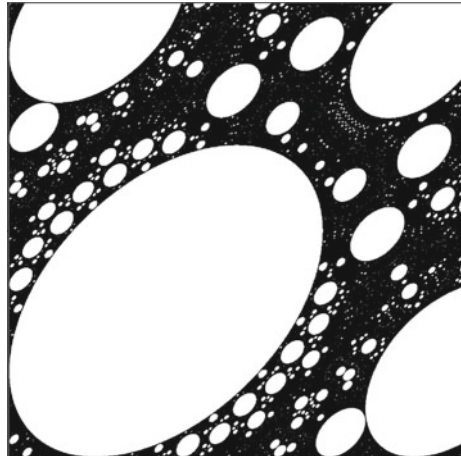
1.2.5 Riddled Basins

When a certain symmetry exists in phase space, the basins of attraction of chaotic attractors may be riddled. This means that inside the basin of a chaotic attractor there are holes belonging to the basin of another attractor (not necessarily chaotic) [64]. Every point in the attractor's basin contains pieces of another attractor's basin arbitrarily nearby. This type of basin topology occurs in systems with a smooth invariant manifold, where any initial condition in a smooth surface in phase space generates an orbit that remains in the surface [65].

Riddled basins can only occur in systems with symmetry. This means that they are so densely intertwined that it is impossible to determine the final state, since the determination of initial conditions is of a finite uncertainty. When all basins are riddled, the basins are said to be *intermingled* [66].

It should be noted that the attractor with a riddled basin is a Milnor attractor, but not a maximal attractor which requires the existence of a neighborhood such that

Fig. 1.12 Riddled basin of attraction. The black region is a set of points within the square $[-1, -7/8]^2$ which orbits accumulate on the discontinuity for the area-preserving map $(x, y) \rightarrow (y, g(-x + 0.9y))$, where $g(x) = x$ for $x \in [-1, 1)$ and $g(x + 2) = g(x)$. Reprinted from [67] by permission from the Springer Nature ©2005



all initial conditions in its neighborhood generate orbits that limit on the attractor (see Sect. 1.2.2). There are points arbitrarily close to an attractor with a riddled basin, such that these points generate orbits that go to another attractor, because the neighborhood mentioned above does not exist.

An example of the riddled basin of attraction is shown in Fig. 1.12. The black region in the figure is a basin of attraction riddled by white dots which belong to the basin of another attractor.

Let us now explain what a riddled basin means. Consider a dynamical system with two coexisting attractors in phase space \mathbb{R} denoted as $\mathcal{A}_1 \in \mathbb{R}$ and $\mathcal{A}_2 \in \mathbb{R}$ with their basins of attraction \mathcal{B}_1 and \mathcal{B}_2 . We say that the basin \mathcal{B}_1 is riddled, if for every point $p \in \mathcal{B}_1$ an ε -radius ball centered at p contains a positive Lebesgue measure (non-zero volume) of points in \mathcal{B}_1 for any $\varepsilon > 0$. Here, a surprising situation may happen. If a phase-space trajectory initiated at p is attracted to \mathcal{A}_2 , then we repeat the experiment. Even with an infinitesimal error in the initial condition, we cannot be sure that the trajectory will go to \mathcal{A}_1 again, but not to \mathcal{A}_2 . Even though the basin \mathcal{A}_1 has a positive Lebesgue measure, the basin \mathcal{B}_1 and its boundary set are the same. Thus, the calculation of riddled basins requires the repeatability of numerical experiments.

Thus, a dynamical system with riddled basins of attraction should satisfy the following five conditions [68]:

1. An invariant subspace $\mathcal{M} \in \mathbb{R}$ should exist.
2. A chaotic attractor $\mathcal{A}_1 \in \mathcal{M}$ should exist.
3. Another attractor $\mathcal{A}_2 \notin \mathcal{M}$ should exist.
4. The attractor \mathcal{A}_1 should be transversely stable in \mathbb{R} , i.e., the Lyapunov exponents for infinitesimal perturbations along the directions transversal to \mathcal{M} should all be negative.
5. A set of unstable periodic orbits embedded in \mathcal{A}_1 should transversely be unstable. As a consequence, at least one of the Lyapunov exponents along directions transverse to \mathcal{M} should exhibit positive finite-time fluctuations.

A riddled basin was first discovered experimentally in an electronic circuit [69]. Then, riddled basins were found in many models, including coupled chaotic oscillators [70], learning [71] and mechanical systems [72], specially coupled maps [73], interacting populations [74], delay-coupled systems [75], chimeras [76], and other systems.

1.3 Stability of Invariant Sets

Consider now the concept of stability, one of the most important properties of invariant sets. Roughly speaking, an invariant set is stable if trajectories initiated in its vicinity remain close to it forever, otherwise the invariant set is unstable. Among different types of stability of solutions of differential equations are Lyapunov stability, asymptotic stability, exponential stability, orbital stability, and structural stability. The detailed description of different stability concepts can be found in [77]. Here, we will only describe the most important concepts.

1.3.1 Lyapunov Stability

We start with Lyapunov stability, which is related to the system behavior with respect to its equilibrium in the sense of Lyapunov, i.e. when the phase-space trajectory wanders nearby the equilibrium point \mathbf{x}^* . The concept of Lyapunov stability is geometrically illustrated in Fig. 1.13.

Let point \mathbf{x}^* is an equilibrium of the system in Eq. 1.7. Then, the system is *stable in the sense of Lyapunov* with respect to \mathbf{x}^* , if for every $\varepsilon > 0$ and $t_0 \geq 0$ there

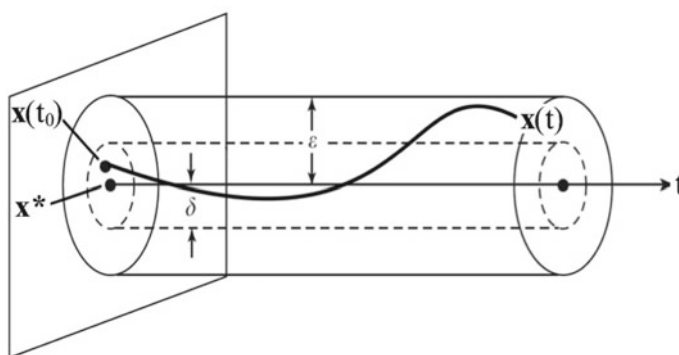


Fig. 1.13 Geometric illustration of stability in the sense of Lyapunov

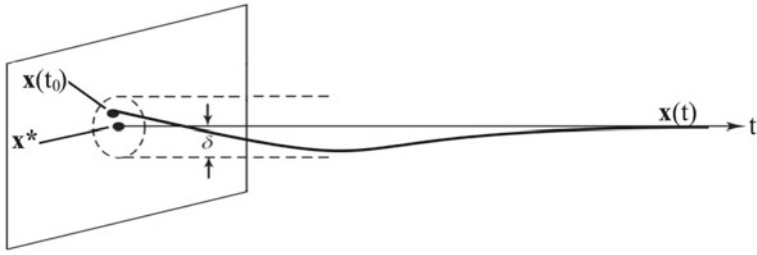


Fig. 1.14 Schematic illustration of the concept of asymptotic stability

exists $\delta > 0$ such that $\|x(t_0) - x^*\| < \delta$ implies that $\|x(t) - x^*\| < \varepsilon$ for all $t \geq t_0$. Otherwise the equilibrium is said to be unstable in the sense of Lyapunov.

1.3.2 Asymptotic Stability

If the trajectory gradually approaches the equilibrium x^* , we deal with asymptotic stability. An invariant set is called *asymptotically stable*, if it is stable in the sense of Lyapunov, and all trajectories initiated within δ converge to x^* as $t \rightarrow \infty$.

Mathematically, asymptotic stability is defined as follows. If there exists $\delta > 0$ such that $\|x(t_0) - x^*\| < \delta$ implies that $\|x(t) - x^*\| \rightarrow 0$ as $t \rightarrow \infty$, the equilibrium x^* is asymptotically stable. The concept of asymptotic stability is schematically illustrated in Fig. 1.14.

The asymptotic stability can be local or global. They are defined as follows. An equilibrium x^* of the system in Eq. 1.7 is called *locally asymptotically stable*, if it is stable according to Lyapunov (cf. Lyapunov stability) and there exists $M > 0$ such that $\|x(t_0) - x^*\| < M$ implies that $\lim_{t \rightarrow \infty} x(t) = x^*$. The equilibrium is called *globally asymptotically stable*, if this holds for all $M > 0$.

1.3.3 Exponential Stability

The equilibrium x^* is said to be *exponentially stable*, if it is asymptotically stable and furthermore all trajectories in the vicinity of δ approach x^* exponentially, that is

$$\|x(t_0)\| < \delta \implies \|x(t)\| \leq ce^{-\delta t}, \quad (1.16)$$

where c and δ are constants. The concept of exponential stability is visualized in Fig. 1.15.

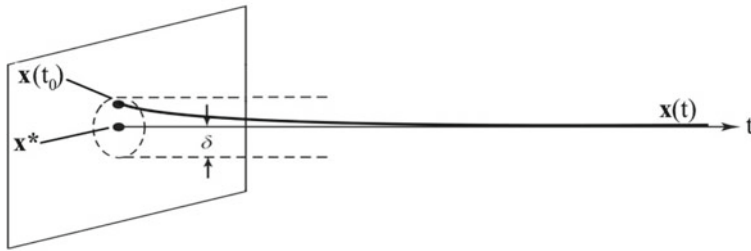


Fig. 1.15 Schematic illustration of the concept of exponential stability

1.3.4 Orbital Stability

Orbital stability describes the behavior of a closed trajectory (orbit) under the action of small external disturbances. The concept of orbital stability is geometrically illustrated in Fig. 1.16.

Let trajectory Γ be a closed orbit of a p -periodic solution $\phi(\mathbf{x}(t_0))$ of the system in Eq. 1.7, namely,

$$\Gamma = \{\mathbf{y} \mid \mathbf{y} = \phi(\mathbf{x}(t_0)), 0 \leq t < p\}. \quad (1.17)$$

The periodic solution $\phi(\mathbf{x}(t_0))$ is *orbitally stable*, if it is stable in the sense of Lyapunov (cf. Lyapunov stability) and for any $\varepsilon > 0$ there exists $\delta > 0$ such that for any $\mathbf{x}(t_0)$ which under small perturbation satisfies

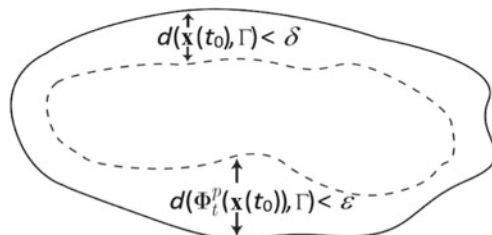
$$d(\mathbf{x}(t_0), \Gamma) := \inf_{\mathbf{y} \in \Gamma} \|\mathbf{x}(t_0) - \mathbf{y}\| < \delta, \quad (1.18)$$

the solution $\phi(\mathbf{x}(t_0))$ satisfies

$$d(\phi(\mathbf{x}(t_0)), \Gamma) < \varepsilon \text{ for all } t \geq t_0. \quad (1.19)$$

By analogy with asymptotic stability in the sense of Lyapunov, the concept of *asymptotic orbital stability* is also used, for example, in systems with a limit cycle.

Fig. 1.16 Schematic illustration of the concept of orbital stability



1.3.5 Structural Stability

Structural stability is related to the sensitivity of the system's structure to small disturbances, for example, a change in the number of attractors or their types, but not their phase-space shapes. In other words, we can say that two systems are topologically orbitally equivalent, if there exists a homeomorphism between them.⁴ This means that the systems are geometrically similar, i.e. there are the same number of attractors, bifurcation branches, etc.

The examples of topologically orbitally equivalent and nonequivalent systems are linear systems $\dot{x} = x + 1$ and $\dot{x} = 3x + 1$, which are topologically equivalent, and nonlinear system $\dot{x} = 2\sqrt{x}$, which is nonequivalent to the linear systems.

Mathematically, structural stability can be formulated as follows. Consider an unperturbed autonomous system $\dot{\mathbf{x}} = \mathbf{F}(\mathbf{x})$ and a perturbed system $\dot{\mathbf{x}} = \mathbf{F}(\mathbf{x}) + \varepsilon \mathbf{g}(\mathbf{x})$. If for any bounded and continuously differentiable vector function $\mathbf{g}(\mathbf{x})$ there exists a number $\varepsilon > 0$ such that the trajectories of the unperturbed and perturbed systems are orbitally topologically equivalent, then such a system is called *structurally stable*.

1.3.6 Linear Stability Analysis

The stability theory of a dynamical system was developed by Russian mathematician Aleksandr Mikhailovich Lyapunov (1857–1918) (Fig. 1.17). The mathematical essence of the Lyapunov theory is in a study of the limiting behavior of solutions of a system of ordinary differential equations when an independent variable tends to infinity [78]. Today, the Lyapunov theory of motion stability is the fundamental scientific basis for various automatic devices, in particular, flight control systems for missiles and aircrafts.

The linear stability analysis in the *local* neighbourhood of an equilibrium \mathbf{x}^* of the dynamical system $\dot{\mathbf{x}} = \mathbf{F}(\mathbf{x})$ under infinitesimal perturbations is known as the *first Lyapunov criterion* (reduced method). The *second Lyapunov criterion* (direct method) implies the stability analysis of \mathbf{x}^* using proper scalar functions, so-called *Lyapunov functions* defined in the phase space.

Linearization determines the local behaviour of the system near stationary points whose eigenvalues of the Jacobian matrix are not on the imaginary axis (for continuous systems) or the unit circle (for discrete systems). Such solutions are called *hyperbolic*, and do not admit local bifurcations. The local bifurcation theory considers the system behaviour near non-hyperbolic solutions, that is local in both the phase and parameter spaces.

⁴ Homeomorphism is one-to-one and continuous mapping in the phase space that transforms the family of trajectories of one system to the family of trajectories of another system with the same directions.

Fig. 1.17 Russian mathematician Aleksandr Mikhailovich Lyapunov (1857–1918)



First Lyapunov criterion. Let us first consider the reduced (or indirect) method of Lyapunov for a continuous-time autonomous system $\dot{\mathbf{x}} = \mathbf{F}(\mathbf{x})$ having an equilibrium at $\mathbf{x}^* = 0$. The system's Jacobian evaluated at the equilibrium point is calculated as $J = [\partial \mathbf{F} / \partial \mathbf{x}]_{\mathbf{x}=\mathbf{x}^*=0}$. The system is asymptotically stable around $\mathbf{x}^* = 0$ if all eigenvalues of J have a negative real part.

The first Lyapunov criterion cannot be applied to nonautonomous systems. A strict asymptotic stability analysis of general nonautonomous systems is provided by the second Lyapunov criterion.

Second Lyapunov criterion for nonautonomous systems. The second method of Lyapunov (or direct Lyapunov criterion) assesses the stability of a continuous-time nonautonomous system $\dot{\mathbf{x}}(t) = \mathbf{F}(\mathbf{x}(t), t)$ under non-infinitesimal perturbations. This system is globally (over entire domain \mathfrak{D}), uniformly (over the entire time interval $[t_0, \infty)$, and asymptotically stable about equilibrium $\mathbf{x}^* = 0$, if there exists a scalar function $V(\mathbf{x}, t)$ defined on $\mathfrak{D} \times [t_0, \infty)$ and functions α , β , and γ , such that

- (a) $V(\mathbf{x}^*, t_0) = 0$,
- (b) $V(\mathbf{x}, t) > 0$, $\forall \mathbf{x} \in \mathfrak{D}$ and $\mathbf{x} \neq \mathbf{x}^*$, $\forall t \geq t_0$,
- (c) $\alpha(\|\mathbf{x}\|) \leq V(\mathbf{x}, t) \leq \beta(\|\mathbf{x}\|)$, $\forall t \geq t_0$,
- (d) $\dot{V}(\mathbf{x}) = \sum_{i=1}^d \frac{\partial V(\mathbf{x})}{\partial x_i} F_i(\mathbf{x}) = (\nabla V) \cdot \mathbf{F} \leq \gamma(\|\mathbf{x}\|) < 0$, $\forall t \geq t_0$.

The function V is called *Lyapunov function*. Note that the above criterion describes conditions necessary for uniform stability of a nonautonomous system, guaranteed by the class of functions α , β , and γ . However, for an autonomous system the condition (c) is not necessary.

Second Lyapunov criterion for autonomous systems. The second method of Lyapunov for autonomous system Eq. 1.7 is reduced to the following form. The system is globally and asymptotically stable about equilibrium $\mathbf{x}^* = 0$, if there exists a scalar function $V(\mathbf{x})$ defined on $\mathfrak{D} \times [t_0, \infty)$ and functions α, β and γ , such that

- (a) $V(\mathbf{x}^*, t_0) = 0$,
- (b) $V(\mathbf{x}, t) > 0, \forall \mathbf{x} \in \mathfrak{D}$ and $\mathbf{x} \neq \mathbf{x}^*$, $\forall t \geq t_0$,
- (c) $\dot{V}(\mathbf{x}) < 0, \forall \mathbf{x} \in \mathfrak{D}$ and $\mathbf{x} \neq \mathbf{x}^*$, $\forall t \geq t_0$.

Local Lyapunov exponents. We talked about the system stability in general. However, it is also interesting to know how a dynamical system resists a perturbation applied when the system is in a particular state. Stability of the dynamical system given by Eq. 1.7 in a particular point of the state space can be estimated by *local Lyapunov exponents*, defined as an instantaneous rate at which the system, starting from this point, converges to an unperturbed trajectory following a perturbation. Negative values of the local Lyapunov exponents indicate that the system is locally stable in the selected point.

In order to define the local Lyapunov exponent, consider the system trajectory starting at \mathbf{x} under infinitesimal perturbation $\delta\mathbf{x}$ which leads the system along a perturbed trajectory starting from $\mathbf{x} + \delta\mathbf{x}$ regulated by the function \mathbf{F} . The linearization procedure around \mathbf{x} using the first-order Taylor expansion of Eq. 1.7 yields

$$\dot{\mathbf{x}} + \delta\dot{\mathbf{x}} = \mathbf{F}(\mathbf{x} + \delta\mathbf{x}) \approx \mathbf{F}(\mathbf{x}) + D_x \mathbf{F}(\mathbf{x}) = \mathbf{F}(\mathbf{x}) + \mathbf{M}(\mathbf{x})\delta\mathbf{x}, \quad (1.20)$$

where $\mathbf{M}(\mathbf{x})$ is the stability matrix such that $M_{ij}(\mathbf{x}) = \frac{\partial F_i}{\partial x_j}(\mathbf{x})$, which describes the instantaneous rate of shearing \mathbf{x} neighbourhood by \mathbf{F} . Following Eq. 1.20, we find $\delta\dot{\mathbf{x}} = \mathbf{M}(\mathbf{x})\delta\mathbf{x}$ and calculate the growth of the perturbation in infinitesimal time dt as

$$\delta\mathbf{x}(dt) = \delta\mathbf{x} + \mathbf{A}(\mathbf{x})\delta\mathbf{x}dt = (\mathbf{I}_{N \times N} + \mathbf{M}(\mathbf{x})dt)\delta\mathbf{x} = \mathbf{J}_{dt}(\mathbf{x})\delta\mathbf{x}, \quad (1.21)$$

where $\mathbf{I}_{N \times N}$ is the $N \times N$ identity matrix and $\mathbf{J}_{dt} = \mathbf{I}_{N \times N} + \mathbf{M}(\mathbf{x})dt$ is the instantaneous Jacobian matrix describing the deformation of an infinitesimal neighbourhood in time dt of the trajectory starting at \mathbf{x} .

The local Lyapunov exponents measuring the rate of stretching are given as [79]

$$\lambda_j(\mathbf{x}) = \frac{1}{dt} \ln(\sigma_j(\mathbf{x})), \quad j = 1, 2, \dots, N, \quad (1.22)$$

where $\sigma_j(\mathbf{x})$ are square roots of eigenvalues of the right (left) Cauchy-Green strain tensor $\mathbf{J}_{dt}^T \mathbf{J}_{dt}$ ($\mathbf{J}_{dt} \mathbf{J}_{dt}^T$) (so-called “principal stretches”), measuring the instantaneous stretching of the neighbourhood of the trajectory at \mathbf{x} .

1.4 Basin Stability

The stability theory of Lyapunov gave impetus to further development of nonlinear dynamics. The diversity of multistable systems and their high sensitivity to initial conditions have required the development of new stability criteria, in particular, the stability of basins of attraction of coexisting attractors under external perturbations, so-called *basin stability* [80].

Quantitatively, the basin volume can be estimated as the number of initial conditions (under certain spatial resolution) leading to the attractor [81]. Alternatively, the basin of attraction of an attractive set can be measured as the probability of the system to return to the attractor after random perturbations. In this sense, the basin volume means how stable the attractor is. The concept of global basin stability proposed by Menck et al. [82] is based on the estimation of the basin volume in phase space. In fact, the basin stability indicates the likelihood of the dynamical system to arrive at one of many solutions when the current state of the system is perturbed. The concept of basin stability also helps to solve some important practical problems arising in complex networks, for example, to find the most critical nodes (power stations) for stability of the power grid [83] (see Sect. 6.1).

Suppose that the dynamical system in Eq. 1.7 exhibits the coexistence of M attractors, which are compact minimal invariant sets $\mathcal{A}_i \in \mathbf{X}$ ($i = 1, 2, \dots, M$) such that their respective basins of attraction \mathcal{B}_i have non-zero volumes, or Lebesgue measures $\mathcal{L}(\mathcal{B}_i) > 0$ of rather general subsets of \mathbb{R}^n [47].

To define the basin stability measure $S(\mathcal{B}_i)$, suppose that the system which resides on attractor \mathcal{A}_i undergoes a random perturbation at time t_0 , that kicks the system to a state $\mathbf{x}(t_0)$. We assume that the system goes to this state with probability distribution $\rho(\mathbf{x})$, such that $\rho(\mathbf{x})d\mathbf{x}$ describes the likelihood that the system is pushed to a state between \mathbf{x} and $d\mathbf{x}$.

Thus, the basin stability for a given attractor \mathcal{A}_i is defined as

$$S(\mathcal{B}_i) = \int_{\mathbf{X}} \chi_{\mathcal{B}_i}(\mathbf{x}) \rho(\mathbf{x}) d\mathbf{x}, \quad (1.23)$$

where $\chi_{\mathcal{B}_i}(\mathbf{x}) = 1$ if the state belongs to the basin of attraction \mathcal{B}_i of attractor \mathcal{A}_i and $\chi_{\mathcal{B}_i}(\mathbf{x}) = 0$ otherwise. The probability that the perturbed system takes a state in the state space \mathbf{X} is unity, that is

$$\int_{\mathbf{X}} \rho(\mathbf{x}) d\mathbf{x} = 1, \quad (1.24)$$

where the integral is taken over the entire state space. Thus, the basin stability can take values between 0 and 1, that is $S(\mathcal{B}_i) \in [0, 1]$ ($\forall i = 1, 2, \dots, M$). The attractor of a monostable system ($M = 1$) is globally stable and therefore its basin of attraction is also stable, that is $S(\mathcal{B}) = 1$.

Analytical estimation of the basin stability in a multistable system is very difficult due to a very high complexity of volume integrals such as Eq. 1.23. However, it can

be done numerically using the Monte Carlo (rejection sampling) method [84, 85]. For estimation of the basin stability of any attractor \mathcal{A}_i , the following algorithm can be used.

- (1) Create a set \mathcal{C} of I initial conditions distributed with probability ρ .
- (2) Starting from each initial condition in the set \mathcal{C} , evolve the system in time until it converges to one of the coexisting attractors.
- (3) Count the number $M_i \in I$ of initial conditions which drive the system to attractor \mathcal{A}_i .
- (4) Estimate the basin stability of attractor \mathcal{A}_i as $\hat{S}(\mathcal{B}_i) = M_i/I$.

Since I independent repeated Bernoulli trials include M_i successful trials leading to attractor \mathcal{A}_i , the estimate basin stability value $\hat{S}(\mathcal{B}_i)$ carries a standard error of $\left[S(\mathcal{B}_i)(1 - S(\mathcal{B}_i))/I \right]^{1/2}$ due to sampling [82].

Thus, basin stability reflects qualitative changes in the system dynamics when the system approaches a critical (or tipping) point. In particular, basin stability was used to characterize climate dynamics in the Amazonian vegetation model [82]. Nevertheless, basin stability does not allow the prediction of the system change when it approaches a critical transition. Only integral stability provides the detection of the tipping point proximity. This important stability measure will be considered in Sect. 1.4.2. However, before describing the integral stability, we have to define such an important stability measure as resilience.

Although this is a rather simplistic theoretical concept, the practical computation of the basin stability involves the extensive Monte Carlo procedure⁵ for basin stability estimation. To simplify this complicated task, Stender and Hoffmann [86] developed a software for computing the basin stability of multistable dynamical systems, which is an open MATLAB toolbox called **bSTAB** freely available through <https://github.com/TUHH-DYN/bSTAB/>.

1.4.1 Resilience

The stability of basins of attraction of coexisting attractors in a multistable system can also be described in terms of *resilience*. This term arose in ecology, as the recovery of an ecosystem after random events, such as windstorms, flooding, fires, tsunamis, etc., or due to human activity. The concept of resilience was introduced by Canadian ecologist Crawford Stanley Holling [87], who blended systems theory and ecology to formulate important ideas about the ability of a natural system to reorganize its behavior (or functioning) after an external disturbance.

⁵ The Monte Carlo procedure is a numerical method for studying random processes. The essence of the method is as follows: the process is described by a mathematical model using a random variable generator, the model is recalculated, and the probabilistic characteristics of this process are calculated based on the data obtained.

There are two concepts of resilience, from engineering and from ecological points of view. The difference between these two concepts is that engineering resilience implies a monostable system, while ecological resilience allows the coexistence of various attractors.

Engineering resilience. Chronologically, engineering resilience was the first type of resilience introduced by Holling [87] as the speed of the returning of an ecosystem to its equilibrium after a disturbance.⁶ Since this type of resilience is related to the system stability and often used in physical and engineering literature, it is called *engineering resilience*.

The engineering resilience is directly related to global exponential stability of the system (see Sect. 1.3.3), i.e. the existence of a single stable equilibrium. For instance, consider a simple one-dimensional dynamical system $\dot{x} = \lambda x$. Under a small perturbation δx , the solution of the system is $x(t) = \delta x e^{\lambda t}$, where $\lambda < 0$ is the rate of the system returning to the equilibrium point $x^* = 0$, or engineering resilience. If $\lambda < 0$, the equilibrium is exponentially stable (see Fig. 1.15).

Ecological resilience. The second type of resilience, so-called *ecological resilience* was introduced by ecologist Brian Walker and colleagues [89] as the system capacity to absorb a disturbance in order to reorganize the system structure. Ecological resilience implies conditions far from equilibrium, so that perturbations can switch the system from one regime to another. Therefore, ecological resilience assumes the coexistence of multiple stable equilibria and transitions among them.

The concept of ecological resilience is illustrated in Fig. 1.18. There are four important characteristics of ecological resilience: latitude (\mathcal{L}), resistance (\mathcal{R}), precariousness (\mathcal{P}), and panarchy.⁷

Let us now consider the characteristics of resilience with an example of an N -dimensional dynamical system represented by state vector $\mathbf{x}(t) = (x_1, x_2, \dots, x_N)^T$ and having M coexisting attractors \mathcal{A}_i ($i = 1, 2, \dots, M$).

Latitude indicates how much the system can be changed being in the same dynamical regime without switching to another state. Geometrically, latitude \mathcal{L}_i is defined as the maximum width of the basin of attraction \mathcal{B}_i of attractor \mathcal{A}_i . Quantitatively, the latitude \mathcal{L}_i is measured as a volume of the basin of attraction \mathcal{B}_i in terms of the relative number of initial conditions leading phase-space trajectories to the attractor \mathcal{A}_i .

Resistance indicates the robustness of the system state to external perturbations, i.e. how large the perturbation should be in order to switch the system to another regime. Geometrically, resistance \mathcal{R}_i is defined as the depth of the basin of attraction \mathcal{B}_i of attractor \mathcal{A}_i . Quantitatively, the resistance \mathcal{R}_i of a state $\mathbf{x}_i \in \mathcal{A}_i$ is estimated as the rate, at which the trajectory returns to the attractor \mathcal{A}_i after a small perturbation. The resistance \mathcal{R} is associated with the negative largest local Lyapunov exponent at the respective point \mathbf{x} as

⁶ Sometimes, it is denoted as the inverse of the return time [88].

⁷ The concept of panarchy was introduced by Allen et al. [90] to describe how complex systems of humans and nature interact across space and time scales.

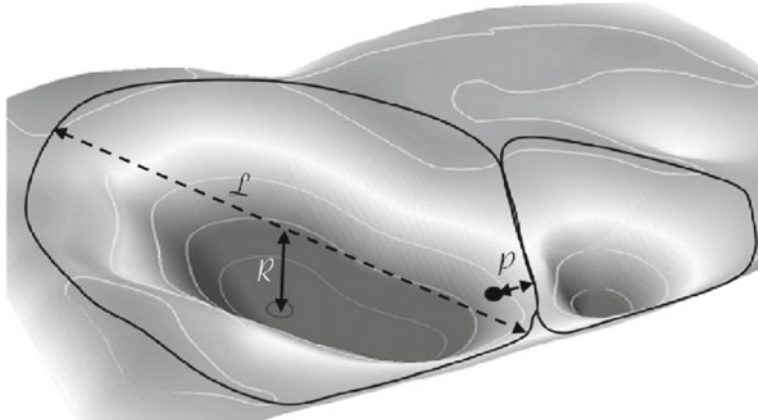


Fig. 1.18 Graphical illustration of ecological resilience of a bistable dynamical system. The basin boundaries are shown by solid lines. The stability landscape is presented in the horizontal plane in terms of latitude \mathcal{L} and precariousness \mathcal{P} , while resistance \mathcal{R} is illustrated in the vertical plane. The deeper the basin of attraction, i.e. the larger the \mathcal{R} , the more stable the attractor. The closed dot shows the current state of the system. The closer the system state to the basin of the neighboring attractor, i.e. the smaller the \mathcal{P} , the less effort is required to switch the system to another state

$$\mathcal{R}(\mathbf{x}) = -\max\{\lambda_1, \lambda_2, \dots, \lambda_N\}, \quad (1.25)$$

where $\lambda(\mathbf{x}) = \lambda_1, \lambda_2, \dots, \lambda_N$ is a set of N local Lyapunov exponents evaluated at \mathbf{x} (see Sect. 1.3.6).

The concept of *dynamical resistance* was introduced by Rings et al. [91] as a fully data-driven indicator of resilience of a complex network structure. They assumed that disturbances can mainly affect the network structure, rather than the dynamics of particular nodes. Structural changes in the network of coupled units can be revealed with a time-resolved clustering analysis (k -means algorithm [92]), implying that the number of different dynamical regimes (number of clusters k) is known. In particular, if each network cluster is identified with different dynamical regime, the minimum distance d between cluster centroids is defined as dynamical resistance of the system to disturbances; the larger d , the higher the system ability to absorb disturbances and reorganize the structure.

The dynamical resistance approach was used to track epileptic seizures and interpreting them as extreme events [91]. Dynamical resistance can be estimated through mutual information, zero-lag cross-correlation, or maximum-lag cross-correlation [93].

Precariousness indicates how close the system current state is to a threshold between different dynamical regimes. Geometrically, precariousness $\mathcal{P}_i(t)$ is the closest distance of the current state $\mathbf{x}_i(t)$ in the basin of attraction \mathcal{B}_i of attractor \mathcal{A}_i to the basin boundary $\delta\mathcal{B}_i$ with the neighboring attractor \mathcal{A}_j . Quantitatively, the precariousness \mathcal{P}_i of a particular stable state $\mathbf{x}_i \in \mathcal{A}_i$ is measured as the minimum

perturbation required to drive the system residing on the attractor \mathcal{A}_i out of its basin of attraction \mathcal{B}_i , i.e.

$$\mathcal{P}_i = \inf \{ \text{dist}(a, b) \mid a \in \mathcal{A}_i, b \in \delta\mathcal{B}_i \}, \quad (1.26)$$

where $\text{dist}(\cdot, \cdot)$ is the Euclidean distance between point a on the attractor \mathcal{A}_i and point b on the basin's boundary $\delta\mathcal{B}_i$ [94].

Panarchy indicates an interacting set of hierarchically structured scales, i.e. the degree to which a certain hierarchical level of an ecosystem is influenced by other levels [90]. Physically, panarchy reflects the interaction between coexisting states and their basins of attraction, describing how a change in one basin affects other basins.

The first three concepts can be applied to both the whole system and its subsystems, associated with the global basin of attraction and basins of attraction of coexisting states, respectively. However, the forth concept is only used for the whole system because it involves the global basin structure.

1.4.2 Integral Stability

As we already mentioned in Sect. 1.4, basin stability says nothing about the proximity to a tipping point when a system parameter is changed. In other words, basin stability is only based on the latitude measure (basin size), regardless of resistance and precariousness. This means that basin stability does not provide us with information about the system robustness to perturbations for different parameter values. Therefore, a new measure is needed to characterize stability of systems with coexisting attractors, which would integrate all aspects of resilience (latitude, resistance, and precariousness). Such a measure was introduced by Vrkoč [95] and named *integral stability*.

The concept of integral stability is connected with stability under constant perturbations, when the perturbations are sufficiently small everywhere excluding a small interval. The integral stability of the i -th attractor of the dynamical system given by Eq. 1.7 is defined as

$$\mathcal{S}_i = \frac{\mathcal{P}_i \int_{\mathbf{x} \in \mathcal{B}_i} \mathcal{R}(\mathbf{x}) d\mathbf{x}}{\sum_{j=1}^M (\mathcal{P}_j \int_{\mathbf{x} \in \mathcal{B}_j} \mathcal{R}(\mathbf{x}) d\mathbf{x})}. \quad (1.27)$$

Datko [96] and Hristova [97] used integral stability to characterize stability of a linear process and nonlinear impulsive functional differential equations, respectively. Later, integral stability was applied to ecological models [98].

1.4.3 Final State Sensitivity

The prediction of a final state and the estimation of basin stability are more difficult tasks in systems with fractal basin boundaries, essentially with Wada property or riddled basins. Let us illustrate the uncertainty in choosing the attractor with the following example. Suppose we randomly choose initial conditions in a box which lies on the boundary between two basins of attraction, and every initial state is selected with a certain error ε . Then, for an initial state closer to the boundary than ε , there is an uncertainty in the preference of the attractor. The fraction of the uncertain initial conditions obeys a power law $f(\varepsilon) \propto \varepsilon^\alpha$ [48], where the uncertainty exponent $0 < \alpha < 1$ indicates *final state sensitivity* [51]. In order to decrease the uncertainty, one needs to substantially improve the resolution in choosing initial conditions by decreasing the box size. We recall that for nonfractal basin boundaries, the condition $f(\varepsilon) \propto \varepsilon$ takes place (i.e. the uncertainty exponent $\alpha = 0$).

The complexity of a fractal basin boundary can be measured in terms of *uncertainty dimension*, defined in an N -dimensional dynamical system as [99]

$$D = N - \alpha. \quad (1.28)$$

There are two main methods to find whether an initial condition is certain or uncertain.

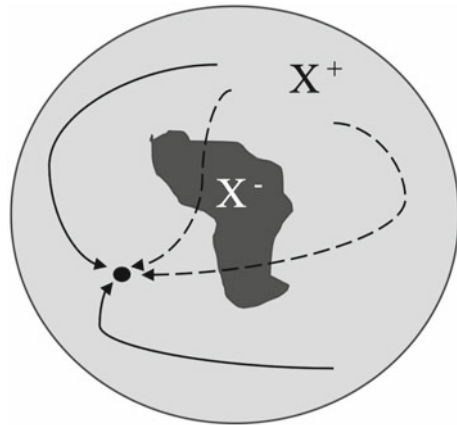
- Calculate an attracting state starting from certain initial conditions x_0 , $(x_0 + \varepsilon)$, and $(x_0 - \varepsilon)$ [51]. If the attractors coincide, then the initial condition x_0 is certain, otherwise it is uncertain.
- Use time-delay function $\Delta T = |T(x_0) - T(x_0 + \varepsilon)|$, where $T(x_0)$ is the time needed for the trajectory, starting from x_0 , to reach the attractor [100]. If $\Delta T > \tau > 0$, we say that x_0 is uncertain with respect to ε , otherwise x_0 is certain.

1.4.4 Survivability

The above assessment of basin stability has at least two disadvantages. First, the stability measure is based on the correct definition of the system asymptotic behavior, which in some cases is difficult to determine, that usually requires prior knowledge of the attractor nature and is meaningful only in multistable systems. Second, the basin stability assessment is insensitive to the undesirable transient behavior, i.e. when the phase-space trajectory visits an undesirable region where the system cannot be modelled. This results in a too rough estimate of the basin stability, unsuitable for some applications. In this case, Helmann et al. [101] suggested a new measure of basin stability, which they called survivability of a dynamical system.

Survivability is a fraction of initial conditions which generate trajectories remaining in the desired region of phase space for a given time. The set of these initial conditions is called *basin of survival*. It is important to note that there also exists

Fig. 1.19 Survivability illustration. X^+ and X^- are sunny (safe) and dark (dead) subspaces. The closed dot indicates a fixed point. The solid and dashed lines are the trajectories which do not pass and pass through the dark region, respectively. The set of trajectories initiating in X^+ and not crossing X^- during time t is called survivability $S(t)$



another set of initial conditions called *basin of death*, which does lead to the attractor, but during transients the trajectory passes through an undesirable (dangerous) phase space zone. In contrast to basin stability based on a linear stability analysis, the survivability of a dynamical system is associated not only with its asymptotic behavior, but also strongly depends on transients.

Imagine now that we want to travel from one country to another and the route passes through a belligerent country. In this case, our travel is not safe because our trajectory crosses a dangerous region where we may die. In the Earth system science, the basin of survival is known as *safe operating space* within planetary boundaries [102] or the *sunny region* [103], and the basin of death is named *dark region*.

The notion of survivability is schematically illustrated in Fig. 1.19. For mathematical definition of survivability, consider trajectories $x_i(t)$ of a dynamical system in phase space $X = X^+ \sqcup X^-$, where X^+ is a desirable (safe, sunny) region and X^- is an undesirable (dead, dark) region.

The survivability $S(t)$ of the dynamical system at time t is defined as a fraction of trajectories starting in X^+ and remaining within X^+ for the entire duration $[0, t]$. In other words, if a trajectory starting in X^+ enters the region X^- , the system dies. So, $S(t)$ denotes a fraction of trajectories starting in X^+ which survive after time t . The part of the X^+ basin of attraction which starting trajectories stay alive during time t is called *t-time basin of survival* X_t^S . Thus, survivability is defined as

$$S(t) = \frac{\text{Vol}(X_t^S)}{\text{Vol}(X^+)}, \quad (1.29)$$

where $\text{Vol}(X_t^S)$ and $\text{Vol}(X^+)$ are basin volumes of sets X_t^S and X^+ , respectively.

Total survivability $S = S_\infty$ is survivability for infinite time ($t \rightarrow \infty$), defined as the limit

$$S_\infty = \lim_{t \rightarrow \infty} S(t). \quad (1.30)$$

Survivability in a restricted state space $C \subset X$ is called *conditional survivability* $S^C(t)$, and defined as the fraction of trajectories starting and remaining in $X^+ \cap C$. For example, conditional survivability in a complex network is related to perturbations applied to a specific node, and given by

$$S^C(t) = \frac{\text{Vol}|_C(X_t^S \cap C)}{\text{Vol}|_C(X^+ \cap C)}, \quad (1.31)$$

where $\text{Vol}|_C$ is the inner measure on the smallest sub-manifold containing C .

There is a strict mathematical relation between survivability and basin stability. If we divide all coexisting attractors of the system X into a set of desirable attractors A^+ and a set of undesirable attractors A^- with their respective sets of basins of attraction X_A^+ and X_A^- , the *basin stability of a desirable set of attractors* A^+ can be defined as

$$S_B = \frac{\text{Vol}(X^0 \cap X_A^+)}{\text{Vol}(X^0)}, \quad (1.32)$$

where X^0 is the initial region.

The survivability concept can be illustrated with an example of an European power grid operating at a nominal frequency of 50 Hz, where deviations must be maintained within ± 200 mHz. If the frequency is out of the (47.5–51.5) Hz range, a blackout may occur. Consequently, the real trajectory on shorter time scales is more important than the long-term asymptotics. This characterizes survivability of a dynamical system as a measure of stability with respect to transient constraints or, in general, a desired phase-space trajectory.

1.4.5 Basin Catastrophe

In some systems, basin boundaries are extremely sensitive to a small change in control parameters. In these systems, the boundary can suddenly jump and even change from being smooth to fractal. This process called *basin boundary metamorphosis* [104] or *basin catastrophe* [105] leads to a change in the boundary structure. The basin catastrophe appears when a basin of attraction suffers a sudden change caused by some kind of collision of the basin with an unstable periodic orbit. The knowledge of basin catastrophes is important for understanding catastrophic events which suddenly emerge in nature. For example, basin boundary metamorphoses can result in catastrophic shifts in ecosystems [105] and destruction of engineering constructions [106].

Among different types of basin boundary metamorphoses, we should mention smooth-fractal metamorphosis [104], fractal-fractal metamorphosis [107], fractal-Wada metamorphosis [58], partially Wada-full Wada metamorphosis [108], and basin reversal [109]. Basin catastrophes can occur in different bifurcations, including

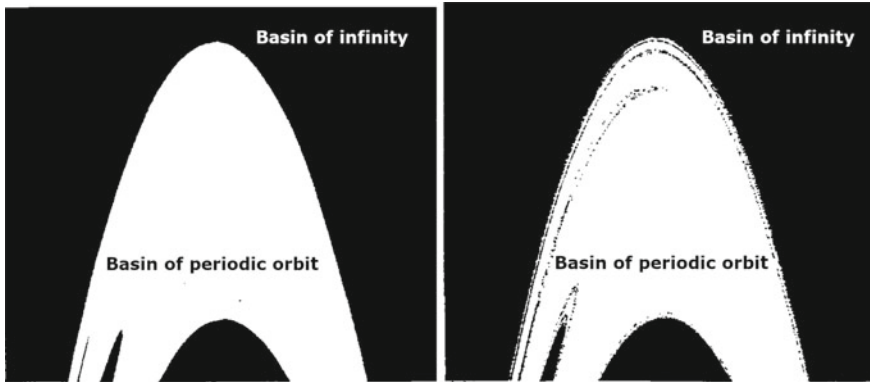


Fig. 1.20 Basin catastrophe in the Hénon map (Eq. 1.11). When a control parameter is increased from (left) $a = 1.314$ to (right) $a = 1.320$, the fractal basin of infinity (black dots) is suddenly expanded inside the basin of attraction of the periodic orbit (white region). Adapted from [107] by permission from the Springer Nature ©1991

saddle-node, period-doubling, homoclinic and heteroclinic bifurcations, as well as in crisis, where boundary metamorphoses give rise to a number of coexisting attractors [110–112].

Below, we will consider two types of basin catastrophes, namely, fractal-fractal metamorphosis and basin reversal.

Fractal-fractal metamorphosis. Let us first demonstrate the fractal-fractal metamorphosis with a simple example of the Hénon map given by Eq. 1.11 with Jacobian $J = 0.3$. This type of metamorphosis is illustrated with the basins of attraction in Fig. 1.20. The black region represents the basin of infinity⁸ and the white region is the basin of a periodic orbit, for $a = 1.314$ (left panel) and $a = 1.320$ (right panel). While in the left panel the basin boundaries are smooth, in the right panel they are fractal. The fractality is revealed as additional black points inside the white area, which are absent in the left panel. This means that there is a critical point $a^* \approx 1.3145$ above which the fractal basin of infinity (black points) is suddenly expanded inside the basin of attraction of the periodic orbit (white region).

In a multistable system with a large number of attractors, basin boundary metamorphoses imply the creation of new and the destruction of old basins, while the existing basins evolve as attractors move and bifurcate [110, 113].

Basin reversal. Another important type of basin catastrophe called *basin reversal* is illustrated in Fig. 1.21 where we present an example of a spiral basin of attraction in two-dimensional driven oscillators. Unlike other types of basin catastrophe, basin reversal changes the direction of basin rotation as a control parameter is varied. While before the catastrophe, all basins spiral outward to the infinity attractor in reverse

⁸ The basin of infinity is a set of initial conditions (x_0, y_0) such that $|x_n, y_n| \rightarrow \infty$ as $n \rightarrow \infty$.

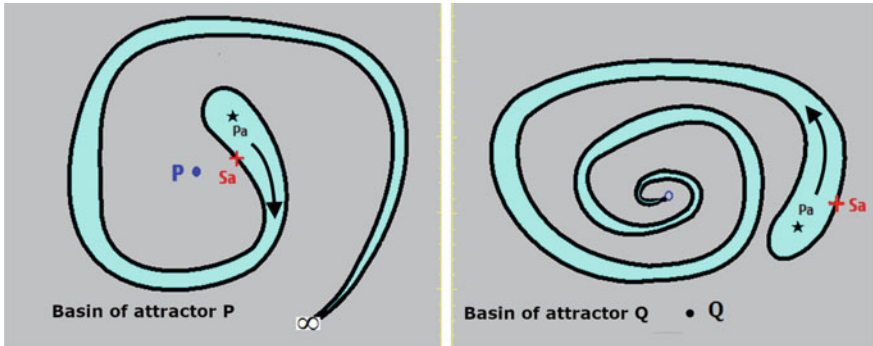


Fig. 1.21 Basin reversal. Basins of attraction (left) before and (right) after catastrophe. The curves are the boundaries between the basins of attraction. **Pa**, **P**, and **Q** are attractors, and **Sa** is a saddle. The arrows show the spiral direction. In the catastrophe, the basin of **Pa** changes its direction, the attractor **P** loses stability and a new attractor **Q** appears. Adapted from [109] with permission of John Wiley & Sons

iteration, after the catastrophe, the systematic basin organization is interrupted and some basins spiral inward to unstable attractors.

As a control parameter is varied, the stable manifold suddenly changes. Simultaneously, the basin suddenly turns around and switches from spiraling outward to spiraling inward, that is called *basin reversal*. The blue region bounded by the solid line is the basin of attraction of **Pa** while the grey region is the basin of attraction of **P** (in the left panel) and **Q** (in the right panel).

The knowledge of the basin reversal helps in understanding attractor properties, that is whether they are hidden or self-extracting (see Sect. 2.4). An important feature of this catastrophic event is that in basin reversal the coexisting hidden attractors cease to be hidden and become self-excited [31].

1.4.6 Basin Integrity

The concept of basin integrity was introduced by Soliman and Thompson [114] as a measure of the erosion of basin boundaries under parameter variation. In many mechanical systems, there is a limit of safe motion and surpassing it can lead to system failure. To model an unbounded motion, the ansatz of the escape from a potential well of a dynamical system can be used (see Sect. 5.1). To avoid undesirable unbounded motion, one needs to predict the parameters and initial conditions leading to this unsafe motion.

Let us first define safe motion. The *safe motion* is a bounded motion inside a safe basin of attraction. The *safe basin*, in turn, is a set of all initial conditions leading asymptotically ($t \rightarrow \infty$) to bounded attractors belonging to a given potential well [115], that is the union of all basins of attraction of bounded solutions.

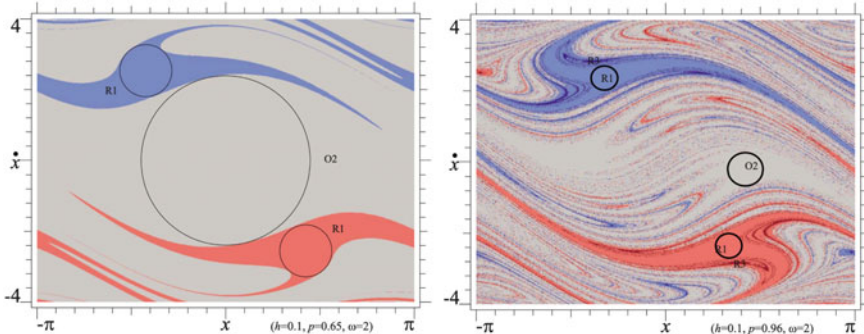


Fig. 1.22 Basins of attraction of the forced pendulum given by Eq. 1.34 with (left) $p = 0.65$ and (right) $p = 0.96$. O_2 , R_1 , and R_3 are the basins of attraction of the period-2 oscillating solution, two period-1 rotating solutions, and two secondary period-3 rotating solutions, respectively. The circles are related to the safe basin integrity factor (IF). Based on data from [117]

To measure the size of safe basins, various indices can be used. The most common measures are *global integrity measure* (GIM), *local integrity measure* (LIM) [114], and *integrity factor* (IF) [116]. The integrity indicators are used to detect erosion profiles.

GIM is defined as the normalized⁹ hypervolume (area in 2D) of the safe basin. Thus, the GIM of the j -th safe basin can be calculated as

$$\text{GIM}_{ij} = \frac{V_j}{\sum_i^N V_i}, \quad (1.33)$$

where V_i is the hipervolume of the i -th basin and N is the number of coexisting attractors.

The main drawback of GIM is the difficulty of its calculation when the basin boundaries are fractal. To solve this problem, LIM is used. The LIM is the minimum distance in the Poincaré section from an attractor to a transient basin boundary.

Finally, IF is the computationally easiest integrity measure defined as the normalized radius of the largest hypersphere (circle in 2D) entirely belonging to the safe basin. To illustrate how IF can be found in practice, consider a periodically forced pendulum modelled by the following equation [118]

$$\ddot{x} + h\dot{x} + [1 + p \cos(\omega t)] \sin x = 0, \quad (1.34)$$

where h is the viscous damping, p and ω are respectively the amplitude and frequency of the pivot vertical oscillation. Figure 1.22 shows the basins of attraction of this pendulum.

⁹ “Normalized” means that the volume of the safe basin, corresponding to the actual value of the varying parameter, is divided by the volume corresponding to a reference value.

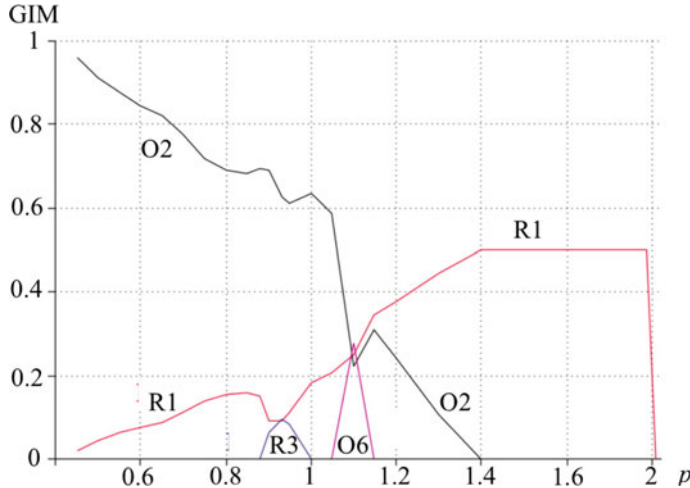


Fig. 1.23 Erosion profile of the excited pendulum modeled by Eq. 1.34 with $\omega = 2$. Based on data from [117]

The integrity measures are specially appealing for a study of the system reliability under a parameter change. As seen from Fig. 1.22, IFs (circle radii) of all basins significantly decrease as the control parameter p is increased from $p = 0.65$ to $p = 0.96$. Such IF reduction is accompanied by an increasing fractality and the emergence of new attractors (R3).

The dependence of GIM on a control parameter is called *erosion profile* and serves to visualize the integrity reduction as the parameter is varied. The erosion profile for the excited pendulum given by Eq. 1.34 is presented in Fig. 1.23. The erosion ends as soon as the safe basin is destroyed, while other dynamical regimes appear. The volume of each of the five basins depicted in Fig. 1.22 is defined as V_i ($i = O2, R1, R1, R3, R3$), and IF is normalized to the largest IF in the erosion profile, that is $IF_{O2}(p = 0.42) = 1$.

Figure 1.23 illustrates the phenomenon of *sudden erosion* around $p \approx 1.8$, when the size of the safe basin suddenly drops down when p is increased beyond $p \approx 1.8$ and the safe R3 basin disappears.

The main features of the integrity profiles are associated with the occurrence of topologically significant dynamic events. In particular, a saddle-node bifurcation, leading to the emergence of a new attractor in a pre-existing basin of attraction, causes its compression, while homoclinic and heteroclinic bifurcations, entailing the penetration of the basin tongue, create conditions for fractal erosion. It can be seen that both of these phenomena cause an instantaneous decrease in some erosion curves. The erosion profiles are important not only from a theoretical point of view, but also provide useful practical information, especially from the viewpoint of a safe use of the considered attractors.

1.5 System Complexity

System complexity is characterized by entropy. The most informative entropy measures for multistable systems are basin entropy, spectral entropy, and sample entropy. The last two measures are especially appealing for systems with infinitely many coexisting attractors [119], and we will now consider them in more detail.

1.5.1 Basin Entropy

Although the uncertainty of the final state can be characterized by the uncertainty dimension α defined in Sect. 1.2.3, it does not account for (i) the number of coexisting attractors in the system, (ii) the number of the phase-space portion occupied by the basin boundary, and (iii) whether the basins are riddled or not. To quantify the uncertainty of the final attractor in a multistable system, Daza et al. [120] introduced the notion of basin entropy. They suggested to construct a mesh in a given region Ω of phase space with a finite number of N_T boxes, so that, through such discretization, the phase space is divided into elements of size ε , each of which could be considered as a random variable with N_A attractors as possible outcomes. Inside each box i , there is a large number of initial conditions and every initial condition converges to one of the N_A attractors. If we mark by different colors the initial conditions inside each box i leading to different attractors, we can compute a so-called *Gibbs entropy* of the i -th box as

$$S_i = \sum_{j=1}^{m_i} p_{i,j} \log(1/p_{i,j}), \quad (1.35)$$

where $m_i \in [1, N_A]$ is the number of different colors inside box i and $p_{i,j}$ is the probability of a certain color j to exist in box i . Then, we calculate the Gibbs entropy of all N_T boxes as the ratio

$$S = \sum_{i=1}^{N_T} S_i. \quad (1.36)$$

Finally, the *basin entropy* is defined as

$$S_b = S/N_T. \quad (1.37)$$

In a monostable system, the basin entropy (or the degree of uncertainty of the basin) is zero ($S_b = 0$), while in systems with completely randomized basins, the basin entropy is $S_b = \log N_A$. The basin entropy not only characterizes the uncertainty of the basin of attraction, but also indicates the presence of some structures in phase space.

If we calculate the number of boxes N_B in the boundary between the basins, i.e. boxes with more than one color, we can compute the *boundary basin entropy* related to the boundary uncertainty as [121]

$$S_{bb} = S/N_B. \quad (1.38)$$

This value quantifies the unpredictability of the basin boundary focusing only on the unpredictable regions of phase space (basin boundaries). The boundary basin entropy is one of the most important measures to characterize fractal basin boundaries where the condition $S_{bb} > \log 2$ is usually fulfilled.

Let us now assume that the colors inside each box are equiprobable, that is $p_{i,j} = 1/m_i$ for all j . By adding the entropy of all trajectories in each box, we obtain the Boltzmann expression for entropy

$$S_i = \log m_i$$

and the equiprobable total entropy becomes

$$S = \sum_{i=1}^N S_i = \sum_{i=1}^N \log m_i.$$

Furthermore, if we locate a grid on a given region of phase space, many boxes will have the same number of colors. In other words, many boxes will be in the interior or near the boundary separating the basins. Assuming that there are N_k boxes with the same number of colors ($k \in [1, k_{max}]$) acting as labels for different boundaries, the basin entropy can be written as

$$S_b = \sum_{k=1}^{k_{max}} \frac{N_k}{N} \log m_k, \quad (1.39)$$

where the number of boxes on the boundary grows with box size as $N_k = n_k \varepsilon^{-D_k}$ (n_k being a positive constant).

The *box-counting dimension* is

$$\begin{aligned} D_k &= D - 1 \quad \text{for smooth basin boundaries,} \\ D_k &\leq D \quad \text{for fractal basin boundaries,} \end{aligned} \quad (1.40)$$

where D is the phase space dimension. Since the number of boxes in the whole phase space grows with box size as $N = \tilde{n} \varepsilon^{-D}$ (\tilde{n} being a positive constant) and recalling that the uncertainty exponent for each boundary is $\alpha_k = D - D_k$ (see Sect. 1.4.3), the basin entropy can be found as

$$S_b = \sum_{k=1}^{k_{\max}} \frac{n_k}{\tilde{n}} \varepsilon^{\alpha_k} \log m_k. \quad (1.41)$$

Thus, the basin entropy is determined by three factors: normalized boundary size n_k/\tilde{n} , uncertainty exponent ε^{α_k} related to boundary fractality and containing the basin entropy variation with box size, and the number of attractors (colors) m_k .

The concepts of basin entropy and boundary basin entropy have been applied to estimate complexity of different systems, including cold atoms [121], chaotic scattering [122, 123], astrophysical models [124, 125], biosystems [126, 127], electronic micro- and nano-devices [128], nonlinear oscillators [129], and the dissipative nontwist map [130].

1.5.2 Spectral Entropy

Spectral entropy allows quantifying the disorder of time sequences using a Fourier transform complexity algorithm [131]. The larger the spectral entropy, the higher the complexity of the sequence. We will show now how spectral entropy is derived.

For a given set of time series of x_n with $n = 0, 1, 2, \dots, N - 1$, we can obtain a new discrete number of length N by subtracting the average of this data set from each data as

$$x_n = x_n - \frac{1}{N} \sum_{n=0}^{N-1} x_n, \quad (1.42)$$

and take a discrete Fourier transform of x_n to get

$$X_k = \sum_{n=0}^{N-1} x_n \exp\left(-\frac{j2\pi nk}{N}\right), \quad (1.43)$$

where $k = 0, 1, 2, \dots, N - 1$ and j is the imaginary unit.

The probability of X_k in the power spectrum is given by

$$P_k = \frac{|X_k|^2}{\sum_{n=0}^{N/2-1} |X_k|^2}. \quad (1.44)$$

Using the above equations, the *normalized spectral entropy* can be calculated as

$$SE = \frac{\sum_{k=0}^{N/2-1} |P_k \ln(P_k)|^2}{\ln(N/2)}, \quad P_k \neq 0. \quad (1.45)$$

1.5.3 Sample Entropy

Sample entropy also measures the complexity of time sequences [132]. The larger the sample entropy, the higher the complexity.

Using a similar approach as for spectral entropy, consider a set of time sequences of length N . This set forms the $(N - m + 1)$ m -dimensional vectors $\mathbf{X}_m(i) = (x_i, x_{i+1}, \dots, x_{i+m-1})$ ($1 \leq i \leq N - m + 1$). The distance between two vectors $\mathbf{X}_m(i)$ and $\mathbf{X}_m(j)$ is defined as the absolute value of the maximum difference in the corresponding element, i.e. $d(\mathbf{X}_m(i), \mathbf{X}_m(j)) = \max(|x_{i+k} - x_{j+k}|)$ ($0 \leq k \leq m - 1$). Defining B_i as the number of $d(\mathbf{X}_m(i), \mathbf{X}_m(j)) \leq r$ ($1 \leq j \leq N - m$, $i \neq j$), we obtain $(N - m + 1)^{-1}$ times B_i as

$$B_i^m(r) = \frac{1}{N - m - 1} B_i \quad (1.46)$$

and define the probability $B^{(m)}(r)$ of the two sequences matching for m points as

$$B_i^{(m)}(r) = \frac{1}{N - m} \sum_{i=1}^{N-m} B_i^m(r). \quad (1.47)$$

In a similar way, $\mathbf{X}_{m+1}(i)$ is defined as an $(m + 1)$ -dimensional vector and A_i is the number of $d(\mathbf{X}_{m+1}(i), \mathbf{X}_{m+1}(j)) < r$. Likewise, $(N - m + 1)^{-1}$ times A_i and the probability $A^{(m)}(r)$ of the two sequences matching for $m + 1$ points are given as

$$\begin{aligned} A_i^m(r) &= \frac{1}{N - m - 1} A_i, \\ A_i^{(m)}(r) &= \frac{1}{N - m} \sum_{i=1}^{N-m} A_i^m(r). \end{aligned} \quad (1.48)$$

Finally, for $N \rightarrow \infty$ the *sample entropy* can be calculated as

$$SE = -\ln \frac{A^n(r)}{B^m(r)}. \quad (1.49)$$

Thus, the concept of basin entropy is important for studying multistable systems. In addition, it allows quantifying the uncertainty of the Wada property (see Sect. 1.2.4). Moreover, the concept of boundary basin entropy yields a sufficient condition for boundary fractality: if the boundary basin entropy is larger than $\log 2$, then the basin is fractal [120]. Unlike other methods, such as box-counting dimension (Eq. 1.40), which require calculations at different resolutions, the $\log 2$ criterion can be used with a fixed resolution. This opens up new possibilities for experimental demonstration of fractal basin boundaries.

References

1. Poincaré H (1890) Sur le problème des trois corps et les équations de la dynamique (Mémoire couronné du prix de S.M. le roi Oscar II de Suède). *Acta Math* 13:1–270
2. Newhouse S (1970) Non-density of axiom A(a) on S^2 . *Proc Am Math Soc Sympos Pure Math* 14:191–202
3. Newhouse S (1974) Diffeomorphism with infinitely many sinks. *Topology* 13:9–18
4. Newhouse S (1979) The abundance of wild hyperbolic sets and nonsmooth stable sets for diffeomorphisms. *Publ Math Inst Hautes Études Sci* 50:101–151
5. Robinson C (1983) Bifurcation to infinitely many sinks. *Commun Math Phys* 90:433–459
6. Gambaudo JM, Tresser C (1990) Diffeomorphisms with infinitely many strange attractors. *J Complex* 6:409–416
7. Mora L, Viana M (1990) Abundance of strange attractors. *Acta Math* 6:1–71
8. Palis J, Viana M (1994) High dimension diffeomorphisms displaying infinitely many periodic attractors. *Ann Math* 140(1):207–250
9. Pumariño A, Rodríguez JA (1997) Coexistence and persistence of strange attractors. Springer, Berlin
10. Colli E (1998) Infinitely many coexisting strange attractors. *Ann Inst H Poincaré Anal Non Linéaire* 15:539–579
11. Atteneave F (1971) Multistability in perception. *Sci Am* 225:63–71
12. Deutsch D (1987) The tritone paradox: effects of spectral variables. *Percept Psychophys* 41:563–575
13. Gibbs HM, Mo Call SL, Venkatesan TNC (1976) Differential gain and bistability using a sodium-filled Fabry-Perot interferometry. *Phys Rev Lett* 36(11):1135–1138
14. Arechi FT, Meucci R, Puccioni G, Tredicce J (1982) Experimental evidence of subharmonic bifurcations, multistability, and turbulence in a Q-switched gas laser. *Phys Rev Lett* 49:1217–1220
15. Otsuka K, Iwamura H (1983) Theory of optical multistability and chaos in a resonant-type semiconductor laser amplifier. *Phys Rev A* 28(5):3153–3155
16. Pisarchik AN, Kuntsevich BK (2002) Control of multistability in a directly modulated diode laser. *IEEE J Quantum Electron* 38:1594–1598
17. Komarov A, Leblond H, Sanchez F (2005) Multistability and hysteresis phenomena in passively mode-locked fiber lasers. *Phys Rev A* 71:053809
18. Pisarchik AN, Kuntsevich BF (2001) Nonlinear dynamics of a CO₂ laser with current modulation and cavity detuning. *J Opt B Quantum Semiclass Opt* 3:363–371
19. Ozbudak EM, Thattai M, Lim HN, Shraiman BI, Van Oudenaarden A (2004) Multistability in the lactose utilization network of *Escherichia coli*. *Nature* 427(6976):737–740
20. Joshi A, Xiao M (2003) Optical multistability in three-level atoms inside an optical ring cavity. *Phys Rev Lett* 91:143904
21. Thomson M, Gunawardena J (2009) Unlimited multistability in multisite phosphorylation systems. *Nature* 460:274–277
22. Laurent M, Kellershohn N (1999) Multistability: a major means of differentiation and evolution in biological systems. *Trends Biochem Sci* 24:418–422
23. Dafilis MP, Frascoli F, Cadusch PJ, Liley DTJ (2009) Chaos and generalised multistability in a mesoscopic model of the electroencephalogram. *Physica D* 238(13):1056–1060
24. Zeng Z, Huang T, Zheng WX (2010) Multistability of recurrent neural networks with time-varying delays and the piecewise linear activation function. *IEEE Trans Neural Netw* 21(8):1371–1377
25. Robinson A, Calov R, Ganopolski A (2012) Multistability and critical thresholds of the Greenland ice sheet. *Nat Clim Change* 2:429–432
26. Ying L, Huang D, Lai YC (2016) Multistability, chaos, and random signal generation in semiconductor superlattices. *Phys Rev E* 93:062204
27. Leonov GA, Vagaitsev VI, Kuznetsov NV (2011) Localization of hidden Chua's attractors. *Phys Lett A* 375(23):2230–2233

28. Leonov GA, Kuznetsov NV, Mokaev TN (2015) Homoclinic orbits, and self-excited and hidden attractors in a Lorenz-like system describing convective fluid motion. *Eur Phys J: Spec Top* 224(8):1421–1458
29. Kuznetsov NV, Leonov GA, Mokaev TN, Prasad A, Shrimali MD (2018) Finite-time Lyapunov dimension and hidden attractor of the Rabinovich system. *Nonlinear Dyn* 92(2):267–285
30. Chen G, Kuznetsov NV, Leonov GA, Mokaev TN (2015) Hidden attractors on one path: Glukhovsky-Dolzhansky, Lorenz, and Rabinovich systems. *Int J Bifurc Chaos Appl Sci Eng* 27(8):1750115
31. Dudkowski D, Jafari S, Kapitaniak T, Kuznetsov NV, Leonov GA, Prasad A (2016) Hidden attractors in dynamical systems. *Phys Rep* 637:1–50
32. Elhadj Z, Sprott JC (2013) Universal basins of attraction in high-dimensional systems. *Int J Bifurc Chaos Appl Sci Eng* 23:50197
33. Sprott JC, Wang X, Chen G (2013) Coexistence of point, periodic and strange attractors. *Int J Bifurc Chaos Appl Sci Eng* 23(5):1350093
34. Sprott JC (2015) Strange attractors with various equilibrium types. *Eur Phys J Spec Topics* 224(8):1409–1419
35. Li C, Sprott CJ (2014) Coexisting hidden attractors in a 4-D simplified Lorenz system. *Int J Bifurc Chaos* 24(3):1450034
36. Li C, Sprott JC, Hu W, Xu Y (2017) Infinite multistability in a self-reproducing chaotic system. *Int J Bifurc Chaos* 27(10):1750160
37. Li C, Thio JCW, Sprott JC, Iu HHC, Xu Y (2018) Constructing infinitely many attractors in a programmable chaotic circuit. *IEEE Access* 6:29003–29012
38. Sun H, Scott S, Showalter K (1999) Uncertain destination dynamics. *Phys Rev E* 60:3876–3880
39. Ngonghala CN, Feudel U, Showalter K (2011) Extreme multistability in a chemical model system. *Phys Rev E* 83:056206
40. Guckenheimer J, Holmes P (1983) Nonlinear oscillations, dynamical systems, and bifurcations of vector fields. Springer, New York
41. Baker GL, Gollub JP (1996) Chaotic dynamics: an introduction, 2nd edn. Cambridge University Press, Cambridge
42. Ott E (2002) Chaos in dynamical systems, 2nd edn. Cambridge University Press, New York
43. Schuster HG, Just W (2005) Deterministic Chaos: an introduction, 4th edn. Wiley-VCH
44. Fuchs A (2013) Nonlinear dynamics in complex systems. Springer, Berlin
45. Strogatz SH (2015) Nonlinear dynamics and chaos: with applications to physics, biology, chemistry, and engineering, 2nd edn. Westview Press, Massachusetts
46. Kuznetsov YA (2013) Elements of applied bifurcation theory, vol 112. Springer Science and Business Media, New York
47. Milnor J (1985) On the concept of an attractor. *Commun Math Phys* 99:177–195
48. McDonald SW, Grebogi C, Ott E, Yorke JA (1985) Fractal basin boundaries. *Physica D* 7:125–153
49. Mandelbrot BB (1975) Les Objets Fractals, Forme. Hasard et Dimension, Flammarion, Paris
50. Hénon M (1976) 2-dimensional mapping with a strange attractor. *Commun Math Phys* 50:69–77
51. Grebogi C, McDonald SW, Ott E, Yorke JA (1983) Final state sensitivity: an obstruction to predictability. *Phys Lett A* 99:415–418
52. Grebogi C, Kostelich E, Ott E, Yorke JA (1986) Multi-dimensioned intertwined basin boundaries and the kicked double rotor. *Phys Lett A* 118:448–452
53. Falconer K (2004) Fractal geometry: mathematical foundations and applications. John, New York
54. Aguirre J, Viana RL, Sanjuán MAF (2009) Fractal structures in nonlinear dynamics. *Rev Mod Phys* 81(1):333–386
55. Yoneyama K (1917) Theory of continuous set of points. *Tohoku Math J* 11–12:43–158
56. Kennedy J, Yorke JA (1991) Basins of Wada. *Physica D* 17:75–86

57. Kennedy J, Yorke JA (1996) Basins of attraction, Wada basin boundaries and basin cells. *Science* 271:1376–1380
58. Nusse HE, Ott E, Yorke JA (1995) Saddle-node bifurcations on fractal basin boundaries. *Phys Rev Lett* 75(13):2482–2485
59. Aguirre J, Sanjuán MAF (2002) Unpredictable behavior in the Duffing oscillator: Wada basins. *Physica D* 171(1):41–51
60. Toroczkai Z, Károlyi G, Péntek A, Tél T, Grebogi C, Yorke JA (1997) Wada dye boundaries in open hydrodynamical flows. *Physica A* 239(1):235–243
61. Portela JSE, Caldas IL, Viana RL, Sanjuán MAF (2007) Fractal and Wada exit basin boundaries in tokamaks. *Int J Bifurc Chaos* 17(11):4067–4079
62. Vandermeer J (2004) Wada basins and qualitative unpredictability in ecological models: a graphical interpretation. *Ecol Modell* 176(1):65–74
63. Daza A, Wagemakers A, Sanjuán AF, Yorke JA (2015) Testing for basins of Wada. *Sci Rep* 5:16579
64. Alexander J, Yorke JA, You Z, Kan I (1992) Riddled basins. *Int J Bifurc Chaos* 2(4):795–813
65. Ott E, Sommerer JC, Alexander JC, Kan I, Yorke JA (1994) The transition to chaotic attractors with riddled basins. *Physica D* 76:384–410
66. Lai YC, Grebogi C (1995) Intermingled basins and two-state on-off intermittency. *Phys Rev E* 52(4):R3313–R3316
67. Ashwin P (2005) Riddled basins and coupled dynamical systems. In: Dynamics of coupled map lattices and of related spatially extended systems. Lecture notes in physics, vol 671, Springer, Berlin, pp 181–207
68. Ott E, Sommerer JC, Alexander JC, Kan I, Yorke JA (1993) Scaling behavior of chaotic systems with riddled basins. *Phys Rev Lett* 71(25):4134–4137
69. Heagy JF, Carroll T, Pecora L (1994) Experimental and numerical evidence for riddled basins in coupled chaotic systems. *Phys Rev Lett* 73:3528–3531
70. Ashwin P, Buescu J, Stewart IN (1994) Bubbling of attractors and synchronisation of oscillators. *Phys Lett A* 193:126–139
71. Nakajima H, Ueda Y (1996) Riddled basins of the optimal states in learning dynamical systems. *Physica D* 99:35–44
72. Woltering M, Markus M (1999) Riddled basins of coupled elastic arches. *Phys Lett A* 260:453–461
73. Hasler M, Maistrenko Y, Popovych O (1998) Simple example of partial synchronization of chaotic systems. *Phys Rev E* 58:6346–6843
74. Bazelles B (2001) Dynamics with riddled basins of attraction in models of interacting populations. *Chaos Solitons Fractals* 12:301–311
75. Saha A, Feudel U (2018) Riddled basins of attraction in systems exhibiting extreme events. *Chaos* 28:033610
76. dos Santos V, Borges FS, Iarosz KC, Viana RL, Baptista MS, Batista AM (2020) Basin of attraction for chimera states in a network of Rössler oscillators. *Chaos* 30:083115
77. Pliss VA, Sell GR (1998) Approximation dynamics and the stability of invariant sets. *J Differ Equ* 149:DE973400
78. Lyapunov AM (1992) The general problem of the stability of motion. *Int J Control* 55(3):531–773
79. Abarbanel HD, Brown R, Kennel MB (1991) Variation of lyapunov exponents on a strange attractor. *J Nonlin Sci* 1:175–199
80. Wiley DA, Strogatz SH, Girvan M (2006) The size of the sync basin. *Chaos* 16:015103
81. Nusse HE, Yorke JA, Kostelich EJ (1994) Basins of attraction. Dynamics: numerical explorations, vol 101. Springer, New York, pp 269–314
82. Menck PJ, Heitzig J, Marwan N, Kurths J (2013) How basin stability complements the linear-stability paradigm. *Nat Phys* 9:89–92
83. Menck PJ, Heitzig J, Kurths J, Schellnhuber HJ (2014) How dead ends undermine power grid stability. *Nat Commun* 5:3969

84. von Neuman J (1951) Various techniques used in connection with random digits. *J Res Nat Bur Stand* 12:36–38
85. Evans M, Swartz T (2000) Approximating integrals via monte carlo and deterministic methods, vol 20. Oxford University Press, Oxford
86. Stender M, Hoffmann N (2021) bSTAB: an open-source software for computing the basin stability of multi-stable dynamical systems. *Nonlinear Dyn*
87. Holling CS (1973) Resilience and stability of ecological systems. *Annu Rev Ecol Evol Syst* 4:1–23
88. Folke C, Carpenter S, Walker B, Scheffer M, Elmqvist T, Gunderson L, Holling CS (2004) Regime shifts, resilience, and biodiversity in ecosystem management. *Annu Rev Ecol Evol Syst* 35:557–581
89. Walker B, Holling CS, Carpenter SR, Kinzig A (2004) Resilience, adaptability and transformability in social-ecological systems. *Ecol Soc* 9(2):5
90. Allen CR, Angeler DG, Garneštani AS, Gunderson LH, Holling CS (2014) Panarchy: theory and application. *Ecosystems* 17:578–589
91. Rings T, Mazarei M, Akhshi A, Geier C, Tabar MRR, Lehnertz K (2019) Traceability and dynamical resistance of precursor of extreme events. *Sci Rep* 9:1744
92. MacQueen JB (1967) Some methods for classification and analysis of multivariate observations. In: Cam ML, Neyman J (eds) *Proceedings of 5th Berkeley symposium on mathematical statistics and probability*. University of California Press, pp 281–297
93. Fischer T, Rings T, Reza Rahimi Tabar M, Lehnertz K (2022) Towards a data-driven estimation of resilience in networked dynamical systems: designing a versatile testbed. *Front Netw Physiol* 2:838142
94. Klinshov VV, Nekorkin VI, Kurths J (2015) Stability threshold approach for complex dynamical systems. *New J Phys* 18(1):013004
95. Vrkoč I (1959) Integral stability. *Czechoslovak Math J* 9(84):71–129 in Russian
96. Datko R (1983) The Laplace transform and the integral stability of certain linear processes. *J Differ Equ* 48:386–403
97. Hristova SG (2010) Integral stability in terms of two measures for impulsive functional differential equations. *Math Comput Model* 51:100–108
98. Mitra C, Kurths J, Donner RV (2015) An integrative quantifier of multistability in complex systems based on ecological resilience. *Sci Rep* 5:16196
99. Ott E, Yorke ED, Yorke JA (1985) A scaling law: How an attractor's volume depends on noise level. *Physica D* 16(1):62–78
100. Lau YT, Finn JM, Ott E (1991) Fractal dimension in nonhyperbolic chaotic scattering. *Phys Rev Lett* 66(8):978–981
101. Hellmann F, Schultz P, Grabow C, Heitzig J, Kurths J (2016) Survivability of deterministic dynamical systems. *Sci Rep* 13(6):129654
102. Rockström J et al (2009) A safe operating space for humanity. *Nature* 461:472–475
103. Heitzig J, Kittel T, Donges JF, Molkenthin N (2016) Topology of sustainable management of dynamical systems with desirable states: from defining planetary boundaries to safe operating spaces in the Earth system. *Earth Syst Dyn* 7:21–50
104. Grebogi C, Ott E, Yorke JA (1986) Metamorphoses of basin boundaries in nonlinear dynamical system. *Phys Rev Lett* 56:1011–1014
105. Scheffer M, Carpenter S, Foley J, Folke C, Walker B (2001) Catastrophic shifts in ecosystems. *Nature* 413:31613–31624
106. Thompson JMT, Soliman MS (1990) Fractal control boundaries of driven oscillators and their relevance to safe engineering design. *Proc R Soc Lond A* 428:1–13
107. Alligood K, Lai LTL, Yorke JA (1991) Metamorphoses: Sudden jumps in basin boundaries. *Commun Math Phys* 141:1–8
108. Zhang Y, Luo G (2013) Wada bifurcations and partially Wada basin boundaries in a two-dimensional cubic map. *Phys Lett A* 377:1274–1281
109. Kong G, Zhang Y (2019) Basin reversal in nonlinear driven oscillators. *Nonlinear Dyn* 96:1213–1231

110. Eschenazi E, Solari HG, Gilmore R (1989) Basins of attraction in driven dynamical systems. *Phys Rev A* 39:2609–2627
111. Soliman MS, Thompson JMT (1992) Global dynamics underlying sharp basin erosion in nonlinear driven oscillators. *Phys Rev A* 45:3425–3431
112. Zhang Y, Luo G, Cao Q, Lin M (2014) Wada basin dynamics of a shallow arch oscillator with more than 20 coexisting low-period periodic attractors. *Int J Nonlinear Mech* 58:151–161
113. Kong G, Zhang Y (2019) A special type of explosion of basin boundary. *Phys Lett A* 383:1151–1156
114. Soliman MS, Thompson JMT (1989) Integrity measures quantifying the erosion of smooth and fractal basins of attraction. *J Sound Vib* 135:453–475
115. Rega G, Lenci S (2005) Identifying, evaluating, and controlling dynamical integrity measures in nonlinear mechanical oscillators. *Nonlinear Anal: Real World Appl* 63:902–914
116. Lenci S, Rega G (2003) Optimal control of nonregular dynamics in a duffing oscillator. *Nonlinear Dyn* 33:71–86
117. Lenci S, Rega G (2008) Competing dynamic solutions in a parametrically excited pendulum: Attractor robustness and basin integrity. *J Comput Nonlinear Dyn* 3(4):041010
118. Szemplinska-Stupnicka W, Tyrkiel E, Zubrzycki A (2000) The global bifurcations that lead to transient tumbling chaos in a parametrically driven pendulum. *Int J Bifurc Chaos Appl Sci Eng* 10:2161–2175
119. Li H, Li K, Chen M, Bao B (2020) Coexisting infinite orbits in an area-preserving Lozi map. *Entropy* 22:1119
120. Daza A, Wagemakers A, Georgeot B, Guéry-Odelin D, Sanjuán MA (2016) Basin entropy: a new tool to analyze uncertainty in dynamical systems. *Sci Rep* 6:31416
121. Daza A, Georgeot B, Guéry-Odelin D, Wagemakers A, Sanjuán MA (2017) Chaotic dynamics and fractal structures in experiments with cold atoms. *Phys Rev A* 95:013629
122. Bernal JD, Seoane JM, Sanjuán MAF (2018) Uncertainty dimension and basin entropy in relativistic chaotic scattering. *Phys Rev E* 97:042214
123. Nieto AR, Seoane JM, Alvarellos J, Sanjuán MAF (2018) Resonant behavior and unpredictability in forced chaotic scattering. *Phys Rev E* 98:062206
124. Zotos EE, Suraj MS (2018) Basins of attraction of equilibrium points in the planar circular restricted five-body problem. *Astrophys Space Sci* 363:20
125. Zotos EE (2018) On the Newton-Raphson basins of convergence of the out-of-plane equilibrium points in the Copenhagen problem with oblate primaries. *Int J Non Linear Mech* 103:93–103
126. Donepudi R, Ramaswamy R (2018) The collective dynamics of NF- κ B in cellular ensembles. *Eur Phys J* 227:851–863
127. Mugnaine M, Andrade F, Szezech JJ, Bazeia D (2019) Basin entropy behavior in a cyclic model of the rock-paper-scissors type. *Europhys Lett* 125:58003
128. Gusso A, Viana RL, Mathias AC, Caldas IL (2019) Nonlinear dynamics and chaos in micro/nanoelectromechanical beam resonators actuated by two-sided electrodes. *Chaos Solitons Fractals* 122:6–16
129. Puy A, Daza A, Wagemakers A, Sanjuán MA (2021) A test for fractal boundaries based on the basin entropy. *Commun Nonlinear Sci Numer Simul* 95:105588
130. Mugnaine M, Batista AM, Caldas IL, Szezech JDJ, de Carvalho RE, Viana RL (2021) Curry-Yorke route to shearless attractors and coexistence of attractors in dissipative nontwist systems. *Chaos* 31:023125
131. He S, Sun K, Wang H (2015) Complexity analysis and DSP implementation of the fractional-order Lorenz hyperchaotic system. *Entropy* 17:8299–8311
132. Richman J, Moorman J (2015) Physiological time-series analysis using approximate entropy and sample entropy. *Am J Physiol Heart Circ Physiol* 278:H2039–H2049

Chapter 2

Emergence of Multistability



Abstract Despite a great variety of underlying mechanisms, the overall behavior of multistable systems is fairly similar. All of them exhibit very complex dynamics due to nonlinear interactions leading to the coexistence of attractors. A particular feature of such systems is their extremely high sensitivity to initial conditions. Even a slight change in the initial condition can lead the system to a different attractive state. This sensitivity is especially pronounced in multistable systems with interwoven basins of attraction. Furthermore, multistable systems are very sensitive to parameter perturbations that can cause a qualitatively different behavior, especially near the bifurcation point, where a tiny change in a control parameter may result in the emergence of a large number of attractors.

2.1 Bifurcations Giving Rise to Multistability

There are many bifurcations where new attractors are born. All these bifurcations can roughly be divided into two large classes: local and global.

A *local bifurcation* occurs when a control parameter, crossing a critical point, changes the local stability of a fixed point or a periodic orbit. At this point, the equilibrium is non-hyperbolic, so that a small deviation of the control parameter near the bifurcation does not affect topological properties of phase space; therefore this bifurcation is called local. Examples of local bifurcations are period-doubling, saddle-node, pitchfork, transcritical, Andronov–Hopf, multiple limit cycles, and Neimark–Saker bifurcations.

A *global bifurcation* appears when an invariant set, for instance, a periodic orbit, collides with another periodic orbit or with an equilibrium point. This leads to topological changes in phase space, which cannot be confined to a small neighbourhood of the fixed point. That is why this bifurcation is called global. Examples of this bifurcation are homoclinic (a limit cycle collides with a saddle point), heteroclinic (a limit cycle collides with two or more saddle points), infinite-period bifurcation (a limit cycle collides with a saddle node and a saddle point simultaneously), blue sky catastrophe (a limit cycle collides with a nonhyperbolic cycle), and codimensional-two gluing bifurcation (two limit cycles collide with each other).

Since there are a huge number of bifurcations, it is impossible to describe all known bifurcations in one book, and we do not set this as a goal. Therefore, here we will consider only those generic bifurcations which give rise to multistability. We will start with local and continue with global bifurcations.

2.1.1 Pitchfork Bifurcation

A pitchfork bifurcation can be either supercritical or subcritical. In a supercritical bifurcation pitchfork bifurcation, a stable fixed point is converted into two stable and one unstable fixed points, while in a subcritical bifurcation, two unstable and one stable fixed points are converted into one unstable fixed point. In other words, the bifurcation diagrams are antisymmetric about supercritical and subcritical bifurcations, so that the state stability is inverted.

Let us now consider a simple dynamical system of fourth-order nonlinearity given by

$$\dot{x} = x(r - x^3), \quad (2.1)$$

where r is the control parameter. In Fig. 2.1 (upper row) we plot the function $f(x) = x(r - x^3)$ for three different values of r . Since the fixed point condition is $\dot{x} = 0$, the fixed points are the points at which the curve intersects the x -axis. A fixed point is stable if the flow goes toward that point, otherwise it is unstable. When r is positive (right panel), the system has two stable ($x_s = \pm\sqrt{r}$) and one unstable ($x_u = 0$) fixed points.

The lower row in Fig. 2.1 illustrates the emergence of bistability with the potential

$$V = -\frac{1}{2}rx^2 + \frac{1}{4}x^4 \quad (2.2)$$

calculated from function $f(x) = -dV/dx$. One can see that the potential is converted from a one-well to a double-well potential, i.e. the system becomes bistable.

The bifurcation diagram with respect to r presented in Fig. 2.2 illustrates the supercritical pitchfork bifurcation. For $r > 0$, there are two branches of two stable solutions (solid lines) and one branch of an unstable solution (dashed line), whereas $r < 0$, there is only one branch of stable solutions.

2.1.2 Saddle-Node Bifurcation

A saddle-node bifurcation arises when a stable manifold (M_s) collides with an unstable manifold (M_u) (Fig. 2.3). This bifurcation is fundamental in nonlinear dynamics since it gives rise to a pair of unstable states [1]. The organization of basins of attraction in a multistable system is governed by the ordering of homoclinic and

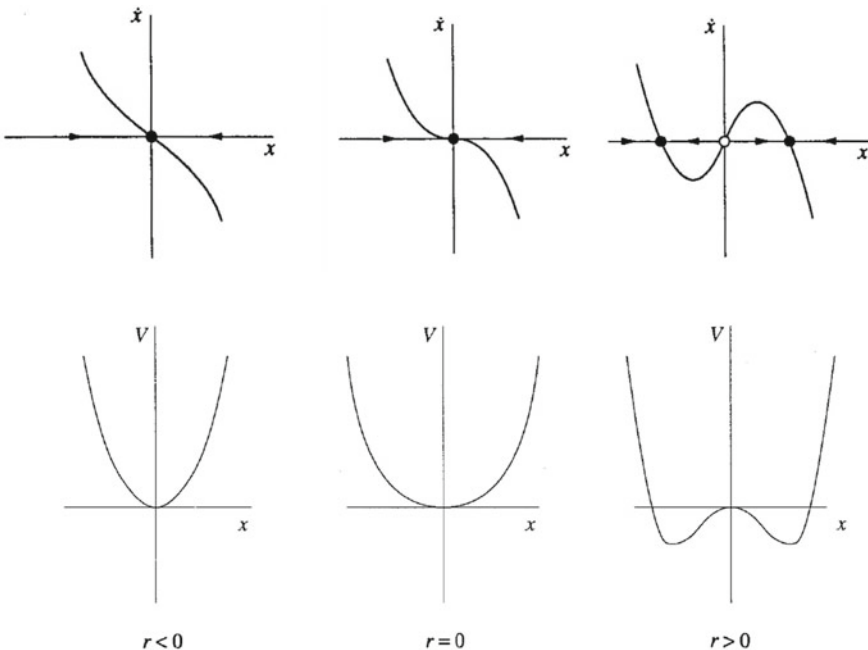
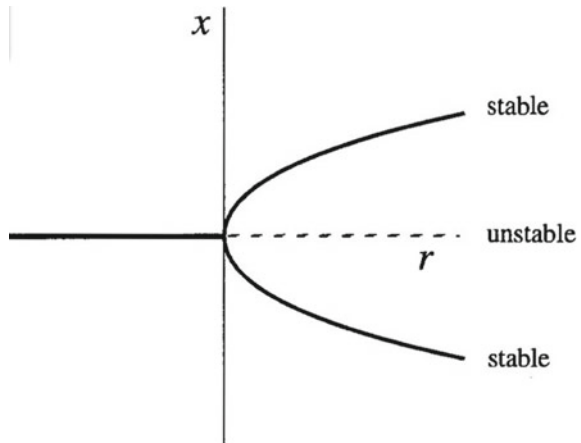


Fig. 2.1 (Upper row) Phase-space plot and (lower row) potential function (Eq. 2.2) illustrating the emergence of bistability in a pitchfork bifurcation. When the control parameter r is increased above zero, two stable (closed dots) and one unstable (open dot) fixed points arise. The arrows indicate the flow direction

Fig. 2.2 Bifurcation diagram of the system in Eq. 2.1 illustrating a supercritical pitchfork bifurcation at $r = 0$ where two stable and one unstable fixed points are born



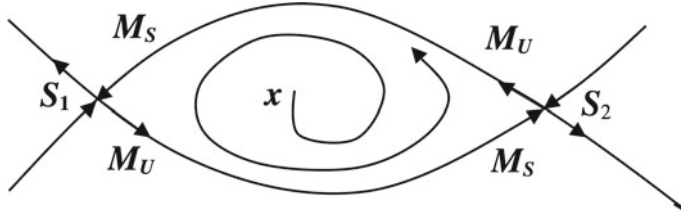


Fig. 2.3 Saddle-node bifurcations S_1 and S_2 connected by a homoclinic orbit (two heteroclinic orbits). x is a phase-space trajectory, M_s and M_u are stable and unstable manifolds

heteroclinic connections of regular saddles [2]. Combined saddle-node bifurcations, also known as *blue sky bifurcation* can generate multistability, since two stable fixed points are suddenly created.

A pair of saddle-node bifurcations (S_1 and S_2) connected by a homoclinic orbit, formed by two heteroclinic orbits, is schematically illustrated in the phase-space plot in Fig. 2.3. The trajectories x approach these bifurcations along stable manifolds M_s and move away from them along unstable manifolds M_u . When a control parameter is changed, the saddle-node points are separated so that the two heteroclinic orbits are transformed into two homoclinic orbits of each fixed point, thus giving rise to bistability.

Let us illustrate the emergence of bistability in a saddle-node bifurcation with an example of a generic energy model used to describe bistable perception (see Sect. 8):

$$\dot{x} = -4ax(x^2 - b) + 4c. \quad (2.3)$$

Here, x is a cognition variable, c is a metabolic activity parameter, and a is an uncertainty parameter. The parameter b reflects a probabilistic character of the synaptic overlap of distinct brain areas responsible for visual perception. Cognition is directly related to both metabolic activity and synaptic connectivity. All these processes are associated with neuronal connectivity. An increase in connectivity enlarges the neural network involved into cognitive processes, thus stimulating metabolic activity. A lack of metabolic activity due to degenerative diseases (for example, Alzheimer disease) leads to the degradation of the neural networks.

The potential function of Eq. 2.3 is

$$U = a(x^4 - 2bx^2) - 4cx. \quad (2.4)$$

The left panel of Fig. 2.4 shows potential functions for different values of parameter b , while the corresponding bifurcation diagrams with respect to c are presented in the right panel of Fig. 2.4. The parameters a and b are related respectively to the depth of the potential wells and the distance between the wells. There is a threshold value of b for which the potential transforms from one-well to two-well, so that the system becomes bistable as b is increased.

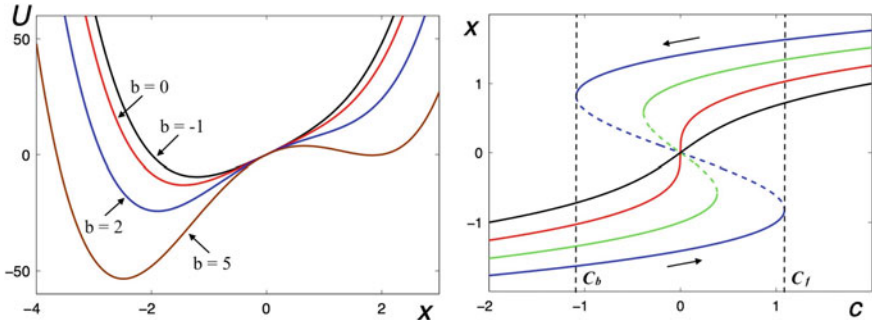


Fig. 2.4 (Left) Potential functions in Eq. 2.4 for $c = -3$ and (right) bifurcation diagrams of Eq. 2.3 for $a = 1$ and different values of b . The arrows show the direction of the parameter change to find hysteresis in the range $c_b < c < c_f$. Bistability is observed between backward (c_b) and forward (c_f) saddle-node bifurcations marked by vertical dashed lines. The dashed curves connecting the two branches (blue) of the bifurcation diagram are unstable fixed points

When the control parameter c is increased, the system follows the lower branch of the bifurcation diagram up to the forward saddle-node bifurcation c_f , where it switches to the upper branch (see Fig. 2.4 (right)). When c is decreased, the system follows the upper branch up to the backward saddle-node bifurcation c_b , where it switches to the lower branch. Therefore, there is a hysteresis in the parameter range $c_b < c < c_f$. Thus, bistability in Eq. 2.3 arises as increasing c crosses c_b and decreasing c crosses c_f . An unstable fixed point is born in these bifurcations simultaneously with a stable fixed point.

While other types of bifurcations are also important in nonlinear dynamics, saddle-node bifurcations giving rise to multistability are most commonly found in biological systems. At the same time, a specific feature of real biological systems is the presence of very strong noise. Therefore, biological models require introducing a stochastic term into underlying nonlinear differential equations. This often greatly complicates the bifurcation structure, causing several coexisting saddle nodes and fixed points.

2.1.3 Andronov–Hopf Bifurcation

Another generic bifurcation where multistability can appear is an inverse subcritical Andronov–Hopf bifurcation.¹ This bifurcation can be either supercritical or subcritical.

To illustrate this bifurcation, we consider a two-dimensional dynamical system given by

¹ In some literature this bifurcation is also referred to as a Poincaré–Andronov–Hopf or simply a Hopf bifurcation.

$$\begin{aligned}\dot{x} &= bx - y + \epsilon x(x^2 - y^2), \\ \dot{y} &= x + by + \epsilon y(x^2 + y^2),\end{aligned}\quad (2.5)$$

where b is a control parameter and $\epsilon = \pm 1$ is a parameter which defines the type of equilibrium.

Figure 2.5 schematically shows supercritical and subcritical Andronov–Hopf bifurcations. The former is observed for $\epsilon = -1$, while the latter for $\epsilon = 1$. In a supercritical Andronov–Hopf bifurcation, a stable focus and an unstable limit cycle

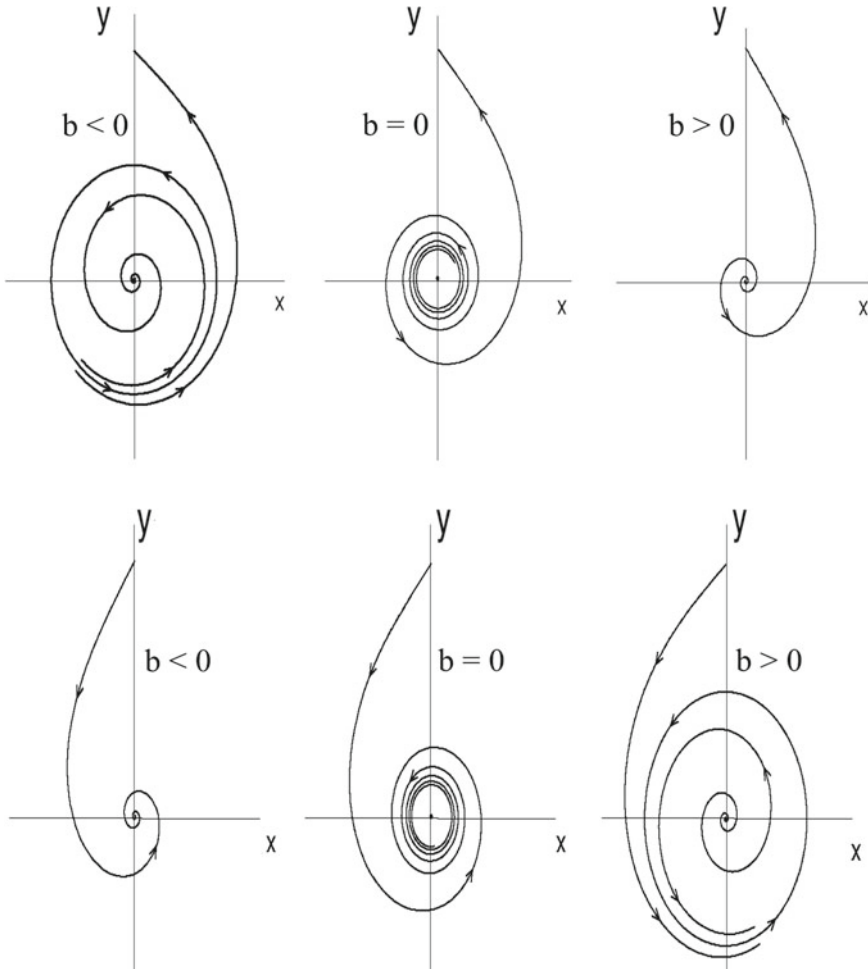


Fig. 2.5 (Upper row) Supercritical and (lower row) subcritical Andronov–Hopf bifurcations for $\epsilon = -1$ and $\epsilon = 1$, respectively

are converted into an unstable focus, while in a subcritical Andronov–Hopf bifurcation, a stable focus is converted into a stable limit cycle.

The application of an external harmonic force can induce bistability in the inverse subcritical Andronov–Hopf bifurcation [3], where decreasing parameter b gives rise to the coexistence of a stable equilibrium in the origin and a stable limit cycle. This case will be considered in Sect. 2.2.7.

In addition, the appearance of bistability in coupled oscillators was associated with the supercritical Andronov–Hopf bifurcation [4].

2.1.4 Neimark–Sacker Bifurcation

A Neimark–Sacker bifurcation is a critical point where a fixed point changes stability via a pair of complex eigenvalues with unit modulus, and a closed invariant curve arises. In fact, the Neimark–Sacker bifurcation is an analog of the Andronov–Hopf bifurcation in discrete systems. The Neimark–Sacker bifurcation can be either supercritical or subcritical. While in a supercritical Neimark–Sacker bifurcation a stable focus loses stability and a quasi-cycle (closed invariant curve) is born, in a subcritical Neimark–Sacker bifurcation, a stable focus loses stability as a control parameter is increased. The qualitative diagrams of the subcritical and supercritical Neimark–Sacker bifurcations are illustrated in Fig. 2.6.

Let us consider a two-dimensional smooth map $M(x, y, b)$ (b being a control parameter) with a focus fixed point $p^* = (x^*, y^*)$, for which the Jacobian matrix DM in p^* has complex conjugate eigenvalues. If the eigenvalues are in modulus less than one (for $b < 0$), the focus is stable and the trajectories in a small neighborhood of p^* belong to spirals and tend to p^* . Whereas, if the eigenvalues are in a modulus greater than one (for $b > 0$, the focus is unstable and local trajectories still belong to spirals, however they have a different asymptotic behavior. The crossing of the complex eigenvalue through the unitary circle $r = \sqrt{x^2 + y^2} = 1$ occurs in the Neimark–Sacker bifurcation at $b = 0$.

Astakhov et al. [4] investigated the bifurcational mechanism of multistability in a van der Pol oscillator through a subcritical Neimark–Sacker bifurcation. They found that the attracting basin boundaries are determined by stable and unstable invariant manifolds of a saddle two-dimensional torus.

2.1.5 Multiple Limit Cycle Bifurcation

In a multiple limit cycle bifurcation two or more stable periodic orbits are created. There are four principal types of bifurcations leading to the birth of limit cycles.

- Multiple Hopf bifurcations from a centre or a focus.
- Separatrix cycle bifurcations from homoclinic or heteroclinic orbits.

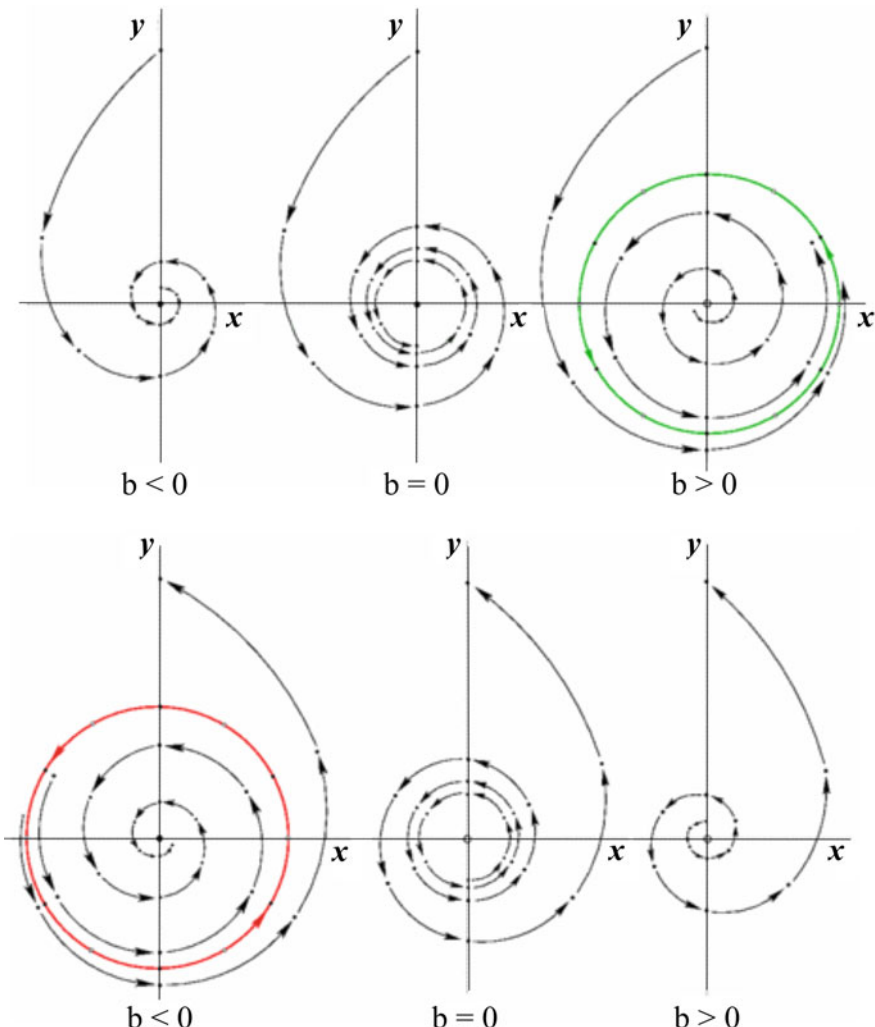


Fig. 2.6 Graphical illustration of Neimark–Sacker bifurcations in a two-dimensional map. (Upper row) Supercritical Neimark–Sacker bifurcation. At $b = 0$ a stable spiral fixed point loses stability and for $b > 0$ an attracting closed invariant curve (green) arises, surrounding the repelling fixed point. (Lower row) Subcritical Neimark–Sacker bifurcation. A repelling closed invariant curve surrounds a stable fixed point for $b < 0$. As b is increased, the size of the closed curve decreases and shrinks merging with the fixed point at $b = 0$, giving rise to a repelling focus. For $b > 0$ the fixed point is unstable



Fig. 2.7 Multiple limit cycle bifurcations in which two periodic orbits are born. The stable limit cycles are shown by the solid lines. (Left) Fixed point, (middle) fixed point and limit cycle, (right) fixed point and two limit cycles

- Global center bifurcation from a periodic annuli.
- Limit cycle bifurcations from multiple limit cycles [5].

The appearance of two limit cycles in the multiple limit cycle bifurcation is illustrated in Fig. 2.7.

2.1.6 Infinite-Period Bifurcation

One of global bifurcations is an infinite-period bifurcation which can give rise to multistability. In this bifurcation, a limit cycle collides simultaneously with a saddle node and a saddle point [6]. To understand how the infinite-period bifurcation arises, let us consider a two-dimensional dynamical system with state variables $x = r \cos \theta$ and $y = r \sin \theta$. In polar coordinates r and θ , the system is described by

$$\dot{r} = r(1 - r^2), \quad (2.6a)$$

$$\dot{\theta} = b - r \cos \theta, \quad (2.6b)$$

where b is a control parameter.

In Fig. 2.8 we plot the phase-space trajectories below (left), at (middle), and above (right) the infinite period bifurcation. The trajectories start at different initial conditions, one from the vicinity of the unstable focus in the origin and another outside of the unit cycle. For $b > 1$, these trajectories go to the saddle point (dot in the left panel). The saddle point and saddle node collide at $b = 1$ giving rise to a stable limit cycle $r = 1$ (green circle in the middle panel). For $b < 1$, there are three fixed points: an unstable focus at the origin ($x = y = 0$), a saddle point (upper dot), and a stable node (lower dot) on the unit circle $r = 1$ with coordinates $(b, +\sqrt{1 - b^2})$ and $(b, -\sqrt{1 - b^2})$, respectively (right panel).

The infinite period bifurcation gives rise to multistability in time-delayed dynamical systems (see Sect. 2.2.6).

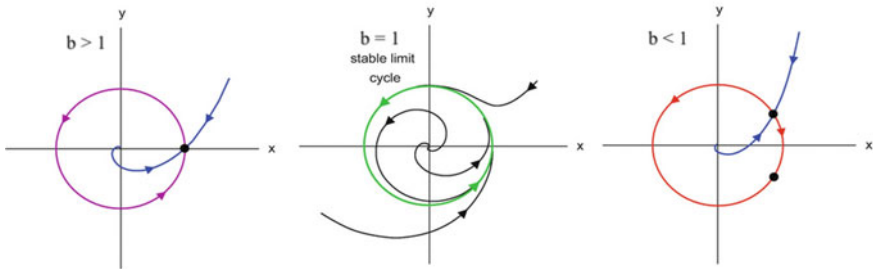


Fig. 2.8 Emergence of an infinite period bifurcation. (Left) Phase-space trajectory below the bifurcation. A stable limit cycle (blue) coexists with a saddle point (dot). (Middle) Homoclinic orbit (green) is created at the critical value. The speed of the oscillation slows down and the period approaches infinity. (Right) Beyond the critical value, two fixed points emerge continuously from each other on a limit cycle (red) to disrupt the oscillation and form two saddle points (dots)

2.1.7 Inverse Gluing Bifurcation

A gluing bifurcation is a codimensional-two bifurcation when two homoclinic orbits collide with each other. Let us suppose that for a certain parameter a dynamical system has a pair of homoclinic orbits. There are two parameters unfolding locally such that if one parameter is zero, one of the homoclinic orbits exists, and if another parameter is zero, another homoclinic orbit exists, whereas both orbits exist at the intersection of the two axes.

A gluing bifurcation was observed in many systems, including hydrodynamics [7], nematic liquid crystals [8], and reaction-diffusion models [9]. It was also found in experiments with liquid crystal flow [10], Taylor-Couette flow [11], optothermal nonlinear device [12], electronic van der Pol oscillator [13], and Chua oscillator [14]. Interestingly, the gluing bifurcation was identified in human heart rate variability [15] in patients with increased arrhythmia.

An inverse gluing (or splitting) bifurcation is schematically illustrated in Fig. 2.9, where one can see how two stable periodic orbits are born. Before this bifurcation, there is a stable limit cycle (left panel). As a control parameter b is increased, the limit cycle doubles at a saddle point S (dot in the middle panel). After the bifurcation, the limit cycle is split into two limit cycles (right panel).

The emergence of bistability in an inverse gluing bifurcation can also be illustrated with an example of a simple nonautonomous system

$$\dot{x} = -4x(x^2 - 1) + 4c, \quad (2.7)$$

where $c = A \cos(\omega t)$ (A and ω being the modulation amplitude and frequency).

Figure 2.10 shows the trajectories in the phase space of c and x . For small modulation amplitudes ($\omega^* < 4.4$), there is a stable limit cycle which intersects with $x = 0$ in the fixed points c_1 and c_2 . As ω is increased, the attractor grows in size, so that the distance between c_1 and c_2 increases. When the modulation frequency approaches

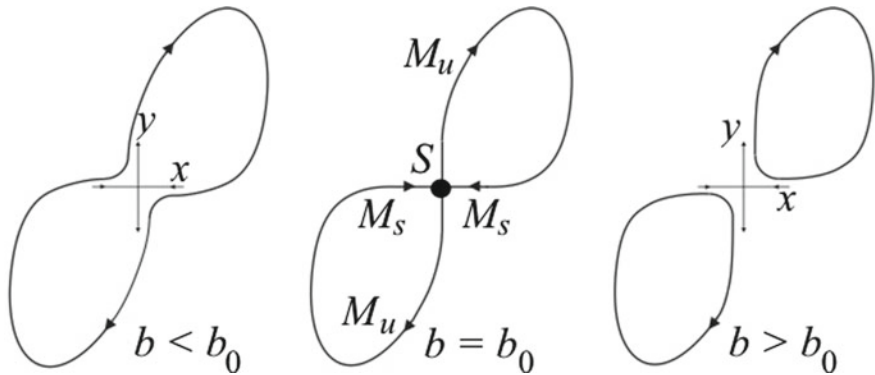
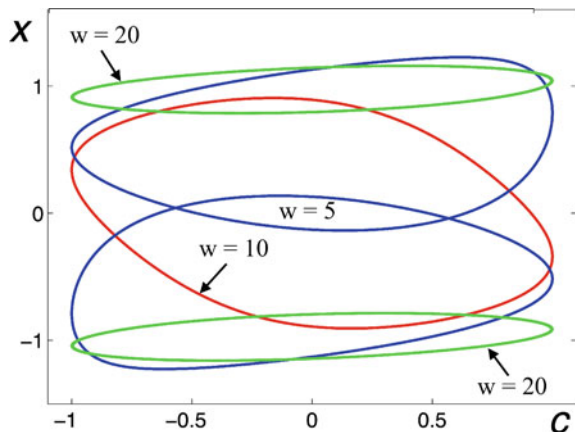


Fig. 2.9 Schematic illustration of an inverse gluing (splitting) bifurcation. (Left) For $b < b_0$ there is only one stable limit cycle. (Middle) At $b = b_0$ the limit cycle doubles giving rise to a saddle point S (dot) with stable (M_s) and unstable (M_u) manifolds. (Right) For $b > b_0$ the limit cycle splits into two stable periodic orbits symmetric over the origin

Fig. 2.10 Schematic representation of an inverse gluing (splitting) bifurcation in the parametrically modulated logistic map (Eq. 2.7). When the frequency ω is increased, the homoclinic orbit is separated into two orbits giving rise to bistability



the critical value $\omega^* = 4.4$, the single limit cycle splits into two coexisting stable limit cycles in the inverse gluing bifurcation.

2.1.8 Symmetry-Increasing Bifurcation

A symmetry-increasing bifurcation is a bifurcation in a symmetric system, associated with spontaneous symmetry breaking, i.e. with new attractors of higher symmetry. When a bifurcation parameter is changed, these attractors increase in size and merge leading to a single attractor with greater symmetry [16]. This bifurcation appears in weakly coupled systems giving rise to the coexistence of chaotic attractors outside

the invariant manifold. As a control parameter is changed, the coexisting attractors merge into a new attractor, symmetric with respect to the invariant manifold, and then this attractor becomes hyperchaotic.

A symmetry-increasing bifurcation is defined as follows. Assuming that the Lie group² Γ acts linearly on \mathbb{R} and that $f: \mathbb{R}^n \rightarrow \mathbb{R}^n$ is continuous and commutes with Γ , for an f -invariant subset A , the symmetry of A to be the subgroup is defined as

$$\Sigma_A = \{\gamma \in \Gamma : \gamma A = A\}, \quad (2.8)$$

where A consists of a single point and Σ_A is just the isotropy group of that point.

Assuming also that f depends on a parameter λ and that A_λ is an attractor for f_λ , we say that f has a *symmetry-increasing bifurcation* at $\lambda = \lambda_0$ if

$$\begin{aligned} \Sigma_\lambda &= \Sigma_1 \text{ for } \lambda < \lambda_0, \\ \Sigma_\lambda &= \Sigma_2 \text{ for } \lambda > \lambda_0, \\ \Sigma_2 &\supset \Sigma_1. \end{aligned} \quad (2.9)$$

Yanchuk and Kapitaniak [17] found the coexistence of chaotic attractors in bidirectionally weakly coupled Rössler oscillators. As a control parameter is increased, the attractors merge in a symmetry-increasing bifurcation creating an attractor symmetric to the invariant manifold control, just before the system undergoes a chaos-hyperchaos transition. After the symmetry-increasing bifurcation, the system exhibits intermittency-like behavior on the new attractor with a relatively low number of switches between the former coexisting attractors. The attractors not located at the invariant manifold can exhibit dynamical behavior similar to bubbling and on-off intermittency previously observed for the attractors located at the invariant manifold.

2.2 Mechanisms Leading to Multistability

There are many mechanisms leading to multistability in dynamical systems, and they are different in different systems. In this section, we discuss the most important mechanisms leading to multistability, such as homoclinic tangency, small dissipation, phase locking in coupled oscillators, time delay, and external forcing.

² In the group theory, a Lie group (named after Sophus Lie) is a real or complex differentiable manifold, in which group operations (multiplication and inverse) are differentiable or analytic functions, as the case may be. The Lie groups are important in mathematical analysis, physics, and geometry, since they help to describe symmetry of analytic structures.

2.2.1 Homoclinic Tangencies

One of the most significant mechanisms of multistability is the existence of a diffeomorphism near a homoclinic tangency in a two-dimensional manifold, leading to infinitely many stable periodic orbits. This mechanism was studied by USA mathematician Sheldon Newhouse, who in 1974 discovered a new phenomenon named after him *Newhouse phenomenon*. He demonstrated the existence of an infinite set of attractors (sinks) for a residual quantity in the space of diffeomorphisms of compact two-dimensional surfaces [18–20]. The construction was based on the existence of *homoclinic tangencies*, i.e. non-transverse cuts of stable and unstable manifolds of a periodic point. Later, this result was extended to higher dimensional systems [21]. It was also proven [22] that in addition to infinitely many sinks, infinitely many strange attractors coexist near homoclinic tangencies.

In the group theory, a *diffeomorphism* is a certain type of invertible mapping between smooth manifolds. Below we give mathematical definitions of various diffeomorphisms.

Definition 2.1 (*Diffeomorphism*) Given two manifolds (M and N), a differentiable map $f : M \rightarrow N$ is called a diffeomorphism if it is a bijection (one-to-one correspondence) and its inverse $f^{-1} : N \rightarrow M$ is differentiable as well. If these functions are r times continuously differentiable, f is called a C^r -diffeomorphism.

Definition 2.2 (*Diffeomorphic manifolds*) Two manifolds (M and N) are diffeomorphic ($M \cong N$) if there is a diffeomorphism f from M to N . They are C^r diffeomorphic if there is an r -times continuously differentiable bijective map between them, whose inverse is also r times continuously differentiable. Manifolds can be diffeomorphic only if they have the same dimension.

Definition 2.3 (*Diffeomorphic subsets of manifolds*) Given a subset X of a manifold M and a subset Y of a manifold N , a function $f : X \rightarrow Y$ is said to be smooth if for all $p \in X$ there is a neighborhood $U \subset M$ of p and a smooth function $g : U \rightarrow N$ such that the restrictions agree $g|_{U \cap X} = f|_{U \cap X}$ (note that g is an extension of f). f is said to be a diffeomorphism if it is bijective, smooth and its inverse is also smooth.

Definition 2.4 (*Group of diffeomorphisms*) The set of diffeomorphisms of a manifold M into itself forms a group called the group of diffeomorphisms M and is denoted by $\text{Diff}(M)$.

Diffeomorphic manifolds and subsets of manifolds are schematically illustrated in Fig. 2.11.

According to Newhouse [19], the coexistence of infinitely many attracting periodic orbits is generic in certain open subsets of the space $\text{Diff}^k(M^2)$ of C^k diffeomorphisms, for any surface M^2 and any $k \leq 2$. These open sets exhibit several interesting phenomena, such as homoclinic tangencies and an exponential growth of the number of periodic orbits.

A *homoclinic tangency* is a non-transverse intersection of a stable and an unstable manifold of a hyperbolic saddle. Figure 2.12 shows a schematic plot of the formation

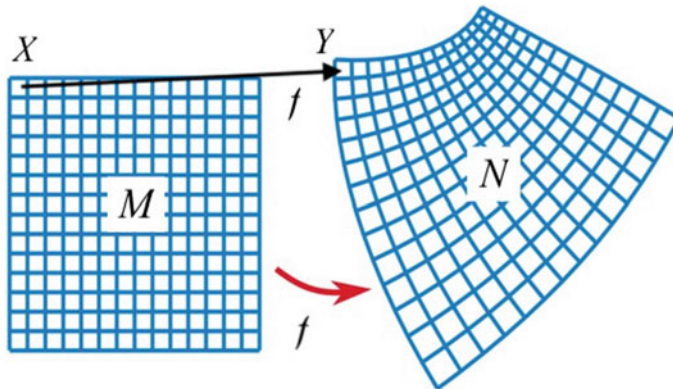
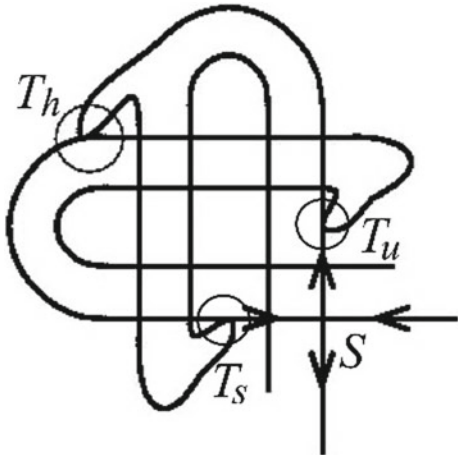


Fig. 2.11 C^2 -diffeomorphism f of manifolds M and N and their subsets X and Y . Each cell in M is mapped into a corresponding cell in N

Fig. 2.12 Homoclinic tangency T_h and transverse intersections (T_s and T_u) of stable and unstable manifolds near a saddle S . All tangencies are marked by circles



of a homoclinic tangency T_h in the vicinity of a hyperbolic saddle S , as well as two transverse intersections (T_s and T_u) of stable and unstable manifolds, respectively. The unfolding of homoclinic tangencies is one of the main bifurcation mechanisms leading to multistability [23].

2.2.2 Weak Dissipation

Another dynamical mechanism leading to multistability is to add a small amount of dissipation to a conservative system. Conservative systems are known to have a large number of coexisting invariant sets (periodic orbits, invariant tori and cantori). A

small dissipation introduced to a conservative system converts some of the invariant sets into attractors. This mechanism of multistability was investigated in a kicked single rotor, the Hénon map, and an optical cavity map [24–26].

Conservative systems are characterized by two types of dynamics: regular motion and Kolmogorov–Arnold–Moser (KAM) tori in the hierarchy of islands³ embedded into a phase-space chaotic sea. Introducing a small damping turns the islands into sinks and the permanent chaotic motion into transient chaos [27]. By such a way, one can obtain a system with an arbitrarily large number of coexisting attractors since the number of attractors scales roughly with the damping factor [25]. This amazing phenomenon referred to as *extreme multistability* will be described in Chap. 7. The dynamics of this class of multistable systems is dominated by a regular motion; almost all attractors are periodic orbits with mainly low periods. Since high-period orbits have very small basins of attraction, it is very difficult to find them.

Forced rotor map. Now, let us demonstrate the emergence of multistability in a weakly dissipative system with a paradigmatic example of the standard map of a forced rotor. In particular, we will consider a two-dimensional map derived from ordinary differential equations [28] of a mechanical pendulum without gravity, when the pendulum is periodically (with period T) kicked at times nT ($n = 1, 2, \dots$). The resulted forced rotor map is given as [25]

$$\begin{aligned} x_{n+1} &= x_n + y_n \mod 2\pi, \\ y_{n+1} &= (1 - \nu)y_n + f_0 \sin(x_n + y_n), \end{aligned} \tag{2.10}$$

where x and y are related to the phase and angular velocity of the rotor after successive kicks. The map dynamics depends on both the kick strength f_0 and the damping parameter $\nu \in [0, 1]$.

For zero damping parameter, the map in Eq. 2.10 is a conservative Hamiltonian system whose phase space represents a chaotic sea with periodic islands inside (see Fig. 2.13). The undamped rotor exhibits infinitely many marginally stable periodic orbits.

On the other hand, for a very strong damping ($\nu = 1$) the rotor contains only two coexisting stable periodic orbits which are in antiphase, as seen from the left panel in Fig. 2.14. When small damping is added, the marginally stable periodic orbits are converted into sinks and stable limit cycles, giving rise to multistability, as illustrated in Fig. 2.15. Although in the conservative case the number of marginally stable orbits is infinite, the number of coexisting attractors in the dissipative system is finite.

The coexisting attractors in this class of systems are usually either fixed points or low-periodic orbits [29], although we cannot preclude the existence of chaotic attractors. In spite of the simplicity of the coexisting attractors, the structure of their basins of attraction is very complex, so that the basin boundaries propagate along

³ The KAM islands are inaccessible regions in phase space where the orbit cannot leave them. They are typical for conservative systems. When the system becomes hyperbolic, the KAM islands are usually destroyed.

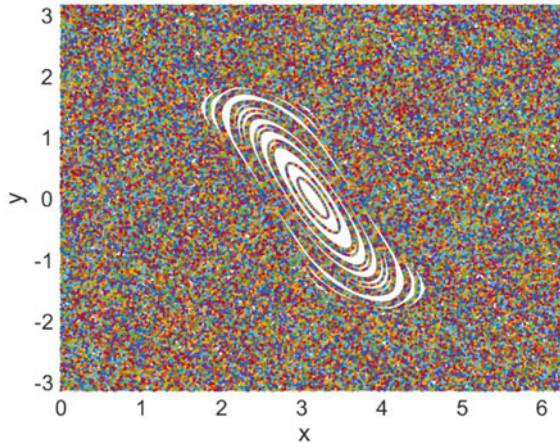


Fig. 2.13 Phase-space plot of the undamped rotor ($\nu = 0$) in Eq. 2.10 at $f_0 = 3$ representing an infinite number of periodic orbits in the chaotic sea

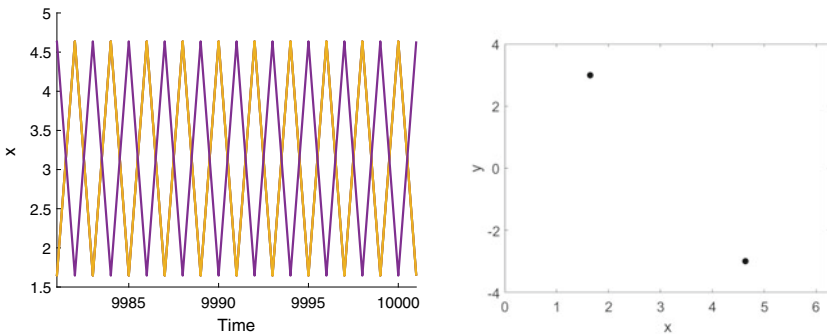


Fig. 2.14 (Left) Time series and (right) attractors in the phase space of the rotor with a very high damping ($\nu = 1$) at $f_0 = 3$. Two periodic orbits coexist and they are in antiphase. The attractors are plotted using 400 initial conditions randomly chosen in the $[-\pi, \pi]$ region

the whole phase space. Due to the complexly interwoven basins of attraction, such systems are highly sensitive to a small amount of noise [30, 31].

Notably, weakly dissipative systems can be considered as an important class of highly multistable systems occurring in many mechanical systems, such as mechanical oscillators [32] and suspension bridges [33]. It can be argued that these two attributes, namely, accessibility to many different states and high sensitivity, are advantages in the sense that they are suitable for simple control of complex systems. However, the transition between different stable states is a delicate problem, since long-term chaotic transients are located near the basin boundary. This problem is related to the migration between different coexisting states and their stability [34, 35].

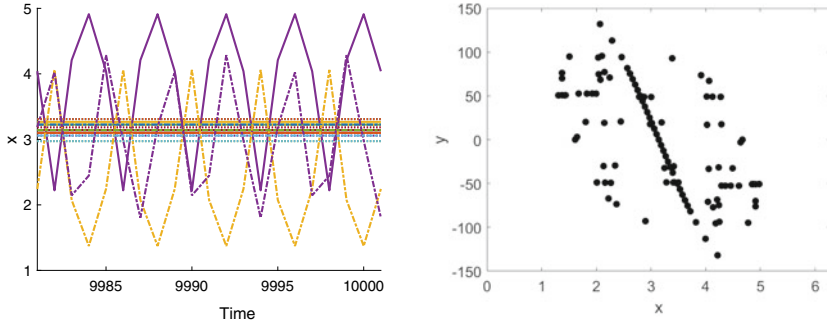


Fig. 2.15 (Left) Time series and (right) phase space of the rotor with a very small damping ($\nu = 0.02$) at $f_0 = 3$. The attractors in the phase space are constructed using 400 initial conditions randomly chosen in the $[0, 2\pi] \times [-200, 200]$ region. For better visualization, only 20 random initial condition are used to plot the time series in the left panel

2.2.3 Clustering

Considering two or more coupled systems, we can find out multistability which can naturally appear due to increasing complexity of the system. One of the mechanisms for coexisting attractors in coupled systems is the formation of clusters [36, 37]. Each attractor in such a system contains a different number of clusters depending on the initial conditions.

Coupled map lattice. To illustrate the emergence of multistability in coupled systems, let us now consider a simple example of a globally coupled map lattice (CML) which was introduced by Kaneko [36, 37]:

$$x_{n+1}(i) = (1 - \epsilon)f(x_n(i)) + \frac{\epsilon}{N} \sum_{j=1}^N f(x_n(j)), \quad (2.11)$$

where n is a discrete time step, ϵ is a coupling strength, $i = 1, 2, \dots, N$ is the index for N elements, and $f(x) = 1 - ax^2$ (a being a nonlinear parameter) is the logistic function. Attractors in this CML are classified by the number of synchronized clusters k and by the number of elements for each cluster N_j . According to Kaneko [35], the CML in Eq. 2.11 exhibits the coexistence of at least

$$\frac{N!}{\prod_{i=1}^k N_i!} \prod_{\text{sets of } N_i=N_j} \frac{1}{m_c!}$$

attractors for each clustering condition, where m_c is the number of clusters with the same value of N_j .

In a two-cluster case, attractors are encoded by a single number N_1 since $N = N_1 + N_2$, while in a three-cluster case, attractors are encoded by both N_1 and N_2 . If each element i is decreased, the number of attractors for each clustering condition exponentially increase. Even in the simplest two-cluster case, there are

$$\frac{N!}{N_1!(N_1!(N - N_1!))}$$

attractors for each N_1 condition.

Wiesenfeld and Hadley [38] studied multistability formation in arrays of coupled Josephson junctions and coupled circle maps. They found that in both cases the number of stable limit cycles can reach $(N - 1)!$ (N being the number of oscillators). The attractor stability is extremely sensitive to noise which induces switching among the coexisting states.

Osipov and Sushchik [39] observed the emergence of a crowd of synchronized clusters in an array of coupled Van der Pol oscillators with frequency mismatch. Each oscillator was diffusively coupled with its two nearest neighbors, and a cluster was denoted as a set of coupled oscillators having the same mean frequency. They found that the number of attractors increase dramatically with the number of oscillators. The cluster formation was experimentally confirmed in coupled electrochemical oscillators [40].

Spiral waves. The clustering was also observed in spatially extended continuous systems. For example, numerical simulations of an extended FitzHung–Nagumo system allowed Postnov et al. [41] to reveal the coexistence of a variety of spiral and travelling waves in a network of potassium-driven neurons.

The dynamics of a single FitzHung–Nagumo neuron is modelled by the following equations

$$\epsilon \dot{x} = x - x^3/3 - y, \quad (2.12a)$$

$$\tau(x)\dot{y} = x + a - Cz, \quad (2.12b)$$

$$\dot{z} = \alpha\Psi(x) - \beta z, \quad (2.12c)$$

where ϵ regulates the time scale separation between fast activator x and slow inhibitor y , $\tau(x)$ is an additional time scale to independently control time scales associated with firing (high x) and refractory (low x) states, $a = a_0 + \sqrt{2D}\xi(t)$ (ξ being zero-mean Gaussian noise of intensity D) is a noisy parameter related to ionic currents, z describes the depolarization effect of the extracellular concentration with factor C (second activator), and β is the rate ion losses. Here, $\Psi(x) = 0.5(1 + \tanh(x/x_s))$ is the sigmoidal function with coefficient α , which tends to 0 for $x \ll 0$ and to 1 for $x \gg 0$, and x_s scales the transition between the states.

The enlarge cell structure of the neural network arrangement is illustrated in the right panel in Fig. 2.16. The excitable neurons (x, y) are located in the non-excitatory field z which diffuses in the remaining space of the two-dimensional medium. The active neurons only interact via the common variable z , while the exterior medium

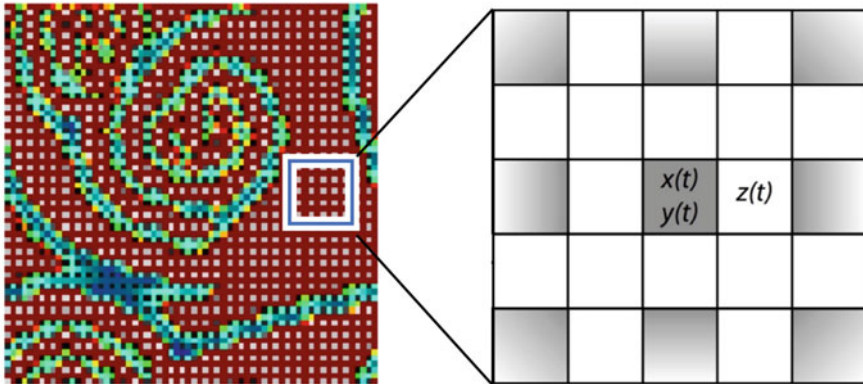


Fig. 2.16 Noise-induced inverted spiral waves with polarized states which appear in the FinzHung–Nagumo neural network of excitable units ($x(t)$, $y(t)$) coupled with z -cells between them. Adapted from [41] with permission from the American Physical Society ©2009

is locally coupled with itself and affected by other neurons. For certain parameter values, the neurons in the network group in clusters forming waves, spots, and spirals, as well as propagating ring-like patterns. These patterns can be distinguished in the left panel in Fig. 2.16. The rotating spirals and target waves run from outward to the center and are called *antispirals* and *antiwaves*. Similar spirals occur in reaction-diffusion systems in the spatially extended Belousov–Zhabotinsky reaction [42].

2.2.4 Phase Multistability

A particular type of multistability, phase multistability, arises in coupled oscillators. *Phase multistability* is the coexistence of multiple synchronous states having different phase shifts between oscillations. In this section, we demonstrate this type of multistability with the simplest case of two coupled pendula which can be synchronized either in-phase or anti-phase depending on the initial conditions. This type of multistability is called *phase bistability*.

Coupled pendula. Let us consider two identical pendula with rods of length l and masses m coupled by a spring with stiffness k to separate them (Fig. 2.17). The pendula displacements x and y are described by the following equations of motion

$$m\ddot{x} = -mg \frac{x}{l} - k(x - y), \quad (2.13a)$$

$$m\ddot{y} = -mg \frac{y}{l} - k(y - x), \quad (2.13b)$$

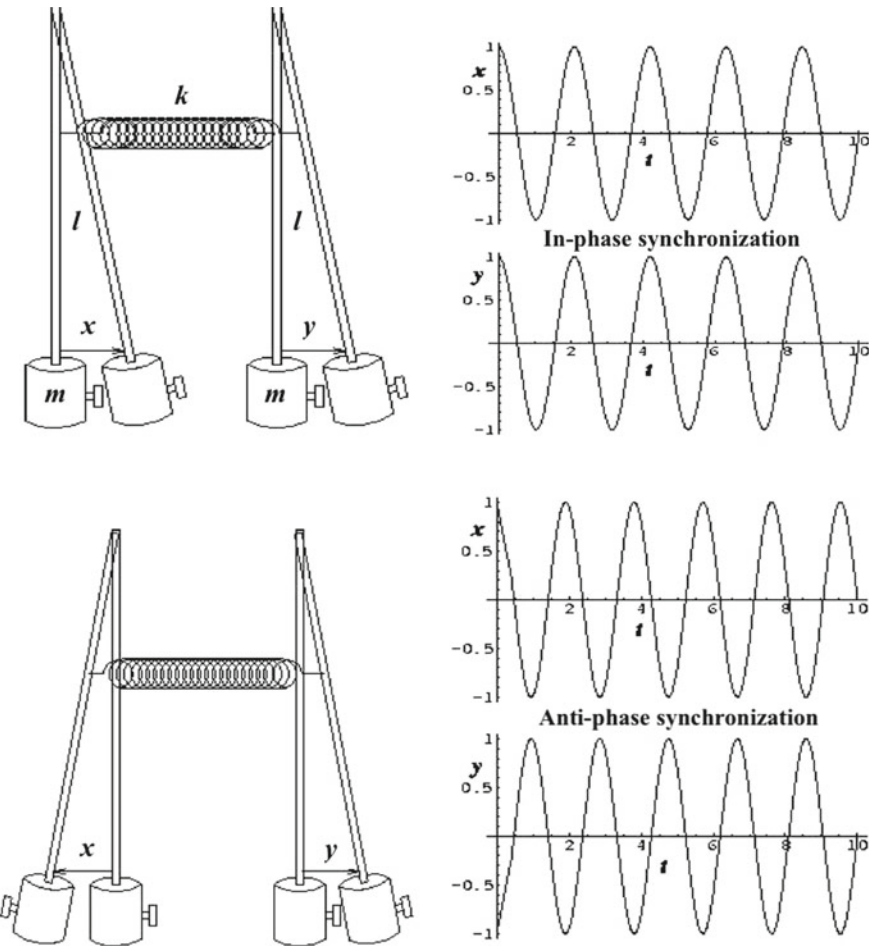


Fig. 2.17 Phase bistability in two coupled pendula. (Upper) In-phase synchronization for initial condition ($x = y$). (Lower) Anti-phase synchronization for initial condition ($x = -y$)

where g is the acceleration of gravity. Since the pendulum natural frequency is given by $\omega_0^2 = g/l$, Eq. 2.13 can be rewritten as

$$\ddot{x} + \omega_0^2 x = -\frac{k}{m}(x - y), \quad (2.14a)$$

$$\ddot{y} + \omega_0^2 y = -\frac{k}{m}(y - x). \quad (2.14b)$$

Summing Eqs. 2.14a and 2.14b and subtracting Eq. 2.14b from Eq. 2.14a, we have

$$\ddot{x} + \ddot{y} + \omega_0^2(x + y) = 0, \quad (2.15a)$$

$$\ddot{x} - \ddot{y} + \omega_0^2(x - y) + \frac{2k}{m}(x - y) = 0. \quad (2.15b)$$

Changing the variables as $x + y = X$ and $x - y = Y$, we obtain two equations of harmonic motion

$$\ddot{X} + \omega_0^2 X = 0, \quad (2.16a)$$

$$\ddot{Y} + \left(\omega_0^2 + \frac{2k}{m}\right) Y = 0, \quad (2.16b)$$

with natural frequencies ω_0 and $(\omega_0^2 + 2k/m)$.

Next, we will consider two variants of initial conditions leading to different stable synchronous states, in-phase and anti-phase (Fig. 2.17).

In-phase synchronization. If the pendula are initially located at the same side (left or right), i.e. $Y = 0$ ($x = y$), the pendula motion is governed by Eq. 2.16a, and they oscillate as a single independent pendulum, so that the spring has no effect (upper row in Fig. 2.17). In this case, both pendula oscillate in-phase and the distance between them is always constant, as shown in the upper panel in Fig. 2.17. The spring length in this case is constant.

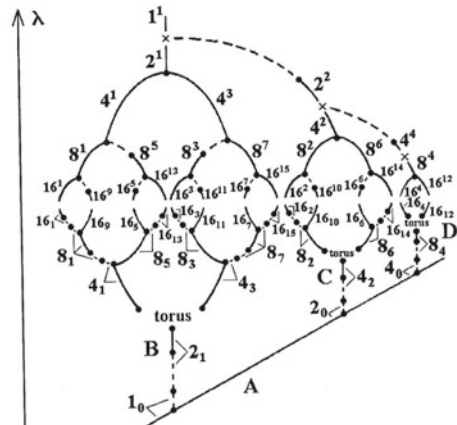
Anti-phase synchronization. If the initial condition is chosen so that the pendula start to oscillate from different sides (one from the left and another from the right), i.e. $X = 0$ ($x = -y$), the motion is regulated by Eq. 2.16b and the pendula synchronize in anti-phase, as illustrated in the lower panel in Fig. 2.17. The oscillation frequency in this case is higher than the natural frequency of the independent pendulum, since the spring is stretched and compresses.

To observe phase multistability in coupled pendula, Dudkowski et al. [43] carried out an experiment with four double pendula located at the same oscillating platform. As a result, they found the coexistence of multiple phase-locked states with different relationships between oscillation phases.

Period-doubling systems. Phase multistability naturally emerges in diffusively coupled period-doubling systems [44–46]. In these systems the number of synchronous stable states increase when more subharmonics of the fundamental frequency appear in the power spectrum.

Let us illustrate how phase bistability arises in a simple system of two coupled oscillators. If both subsystems oscillate in a period-1 regime with period T_0 , there is only one peak in the power spectrum at fundamental frequency ω_0 , and only one phase difference ϕ_0 exists between their phases. However, in a period-2 regime, the power spectrum contains two peaks, one at ω_0 and another at its subharmonic frequency $\omega_0/2$. In this case, two phase differences are possible, $\phi_0/2$ and $(\phi_0 + 2\pi)/2$. A 2π interval corresponds to one period of the period-2 regime ($2T_0$). Consequently, in a p -periodic regime there are 2^p phase differences distributed over interval $[0, 2\pi]$, i.e. $\delta\phi = (\phi_0 + 2\pi i)/2^p$ ($i = 0, 1, 2, \dots, 2^p - 1$). This means that a period- p regime

Fig. 2.18 Bifurcation diagram of coupled logistic maps (Eq. 2.18) representing the coexistence of period-bubbling branches of attractors for $k = 0.006$. The solid and dashed lines represent stable and unstable regimes, respectively. A, B, C, and D are branches of attractors. The bifurcations are marked by dots, and the numbers indicate the orbit periods. Reprinted from [52] ©2003 with permission from Elsevier



can give rise to p stable fixed points in the $\dot{\phi}/(\delta\phi)$ phase space. This type of multistability is structurally stable with respect to the mismatch between fundamental frequencies of coupled oscillators [47].

Phase multistability was found in a variety of discrete and continuous period-doubling systems with dissipative and inertial coupling, including logistic maps [48–52], Hénon maps [53], Van der Pol oscillators [3], etc. To illustrate how multistability appears in such systems, let us consider the simplest case of two dissipatively coupled maps [52]

$$\begin{aligned} x_{n+1} &= f(x_n) + k[f(y_n) - f(x_n)], \\ y_{n+1} &= f(y_n) + k[f(x_n) - f(y_n)], \end{aligned} \quad (2.17)$$

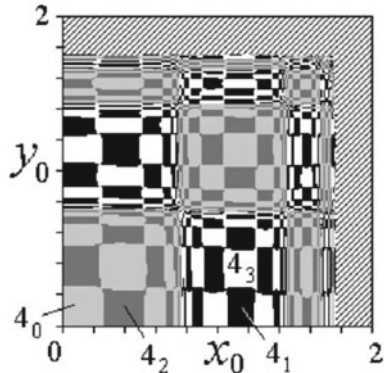
where f is the map function and k is the coupling strength. This kind of coupling can be found in population dynamics, where x and y are species (for example, fishes or birds) located in different places and migrated from one location to another, and $0 < k < 1$ represents a fraction of the migrated specie. If f is a logistic function, Eq. 2.17 takes the following form:

$$\begin{aligned} x_{n+1} &= \lambda - x_n^2 + k(x_n^2 - y_n^2), \\ y_{n+1} &= \lambda - y_n^2 + k(y_n^2 - x_n^2). \end{aligned} \quad (2.18)$$

The bifurcation diagram of x with respect to the control parameter λ is shown in Fig. 2.18. The diagram obtained by using different initial conditions contains four branches: A, B, C, and D. The branch B begins with a period-2 cycle, branch C with a period-4 cycle, and branch D with a period-8 cycle. The states in branch A are in the in-phase regime, while the states in other branches are in the out-of-phase regime.

The basins of attraction of the coexisting attractors exhibit a chess-like structure shown in Fig. 2.19. When the control parameter approaches the Feigenbaum period-doubling accumulation point, a very large number of stable periodic orbits appear

Fig. 2.19 Basins of attraction of coexisting cycles $4^0, 4^1, 4^2$, and 4^3 for $\lambda = 1.3$ and $k = 0.008$ of Eq. 2.18. Reprinted from [52] ©2003 with permission from Elsevier



[50]. Because of the flip properties, the Feigenbaum attractor at this point coexists with an infinite set of unstable periodic orbits, and due to the coupling, the arbitrarily large number of orbits become stable [51]. Studying the emergence of multistability in two coupled Van der Pol oscillators, Astakhov and colleagues [3] found that asymmetrical repulsive coupling is responsible for the appearance of an Andronov–Hopf bifurcation which gives rise to the coexistence of phase-shifted periodic orbits.

A more sophisticated case of phase multistability was observed in spatially extended systems with coexisting running or rotating waves which propagate along a discrete medium with a constant phase velocity [54–57]. This type of phase multistability was first discovered in a chain of N weakly coupled oscillators. The coupling is so weak that each oscillator is reduced to a single variable that describes the phase as

$$\dot{\phi} = \omega_i + H_i(\phi_1 - \phi_i, \dots, \phi_N - \phi_i), \quad i = 1, \dots, N, \quad (2.19)$$

where ϕ_i is the phase of i th oscillator, ω_i is its fundamental frequency of the uncoupled case, and H_i is a 2π -periodic function. Equation 2.19 has periodic solutions in the form $\phi_i(t + T) = \phi_i(t) + 2\pi$. If the oscillators in the chain is coupled with their nearest neighbors, each solution corresponds to a traveling wave.

Coexisting running waves were discovered in a chain of diffusively coupled period-doubling oscillators with the same amplitude and frequency, but their phases were locked with different phase shifts [56]. In a ring of unidirectionally coupled chaotic oscillators, phase multistability manifests itself as the coexistence of rotating waves with different phase shifts [57].

In this regard, an interesting question arises: Is there a biological analog of such rotating waves? The experiments of Kleinfeld et al. [58] gave a positive answer to this question. Using electrical potential imaging, they found rotating waves in the olfactory network of a terrestrial mollusc.

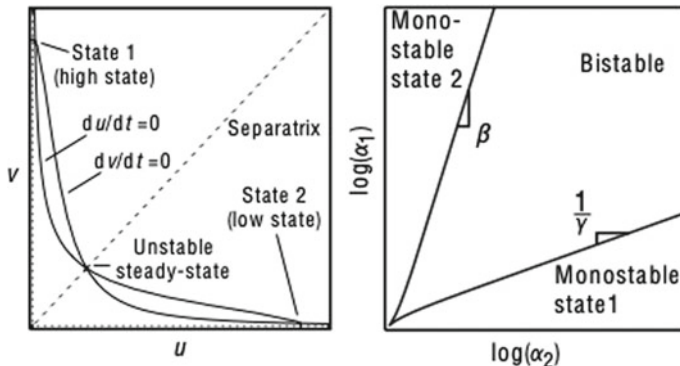


Fig. 2.20 (Left) Phase-space states and (right) two-parameter bifurcation diagram of Eq. 2.20. The bifurcation lines separate bistable and monostable regions and their slopes are determined by β and γ . Reprinted by permission from Springer Nature [63] ©2000

2.2.5 Positive Feedback

Cinquin and Demongeot [59] showed that positive feedback can induce multistability in a wide class of systems, and, in particular, in complex networks of signaling proteins [60–62]. A simple example of such a system is a biochemical rate equation model of gene expression [63]:

$$\dot{u} = \frac{\alpha_1}{1 + v^\beta} - u, \quad (2.20a)$$

$$\dot{v} = \frac{\alpha_2}{1 + u^\gamma} - v, \quad (2.20b)$$

where u and v are the concentrations of repressors 1 and 2, respectively, α_1 and α_2 are the effective rates of these repressors, and β and γ are the cooperativity of repression of promoters 2 and 1, respectively.

The phase-space states of Eq. 2.20 are schematically presented in Fig. 2.20. Due to a sigmoidal shape, the nullclines $\dot{u} = 0$ and $\dot{v} = 0$ intersect at three points, giving rise to one unstable and two stable steady states. A toggle with an initial condition above the separatrix is attracted to State 1, whereas a toggle starting below the separatrix goes to State 2.

The two-parameter bifurcation diagram in Fig. 2.20 shows the range of bistability. One can see that the size of the bistable region enlarges, as the repressor rates are increased. Since the slopes of the bifurcation lines are determined by β and γ , to obtain bistability at least one of the inhibitors must repress expression with cooperativity greater than one. Furthermore, higher cooperativity increases the system robustness, allowing weaker promoters to achieve bistability and producing a broader bistable region.

2.2.6 Delayed Feedback

The fact that a delayed feedback can induce bistability was first noted by Ikeda et al. [64] in 1979, who studied the light transmission through a Fabri–Perot cavity containing a two-level saturable absorber. They found a hierarchy of coexisting periodic orbits in numerical simulations of the delay-differential equation model with a time-delayed feedback [65]. In 1981, the Ikeda’s prediction was confirmed experimentally in an electro-optical bistable device with a computer delay [66]. Later, a very large number of multistable self-oscillatory modes were observed in a laser diode pumped hybrid bistable system with a large delay [67]. The main difference between the cases of large and small delays is the variety of coexisting attractors. When the delay time is much larger than the response time, there is a fundamental oscillation mode which exhibits period-doubling bifurcations, and there are also multiple harmonic oscillation modes, each of which exhibits a sequence of bifurcations. A systematic analysis of delayed-induced stability for oscillatory systems whose oscillations result from a supercritical Hopf bifurcation can be found in the book [68].

Here, we will show how a delayed feedback induces multistability in a nonlinear system. One of the methods was introduced by Pyragas [69] with the aim to control chaos. The method is based on stabilization of unstable periodic orbits embedded into a chaotic attractor by the construction of a special form of time-continuous perturbations, which do not change the form of a desired unstable periodic orbit, but under certain conditions can stabilize it. Pyragas considered a chaotic system governed by the delay ordinary differential equations

$$\begin{aligned}\dot{\mathbf{x}} &= \mathbf{Q}(\mathbf{x}, x) + F(f), \\ \dot{x} &= P(\mathbf{x}, x),\end{aligned}\tag{2.21}$$

where $\mathbf{x} \in \mathbb{R}^{n-1}$ describes the system variables which are not available or not of interest and only $x \in \mathbb{R}$ can be measured as the system output, $\mathbf{Q} : \mathbb{R}^{n-1} \times \mathbb{R} \rightarrow \mathbb{R}^{n-1}$ and $P : \mathbb{R}^{n-1} \times \mathbb{R} \rightarrow \mathbb{R}$.

To stabilize unstable periodic orbits, the delayed feedback signal $F(t)$ is applied as follows [70]

$$F(t) = \eta[x(t - \tau) - x(t)],\tag{2.22}$$

where η is the feedback strength and τ is the delay time. The form of the feedback function $F(t)$ can differ from that given by Eq. 2.22. For instance, it can take a simpler form $F(t) = \eta x(-\tau)$, or contains multiple delays, or a combination of delayed and instantaneous feedback. The equivalent structural scheme of the chaos control is presented in Fig. 2.21.

Let us consider now the simplest example of the delayed logistic map to demonstrate that the delayed feedback can stabilize not only a single periodic orbit, but also induce bistability. The map reads [71]

$$x_{n+1} = ax_n(1 - x_n) - \eta x_{n-k},\tag{2.23}$$

Fig. 2.21 Pyragas chaos control scheme with delayed feedback loop D. Part of the output signal is delayed with time τ and reinjected into the system with amplification factor η

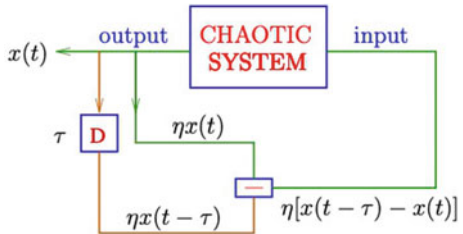
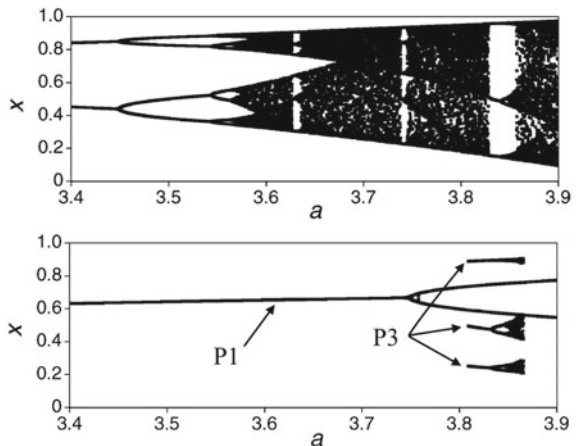


Fig. 2.22 Bifurcation diagrams of Eq. 2.23 (upper) without feedback ($\eta = 0$) and (lower) with delayed feedback ($\eta = 0.25$, $\tau = 1$). P1 and P3 are the coexisting period-1 and period-3 branches of attractors obtained using different initial conditions



where k is a discrete time delay. The bifurcation diagram of the map without feedback ($\eta = 0$) displays a cascade of period-doubling bifurcations to chaos depicted in the upper panel in Fig. 2.22. Whereas, a short delay feedback induces bistability in the form of the coexistence of two periodic orbits (P1 and P3) within a certain range of the control parameter, as seen in the lower panel in Fig. 2.22. We should note that the period-3 branch is very similar to the part of the bifurcation diagram in the upper panel (without feedback), while the feedback signal stabilizes the period-1 branch.

Delay-induced multistability was found not only in logistic maps [71, 72], but also in many discrete and continuous systems, including Mackey–Glass model [73], Rössler oscillator [74, 75], Van der Pol oscillator [76], CO₂ [71] and semiconductor [77] lasers, optoelectronic ring-coupled oscillators [78], biochemical oscillators [79], cortical rhythms [80], ecological [81], and neural [82–84] models. The requirement for the emergence of multistability in systems with delayed feedback is that the time delay be longer than an intrinsic time scale of the element experiencing feedback, such as the oscillation period or a response time.

The emergence of multistability in a class of excitable systems with time-delayed feedback was analyzed by Hizanidis et al. [85]. The dynamics of such systems without delay is regulated by a type of global bifurcation, in particular, a saddle-node bifurcation on a limit cycle, so-called *saddle-node infinite period bifurcation* (see Sect. 2.1.6). This bifurcation was first observed experimentally in a semiconductor

device [86], and then found in various models, including superlattices [87, 88] and lasers [89–91]. Due to the delay, the saddle possesses no longer two distinct eigenvalues (one positive, i.e. unstable, and one negative, i.e. stable) but infinitely many. Moreover, complex eigenvalues also exist. However, the eigenvalues responsible for the behaviour of the colliding homoclinic orbit play a key role.

In addition, the coexistence of attractors often occurs in coupled systems with delayed coupling. It was observed, for instance, in a ring of unidirectionally coupled FitzHun–Nagumo oscillators [92], globally coupled phase oscillators [93, 94], coupled chemical oscillators [95], coupled neurons [96–98], and coupled semiconductor lasers [99]. Some examples are given in Chaps. 3 and 4.

2.2.7 Periodic Forcing

Next, we will show how multistability can be induced by an additional resonant perturbation. Let us consider a classical example of the quadratic map [100]

$$x_{pn+j+1} = \lambda - x_{pn+1}^2 + \epsilon \cos(2\pi j/p), \quad j = 0, 1, \dots, p-1, \quad (2.24)$$

where λ is the map parameter, and ϵ and p are the modulation amplitude and period, respectively. Sahju and Varna [100] found that the modulation with period $p > 2$ posses a maximum of p noncomplementary attractors.

Figure 2.23 shows the bifurcation diagram of Eq. 2.24 obtained by varying initial condition. One can see two coexisting branches. The upper branch x_b^* yields the map values without modulation, while the lower branch x_d^* represents stable solutions induced by a period-2 modulation ($p = 2$). The new branch is born in the saddle-node bifurcation λ_2 together with the unstable x_c^* branch.

Bistability induced by a resonant perturbation at the first subharmonic frequency was also found in a fiber laser with dual-frequency modulated pumping [101] and in a loss-driven CO₂ laser [102, 103] (see Sect. 4.3.3). In particular, Chizhevsky [104] has shown that a loss-driven laser CO₂ with frequencies f_d and f_d/n ($n = 3, 4, 8, 16, \dots$) exhibits the coexistence of n attractors. Since the modulated laser can be considered as a nonautonomous system with a Toda potential, a similar behavior is expected in a large class of periodically modulated asymmetric oscillators.

In addition, Astakhov et al. [3] found that harmonic external forcing can induce multistability in the Andronov–Hopf bifurcation (see Sect. 2.1.3). They considered a system of two asymmetrically coupled Van der Pol oscillators with an external harmonic force:

$$\ddot{x} - \epsilon(1 - x^2)\dot{x} + \omega_1^2 x = \gamma_1(\dot{y} - \dot{x}) + C_0 \cos(\omega_0 t), \quad (2.25a)$$

$$\ddot{y} - \epsilon(1 - y^2)\dot{y} + \omega_2^2 y = \gamma_2(\dot{x} - \dot{y}), \quad (2.25b)$$

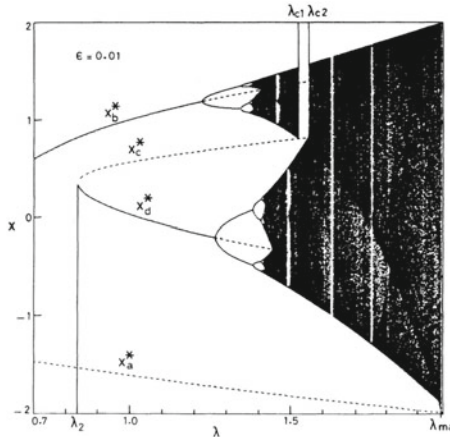


Fig. 2.23 Bifurcation diagram of the logistic map in Eq. 2.24 with external period-2 modulation for $\epsilon = 0.01$. x_b^* and x_d^* mark coexisting branches of attractors, and x_c^* and x_a^* mark unstable orbits. λ_2 , λ_{c1} and λ_{c2} mark saddle-node bifurcation and crisis points, respectively. Branches of unstable fixed points are marked by dashed lines. Reprinted figure with permission from [100] ©1993 by the American Physical Society

where x and y are dynamical variables, ϵ is a nonlinearity parameter, $\omega_{1,2}$ are natural frequencies of the coupled oscillators, $\gamma_{1,2}$ are coupling coefficients, and C_0 and ω_0 are the amplitude and frequency of the external force, respectively.

Using the quasiharmonic approximation, the state variables of the coupled oscillators x and y can be written as follows

$$x = a_1(t) \cos(\omega_0 t + \phi_1(t)), \quad (2.26a)$$

$$y = a_2(t) \cos(\omega_0 t + \phi_2(t)), \quad (2.26b)$$

where ϕ_1 and ϕ_2 are the phases of the first and second van der Pol oscillators, respectively. The phase-reduced model of Eq. 2.25 yields

$$\dot{\phi}_1 = \Delta_1 + g_1 \sin(\phi_1 - \phi_2) - \frac{C}{1 - \Delta_1} \cos \phi_1, \quad (2.27a)$$

$$\dot{\phi}_2 = \Delta_2 + \delta - g_2 \sin(\phi_1 - \phi_2), \quad (2.27b)$$

where $g_{1,2} = \gamma_{1,2}/2$ are the coupling strengths, $\Delta_{1,2} = (\omega_{1,2}^2 - \omega_0^2)/(2\omega_0)$, $\delta = \Delta_2 - \Delta_1$, and $C = C_0/(2a_1)$.

The emergence of multistability in the Andronov–Hopf bifurcation is illustrated in Fig. 2.24 with the phase-space plot. In the phase-reduced system in Eq. 2.27, the stable limit cycles appears (see Figs. 2.24a, b). This corresponds to the appearance of a two-dimensional invariant torus in the non-reduced system in Eq. 2.25 (2' in

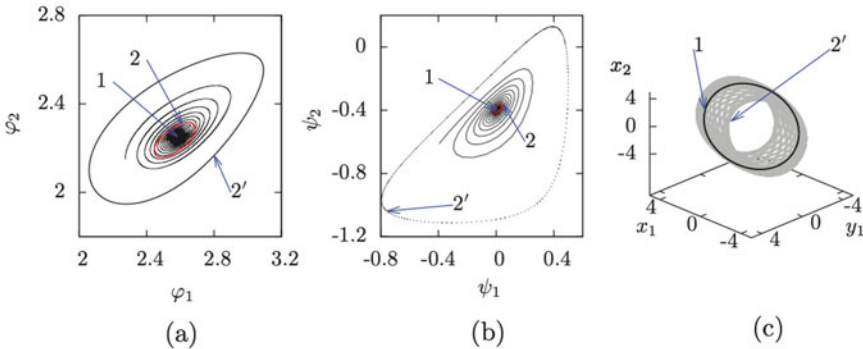


Fig. 2.24 **a, b** Multistability emergence in the reduced system in Eq. 2.27 with $\Delta_1 = -0.08$, $g_1 = 0.15$, $g_2 = -0.0616$, and $\delta = 0.1$. **a** Before the bifurcation ($C = 0.16$) the system possesses the stable focus 1 on the phase plane. **b** After the bifurcation ($C = 0.1659$) the stable limit cycle 2 emerges in the Andronov–Hopf bifurcation. 2' is the limit cycle which appears at $C = 0.17$. **c** In the non-reduced system in Eq. 2.25, 1 and 2' are the stable limit cycle and the two-dimensional torus, respectively. Reprinted with permission from [3] ©2013 by the American Physical Society

Fig. 2.24c), which is born in the Neimark–Sacker bifurcation. The two-dimensional torus 2' arises in the phase-modulated oscillations.

2.2.8 Symmetry

Symmetric dynamical systems often exhibit a symmetric pair of coexisting attractors [105, 106], and sometimes they persist even when symmetry is broken, but attractors usually lose their symmetry. Multistability can also be associated with local symmetry, i.e. so-called *conditionally symmetric structures* that are locally symmetric in a certain region of phase space [107].

Here, we give the definitions of different types of symmetry in dynamical systems.

Symmetric systems. A dynamical system is *symmetric* if there exists a variable substitution $u_{i_1} = -x_i$, $u_{i_2} = -x_{i_2}$, ..., $u_{i_k} = -x_{i_k}$, $u_i = x_i$ which satisfies $\dot{\mathbf{U}} = \mathbf{F}(\mathbf{U})$, where $\mathbf{U} = (u_1, u_2, \dots, u_n)$.

Reflectional symmetric systems. A three-dimensional dynamical system is *reflection symmetric* if $x_{i_0} = -u_{i_0}$ ($i_0 \in \{1, 2, 3\}$) obeys the same basin equation.

Rotational symmetric systems. A three-dimensional dynamical system is *rotational symmetric* if $x_{i_0} = -u_{i_0}$ and $x_{j_0} = -u_{j_0}$ ($i_0, j_0 \in \{1, 2, 3\}$, $i_0 \neq j_0$) obeys the same basin equation.

Inversion symmetric systems. A three-dimensional dynamical system is *inversion symmetric* if $x_1 = -u_1$, $x_2 = -u_2$, and $x_3 = -u_3$ obey the same basin equation.

Conditionally symmetric systems. A dynamical system is *conditionally symmetric* if there exists a variable substitution $u_{i_0} = x_{i_0} + c_0$, $u_i = x_i$, which induces asymmetry to the deduced system $\dot{\mathbf{U}} = \mathbf{F}^*(\mathbf{U}) = (f_1^*, f_2^*, \dots, f_N^*)$, but the system becomes symmetric when $f_{j_0}^*$ ($1 \leq j_0 \leq N$, $j_0 \neq i_0$) is revised.

As an example, let us consider now the last type of symmetry. A method for producing conventional symmetric systems was proposed by Li, Sprott, and Xing [108]. They found that conditional symmetry occurs in variable-boostable dynamical systems and constructed two modes of conditional symmetry (conditional reflection symmetry and conditional rotational symmetry) in which a symmetric pair of strange attractors are located in asymmetric basins of attraction.

Figure 2.25 illustrates the examples of conditional reflection and rotational symmetric attractors in three-dimensional systems:

$$\begin{aligned}\dot{x} &= y^2 - 0.4z^2, \\ \dot{y} &= -z^2 - 1.75y + 3, \\ \dot{z} &= yz + (|x| - 3),\end{aligned}\tag{2.28}$$

and

$$\begin{aligned}\dot{x} &= y^2 - 1.22, \\ \dot{y} &= 8.48z, \\ \dot{z} &= -y - z + (|x| - 3).\end{aligned}\tag{2.29}$$

The coexisting attractors shown in Fig. 2.25 arise in variable-boostable systems which are defined as follows.

A dynamical system $\dot{\mathbf{X}} = \mathbf{F}(\mathbf{X})$, where $\mathbf{X} = (x_1, x_2, \dots, x_N)$, $\mathbf{F} = (f_1, f_2, \dots, f_N)$, is called *variable-boostable* if $u_{i_0} = x_{i_0} + c$ with $i_0 \in \{1, 2, \dots, N\}$ obeys the same basic equations after introducing a single constant c into one and only one of the other equation, i.e. $\dot{\mathbf{Y}} = \mathbf{F}(\mathbf{Y})$, where $\mathbf{Y} = (y_1, y_2, \dots, u_{i_0}, \dots, y_N)$. Changing x_{i_0} to $x_{i_0} + c$ introduces a new constant c into the variable x_{i_0} , which changes the average value of x_{i_0} . For such a system, there exists one and only one function $f_{j_0} = h_{j_0}(x_1, x_2, \dots, x_{i_0}, \dots, x_N)$ ($i_0 \neq j_0$) which satisfies $f_{j_0}(x_1, x_2, \dots, x_{i_0}, \dots, x_N) = h_{j_0}(x_1, x_2, \dots, x_{i_0-1}, x_{i_0+1}, \dots, x_N) + kx_{i_0}$, where k is a nonzero constant.

Multistability often arises in symmetric systems, and even if the symmetry is broken, parts of the original attractor can be found. However, in some dynamical systems the coexisting symmetric attractor is not located near the origin, but occurs far along a certain coordinate. This happens in systems with conditional symmetry associated with offset boosting, that usually gives rise to coexisting symmetric attractors at different locations of the boostable variable. The coexisting symmetric attractors are located in the corresponding asymmetric regions with symmetric cross-sections.

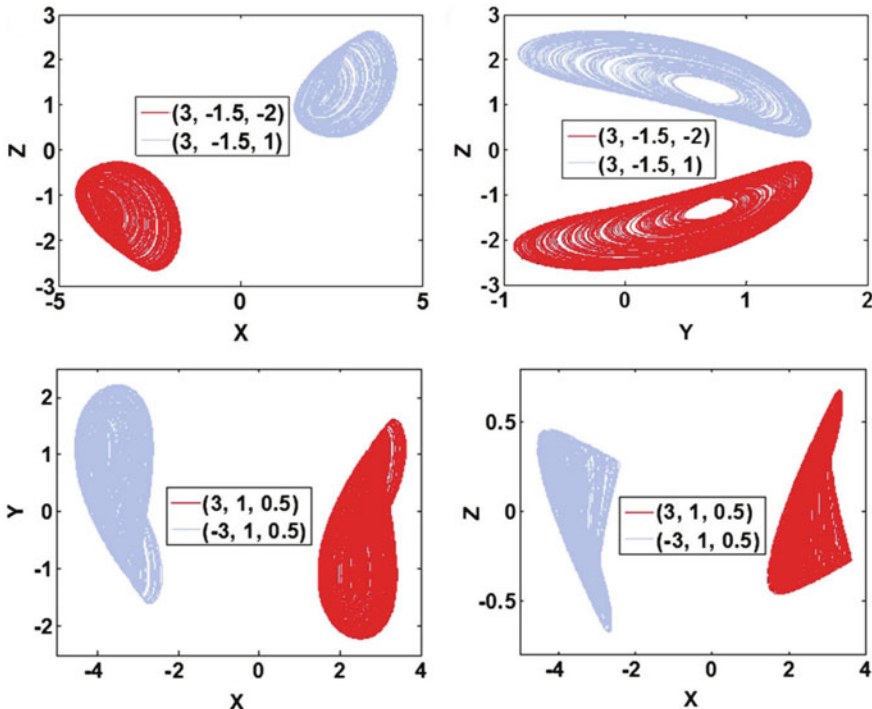


Fig. 2.25 Coexisting strange attractors with conditional (upper row) reflection and (lower row) rotational symmetries in Eqs. 2.28 and 2.29, respectively. Reprinted by permission from the Springer Nature [108] ©2017

2.2.9 Structural Multistability

A particular type of multistability, so-called *structural multistability*, arises in the geometrical structure of *metamaterials* with unusual properties. Due to their mesoscopic architecture, metamaterials can take different shapes after deformation caused by an external force, even if the force is the same [109]. The reasons of structural multistability in metamaterials are their periodic structure and chemical composition.

Among various metamaterial, auxetic materials, such as origami or papiroflexia⁴ and kirigami, take a special place. The former is the handcrafted art of folding paper without using scissors, while the latter is the art of paper cutting; the both do not use glue, to create various shapes, many of which can be thought of as paper sculptures. Other auxetic materials are honeycombs [110], special subsets of foams [111], auxetic microporous polymers [112], long fibre composites [113], and prismatic composites [114]. In addition, materials with soft and porous structures (mechanical cloak) [115, 116] and non-reciprocal materials [117] can also exhibit structural multistability.

⁴ In Latin *papyrus* is “paper” and *flexus* is “folding”.

The mechanical behavior of metamaterials depends on the Poisson's ratio $\nu = \varepsilon_1/\varepsilon_l$. This is the ratio between the transverse strain ε_t and the longitudinal strain ε_l in the loading direction. The material is stable if the Poisson's ratio $\nu \in (-1, 0.5)$ for isotropic 3D materials and $\nu \in (-1, 1)$ for isotropic 2D materials [118]. In a stable state, the stiffness tensor of the solid material must be positive definite [119]. The Poisson's ratio for solid materials, such as metals, polymers, and ceramics, varies in a very narrow band, typically $\nu \in (0.25, 0.35)$. Therefore, these materials shrink in the transverse direction if they are stretched in the longitudinal direction. In contrast, auxetics materials have a negative Poisson's ratio. For example, rotating unit auxetics are comprised of square and equilateral triangular units connected together by hinges at their vertices (Fig. 2.26). If pulled in one direction, the collective motion of their rotating units expands the material in the transverse direction, thus resulting in $\nu = -1$. A similar behavior is observed for chiral auxetics [120] and bar-and-joint lattices [121].

The examples of multistability in prismatic structures are presented in Fig. 2.27. To simulate origami, the deformation of faces is typically modeled using bending. The computational cost can be reduced, if the observed deformation is approximated using in-plane stretching only [123]. This also allows one to decrease the number of parameters used in the simulation, for example, bending stiffness of the faces. The deformation of prismatic structures was numerically simulated using the method based on the minimization of the elastic energy [114].

The materials with a negative Poisson's ratio have several advantages over conventional composite materials. These are higher stiffness, higher strength, lighter weight, higher shear modulus, higher damping resistance, high fracture toughness, enhanced crack growth resistance, and higher energy absorption capability. All these advantages make auxetic composites very promising for engineering applications, such as automotive and aerospace. However, auxetic composites are difficult to manufacture. Nevertheless, rapid development of multi-material 3D-printing technologies allows printing auxetic structures in the nearest future [124]. For instance, 4D bioprinting⁵ advantage lies in the creation of three-dimensional complex tissue structures based on sensitive materials, which can restore or change their shape upon external stimulation. In addition, 4D bioprinting can generate cell populations with programmable scaffolds.

Multistable structures can also be potentially useful for tissue engineering, such as dynamic tissue healing and regeneration of damaged organs, as these technologies can provide large and well-controlled shape changes. Microscale multistable structures can be triggered by various external stimuli (heat, light, magnetic fields, etc.).

⁵ 4D printing adds the dimension of transformation over time, when after the fabrication process the printed product changes its shape depending on the environment parameters, such as humidity, temperature, atmospheric pressure, etc.

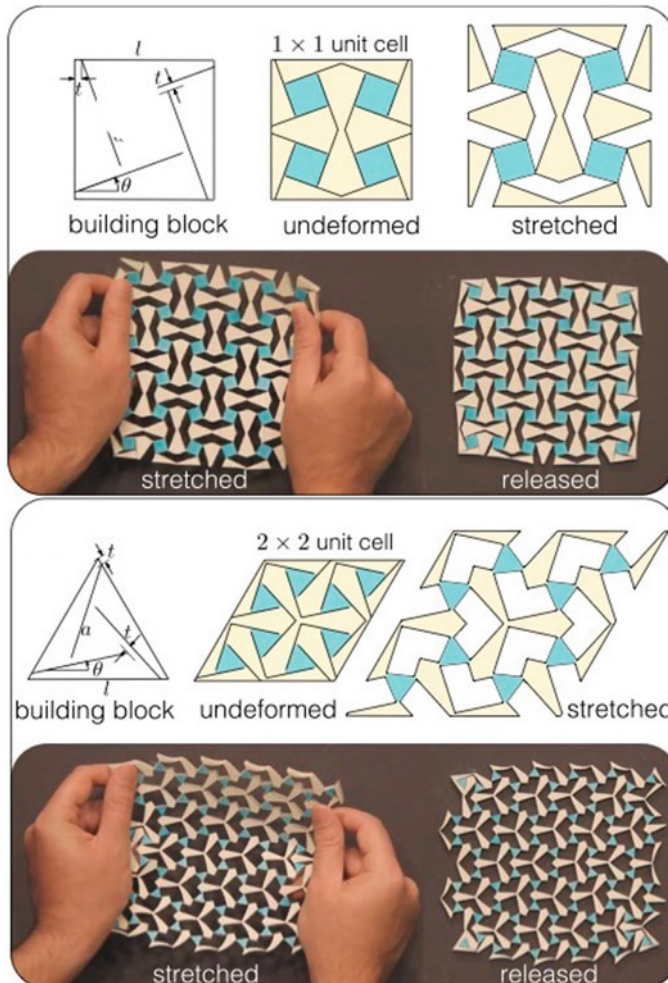


Fig. 2.26 Bistable auxetic materials. The building block and the corresponding unit cell in the undeformed and deformed state contain square and triangular rotating blocks with inclined cutouts, which can maintain a stable deformation structure after the load is removed. Reprinted from [122] ©2016 with permission from Elsevier

2.3 Methods to Reveal Multistability

One of the important tasks of numerical modeling and experimental research is the identification of coexisting attractors in the system under study. There are several approaches to find coexisting attractors and their basins of attraction. At first glance, there is nothing difficult here. What we need is to look for numerical solutions of differential equations by taking different initial conditions. However, sometimes it is

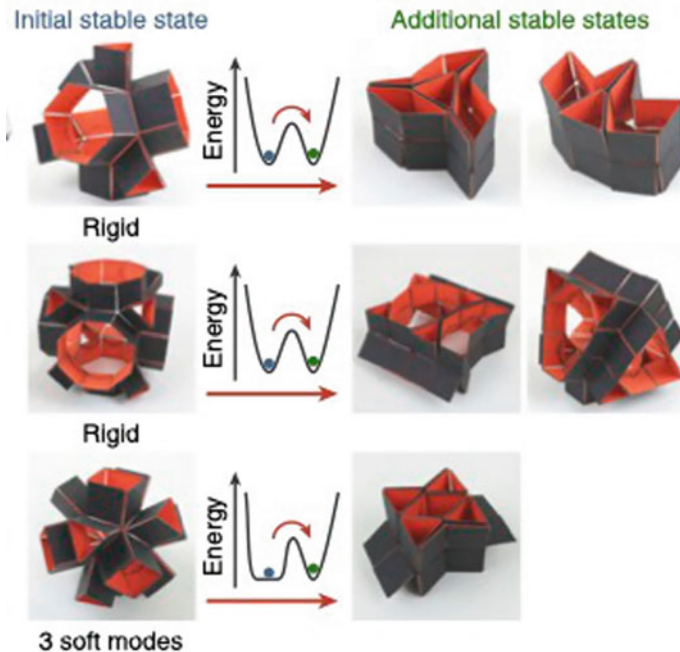


Fig. 2.27 Multistability in prismatic structures based on (upper raw) a truncated tetrahedron, (middle raw) a truncated cube and (lower raw) a cuboctahedron. The coexisting stable states can be reached by going over a finite energy barrier caused by deformation of the structure faces. Adapted from [114]

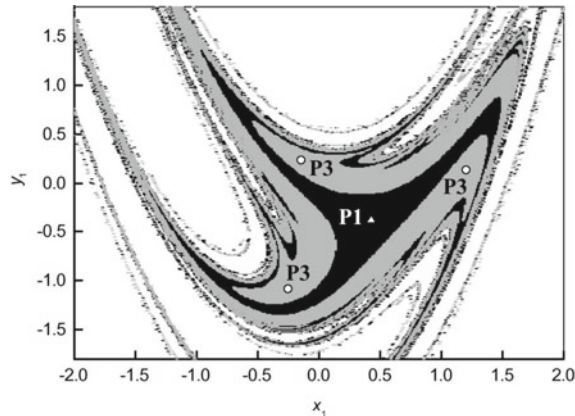
not so easy, because, some attractors have very tiny basins of attraction, and in order to find them a mesh of initial conditions should be so fine that the calculation requires an extremely long time. Moreover, initial conditions cannot be varied from minus infinity to plus infinity. On the other hand, varying initial conditions is not possible in experiments. In addition, some attractor are fractal and even hidden; their basins of attraction do not contain a small neighborhood of unstable equilibrium points.

In this section, we describe some methods and tricks which can be used to find multistability in dynamical systems.

2.3.1 Varying Initial Conditions

The simplest and evident way to find stable solutions of a dynamical system is to numerically calculate differential equations using a mesh of initial conditions. This method is called *cell-to-cell-mapping* [125]. Each cell of the initial condition has a sufficiently small size. Starting from a certain cell of the initial condition, the system trajectory after transients will be attracted to a particular stable solution or go to

Fig. 2.28 Basins of attraction of coexisting period-1 (triangle) and period-3 (open dots) attractors of the Hénon map in Eq. 1.11 for $\mu = 0.95$, calculated using a mesh of 100×100 initial conditions



infinity (negative or positive), which sometimes is referred to as *infinity attractor*. So, any initial condition will belong to either a stable attractor or infinity attractor.

The natural transient process is used to identify the cell to a concrete basin of attraction. This is done by the calculation of the transient process starting from the cell center. The process ends on one of the attractors, and thus defines to which basin of attraction the cell belongs. If we repeat the calculation for all cells of the plane and choose a fill color for them according to the attractor, the resulting mapping will define the boundaries of the basins with an accuracy determined by the size of the cell.

Let us illustrate this procedure with the Hénon map in Eq. 1.11 (see Sect. 1.2.3). The map exhibits the coexistence of period-1 and period-3 attractors in the parameter range $0.915 < \mu < 1.171$ [126]. The fixed points for the period-1 regime are

$$X_{1,2}^* = (x_{1,2}^*, y_{1,2}^*) = \left(-\frac{J+1}{2\mu} \pm \sqrt{\left(\frac{J+1}{2\mu}\right)^2 + \frac{1}{\mu}}, -Jx_{1,2}^* \right). \quad (2.30)$$

These two equilibrium points produce four eigenvalues (two real and two complex conjugates):

$$\lambda_{1,2,3,4} = -\mu X_{1,2}^* \pm \sqrt{(\mu X_{1,2}^*)^2 - J}. \quad (2.31)$$

For $J = 0.9$ and $\mu = 1.05$, the period-1 attractor is located at ($x_1^* = 0.426$, $y_1^* = -0.3834$). Similar analysis can be performed for the period-3 attractor, which has eight fixed points, three of which are stable within the range $0.915 < \mu < 1.171$. The period-1 and period-3 attractors and their basins of attraction are shown in the phase-space plot in Fig. 2.28.

The main disadvantage of the cell-to-cell-mapping is the difficulty of its application to experiments, although some electronic tricks make this possible. An alternative approach to change initial conditions is the *Monte Carlo method* [127], which

implies a random variation of initial conditions. Using this method, one needs to test what fraction of uniform random initial conditions converge to the attractor. The Monte Carlo method is used in experiments, for example, in lasers by multiple on and off switching of the generator (see Chap. 4).

2.3.2 Continuation Method

The continuation method is a technique for producing a sequence of closely-located solutions of a dynamical system. In particular, the *parametric continuation method* facilitates computing bifurcation diagrams of multistable systems, which have branches belonging to different attractors.

Briefly speaking, the continuation (or homotopy) method can be described as follows. Suppose, we wish to find a solution of a system of N nonlinear discrete equations $\mathbf{F}(\mathbf{X})$, where $\mathbf{F} : \mathbb{R}^N \rightarrow \mathbb{R}^N$ is a smooth mapping. Starting from a certain initial condition x_0 , the variable x_i can be calculated by the iteration

$$x_{i+1} := x_i - J_i^{-1} F(x_i), \quad i = 0, 1, \dots, \quad (2.32)$$

where $J_i = F'(x_i)$ is the Jacobian.

In general, the continuation (homotopy) or deformation $H : \mathbb{R}^N \times \mathbb{R} \rightarrow \mathbb{R}^N$ is defined as

$$H(x, \lambda_1) = F(x), \quad H(x, \lambda_2) = G(x), \quad (2.33)$$

where $G : \mathbb{R}^N \rightarrow \mathbb{R}^N$ is a smooth map and λ is a control parameter.

To find H , either convex or global homotopy can be applied. The *convex homotopy* is defined as

$$H(x, \lambda) := \lambda G(x) + (1 - \lambda) F(x). \quad (2.34)$$

The continuation method allows one to trace a curve $c(s) \in H^{-1}(0)$ from a starting point $(x_0, \lambda = 0)$ to a solution point $(x_i, \lambda = 1)$. The *global homotopy* implies

$$H(x, \lambda) := F(x) - \lambda F(x_1). \quad (2.35)$$

The idea behind the continuation method is as follows. If the increment $\Delta\lambda$ is chosen to be sufficiently small, then the iterative process will generally converge because the starting value x_0 will be close to the solution of $H(x_i, \lambda) = 0$. The subsequent solution x_{i+1} for every $\Delta\lambda_i$ is searched starting from the previous value x_i (see Fig. 2.29). The method fails if there are turning points τ on the curve with respect to the control parameter λ . After these points, the solution switches to another branch (for instance, from x_3 to x_4 or from x_8 to x_9). The upper branch can be found by increasing the control parameter λ , while the lower branch by decreasing λ . It is more difficult to find the middle branch between the turning points τ . However, it is

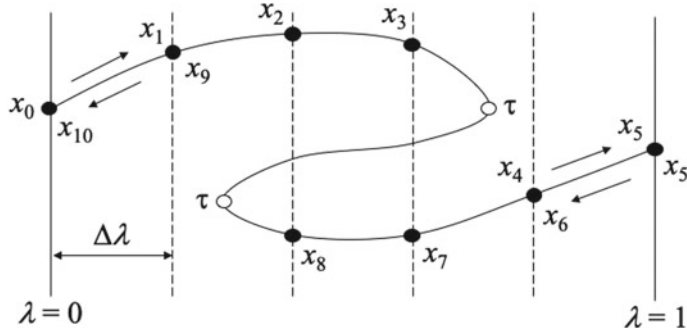


Fig. 2.29 Illustration of the continuation method to trace the solution from $\lambda = 0$ from $\lambda = 1$ and back. The arrows show the direction of the continuation solutions and τ are the turning points

also possible if we diminish the step $\Delta\lambda$ to approach τ as soon as possible, and then change the direction of the parameter change.

For the readers who are interested in deeper understanding of continuation methods, we recommend the monographs [128, 129].

2.3.3 External Short Pulse

One of the ways to reveal multistability is to perturb the system by a short external pulse to direct the trajectory from the basin of attraction of one attractor to the basin of another attractor and wait until the trajectory approaches that attractor. This method was first applied by Kaneko [36, 37] to coupled logistic maps and later by Chizhevsky et al. [130] to a CO₂ laser (see Sect. 4.3.2).

A short external pulse, which can be modeled by a delta function, pushes the phase-space trajectory far away from the attractor, and then the trajectory either returns back to the same attractor or falls into the basin of another coexisting attractor. Since the external pulse is added at different moments of time, this is equivalent to a random choice of initial conditions.

Now, we will show how the method works in a coupled map lattice. A globally coupled map lattice was introduced by Kaneko [36, 37] as a prototype of a chaotic spatially extended system:

$$x_{n+1}(i) = (1 - \epsilon)f(x_n(i)) + \frac{\epsilon}{N} \sum_{j=1}^N f(x_n(j)), \quad (2.36)$$

where n is a discrete time step, i is the index of an element $i = 1, 2, \dots, N$, and $f(x)$ is a nonlinear map function.

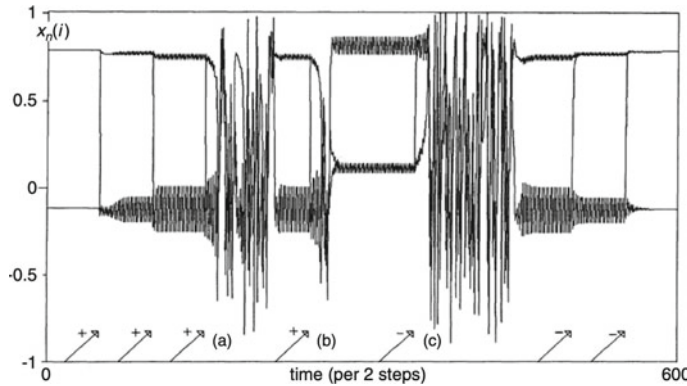


Fig. 2.30 Time series showing switches among coexisting attractors in a coupled map lattice (Eq. 2.36). The arrows indicate the inputs $\delta = -0.7$ on a site belonging to the $+/-$ cluster. After each input, the system either changes the attractor or returns back to the same attractor after chaotic transients (a), (b), and (c). $a = 1.9$, $\epsilon = 0.3$, and $N = 50$. Reprinted figure with permission from [36] ©1989 by the American Physical Society

The input $\delta_n(j)$ applied to a single node j at a single time step n , can cause the system to jump from one attractive state to another. The input pulse changes the value of j from $x_n(j)$ to $x_n(j) + \delta_n(j)$. After the input is applied, the map is iterated until the trajectory of the system is attracted to another state or returns to the original attractor after transient processes. In other words, if the pulse amplitude $|\delta|$ is small, the system returns to the same attractor after several iterations, otherwise the system changes the attractor.

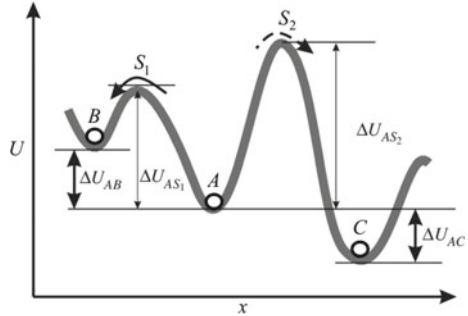
The time series in Fig. 2.30 illustrates switching between coexisting clusters in globally connected logistic maps $f(x) = 1 - ax^2$ after successive inputs. Switching between attractors is often accompanied by intermittent chaotic transient processes, after which the system either returns back to the original attractor (a), or passes to another attractor (cases (b) and (c)). The target attractor is determined by two parameters of the external pulse, namely, its amplitude and the moment of time when the short pulse is applied.

Kaneko [36, 37] suggested that switching between attractors can explain the processing of biological information if the neural network is viewed as a network of globally connected oscillators.

2.3.4 Stochastic Perturbation

Multistability can also be revealed by adding noise. Noise converts a multistable system to a metastable one, so that the trajectory eventually visits the coexisting metastable states. The frequency of switches between these state is determined by

Fig. 2.31 Quasipotential and transitions among metastable states in the presence of noise. A , B , and C are stable equilibria and S_1 and S_2 are saddles. The transition rate is determined by the Kramers time and different ΔU . Modified from [131]



the Kramers time, that is the rate at which a particle under noise escapes from a potential well over a potential barrier (Fig. 2.31).

A multistable dynamical system

$$\dot{\mathbf{x}} = \mathbf{F}(\mathbf{x}) \quad (2.37)$$

can be described by a second-order differential equation with a single variable x :

$$\ddot{x} - A\dot{x} \approx \nabla U, \quad (2.38)$$

where A is the damping parameter, $\nabla \equiv d/dx$, and U is a potential function. Supposing that the deterministic system in Eq. 2.37 has three stable steady states A , B , and C , the difference between the potential energies of states A and B can be found as

$$\Delta U_{AB} = U_B - U_A = \int_{x_A}^{x_B} \mathbf{F}(x) dx. \quad (2.39)$$

In the presence of noise, the particle jumps over the potential barrier S_1 with probability obeyed by the Arrhenius equation

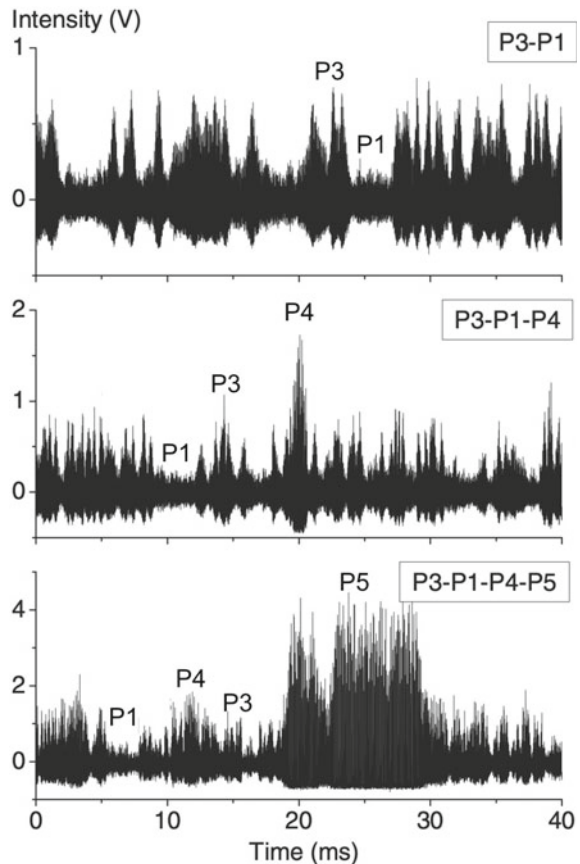
$$P_{A \rightarrow B} = \exp(-U_{AB}/\varepsilon^2), \quad (2.40)$$

where ε is the noise intensity.

Under the influence of noise, the system in Eq. 2.37 visits from time to time different metastable states. This phenomenon is often called *attractor hopping* [133]. The switching between coexisting chaotic and periodic states is closely related to *chaotic itinerancy* [134] observed in high-dimensional systems such as globally coupled maps [37] and networks of neuronal oscillators⁶ [135].

⁶ One should distinguish noise-induced attractor hopping from a low-dimensional ordered motion in chaotic itinerancy, since the latter takes place between stable and unstable manifolds and therefore involves a saddle point.

Fig. 2.32 Noise-induced hopping between coexisting states in a pumped-modulated erbium-doped fiber laser with different intensities of noise applied to the diode-pumped current (upper) $\varepsilon = 0.5$ V, (middle) $\varepsilon = 0.9$ V, and (lower) $\varepsilon = 0.5$ V. The states are distinguished by their amplitudes. Based on data from [132]



A particular case of attractor hopping in a bistable system is two-state on-off intermittency [136] which was observed experimentally in a semiconductor laser [137]. In contrast to a bistable system, attractor hopping in a multistable system depends on the structure of chaotic saddles separating attractors [133].

Figure 2.32 shows the experimental noise-induced switches between different coexisting states in an erbium-doped fiber laser [132]. One can see that depending on the noise intensity ε , the intensity I of laser oscillations changes from very small (around 0.1–0.2 V) to very large (around 4 V) values, representing switches between period-1 (P1) and period-3 (P3) oscillations (upper panel), or between P3, P1, and period-4 (P4) oscillations (middle panel), or between P1, P3, P4, and period-5 (P5) oscillations (lower panel). As soon as the system reaches one of the states, noise can be stopped, and the system will stay in this state forever if the state is an attractor. Note, that P5 with largest amplitude only exists in the presence of external noise added to the pump current of the diode laser [132, 138].

2.3.5 Critical Velocity Surfaces

A powerful tool for revealing multistability is the critical velocity surfaces method introduced by Godara et al. [139]. This method is related to the architecture of attractors since their location in phase space determines possible flows according to which the trajectories can appear and consequently affect the attractors.

To understand how this method works, let us consider a general N -dimensional dynamical system $\dot{\mathbf{x}} = \mathbf{F}(\mathbf{x})$. Some of the trajectories asymptote to an attracting set $\mathbf{A} \subset \mathbb{R}^N$. The first derivative $\dot{x}_i(t)$ ($i \in 1, \dots, N$) or the velocity can take either positive or negative values, i.e. $x_i(t)$ can be increasing or decreasing with time. There are also some points on the attractor \mathbf{A} where $\dot{x}_i = 0$. These points form geometrical shapes in the phase space called x_i -critical velocity surfaces. The location of these surfaces provides us with important information about attractors and their basins of attraction as well. Therefore, instead of searching for initial conditions leading to attractors in the N -dimensional phase space, one can search for $(N - 1)$ -dimensional subspaces of critical velocity surfaces.⁷

In a similar way, additional information about the phase-space structure can be extracted from higher derivatives. In particular, the x_i -critical acceleration surface is defined as phase-space points at which the second derivative crosses zero, i.e. $\ddot{x}_i = 0$. Every critical velocity surface $\dot{x}_i = 0$ divides the phase space into two regions, the region where $\dot{x}_i > 0$ and the region where $\dot{x}_i < 0$. The direction of the flow $x_i(t)$ when crossing the x_i -critical velocity surface is determined by the sign of \ddot{x}_i on the surface $\dot{x}_i = 0$. The trajectories starting from this surface and going towards ($\dot{x}_i > 0$) region imply $\ddot{x}_i > 0$, whereas the trajectories going towards ($\dot{x}_i < 0$) region imply $\ddot{x}_i > 0$. Similar to the critical velocity surface, the critical acceleration surface $\ddot{x}_i = 0$ divides phase space into two regions ($\ddot{x}_i > 0$ and $\ddot{x}_i < 0$), and intersects with the critical velocity surface at the points where $\dot{x}_i(t) = \ddot{x}_i(t) = 0$. These points form the x_i -critical curve, that is the boundary between positive ($x_i > 0$) and negative ($x_i < 0$) flows on the x_i -critical velocity surface.

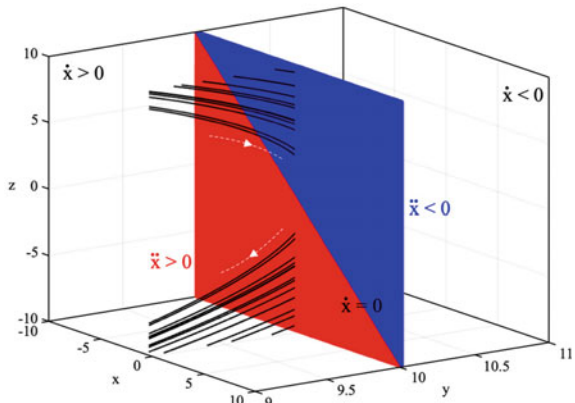
Let us explain how the method works with the example of a three-dimensional dynamical system given by [140]

$$\begin{aligned}\dot{x} &= -0.1y + 1, \\ \dot{y} &= x + z, \\ \dot{z} &= xz - 3y.\end{aligned}\tag{2.41}$$

The x -critical velocity surface ($\dot{x} = 0$) is shown in Fig. 2.33. It divides the whole phase space \mathbb{R}^3 into two parts, namely, $\dot{x} > 0$ ($y < 10$) and $\dot{x} < 0$ ($y > 10$). The plane is also divided by the x -critical curve into two regions: dark, where $\ddot{x} < 0$ and light, where $\ddot{x} > 0$. The flow crossing the plane from the front to back goes only through the blue region. However, when crossing from back to front, the flow crosses the red one.

⁷ It should be noted that this approach can only be applied to smooth dynamical systems.

Fig. 2.33 Critical velocity surface ($\dot{x} = 0$) for the system in Eq. 2.41 divided by the x -critical curve into regions of positive (red) and negative (blue) acceleration \ddot{x} . Black lines show the part of trajectories crossing the surface. The flow direction is shown by the arrows. $y = 10$. Reproduced from [139] with permission of AIP Publishing



The procedure of looking for intersections with a critical velocity surface reduces the range of initial conditions leading to rare or hidden attractors. The algorithm for searching attractors in any model can be summarized as follows.

- Find all N critical velocity ($\dot{x}_i = 0$) and acceleration surfaces ($\ddot{x}_i = 0$) analytically ($i = 1, \dots, N$).
- Find all N critical curves for both $\dot{x}_i = 0$ and $\ddot{x}_i = 0$.
- Find the smallest regions on the critical velocity surfaces after the separation by critical curves (the parts distinguished by positive and negative acceleration).
- Apply the searching method for the smallest possible region of critical velocity surfaces.

Practically, when looking at system equations, one can select the variable whose critical velocity surface allows reducing complexity as much as possible. In the model in Eq. 2.41 described above, the surface is chosen on the y -variable only.

2.3.6 Complete Bifurcation Group

There are a class of attractors called *rare attractors* which are very difficult to find. These attractors have extremely small basins of attraction, as compared to basins of other coexisting attractors. Rare attractors were found in many dynamical systems [141–143]. They can be either periodic, quasi-periodic, or chaotic.

The traditional methods of analysis are ineffective for rare attractors. Bifurcation diagrams constructed by traditional methods, are usually incomplete, since, as a rule, not all attractors found and the branches of periodic regimes acquire discontinuities. To overcome this drawback, Zakrzhevsky [141] developed a *method of complete bifurcation groups* (MCBG) which allows carrying out a profound analysis of the parameter space. This method is especially appealing for the systems with many degrees of freedom, since it is based on the idea of motion along the branches of

periodic regime in the parameter space, regardless of whether the regime is stable or unstable.

The MCBG was applied to find rare attractors in a damped pendulum, including periodic and chaotic orbits. Some of these regimes are rare attractors, since they exist, as a rule, in quite narrow ranges of system parameters. Rare attractors can be found as a result of continuation of an unstable periodic regime along the solution branch in the parameter space.

The simplest implementation of the MCBG can be achieved by a cell-to-cell mapping (see Sect. 2.3.1), which implies the division of the studied region into cells. Each cell is assumed atomic, meaning that all its points are considered to belong to the same basin of attraction. This assumption does not lead to significant errors at a sufficiently small cell. Starting from the center of the cell, the natural transient process is used to identify the cell to a particular basin of attraction. The process ends with one of the stationary orbit and thus defines to which basin of attraction the source cell belongs. For example, if the validation of one of the cells of the transient process completes by a period-1 attractor, therefore, the tested cell belongs to the basin of attraction this attractor. If we repeat the calculation for all cells of the plane and select a fill color for them in accordance with the attractor, then the resulting mapping will determine the boundaries of the basins of attraction within the cell size.

Another approach is the *method of separatrices* of the saddle point. The separatrices are the boundaries that divide basins of attraction according to different regimes. Therefore, in this case the checking process of each point on the phase plane in the algorithm of the cell-to-cell mapping is replaced by a significantly faster process of constructing separating lines. The initial data for the beginning of the calculation are the coordinates of the saddle point, around which the algorithm is used to display a straight line in reverse time. If the line size is sufficiently small and the number of points on the line is large enough, the first few steps of mapping in reverse time will not lead to significant spread of the points. The points will be located on the separatrix and will determine its position. Such mapping allows getting the set of points (inset), which define the boundaries of the basins of attraction and the location of a saddle point between them. A similar mapping provided in the direct time (outset) shows the location of the fixed points, whose basins of attraction are separated by the constructed boundaries.

The considered approaches of construction of the basins of attraction are designed for the study of the systems with one degree of freedom, although they can also be used for systems with a large number of phase coordinates. In this case we are talking about the core of the basin of attraction. In order to evaluate it, a contour map from some figure in the direct time can be used [144]. If all points of the contour will converge to the same attractor, then all points inside the contour belong to the given attractor. The combination of these points forms a core of the basin of attraction of the corresponding regime.

The main features of the method of complete bifurcation group are illustrated with a three-dimensional driven damped pendulum shown in Fig. 2.34 (left). The

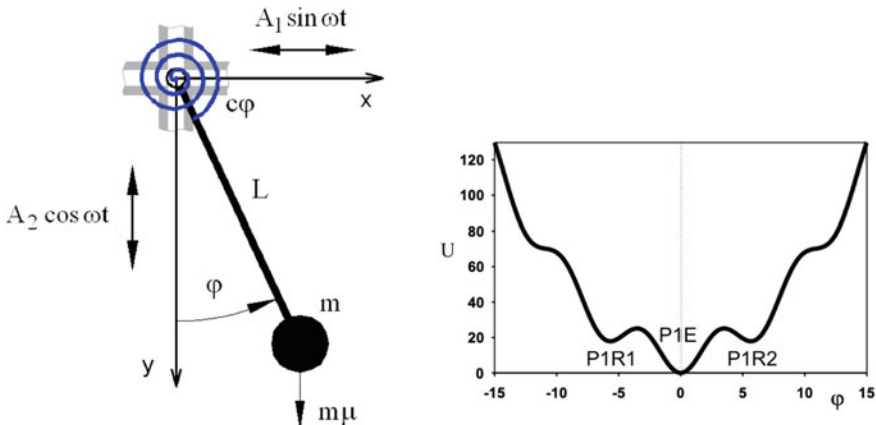


Fig. 2.34 (Left) Driven damped pendulum and (right) corresponding potential with three stable period-1 states: evident P1E and two rare P1R1 an P1R2. Adapted from [142]

pendulum has three period-1 (P1) attractors, one is evident (P1E) and two are rear (P1R1 (left) and P1R2 (right)), as shown in the potential in Fig. 2.34 (right).

The pendulum motion is described by the following equation

$$mL^2\ddot{\varphi} + b\dot{\varphi} + c\varphi + mL(\mu - A_2\omega^2 \cos(\omega t)) \sin(\omega t) + mL A_1 \omega^2 \sin(\omega t) \cos \varphi = 0, \quad (2.42)$$

where φ is the rotation angle, read-out from a vertical line, $\dot{\varphi}$ is the angular velocity of the pendulum, m and L are the pendulum mass and length, μ is the gravitation constant, b and c are the linear damping and linear stiffness coefficients, A_1 , A_2 , and ω are oscillation amplitudes and frequency of the point of suspension on a horizontal and a vertical direction.

The phase-space plot and basins of attraction of three coexisting period-1 attractors of Eq. 2.42 are shown in Fig. 2.35.

The dynamic wells in the phase space are built by line mapping from a line $(-10, -0.1; 10, -0.1)$ on the Poincaré map. The basins of attraction were found by using cell-to-cell mapping with 501×501 grid of initial conditions obtained for cross-section at $A_1 = 0.5$.

2.3.7 Quantifying Basins of Attraction

The shape and size of basins of attraction are important characteristics of multistable systems. Sprott and Xiong [145] proposed to classify and quantify basins of attraction by calculating the probability $P(r)$ that an initial condition at a distance r from the attractor lies within the attractor's basin. They found that the majority of attractors are characterized by the power law $P(r) = P_0/r^\gamma$ as $r \rightarrow \infty$, where P_0 is a constant

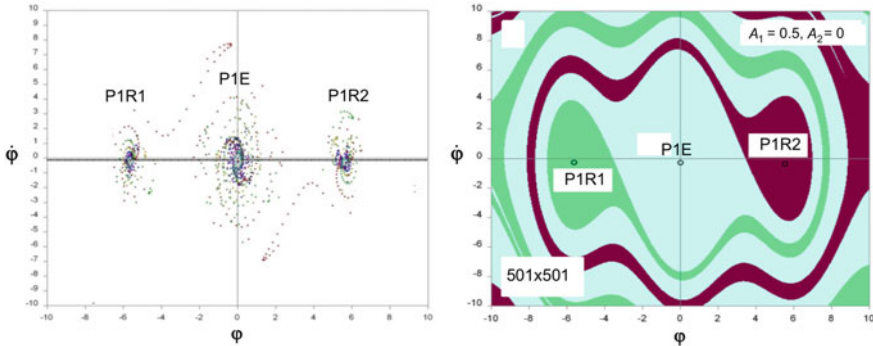


Fig. 2.35 (Left) Phase-space plot and (right) basins of attraction of the driven damped pendulum in Eq. 2.42 with three coexisting period-1 attractors. $m = 1$, $L = 1$, $b = 0.2$, $c = 1$, $\mu = 9.81$, $\omega = 1.5$, $A_1 = 0.5$, $A_2 = 0$. Based on data from [142]

probability and γ is the basin codimension, not necessarily integer. The basins are classified into one of four classes, according to the parameters P_0 and γ .

Class 1: $P_0 = 1$ and $\gamma = 0$. Almost all initial conditions lead to the attractor.

Class 2: $P_0 < 1$ and $\gamma = 0$. A fixed fraction of initial conditions lead to the attractor.

Class 3: $0 < \gamma < D$ (D being the dimension of the state space).

Class 4: $\gamma = D$. The basin is bounded with a fixed, well-defined linear size, given in normalized form by $r_0 = P_0^{1/D}$.

To find what class the basin belongs to, one has to choose random initial conditions uniformly distributed in a D -dimensional hypersphere of radius $r = 1$ and calculate what fraction of them lies within the basin to obtain the probability value $P(1)$. Then, consider a hypersphere of radius $r = 2$ with random initial conditions uniformly distributed in the shell between $r = 1$ and $r = 2$ and calculate the fraction $\Delta P(1)$ of the initial conditions which lies within the basin to compute $P(2) = P(1)(1 - 1/2^D) + \Delta P(1)/2^D$. The procedure is repeated for larger r .

To find whether or not an initial condition lies within the basin, one needs to calculate a running average of the Euclidean distance $\rho(t)$ of the trajectory from the center of mass of the attractor. If $\rho(t) \rightarrow 0$ or at least $\rho(t) < S/10$, we assume that the initial condition is in the basin. For monostable systems, initial conditions which diverge the trajectory to infinity, can easily be detected if $\rho(t)$ exceeds some large value (say, $1000r$). However, in the case of coexisting attractors, one has to add a condition which excludes points leading to either $\rho(t) \rightarrow 0$ or $\rho(t) \rightarrow \infty$.

Then, one has to plot $\log_2 P$ versus $\log_2 r$ and fit to a straight line at large r using linear regression. The intercept of that line with $\log_2 r = 0$ yields P_0 , and the negative of its slope gives γ . The example of this plot is shown in Fig. 2.36 for the Tinkerbell map [147]:

$$\begin{aligned} x_{n+1} &= x_n^2 - y_n^2 + ax_n + by_n, \\ y_{n+1} &= 2x_n y_n + cx_n + dy_n, \end{aligned} \quad (2.43)$$

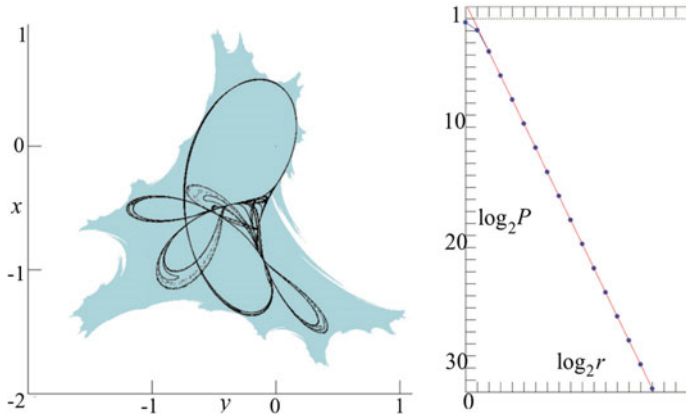


Fig. 2.36 (Left) Chaotic attractor (black line) and its basin of attraction of the Tinkerbell map in Eq. 2.43 and (right) log-log plot approximated (straight line). Based on data from [146]

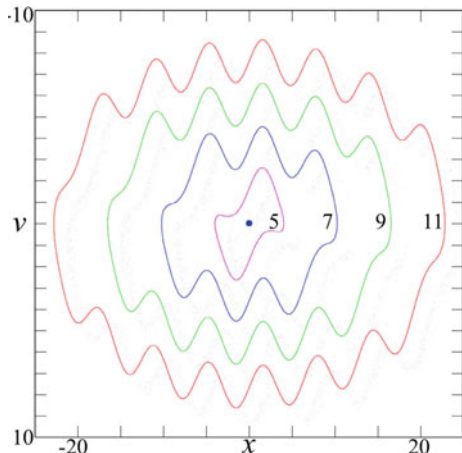
with parameters $a = 0.9$, $b = -0.6$, $c = 2$, and $d = 0.5$. The basin of attraction has a fractal boundary and its size is comparable to the size of the chaotic attractor. With $P_0 = 2.4029$ and $\gamma = 2$ the basin belongs to Class 4 since $\gamma = D$.

2.4 Methods for Detecting Hidden Attractors

Hidden attractors are attractors which basins of attraction do not contain a small neighborhood of any unstable equilibrium points, otherwise they are called *self-excited attractors*. Self-excited attractors are classical stable equilibrium states with attraction domain, which can be localized by a standard procedure described in Sect. 2.3.1, when starting from a point of unstable manifold in a neighborhood of equilibrium, the trajectory reaches the attractor. Hidden attractors can be either periodic or chaotic in systems without equilibria or with the only stable equilibrium. Since the basin of hidden attractors does not intersect with small neighborhoods of equilibria, the standard methods to find such attractors do not work. Therefore, the localization of hidden attractors requires a special computational procedure. General discussions on hidden and rare attractors can be found in surveys [43, 148].

The second part of the Hilbert's 16th problem [149] for two-dimensional polynomial systems piqued the interest of many scientists to a study of hidden oscillations, that was spurred by the crashed of Boing YF-22 [150, 151], Saab JAS 39 Gripen [152], and Olympic Airways Falcon 900 aircrafts in 1992, 1993, and 1999, respectively, due to so-called “pilot-induced oscillation”, that was later interpreted as a hidden attractor. These incidents stimulated extensive research for the development of efficient control systems [153–156] and the theory of absolute stability [157]. There exists a relationship between multistability and the occurrence of hidden attractors.

Fig. 2.37 First four limit cycles of system $\dot{x} = v$, $\dot{v} = -x + v \cos x$ for initial conditions $(x_0, v_0) = (n\pi, 0)$ with $n = 5, 7, 9, 11$. The central blue dot is an unstable focus at the origin $(0, 0)$. The limit cycles are hidden attractors since their basins of attraction do not include the neighborhood of any equilibria. Based on data from [177]



At the beginning of the 21st century, chaotic hidden attractors were discovered in Chua circuits [158, 159] and then in other dynamical systems (see [43] and references therein). After that, hidden attractors were found in many nonlinear system regardless the number of stable equilibrium points [160, 161]. In particular, such attractors were revealed in systems without equilibria [140, 162–165], with non-hyperbolic equilibria [166, 167], with one stable equilibrium [168–171], with curves of equilibria [172–174], with surfaces of equilibria [175, 176], and with multilayer equilibria [177]. In the last class of the systems, an infinite number of nested coexisting hidden attractors of different types, including limit cycles, tori, and strange attractors, were found. The coexisting attractors form a layered structure similar to those shown in Fig. 2.37.

To characterize the stability of such systems with infinite number of attractors Sprott et al. [177] introduced the term *megastability*. Later, megastable oscillators with infinite number of hidden and self-excited attractors were found by other researchers [178–181].

2.4.1 Homotopy and Continuation Methods

The detection of hidden attractors is not an easy task. Nevertheless, Leonov et al. [159] developed an approach which allows one to localize them. Their method is based on homotopy and continuation and consists in the creation of a similar system, analytical finding of a self-excited oscillatory attractor, and then numerically tracking this solution to transform the starting oscillation into a hidden attractor by varying a control parameter, i.e. using the continuation method (see Sect. 2.3.2).

The method consists as follows [182]. Considering a system with vector nonlinearity

$$\dot{\mathbf{x}} = \mathbf{P}\mathbf{x} + \psi(\mathbf{x}), \quad \mathbf{x} \in \mathbb{R}^n, \quad (2.44)$$

where \mathbf{P} is a constant $(n \times n)$ -matrix, $\psi(\mathbf{x})$ is a continuous vector function, and $\psi(\mathbf{0}) = 0$, we define a matrix \mathbf{K} such that the matrix

$$\mathbf{P}_0 = \mathbf{P} + \mathbf{K}$$

has a pair of purely imaginary eigenvalues $\lambda_{1,2} = \pm i\omega_0$ and the rest of eigenvalues have negative real parts. Then, we rewrite the system Eq. 2.44 as

$$\dot{\mathbf{x}} = \mathbf{P}_0\mathbf{x} + \varphi(\mathbf{x}), \quad (2.45)$$

where $\varphi(\mathbf{x}) = \psi(\mathbf{x}) - \mathbf{K}\mathbf{x}$.

Next, we introduce a sequence of small functions $\varphi^0(\mathbf{x}), \varphi^1(\mathbf{x}), \dots, \varphi^m(\mathbf{x})$ such that the sequences of neighbouring functions $\varphi^j(\mathbf{x})$ and $\varphi^{j+1}(\mathbf{x})$ ($j = 0, 1, \dots, m$) are slightly different from each another. The function $\varphi^m(\mathbf{x})$ is the original function $\varphi(\mathbf{x})$ in Eq. 2.44. Since the function $\varphi^0(\mathbf{x})$ is small, we can use the method of harmonic linearization for the system in Eq. 2.45 with $\varphi(\mathbf{x}) = \varphi^0(\mathbf{x})$ and find a stable nontrivial periodic solution $\mathbf{x}^0(t)$ or starting oscillating attractor \mathcal{A}_0 .

In order to localize the attractor of the original system in Eq. 2.45, one has to numerically continue the transformation of the attractor \mathcal{A}_0 by increasing j and consequently finding attractors $\mathcal{A}_1, \mathcal{A}_2, \dots, \mathcal{A}_m$, being oscillating attractors of the system

$$\dot{\mathbf{x}} = \mathbf{P}_0\mathbf{x} + \varphi^j(\mathbf{x}). \quad (2.46)$$

When computing the next attractor \mathcal{A}_1 , two cases are possible: (i) all points of \mathcal{A}_0 lie in an attraction domain of the attractor \mathcal{A}_1 or (ii) the system loses stability and attractor \mathcal{A}_0 is annihilated.

In the former case, the solution $\mathbf{x}^1(t)$ can be found numerically by starting a trajectory of the system in Eq. 2.46 with $j = 1$ from the initial point $\mathbf{x}^0(0)$. If during the computational process with a sufficiently large computational interval $t \in [0, T]$ the solution $\mathbf{x}^1(t)$ neither is attracted to an equilibrium nor goes to infinity, it arrives in the attractor \mathcal{A}_1 . Then, one can start to search for the solution of Eq. 2.46 with $j = 2$ by performing a similar procedure to find attractor \mathcal{A}_2 by initiating from the initial condition in $\mathbf{x}^1(t)$. One has to sequentially repeat these calculations by increasing j up to $j = m$ to find all oscillatory attractors \mathcal{A}_j up to attractor \mathcal{A}_m of the original system in Eq. 2.44, since $\varphi^m(\mathbf{x}) = \varphi(\mathbf{x})$.

To determine the initial condition $\mathbf{x}^0(0)$ of the periodic solution \mathcal{A}_0 , a linear nonsingular transformation \mathbf{S} is used such that $\mathbf{x}_0(0) = \mathbf{S}(y_1(0), y_2(0), y_3(0))^*$. As a result, the system in Eq. 2.46 is transformed into the form

$$\begin{aligned} \dot{y}_1 &= -\omega_0 x_2 + \varepsilon \varphi_1(y_1, y_2, y_3), \\ \dot{y}_2 &= \omega_0 x_1 + \varepsilon \varphi_2(y_1, y_2, y_3), \\ \dot{y}_3 &= \mathbf{A}\mathbf{x}_3 + \varepsilon \varphi_3(y_1, y_2, y_3), \end{aligned} \quad (2.47)$$

where y_1 and y_2 are scalar values, \mathbf{y}_3 is an $(n - 2)$ -dimensional vector, φ_1 and φ_1 are scalar functions, φ_3 is an $(n - 2)$ -dimensional vector function, and \mathbf{A} is an $(n - 2) \times (n - 2)$ -matrix whose all eigenvalues have negative real parts.

It is assumed that for the matrix \mathbf{A} there exists a positive number $d > 0$ such that

$$\mathbf{y}_3^*(\mathbf{A} + \mathbf{A}^*)\mathbf{y}_3^* \leq -2d|\mathbf{y}_3|^2, \quad \forall \mathbf{w} \in \mathbb{R}^{n-2}.$$

It is supposed that the vector function $\varphi(\mathbf{x})$ satisfies the condition

$$|\varphi(\mathbf{x}') - \varphi(\mathbf{x}'')| \leq L|\mathbf{x}' - \mathbf{x}''|, \quad \forall \mathbf{x}', \mathbf{x}'' \in \mathbb{R}^n.$$

The following describing function is introduced

$$\Phi(a) = \int_0^{2\pi/\omega_0} \left[\varphi_1(a \cos(\omega_0 t), a \sin(\omega_0 t), 0) \cos(\omega_0 t) \right. \\ \left. + \varphi_2(a \cos(\omega_0 t), a \sin(\omega_0 t), 0) \sin(\omega_0 t) \right] dt. \quad (2.48)$$

The initial data for the first step of the algorithm can be found according to the following theorem [158].

Theorem 2.1 *If it can be found a positive a_0 such that $\Phi(a_0) = 0$, then for the initial data of periodic solution $\mathbf{x}_0(0) = \mathbf{S}(y_1(0), y_2(0), \mathbf{y}_3(0))^*$ at the first step of algorithm we have*

$$y_1(0) = a_0 - O(\varepsilon), \quad y_2(0) = 0, \quad \mathbf{y}_3 = \mathbf{O}_{n-2}(\varepsilon), \quad (2.49)$$

where $\mathbf{y}_3 = \mathbf{O}_{n-2}(\varepsilon)$ is an $(n - 2)$ -dimensional vector such that all its components are $O(\varepsilon)$.

Let us illustrate this process with an example of the Chua system

$$\begin{aligned} \dot{x} &= \alpha[(y - x) - f(x)], \\ \dot{y} &= x - y + z, \\ \dot{z} &= -\beta y - \gamma z, \end{aligned} \quad (2.50)$$

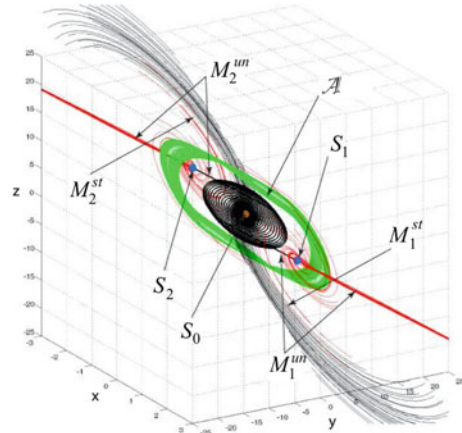
with function $f(x) = m_1x + (m_0 - m_1)\tanh(\sigma)$ and parameters $\alpha, \beta, \gamma, m_0$, and m_1 .

According to the above procedure, we rewrite Eq. 2.50 in the vector form as

$$\dot{\mathbf{x}} = \mathbf{P}\mathbf{x} + \mathbf{q}\psi(\mathbf{r}^*\mathbf{x}), \quad \mathbf{x} \in \mathbb{R}^3, \quad (2.51)$$

where

Fig. 2.38 Localization of hidden attractors in the Chua system modelled by Eq. 2.50. S_0 is a stable equilibrium, S_1 and S_2 are saddle points with their stable and unstable manifolds M_1^{st} and M_1^{un} , respectively, and \mathcal{A} is a hidden attractor. Based on data from [182]



$$\mathbf{P} = \begin{pmatrix} -\alpha(m_1 + 1) & \alpha & 0 \\ 1 & -1 & 1 \\ 0 & -\beta & \gamma \end{pmatrix}, \quad \mathbf{q} = \begin{pmatrix} -\alpha \\ 0 \\ 0 \end{pmatrix}, \quad \mathbf{r} = \begin{pmatrix} 1 \\ 0 \\ 0 \end{pmatrix},$$

$$\psi(\sigma) = (m_0 - m_1) \tanh(\sigma).$$

Then, we introduce a coefficient of harmonic linearization k in such a way that the matrix

$$\mathbf{P}_0 = \mathbf{P} + k\mathbf{qr}^* = \begin{pmatrix} -\alpha(m_1 + 1) + k & \alpha & 0 \\ 1 & -1 & 1 \\ 0 & -\beta & \gamma \end{pmatrix} \quad (2.52)$$

has a pair of purely imaginary eigenvalues $\lambda_{1,2} = \pm i\omega_0$ (ω_0 being a starting frequency) and real negative eigenvalue $\lambda_3 = -d$.

After that, Eq. 2.51 can be rewritten as

$$\dot{\mathbf{x}} = \mathbf{P}_0 \mathbf{x} + \mathbf{q}\varepsilon\varphi(\mathbf{r}^*\mathbf{x}), \quad (2.53)$$

where $\varphi(\sigma) = \psi(\sigma) - k\sigma = (m_0 - m_1) \tanh(\sigma) - k\sigma$.

The system in Eq. 2.53 with parameters $\alpha = 8.4562$, $\beta = 12.0732$, $\gamma = 0.0052$, $m_0 = 0.35$, and $m_1 = -1.1468$ has three equilibria: a locally stable equilibrium in origin (S_0) and two saddle points (S_1 and S_2), as illustrated in Fig. 2.38. To localize a hidden attractor, one has to apply the numerical continuation procedure to Eq. 2.51 keeping the same parameters.

First, one needs to compute a starting frequency $\omega_0 = 2.0392$ and the coefficient of nonlinearity $k = 0.2098$. Then, one has to find the solutions of Eq. 2.53 containing the nonlinearity term $\varepsilon\varphi(x) = \varepsilon(\psi(x) - kx)$, by sequentially increasing ε from $\varepsilon_1 = 0.1$ to $\varepsilon_{10} = 1$ with a step of 0.1.

The initial condition $\mathbf{x}(0)$ for the first step is obtained according to Eq. 2.49, and using the above computational procedure the hidden attractor \mathcal{A} of the original Chua system Eq. 3.12 can be localized, as illustrated in Fig. 2.38.

2.4.2 Amplitude Control

Another useful method for detecting coexisting hidden attractors is *amplitude control* [183]. The amplitude control increases or decreases the attractor size by rescaling some or all of the variables without changing dynamical and topological properties of the attractor. If there are several coexisting attractors in the system, one needs to scale the initial conditions in order to remain in the desired basin of attraction.

Let us consider how the amplitude control works on the example of three-dimension chaotic system with coexisting attractors given by [184]

$$\begin{aligned}\dot{x} &= yz + 0.01, \\ \dot{y} &= x^2 - y, \\ \dot{z} &= 1 - 4x.\end{aligned}\tag{2.54}$$

This system has three coexisting attractors: a fixed point, a limit cycle, and a strange attractor. The limit cycle and strange attractor are hidden attractors in the sense that they cannot be found by using an initial condition in any vicinity of an unstable equilibrium.

The amplitude control can be realized by introducing multiplicator c to the system variables by different ways. Three examples of this type of control are

$$\begin{array}{lll}\dot{x} = (1/c)yz + 0.01c, & \dot{x} = (1/c)yz + 0.01, & \dot{x} = yz + 0.01c, \\ \dot{y} = (1/c)x^2 - y, & \dot{y} = cx^2 - y, & \dot{y} = (1/c)x^2 - y, \\ \dot{z} = c - 4x, & \dot{z} = 1 - 4x, & \dot{z} = 1 - (4/c)x.\end{array}\tag{2.55}$$

Amplitude control rescales the amplitudes of variables x , y , and z according to c . For fixed initial conditions $(0, 1, 0)$, a change in $c \in [-2, 2]$ causes a change in the Lyapunov exponents when the system passes through a bifurcation point, as seen from Fig. 2.39. In all three cases presented in Eq. 2.55, the coexisting attractors occur visible in the Lyapunov exponent spectrum.

Although amplitude control is a fairly reliable method for detecting hidden attractors, it has some drawbacks. In particular, the method does not allow distinguishing between two symmetric attractors with the same spectra of Lyapunov exponents, which is a common phenomenon in systems with symmetries. Moreover, crisis in amplitude control may occurs [185]. Therefore, in some cases, amplitude control should be used in conjunction with other techniques such as, for example, the offset boosting method, which will be introduced in the next section.

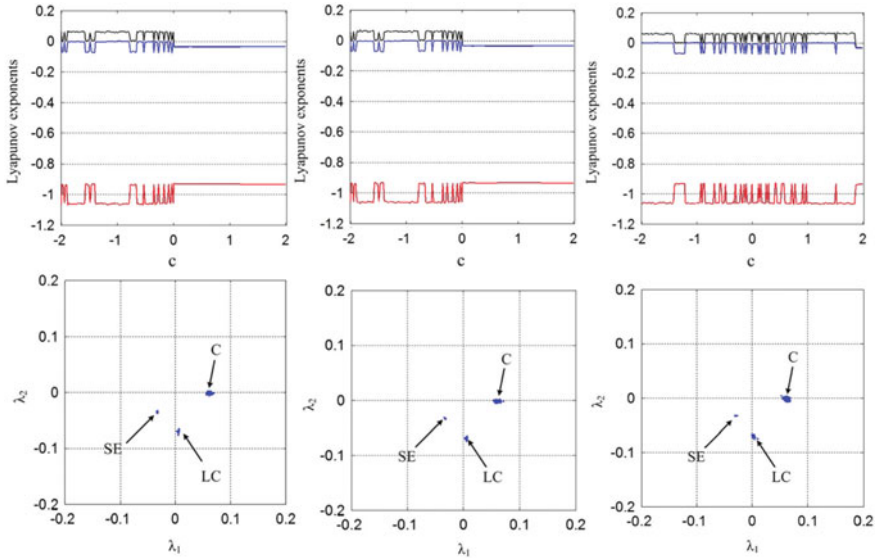


Fig. 2.39 Two largest Lyapunov exponents of the systems in Eq. 2.55 (upper raw) under amplitude control with $c \in [-2, 2]$. (Lower raw) Coexisting stable equilibrium (SE), limit cycle (LC), and chaotic attractor (C) in the Lyapunov spectrum space. Modified from [183]

2.4.3 Offset Boosting

The rescaling of the basins of attraction using amplitude control does not allow finding all coexisting attractors, especially for those attractors whose basin of attraction extends to $\pm\infty$ in one direction. Evidently, the basin in this direction cannot be rescaled because it remains equal to $\pm\infty$. To identify these attractors, the *offset-boosting method* can be used [186]. This method shifts the basin of attraction in any direction, thus generating dynamical dispersion that allows detecting multiple hidden and self-extracted attractors.

The offset-boosting method consists in the addition of a constant vector $\mathbf{a} = (a_1, a_2, \dots, a_n)$ into each variable (x_1, x_2, \dots, x_n) . This operation provides the system offset boosting within the \mathbf{a} interval. Specifically, we transform a smooth dynamical system $\dot{\mathbf{X}} = \mathbf{F}(\mathbf{X})$ into $\dot{\mathbf{Y}} = \mathbf{F}(\mathbf{X} + \mathbf{a})$ so that we obtain the same solution with a constant offset \mathbf{a} . For instance, if the offset boosting is applied to x direction, all basins of attraction will move according to the constant a . If $a > 0$, the basins of attraction will move in a negative direction, and vice versa. When the offset boosting in one direction reaches the basin boundary and falls into another basin of attraction, a new attractor appears, which can then be diagnosed. Since different types of attractors have different Lyapunov exponents, the offset boosting with a fixed initial condition will accordingly change the Lyapunov exponents and display different coexisting attractors.

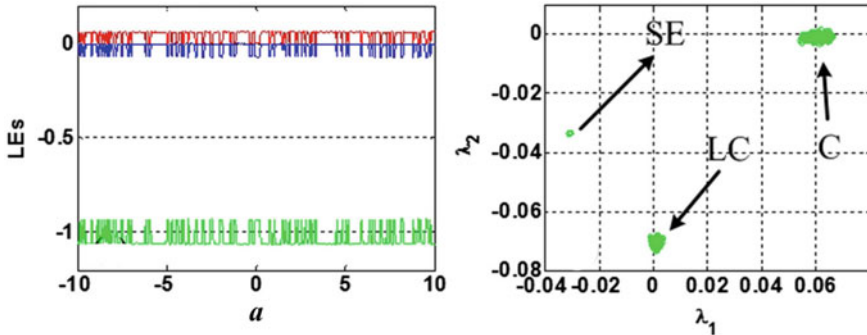


Fig. 2.40 (Left) Two largest Lyapunov exponents of the systems in Eq. 2.56 under offset boosting with $a \in [-10, 10]$. (Right) Coexisting shifted stable equilibrium (SE), limit cycle (LC), and chaotic attractor (C) in the Lyapunov spectrum space. Modified from [186]

Now, we will show how the offset boosting method works on the example of the simplest chaotic system given by Eq. 2.54. As was demonstrated in the previous section, this system has three coexisting attractors: a fixed point, a limit cycle, and a strange attractor. To identify these attractors, the offset boosting is applied in z direction, as we will show below,

$$\begin{aligned}\dot{x} &= y(z + a) + 0.01, \\ \dot{y} &= x^2 - y, \\ \dot{z} &= 1 - 4x,\end{aligned}\tag{2.56}$$

As a result, the basins of attraction are shifted in the z direction and a stable equilibrium (SE) has different basins of attraction leading to intermittent collapses of Lyapunov exponents. This behavior is illustrated in Fig. 2.40 which shows the two largest Lyapunov exponent as a function of $a \in [-10, 10]$ and the distribution of the Lyapunov exponents for the former case. Thus, the coexisting hidden and self-excited attractors can be identified.

The offset boosting method has some advantages over the amplitude control, because it is more convenient to introduce a desired displacement parameter into any desired variable. Moreover, offset boosting can easily detect coexisting symmetric pairs of attractors without the need to calculate Lyapunov exponents, which can be quite problematic for multidimensional systems with strong nonlinearity. However, the offset boosting method can be difficult to apply, especially for engineering applications. For example, offset boosting may require a complex constant, which may require expensive additional hardware or time-consuming data preprocessing.

2.4.4 Nested Double-Scroll Attractors

One of the methods for creating multistability is the use a nonlinear function to form coexisting self-excited attractors at certain phase-space locations. In this case, a hidden attractor appears for each pair of self-excited attractors, while each pair of these hidden attractors results in the emergence of a larger hidden attractor. Thus, self-excited attractors create hidden nested attractors.

In order to create a dynamical system with nested attractors, Escalante-González and Campos [187] proposed to choose parameters related to the oscillatory behavior. Then, the parameters responsible for the equilibrium are selected to create a bistable behavior with two self-excited attractors, each of which is generated by a pair of equilibrium points. When the connection between two pairs of equilibria is strong enough, two self-excited attractors arise.

To illustrate this approach, let us consider a piecewise linear dynamical system

$$\dot{\mathbf{x}} = A\mathbf{x} + f(\mathbf{x})B, \quad (2.57)$$

where $\mathbf{x} = (x_1, x_2, x_3)^T \in \mathbb{R}^3$ is the state vector, $A = \alpha_{ij} \in \mathbb{R}^{3 \times 3}$ is a linear operator, $B = (\beta_1, \beta_2, \beta_3)^T$ is a constant vector, and f is a functional. Here, $f(\mathbf{x})B$ is a constant vector in each unit P_i such that the equilibria are given by $\mathbf{x}_{eq_i}^* = (x_{1eq_i}^*, x_{2eq_i}^*, x_{3eq_i}^*)^T = -f(\mathbf{x})A^{-1}B \in P_i$ with $i = 1, \dots, v$.

The selection of the linear operator A is based on the proposition that each equilibrium point $\mathbf{x}_{eq_i}^*$ is a saddle point. Moreover, if two equilibria $\mathbf{x}_{eq_1}^*$ and $\mathbf{x}_{eq_2}^*$ are symmetrically separated along axis x_1 from a surface $\Sigma = \{\mathbf{x} \in \mathbb{R}^3 : x_1 = \rho \in \mathbb{R}\}$, then the unstable and stable manifolds of the saddle points 1 and 2 are related as $W_{\mathbf{x}_{eq_1}^*}^U \cap W_{\mathbf{x}_{eq_2}^*}^S \cap \Sigma = \emptyset$ and $W_{\mathbf{x}_{eq_1}^*}^S \cap W_{\mathbf{x}_{eq_2}^*}^U \cap \Sigma = \emptyset$.

With the above condition which implies the existence of a hidden attractor, the matrix A and constant vector $B \in \mathbb{R}^3$ are defined as follows

$$A = \begin{pmatrix} a/3 + 2c/3 & b & 2c - 2a/3 \\ -b/3 & a & 2b/3 \\ c/3 - a/3 & -b & 2a/3 + c/3 \end{pmatrix}, \quad B = \begin{pmatrix} -a/3 - 2c/3 \\ b/3 \\ a/3 - c/3 \end{pmatrix},$$

where $a, b \in \mathbb{R}^+$ and $c \in \mathbb{R}^-$.

The functional $f(\mathbf{x})$ responsible for the equilibria location is taken as

$$f(\mathbf{x}) = \alpha u \left(2x_1 - 2 \sum_{i=1}^m w_i - x_3, x_3 \right) + \sum_{i=1}^m w_i, \quad m \in \mathbb{N}, \quad (2.58)$$

where $w_0 = 0$ and

$$w_i = \gamma^{m+1-i} u \left(x_1 - \sum_{j=0}^{i-1} w_j, x_3 \right) \quad \text{for } i = 1, \dots, m, \quad \gamma \in \mathbb{R}, \quad (2.59)$$

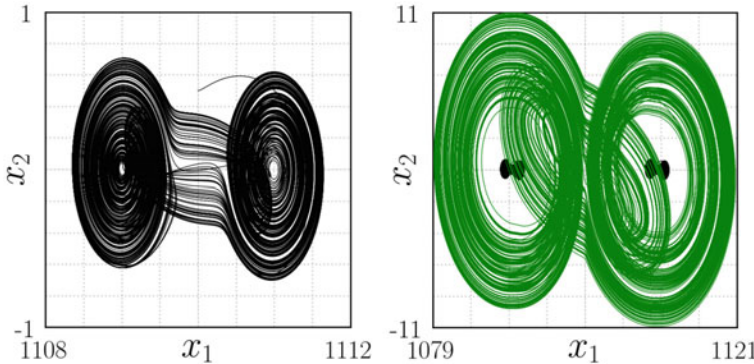


Fig. 2.41 Projections of (left) self-excited double-scroll attractor and (right) hidden double-scroll (green) and two self-excited double-scroll attractors (black) of fifteen coexisting attractors generated by Eqs. 2.57–2.58 with $a = 0.2$, $b = 5$, $c = -3$, $m = 3$, $\alpha = 1$, and $\gamma = 10$. Reprinted by permission from the Springer Nature [187] ©2021

where $u(x_1, x_3)$ is a binary function with two arguments, x_1 and x_3 , which takes values either 1 or -1 depending on x_1 and x_3 , defined as

$$u(x_1, x_3) = \begin{cases} 1, & \text{if } x_1 > 0 \text{ and } x_3 \geq 0, \\ -1, & \text{if } x_1 \leq 0 \text{ and } x_3 \geq 0, \\ 1, & \text{if } x_1 \geq 0 \text{ and } x_3 < 0, \\ 1, & \text{if } x_1 > 0 \text{ and } x_3 < 0. \end{cases} \quad (2.60)$$

For $m = 1$, there are two self-excited attractors and one hidden attractor. As m is increased, the number of attractors is multiplied by two, and a new hidden attractor may appear. Therefore, the total number of hidden attractors is $2^m - 1$, and the total number of self-excited attractors is 2^m . Thus, the total number of coexisting attractors is $2^{m+1} - 1$.

As an example, for $m = 3$, $\alpha = 1$, and $\gamma = 10$ the system exhibits fifteen nested double-scroll attractors (eight self-excited and seven hidden). The projections of the attractors onto the (x_1, x_2) plane are shown in Fig. 2.41. There are eight self-excited double-scroll attractors (black), one of them is shown in the left panel of Fig. 2.41. A pair of self-excited double scroll attractors generates a hidden double-scroll attractor shown in green in the right panel of Fig. 2.41. Then, a pair of hidden attractors generate a larger double-scroll hidden attractor, and so on.

Figure 2.42 shows the basins of attraction of the fifteen coexisting attractors, which arise as disjoint sets in the phase space due to the nested geometry of the attractors. For example, the basin of attraction of a hidden green attractor shown in the right panel of Fig. 2.41 surrounds four equilibrium points, but the equilibria are not part of it, neither the two self-excited attractors highlighted in black. The area of attraction of each self-excited attractor surrounds two equilibria, but it is also surrounded by the area of attraction of the hidden attractor.

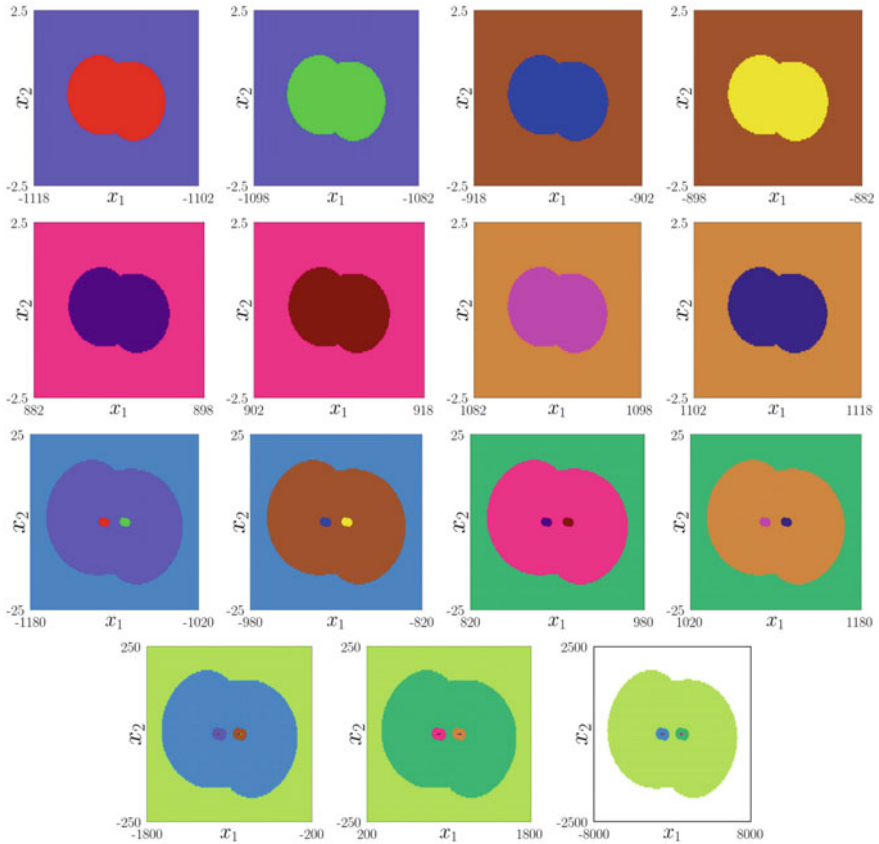


Fig. 2.42 Basins of attraction of fifteen double-scroll self-excited and hidden attractors generated by Eqs. 2.57–2.58 with the same parameters as in Fig. 2.41, on the plane $\{\mathbf{x} \in \mathbb{R}^3 : x_3 = 0\}$. Different basins are shown by different colors, the white region does not belong to any basin of attraction. Reprinted by permission from the Springer Nature [187] ©2021

This approach can also be applied to other systems which exhibit not only double scroll attractors, but different number of scrolls, or even nested hidden grid attractors. The prominent application of the systems with coexisting multiscroll hidden and self-excited attractors is chaotic cryptography and secure communication. On the base of such systems, a pseudorandom number generator can be created to generate a chaotic sequence with specific properties (see Sect. 7.4.2).

2.4.5 Final-State Machine

The described methods for estimating the basin size require the approximation of a system and comprehensive calculations. However, in the current era of computers, the calculation process for searching attractors and their basins can be automatized. To do this, Datseris and Wagemakers [188] developed an algorithm which allows attractor identification for arbitrarily high-dimensional dynamical systems without prior knowledge of the number, location, or nature of the attractors. The algorithm defines an appropriate finite-state machine on the state space.

A *finite-state machine* in the theory of algorithms is a mathematical abstraction, a model of a discrete device that has one input, one output and at each moment of time is in one state out of many possible ones. This is a special case of an abstract discrete automaton, the number of possible internal states of which is finite. The method developed in [188] is based on the Poincaré recurrence theorem, which states that, while on the attractor, the trajectory will sooner or later visit the same region of the phase space. The attractors first are located by searching for recurrences on the phase-state discretization using the dynamical system transformation to a finite state machine, and then the initial conditions are matched with the attractors.

The algorithm works as follows. First, a grid of initial conditions is applied to that part of the phase space in which the attractor is supposed to be located, and the information is stored in a data array which has the dimensions of the grid. In addition, an integrator is introduced that moves a point in the state space in time, and at each step the algorithm determines which cell the current point belongs to.

To identify the attractor, the trajectory successive steps are tracked on a grid of initial conditions, as illustrated in Fig. 2.43. As the trajectory develops, the algorithm leaves a red mark on each visited cell, and when the orbit reaches the already marked cell, the algorithm starts counting repetitions. When the trajectory passes through already marked cells, these cells are marked in blue. The blue cells form a new attractor.

A finite state machine formalism provides a flexible structure of the algorithm, which allows, if necessary, to expand its functionality. Specifically, the machine input to one of the five possible numbers stored in the current grid cell. Initially, each cell of the grid is coded by the number 1 meaning that there is an unknown basin or attractor. Cells containing attractor points are coded with an even number n , while cells containing basin points are coded with an odd number $n + 1$. Cells associated with initial conditions for a diverging trajectory are coded with -1 . Finally, cells encoded with 1 that are visited by the trajectory are coded as “marked”.

Transitions between these five states are controlled by an internal counter and a state machine input. At each step of the process, the integrator of the dynamical system develops the current point of the trajectory in one step of time Δt . The new phase-space pathpoint is mapped to the corresponding grid cell, and the encoding of the grid cell is passed to the finite state machine as input. The machine’s internal counter is incremented by one if the given input leaves the machine in the same state as before, while it is set to zero when in case of a transition between states.

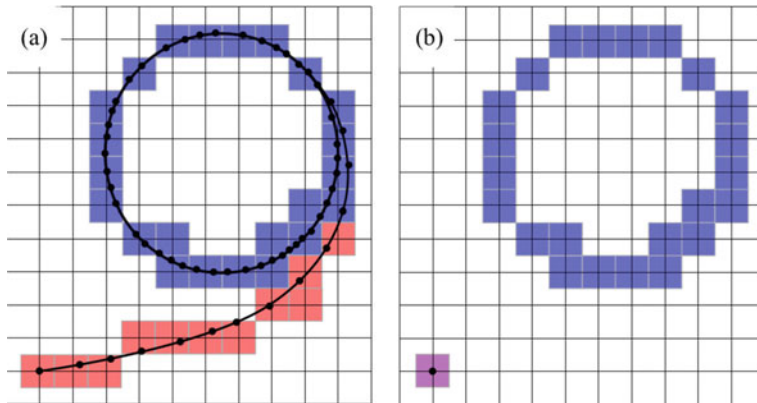


Fig. 2.43 Attractor identification on the grid. The intersections of the grid correspond to the initial conditions, the black dots correspond to the states of the dynamical system during integration, and the solid line serves as a reference during the process. The color areas around the intersections are cells that are used to define the attractors and its basin of attraction. **a** Searching an attractor. Each visited cell is marked in red in the path to the attractor (blue cells), and the process continues until the trajectory visits all blue cells in a raw. **b** Finding a basin of attraction. At this stage, the algorithm marks the cell of the initial state (bottom left) as part of the basin of attraction of the attractor marked by blue cells. Adapted from [188]

The finite-state machine enables to find attractors of different types and their basins of attraction, including hidden attractors and riddled basins of attraction. To calculate basins with fractal boundaries, a zoom of some basins near the boundary is required. For this, the algorithm uses the operation mode which works with already identified attractors. In this mode, the algorithm calculates the minimum distance to the current point relative to all attractors. When one of these distances is below a given threshold, the initial condition is consistent with the corresponding attractor. Thus, the original algorithm can be used for the initial detection of attractors on a coarser and coarser phase space grid, which is then refined in the second operation mode.

The algorithm is easy to use, computationally efficient, and is implemented in the general-purpose library `DynamicalSystems.jl` [189]. In addition to the open source implementation, the entire codebase is available on the Internet for free [190, 191].

It should be noted that the described method has certain limitations. First of all, there is no guarantee that all attractors existing in the phase space will be found at a given grid resolution. The overall length of the grid must also be carefully chosen to be large enough to actually contain attractors. Another difficulty is the correct choice of the integrator step Δt in the case of continuous systems. It should be large enough so that the trajectory enters different cells at each step. However, if it is too large, we may lose the basin details. On the other hand, if the step is too small, then

some of the results may be incorrect and the computational cost will also be higher. We have to emphasize that the array size grows exponentially with the phase-space dimension.

References

1. Tufillaro NB, Reilly J, Abbott T (1992) An experimental approach to nonlinear dynamics and Chaos. Addison-Wesley
2. Eschenazi E, Solari HG, Gilmore R (1989) Basins of attraction in driven dynamical systems. *Phys Rev A* 39:2609–2627
3. Astakhov V, Fujiwara N, Gulay A, Tsukamoto N, Kurths J (2013) Hopf bifurcation and multistability in a system of phase oscillators. *Phys Rev E* 88:032908
4. Astakhov S, Astakhov O, Astakhov V, Kurths J (2016) Bifurcational mechanism of multi-stability formation and frequency entrainment in a van der pol oscillator with an additional oscillatory circuit. *Int J Bifur Chaos* 26(7):1650124
5. Yu P, Lin W (2016) Complex dynamics in biological systems arising from multiple limit cycle bifurcation. *J Biol Dyn* 10:263–285
6. Keener JP (1981) Infinite period bifurcation and global bifurcation branches. *SIAM J Appl Math* 41(1):127–144
7. Rucklidge AM (1994) Chaos in magnetoconvection. *Nonlinearity* 7(6):1565–1591
8. Demeter G, Kramer L (1999) Transition to chaos via gluing bifurcations in optically excited nematic liquid crystals. *Phys Rev Lett* 83(23):4744–4747
9. Pazó D, Pérez-Muñozuri V (2003) Traveling fronts in an array of coupled symmetric bistable units. *Chaos* 13(3):812–823
10. Peacock T, Mullin T (2001) Homoclinic bifurcation in a liquid crystal flow. *J Fluid Mech* 432:369–386
11. Marques F, Lopez JM, Irano V (2002) Imperfect gluing bifurcation in a temporal glide-symmetric Taylor-Couette flow. *Phys Fluids* 14:L33–L36
12. Herrero R, Farjas J, Pons R, Pi F, Orriols G (1998) Gluing bifurcations in optothermal nonlinear devices. *Phys Rev E* 57:5366–5377
13. Glendinning P, Absaghen J, Mullin T (2001) Imperfect gluing bifurcation. *Phys Rev E* 64:36208
14. Roy PK, Daha SK (2006) Gluing bifurcations in Chua oscillator. *Int J Bifurc Chaos* 16(12):3497–3508
15. Zebrowski JJ, Baranowski R (2003) Direct observation of homoclinic orbits in human heart rate variability. *Phys Rev E* 67:056216
16. Chossat P, Golubitsky M (1988) Symmetry-increasing bifurcation of chaotic attractors. *Physica D* 32:423–436
17. Yanchuk S, Kapitaniak T (2001) Symmetry-increasing bifurcation as a predictor of a chaos-hyperchaos transition in coupled systems. *Phys Rev E* 64:056235
18. Newhouse S (1970) Non-density of axiom A(a) on S^2 . *Proc Am Math Soc Symp Pure Math* 14:191–202
19. Newhouse S (1974) Diffeomorphism with infinitely many sinks. *Topology* 13:9–18
20. Newhouse S (1979) The abundance of wild hyperbolic sets and nonsmooth stable sets for diffeomorphisms. *Publ Math Inst Hautes Études Sci* 50:101–151
21. Palis J, Viana M (1994) High dimension diffeomorphisms displaying infinitely many periodic attractors. *Ann Math* 140(1):207–250
22. Colli E (1998) Infinitely many coexisting strange attractors. *Ann Inst H Poincaré Anal Non Linéaire* 15:539–579
23. Palis J, Taken F (1993) Hyperbolicity and sensitive chaotic dynamics at homoclinic bifurcations. Cambridge University Press, New York

24. Poon L, Grebogi C (1995) Controlling complexity. *Phys Rev Lett* 75:4023–4026
25. Feudel U, Grebogi C, Hunt BR, Yorke JA (1996) Map with more than 100 coexisting low-period periodic attractors. *Phys Rev E* 54(1):71–81
26. Feudel U, Grebogi C (1997) Multistability and the control of complexity. *Chaos* 7:597–604
27. Lieberman MA, Tsang KY (1985) Transient chaos in dissipatively perturbed, near-integrable hamiltonian systems. *Phys Rev Lett* 55:908–911
28. Zaslavskii GM (1978) The simplest case of a strange attractor. *Phys Lett A* 69(3):145–147
29. Rech P, Beims M, Gallas J (2006) Basin size evolution between dissipative and conservative limits. *Phys Rev E* 71:017202
30. Kraut S, Feudel U, Grebogi C (1999) Preference of attractors in noisy multistable systems. *Phys Rev E* 59:5253–5260
31. Kraut S, Feudel U (2003) Enhancement of noise-induced escape through the existence of a chaotic saddle. *Phys Rev E* 67:015204(R)
32. Blazejczyk-Okolewska B, Kapitaniak T (1998) Co-existing attractors of impact oscillator. *Chaos, Solitons Fractals* 9:1439–1443
33. Mário de Freitas ST, Viana RL, Grebogi C (2004) Basins of attraction of periodic oscillations in suspension bridges. *Nonlinear Dyn* 37:207–226
34. Weigel R, Atlee Jackson E (1998) Multistability and the control of complexity. *Int J Bifurc Chaos* 8:173–178
35. Kaneko K (1997) Dominance of milnor attractors and noise-induced selection in a multiattractor system. *Phys Rev Lett* 78:2736–2739
36. Kaneko K (1989) Chaotic but regular posi-nega switch among coded attractors by cluster size variation. *Phys Rev Lett* 63:219–223
37. Kaneko K (1990) Clustering, coding, switching, hierarchical ordering, and control in network of chaotic elements. *Physica D* 41:137–172
38. Wiesenfeld K, Hadley P (1998) Attractor crowding in oscillator array. *Phys Rev Lett* 62:1335–1338
39. Osipov GV, Sushchik MM (1998) Synchronized clusters and multistability in arrays of oscillators with different natural frequencies. *Phys Rev E* 58(6):7198–7207
40. Wang W, Kiss IZ, Hudson JL (2000) Experiments on arrays of globally coupled chaotic electrochemical oscillators: synchronization and clustering. *Chaos* 10(1):248–256
41. Postnov DE, Müller F, Schuppner RB, Schimansky-Geier L (2009) Dynamical structures in binary media of potassium-driven neurons. *Phys Rev E* 80(3):031921
42. Vanag VK, Epstein IR (2001) Inwardly rotating spiral waves in a reaction-diffusion system. *Science* 294:835–837
43. Dudkowski D, Jafari S, Kapitaniak T, Kuznetsov NV, Leonov GA, Prasad A (2016) Hidden attractors in dynamical systems. *Phys Rep* 637:1–50
44. Astakhov VV, Bezruchko BP, Erastova EN, Seleznev EP (1990) Oscillation types and their evolution in dissipatively coupled Feigenbaum systems. *Sov Phys Tech Phys* 35:1122–1129, zh. Tekh. Fiz. 60 (1990) 19–26
45. Vadivasova TE, Sosnovtseva OV, Balanov AG, Astakhov V (2000) Phase multistability of synchronous chaotic oscillations. *Discret Dyn Nat Soc* 4:231–243
46. Mosekilde E, Postnov DE, DE, Sosnovtseva OS, (2003) Phase multistability in coupled oscillator systems. *Prog Theor Phys Suppl* 150:147–164
47. Postnov DE, Vadivasova TE, Sosnovtseva OV, Balanov AG, Anishchenko VS, Mosekilde E (1999) Role of multistability in the transition to chaotic phase synchronization. *Chaos* 9(1):227–232
48. Gu Y, Tung M, Yuan JM, Feng DH, Narducci LM (1984) Crises and hysteresis in coupled logistic maps. *Phys Rev Lett* 52(9):701–704
49. Ferretti A, Rahman NK (1987) Coupled logistic maps in physico-chemical processes: Coexisting attractors and their applications. *Chem Phys Lett* 140:71–75
50. Carvalho R, Vilela Mendes R, Seixas J (1999) Feigenbaum networks. *Physica D* 126(1–2):27–37

51. Carvalho R, Fernandez B, Vilela Mendes R (2001) From synchronization to multistability in two coupled quadratic maps. *Phys Lett A* 285(5–6):327–338
52. Bezruchko BP, Prokhorov MD, Seleznev YP (2003) Oscillation types, multistability, and basins of attractors in symmetrically coupled period-doubling systems. *Chaos Soliton Fraction* 15:695–711
53. Astakhov V, Shabunin A, A, Uhm W, Kim S, (2001) Multistability formation and synchronization loss in coupled Hénon maps: Two sides of the single bifurcational mechanism. *Phys Rev E* 63:056212
54. Ermentrout GB (1985) The behavior of rings of coupled oscillators. *J Math Biol* 23(1):55–74
55. Ren L, Ermentrout GB (2000) Phase locking in chains of multiple-coupled oscillators. *Physica D* 143:56–73
56. Shabunin A, Feudel U, Astakhov V (2009) Phase multistability and phase synchronization in an array of locally coupled period-doubling oscillators. *Phys Rev E* 80:026211
57. Matías MA, Pérez-Muñoz V, Lorenzo MN, Mariño IP, Pérez-Villar V (1997) Observation of a fast rotating wave in rings of coupled chaotic oscillators. *Phys Rev Lett* 78(2):219–222
58. Kleinfeld D, Delaney KR, Fee M, Flores JA, Tank DW, Gelperin A (1994) Dynamics of propagating waves in the olfactory network of a terrestrial mollusc: an electrical and optical study. *J Neurophysiol* 72:1402–1419
59. Cinquin O, Demongeot J (2002) Positive and negative feedback: striking a balance between necessary antagonists. *J Theor Biol* 216:229–241
60. MacArthur BD et al (2004) Nanog-dependent feedback loops regulate murine embryonic stem cell heterogeneity. *Nat Cell Biol* 14(11):1139–1147
61. Angeli D, Ferrell JJE, Sontag ED (2004) Detection of multistability, bifurcations, and hysteresis in a large class of biological positive-feedback systems. *Proc Natl Acad Sci USA* 101(7):1822–1827
62. Housden BE, Perrimon N (2014) Spatial and temporal organization of signaling pathways. *Trends Biochem Sci* 39:457–464
63. Gardner TS, Cantor CR, Collins JJ (2000) Construction of a genetic toggle switch in *Escherichia coli*. *Nature* 403:324–339
64. Ikeda K (1979) Multiple-valued stationary state and its instability of the transmitted light by a ring cavity system. *Opt Commun* 30:257–261
65. Ikeda K, Matsumoto K (1987) High-dimensional chaotic behavior in systems with time-delayed feedback. *Physica D* 29(1–2):223–235
66. Gibbs HM, Hopf FA, Kaplan DL, Shoemaker RL (1981) Observation of chaos in optical bistability. *Phys Rev Lett* 46:474–477
67. Aida T, Davis P (1992) Oscillation modes of laser diode pumped hybrid bistable system with large delay and application to dynamical memory. *IEEE J Quantum Electron* 28(3):686–699
68. Atay FM (ed) (2010) Complex time-delay systems: theory and applications. Understanding complex systems, Springer, Berlin
69. Pyragas K (1992) Continuous control of chaos by self-controlling feedback. *Phys Lett A* 170(6):421–428
70. Pyragas K (1992) Control of chaos via extended delay feedback. *Phys Lett A* 206:323–330
71. Martínez-Zéregá BE, Pisarchik AN (2005) Efficiency of the control of coexisting attractors by harmonic modulation applied in different ways. *Phys Lett A* 340(1–4):212–219
72. Martínez-Zéregá BE, Pisarchik AN, Tsimring L (2003) Using periodic modulation to control coexisting attractors induced by delayed feedback. *Phys Lett A* 318:102–111
73. Mensour B, Longtin A (1998) Chaos control in multistable delay-differential equations and their singular limit maps. *Phys Rev E* 58(1):410–422
74. Balanov A, Janson N, Schöll E (2005) Delayed feedback control of chaos: bifurcation analysis. *Phys Rev E* 71:016222
75. Jaimes-Reátegui R, Vera-Ávila VP, Sevilla-Escoboza R, Huerta-Cuéllar G, Castañeda-Hernández CE, Chiu-Zarate R, Pisarchik AN (2016) Synchronization of unidirectionally delay-coupled chaotic oscillators with memory. *Eur Phys J Spec Top* 13:2707–2715

76. Balakin MI, Ryskin NM (2017) Bifurcational mechanism of formation of developed multistability in a van der Pol oscillator with time-delayed feedback. *Rus J Nonlinear Dyn* 13(2):151–164
77. Xia GQ, Chan SC, Liu JM (2007) Multistability in a semiconductor laser with optoelectronic feedback. *Opt Express* 15:572–576
78. Williams CR, Sorrentino F, Murphy TE, Roy R (2013) Synchronization states and multistability in a ring of periodic oscillators: experimentally variable coupling delays. *Chaos* 23:043117
79. de la Fuente IM, Martinez L, Aguirregabiria JM, Veguillas J (1998) Coexistence of multiple periodic and chaotic regimes in biochemical oscillations with phase shifts. *Acta Biotheor* 46(1):37–51
80. Freyer F, Roberts JA, Becker R, Robinson PA, Ritter P, Breakspear M (2011) Biophysical mechanisms of multistability in resting-state cortical rhythms. *J Neurosci* 31(17):6353–6361
81. Neverova GP, Yarovenko IP, Frisman EY (2016) Dynamics of populations with delayed density dependent birth rate regulation. *Ecol Model* 340:64–73
82. Foss J, Longtin A, Mensour B, Milton J (1996) Multistability and delayed recurrent loops. *Phys Rev Lett* 76(4):708–711
83. Foss J, Milton J (2000) Multistability in recurrent neural loops arising from delay. *J Neurophysiol* 84:975–985
84. Song Z, Wang C, Zhen B (2016) Codimension-two bifurcation and multistability coexistence in an inertial two-neuron system with multiple delays. *Nonlinear Dyn* 85:2099–2113
85. Hizanidis J, Aust R, Schöll E (2008) Delay-induced multistability near a global bifurcation. *Int J Bifurc Chaos* 18(6):1759–1765
86. Peinke J, Rau U, Clauss W, Richter R, Parisi J (1989) Critical dynamics near the onset of spontaneous oscillations in p-germanium. *Europhys Lett* 9(8):743–748
87. Patra M, Schwarz G, Schöll E (1998) Bifurcation analysis of stationary and oscillating field domains in semiconductor superlattices with doping fluctuations. *Phys Rev B* 57:1824–1833
88. Hizanidis J, Balanov AG, Amann A, Schöll E (2006) Noise-induced front motion: signature of a global bifurcation. *Phys Rev Lett* 96:244104
89. Dubbeldam JLA, Krauskopf B, Lenstra D (1999) Excitability and coherence resonance in lasers with saturable absorber. *Phys Rev E* 60(6):6580–6588
90. Wieczorek SM, Krauskopf B, Lenstra D (2002) Multipulse excitability in a semiconductor laser with optical injection. *Phys Rev Lett* 88:063901
91. Krauskopf B, Schneider K, Sieber J, Wieczorek S, Wolfrum M (2003) Excitability and self-pulsations near homoclinic bifurcations in semiconductor laser systems. *Opt Commun* 215(4–5):367–379
92. Perlikowski P, Yanchuk S, Popovych OV, Tass PA (2000) Periodic patterns in a ring of delay-coupled oscillators. *Phys Rev E* 82(3):036208
93. Kim S, Park SH, Ryu CS (1997) Multistability in coupled oscillator systems with time delay. *Phys Rev Lett* 79:2911–2914
94. Zanette DH (2000) Propagating structures in globally coupled systems with time delays. *Phys Rev E* 62:3167–3172
95. Tinsley MR, Nkomo S, Showalter K (2012) Chimera and phase-cluster states in populations of coupled chemical oscillators. *Nat Phys* 8(9):662–665
96. Shayer LP, Campbell SA (2000) Stability, bifurcation, and multistability in a system of two coupled neurons with multiple time delays. *SIAM J Appl Math* 61(2):673–700
97. Park SH, Kim S, Pyo HB, Lee S, Lee SK (2000) Time delay effects on dynamic patterns in a coupled neural model. In: Lee SW, Bühlhoff HH, Poggio T (eds) *Biologically motivated computer vision. BMVC 2000. Lecture notes in computer science*, vol 1811, Springer, Berlin
98. Song Y, Makarov VA, Velarde MG (2009) Stability switches, oscillatory multistability, and spatio-temporal patterns of nonlinear oscillations in recurrently delay coupled neural networks. *Biol Cybern* 101:147–167
99. Erzgräber H, Wille E, Krauskopf B, Fischer I (2009) Amplitude-phase dynamics near the locking region of two delay-coupled semiconductor lasers. *Nonlinearity* 22:585–600

100. Sanju Varma VS (1993) Quadratic map modulated by additive periodic forcing. *Phys Rev E* 48:1670–1675
101. Newell TC, Gavrielides A, Kovanis V, Sukow D, Erneux T, Glasgow SA (1997) Unfolding of the period-two bifurcation in a fiber laser pumped with two modulation tones. *Phys Rev E* 56:7223–7231
102. Chizhevsky VN, Corbalán R, Pisarchik AN, (1997) Attractor splitting induced by resonant perturbations. *Phys Rev E* 56(2):1580–1584
103. Chizhevsky VN, Vilaseca R, Corbalán R (1998) Experimental switchings in bistability domains induced by resonant perturbations. *Int J Bifurc Chaos* 8:1777–1782
104. Chizhevsky VN (2001) Multistability in dynamical systems induced by weak periodic perturbations. *Phys Rev E* 64:036223
105. Sprott JC (2014) Simplest chaotic flows with involutorial symmetries. *Int J Bifurc Chaos* 24:1450009
106. Li C, Hu W, Sprott JC, Wang X (2015) Multistability in symmetric chaotic systems. *Eur Phys J Spec Top* 224:1493–1506
107. Barrio R, Blesa F, Serrano S (2009) Qualitative analysis of the Rössler equations: bifurcations of limit cycles and chaotic attractors. *Physica D* 238(13):1087–1100
108. Li C, Sprott JC, Xing H (2017) Constructing chaotic systems with conditional symmetry. *Nonlinear Dyn* 87:1351–1358
109. Bertoldi K, Vitelli V, Christensen J, Van Hecke M (2017) Flexible mechanical metamaterials. *Nat Rev Mater* 2:1–11
110. Novak N, Vesenjak M, Ren Z (2016) Auxetic cellular materials—a Review. *J Mech Eng* 62(9):485–493
111. Lakes R (1987) Foam structures with a negative Poisson's ratio. *Science* 235:1038–1041
112. Alderson KL, Alderson A, Evans KE (1997) The interpretation of strain dependent Poisson's ratio in auxetic polyethylene. *J Strain Anal* 32(3):201–212
113. Herakovich CT (1984) Composite laminates with negative through-the-thickness Poisson's ratios. *Compos Mater* 18(5):447–455
114. Iniguez-Rabago A, Li Y, Overvelde JTB (2019) Exploring multistability in prismatic metamaterials through local actuation. *Nat Commun* 10:5577
115. Overvelde JTB, Shan S, Bertoldi K (2012) Compaction through buckling in 2D periodic, soft and porous structures: Effect of pore shape. *Adv Mater* 24:2337–2342
116. Bückmann T, Kadlec M, Schittny R, Wegener M (2015) Mechanical cloak design by direct lattice transformation. *Proc Natl Acad Sci* 112:4930–4934
117. Coulais C, Sounas D, Alù A (2017) Static non-reciprocity in mechanical metamaterials. *Nature* 542:461–464
118. Grima JN, Alderson A, Evans KE (2005) Auxetic behaviour from rotating rigid units. *Phys Stat Sol B* 242(3):561–575
119. Lakes R, Wojciechowski KW (2008) Negative compressibility, negative Poisson's ratio, and stability. *Phys Stat Sol B* 245(3):545–551
120. Scarpa F, Blain S, Lew T, Perrott D, Ruzzene M, Yates JR (2007) Elastic buckling of hexagonal chiral cell honeycombs. *Compos A* 38(2):280–289
121. Cabras L, Brun M (2014) Auxetic two-dimensional lattices with Poisson's ratio arbitrarily close to -1. *Proc R Soc A* 470:20140538
122. Rafsanjani A, Pasini D (2016) Bistable auxetic mechanical metamaterials inspired by ancient geometric motifs. *Extrem Mech Lett* 9:291–296
123. Faber JA, Arrieta AF, Studart AR (2018) Bioinspired spring origami. *Science* 359:1386–1391
124. Jeong HY, An SC, Lim Y, Jeong MJ, Kim N, Jun YC (2020) 3D and 4D printing of multistable structures. *Appl Sci* 9:291–296
125. Hsu CS (1987) Cell-to-cell mapping: a method of global analysis for nonlinear systems. Springer, New York
126. Saucedo-Solorio JM, Pisarchik AN, Aboites V (2002) Shift of critical points in the parametrically modulated Hénon map with coexisting attractors. *Phys Lett A* 304:21–29
127. Metropolis N, Ulam S (1949) The monte carlo method. *J Am Stat Assoc* 44:335–341

128. Allgower EL, Georg K (1990) Numerical continuation methods: an introduction. Springer, Berlin
129. Krauskopf B, Osinga HM, Galán-Vioque J (eds) (2007) Numerical continuation methods for dynamical systems. Springer, Berlin
130. Chizhevsky VN, Turovets SI (1993) Small signal amplification and classical squeezing near period-doubling bifurcations in a modulated CO₂-laser. Opt Commun 102:175–182
131. Zhou JX, Aliyu MDS, Aurell E, Huang S (2012) Quasi-potential landscape in complex multi-stable systems. J R Soc Interface 9:3539–3553
132. Huerta-Cuellar G, Pisarchik AN, Barmenkov YO (2008) Experimental characterization of hopping dynamics in a multistable fiber laser. Phys Rev E 78:035202(R)
133. Kraut S, Feudel U (2002) Multistability, noise, and attractor hopping: the crucial role of chaotic saddles. Phys Rev E 66:015207
134. Ikeda K, Matsumoto K, Otsuka K (1989) Maxwell-Bloch turbulence. Prog Theor Phys Suppl 99:295–324
135. Timme M, Wolf F, Geisel T (2002) Prevalence of unstable attractors in networks of pulse-coupled oscillators. Phys Rev Lett 89:154105
136. Lai YC, Grebogi C (1995) Intermingled basins and two-state on-off intermittency. Phys Rev E 52(4):R3313–R3316
137. Pisarchik AN, Pinto-Robledo VJ (2002) Experimental observation of two-state on-off intermittency. Phys Rev E 66(2):027203
138. Pisarchik AN, Jaimes-Reátegui R, Sevilla-Escoboza R, Huerta-Cuellar G (2012) Multistate intermittency and extreme pulses in a fiber laser. Phys Rev E 86:056219
139. Godara P, Dudkowski D, Prasad A, Kapitaniak T (2018) New topological tool for multistable dynamical systems. Chaos 28:111101
140. Jafari S, Sprott JC, Golpayegani SMRH (2013) Elementary quadratic chaotic flows with no equilibria. Phys Lett A 377(1):699–702
141. Zakrzhevsky MV (2008) New concepts of nonlinear dynamics: complete bifurcation groups, protuberances, unstable periodic infinitums and rare attractors. J Vibroengineering 10(4):421–441
142. Klokov AV, Zakrzhevsky MV (2011) Parametrically excited pendulum systems with several equilibrium positions: bifurcation analysis and rare attractors. Int J Bifurc Chaos 21(10):2825–2836
143. Chudzik A, Perlikowski P, Stefanski A, Kapitaniak T (2011) Multistability and rare attractors in van der Pol-Duffing oscillator. Int J Bifurc Chaos 21(7):1907–1912
144. Zakrzhevsky M, Smirnova R, Schukin I, Yevstignejev V, V F, Klokov A, Shilvan E (2012) Nonlinear dynamics and Chaos. RTU Publishing House, Riga, Bifurcation Groups and Rare Attractors
145. Sprott JC (2015) Strange attractors with various equilibrium types. Eur Phys J Spec Topics 224(8):1409–1419
146. Sprott JC, Xiong A (2015) Classifying and quantifying basins of attraction. Chaos 25:083101
147. Nusse HE, Yorke JA, Kostelich EJ (1994) Basins of attraction. dynamics: numerical explorations, vol 101. Springer, New York, pp 269–314
148. Leonov GA, Kuznetsov NV (2013) Hidden attractors in dynamical systems: From hidden oscillations in Hilbert-Kolmogorov, Aizerman, and Kalman problems to hidden chaotic attractor in Chua circuits. Int J Bifurc Chaos 23:1330002
149. Hilbert D (1902) Mathematical problems. Bull Am Math Soc 8(10):437–479
150. Dornheim MA (1992) Report pinpoints factors leading to YF-22 crash. Aviation Week Space Technol 137(19):53
151. Buchholz JJ (1992) Time delay induced by control surface rate saturation. Z Flugwiss Weltraumforsch 17:287–293
152. Shifrin C (1993) Sweden seeks cause of Gripen crash. Aviat Week Space Technol 139:78–79
153. Lauvdal T, Murray R, Fossen T (1997) Stabilization of integrator chains in the presence of magnitude and rate saturations: a gain scheduling approach. In: Proceeding IEEE control and decision conference, pp 4404–4005

154. Klyde DH, McRuer DT, Myers TT (1997) Pilot-induced oscillation analysis and prediction with actuator rate limiting. *J Guid Control Dyn* 20(1):81–89
155. Mitchell DG, Klyde DH (2008) Identifying a pilot-induced oscillation signature: New techniques applied to old problems. *J Guid Control Dyn* 31(1):215–224
156. Andrievsky B, Kuznetsov NV, Kuznetsova OA (2018) Hidden nonlinear oscillations in controlled aircraft with saturated inputs. In: 2018 15th international conference on control, automation, robotics and vision (ICARCV), pp 704–709
157. Liberzon MR (2006) Essays on the absolute stability theory. *Automat Rem Control* 67:1610–1644
158. Leonov GA, Vagaitsev VI, Kuznetsov NV (2010) Algorithm for localizing Chua attractors based on the harmonic linearization method. *Doklady Math* 82(1):663–666
159. Leonov GA, Vagaitsev VI, Kuznetsov NV (2011) Localization of hidden Chua’s attractors. *Phys Lett A* 375(23):2230–2233
160. Jafari S, Sprott JC, Nazarimehr F (2015) Recent new examples of hidden attractors. *Eur Phys J Spec Top* 224(1):1469–1476
161. Wang X, Chen G (2013) Constructing a chaotic system with any number of equilibria. *Nonlinear Dyn* 71:429–436
162. Pham VT, Volos C, Jafari S, Wei Z, Wang X (2014) Constructing a novel no-equilibrium chaotic system. *Int J Bifurc Chaos* 24:1450073
163. Tahir FR, Jafari S, Pham VT, Volos C, Wang X (2015) Generating a novel hyperchaotic system out of equilibrium. *Int J Bifurc Chaos* 25:1550056
164. Jafari S, Pham VT, Kapitaniak T (2016) Multiscroll chaotic sea obtained from a simple 3D system without equilibrium. *Int J Bifurc Chaos* 26:1650031
165. Nag Chowdhury S, Ghosh D (2020) Hidden attractors: a new chaotic system without equilibria. *Eur Phys J Spec Top* 229:1299–1308
166. Wei Z, Sprott J, Chen H (2015) Elementary quadratic chaotic flows with a single non-hyperbolic equilibrium. *Phys Lett A* 379:2184–2187
167. Wei Z, Zhang W, Yao M (2015) On the periodic orbit bifurcating from one single non-hyperbolic equilibrium in a chaotic jerk system. *Nonlinear Dyn* 82:1251–1258
168. Wang X, Chen G (2012) A chaotic system with only one stable equilibrium. *Comm Nonlin Sci Numer Simul* 17:1264–1272
169. Molaie M, Jafari S, Sprott JC, Golpayegani SMRH (2013) Simple chaotic flows with one stable equilibrium. *Int J Bifurc Chaos* 23:1350188
170. Kingni S, Jafari S, Simo H, Woaf P (2014) Three-dimensional chaotic autonomous system with only one stable equilibrium: Analysis, circuit design, parameter estimation, control, synchronization and its fractional-order form. *Eur Phys J Plus* 129:76
171. Wei Z, Zhang W (2014) Hidden hyperchaotic attractors in a modified Lorenz-Stenflo system with only one stable equilibrium. *Int J Bifurc Chaos* 24(10):1450127
172. Jafari S, Sprott JC (2013) Simple chaotic flows with a line equilibrium. *Chaos Solitons Fractals* 57:79–84
173. Pham VT, Jafari S, Kapitaniak T (2016) Constructing a chaotic system with an infinite number of equilibrium points. *Int J Bifurc Chaos* 26:1650225
174. Wang X, Pham VT, Volos C (2017) Dynamics, circuit design, and synchronization of a new chaotic system with closed curve equilibrium. *Complexity* 2017:7138971
175. Jafari S, Sprott J, Molaie M (2016) A simple chaotic flow with a plane of equilibria. *Int J Bifurc Chaos* 26(6):1650098
176. Jafari S, Sprott J, Pham VT, Volos C, Li C (2016) Simple chaotic 3d flows with surfaces of equilibria. *Nonlinear Dyn* 86:1349–1358
177. Sprott JC, Jafari S, Khalaf AJM, Kapitaniak T (2017) Megastability: coexistence of a countable infinity of nested attractors in a periodically-forced oscillator with spatially-periodic damping. *Eur Phys J Spec Top* 226(9):1979–1985
178. Tang Y, Abdolmohammadi HR, Khalaf AJM, Tian Y, Kapitaniak T (2018) Carpet oscillator: a new megastable nonlinear oscillator with infinite islands of self-excited and hidden attractors. *Pramana* 91:11

179. Prakash P, Rajagopal K, Singh JP, Roy BK (2018) Megastability in a quasi-periodically forced system exhibiting multistability, quasi-periodic behaviour, and its analogue circuit simulation. *Int J Electron Commun* 92:111–115
180. Wang Z, Hamarash II, Shabestari PS, Jafari S (2019) A new megastable oscillator with rational and irrational parameters. *Internat J Bifurcat Chaos* 29(7):1850085
181. Leutcho TGD, Khalaf AJM, Tabekoueng ZN, Fozin TF, Kengne J, Jafari S, Hussain I (2020) A new oscillator with mega-stability and its Hamilton energy: infinite coexisting hidden and self-excited attractors. *Chaos* 30(3):033112
182. Kuznetsov NV, Vagaitsev VI, Leonov GA, Seledzhi SM (2011) Localization of hidden attractors in smooth Chua's systems. In: ICACM'11: Proceedings of the 2011 international conference on applied and computational mathematics, pp 26–33
183. Li C, Sprott JC (2014) Finding coexisting attractors using amplitude control. *Nonlinear Dyn* 78(3):2059–2064
184. Sprott JC, Wang X, Chen G (2013) Coexistence of point, periodic and strange attractors. *Int J Bifurc Chaos Appl Sci Eng* 23(5):1350093
185. Li C, Sprott JC, Xing H (2016) Crisis in amplitude control hides in multistability. *Int J Bifurc Chaos* 26:1650233
186. Li C, Wang X, Chen G (2017) Diagnosing multistability by offset boosting. *Nonlinear Dyn* 90(6):1335–1341
187. Escalante-González RJ, Campos E (2021) Multistable systems with nested hidden and self-excited double scroll attractors. *Eur Phys J Spec Top.* <https://doi.org/10.1140/epjs/s11734-021-00350-3>
188. Datseris G, Wagemakers A (2021) Effortless estimation of basins of attraction. [arXiv:211004358](https://arxiv.org/abs/211004358)
189. Datseris G (2018) Dynamical systems.jl: a julia software library for chaos and nonlinear dynamics. *J Open Source Softw* 3:598
190. Datseris G (2021). Archived basinspaper codebase. <https://doi.org/10.5281/zenodo.5553936>
191. Datseris G (2021b) Online basinspaper codebase. <https://github.com/Datseris/BasinsPaper>. Accessed 7 Oct 2021

Chapter 3

Manifestation of Multistability in Different Systems



Abstract Multistability is a widespread phenomenon observed in diverse dynamical systems. In this chapter, we give the most representative examples of multistability in discrete and continuous systems, including fractional-order systems. Particular attention is given to multistability in coupled oscillators and popular neural models. Finally, we present the most interesting examples of the manifestation of multistability in various dynamical systems, from mechanical and thermochemical to climatic and space systems.

3.1 Multistability in Discrete Systems

We have already demonstrated in Sect. 2.2.6 how multistability emerges in the delayed logistic map. Here, we will show how multistability arises in two-dimensional discrete systems, namely, in the Hénon map and in the dissipative standard nontwist map. There are also other discrete systems where the coexistence of attractors was observed and which are not included in this book, namely, square root map [1], piecewise linear map [2], quasiperiodically forced circle map [3], kicked rotor map [4], etc.

3.1.1 *Hénon Map*

The Hénon map is a popular example of two-dimensional quadratic mapping. As we have shown in Sect. 1.2.3, even such a simple dynamical system allows the coexistence of attractors with fractal basin boundaries (see Fig. 1.9). Here, we will demonstrate how multistability appears in this map.

The dynamics of the Hénon map is well studied (see, for instance, [5]). The fixed points corresponding eigenvalues are given by Eqs. 1.11 and 2.31. As seen from the bifurcation diagram of the x variable in Fig. 3.1, this map exhibits the coexistence

Fig. 3.1 Bifurcation diagram of the Hénon map in Eq. 1.11 for $J = 0.9$. Period-1 (P_1) (red), period-3 (P_3) (black), and period-9 (P_9) (blue) branches of attractors are shown by the arrows

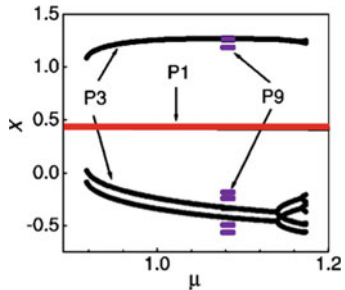
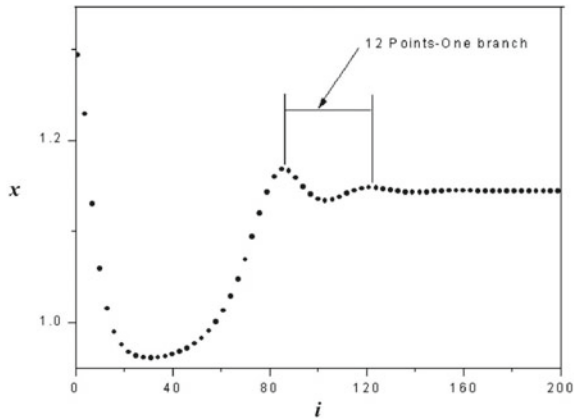


Fig. 3.2 Relaxation oscillations in transients in one branch of the period 3 for $\mu = 0.926$



of period-1, period-3, and period-9 attractors in the parameter range $1.077 < \mu < 1.089$, while the period 3 coexists with the period 1 in the range $0.92 < \mu < 1.18$.

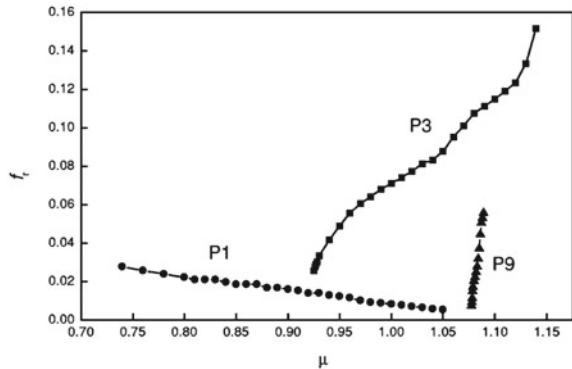
The attractors have different relaxation oscillation frequencies f_r , which depend on the parameter. The frequency f_r can be measured numerically from a time series as an inverse period of damped oscillations after a small disturbance from the equilibrium point, as illustrated in Fig. 3.2, where we present the relaxation oscillations in the period 3. The period of the relaxation oscillations is $p = 12 \times 3 = 36$. The factor 3 appears because the period 3 has three branches in the bifurcation diagram.

The relaxation oscillation frequency is equal to the imaginary part of the eigenvalue of the corresponding fixed point. Unfortunately, it is impossible to find these values analytically because for the period-3 attractor one would need to solve an eighth-order characteristic algebraic equation.

The dependences of f_r on the parameter μ for different attractors are shown in Fig. 3.3.

A similar approach can be used for searching relaxation oscillation frequencies for more complex dynamical systems.

Fig. 3.3 Relaxation oscillation frequencies of the system in the period-1 (dots), period-3 (squares), and period-9 (triangles) regimes as a function of parameter μ



3.1.2 Dissipative Standard Nontwist Map

The labyrinthic standard nontwist map is an interesting example of a discrete system proposed by Simó [6] and later investigated by other researchers [7–10].

This map is defined as

$$\begin{aligned} x_{n+1} &= x_n - a(y_{n+1} - r_1)(y_{n+1} - r_2), \\ y_{n+1} &= (1 - \gamma)y_n - b[\sin(2\pi x_n) + \sin(\nu 2\pi x_n)], \end{aligned} \quad (3.1)$$

where γ is the dissipation parameter (the system is conservative for $\gamma = 0$). The parameters a and b are responsible for the nontwist term and nonlinearity, respectively, both affect the width of the chaotic sea. The parameters r_1 and r_2 indicate the location of resonances in the phase space, and ν is the bifurcation parameter inside the resonance islands. The variable $x \in [0, 1)$ has a period of 1.

The phase spaces of the system in Eq. 3.1 are shown in Fig. 3.4 for the conservative (left) and dissipative (right) cases. While for the conservative map we observe the coexistence of chaotic (disperse points), quasiperiodic (blue and red curves), and periodic (colored closed curves) solutions, a small dissipation transform these solution to a quasiperiodic attractor and two stable steady states.

Thus, the dissipative map exhibits the coexistence of multiple shearless attractors, which are robust due to their origin on shearless torus and survive under generic perturbations. The shearless attractor appears as a result of the dissipation of the shearless curve. This example demonstrates once more that adding a small amount of dissipation turns a conservative system into a multistable one, as we have already demonstrated in Sect. 2.2.2.

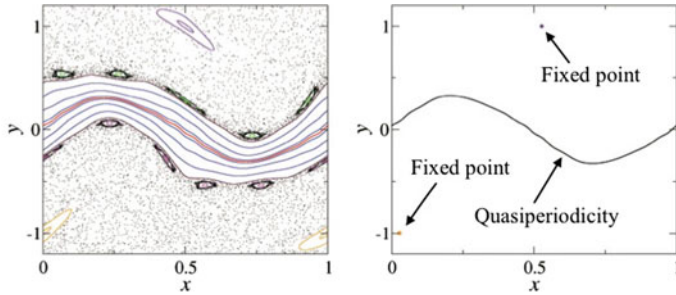


Fig. 3.4 Phase-space plots of (left) conservative ($\gamma = 0$) and (right) dissipative ($\gamma = 0.1$) nontwist maps in Eq. 3.1 for $a = 0.47$, $b = 0.6$, $\nu = 0$, $r_1 = 1$, and $r_2 = -1$. The disperse points represent a chaotic sea, blue and red curves indicate quasiperiodicity, and closed color curves show periodic states. The shearless curve (left) and quasiperiodic attractor (right) are indicated by the red and black curves, respectively. The orange and purple points indicate the fixed point attractors. Reproduced from [10] with permission of AIP Publishing

3.2 Multistability in Continuous Systems

We continue our consideration of multistability with popular continuous-time systems, such as Duffing, Rössler, Lorenz, Chua, and jerk equations.

3.2.1 Duffing Oscillator

The damped Duffing oscillator with a double-well potential is a classical example of a bistable system with two coexisting steady-state attractors. The Duffing system, as a second-order differential equation with third-order nonlinearity, was introduced by the German electrical engineer Georg Duffing [11] to describe forced vibrations of industrial equipment. This prototype dynamical system was then successfully investigated to simulate various physical processes such as string amplification and beam bending. The Duffing equations were also used to model an elastic pendulum, nonlinear electronic circuits, superconducting Josephson parametric amplifiers, plasma ionization waves, and biological processes [12]. An interesting feature of this oscillator is that it exhibits the coexistence of two stable limit cycles for certain parameters.

The Duffing system is given by

$$\ddot{x} + \gamma \dot{x} + \alpha x + \beta x^3 = 0, \quad (3.2)$$

where the first term represents inertia, $\gamma > 0$ is the damping coefficient, α is the spring elasticity, and β is the coefficient of cubic nonlinearity related to stiffness. The corresponding potential energy function can be written as

$$V(x) = \frac{1}{2}\alpha x^2 + \frac{1}{4}\beta x^4. \quad (3.3)$$

Depending on the parameters α and β , we can distinguish four different cases:

- If $\alpha > 0$ and $\beta < 0$ then the potential has a double-hump well with a local minimum at $x = 0$ and two maxima at $\pm\sqrt{\alpha/|\beta|}$.
- If $\alpha > 0$ and $\beta > 0$ then the potential has a single well with a local minimum at $x = 0$.
- If $\alpha < 0$ and $\beta < 0$ then the potential has a single hump with a local maximum at $x = 0$.
- If $\alpha < 0$ and $\beta > 0$ then the potential has a double well with two minima at $\pm\sqrt{|\alpha|/\beta}$ and a local maximum at $x = 0$.

In the last case, we deal with bistability, when the motion is ruled by the potential in Eq. 3.3 with dissipation until the trajectory is attracted to one of the stable fixed points depending on the initial condition. The potential shape in this case is illustrated in Fig. 3.5.

The structure of the basins of attraction of the coexisting fixed points in the Duffing oscillator in Eq. 3.2 is determined by the system parameters. As seen from Fig. 3.6, the basin structure becomes finer as the damping parameter γ is decreased.

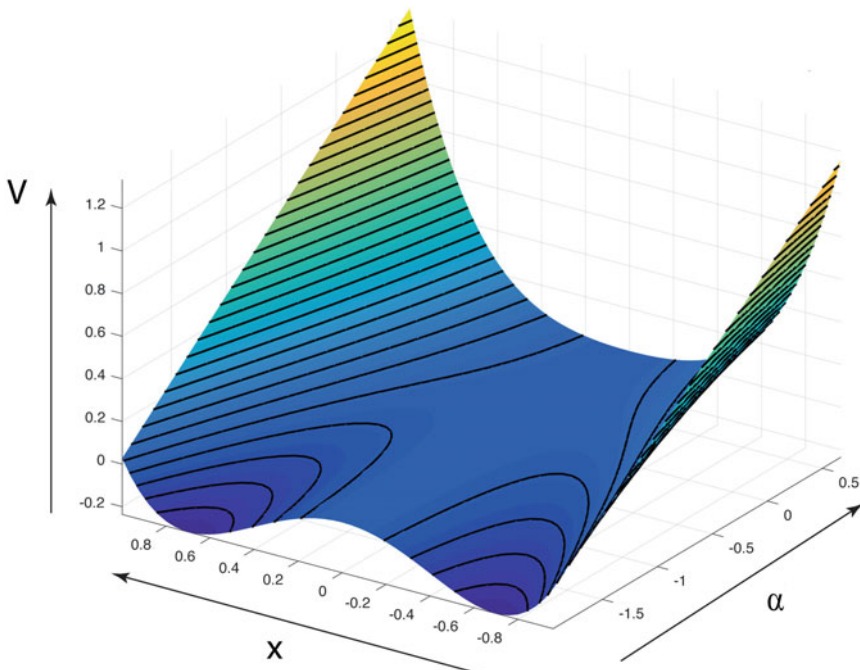
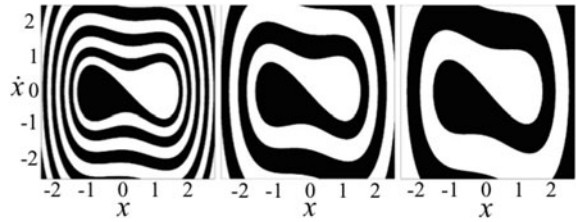


Fig. 3.5 Potential energy of the Duffing oscillator in Eq. 3.2 as a function of α

Fig. 3.6 Basins of attraction of the coexisting fixed points in the bistable Duffing oscillator in Eq. 3.2 for $\alpha = -1$, $\beta = 1$, and $\gamma = 0.1$ (left), $\gamma = 0.2$ (middle), and $\gamma = 0.3$ (right). Adapted from [13]



Although the potential of a damped system cannot always be defined, nevertheless, it is possible to reveal it, if the damping coefficient is written as a logarithmic derivative of a certain function [14]. Now, we will show how a proper potential can be defined for the Duffing oscillator. More explicitly, if we have a motion equation with time-dependent damping coefficient $\gamma(t)$:

$$\ddot{x} + \gamma(t)\dot{x} + \delta(x, t) = 0, \quad (3.4)$$

it can be described by the Langrangian

$$L = \frac{1}{2}m(t)\dot{x}^2 - V(x, t), \quad (3.5)$$

where

$$\gamma(t) = \dot{m}/m, \quad V(x, t) = m(t) \int^x \delta(z, t) dz. \quad (3.6)$$

In other words, Eq. 3.4 can be viewed as an undamped motion with variable mass $m(t)$. Introducing $\gamma(t)$ into Eq. 3.2 we get

$$\ddot{x} + \gamma(t)\dot{x} + \alpha x + \beta x^3 = 0, \quad (3.7)$$

and the corresponding potential becomes time dependent:

$$V(x, t) = m(t) \left[\frac{1}{2}\alpha x^2 + \frac{1}{4}\beta x^4 \right], \quad (3.8)$$

where $\gamma(t) = \dot{m}/m$. Thus, we will have the same potential as Eq. 3.3 with similar fixed points but with a scaling factor $m(t)$.

The double-well Duffing oscillator was successfully used to model a large variety of nonlinear systems including slender aerostructures that may buckle under heavy loads [15], microelectromechanical switches [16], vibration-based energy harvesters [17], and optical systems [18].

3.2.2 Rössler-Like Oscillator

The classical Rössler oscillator [19] with a smooth function has only one attractor. However, a small modification of the Rössler equations by replacing the nonlinear element with a piecewise linear function allows the coexistence of two chaotic attractors [20, 21].

The modified Rössler oscillator with a piecewise linear function is given as follows [22]:

$$\begin{aligned}\dot{x} &= -\alpha_1(x + \beta y + \Gamma z), \\ \dot{y} &= -\alpha_2[-\gamma x - (1 - \delta)y], \\ \dot{z} &= -\alpha_3[-g(x) + z], \\ g(x) &= \begin{cases} 0 & x \leq 3, \\ \mu(x - 3) & x > 3, \end{cases}\end{aligned}\tag{3.9}$$

where x , y , and z are the state variables. For parameters $\alpha_1 = 500$, $\alpha_2 = 200$, $\alpha_3 = 10000$, $\beta = 10$, $\Gamma = 20$, $\gamma = 50$, $\delta = 14.625$, and $\mu = 15$ the system exhibits the coexistence of two chaotic attractors shown in Fig. 3.7.

There is also another type of multistability in the Rössler-like system. This is phase bistability due to symmetry breaking. This phenomenon is observed in the period-doubling regime in the bifurcation diagram illustrated in Fig. 3.8. When parameter $R \sim \delta$ is increased (left panel), the phase switches between two branches of the period doubling. At the same time, another attractor coexists, which can be revealed when R is decreased, i.e. the branches follow their usual ways and the phase does not change (right panel). Thus, there exists phase bistability in the period-doubling range [23].

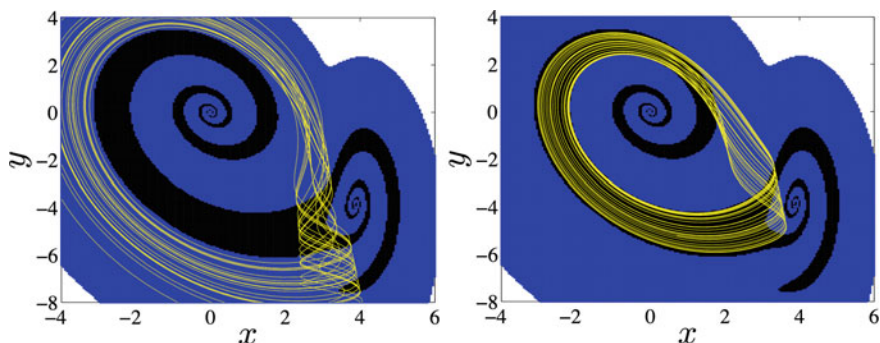


Fig. 3.7 Phase portraits of chaotic attractors (yellow curves) and their basins of attraction (blue and black areas) of the system in Eq. 3.9

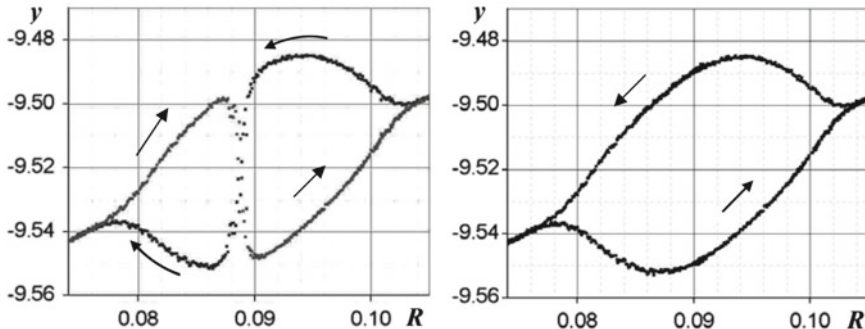


Fig. 3.8 Phase bistability and change of symmetry in the period-bubbling in the Rössler-like system in Eq. 3.9. The arrows indicate the direction of the parameter change. The symmetry breaking is seen in the left panel

3.2.3 Lorenz-Like System

The classical Lorenz system [24]

$$\begin{aligned}\dot{x} &= \sigma(x - y), \\ \dot{y} &= rx - y - yz, \\ \dot{z} &= xy - bz\end{aligned}\tag{3.10}$$

has a single symmetric double-wing chaotic attractor for standard parameter values $\sigma = 10$, $r = 28$, $b = 8/3$. However, for different parameters, in particular, for $r = 0$ and $b < 0$, the classic butterfly attractor is splitted into a symmetric pair of strange attractors, or it shrinks into a small attractor basin intermingled with the basins of a symmetric pair of limit cycles, resulting in bistability or tristability [25] (Fig. 3.9).

Multistability was also found in other modifications of the Lorenz system. In particular, Leonov and his colleagues [26] studied the modified Lorenz system

$$\begin{aligned}\dot{x} &= \sigma(x - y) - ayz, \\ \dot{y} &= rx - y - xz, \\ \dot{z} &= xy - bz,\end{aligned}\tag{3.11}$$

where they found the coexistence of self-excited and hidden attractors by homotopy and numerical continuation. For $a = 0$, the system in Eq. 3.11 coincides with the classical Lorenz system Eq. 3.10.

The coexisting attractors in Eq. 3.11 are shown in Fig. 3.10. The self-excited attractors can be found using the standard computational procedure with initial data in the vicinity of one of the equilibria $S_{0,1,2}$ on the corresponding unstable manifolds, while the hidden attractor is localized by a special numerical method because its basin of attraction does not intersect the small neighborhoods of the unstable manifolds of the equilibria.

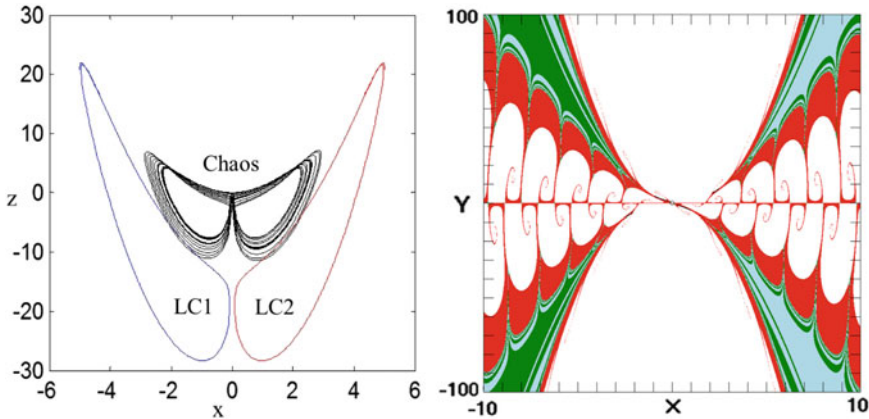


Fig. 3.9 Tristability in the Lorenz-like system in Eq. 3.10 for $b = 0$, $r = -3$ and $\sigma = 0.279$ and initial conditions $(-0.1, 0.1, -2)$ and $(\mp 0.1, \pm 0.1, -14)$. (Left) Two coexisting symmetric limit cycles (LC1 and LC2) and chaotic attractor. (Right) Cross-section for $z = 0$ of the basins of attraction of periodic cycles (blue and green) and chaos (red). Adapted from [25]

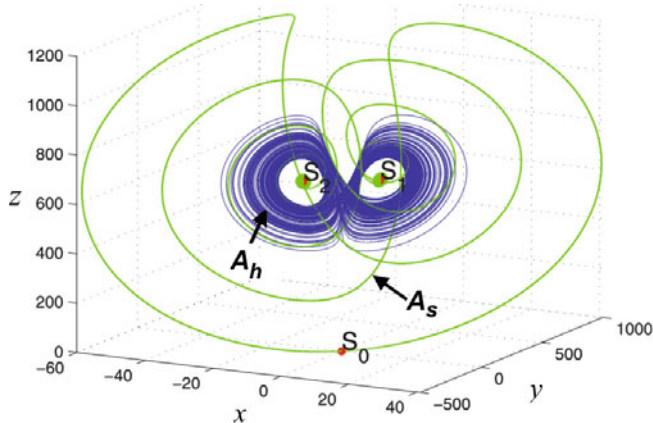


Fig. 3.10 Coexistence of hidden A_h (blue) and self-excited A_s (green) attractors in the Lorenz system in Eq. 3.11. $S_{0,1,2}$ are saddle points. Adapted from [26]

In addition, the coexistence of hidden attractors was also observed in a four-dimensional Lorenz-like system. In a certain range of parameters, Li and Sprott [25] found coexisting stable torus with either a symmetric pair of strange attractors or with a symmetric pair of limit cycles. For other set of parameters, the authors observed three coexisting limit cycles and Arnold tongues. All the attractors are hidden because no equilibria exist.

3.2.4 Chua Oscillator

The first electronic circuit exhibiting chaos was constructed on the base of the Chua model [27]. The first hidden attractor was also discovered in the Chua system with piecewise-linear nonlinearity [28]. The coexistence of stable equilibria and hidden periodic limit cycle was observed in a modified smooth Chua system [29].

The Chua oscillator with smooth cubic nonlinearity is given as [27]:

$$\begin{aligned}\dot{x} &= \alpha[x - y + f(x)], \\ \dot{y} &= -x + y - z, \\ \dot{z} &= \beta y + \gamma z,\end{aligned}\tag{3.12}$$

where $f(x) = ax^3 + bx$.

It should be noted that the system in Eq. 3.12 is symmetric to the system in Eq. 2.50 introduced in Sect. 2.4.1, i.e. $(x, y, z) = (-x, -y, -z)$.

The Chua system in Eq. 3.12 allows the coexistence multiple attractors being self-excited or hidden. The attractors are shown in Fig. 3.11 for $a = -0.0375582129$, $b = -0.8415410391$, $\alpha = 16.6$, $\beta = 53.6$, and $\gamma = -0.75087096$. The localization of hidden attractors is possible using the algorithm described in Sect. 2.4.

Multistability was also found in other modifications of the Chua system and experimentally verified in corresponding electronic circuits [31, 32].

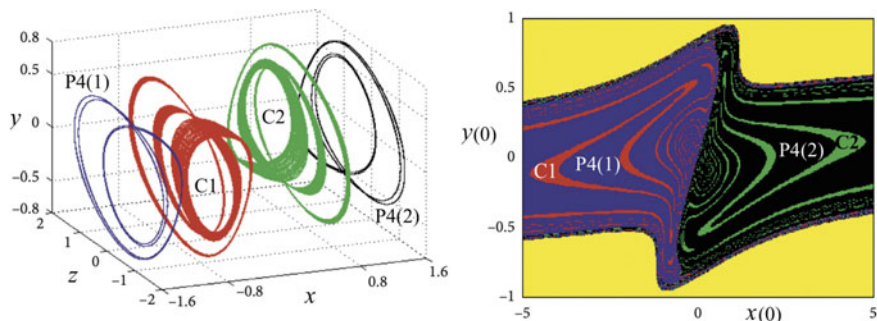


Fig. 3.11 (Left) Coexistence of four attractors (a pair of chaotic attractors and a pair of period-4 limit cycles) in the Chua oscillator in Eq. 3.12. (Right) Cross-section of the basin of attraction at $z(0) = 0$ corresponding to the asymmetric pair of period-4 cycles $P4(1)$ and $P4(2)$ (blue and black) and the pair of chaotic attractors $C1$ and $C2$ (red and green). Yellow region corresponds to unbounded motion. Modified from [30]

3.2.5 Jerk Systems

Jerk systems are third-order differential equations of the form $\ddot{x} = J(\ddot{x}, \dot{x}, x)$, where the nonlinear jerk function J describes the third-time derivative of x . Kengne et al. [33] have shown that a simple 3D autonomous jerk system with a cubic nonlinearity exhibits the coexistence of four attractors.

The mathematical model of the jerk equation is given as follows [34]

$$\ddot{x} = -\ddot{x} - ab\dot{x} + ax - ax^3. \quad (3.13)$$

Changing the variables, this system can be rewritten as

$$\begin{aligned}\dot{x} &= y, \\ \dot{y} &= az, \\ \dot{z} &= x - by - z - x^3.\end{aligned} \quad (3.14)$$

For parameter values $a = 18$ and $b = 0.725$ the system in Eq. 3.14 exhibits the coexistence of four attractors shown in Fig. 3.12.

Multistability was also observed in other jerk systems with different nonlinearity [35, 36]. For example, a simple jerk system with hyperbolic sine nonlinearity was considered by Njitacke et al. [37]:

$$\ddot{x} = -b\ddot{x} - ac\dot{x} + ax - a\varepsilon \sinh(\rho x). \quad (3.15)$$

In this model, the third-order nonlinearity is replaced by the hyperbolic sine function $f(x) = \sinh(x)$ with its parametric generalization $f_k(x) = 0.5(e^{kx} - e^{-x})$. The bifurcation diagram in Fig. 3.13 displays the number of coexisting branches of attractors of the jerk system Eq. 3.15.

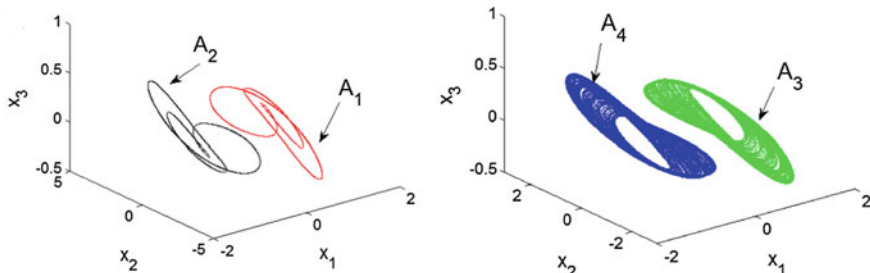


Fig. 3.12 Coexisting attractors of jerk Eq. 3.14. (Left) A₁ and A₂ are period-3 limit cycles. (Right) A₃ and A₄ are chaotic attractors. The attractors are found using initial conditions $x(0), y(0), z(0) = (0, \pm 0.5, \pm 0.5)$ and $(\pm 0.5, 0, 0)$, respectively. Reprinted by permission from the Springer Nature [33] ©2016

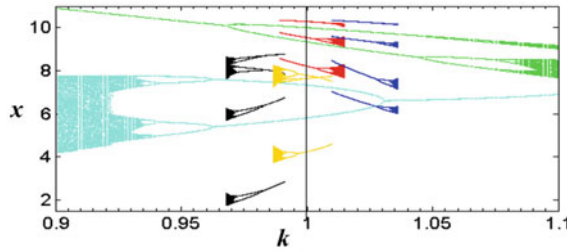


Fig. 3.13 Bifurcation diagram of the jerk system in Eq. 3.15 versus k for $a = 9.69$, $b = 0.6$, and $c = 1$. Coexisting attractors are shown by different colors. Reprinted by permission from the Springer Nature [38] ©2019

A similar multistable behavior was observed in jerk systems with hyperbolic tangent $f(x) = \tanh(x)$ [39, 40], tangent-cubic $f(x) = \tanh x^3$ [41], and piecewise quadratic $f(x) = |x|$ [42] nonlinearities.

3.2.6 Fractional-Order systems

Fractional-order systems are dynamical systems described by using fractional-order derivative and integral operators. Fractional-order derivative has shown great practical value in many areas of science, economy [43], engineering [44], mechanics [45, 46], and secure communications [47]. The main advantages of fractional-order systems over classical integer-order models is that the former systems are characterized by global correlation and infinite memory that provides a good tool for description of hereditary properties of neural networks [48].

Coexistence of attractors were found in many fractional-order models including the Lorenz [49, 50], Chua [50], Rabinovich–Fabrikant [50], Bloch systems [51], neural networks [52], coronary artery system [53], microscopic chemical system [54], centrifugal flywheel governor system [55], and multiscroll system [56].

According to Samko et al. [57], the fractional-order derivative is defined as

$$\frac{d^\alpha x(t)}{dt^\alpha} = J^{n-\alpha} \frac{d^n x(t)}{dt^n}, \quad (3.16)$$

where α is the ordinary n th derivative of $x(t)$, n is the first integer which is not less than α , and J^θ is the θ -order Riemann–Liouville Integral operator given as

$$J^\theta \phi(t) = \frac{1}{\Gamma(\theta)} \int_0^t (t - \tau)^{(\theta-1)} \phi(\tau) d\tau, \quad (3.17)$$

where $\Gamma(\theta)$ is the Gamma function with $0 < \theta \leq 1$.

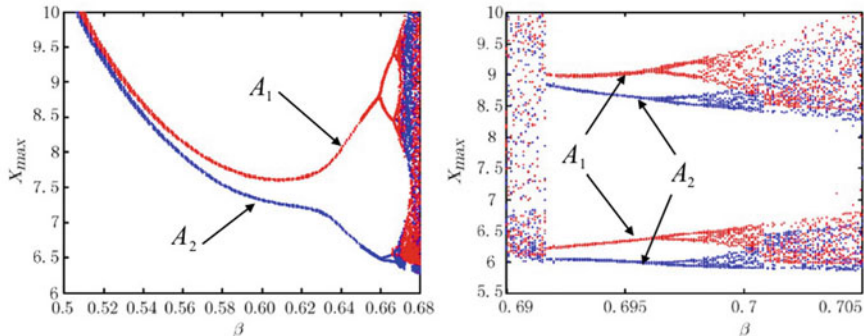


Fig. 3.14 Bifurcation diagrams of peak values of x as a function of β at $\alpha = \gamma = 1$. Attractors A_1 and A_2 correspond to two symmetric initial conditions $x(0) = -8.3458$, $y(0) = -10.6753$, and $z(0) = 12.3088$. Adapted from [49]

As an example consider the fractional-order simplified Lorenz system [49]:

$$\begin{aligned} \frac{d^\alpha x}{dt^\alpha} &= a(x - y), \\ \frac{d^\beta y}{dt^\beta} &= -xz + (b - 4c)x + cy, \\ \frac{d^\beta y}{dt^\beta} &= xy - dz, \end{aligned} \quad (3.18)$$

where α , β , and γ are fractional orders of the time derivatives and $a = 10$, $b = 24$, $c = 5$, $d = 8/3$ are parameters. For $\alpha = \beta = \gamma = 1$, the system Eq. 3.18 coincides with the integer-order simplified Lorenz system [58].

Figure 3.14 depicts the bifurcation diagram of the peak values of x of the system Eq. 3.18 with respect to β . One can see that as β is increased, the system goes to chaos through a cascade of period-doubling bifurcations, where two limit cycles A_1 and A_2 coexist. The right panel illustrates interior crisis of the two coexisting chaotic attractors.

3.3 Multistability in Coupled Systems

Multistability often occurs in coupled dynamical systems because of their higher complexity as compared with solitary systems. First, we will demonstrate the appearance of multistability with the examples of simplest coupled one- and two-dimensional discrete systems, such as coupled quadratic and Hénon maps, and then we will consider popular continuous systems, in particular, coupled Duffing, Rössler, and Lorenz oscillators. We will focus on the dynamics of very simple

coupled systems formed by only two or three oscillators. The dynamics of coupled multistable systems with larger number of oscillators will be considered in Chap. 6. In this section, we mainly focus on system dynamics rather than synchronization.

3.3.1 Coupled Quadratic Maps

One of the simplest discrete systems is a quadratic map. Although in an isolated one-dimensional map multistability is impossible, it occurs in the coupled maps. In particular, Carvalho et al. [59] demonstrated that near accumulation point μ_∞ of the Feigenbaum period-doubling bifurcation cascade, a set of symmetrically coupled quadratic maps exhibit the coexistence of many periodic orbits. A set of coupled quadratic maps is given as [59]

$$x_{i+1} = 1 - \mu_\infty \left\{ \sum_j W_{ij} x_j(t) \right\}^2, \quad (3.19)$$

where $x \in [-1, 1]$, $\mu_\infty = 1.401155\dots$, $\sum_j W_{ij} = 1 \forall i$ and $W_{ij} > 0 \forall i, j$.

In the simplest case of two coupled quadratic maps, the system in Eq. 3.19 can be written as

$$\begin{aligned} x_{i+1} &= (1 - \varepsilon)f(x) + \varepsilon f(y), \\ y_{i+1} &= (1 - \varepsilon)f(y) + \varepsilon f(x), \end{aligned} \quad (3.20)$$

where $f(x) = 1 - \mu x_n^2$, $0 \leq \varepsilon \leq 1/2$, and $0 < \mu < 2$. For $\mu = \mu_\infty$ the map f has a period- 2^p orbit for each $p \in N$, whose components for periods up to $p = 5$ are shown in Fig. 3.15.

It should be noted that multistability in two coupled quadratic maps arises only for the parameters close the Feigenbaum accumulation point μ_∞ .

3.3.2 Coupled Hénon Maps

The Hénon map is a two-dimensional discrete system where multistability appears even in one isolated map (see Sect. 3.1.1). Multistability in mutually coupled Hénon maps was studied by Astakhov and colleagues [61, 62]. Here, we will consider multistability in two unidirectionally coupled Hénon map, so-called master-slave configuration. An interesting feature of this configuration is that the attractor of the master system always exists in the slave system regardless the coupling strength [63].

The Hénon map is given by Eq. 1.11. In the isolated map, multistability exists within a certain range of the parameters μ and J , as illustrated in Fig. 3.16.

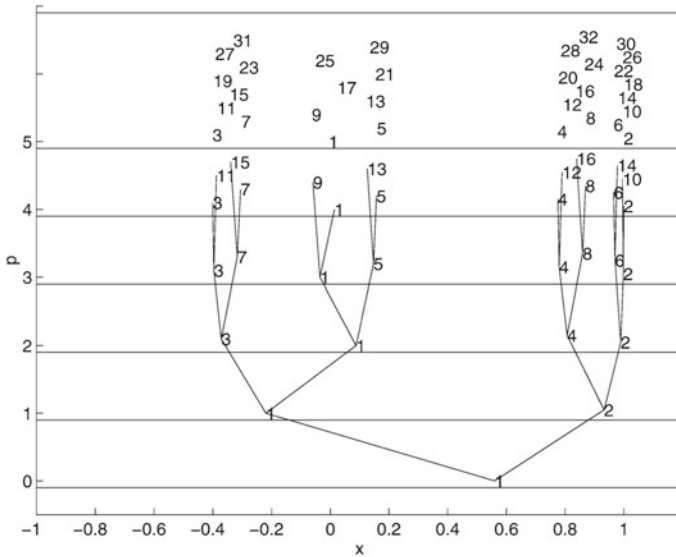
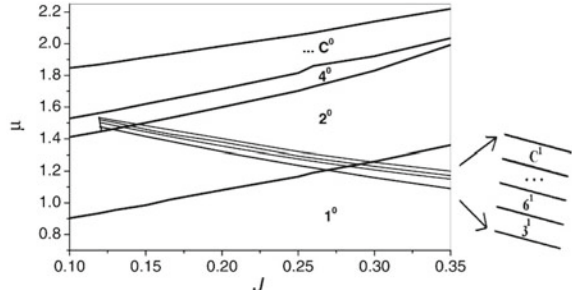


Fig. 3.15 Coexisting periodic orbits at $\mu = \mu_\infty$. The numbers reflect the order in which the components are visited and the tree structure represents the origin of each component in the bifurcation cascade. Reprinted from [60] ©2001 with permission from Elsevier

Fig. 3.16 State diagram of the Hénon map in the parameter space. $1^0, 2^0, 4^0, 3^1, 6^1, C^0$ and C^1 denote periods 1, 2, 4, 3, 6 and two chaotic states, respectively



In the figure, one can see two intersected cascades of period-doubling bifurcations terminated in chaos. The lines are period-doubling bifurcations which separate different periodic regimes. One cascade starting from period 1 is denoted by super-index 0, while another cascade starting from period 3 is denoted by super-index 1. Bistability exists in the parameter range $J > 0.12$ and $\mu \in [1.1, 1.5]$.

Let us fix the parameter $J = 0.166$ and vary μ from $\mu = 1.38$ to $\mu = 1.45$ to explore the coexistence of periods 2^0 and 3^1 and period 2^0 with chaos C^1 . The corresponding bifurcation diagram of x with respect to μ is present in Fig. 3.17.

Fig. 3.17 Bifurcation diagram of the Hénon map at $J = 0.166$. The period 2^0 (P2) coexists with the period 3^1 (P3)

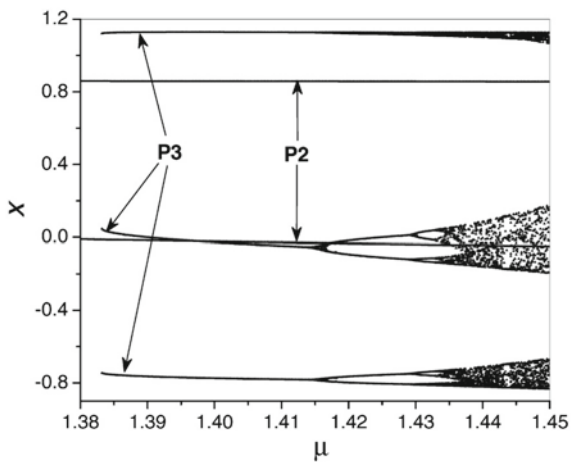
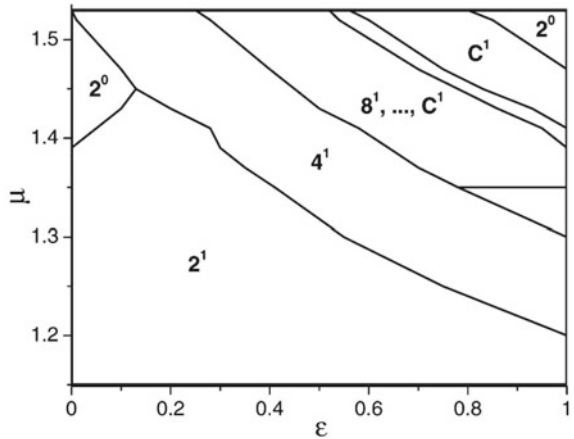


Fig. 3.18 State diagram of the slave map in the (ε, μ) -parameter space for $J = 0.166$

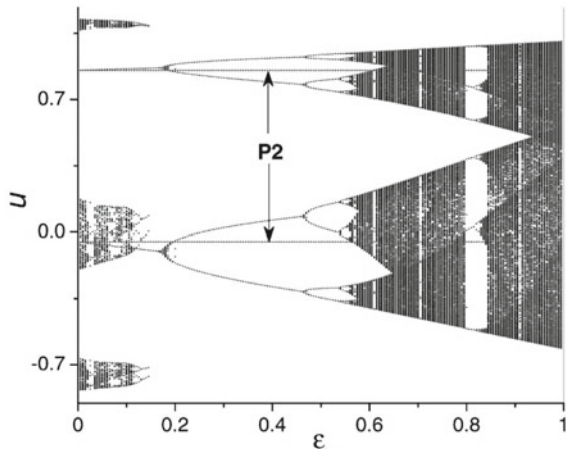


Now, if we couple two Hénon maps as

$$\begin{aligned} x_{n+1} &= 1 - \mu x^2 + y_n, \\ y_{n+1} &= -J x_n, \\ u_{n+1} &= 1 - \mu u^2 + v_n + \varepsilon(y_n - v_n), \\ v_{n+1} &= -Ju_n, \end{aligned} \quad (3.21)$$

where u and v denote the slave map state variables and $\varepsilon \in [0, 1]$ is the coupling strength, we get a multistable system whose state diagram in the (ε, μ) -parameter space has a form shown in Fig. 3.18. One can see from the figure that the coupling induces new attractors in the slave system which always coexist with the period 2^0 of the master system.

Fig. 3.19 Bifurcation diagram of the slave map with the coupling strength as a control parameter when the master map is in the period 2, while the isolated slave map initially stays in chaos



As an example, explore the parameters $\mu = 1.45$ and $J = 0.166$, and consider the case when the master map is in the period-2 regime, while the isolated slave map is in the chaotic regime. The bifurcation diagram of u with respect to ε is shown in Fig. 3.19. One can see that the master attractor (period 2) always exists in the slave map and does not change as ε is increased, whereas the slave map undergoes inverse period-doubling bifurcations leading to the disappearance of the initial chaotic attractor. At the same time, even a very weak coupling induces a different period-2 attractor which undergoes a cascade of period-doubling bifurcations terminated in chaos.

Below we will demonstrate multistability in coupled continuous-time systems.

3.3.3 Coupled Duffing Oscillators

Generally, dynamics of identical oscillators is governed by the following two-dimensional differential equation

$$\ddot{\mathbf{x}} + \gamma \dot{\mathbf{x}} = -\frac{dV(\mathbf{x})}{d\mathbf{x}}, \quad (3.22)$$

where \mathbf{x} is a vector of state variables, γ is a damping factor, and $V(\mathbf{x})$ is a vector of a harmonic potential function of the coupled oscillators. In the case of two symmetric mutually coupled Duffing oscillators, i.e. $\mathbf{x} \equiv (x, y)$, their potential functions can be written as

$$\begin{aligned} V(x, y) &= \frac{a}{2}x^2 + \frac{b}{4}x^4 + \frac{c}{2}x^2y^2, \\ V(y, x) &= \frac{a}{2}y^2 + \frac{b}{4}y^4 + \frac{c}{2}y^2x^2, \end{aligned} \quad (3.23)$$

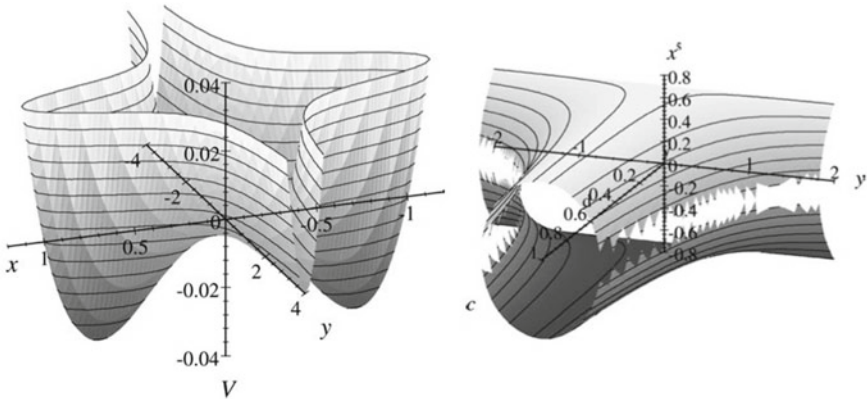


Fig. 3.20 (Left) Double-well potential function Eq. 3.23 and (right) position of stable equilibrium points x^s with respect to variable y and coupling strength c

where a and b are parameters and c is a coupling coefficient. Here, we are interested in the case when the system Eq. 3.22 is bistable, which occurs for $a < 0$ and $b > 0$.

The analysis of steady states of the two coupled Duffing oscillators yields nine possible steady states $Q_i = (\bar{x}_1, \bar{x}_2, \bar{x}_3, \bar{x}_4)$, ($i = 1, \dots, 9$):

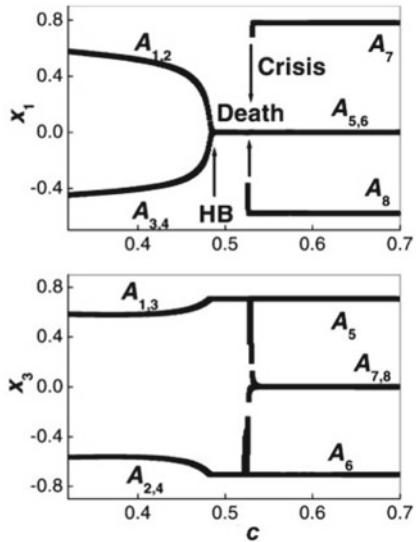
$$\begin{aligned} Q_1 &(0, 0, 0, 0), \quad Q_{2,3} \left(0, 0, \pm \sqrt{-\frac{a}{b}}, 0\right), \quad Q_{4,5} \left(\pm \sqrt{-\frac{a}{b}}, 0, 0, 0\right), \\ Q_{6-9} &\left(\pm \sqrt{-\frac{a}{b+c}}, 0, \pm \sqrt{-\frac{a}{b+c}}, 0\right). \end{aligned} \quad (3.24)$$

To be specific, let us consider the following parameter values: $\gamma = 0.4$, $a = -0.25$, and $b = 0.5$. The resulting three-dimensional potential function $V(x, y)$ is represented in the left panel of Fig. 3.20.

There exists a saddle equilibrium point at $x^u = 0$ and a conjugate pair of stable equilibrium points at $x^s = \pm\sqrt{0.5 - cy^2}$, whose positions depend on the coupling strength c , as illustrated in the right panel of Fig. 3.20. For the double-well potential function $V(y, x)$ of another subsystem, the equilibrium points are $y^u = 0$ and $y^s = \pm\sqrt{0.5 - cx^2}$. For the set of selected parameters, point Q_1 is a saddle and points Q_{2-5} are sinks for any value of $c \geq 0$, while the stability of other four solutions, Q_{6-9} , is defined by c , i.e. they are sinks for $c < 0.5$ and saddles for $c \geq 0.5$.

Thus, one can see that the system has two stable equilibria. Now, let us consider what happens with the system stability if we apply a harmonic modulation to one of the system parameters, for example, to the parameter a of one of the oscillators, i.e. we consider the case when $a = a_0[1 - m \sin(2\pi f t)]$ (a_0 , m and f being the modulation amplitude, depth and frequency). To analyze the system stability and perform numerical simulations, it is convenient to convert the system in Eqs. 3.22 and 3.23

Fig. 3.21 Bifurcation diagrams of the peak values of oscillators x_1 and x_3 with respect to coupling strength c demonstrating the coexistence of stable equilibria and oscillatory states, Hopf bifurcation (HB), and crisis of attractors for $f = 0.2$ and $m = 0.8$



with parametric modulation into a system of first-order differential equations by introducing four new variables: $x_1 = x$, $x_2 = \dot{x}$, $x_3 = y$, $x_4 = \dot{y}$, and $x_5 = m a_0 \sin(2\pi f)$. After the change of the variables, the system becomes [64]

$$\begin{aligned} \dot{x}_1 &= x_2, \\ \dot{x}_2 &= -\gamma x_2 - (a_0 - x_5)x_1 - bx_1^3 - cx_1x_3^2, \\ \dot{x}_3 &= x_4, \\ \dot{x}_4 &= -\gamma x_4 - a_0 x_3 - bx_3^3 - cx_1^2 x_3, \\ \dot{x}_5 &= \pm 2\pi f \sqrt{(a_0 m)^2 - x_5^2}. \end{aligned} \quad (3.25)$$

The bifurcation diagrams of peak amplitudes of oscillators x_1 and x_3 versus coupling strength c are shown in Fig. 3.21. The diagrams demonstrate the coexistence of oscillatory and steady state regimes. As the coupling strength c is increased, the stable equilibrium appears in the Hopf bifurcation at $c \approx 0.48$ when the oscillators pull each other off their limit cycles A_{1-4} and collapse to steady states $A_{5,6}$. The periodic attractors $A_{7,8}$ coexist with the steady state for $c > 0.53$ (partial death), whereas at $c \approx 0.53$ they undergo boundary crisis and disappear, and in the region $0.48 < c < 0.53$ only the steady state exists (pure death).

The general information analysis of the results performed on the basis of the consideration of bifurcation diagrams and time series allows revealing the following possible situations which can be expected from the system of two coupled oscillators with parametric modulation.

- When both the coupling strength and the modulation frequency are sufficiently small ($c \lesssim 0.1$ and $m \lesssim 0.1$), the oscillators respond linearly to external modulation displaying resonance at the fundamental frequency.

- As the coupling strength c is increased, the response becomes nonlinear and the resonance is shifted to the high-frequency range and finally disappears at $c \approx 0.5$. However, for $c \leq 0.5$ both oscillators are in a periodic regime at the modulation frequency (period one) over all frequency ranges.
- A further increase in coupling strength leads to the appearance of coexisting periodic and dead states. The dead states are stable equilibria independent of either f or c , which correspond to the stable equilibria of the three-dimensional double-well potential (left panel of Fig. 3.20). For certain parameter values, the dead states coexist with periodic or chaotic attractors. Thus, the whole system may be either oscillating or not depending on its previous history. The dead states arise in the Hopf bifurcation (HB) where the oscillators pull each other off their limit cycles and collapse to steady states. The coexistence of a stable limit cycle with a stable equilibrium is called *partial amplitude death*.
- Finally, at high coupling strengths all periodic and chaotic attractors are destroyed in boundary crisis and only the stable equilibrium remains. This regime is referred to as *pure amplitude death*. This regime is located between the HB and crisis points (Fig. 3.21).

3.3.4 Coupled Rössler Oscillators

Hens et al. [65] demonstrated that two Rössler oscillators coupled in an appropriate way can exhibit infinitely many coexisting states, so-called *extreme multistability* being considered in Sect. 7. Later, Sprott and Li [66] contended that “*the reason for such a behavior is that the resulting system collapses to one of lower dimension in which the initial conditions of the extraneous equations become parameters in the remaining equations*”. Therefore, the proposed coupling scheme recomposes the coupled systems in such a way that initial conditions become the system parameters, so that a change in the initial conditions of the six-dimensional system is related to a change in the parameter leading to another stable solution. Nevertheless, an artificial six-dimensional system composed of a pair of Rössler oscillators can be created so that it poses extreme multistability. The evidence of extreme multistability in such a system was experimentally verified by Patel et al. [67].

Let us consider two coupled Rössler systems introduced by Hens et al. [65]

$$\begin{aligned}\dot{x}_1 &= -x_2 - x_3, \\ \dot{x}_2 &= x_1 + c_1 x_3, \\ \dot{x}_3 &= c_2 - c_3 x_3 + x_4 x_6, \\ \dot{x}_4 &= x_1 - x_2 - x_3 - x_4, \\ \dot{x}_5 &= x_4 + c_1 x_5, \\ \dot{x}_6 &= c_2 - x_6(x_4 - c_3),\end{aligned}\tag{3.26}$$

where $c_1 = 0.2$, $c_2 = 0.2$, and $c_3 = 5.7$. Initial conditions are given as follows: $x_{01} = -0.1$, $x_{02} = 0.01$, $x_{03} = 0.3$, $x_{04} \in [-8, 8]$, $x_{05} \in [-2, 2]$, and $x_{06} = 2.0$.

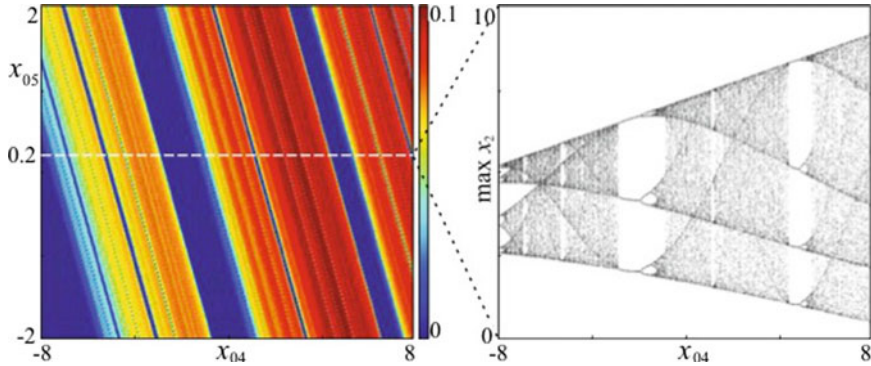


Fig. 3.22 (Left) Maximum Lyapunov exponent in the space of initial conditions $x_{04} \in [-8, 8]$ and $x_{05} \in [-2, 2]$ of coupled Rössler oscillators in Eq. 3.26 and (right) Poincaré map of solutions obtained for fixed $x_{05} = 0.2$ marked by the dashed line in the left panel. Modified from [68]

The coupling in Eq. 3.26 is selected in such a way that after certain time the following relationships are obtained: $x_1 - x_4 = 0, x_2 - x_5 = \text{const}, x_3 - x_6 = 0$, and the complete system Eq. 3.26 poses infinitely many equilibria given by $x_1 = p, x_2 = c_2/(p - c_3), x_3 = c_2/(c_3 - p), x_4 = p, x_5 = -p/c_1, x_6 = c_2/(c_3 - p)$, where p is a parameter. One can see that changes in the initial conditions result in changes in the parameters of the coupled subsystems x_1, x_2, x_3 and x_4, x_5, x_6 .

The coexistence of multiple attractors can be seen in Fig. 3.22 (left panel), where we present a two-dimensional bifurcation diagram of the maximum Lyapunov exponent in the space of the initial conditions x_{04} and x_{05} . The other initial conditions are fixed and given above. In the right panel of the same figure we plot the section of this diagram (Poincaré map) for the fixed value of $x_{05} = 0.2$. Since the initial conditions are used as a control parameter, there is an infinite number of coexisting attractors.

3.3.5 Coupled Lorenz Oscillators

Similar to the coupled Rössler system described above, coupled Lorenz oscillators also exhibit the coexistence of a large number of attractors near a Hopf bifurcation point [69]. To demonstrate this phenomenon, let us consider two mutually coupled identical Lorenz oscillators given by

$$\begin{aligned}\dot{x}_1 &= \alpha(y_1 - x_1), \\ \dot{y}_1 &= \beta x_1 - y_1 - x_1 z_1, \\ \dot{z}_1 &= -\gamma z_1 + x_1 y_1 + \varepsilon(z_2 - z_1), \\ \dot{x}_2 &= \alpha(y_2 - x_2), \\ \dot{y}_2 &= \beta x_2 - y_2 - x_2 z_2, \\ \dot{z}_2 &= -\gamma z_2 + x_2 y_2 + \varepsilon(z_1 - z_2),\end{aligned}\tag{3.27}$$

where $\alpha = 10, \beta < 24.74$, and $\gamma = 8/3$ are parameters and ε is a coupling strength.

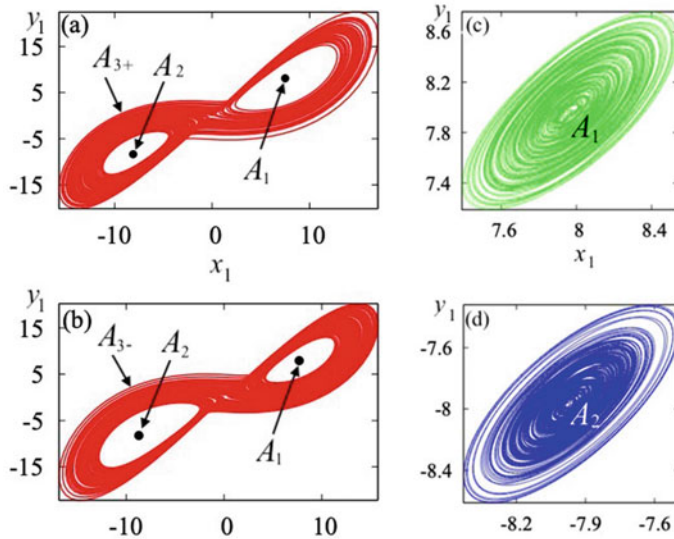


Fig. 3.23 Coexistence of four attractors in two coupled Lorenz oscillators in Eq. 3.10 for $\beta = 24.76$ and $\varepsilon = 0.05$. **a, b** Coexisting butterfly-shape Lorenz attractors A_{3+} and A_{3-} and small chaotic attractors A_1 and A_2 inside the loops, shown by the arrows. **c, d** Enlarged view of small chaotic attractors A_1 and A_2 . Based on data from [69]

For weak coupling, the system Eq. 3.27 displays the coexistence of four attractors, as illustrated with the phase portraits in Fig. 3.23a, b. In particular, there coexist two symmetric chaotic attractors with a butterfly shape (A_{3+} and A_{3-}) similar to the butterfly-like attractor of the isolated Lorenz system, and two small chaotic attractors (A_1 and A_2) inside the spiral loops. The latter attractors are shown in the enlarged pictures in Fig. 3.23c, d.

3.4 Multistability in Neuronal Systems

Let us now consider living systems, specifically, neurons. Multistability is perhaps the most interesting property of living systems and the fundamental attribute of neural dynamics. The coexistence of attractors was evidenced in a number of biological experiments (see, for example, [70–74]). This property is very important for the normal functioning of neurons and the organism as a whole, since multistability in cells can result in multipotentiality, for example, cancer attractors [75, 76].

The importance of multistability in neuronal networks is primarily associated with the interaction of neurons and their synchronization, which plays a key role in the pathogenesis of some neurological diseases, such as Parkinson's disease and essential

tremor [77, 78]. For example, the symptoms of Parkinson’s disease are thought to be caused by an asynchronous pacemaker-like activity in many basal ganglia neurons [79].

The coexistence of attractors was found in many neuronal models. Bifurcation analysis of low-dimensional models (for example, a simplified leech neuron model [80]) revealed at least six types of multistability:

- coexistence of bursting and silent regimes;
- coexistence of tonic spiking and silence;
- coexistence of tonic spiking and subthreshold oscillations;
- coexistence of bursting and subthreshold oscillations;
- coexistence of bursting, subthreshold oscillations and silence;
- coexistence of bursting and tonic spiking.

The first five types occur due to the presence of a separating regime that is either a saddle periodic orbit or a saddle equilibrium.

Below, we consider only two specific cases of multistability in neuronal models, the coexistence of silence and tonic spikes in a single neuron and the coexistence of attractors in asymmetrically coupled neurons. Multistability in neural networks is described in Sect. 6.3.

3.4.1 Single Neuron

The neuron is a fundamental building block of the central nervous system, and consists of three functionally distinct parts, namely, dendrites, soma (or cell body), and axon (see Fig. 3.24). Dendrites act as input devices that collect signals from other neurons and transmit them to the soma, while the soma generates a signal transmitted through the axon to other neurons. The axons of other neurons link to dendrite and soma surfaces using connectors called synapses.

The neuron dynamics is well described using an electrochemical potential gradient across the cell membrane. If the voltage gradient across the membrane increases to a critical threshold value, then there is a subsequent sharp stepwise increase in the potential gradient, so-called *action potential*, transmitted from the soma along the axon to the dendrite of the receiving neuron. The action potential causes the release of neurotransmitter molecules that diffuse to the dendrite of the receiving neuron resulting in a change in the voltage gradient across the receiving neuron.

Neurons can be either excitatory or inhibitory, depending on whether the postsynaptic potential increases or decreases the receiving neuron potential. Excitatory neurotransmitters depolarize postsynaptic membranes by increasing the membrane potential and can generate an action potential. Inhibitory neurotransmitters hyperpolarize the postsynaptic membrane, decreasing membrane potential, thereby negating the action of excitatory neurotransmitters and, in some cases, inhibiting them.

Many researchers consider collective dynamics of neurons in a neuronal network assuming that every neuron is monostable. However, even a single neuron can exhibit

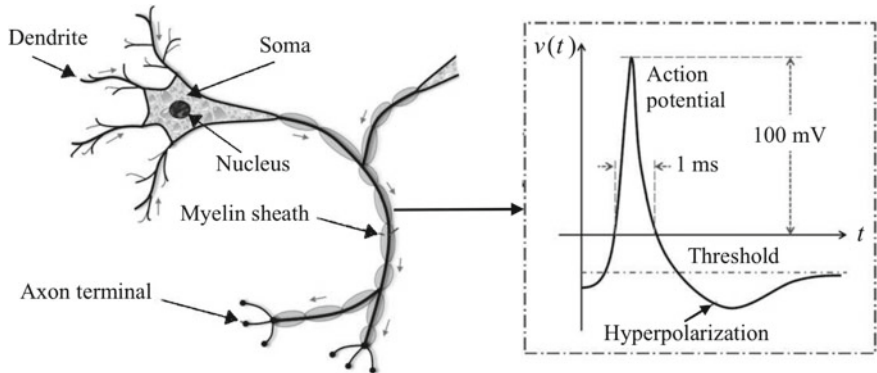


Fig. 3.24 (Left) Neuron anatomy and (right) action potential

bistability in a narrow range of control parameters near the excitation threshold [81]. To demonstrate this type of bistability, consider a physiological membrane potential model proposed by Hodgkin and Huxley [82]:

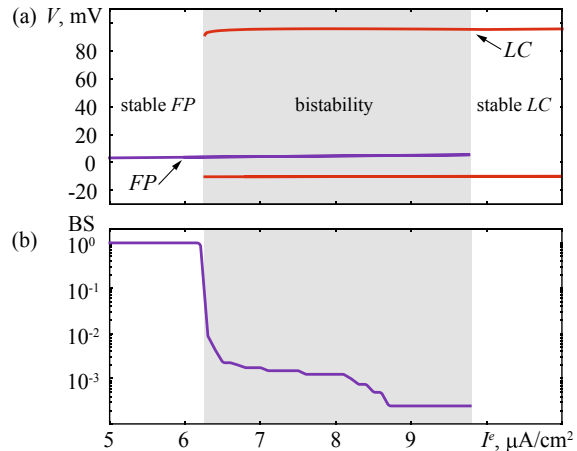
$$\begin{aligned} C_m \dot{V} &= -g_{Na}^{max} m^3 h(V - V_{Na}) - g_K^{max} n^4 (V - V_K) - g_L^{max} (V - V_L) + I^e, \\ \dot{x} &= \alpha_x(V)(1 - x) - \beta_x(V)x, \quad x = m, n, h, \end{aligned} \quad (3.28)$$

where $C_m = 1 \mu\text{F}/\text{cm}^2$ is the capacity of the cell membrane, I^e is the external bias current (in $\mu\text{A}/\text{cm}^2$), V is the membrane potential (in mV), $g_{Na}^{max} = 120 \text{ mS}/\text{cm}^2$, $g_K^{max} = 36 \text{ mS}/\text{cm}^2$ and $g_L^{max} = 0.3 \text{ mS}/\text{cm}^2$ are maximal sodium, potassium and leakage conductances, respectively, when all ion channels are open, $V_{Na} = 115 \text{ mV}$, $V_K = -12 \text{ mV}$ and $V_L = -10.6 \text{ mV}$ are reversal potentials for sodium, potassium and leak channels, respectively, m , n and h represent mean ratios of open gates of specific ion channels, n^4 and $m^3 h$ are mean portions of open potassium and sodium ion channels within a membrane patch, $\alpha_x(V)$ and $\beta_x(V)$ are rate functions given as [83]

$$\begin{aligned} \alpha_m(V) &= \frac{0.1(25 - V)}{\exp[(25 - V)/10] - 1}, \\ \beta_m(V) &= 4 \exp(-V/18), \\ \alpha_h(V) &= 0.07 \exp(-V/20), \\ \beta_h(V) &= \frac{1}{1 + \exp[(30 - V)/10]}, \\ \alpha_n(V) &= \frac{0.01(10 - V)}{\exp[(10 - V)/10] - 1}, \\ \beta_n(V) &= 0.125 \exp(-V/80). \end{aligned} \quad (3.29)$$

The neural dynamics is controlled by the external current I^e . Depending on I^e , the neuron can be either in a silent (fixed point FP) or a spiking (limit cycle LC)

Fig. 3.25 **a** Membrane potential bifurcation diagram of the Hodgkin–Huxley neuron using external current I^e as a control parameter. FP and LC are a stable fixed point and a limit cycle which coexist in the grey region. **b** Basin stability (BS) of the FP basin of attraction. Reprinted figure with permission from [84] ©2019 by the American Physical Society



regime. Within a narrow range of I^e , the two attractors coexist, as shown in the bifurcation diagram in Fig. 3.25 (grey region). For $I^e < 6.24 \mu\text{A}/\text{cm}^2$ only a stable fixed point (FP) exists, whereas for $I^e \geq 9.78 \mu\text{A}/\text{cm}^2$ there is only a stable limit cycle (LC). When the external current is increased, bistability arises in the saddle-node bifurcation at $I^e = 6.24 \mu\text{A}/\text{cm}^2$.

The basin stability (BS) of the resting state (fixed-point attractor FP) can be estimated as a relative volume of the basin of attraction of FP using the approach described in Sect. 1.23. The FP basin size is estimated as the ratio $BS_{FP} = M_{FP}/M$, where M_{FP} is the number of trajectories terminated at FP . One can see that the FP basin volume abruptly decreases when the external current passes the critical point at $I^e = 6.24 \mu\text{A}/\text{cm}^2$, as shown in Fig. 3.25b.

A small perturbation of the external current ($\tilde{I}^e(t)$) allows switches between the coexisting FP and LC states. The effect of this perturbation is shown in Fig. 3.26, where a short perturbation of the external current modeled by a boxcar function $\tilde{I}^e(t) = I^e + I_0^e[H(t - t_0) - H(t - t_0 - \Delta t)]$ is applied. Here, I_0^e is the amplitude of the external current perturbation, $H(\bullet)$ is the Heaviside step-function, t_0 is the moment of time when the perturbation is applied, and Δt is the duration of the external pulse.

It should be noted that the Hodgkin–Huxley model is rather bulky and therefore computationally expensive. To reduce computational cost, the HH model was simplified. Among a variety of reduced neural models, we should mention popular discrete models such as Rulkov and Izhikevich maps, as well as continuous models such as FinzHung–Nagumo, Morris–Lecar [85], and Hindmarsh–Rose [86]. However, the reduced models do not allow multistability in a single neuron. In order to observe multistability in the reduced models, one has to add either a delayed feedback or couple two or more neurons. In the following sections, we will show how multistability arises in coupled neurons.

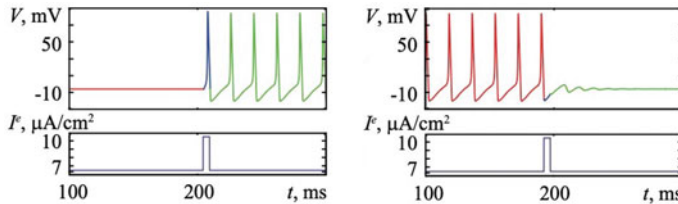


Fig. 3.26 Switches of neural dynamics (left) from a resting to a spiking state and (right) from a spiking to a resting state, by applying a 5-ms perturbation $I^e = 6.5 \mu\text{A}/\text{cm}^2$ to external current $I_0^e = 4 \mu\text{A}/\text{cm}^2$

3.4.2 Coupled Neurons

The coexistence of two different firing patterns was observed in the Morris-Lecar [85] and two-compartment motor [87] neural models in the presence of an asymmetry in electrotonic coupling between the soma and dendrites [88]. Due to the simplicity of the Morris–Lecar mechanisms, the authors found bistability only for a unique set of system parameters. However, coexistence of attractors also occurs in other models of asymmetrically coupled neurons. In particular, it was found in the Hindmarsh–Rose model [86] which is a simplified version of the physiological Hodgkin–Huxley model. Nevertheless, the Hindmarsh–Rose model allows a basic phenomenological description of neuron dynamics, such as resting, spiking, and bursting behaviors, and reveals nonlinear mechanisms underlying important physiological processes.

To demonstrate multistability in coupled neurons, let us consider the system of two Hindmarsh–Rose neurons asymmetrically coupled as [89]

$$\begin{aligned}\dot{x}_1 &= y_1 - ax_1^3 + bx_1^2 - z_1 + I_{\text{ext}1} + \sigma_1(x_2 - x_1), \\ \dot{y}_1 &= c - dx_1^2 - y_1, \\ \dot{z}_1 &= r[s(x_1 - x_0) - z_1], \\ \dot{x}_2 &= y_2 - ax_2^3 + bx_2^2 - z_2 + I_{\text{ext}2} + \sigma_2(x_1 - x_2), \\ \dot{y}_2 &= c - dx_2^2 - y_2, \\ \dot{z}_2 &= r[s(x_2 - x_0) - z_2],\end{aligned}\tag{3.30}$$

where $x_{1,2}$ are membrane potentials of neuron 1 and neuron 2, $y_{1,2}$ are recovery variables associated with a fast current of Na^+ or K^+ ions, $z_{1,2}$ are adaptation currents associated with a slow current of Ca_2^+ ions, $I_{\text{ext}1,2}$ are external input currents, $x_0 = -1.6$ is the x -component of the stable equilibrium point without input ($I_{\text{ext}} = 0$), and $0 < \sigma_{1,2} < 1$ are electrical coupling strengths used as control parameters. For parameter values $a = 1, b = 3, c = 1, d = 5, s = 4$, and $r = 0.006$ the solitary (uncoupled) neurons oscillate periodically at small ($1.4 < I_{\text{ext}} < 2.9$) and large ($I_{\text{ext}} > 3.4$) external currents, whereas for intermediate currents ($2.9 < I_{\text{ext}} < 3.4$) they are chaotic. If the neuron currents are fixed at $I_{\text{ext}1} = I_{\text{ext}2} = I_{\text{ext}} = 1.4$, the uncoupled neurons oscillate in a periodic spiking regime.

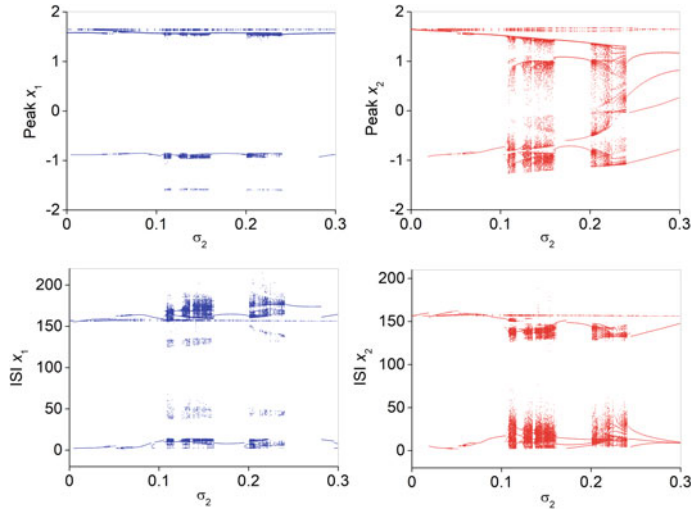


Fig. 3.27 Bifurcation diagrams of local maxima of membrane potentials x_1 and x_2 (upper row) and inter-spike intervals (ISI) of membrane potentials (lower row) of two coupled neurons with respect to coupling strength σ_2 for fixed $\sigma_1 = 0.051$

The bifurcation diagrams with respect to the coupling strength σ_2 shown in Fig. 3.27 reveal multistability in the coupled neurons. The diagrams are obtained for fixed parameters and randomly varied initial conditions.

For a small enough coupling σ_2 , the system is monostable; the two neurons generate tonic spikes since both couplings are too weak. However, when σ_2 is increased, the coexistence of three different regimes appears. In particular, for $0.12 \lesssim \sigma_2 \lesssim 0.16$ and $0.20 \lesssim \sigma_2 \lesssim 0.24$ tonic spikes, bursts, and chaos coexist. The upper horizontal branch of the bifurcation diagrams in Fig. 3.27 correspond to the tonic spikes shown in the upper row in Fig. 3.28, while lower branches correspond to the bursting and chaotic regimes represented in the middle and lower rows.

The section of the basins of attraction of three coexisting states is shown in Fig. 3.29. As we already mentioned above, since the system is six-dimensional, it is impossible to visualize the complete phase space. However, we can plot the $(y_1(0), y_2(0))$ section of the basins of attraction, keeping other initial conditions fixed ($x_1(0) = -0.9221$, $y_1(0) = 1.2556$, $z_1(0) = 1.2556$, $x_2(0) = -0.9127$, $y_2(0) = 1.2603$, $z_2(0) = 1.2603$), for the fixed coupling strengths $\sigma_1 = 0.051$ and $\sigma_2 = 0.2$.

One can see that the tonic spikes attractor (green area) has the largest basin of attraction, and the chaotic attractor more often occurs when the initial conditions for the coupled oscillators are close to each other, i.e. when $y_1(0) \approx y_2(0)$ (blue dots on the diagonal).

Fig. 3.28 Time series (left column) and phase portrait (right column) of the membrane potential representing the coexisting tonic spikes (upper row), bursts (middle row), and chaos (lower row) for fixed parameters at the coupling strengths $\sigma_1 = 0.051$ and $\sigma_2 = 0.2$

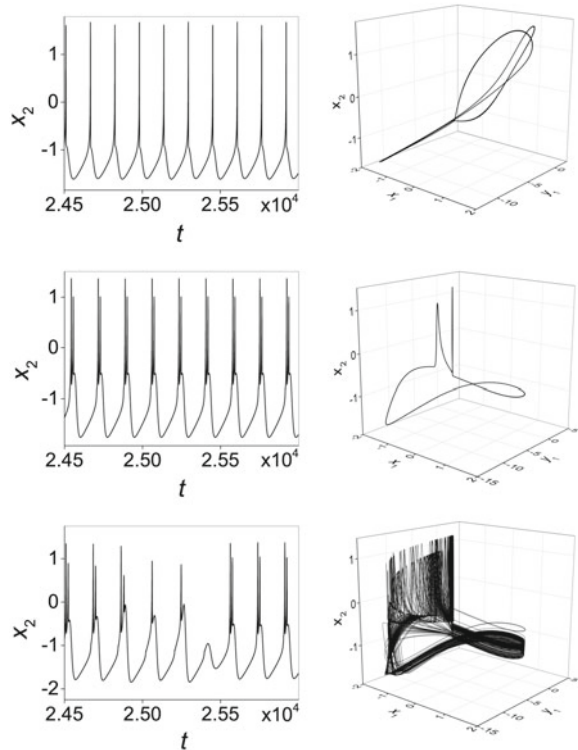
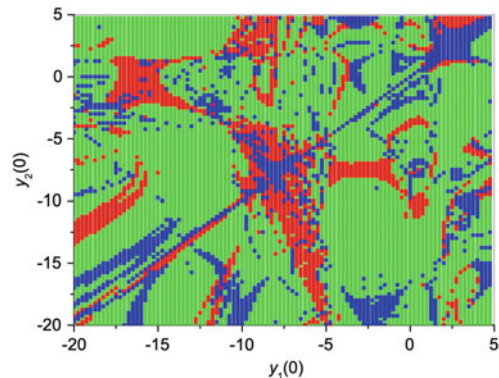


Fig. 3.29 Section of basins of attraction of three coexisting attractors: tonic spikes (green), bursts (red), and chaos (blue)



Bistable behavior was found in real neurons. For example, the coexistence of silent and spiking regimes was observed in the membrane potential response of squid [90] and *Hermissenda* [91] neurons. Biorhythmicity was found in the *Aplysia* neuron, which, when disturbed, switches between spiking and bursting regimes [92].

3.5 Other Examples of Multistable Systems

Multistability is such a widespread phenomenon in nature that it is impossible to describe in one book all the varieties of dynamical systems where coexisting attractors were discovered. Therefore, here we only present the most interesting, in our opinion, examples of such systems in terms of distinctive features of multistability manifestation. In particular, we consider multistability in mechanical, thermochemical, climatic, ecological, biological, astronomical, and fractional-order systems.

3.5.1 Mechanical Systems

The coexistence of in-phase and anti-phase synchronization states (phase bistability) in coupled pendula is described in Sect. 2.2.4. Here, we consider another interesting mechanical system that can be essential in robotics. The problem is how to get the robot to bring a cup of coffee without spilling a drop. In real life, not every person can easily cope with this task. However, persistent experiments allowed nevertheless developing some strategies [93].

In particular, Wallace et al. [94] proposed a paradigmatic model to simulate the handling of a cup of coffee, namely, a forced cart-pendulum system illustrated in Fig. 3.30. The strategies are slow or high sinusoidal modulation of the cup position in x direction.

The model contains an oscillatory pendulum whose amplitude is controlled by an external force derived as

$$F_{\text{inter}}(t) = F_{\text{input}}(t) - K(x - x_{\text{des}}) - B(\dot{x} - \dot{x}_{\text{des}}) \quad (3.31)$$

with K being stiffness, B being a damping coefficient, and

$$F_{\text{input}}(t) = (m_c + m_p)\ddot{x}_{\text{des}}(t) = F \sin(2\pi ft + \pi/2) \quad (3.32)$$

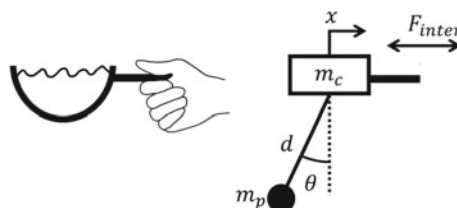


Fig. 3.30 (Left) Conceptual and (right) mechanical models of handling a cup of coffee. F_{inter} is the human interaction force in x direction, m_c is the cup mass, d , m_p , and θ are respectively the pendulum length, mass, and angle

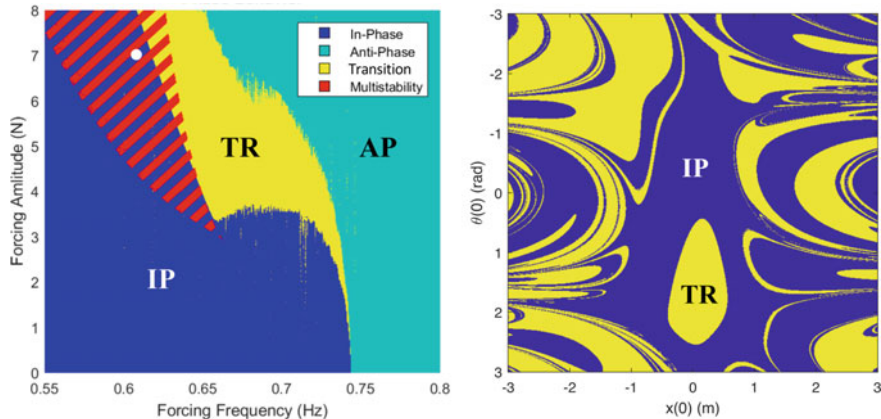


Fig. 3.31 (Left) Localization of different synchronization regimes in the parameter space of the forcing frequency f and amplitude F . IP, AP, and TR are in-phase, anti-phase, and transient regions. The bistable region is shown by the diagonal stripes. (Right) Section of fractal basins of attraction of IP (blue) and TR (yellow) states for $f = 0.62$ Hz and $F = 7$ N (white dot in the left-upper corner in the left panel). Based on data from [94]

being the driving force. Here, the human periodically tracks the desired cart position with a reference trajectory

$$x_{des}(T) = A \sin(2\pi f t + \pi/2), \quad (3.33)$$

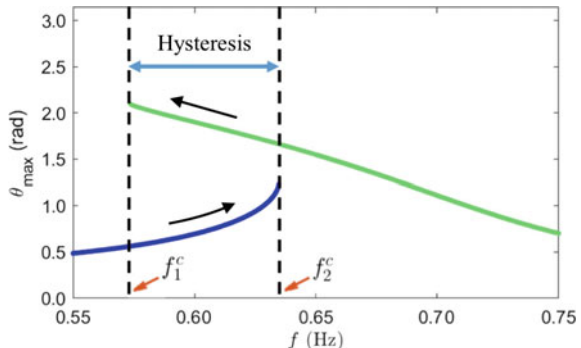
where A and f are the amplitude and frequency, and $F = -A(m_c + m_p)(2\pi f)^2$ is the forcing amplitude.

The slow- or high-frequency driving locks the pendulum either in-phase or anti-phase, which results in a relatively small amplitude of the pendulum oscillations, whereas the driving with intermediate frequencies swings the pendulum in resonance with its natural frequency leading to large-amplitude oscillations. Thus, depending on the driving frequency, there exist three different regimes, regimes with harmonic responses of x and θ which synchronize in-phase or anti-phase, and a regime with a harmonic x response located at the boundary between the harmonic responses, as illustrated in Fig. 3.31.

The bifurcation diagram with respect to the frequency is presented in Fig. 3.32. For $f < f_2^c$ there are in-phase attractors. Bistability exists for $f \in (f_1^c, f_2^c)$.

Analysis of the model showed that a person is able to switch abruptly and efficiently from one synchronous attractor to another. However, there is currently no experimental data on the characteristics of human movements collected in such a way as to be compared with this prediction. There also exists the possibility that a person is not able to perform such movements. The problem with fast movements is minimizing jerks (acceleration or third derivative). We hope that these results will motivate further experimental research in this direction.

Fig. 3.32 Bifurcation diagram of the maximum value of the pendulum angle θ_{\max} with respect to the frequency f for $F = 6$ N. Hysteresis occurs between two saddle-node points at f_1^c and f_2^c when f is increased and decreased, as shown by the arrows. Based on data from [94]



3.5.2 Micro- and Nanosystems

The phenomenon of multistability should be taken into account when designing nonlinear mechanical devices. Coexistence of attractors was found in various microscale and nanoscale systems. For instance, in microsystems, multistability was uncovered in microelectromechanical resonators [95] and multistable microactuators with serially connected bistable elements [96]. In nanosystems, multistability was found in electrostatically driven nanowire systems, semiconductor superlattices, and systems of a coupled ferromagnetic and a topological insulator.

As an example, we consider here a driven nanowire system schematically shown in Fig. 3.33 [97]. This system is characterized by very low power consumption and ultrafast communication speed and has many applications, such as single electron spin detection [98], RF communication [99], semiconductor superlattice [100], nanotube nanotweezers [101], carbon nanotube for molecular computing [102], and others.

The driven nanowire system is described by the partial differential equations of motion:

$$\begin{aligned} \rho A \frac{\partial^2 Y}{\partial t^2} + EI \frac{\partial^4 Y}{\partial x^4} - \frac{EA}{2L} I_0 \frac{\partial^2 Y}{\partial x^2} &= F_f^Y, \\ \rho A \frac{\partial^2 Z}{\partial t^2} + EI \frac{\partial^4 Z}{\partial x^4} - \frac{EA}{2L} I_0 \frac{\partial^2 Z}{\partial x^2} &= F_f^Z + F_e, \end{aligned} \quad (3.34)$$

where $Y(x, t)$ and $Z(x, t)$ are the displacements in y and z directions, respectively, E is the Young's modulus, ρ is the volume density, L is the original wire length, A is the cross-sectional area, $I = \pi r^4/4$ is the cross-sectional moment of inertia of the wire, F_f^Y and F_f^Z are viscous damping forces in y and z directions, respectively, proportional to the wire velocity, and I_0 is an integral proportional to the length increment of the wire under stretch, which is given as

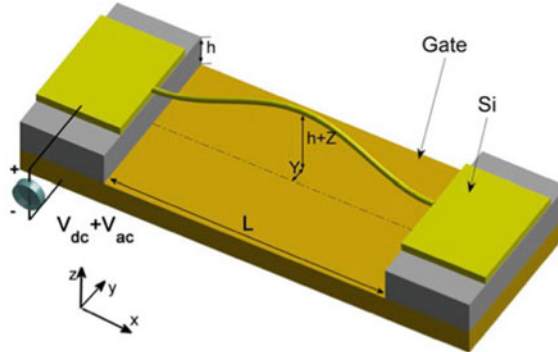


Fig. 3.33 Schematic illustration of a driven nanowire system. The electrostatically driven Si nanowire of length L and diameter d is suspended on a U-shaped gate. h is the gap between the wire and the gate. Electrostatic force is applied on the nanowire in the $-z$ direction due to an externally applied electric potential between the nanowire and the substrate. The potential has dc and ac components (V_{dc} and V_{ac}) with adjustable frequency f . Reprinted figure with permission from [97] ©2013 by the American Physical Society

$$I_0 = \int_0^L \left[\left(\frac{\partial Y}{\partial x} \right)^2 + \left(\frac{\partial Z}{\partial x} \right)^2 \right] dx. \quad (3.35)$$

The electrostatic force F_e and the viscous damping forces $F_f^{Y,Z}$ are given as

$$F_e = -\frac{\pi \varepsilon_0 V^2(t)}{(Z+h) \left[\ln \left(4 \frac{Z+h}{d} \right) \right]^2}, \quad (3.36)$$

$$F_f^{Y,Z} = \frac{\pi P d}{4 v_T} \frac{\partial(Y, Z)}{\partial t},$$

where P is the air pressure, and $v_T = \sqrt{k_B T/m}$ is the air molecule velocity at temperature T .

Multistability was found in a wide range of parameters of the driven nanowire system. The phase-space and bifurcation diagrams with respect to the driven frequency are shown in Fig. 3.34. One can see that several different regimes coexist at certain values of f/f_0 .

The origin of multistable dynamics was attributed to high-dimensional transient chaos permeating the phase space. For practical implementation of nanowire devices, the parameter ranges for which multistability arises should be avoided because of the intrinsic difficulty to predict the final state of the system and to exclude occasional switches from one stable state to another under external perturbations.

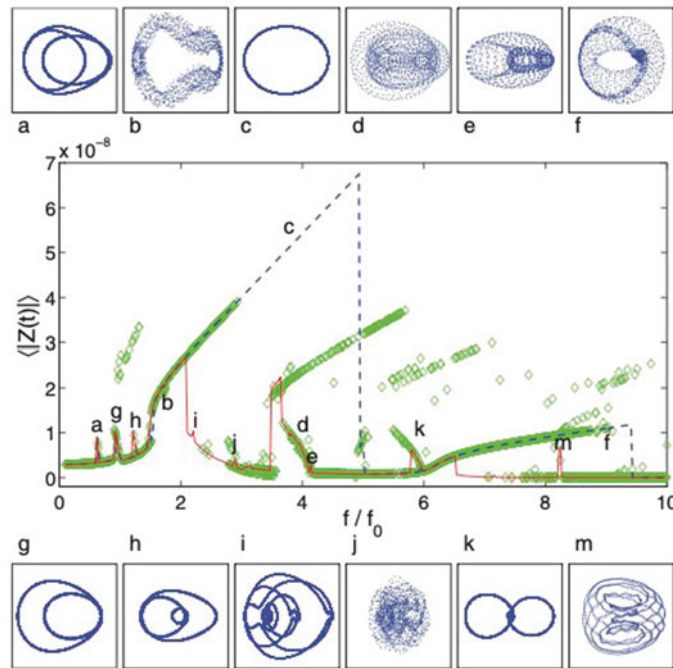


Fig. 3.34 Phase-space (z versus v_z) trajectories (up and down) and bifurcation diagrams (middle) with respect to driving frequency. Different branches of the bifurcation diagrams correspond to different dynamical regimes. Reprinted figure with permission from [97] ©2013 by the American Physical Society

3.5.3 Thermochemical Systems

Another interesting example of a multistable system can be found in a popular non-linear model of a thermochemical reactor [103]. The reactor contains the reactant A , the product B , and the catalyst C . The system exchanges energy with its surroundings by the Newtonian heat flow through the boundaries, which are kept at constant temperature T_b via the following reactions:



The first reaction is exothermic with a reaction heat Q , while the second reaction occurs on the walls of the system. This reaction simulates a mechanism allowing for the supply of the reactant A and the removal of the product B .

If we consider the diluted gas system, the dependence of the internal energy U on the temperature T obeys $U = (3/2)Nk_B T$ (N and k_B being the number of particles and the Boltzmann constant, respectively). Thus, the system dynamics can be described as

$$\begin{aligned} V\dot{n}_A &= -k_1 n_A n_C V + k_2 n_B S, \\ (3/2)Nk_B \dot{T} &= k_1 n_A n_C V Q - knS k_B (T - T_b), \end{aligned} \quad (3.39)$$

where V and S are the volume and the surface of the system, respectively, n is the total number density, n_A , n_B , and n_C are the number densities of A , B , and C , respectively, and k is the coefficient of heat exchange. Taking into account that $n = (n_A + n_B + n_C)$, the density of B is eliminated from Eq. 3.40.

In the dimensionless form Eq. 3.40 can be written as follows

$$\begin{aligned} \dot{x} &= \sqrt{y}(-x \exp(-\delta/y) + p(1-x)), \\ \dot{y} &= (2/3)q\sqrt{y}(x \exp(-\delta/y) + r(1-y)), \end{aligned} \quad (3.40)$$

where x and y are the dimensionless concentration and temperature, respectively, and p, q, r and δ are positive parameters.

Bashkirtseva et al. [104] studied the transition from monostability to bistability in the thermochemical reactor with well mixing modelled by Eq. 3.40. They have shown that the additional attractor arises in a saddle-node bifurcation.

The coordinates of equilibria of Eq. 3.40 satisfy the following condition:

$$z(y) = \frac{p}{p \exp(\delta/y) + 1} + r(1 - y) = 0, \quad (3.41)$$

where the function $z(y)$ is plotted in Fig. 3.35 for three values of parameter p , while other parameters are fixed at $\delta = 5$ and $r = 0.07$. One can see that for relatively large p , the system exhibits the coexistence of two fixed points.

In the presence of noise, the system dynamics displays random switching between two fixed points.

3.5.4 Climate

The climate is a high-dimensional complex system with many variables regulated by a large number of parameters inherent to atmosphere, hydrosphere, lithosphere (upper solid layer), cryosphere (glaciers), and biosphere. The climate is also influenced by the solar radiation and the Moon phases. The climate system is always at a nonequilibrium steady state due to the interplay of forcing, dissipation, positive and negative feedbacks, instabilities and saturation mechanisms. We remember that deterministic chaos was first found by the American meteorologist Edward Lorenz (see Fig. 3.36) in numerical simulations of a three-dimensional model based on

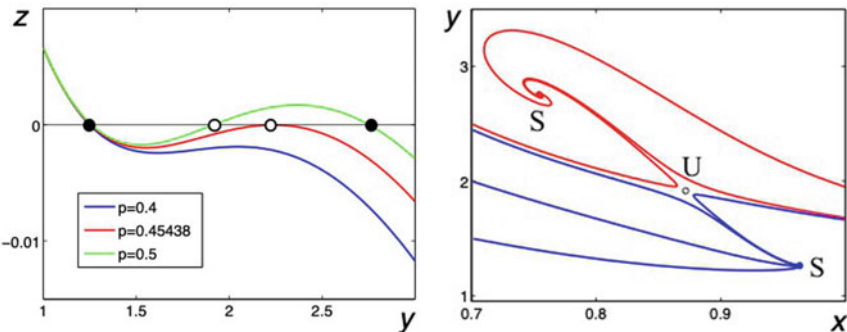
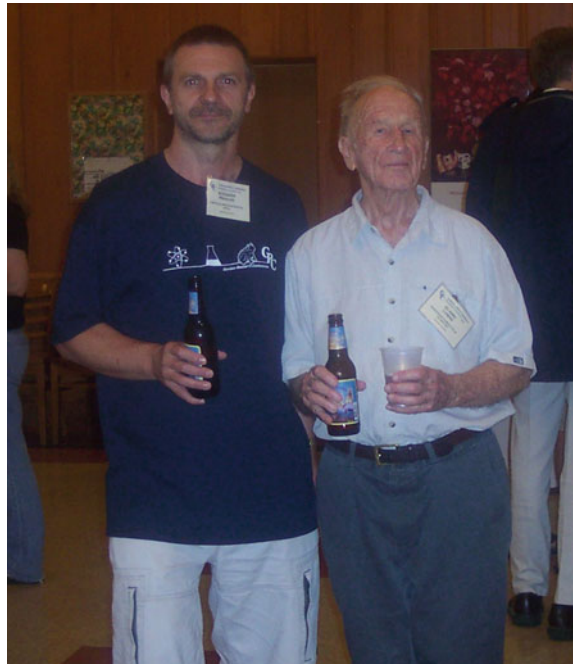


Fig. 3.35 Bistability in the termochemical system in Eq. 3.41. (Left) Function $z(y)$. The dots indicate fixed points. For $p = 0$ the system has a single equilibrium, whereas for $p = 0.5$ there are three equilibria (closed dots). At $p = 0.45438$, where $z(y)$ is tangent to the y -axis, a saddle-node bifurcation is born (open dot). (Right) Phase-space trajectories for $p = 0.5$. S and U are stable and unstable equilibria

Fig. 3.36 Edward Lorenz (right) and Alexander Pisarchik (left) at the Gordon Research Conference at Colby College, USA in 2005



meteorological data (see Eq. 3.10). Lorenz concluded that due to extreme sensitivity to initial conditions it is impossible to predict the weather beyond more than two weeks with a reasonable degree of accuracy.

Our knowledge about global Earth temperatures in ancient times is obtained from the analysis of the concentration of the oxygen isotope ^{18}O in seawater. Although

the absolute content of minor isotopes (for example, ^{18}O) cannot be accurately determined, one can obtain a quantitative value by comparing the result obtained for a known external standard with the result for an unknown sample. These isotope ratio differences are known as δ defined as [105]

$$\delta_{\text{sam}} = \frac{R_{\text{sam}} - R_{\text{std}}}{R_{\text{std}}} \times 1000,$$

where the subindex “sam” is referred to the sample value and “std” to the standard or reference value. These variations in composition δ are reported in parts per thousand (per mille, ‰). R denotes the heavy/light ratio between the abundances of any two isotopes (for example, $^{18}\text{O}/^{16}\text{O}$). A positive δ indicates enrichment in the heavy isotope relative to the standard, while depletion is indicated by a negative δ . There is a certain relationship between temperature and $\delta^{18}\text{O}$.

Figure 3.37 shows the variation of $\delta^{18}\text{O}$ over the last 3,000,000 years (or 3000 ka). One can note the existence of different time scales in the temperature oscillations, whose period and amplitude increase with time. An increase in the range of the amplitude variation is known to occur when the dynamical system approaches a critical point due to noise amplification by the system near the bifurcation. In the climate system, such a bifurcation is called a *tipping point*. This point can be associated with a switch to another coexisting attractor where the system undergoes abrupt and sometimes irreversible changes. It is inherently difficult to predict the time when the Earth’s climate will reach this point, and this is a serious scientific challenge when developing climate models.

Among many models of climate, there are models which assume the existence of multiple attractors. Historically, bistability in the Earth’s system was discovered in the late 1960s when scientists were interested in the possible effects of the nuclear winter. During that time, Budyko [106] and Sellers [107] independently introduced low-order continuous (“Sellers-type”) and discontinuous (“Budyko-type”) climate models. They found that a prolonged nuclear winter might cause a global glaciation on Earth. They suggested that for a wide range of values of the incoming solar radiation,

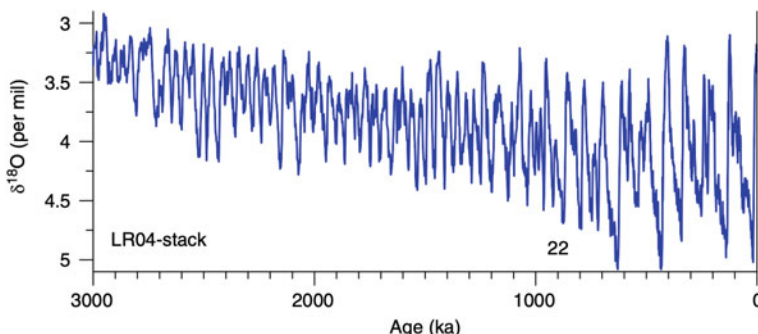


Fig. 3.37 Time series of $\delta^{18}\text{O}$. Adapted from [109] ©2006 with permission from Elsevier

the Earth has at least two attracting states, which correspond to competing climatic states, warm and snowball. The former is similar to the present climate, while the latter is related to global glaciation and conditions that can hardly support life forms. Paleoclimatic evidences suggest that in the past our planet flipped between these two states. The main physical mechanism responsible for such instability is the ice-albedo feedback. Lucarini and Bódai [108] supposed that there is a Melancholia state located between the warm and snowball climates. The Melancholia state is embedded in the boundaries between the two basins of attraction and features extensive glaciation down to relatively low latitudes.

Random perturbations of the incoming solar radiation induce transitions between the competing basins of attractions. In the weak noise limit, large deviation laws define the invariant measure and the statistics of escape times. The Melancholia states are the gateways for the noise-induced transitions. In the region of multistability without noise, the system is in one of the competing attractors. For low/high values of the solar irradiance, the limit measure is the snowball/warm climate. The switching between the two regimes corresponds to a first order phase transition in the system.

Mathematically, climate dynamics is modelled by a set of partial differential equations that describe the budget of mass, momentum and energy. Because of the impossibility to solve these equations analytically, numerical simulation is usually used. The simplest climate models are energy balance models that estimate changes in the climate system from the analysis of the energy budget of the Earth. These are low-scale one-dimensional climate models, so-called *energy budget models* (EBM), based on the energy exchange in the atmosphere or triggered by solar radiation [110] and atmospheric dynamics [111].

In the reduces zero-dimensional (0D) (in physical space) energy budget model only the global averaged effective temperature T is used as a state variable as follows [112]:

$$C\dot{T}(t) = I(1 - \alpha(T)) - O(T) \rightarrow \dot{T}(t) = -\frac{d}{dT}V(T), \quad (3.42)$$

where C is an effective average heat capacity per unit area, $I = S_*/4$ is the average incoming solar radiation per unit area, S_* is the solar constant (the factor 4 emerges looking at the geometry of the Earth-Sun system, α is the albedo, which is parameterised as a non-increasing function of T , and O is the outgoing radiation per unit area. $O(T)$ is a monotonically increasing function of T , i.e. an increasing surface temperature leads to an increase in the outgoing radiation, which is the basic mechanism behind the Boltzmann (negative) radiative feedback.

A reasonable choice of the parameters α and O allows finding bistability in the bifurcation diagrams using the solar constant S_* as a control parameter (Fig. 3.38).

The global temperature evolution for one-dimensional EBMs (1D-EBMs) is governed by the following partial differential equation:

$$C(\varphi)\partial_t T(t, \varphi) = I(\varphi)(1 - \alpha(\varphi, T)) - O(T) - D[T, \varphi], \quad (3.43)$$

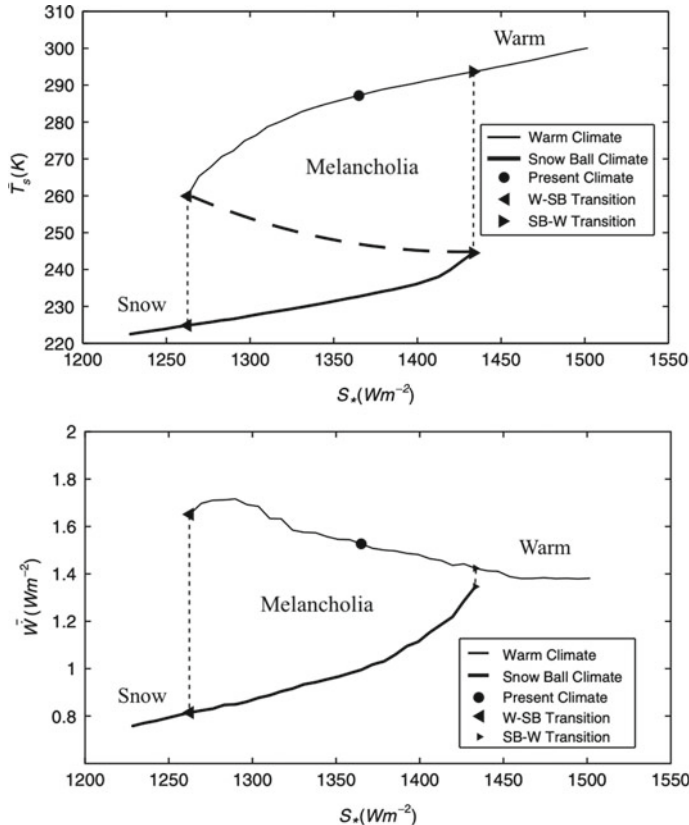


Fig. 3.38 Coexistence of warm and snowball states in the climate system. (Upper) Globally averaged surface temperature T_s versus solar constant. The long dashed line shows unstable states. (Lower) Average intensity of the Lorenz energy cycle $C(P, K)$. The dashed line indicates the branch of unstable states. Based on data from [108]

where C is the heat capacity, I is the incoming radiation, the albedo α are explicitly dependent on the latitude φ , and $D[T, \varphi]$ is the diffusion operator or the divergence of energy transport performed by the geophysical fluids. The diffusion operator is related to the negative feedbacks associated to the meridional temperature gradient, which acts through the meridional heat transport facilitated by atmospheric and oceanic motions. With a suitable choice of the parameters controlling the terms responsible for the energy budget in Eq. 3.43, we obtain a range of values of S_* where bistability is found, as seen from Fig. 3.38 (upper panel), where the unstable solution is between the two stable solutions.

The presence of multistability for the Earth's climatic conditions is compelling evidence for the entire modelling hierarchy, from the simple EBMs described above to global climate models. Global climate models are characterized by the bistability (hysteresis) region for a certain range of the solar constant S_* (Fig. 3.38 (upper

panel)). While in simple EBMs, stable solutions correspond to fixed points in phase space, in global climate models attractive solutions are associated with a generally chaotic behavior. At the same time, 1D-EBMs provide the global stable temperature regulated by Eq. 3.43 with a suitable choice of parameters which usually match the values obtained by complex general circulation models [113].

For a given S_* in the bistability range, the atmosphere in the warm climate is very active and has a large meridional temperature gradient. There exist eddies due to the baroclinic conversion between potential and kinetic energy, whereas the snowball climate is characterized by a much lower atmospheric variability with a low meridional temperature gradient. As seen in Fig. 3.38 (lower panel), the intensity of the Lorenz energy cycle $C(P, K)$ is determined by the average rate of conversion of the kinetic energy potential, which in the steady state is equal to the average rate of kinetic energy dissipation due to friction, much higher in the warm state than in the snow state [114]. A detailed analysis of the mechanisms underlying multistability in the Earth's climate, using models capable of accurately determining the time scales of the ocean, suggests the possibility of the existence of the additional climate, so-called a Melancholic state, that coexists with the warm and snow states. A complete analysis of the Melancholic state located between possible climatic states would reveal global dynamical properties of the Earth's system and, possibly, identify non-trivial stable climates associated with the paleoclimate and climates at exoplanets [108].

Interestingly, Pati et al. [115] found the coexistence of nonlinear acoustic-gravity waves in the Earth's rotational atmosphere modelled by low-order nonlinear flow equations. They have shown that the transition to an unsteady motion can occur either catastrophically or non-catastrophically due to the Earth's rotation. Their research revealed that the rotation parameter gives rise to heterogeneous coexisting attractors, leading to unpredictable dynamics. They conclude that the Earth's rotation causes a Hopf bifurcation even when the air Prandtl number¹ is less than one.

3.5.5 Ecology

Ecosystems are highly nonlinear dissipative systems characterized by multiplicity of stable and unstable states. Therefore, multistability is a common feature of ecosystems. Since differences in the composition of biological communities often lead to differences in their functions, studying the mechanisms of community multistability is necessary to understand the role of biodiversity in maintaining ecosystems. Research in biological communities has long recognized that the order and timing of migration and extinction of species affect the structure and function of communities. At the same time, multistability in ecosystems is associated with an increased likelihood of extreme climate events on a regional scale, such as droughts, floods and heat waves, which can lead to disruption of ecosystem functioning. Another reason

¹ The Prandtl number is defined as the ratio of momentum diffusivity to thermal diffusivity. The air Prandtl number at room temperature is 0.71.

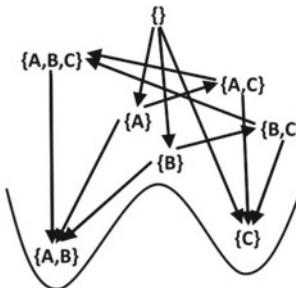


Fig. 3.39 Example of a stability landscape for a conceptual three-species system. A, B and C are different species. Arrows indicate transitions of community composition when species join the system one-by-one. The curve represents the potential landscape of a network connecting different species compositions when capturing compositional stability. Adapted from [118]

is associated with the dominant role of humans in the formation and transformation of the Earth ecology, as well as with the catastrophic consequences that such transformations often have.

Mutual inhibition, often encountered in ecology, can also lead to multistability when the competition of two species populations for the same resource lead either to their coexistence or to the destruction of one or the other population, depending on the initial conditions. This situation represents, starting with Volterra's work on competing animal populations, a classic problem in theoretical ecology.

Many researchers working on multistability in ecology are focused on low-dimensional models where changes in dynamical stability are studied as functions of environmental parameters [116, 117]. To characterize multistable behavior in a larger-dimensional space, Suzuki et al. [118] introduced the concept of *stability landscape*. They defined the stability landscape as a structure that regulates compositional stability of ecological communities (Fig. 3.39) and used the pairwise maximum entropy models to study the stability landscape of multispecies communities. They supposed that the species A and B cooperate and can exclude specie C if the both are present. On the other hand, C excludes either A or B as long as they are present alone. The transition from {A, C} (or {B, C}) to {A, B, C} is only valid when {B} ({A}) appears before exclusion occur. The compositions {A, B} and {C} are stable states located in the two potential wells. The remaining six compositions are transient states located either in the basins of either stable state (in terms of the result of competition among the species present) or on the ridge between the basins.

The study of multistability in ecosystems is also important for the science-policy interface in problems of fisheries collapse, climate changes, vegetation changes, and invasive species. These issues are often consequences of regime shifts that diminish ecosystem services [119]. Since ecological systems are constantly exposed to anthropogenic impact, including remote sensing systems, they are considered as interconnected socioeconomic ecological systems (SES), in which human behavior acts as a feedback affecting ecological variables. Solving environmental problems

requires a change in the landscape or SES stability topology (basins of attraction) to move the system towards the desired result. This result is achieved by introducing appropriate norms and rules or changes in economic conditions affecting a person's response.

Horan et al. [120] analyzed a problem related to intraguild predation (IGP), that is, mutual predation and competition, a common ecological phenomenon, and one of several types of interactions between species that create multistability without human intervention. The numerical example involves the interactions between high-value sportfish, smallmouth bass (*Micropterus dolomieu*), aggressive rusty crayfish (*Orconectes rusticus*), anglers, and resource managers.

The coexistence of microbial communities was investigated by Dubinkina et al. [121]. Such communities usually have several possible species or conditions observed under the same environmental parameters. Using a consumer-resource model in which microbes compete for two types of essential nutrients, each with many different metabolites, the authors observed multistability and shift in stable states. They found that multistability requires microbial species to have different stoichiometry of essential nutrients. It was also shown that a balanced nutrient supply promotes multistability and species diversity, making certain states of the community less stable.

The dynamics of multiple interacting species is often simulated by the generalized Lotka–Volterra model given as

$$\dot{N}_i = N_i \left(b_i + \sum_{j=1}^S a_{ij} N_j \right), \quad (3.44)$$

where N_i is the size of the i -th population at a given time t , S is the total number of interacting species, b_i is inherent per-capita growth rate, and a_{ij} represents the effect the species i has on the population j . For simplicity all self-interacting terms a_{ii} are often set to 1. It is assumed that all values in the interaction matrix based on Eq. 3.44 are positive or 0 ($a_{ij} \leq 0 \forall i, j$).

In the matrix form Eq. 3.44 can be written as

$$\dot{\mathbf{N}} = \mathbf{N}(\mathbf{b} + \mathbf{A}\mathbf{N}), \quad (3.45)$$

where \mathbf{A} is the interaction of a species network.

The stability of Eq. 3.45 with \mathbf{A} which elements are drawn by a normal distribution with zero mean and standard deviation α , is regulated by the Wigner–May theorem [122], which states that the probability $P(S, \alpha, C)$ for a system composed of S species with connectivity C ($0 < C < 1$) is given as

$$\begin{aligned} \text{if } \alpha^2 SC < 1 \text{ then } P(S, \alpha, C) &\rightarrow 1 \text{ as } S \rightarrow \infty, \\ \text{if } \alpha^2 SC > 1 \text{ then } P(S, \alpha, C) &\rightarrow 0 \text{ as } S \rightarrow \infty. \end{aligned} \quad (3.46)$$

The coexistence of multiple stable steady states can be illustrated with a variant of the Lotka–Volterra model in which the growth rates are described by “inhibitory” Hill function f . For three-species system

$$\begin{aligned}\dot{X}_1 &= X_1(b_1 f_1(X_2, X_3) - k_1 X_1), \\ \dot{X}_2 &= X_2(b_2 f_2(X_1, X_3) - k_2 X_2), \\ \dot{X}_3 &= X_3(b_3 f_3(X_1, X_2) - k_3 X_3),\end{aligned}\quad (3.47)$$

these functions are

$$f_1(X_2, X_3) = \frac{K_{12}^n}{K_{12}^n + X_2^n} \frac{K_{13}^n}{K_{13}^n + X_3^n}, \quad (3.48)$$

$$f_2(X_1, X_3) = \frac{K_{21}^n}{K_{21}^n + X_1^n} \frac{K_{23}^n}{K_{23}^n + X_3^n}, \quad (3.49)$$

$$f_3(X_1, X_2) = \frac{K_{31}^n}{K_{31}^n + X_1^n} \frac{K_{32}^n}{K_{32}^n + X_2^n}. \quad (3.50)$$

The growth of each species is inhibited by the two others. The numerical simulation of Eq. 3.47 with parameters $K_{ij} = 0.1 \forall i = j, n = 2$, and $k_i = 0.1 \forall i, b_1 = 1$, $b_2 = 0.95$, and $b_3 = 1.05$ demonstrates the coexistence of three stable states for different initial conditions. They can be observed in the bifurcation diagrams shown in Fig. 3.40.

For the interpretation of microbial sequencing data, it is important to know whether the community of interest is multistable. If the microbial community associated with the host is multistable, there is no need to explain differences in microbial composition from different hosts to differences in physiology, lifestyle, genetics, or other properties of the host, since alternative stable states may be the result of past disturbances rather than current differences in host properties. Therefore, the generative mechanisms underlying the types of communities are of great importance for understanding the variability of communities.

3.5.6 Biosystems

Multistability is known to play an essential role in the dynamics of living cells and organisms. Why is multistability common in biological systems? Since life is inherently nonlinear, many different forms of movement coexist. The nonlinearity is susceptible to instability and arises from the cooperation of allosteric proteins such as enzymes, ion channels, or receptors, as well as from many feedback loops that control the functioning of biological systems at all levels, from cells to tissues and from organs to animal populations [124].

In the middle of the 20th century, a German–American biophysicist Max Delbrück [125] suggested the possibility of the coexistence of several stable steady states in a

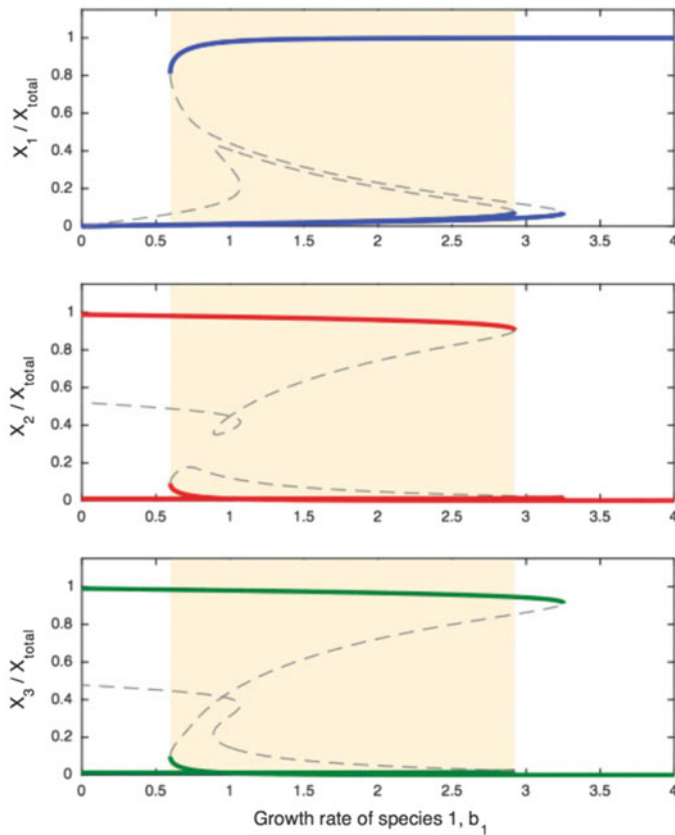


Fig. 3.40 Bifurcation diagrams representing tristability in a multistable community of three species, each of which competes with the other two. The three bifurcation diagrams show the range of the three stable states for each species. Reprinted by permission from Springer Nature [123] ©2017

genetic regulatory network. A few years later, bistability was theoretically considered in the model of a structured enzyme system [126]. Advances in thermodynamics in the 1960s and the discovery of chemical oscillations in the Belousov–Zhabotinsky reaction, as well as a number of theoretical studies in the early 1970s, caused an increased interest in multistability.

The coexistence of different attractors explains many biological phenomena, such as ecological catastrophes [127], cascades of mitogen-activated protein kinases in animal cells [128], generation of switching biochemical responses [129] regulatory circuits of the cell cycle in *Xenopus* and *Saccharomyces cerevisiae* [130], cell cycle oscillations and mutually cell-cycle exclusive phases [131], bistable growth rate of bacteria in response to antibiotics [132, 133], biological switches [134, 135],

adaptation to different environments through bet hedging [136], cell signaling [137], decision making [138, 139], etc., and can be used for cellular reprogramming [140].

Santillán et al. [141] have shown that bistability ensures that *Escherichia coli* efficiently consumes glucose and lactose. By studying the *lac* operon, they found that the level of induction of the operon rises sharply when the level of glucose in the environment drops to very low values. Bistability is necessary to maintain the stability of the induced and non-induced states. This effect was demonstrated in genetically identical cells, where bistability creates two distinct cellular states or phenotypes. It can also store memory of past stimuli through hysteresis and induce cell-cycle oscillations [142, 143].

Bistability was also observed in the pathophysiology of a number of diseases, including type II diabetes [144], prion diseases [145], Alzheimer's disease [146], and autoimmune diseases [147].

In many models demonstrating bistability, two branches of stable states correspond to healthy and diseased states, respectively. In contrast, in the bipolar disorder model [148], two stable states correspond to the two poles of the disease—mania and depression.

As was already mentioned in Sect. 2.2.5, bistability can be induced by positive feedback [149]. The feedback loops exist in many biological systems, for example, in biomolecules which either directly or indirectly promote their own creation [150–152]. In addition, it is generally accepted that two paradigmatic regulatory gene networks in bacteria, phage switch 1 and *lac* operon, are caused, respectively, by double negative and positive feedback, both resulting in bistability [153].

Despite a huge range of issues where multistability was involved in biological systems at the cellular and supracellular levels, cell differentiation remains an area in which the coexistence of multiple attractors is often emphasized [154–157] as the main specification of cell fate. Multistability was suggested [155] to require the presence of a positive feedback in the main control network. Such positive circuits usually arise in genetic regulatory networks as a result of mutual inhibition [152]. Cell fate specification often involves a sequence of binary choices between two stable steady states due to mutual inhibition of two transcription factors [158]. Theoretical models show that the specification of cell fates can sometimes include more than two stable states [159, 160].

Another example of multistability in biological systems is platelet aggregation, which plays a key physiological role [161]. In hemostasis, platelet aggregation underlies the formation of a hemostatic plug, which leads to the cessation of bleeding due to minor vascular damage, while in pathological conditions, platelet aggregation can lead to thrombosis. Activated platelets secrete ADP in response to ADP stimulation. This self-amplification is a form of direct positive feedback.

In addition to direct positive feedback, mutual inhibition as a source of bistability is a repetitive regulatory motif in biological systems [152]. This explains why the same regulatory structure generates similar dynamical phenomena at different levels of biological organization. Gardner and colleagues [162] showed that two mutually inhibiting repressors enable to create bistability in a synthetic genetic network called *toggle switch*. Mutual inhibition was also considered as a source of multistability

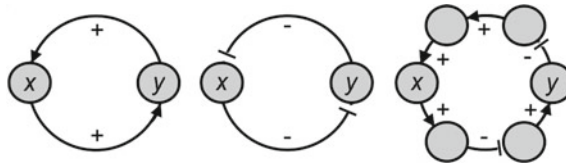


Fig. 3.41 Different feedback loops in cell system induce bistability. (Left) Positive feedback loop, (middle) mutually inhibitory double negative feedback loop, and (right) mutually inhibitory feedback loop of ring-coupled cells. Reprinted from [153] ©2004 National Academy of Sciences, U.S.A

at other levels of biological organization. Two putative mutually inhibitory neural circuits that produce bistability were used in theoretical studies underlying the REM-non-REM transitions during sleep [163] and the transitions between mania and depression in bipolar disorders [148].

Transitions between multistable states resulting from positive feedback are numerous in the cell cycle. A network of enzymes known as cyclin-dependent kinases (Cdks) controls progression in successive phases of the cell cycle [164]. It has been shown theoretically and experimentally that positive feedback in the regulation of Cdk leads to bistable transitions [130]. The Cdk network provides many loops of positive feedback that facilitate the irreversible transition from one phase of the cycle to the next [165]. Theoretical studies of the Cdk network models have shown that the multiplicity of positive feedback loops increases the robustness of Cdk oscillations to molecular noise by increasing the bistability range in different Cdk modules.

Figure 3.41 shows three general feedback schemes representing a positive feedback loop, a mutually inhibitory, double negative feedback loop, and mutually inhibitory feedback loop in a ring of cells.

Angeli et al. [153] showed that for a large class of biological systems with positive feedback of arbitrary order, it is possible to determine whether the system is bistable. To study the stability of the feedback scheme presented in the middle panel of Fig. 3.41, they carried out the phase plane analysis by supposing that one of the proteins is the Cdc2-cyclin B complex (x) and another is the Wee1 protein (y). They assumed that Cdc2-cyclin B and Wee1 each exist in only two forms: an active form (x_1, y_1) and an inactive form ($x_2 = 1 - x_1$ and $y_2 = 1 - y_1$). Then, the inhibition of each kinase by another is approximated by the Hill equations

$$\begin{aligned}\dot{x} &= \alpha_1(1-x) - \frac{\beta_1 x \omega^{\gamma_1}}{K_1 + \omega^{\gamma_1}}, \\ \dot{y} &= \alpha_2(1-y) - \frac{\beta_2 \eta x^{\gamma_2}}{K_2 + x^{\gamma_2}},\end{aligned}\tag{3.51}$$

where $x = x_1$ is active Cdc2, $\omega = \nu y_1$ is the input (stimulus) variable, $\eta = y_1$ is active Wee1 or the output (response) variable, α and β are rate constants, K are Michaelis (saturation) constants, and γ are Hill coefficients.

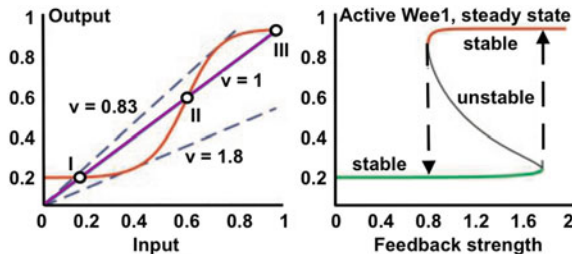


Fig. 3.42 (Left) Steady-state I/O static characteristic curve (curved line). The solid straight line is I/O for unitary feedback. The intersections represent stable (I and III) and unstable (II) steady states. The dashed straight lines are the slopes, whose sign indicates stability of these states. (Right) Bifurcation diagram showing bistability. Reprinted from [153] ©2004 National Academy of Sciences, U.S.A

The steady-state output η as a function of the constant input ω and the bifurcation diagram of the steady-state active Wee1 with respect to the feedback strength v are shown respectively in the left and right panels of Fig. 3.42. One can see that the I/O function (red line) has three intersections with the diagonal line ($\eta = \omega$), i.e. there are three equilibrium points (I, II, and III). The slope of the I/O at these points indicates its stability. If the slope is lower than unity, the state is stable, and if it is greater than unity, it is unstable. One can see from the figure that the points I and III are stable, while the point II is unstable.

The bifurcation diagram for the Cdc2-cyclin B/Wee1 system represents possible steady states as a function of the feedback strength v . The hysteresis loop and bistability are clearly seen in the diagram for the feedback strength $v \in [0.83, 1.8]$.

Coexisting attractors are regulated by feedback loops. While positive feedback is important for multistability, negative feedback is associated with oscillatory behavior. Both types of feedback are often intertwined. Thus, the system has two critical properties: (i) the open-loop system has a monostable steady-state response to constant inputs and (ii) there are no possible negative feedback loops, even when the system is closed under positive feedback. Such an analysis can also be made in experiments to find the steady-state I/O ratio of a feedback loop when feedback is blocked, for example, by inhibitors or small interfering RNAs.

The examples of the cell cycle and circadian clock illustrate well how positive and negative feedback loops interact, endowing a complex regulatory network with the ability of temporary self-organization in the form of stable oscillations. The occurrence of nonlinear interactions that can cause multistability or oscillation may actually be more common than the identified feedback loops would suggest. Although a single cycle of protein phosphorylation-dephosphorylation can induce steep threshold hypersensitivity [166], multiple protein phosphorylation, which usually occurs during cellular regulation itself can induce bistability under appropriate conditions [167]. Other types of protein-protein interactions provide additional potential mechanisms of a bistable behavior [168].

3.5.7 Astrosystems

Studying the escape dynamics of a small body under the influence of the potential of the Earth–Moon system with fractal basins boundaries, Zotos [169] found that the trajectory of a spacecraft, comet, or asteroid, starting near the Moon, can develop into basins of coexisting orbits of five types: (i) limited regular orbits around the Moon, (ii) trapped chaotic orbits around the Moon; (iii) escaping orbits to Earth realm, (iv) escaping orbits to the outside realm, and (v) leaking orbit due to collisions with the lunar surface. He proved that the escape and collision times of orbits are directly related to the escape and collision basins. Specifically, the lowest escape and collision rates of the orbits were found for initial conditions inside the escape or collision basins, as well as at relatively long distances from fractal regions, whereas the longest escape or collision rates correspond to the initial orbital conditions located near fractal boundaries between escape or collision basins or near stability islands.

Another interesting manifestation of coexisting exit basins is a binary black hole system or so-called *dihole*. In particular, any point of the boundary of one basin is also on the boundary of at least two additional basins. As known from Einstein’s theory, massive objects such as stars or black holes distort the space-time continuum, causing the trajectories of photons to deviate from a straight line. This phenomenon is known as *gravitational lensing of light*. The shadow of a black hole, i.e., an area in the sky that cannot be illuminated by distant light sources because it is blocked by the black hole, can be detected by tracing the path of all photons in the opposite direction from the observer to the event horizon of the black hole. In the model of an open Hamiltonian dynamical system, this black hole shadow is an exit basin defined as a set of initial conditions which lead to a specific region of phase space (event horizon).

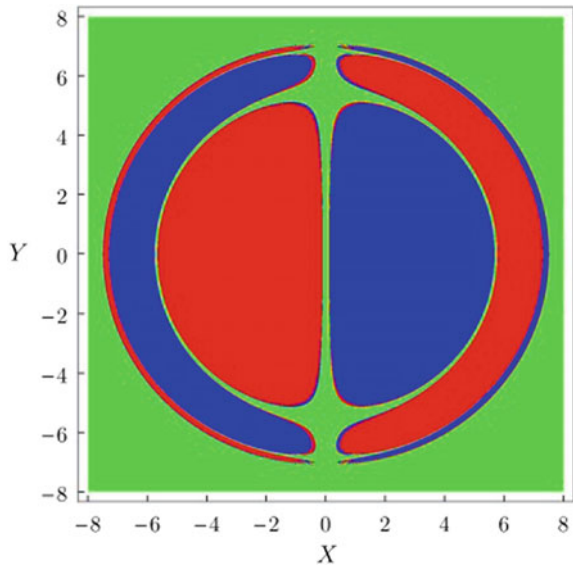
Astrophysical models usually deal with Hamiltonian systems with escapes known as open or leaking Hamiltonian systems with a finite escape energy. The basins of escape in leaking Hamiltonian systems are similar to basins of attraction in dissipative systems or to Newton–Raphson fractal basins. The boundaries between the several basins of escape may be fractal and obey the Wada property (see Sect. 1.2.4). In order to predict Newtonian motion of planets, astrophysicists and mathematicians try to solve the three-body problem which deals with the gravitationally interacting celestial bodies. Sun–planet–asteroid and Sun–planet–Moon systems are typical examples of the three-body problem [169, 170].

The galactic dynamics is often modeled by the Hénon–Heiles Hamiltonian which described the motion of a body (star) around a galactic center in the (x, y) plane [171]:

$$H = \frac{P_x^2}{2m} + \frac{P_y^2}{2m} + \frac{1}{2}k(x^2 + y^2) + \lambda\left(x^2y - \frac{1}{3}y^3\right) = E, \quad (3.52)$$

where $P_x = m\dot{x}$ and $P_y = m\dot{y}$ are the body’s momentum (m being the body’s mass), k and λ are coefficients, and E is the energy. Taking $k = \lambda = 1$, Eq. 3.52 in the dimensionless normalized form becomes

Fig. 3.43 Shadows (exit basins) cast by a binary black hole. Three coexisting exit basins for photons which go to two black holes and to infinity. Reprinted figure with permission from [172] ©2018 by the American Physical Society



$$E = \frac{1}{2}(\dot{x}^2 + \dot{y}^2) + \frac{1}{2}(x^2 + y^2) + x^2y - \frac{1}{3}y^3, \quad (3.53)$$

The resulting motion equations are written as

$$\begin{aligned} \ddot{x} &= -x - 2xy, \\ \ddot{y} &= -y - x^2 + y^2. \end{aligned} \quad (3.54)$$

A photon passing near a dihole has three choices: either it falls into one of the holes or it flies off to infinity. Thus, there are three exit basins which can have either a regular or a fractal structure (Fig. 3.43). Moreover, in certain parts of the phase space, the basins can have the Wada property, that is all three basins share a common fractal boundary.

Figure 3.43 shows the dihole shadows. The initial conditions painted in red and blue lead to the black holes, while the green shadow means infinity. There is a pair of globular shadows in the outlet basin diagram that correspond to individual black holes. Around these basic shadows, there is a similar hierarchy of eyebrow-like traits. The shadow boundary of the binary black hole corresponds to a set of initial conditions that are asymptotic with respect to the unstable eternal orbits that form the Cantor-like set.

The Wada properties of basins of attraction are similar to the example discussed in Sect. 1.2.2. Simply put, if you navigate a spaceship in the vicinity of a binary black hole and approach one of them, you may surprisingly find yourself in the arms of another black hole.

References

1. Staunton EJ, Piroinen PT (2018) Noise and multistability in the square root map. *Physica D* 380–381:31–44
2. Tikhha W, Gardini L (2020) Bifurcation sequences and multistability in a two-dimensional piecewise linear map. *Int J Bifurc Chaos* 30(6):2030014
3. Osinga H, Wiersig J, Glendinning P, Feudel U (2001) Multistability and nonsmooth bifurcations in the quasiperiodically forced circle map. *Int J Bifurc Chaos* 11(12):3085–3105
4. Camargo L, Martins A, C GJA, (2008) Multistability, phase diagrams and statistical properties of the kicked rotor: a map with many coexisting attractors. *Int J Bifurc Chaos* 18(6):1705–1717
5. Devaney RL (1989) An introduction to chaotic dynamical systems. Redwood City
6. Simó C (1998) Invariant curves of analytic perturbed nontwist area preserving maps. *Regul Chaotic Dyn* 3:180–195
7. Martins CGL, De Carvalho RE, Caldas IL, Roberto M (2010) Labyrinthic standard non-twist map. *J Phys A* 44:045102
8. De Carvalho RE, Abud CV (2015) Robust attractor of non-twist systems. *Physica A* 440:42–48
9. Kato LK, De Carvalho RE (2019) Transport barriers with shearless attractors. *Phys Rev E* 99:032218
10. Mugnaine M, Batista AM, Caldas IL, Szezech JDJ, de Carvalho RE, Viana RL (2021) Curry-Yorke route to shearless attractors and coexistence of attractors in dissipative nontwist systems. *Chaos* 31:023125
11. Duffing G (1918) Erzwungene Schwingungen bei veränderlicher Eigenfrequenz und ihre technische Bedeutung. Vieweg & Sohn, Braunschweig
12. Lakshmanan M, Murali K (1996) Chaos in non-linear oscillators: controlling and synchronization. World Scientific
13. Daza A, Wagelmakers A, Georgeot B, Guéry-Odelin D, Sanjuán MA (2016) Basin entropy: a new tool to analyze uncertainty in dynamical systems. *Sci Rep* 6:31416
14. Cieślinski JL, Nikiciuk T (2010) A direct approach to the construction of standard and non-standard Lagrangians for dissipative-like dynamical systems with variable coefficients. *J Phys A* 43:175205
15. Virgin LN (2007) Vibration of axially-loaded structures. Cambridge University Press, Cambridge
16. Qiu J, Lang JH, Slocum JH (2004) A curved-beam bistable mechanism. *J Microelectromech Syst* 13:137–146
17. Kazmierski TJ, Beeby S (2014) Energy harvesting systems. Springer, Berlin
18. Dykman M, Velikovich A, Golubev G, Luchinskii D, Tsuprikov S (1991) Stochastic resonance in an all-optical passive bistable system. *J Exp Theor Phys Lett* 53:193–197
19. Rössler OE (1976) An equation for continuous chaos. *Phys Lett A* 57:397–398
20. Carroll T, Pecora L (1995) Nonlinear dynamics in circuits. World Scientific Publishing, Singapore
21. Pisarchik AN, Jaimes-Reátegui R, García-Lopez JH (2008) Synchronization of coupled bistable chaotic systems: Experimental study. *Phil Trans R Soc, Ser A* 366:459–473
22. Pisarchik AN, Jaimes-Reátegui R (2005) Intermittent lag synchronization in a nonautonomous system of coupled oscillators. *Phys Lett A* 338:141–149
23. Pisarchik AN, Jaimes-Reátegui R (2005) Homoclinic orbits in a piecewise linear Rössler circuit. *J Phys Conf Ser* 23:122–127
24. Lorenz EN (1963) Deterministic nonperiodic flow. *J Atmos Sci* 20(2):130–141
25. Li C, Sprott CJ (2014) Coexisting hidden attractors in a 4-D simplified Lorenz system. *Int J Bifurc Chaos* 24(3):1450034
26. Leonov GA, Kuznetsov NV, Mokaev TN (2015) Homoclinic orbits, and self-excited and hidden attractors in a Lorenz-like system describing convective fluid motion. *Eur Phys J: Spec Top* 224(8):1421–1458
27. Fortuna L (2009) Chua's circuit implementations: yesterday, today and tomorrow. World Scientific, Singapore

28. Kuznetsov NV, Leonov GA, Vagaitsev VI (2010) Analytical-numerical method for attractor localization of generalized Chua's system. *IFAC Proc* 43(11):29–33
29. Zhao H, Lin Y, Dai Y (2017) Hopf bifurcation and hidden attractor of a modified Chua's equation. *Nonlinear Dyn* 90(11):2013–2021
30. Njitacke ZT, Fozin TF, Tchapga CT, Leutcho GD, Wouapi KM, Kengne J (2020) Control of coexisting attractors with preselection of the survived attractor in multistable Chua's system: a case study. *Complexity* 2020:5191085
31. Bao B, Li Q, Wang N, Xu Q (2016) Multistability in Chua's circuit with two stable node-foci. *Chaos* 26:043111
32. Wang N, Zhang G, Kuznetsov NV, Bao H (2021) Hidden attractors and multistability in a modified Chua's circuit. *Commun Nonlinear Sci Numer Simul* 92:105494
33. Kengne J, Njitacke ZT, Fotsin HB (2016) Dynamical analysis of a simple autonomous jerk system with multiple attractors. *Nonlinear Dyn* 83:751–765
34. Sprott JC (2000) Simple chaotic systems and circuits. *Am J Phys* 68:758–763
35. Chen H, He S, Azucena ADP, Yousefpour A, Jahanshahi H, López MA, Alcaraz R (2020) A multistable chaotic jerk system with coexisting and hidden attractors: Dynamical and complexity analysis, FPGA-based realization, and chaos stabilization using a robust controller. *Symmetry* 12:569
36. Tsotsop MF, Kengne J, Kenne G, Njitacke ZT (2020) Coexistence of multiple points, limit cycles, and strange attractors in a simple autonomous hyperjerk circuit with hyperbolic sine function. *Complexity* 2020:6182183
37. Njitacke ZT, Kengne J, Ngoumkam NA, Fouodji TM, Fotsin HB (2015) Coexistence of multiple attractors and crisis route to chaos in a novel chaotic Jerk circuit. *Int J Bifurc Chaos* 25(4):1550052
38. Tagne RLM, Kengne J, Negou AN (2019) Multistability and chaotic dynamics of a simple Jerk system with a smoothly tuneable symmetry and nonlinearity. *Int J Dyn Control* 7:476–495
39. Kengne J, Njikam SM, Signing VRF (2018) A plethora of coexisting strange attractors in a simple jerk system with hyperbolic tangent nonlinearity. *Chaos Soliton Fractals* 106:201–213
40. Kengne LK, Kengne J, Pone JRM, Tagne HTK (2020) Symmetry breaking, coexisting bubbles, multistability, and its control for a simple jerk system with hyperbolic tangent nonlinearity. *Complexity* 2020:2340934
41. Kengne J, Mogue RLT (2019) Dynamic analysis of a novel jerk system with composite tanh-cubic nonlinearity: chaos, multi-scroll, and multiple coexisting attractors. *Int J Dyn Control* 7:112–133
42. Kengne J, Signing VRF, Chedjou JC, Leutcho GD (2018) Nonlinear behavior of a novel chaotic jerk system: antimonotonicity, crises, and multiple coexisting attractors. *Int J Dyn Control* 6:468–485
43. Scalas E, Gorenflo R, Mainardi FL (2000) Fractional calculus and continuous-time finance. *Physica A* 285(1–4):376–384
44. Magin RL (2006) Fractional calculus in bioengineering. Begell House, Danbury, CT
45. Atanacković TM (2003) On a distributed derivative model of a viscoelastic body. *C R Mecanique* 331(10):687–692
46. Shen Y, Yang S, Xing H, Ma H (2012) Primary resonance of Duffing oscillator with two kinds of fractional-order derivatives. *Int J Non-Linear Mech* 47(9):975–983
47. Montesinos-García JJ, Martínez-Guerra R (2019) A numerical estimation of the fractional-order Liouvillian systems and its application to secure communications. *Int J Syst Sci* 50(4):791–806
48. Rudolf H (2000) Applications of fractional calculus in physics. World Scientific, Singapore
49. Sun K, Wang X, Sprott JC (2010) Bifurcations and chaos in fractional-order simplified Lorenz system. *Int J Bifurc Chaos* 20:1209–1219
50. Danca M (2017) Hidden chaotic attractors in fractional-order systems. *Nonlinear Dyn* 89:577–586
51. Hamri N, Houmor T (2011) Chaotic dynamics of the fractional order nonlinear Bloch systems. *Electron J Theor Phys* 25:233–244

52. Kaslik E, Sivasundaram S (2012) Nonlinear dynamics and chaos in fractional-order neural networks. *Neural Netw* 32:245–256
53. Rajagopal K, Pham VT, Alsaadi FE, Alsaadi FE, Karthikeyan A, Duraisamy P (2018) Multistability and coexisting attractors in a fractional order Coronary artery system. *Eur Phys J Spec Top* 227:837–850
54. He S, Banerjee S, Sun K (2019) Complex dynamics and multiple coexisting attractors in a fractional-order microscopic chemical system. *Eur Phys J Spec Top* 228:195–207
55. Yan B, He S, Sun K, Wang S (2020) Complexity and multistability in the centrifugal flywheel governor system with stochastic noise. *IEEE Access* 8:30092–30103
56. Echenausía-Monroy JL, Huerta-Cuellar G, Jaimes-Reátegui R, García-López JH, Aboites V, Cassal-Quiroga BB, Gilardi-Velázquez HE (2020) Multistability emergence through fractional-order-derivatives in a PWL multi-scroll system. *Electronics* 9:880
57. Samko SG, Kilbas AA, Marichev OI (1993) Fractional integrals and derivatives: theory and applications. Gordan and Breach, New York
58. Sun K, Sprott JC (2009) Dynamics of a simplified Lorenz system. *Int J Bifurc Chaos* 19(4):1357–1366
59. Carvalho R, Vilela Mendes R, Seixas J (1999) Feigenbaum networks. *Physica D* 126(1–2):27–37
60. Carvalho R, Fernandez B, Vilela Mendes R (2001) From synchronization to multistability in two coupled quadratic maps. *Phys Lett A* 285(5–6):327–338
61. Astakhov V, Shabunin A, A, Uhm W, Kim S (2001) Multistability formation and synchronization loss in coupled Hénon maps: two sides of the single bifurcational mechanism. *Phys Rev E* 63:056212
62. Uhm W, Astakhov V, Akopov A, Kim S (2003) Multistability formation and loss of chaos synchronization in coupled period-doubling systems. *Int J Mod Phys B* 17(22–24):4013–4022
63. Sausedo-Solorio JM, Pisarchik AN (2011) Dynamics of unidirectionally coupled Hénon maps. *Phys Lett A* 375:3677–3681
64. Pisarchik AN (2003) Oscillation death in coupled nonautonomous systems with parametrical modulation. *Phys Lett A* 318:65–70
65. Hens CR, Banerjee R, Feudel U, Dana SK (2012) How to obtain extreme multistability in coupled dynamical systems. *Phys Rev E* 85:035202(R)
66. Sprott JC (2014) Simplest chaotic flows with involutional symmetries. *Int J Bifurc Chaos* 24:1450009
67. Patel MS, Patel U, Sen A, Sethia GC, Hens C, Dana SK, Feudel U, Showalter K, Ngonghala CN, Amritkar RE (2014) Experimental observation of extreme multistability in an electronic system of two coupled Rössler oscillators. *Phys Rev E* 89:022918
68. Jaros P, Perlikowski P, Kapitaniak T (2015) Synchronization and multistability in the ring of modified Rössler oscillators. *Eur Phys J Spec Top* 224:1541–1552
69. Wontchui TT, Effa JY, Ekobena Fouad HP, Ujjwal SR, Ramaswamy R (2017) Coupled Lorenz oscillators near the Hopf boundary: Multistability, intermingled basins, and quasiriddling. *Phys Rev E* 96:062203
70. Hounsgaard J, Kiehn O (1989) Serotonin-induced bistability of turtle motoneurons caused by a nifedipine-sensitive calcium plateau potential. *J Physiol* 414:265–282
71. Lee RH, Heckman CJ (1998) Bistability in spinal motoneurons *In vivo*: systematic variations in persistent inward currents. *J Neurophysiol* 80:583–593
72. Perrier JF, Hounsgaard J (2000) Development and regulation of response properties in spinal cord motoneurons. *Brain Res Bull* 53:265–282
73. Heyward P, Ennis M, Keller A, Shipley MT (2001) Membrane bistability in olfactory bulb mitral cells. *J Neurosci* 21:5311–5320
74. Loewenstein Y, Mahon S, Chadderton P, Kitamura K, Sompolinsky H, Yarom Y, Häusseret M (2005) Bistability of cerebellar Purkinje cells modulated by sensory stimulation. *Nat Neurosci* 8:202–211
75. Huang S, Ernberg I, Kauffman S (2009) Cancer attractors: A system view of tumors from a gene network dynamics and developmental perspective. *Semin Cell Dev Biol* 20:869–876

76. Li Q, Wennborg A, Aurell E, Dekel E, Zou JZ, Xu Y, Huang S, Ernberg I (2016) Dynamics inside the cancer cell attractors reveal cell heterogeneity, limits of stability, and escape. *Proc Natl Acad Sci U S A* 113(10):2672–2677
77. Tass PA (1999) Phase resetting in medicine and biology. Stochastic modelling and data analysis. Springer, Berlin
78. Buzsaki G, Draguhn A (2004) Neuronal oscillations in cortical networks. *Science* 304:1926–1929
79. Bergman H, Feingold A, Nini A, Raz A, Slovin H, Abeles M, Vaadia E (1998) Physiological aspects of information processing in the basal ganglia of normal and parkinsonian primates. *Trends Neurosci* 21:32–38
80. Malashchenko T, Shilnikov A, Cymbalyuk G (2011) Six types of multistability in a neuronal model based on slow calcium current. *PLoS One* 6(7):1–10
81. Keener J, Sneyd J (2010) Mathematical physiology, 2nd edn. Springer, New York
82. Hodgkin AL, Huxley AF (1952) Propagation of electrical signals along giant nerve fibres. *Proc R Soc Lond B* 140:177–183
83. Pankratova EV, Polovinkin AV, Mosekilde E (1995) Resonant activation in a stochastic Hodgkin-Huxley model: Interplay between noise and suprathreshold driving effects. *Eur Phys J B* 45:391–397
84. Andreev AV, Frolov NS, Pisarchik AN, Hramov AE (2019) Chimera state in complex networks of bistable Hodgkin-Huxley neurons. *Phys Rev E* 100:022224
85. Morris C, Lecar H (1981) Voltage oscillations in the barnacle giant muscle fiber. *Biophys J* 35(1):193–213
86. Hindmarsh JL, Rose RM (1984) A model of neuronal bursting using three coupled first order differential equations. *Proc R Soc Lond B* 221(1222):87–102
87. Booth V, Rinzel J (1995) Compartmental model of vertebrate motoneurons for Ca^{2+} -dependent spiking and plateau potentials under pharmacological treatment. *J Comput Neurosci* 2:3371–3385
88. Kim H, Jones KE (2011) Asymmetric electrotonic coupling between the soma and dendrites alters the bistable firing behaviour of reduced models. *J Comput Neurosci* 30:659–674
89. Pisarchik AN, Jaimes-Reátegui R, M A García-Vellisca MA (2018) Asymmetry in electrical coupling between neurons alters multistable firing behavior. *Chaos* 28:033605
90. Guttman R, Lewis S, Rinzel J (1980) Control of repetitive firing in squid axon membrane as a model for a neuroneoscillator. *J Physiol* 305:377–395
91. Jacklet JW (1986) Bistability of membrane potential and anomalous rectification in neuron LP1 of Hermissona. *Comp Biochem Physiol A* 83:555–559
92. Lechner HA, Baxter DA, Clark JW, Byrne JH (1996) Bistability and its regulation by serotonin in the endogenously bursting neuron R15 in Aplysia. *J Neurophysiol* 75:957–962
93. Mayer HC, Krechetnikov R (2012) Walking with coffee: why does it spill? *Phys Rev E* 85:046117
94. Wallace B, Kong LW, Rodriguez A, Lai YC (2021) Synchronous transition in complex object control. *Phys Rev Appl* 16:034012
95. Kacem N, Hertz S (2009) Bifurcation topology tuning of a mixed behavior in nonlinear micromechanical resonators. *Appl Phys Lett* 95:183104
96. Gerson Y, Krylov S, S, Ilic B, Schreiber D (2012) Design considerations of a large-displacement multistable micro actuator with serially connected bistable elements. *Finite Elem Anal Des* 49(1):58–69
97. Ni X, Ying L, Lai YC, Do Y, Grebogi C (2013) Complex dynamics in nanosystems. *Phys Rev E* 87:052911
98. Rugar D, Budakian R, Mamin HJ, Chui BW (2004) Single spin detection by magnetic resonance force microscopy. *Nature* 430(4):329–332
99. Gammel P, Fischer G, Bouchaud J (2005) RF MEMS and NEMS technology, devices, and applications. *Bell Labs Tech J* 10(3):29–59
100. Bomze Y, Hey R, Grahn HT, Teitsworth SW (2012) Noise-induced current switching in semiconductor superlattices: observation of nonexponential kinetics in a high-dimensional system. *Phys Rev Lett* 109(2):026801

101. Kim P, Lieber CM (1999) Nanotube nanotweezers. *Science* 286:2148–2150
102. Rueckes T, Kim K, Joselevich E, Tseng GY, Cheung CL, Lieber CM (2000) Carbon nanotube-based nonvolatile random access memory for molecular computing. *Science* 289:94–97
103. Kawczyński AL, Nowakowski B (2008) Stochastic transitions through unstable limit cycles in a model of bistable thermochemical system. *Phys Chem Chem Phys* 10:289–296
104. Bashkirtseva I, Pisarchik AN, Ryashko L (2017) Multistability and stochastic phenomena in a randomly forced thermochemical system. *IOP Conf Ser: Mater Sci Eng* 192(14):012011
105. Rohling EJ (2013) Oxygen isotope composition of seawater. *Encycl Quat Sci* 2:915–922
106. Budyko MI (1969) The effect of solar radiation variation on the climate of the Earth. *Tellus* 21:611–619
107. Sellers WD (1969) A global climatic model based on the energy balance of the Earth-Atmosphere system. *J Appl Meteor* 8:392–400
108. Lucarini V, Bódai T (2017) Edge states in the climate system: exploring global instabilities and critical transitions. *Nonlinearity* 30:R32–R66
109. Clark PU, Archer D, Pollard D, Blum JD, Rial JA, Brovkin V, Mix AC, Pisias NG, Roy M (2006) The middle Pleistocene transition: characteristics, mechanisms, and implications for long-term changes in atmospheric pCO₂. *Quat Sci Rev* 25:3150–3184
110. Ghil M (1976) Climate stability for a sellers-type model. *J Atmos Sci* 33:3–20
111. Lorenz EN (1996) Predictability—a problem partly solved. In: Palmer T, Hagedorn R (eds) *Predictability of weather and climate*. Cambridge University Press, pp 40–58
112. Saltzman B (2001) *Dynamical paleoclimatology*. Academic, New York
113. Bódai T, Lucarini V, Lunkeit F, Boschi R (2014) Global instability in the Ghil-sellers model. *Clim Dyn* 44:3361–3381
114. Pierrehumbert RT, Abbot D, Voigt A, Koll D (2011) Climate of the neoproterozoic. *Ann Rev Earth Planet Sci* 39(1):417–460
115. Pati NC, Rech PC, Layek GC (2021) Multistability for nonlinear acoustic-gravity waves in a rotating atmosphere. *Chaos* 31:023108
116. Mitra C, Kurths J, Donner RV (2015) An integrative quantifier of multistability in complex systems based on ecological resilience. *Sci Rep* 5:16196
117. Sprott JC, Vano JA, Wildenberg JC, Anderson MB, Noel JK (2005) Coexistence and chaos in complex ecologies. *Phys Lett A* 335(1):207–212
118. Suzuki K, Nakaoka S, Fukuda S, Masuya H (2021) Energy landscape analysis elucidates the multistability of ecological communities across environmental gradient. *Ecol Monogr* 91(3):e01469
119. Carpenter SR, Bennett EA, Peterson GD (2006) Scenarios for ecosystem services: An overview. *Ecol Soc* 11(1):29
120. Horan RD, Fenichel EP, Drury KLS, Lodge DM (2011) Managing ecological thresholds in coupled environmental-human systems. *PNAS* 108(18):7333–7338
121. Dubinkina V, Fridman Y, Pandey PP, Maslov S (2019) Multistability and regime shifts in microbial communities explained by competition for essential nutrients. *eLife* 8:e49720
122. May RM (1972) Will a large complex system be stable? *Nature* 238(5364):413–414
123. Gonze D, Lahti L, Raes J, Faust K (2017) Multi-stability and the origin of microbial community types. *ISME J* 11:2159–2166
124. Goldbeter A (2018) Dissipative structures in biological systems: bistability, oscillations, spatial patterns and waves. *Philos Trans R Soc A* 376:20170376
125. Delbrück M (1949) Discussion. Editions du CNRS, Lyon, pp 33–35
126. Bierman A (1954) Studies on the effects of structure on the behavior of enzymes. *Bull Math Biophys* 16(9):203–257
127. Rietkerk M, Dekker SF, de Ruiter PC, van de Koppel J (2004) Self-organized patchiness and catastrophic shifts in ecosystems. *Science* 305:1926–1929
128. Bhalla US, Ram PT, Iyengar R (2002) MAP kinase phosphatase as a locus of flexibility in a mitogen-activated protein kinase signaling network. *Science* 297:1018–1023
129. Bagowski C, Besser J, Frey CR, Ferrell JE (2003) The JNK cascade as a biochemical switch in mammalian cells: ultrasensitive and all-or-none responses. *Curr Biol* 13:315–320

130. Pomerening JR, Sontag ED, Ferrell JE Jr (2003) Building a cell cycle oscillator: hysteresis and bistability in the activation of Cdc2. *Nat Cell Biol* 5:346–351
131. Sha W, Moore J, Chen K, Lassaletta AD, Yi CS, Tyson JJ, Sible JC (2003) Hysteresis drives cell-cycle transitions in *Xenopus laevis* EGG extracts. *Proc Natl Acad Sci USA* 100:975–980
132. Elf J, Nilsson K, Tenson T, Ehrenberg M (2006) Bistable bacterial growth rate in response to antibiotics with low membrane permeability. *Phys Rev Lett* 97:258104
133. Meredith HR, Srimani JK, Lee AJ, Lopatkin AJ, You L (2015) Collective antibiotic tolerance: mechanisms, dynamics and intervention. *Nat Chem Biol* 11:182–188
134. Slepchenko BM, Terasaki M (2003) Bio-switches: what makes them robust? *Curr Opin Genet Dev* 14:428–434
135. Yao G, Lee TJ, Mori S, Nevins JR, You L (2008) A bistable Rb-E2F switch underlies the restriction point. *Nat Cell Biol* 10(4):476–482
136. Veening JW, Smits WK, Kuipers OP (2008) Bistability, epigenetics, and bet-hedging in bacteria. *Annu Rev Microbiol* 62:193–210
137. Ferrell JJE, Xiong W (2001) Bistability in cell signaling: how to make continuous processes discontinuous, and reversible processes irreversible. *Chaos* 11(1):227–236
138. Tiwari A, Igoshin OA (2012) Coupling between feedback loops in autoregulatory networks affects bistability range, open-loop gain and switching times. *Phys Biol* 9(5):055003
139. Xiong W, Ferrell JE (2003) A positive-feedback-based bistable ‘memory module’ that governs a cell fate decision. *Nature* 426(6965):460–465
140. Ladewig J, Koch P, Brustle O (2013) Leveling waddington: The emergence of direct programming and the loss of cell fate hierarchies. *Nat Rev Mol Cell Biol* 14:225–236
141. Santillán M, Mackey MC, Zeron ES (2007) Origin of bistability in the lac operon. *Biophys J* 92(2):3830–3842
142. Sabouri-Ghomí M, Ciliberto A, Kar S, Novak B, Tyson JJ (2008) Antagonism and bistability in protein interaction networks. *J Theor Biol* 250:209–218
143. Straube R, Conradi C (2013) Reciprocal enzyme regulation as a source of bistability in covalent modification cycles. *J Theor Biol* 330:56–274
144. Ha J, Satin LS, Sherman AS (2016) A mathematical model of the pathogenesis, prevention, and reversal of type 2 diabetes. *Endocrinology* 157:624–635
145. Laurent M (1996) Prion diseases and the ‘protein only’ hypothesis: a theoretical dynamic study. *Biochem J* 318:35–39
146. De Caluwé J, Dupont G (2013) The progression towards Alzheimer’s disease described as a bistable switch arising from the positive loop between amyloids and Ca²⁺. *J Theor Biol* 331:12–18
147. Rapin N, Mosekilde E, Lund O (2011) Bistability in autoimmune diseases. *Autoimmunity* 44:256–260
148. Goldbeter A (2013) Origin of cyclicity in bipolar disorders: A computational approach. *Pharmacopsychiatry* 46(Suppl. 1):S44–S52
149. Cinquin O, Demongeot J (2002) Positive and negative feedback: striking a balance between necessary antagonists. *J Theor Biol* 216:229–241
150. Ozbudak EM, Thattai M, Lim HN, Shraiman BI, Van Oudenaarden A (2004) Multistability in the lactose utilization network of *Escherichia coli*. *Nature* 427(6976):737–740
151. Tan C, Marguet P, You L (2009) Emergent bistability by a growth-modulating positive feedback circuit. *Nat Chem Biol* 5(11):842–848
152. Ferrell JE Jr (2002) Self-perpetuating states in signal transduction: Positive feedback, double-negative feedback, and bistability. *Curr Opin Chem Biol* 6:140–148
153. Angeli D, Ferrell JJE, Sontag ED (2004) Detection of multistability, bifurcations, and hysteresis in a large class of biological positive-feedback systems. *Proc Natl Acad Sci USA* 101(7):1822–1827
154. Laurent M, Kellershohn N (1999) Multistability: A major means of differentiation and evolution in biological systems. *Trends Biochem Sci* 24:418–422
155. Thomas R, Kaufman M (2001) Multistationarity, the basis of cell differentiation and memory. I. Structural conditions of multistationarity and other nontrivial behavior. *Chaos* 11:170–179

156. Guantes R, Poyatos JF (2008) Multistable decision switches for flexible control of epigenetic differentiation. *PLoS Comput Biol* 4:e1000235
157. Rouault H, Hakim V (2012) Different cell fates from cell-cell interactions: core architectures of two-cell bistable networks. *Biophys J* 102:417–426
158. Zhou JX, Huang S (2011) Understanding gene circuits at cell-fate branch points for rational cell reprogramming. *Trends Genet* 27:55–62
159. De Mot L, Gonze D, Bessonard S, Chazaud C, Goldbeter A, Dupont G (2015) Cell fate specification based on tristability in the inner cell mass of mouse blastocysts. *Biophys J* 110:710–722
160. Jia D, Jolly MK, Harrison W, Boareto M, Ben-Jacob E, Levine H (2017) Operating principles of tristable circuits regulating cellular differentiation. *Phys Biol* 14:035007
161. Born GV (1962) Aggregation of blood platelets by adenosine diphosphate and its reversal. *Nature* 194:927–929
162. Gardner TS, Cantor CR, Collins JJ (2000) Construction of a genetic toggle switch in *Escherichia coli*. *Nature* 403:339–324
163. Lu J, Sherman D, Devor M, Saper CB (2006) A putative flip-flop switch for control of REM sleep. *Nature* 441:589–594
164. Morgan DO (2006) The cell cycle: principles of control. Oxford University Press, Oxford, UK
165. Mochida S, Rata S, Hino H, Nagai T, Novák B (2016) Two bistable switches govern M phase entry. *Curr Biol* 26:3361–3367
166. Goldbeter A, Koshland DE Jr (1981) An amplified sensitivity arising from covalent modification in biological systems. *Proc Natl Acad Sci USA* 78:6840–6844
167. Kapuy O, Barik D, Sananes MR, Tyson JJ, Novak B (2009) Bistability by multiple phosphorylation of regulatory proteins. *Prog Biophys Mol Biol* 100:47–56
168. Varusai TM, Kolch W, Kholodenko BN, Nguyen LK (2015) Protein-protein interactions generate hidden feedback and feed-forward loops to trigger bistable switches, oscillations and biphasic dose-responses. *Mol BioSyst* 11:2750–2762
169. Zotos EE (2016) Escape dynamics and fractal basins boundaries in the three-dimensional Earth-Moon system. *Astrophys Space Sci* 361:94
170. de Assis S, Terra M (2014) Escape dynamics and fractal basins boundaries in the planar Earth-Moon system. *Celest Mech Dyn Astron* 120:105–130
171. Hénon M, Heiles C (1964) The applicability of the third integral of motion: some numerical experiments. *Astron J* 69:73–79
172. Daza A, Shipley JO, Dolan SR, Sanjuán MAF (2018) Wada structures in a binary black hole system. *Phys Rev D* 98:084050

Chapter 4

Multistability in Lasers



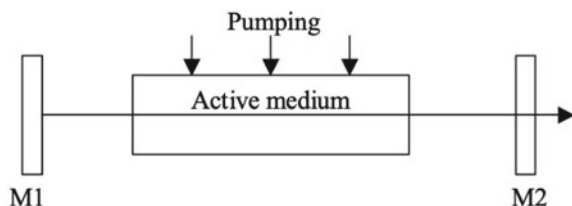
Abstract Lasers are nonlinear optical devices where multistability has been extensively studied. That is why in this book we pay special attention to multistability in lasers and devote an entire chapter to this topic. After introducing the reader to the main principles of laser dynamics, we start our consideration of laser multistability with the so-called *optical bistability* or the coexistence of two different outputs of the laser light transmitted through an optical cavity filled with a resonant medium. In fact, an optical bistable system is the passive counterpart of a laser. The phenomenon of optical bistability theoretically predicted by Szoke et al. [1] was observed in the experiments of Gibbs and colleagues [2]. Their findings stimulated intensive theoretical and experimental research in this direction. It was only in the early 1980s that multistability became a noticeable phenomenon in laser physics. Here, after a short excursion back to the history of nonlinear laser dynamics, we will describe the main features of optical bistability and generalized multistability in laser systems of different types.

4.1 Laser as a Nonlinear Dynamical System

4.1.1 History of Laser Dynamics

A laser is an electro-optical device that produces coherent radiation. The term “laser” has been widely used since about 1965. LASER is the abbreviation for the word “Light Amplification by Stimulated Emission of Radiation.” At first it was called an “optical quantum generator” or “optical MASER” (Microwave Amplification by Stimulated Emission of Radiation). The first masers were created in 1953–1954 by Russian physicists Nikolai G. Basov and Alexander M. Prokhorov and independently by American physicist Charles Townes. In 1955, Prokhorov and Basov proposed optical pumping of a multilevel system as a method for obtaining a population inversion, which later became one of the main methods of laser pumping. In 1964, Townes, Basov and Prokhorov shared the Nobel Prize in Physics “*For fundamental work in the field of quantum electronics, which led to the creation of oscillators and amplifiers*

Fig. 4.1 A laser construction with a Fabry–Pérot cavity. M1 and M2 are full reflective and semitransparent mirrors, respectively



based on the maser-laser principle.” Indeed, the laser has revolutionized optical technology and has had a far-reaching influence in various fields of science and life in general.

As a rule, a laser consists of an amplifying (active) medium with inverted population and a cavity formed by two mirrors M1 and M2, which form a Fabry–Pérot resonator confining light between the mirrors (Fig. 4.1). Instead of flat mirrors, concave mirrors, diffraction gratings or Bragg reflectors are also used, and sometimes an optical cavity with more than two mirrors is utilized. The active medium is excited from an external energy source (electrical, chemical, or optical). The active medium plays an important role in the light amplification by population inversion and stimulated emission. There are many types of active media that can be used to produce lasing at different wavelengths. Thus, we can say that a laser is a nonlinear optical oscillator or an amplifier of light waves.

Since its discovery and until the mid-1960s, the laser was thought as a “stable” device whose instability was treated as a consequence of mechanical vibration or bad cavity alignment. Nonlinear laser dynamics was conceived by Russian physicists Grazyuk and Oraevsky [3], who found that the coherent single-mode laser equations, which are a simplified version of the more modern Maxwell–Bloch theory, predict instabilities and stable oscillations without well-defined mathematical conditions that do not affect the unsaturated gain of the active medium in the cavity and the rate of atomic relaxation.

By coherent laser equations, we mean a theory based on the existence of an interaction between an optical wave and atomic dipoles, which assumes a relationship between an optical wave and macroscopic polarization in accordance with Maxwell’s electrodynamics. In numerical studies of equations describing the simplest (uniformly broadened, single-mode, traveling wave, resonantly tuned) laser, they found a non-stationary solution consisting of pulses that irregularly vary in time. At the time, they even used the term “chaotic” to describe this irregular, pulsating behavior.

Laser dynamics was in its infancy for over a decade until the mid-1970s, when the German theoretical physicist Hermann Haken, based on the isomorphism of the laser with Lorentz equations, came to the conclusion that lasers should exhibit non-periodic pulses. However, in the early 1980s, many researchers did not believe that the Lorentz–Haken instability was inherent in real laser systems. They thought it was just an academic curiosity invented by theoreticians far remote from the daily reality of experimental laser physics. Nevertheless, chaos and multistability were soon discovered in lasers giving rise to a new research field named *Nonlinear Laser Dynamics*.

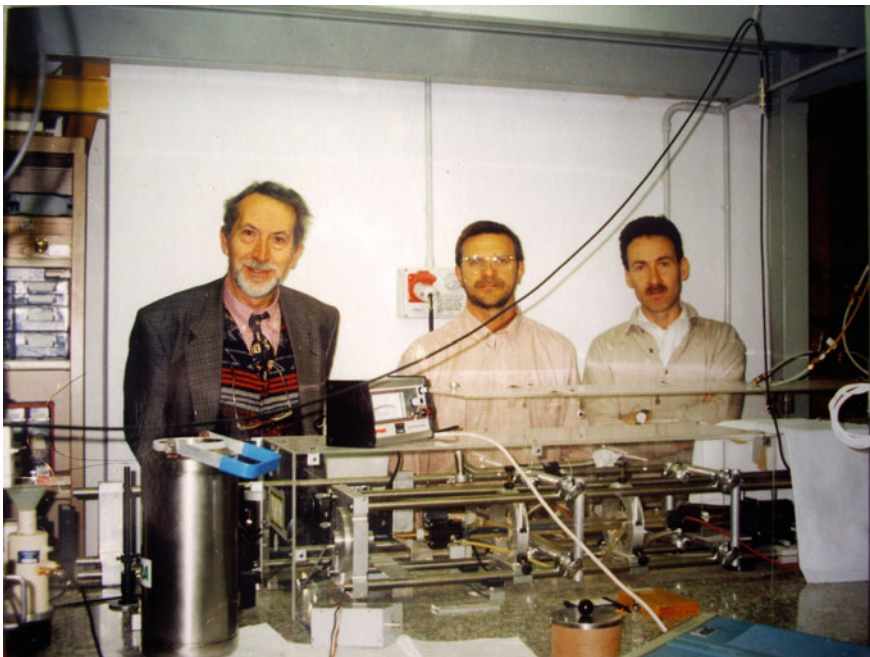


Fig. 4.2 Tito Arecchi (left), Alexander Pisarchik (center), and Riccardo Meucci (right) behind the CO₂ laser setup at the National Institute of Applied Optics (Istituto Nazionale di Ottica Applicata). Florence, Italy, April 1999

The first clear experimental evidence of multistability in laser systems was demonstrated in 1982 by the group of Tito Arecchi [4], who found the coexistence of two oscillatory regimes in a loss-modulated CO₂ laser (see Fig. 4.2). They called this phenomenon *generalized multistability* to distinguish it from “optical bistability” meaning the coexistence of two stable steady states. At the same year, bistability was experimentally observed in a multimode infrared He–Ne laser by the group of Carl Weiss [5]. Later, Brun and colleagues [6] observed the coexistence of periodic and chaotic pulsations in a nuclear spin-flip laser. Since then, the coexistence of various attractors has been found in other types of lasers, including solid-state lasers with intracavity second harmonic generation [7], semiconductor [8, 9], and fiber lasers [10, 11]. These results sharpened the concept of lasers as “unstable” systems and stimulated new experimental and theoretical research.

From the very beginning of the laser industry, stabilization of irregular fluctuations in the intensity of laser radiation has been an important problem. However, instability and chaos are inherent in the nonlinear nature of laser systems with three or more degrees of freedom. For example, in multimode lasers or in lasers with nonlinear intracavity devices, nonlinear coupling between modes can lead to instability and multistability of the laser intensity. It is quite obvious that the irregular behavior of such lasers is an undesirable situation for many practical applications. Scientists

faced this problem first in a diode-pumped Nd:YAG (neodymium-doped yttrium-aluminum garnet) ($1.06\text{ }\mu\text{m}$) with intracavity second harmonic generation (green light) and thus called “green problem” [7]. Several theoretical and experimental works have been devoted to avoiding such irregular behavior and switching between coexisting states [12].

A special type of multistability, *spatial multistability* was also found in lasers in the form of coexisting transverse spatial patterns which appear due to the interaction of cavity modes. In order to describe spatial multistability in optical patterns, Brambilla et al. [13] argued a general connection between laser physics and hydrodynamics, reformulating the equations of laser dynamics in the form as the equations of hydrodynamics for a compressible fluid in accordance with the law of conservation of mass and the Bernoulli equation. Two-dimensional optical patterns can also result from synchronization of several wave vectors of different lengths and orientations [14]. Multistability of optical structures can be useful for information processing, associative memory, and pattern recognition [15].

4.1.2 *Dynamical Classification of Lasers*

Lasers are usually classified according to the active medium providing optical amplification. This material largely determines the properties of the laser: operating mode (pulsed or continuous), radiation wavelength, output power/energy, and coherence properties. Gases, liquids and solids can provide optical amplification when properly excited.

Another classification of lasers is based on timescale considerations. This classification was introduced by Arecchi et al. [16], who opened a new view of lasers as dynamical systems and can be regarded as one of the most important advances in laser dynamics. Similar to other nonlinear devices, the laser can be modeled by rate equations. In particular, many lasers are described by three differential equations. Three relevant variables (field, population, and polarization) decay at different time scales, which are given by the corresponding relaxation rates (κ , γ_{\parallel} , and γ_{\perp}). If one of these constants is larger compared to the others, the corresponding variables are rapidly weakened and therefore adjust adiabatically to the other variables. Thus, the number of equations describing the laser can be reduced. More precisely, single-mode lasers are named classes A, B, and C depending on whether the laser dynamics is ruled, after appropriate adiabatic elimination of fast variables, by one, two, or three equations, respectively.

Thus, the following laser classification is now widely accepted.

Class A (for example, He-Ne, Ar, Kr, dye lasers): $\gamma_{\perp} \simeq \gamma_{\parallel} \gg \kappa$. The dynamics of these lasers are modeled by only one nonlinear field equation resulting in a stable coherent emission.

Class B (for example, ruby, Nd:YAG, CO, CO₂, semiconductor, fiber lasers): $\gamma_{\perp} \gg \kappa \leq \gamma_{\parallel}$. Only polarization is adiabatically eliminated so that the dynamics is

ruled by two rate equations for field and population that allows for damped oscillations (relaxation oscillations) of the energy between field and inversion.

Class C (for example, He-Cd, He-Xe, far-infrared gas lasers): $\gamma_{\perp} \simeq \kappa \simeq \gamma_{\parallel}$. The complete set of three rate equations has to be used, and therefore chaos is possible.

Thus, chaotic dynamics and multistability are impossible in class A and B lasers without adding additional degrees of freedom, which can be introduced using either an external action (for example, parametric modulation or injection of external light), an intracavity nonlinear medium (saturable absorber), a feedback, or in a bidirectional ring cavity.

In general, a small change in one or more laser parameters causes small (smooth) changes in the laser output, so that the laser is considered “structurally stable”. However, for some specific values of the parameters, one of the solutions (or attractors) can undergo a strong qualitative change (bifurcation), and the laser is considered “structurally unstable”. Very often, when the control parameter is changed and a bifurcation appears at a certain critical value, the laser undergoes a sequence of new bifurcations at higher values of the parameter. Each new attractor that appears in the chain of bifurcations is usually more complex than the previous one and eventually becomes chaotic. Such a sequence of bifurcations is called “the road (or route) to chaos.” The number of types of routes to chaos in lasers is large and exactly unknown, but it has been observed that some of them appear very often, and for this reason they are called “scenarios.” The most often scenarios are the Feigenbaum (or period-doubling), Ruelle–Takens–Newhouse (or quasiperiodicity), and intermittency (types I–III, Pomeau–Manneville, on-off, crisis-induced) routes to chaos.

4.2 Multistability in Optical Systems

In this section, we describe different types of multistability in optical and laser systems, in particular, optical bistability, spatial multistability, and polarization multistability.

4.2.1 Optical Bistability

Optical bistability is the general name for a number of static and dynamic phenomena that arise from the interaction of optical nonlinearity and feedback. The comprehensive reviews can be found in Refs. [17–19].

An optically bistable system is a system that exhibits two stable output signal states at the same input radiation intensity. The simplest example of such a device consists of a Fabry–Perot cavity filled with a nonlinear media whose refractive index depends on the radiation intensity I as $n = n_0 + n_2 I$ (n_0 and n_2 being constants), as illustrated in the left panel in Fig. 4.3.

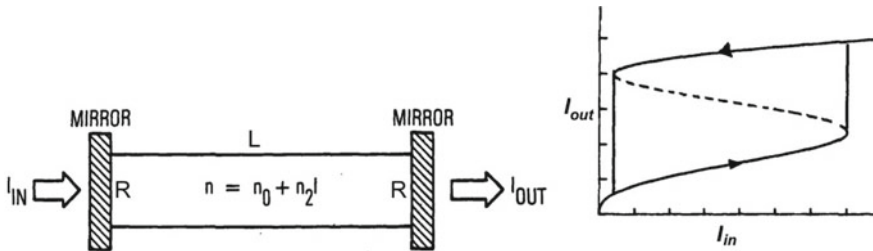


Fig. 4.3 (Left) Fabry–Perot interferometer of length L and mirror reflectivity R . I_{in} and I_{out} are incident and transmitted intensities. (Right) Characteristic curve of the optical cavity showing bistability. As the input intensity I_{in} varies, the transmitted intensity I_{out} exhibits a hysteresis cycle. The dashed line indicates unstable equilibria

The transfer function of the Fabry–Perot interferometer, that is the ratio of the output intensity to the input intensity, as known to depend on the radiation wavelength λ as [20]

$$\frac{I_{in}}{I_{out}} = \frac{1}{1 + F \sin^2(\Phi/2)}, \quad (4.1)$$

where $F = 4R/(1 - R)^2$ is the cavity finesse and

$$\Phi = 2\pi n_o \frac{L}{\lambda} + \frac{4\pi n_2 L}{\lambda} I_{in} \quad (4.2)$$

is the round-trip phase shift.

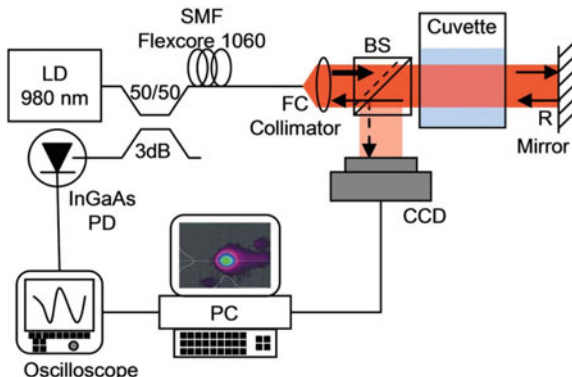
An increase in the input intensity causes a decrease in the effective wavelength and, accordingly, an increase in the transmission. As a result, the cavity optical length nL is a periodic function of I . One can see in the right panel in Fig. 4.3 that the transfer function displays a hysteresis behavior, i.e. there is a region of input intensities for which the output intensity has two stable values for a given input intensity. The two values represent high and low transmitting levels or states. This is a typical example of bistability which arises in saddle-node bifurcations (see Sect. 2.1.2).

Miller and colleagues [21] were the first to experimentally observe optical bistability in InSb at 1895 cm^{-1} near the absorption edge at 5 K. The nonlinear term in Eq. 4.2 indicates that the longer the cavity, the lower the intensity required for these effects, but if the cavity is too long, then linear absorption becomes important, and this leads to a decrease in efficiency, and therefore bistability may not occur.

Bistable optical systems usually contain either a saturable absorber or a nonlinear dispersive medium and an optical feedback loop. However, aerosols and suspensions of dielectric nanoparticles (soft matter) can also be used as nonlinear media, since in this case nonlinear effects can be observed at very low power levels [22].

Pobegalov et al. [23] discovered a new type of optical bistability obtained with low-power lasers and using defocusing nonlinearity in nanoparticle suspensions. The ability to use light to control properties of nanosuspensions at a mesoscopic

Fig. 4.4 Experimental setup for observation of low-power optical bistability in the optoliquid system. It includes a fiber pigtailed semiconductor laser diode (LD) with nonlinear incoherent optical feedback. To visualize coexisting optical patterns, a CCD camera is used. Reprinted with permission from [23] ©2014 The Optical Society



level makes such a system very attractive for the rapidly developing field of optofluidics [24, 25] which combines microfluids and photonics, creating new possibilities for optical information processing. In addition, low-power optoliquid systems are especially promising for biomedical applications, as they can provide nondestructive inspection and verification of biological objects. Using a semiconductor laser diode operating near the threshold at a 980-nm wavelength and a colloidal solution of LaF₃:Er and Yb nanocrystals with resonant optical absorption at the same wavelength, optical switching of several milliwatts was obtained. Figure 4.4 shows the experimental setup for studying optical bistability.

The bifurcation diagram of the laser intensity at the center of the laser beam is presented in Fig. 4.5a. It displays hysteresis with respect to the pump current. Optical bistability is observed as switching between high-power and low-power states of the photodetector signal, accompanied by a radical change in the cross-section profile of the optical feedback beam, i.e. the transition from a simple bell-shaped profile to an annular one, meaning, respectively, high-power and low-power states illustrated in Fig. 4.5b,c. In the hysteresis range, two different laser beam profiles coexist and can be found by changing the direction of the pump current change. The origin of optical bistability relies on the incoherent optical feedback and thermal defocusing nonlinear optical response of the nanosuspension.

The change in the beam profile can also be interpreted as spatial bistability caused by spontaneous emission of four-wave mixing in the off-axis direction. The hysteresis appears due to a special operation mode of the laser with incoherent optical feedback.

4.2.2 Spatial Multistability

Spatial multistability is a specific type of multistability which reveals itself as the coexistence of different patterns in space for the same set of system parameters. Spatial bistability, was first experimentally observed in 1990 in a helium-neon (He-Ne)

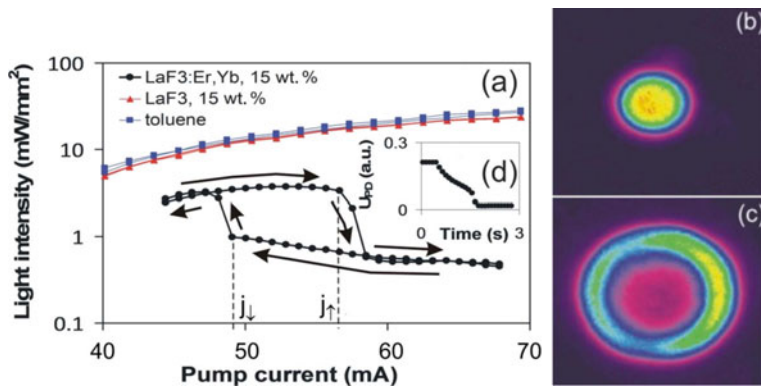


Fig. 4.5 Optical bistability in a laser system. **a** Output light intensity at the beam center at the CCD camera as a function of laser-diode current for pure toluene (squares). **b, c** Coexisting output beam profiles in high- and low-intensity states. Adapted from [23]

laser oscillating in the TEM_{01}^* hybrid optical-resonator mode [26]. One year later, Brambilla and colleagues [13] reported on their findings of the coexistence of three and four different pattern configurations of the laser field. Then, this phenomenon was observed in other nonlinear systems, such as cell replication models [27], continuous stirred tank reactors [28], protein-protein interactions [29], reaction-diffusion systems [28, 30, 31], ecosystems [32–34], planar exciton-polariton condensates [35], multimode vertical-cavity lasers [36], and arrays of graphene [37].

We can distinguish two types of spatial multistability conventionally called *exogenous* and *endogenous*. The former type is referred to the case when coexisting patterns are caused by an external source, while the latter type results from synchronization of coupled systems. For example, the coexistence of different laser modes caused by a laser beam passed through a Fabry–Perot resonator belongs to the exogenous type of spatial multistability. Another example of exogenous spatial multistability is the coexistence of different patterns in brain imaging of electrical or magnetic activity induced by ambiguous stimuli (see Chap. 8). Examples of endogenous spatial multistability are multistable spatial dynamics of reaction-diffusion systems and multistability in cell replication. In addition, spatial multistability in complex networks can manifest itself as the coexistence of synchronous and asynchronous oscillations. Such a behavior referred to as *multistable chimeras* [38, 39] will be described in Chap. 6.

The first example demonstrating that laser dynamics can be characterized by the transverse structure of the laser field was given by Lugiato and Milani [40]. They showed that for a fixed Gaussian transverse distribution of the intensity of laser modes in a uniformly broadened laser, there are no “bad-cavity” or “good-cavity” single-mode laser instabilities. In other words, neither single-mode instabilities nor instabilities with the participation of several longitudinal modes arise.

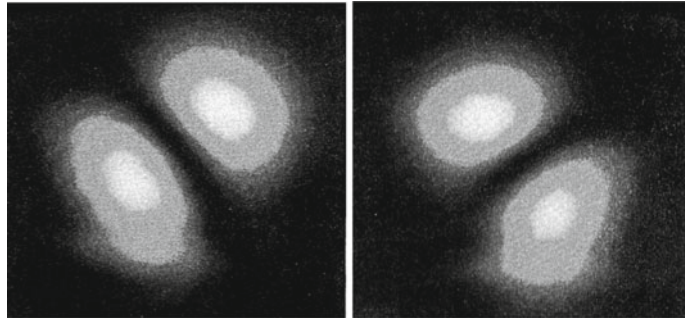


Fig. 4.6 Coexisting TEM_{01} and TEM_{10} laser modes. Reprinted with permission from [26] ©1990 The Optical Society

Tamm and Weiss [26] were the first who experimentally observed spatial bistability. It was achieved with a small screen placed at the center of the He–Ne laser beam waist. When the laser is tuned to cavity modes with zero intensity at the center, it usually emits in TEM_{01} or TEM_{10} mode, or both, as illustrated in Fig. 4.6. By moving the point of the absorber, it is possible to make the intensities of both modes more or less equal. At the same time, switching between these two modes occur due to inherent laser noise.

4.2.3 *Polarization Multistability*

Due to a vector character of electromagnetic field \mathbf{E} , there is a phase difference between two components E_x and E_y of output light passed through a nonlinear medium. The coexistence of two laser beams with orthogonal polarization was first observed by Chen and Liu [41] in an edge-emitting semiconductor laser. This type of optical bistability was revealed near the polarization transition temperature with a hysteresis in the laser power versus the injection current. Later, polarization bistability was also found and extensively studied in vertical cavity surface lasers (VCSELs) [42].

VCSELs are widely used as light sources in optoelectronic devices, optical communications and measuring systems, in particular, in communication systems for data transmission, laser printers, autodyne interferometry, atomic clocks, various spectroscopic schemes, etc. [43]. VCSELs have a number of advantages over other types of semiconductor lasers. In particular, they are relatively cheap, the laser beam is of a high quality, and the lasing threshold is low. In addition, these lasers provide broadband modulation that is important for communication. Extensive efforts were concentrated on the stabilization of polarization that is important for the application of these lasers in a polarization-sensitive equipment, such as, magneto-optic

disks and coherent detection systems. On the other hand, fast switching between two orthogonal polarization states can be useful for applications in all-optical switching and optical memory.

The physical mechanism underlying polarization multistability in VCSEL lies in the fact that the guided fundamental laser mode does not have azimuthal changes and, therefore, the distribution of the optical field depends only on the lateral position. Since a preferential axis of symmetry in the circular cross-section does not exist, the electric field can be directed so that it is everywhere parallel to one of the arbitrary pair of orthogonal directions. Moreover, the two orthogonally polarized beams are amplified in the active layer of an isotropic quantum well active, so that the two polarization states become nearly degenerated. Dispersive bistability is caused by gain saturation that can be obtained through the input Y-polarized beam when the optical gain is depleted during the amplification of the Y-polarized beam, and hence X-polarized mode is suppressed. At the same time, the amplification of the Y-polarized mode is accompanied by a decrease in carrier concentration, which in turn causes an increase in the refractive index of the active medium. Dispersive bistability in both X- and Y-polarized outputs appears if the wavelength of the injected Y-polarized light is slightly larger than the wavelength of the Y-polarized light in the cavity without external optical injection. It was found that the dispersive bistability and gain saturation powers of the X- and Y-polarized models depend on the temperature, dispersion, and the VCSEL structure.

As a rule, bistability in single-mode VCSEL lasers is observed as spontaneous polarization switching during the scanning of the pump current that leads to hysteresis. Multimodal VCSELs behave in a similar way, however, several polarization states can coexist at high pump currents, namely, three [44], four, and five [45] polarization states were observed. In addition, two types of multistability (polarization and spatial) simultaneously exist in this laser [36].

Figure 4.7 shows the experimentally observed coexisting spatial patterns of the VCSEL intensity corresponding to different polarization states which were obtained for the same parameters using different initial conditions. The measurements were performed with a 852-nm VCSEL. The collimated laser beam was split into two equal beams. One was recorded by a photodiode to analyze the integrated intensity, and another passed through a half-wave plate and split by a Glan prism into two orthogonal polarization components. One of these components was recorded by a CCD camera to analyze spatial beam profile, while another component was recorded by a second photodiode to analyze laser dynamics of a particular polarization. A spatial beam profile was recorded by the CCD camera.

As seen from Fig. 4.7, polarization multistability manifests itself in the form of coexisting spatial structures or, in other words, different distributions of laser radiation intensity in the beam cross-section at the same parameters. The coexistence of two, three, and four spatial distributions of the laser intensity were experimentally observed in this laser. Thus, polarization multistability leads to spatial multistability in the integral laser intensity.

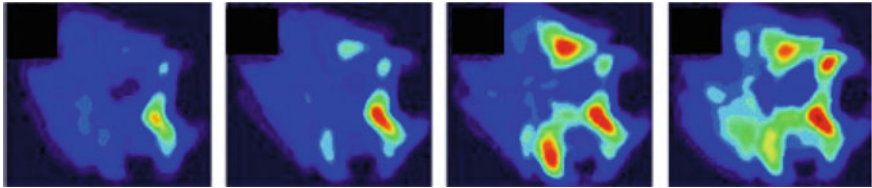
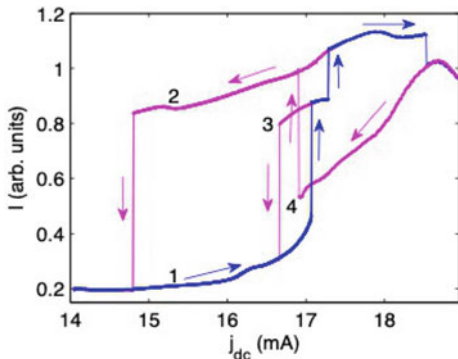


Fig. 4.7 Four coexisting spatial distributions of the VCSEL intensity corresponding to different polarization states. Based on data from [46]

Fig. 4.8 Laser intensity of different polarization versus dc pump current. The arrows show the directions of the current changes and switches between different polarization states. The hysteresis is obtained by increasing and decreasing pump currents starting from different initial conditions



Polarization multistability is clearly seen in Fig. 4.8 which displays the laser intensity when the bias current is slowly increased and decreased. One can see that for certain currents two, three, and even four polarization states coexist.

The theoretical analysis of polarization bistability in VECSELs and conditions necessary for its occurrence were derived by Yu [47]. In particular, he substantiated that (i) the input power required to achieve polarization bistability depends on the matching between the gain and the resonator mode. When the gain is blue-shifted relative to the resonator mode, then the hysteresis loops are shifted towards the low-power side of the input Y-polarized light. However, the opposite situation occurs for the red-shift alignment. (ii) Self-heating effect is minimized for the blue-shifted alignment because the low injection power is required for bistability. (iii) The reflectivity of Bragg reflectors affects the bistable performance of the VCSEL. Devices with low reflectivity require low input power to achieve bistability, but the strength of the coupling between the injected light and the active layer is reduced. Therefore, the use of polarization bistability in VCSELs for all-optical switching and optical memory requires a blue-shifted gain relative to the cavity mode to reduce input power and self-heating.

It should be noted that polarization bistability was found not only in semiconductor laser, but also in liquid crystals in the Fabry-Pérot optical resonator [48–50], counter-propagating laser beams through a nonlinear medium [51], and in a He-Ne laser with saturable absorber [52].

4.3 Multistability in CO₂ Lasers

The CO₂ laser with harmonic modulation of cavity losses was the first laser system where the coexistence of different periodic orbits was observed [4]. Using an intracavity electro-optical modulator, Arrecchi and colleagues found that at certain modulation frequencies the laser operated either in a period-3 or in a period-4 regime. The coexistence of these regimes was found in the average power spectrum of the laser output intensity, where the both subharmonic frequencies were observed, as illustrated in Fig. 4.9. The switching between the two periodic orbits was explained by the influence of internal laser noise.

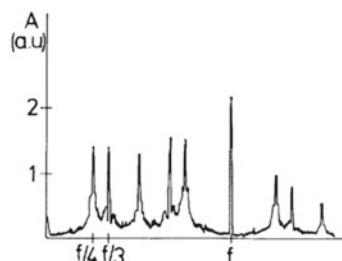
Later, bistability in a CO₂ laser was observed under harmonic modulation of the cavity optical length [53], optical injection [54, 55], delayed feedback [56], pump current modulation, and cavity detuning [57].

4.3.1 Loss-Modulated CO₂ Laser

A CO₂ laser belongs to class-B lasers, i.e. the polarization term can be adiabatically eliminated so that the laser can be described by two rate equations, for the laser intensity and for population inversion. Nevertheless, it is possible to observe nonlinear dynamical effects in this class of lasers, including chaos and multistability if we add an additional degree of freedom in the form of external modulation, intracavity saturable absorber, or feedback.

The simplest two-level model of the active medium of a single-mode CO₂ laser contains two dimensionless variables that describe radiation power density u in the cavity and gain y in the active medium [58, 59]:

Fig. 4.9 Experimental averaged power spectrum of the CO₂ laser intensity demonstrating the coexistence of period-3 and period-4 regimes. $f/3$ and $f/4$ are subharmonics of the modulation frequency f



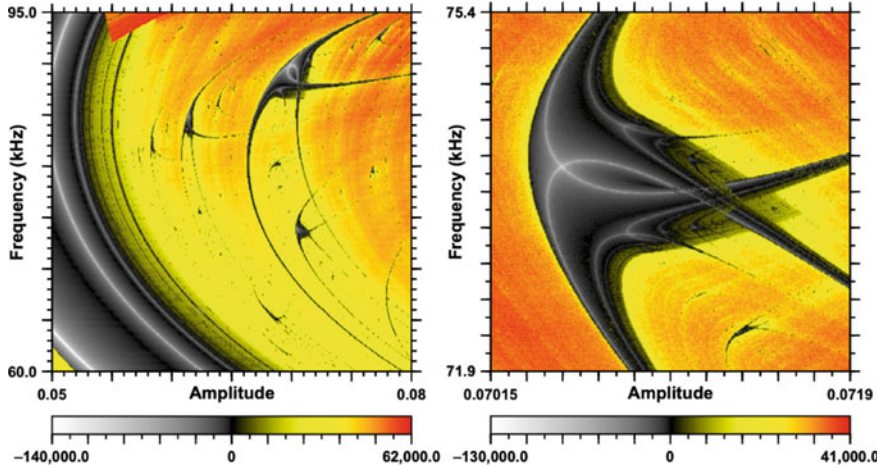


Fig. 4.10 Lyapunov exponents in the CO₂ laser (Eq. 4.3) with loss modulation (Eq. 4.4) in the space of modulation amplitude k_d and frequency f_d . The right diagram is the enlarged area of the left diagram. Negative exponents (in grey) represent periodic regimes, while positive exponents (in colors) indicate the regime of chaotic oscillations. Reprinted from [60] ©2016 with permission from Elsevier

$$\begin{aligned}\dot{u} &= \tau^{-1}(y - k)u, \\ \dot{y} &= (y_0 - y)\gamma - uy,\end{aligned}\tag{4.3}$$

where y_0 is unsaturated gain, τ is half of the round-trip time of light in the laser cavity, γ is the gain decay rate, and k is the total cavity losses.

Complex dynamics in a class-B laser appears when cavity losses are periodically modulated as follows

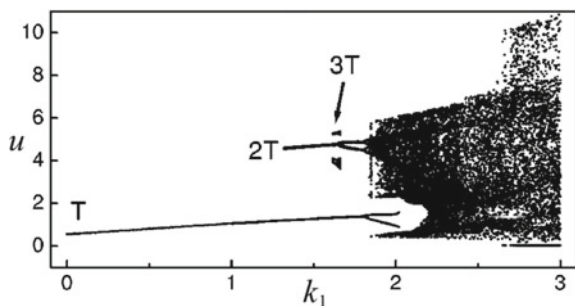
$$k(t) = k_0(1 + k_d \cos(2\pi f_d t)),\tag{4.4}$$

where k_0 is the constant part of the losses, and k_d and f_d are the driving amplitude and frequency.

For parameter values $\tau = 3.5 \times 10^9$ s, $\gamma = 1.978 \times 10^5$ s⁻¹, $y_0 = 0.175$, and $k_0 = 0.1731$ and using a and f as control parameters, the phase-space structure of the system stability (in terms of Lyapunov exponents) exhibits so-called *shrimps* illustrated in Fig. 4.10. The shrimps represent a complex structure consisting of a doubly infinite sequence of period-doubling bifurcations, followed by chaotic oscillations.

Figure 4.11 shows the bifurcation diagram of peak values of u versus driving amplitude f_d obtained by numerical simulations of Eqs. 4.3 and 4.4 using random initial conditions [61]. One can see three branches (T, 2T, and 3T) which correspond to different attractors starting from period-1, period-2, and period-3 orbits. As k_d is increased, these orbits undergo period-doubling bifurcations followed by crisis and chaos. For certain values of k_d , there is bistability and tristability.

Fig. 4.11 Bifurcation diagram of the peak values of laser density u as a function of the driving amplitude k_d . T, 2T, and 3T are stable branches of the period-1, -2, and -3 orbits. $y_0 = 0.1805$, $f_d = 112$ kHz



4.3.2 Targeting Attractors by Short Pulses

To find coexisting attractors in a loss-modulated CO₂ laser, Chizhevsky and colleagues [62, 63] applied a short (as compared to characteristic times in the system) perturbation to the laser field. In fact, the method is equivalent to the Monte Carlo method (see Sect. 2.3.2), when the initial condition is randomly changed. In this case, the laser turns off for a very short time, and then turns on again, but under different initial condition and, therefore, can be instantly sent to the basin of attraction of another coexisting attractor. An important advantage of this method is that it can easily be used in experiments, since it does not require any prior knowledge of the model. Since the pulse is very short, no significant changes in the laser parameters occur during the switching time, so that the global structure of attractors in phase space remains unchanged. In addition, switching with short pulses is a well-controlled deterministic process, so that the laser response is reproduced with a very high accuracy.

A scheme of the experimental setup for identifying coexisting attractors in a CO₂ laser is drawn in Fig. 4.12. A 15-ns pulse of a Nd³⁺:YAG laser is applied to a GaAs plate inside the cavity of a single-mode cw CO₂ laser, which leads to an increase in the concentration of nonequilibrium carriers, which, in turn, increases the absorption of CO₂ laser radiation. As a result, the CO₂ laser stops generating radiation for a short pulse time. The back edge of the induced losses is determined by the lifetime of nonequilibrium charge carriers in GaAs, which does not exceed 300 ns. Both time constants are much shorter than the period of loss modulation by an acousto-optic modulator based on a Thallium Halogenide (KRS-5) crystal, exceeding 10 μ s.

To obtain a particular coexisting attractor, the amplitude and phase of the Nd:YAG laser pulse must be matched with the phase of loss modulation of the CO₂ laser. For this, the following procedure is used. For a fixed pulse amplitude, its phase (i.e. its delivery time) is shifted relative to the phase of modulation of the CO₂ laser losses. By shifting the pulse phase, all coexisting states can be found.

Using this approach, the coexistence of four periodic orbits was revealed in the loss-modulated CO₂ laser, namely, period 1 (T), period 3 (3T), period 4 (4T), and period 5 (5T), for the same set of the laser parameters. The switching between different coexisting attractors is illustrated with the oscilloscope recordings in the left

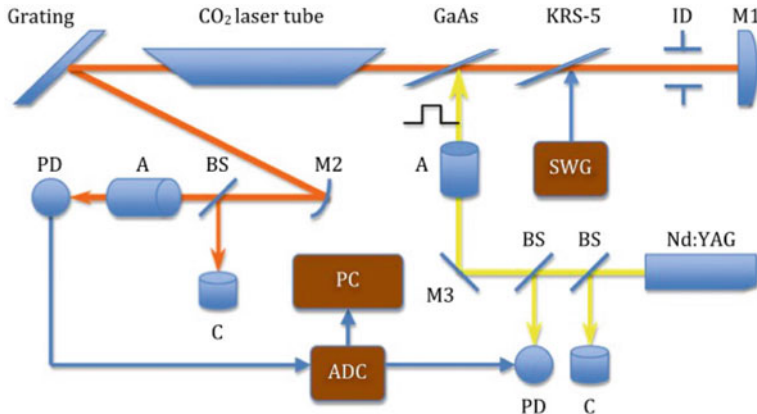


Fig. 4.12 Experimental setup for searching coexisting attractors in a loss-modulated CO₂ laser by an external short-pulsed perturbation from a Nd:YAG laser. M₁, M₂, and M₃ are a totally reflecting mirror. The cavity losses are modulated by a harmonic signal applied from a sine wave generator (SWG) to an acousto-optical modulator (KRS-5). Switching between coexisting attractors is realized by short pulses of the Nd³⁺:YAG laser applied to a GaAs plate. ID is an iris diaphragm, BS are beam splitters, PD are photodetectors, A are optical attenuators, C are calorimeters, ADC is an analog-to-digital converter, and PC is a computer

panel in Fig. 4.13. Multistability is clearly seen in the experimentally reconstructed bifurcation diagrams of the CO₂-laser peak amplitude versus the driving amplitude applied to the acousto-optical modulator, presented in the right panel in Fig. 4.13.

It should be noted that the same approach can be applied to detect not only stable but also unstable orbits. Indeed, using this technique, unstable periodic orbits have been found in a loss-modulated CO₂ laser [65].

4.3.3 Bistability Induced by Resonant Perturbations

Chizhevsky et al. [59] discovered that similar to other dynamical systems (see Sect. 2.2.7), bistability can be induced by additional resonant perturbation. It was found that in a loss-modulated CO₂ laser the addition of another modulation at a subharmonic frequency of the driving loss modulation splits the bifurcation diagram into two diagrams shifted in different directions with respect to the driving amplitude which is used as a control parameter.

The double-frequency modulation is applied to the cavity loss in Eq. 4.3 as

$$k(t) = k_0 + k_d \cos(2\pi f_d t) + k_p \cos(2\pi \frac{f_d}{n} t + \phi),$$

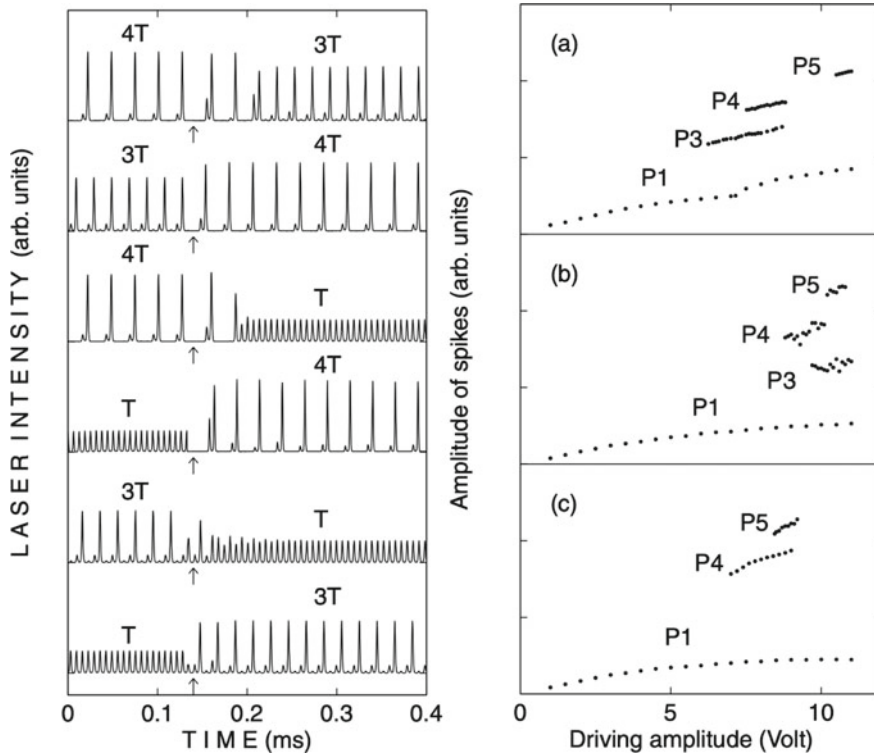


Fig. 4.13 (Left) Experimental time series showing switches between coexisting periodic orbits and (right) bifurcation diagrams of the peak laser intensity as a function of the driving amplitude applied to the loss modulator, showing the coexisting branches of periodic orbits P1, P3, P4, and P5, for modulation frequencies **a** 150, **b** 170, and **c** 180 kHz. Reprinted by permission from IOP Publishing [64]

where k_p is the perturbation amplitude at subharmonic frequency f_d/n ($n = 3, 4, 8, 16$) and ϕ is the perturbation phase.

The bifurcation diagram of the peak laser intensity with respect to the control parameter $\mu = k_d/k_{1/2}$ ($k_{1/2}$ being the first period-doubling bifurcation in the absence of the resonant perturbation) for the parameters $\tau = 3.5 \times 10^{-9}$ s, $\gamma = 1.978 \times 10^5$ s $^{-1}$, $y_0 = 0.1735$, $k_0 = 0.1731$, $f_d = 129$ kHz, $k_{1/2} = 4.76 \times 10^{-3}$, and $\phi = 0$.

A common feature of periodically driven nonlinear systems, apart from a period-doubling route to chaos, is the presence of n subharmonic isolated branches called *isolas*, which are born in saddle-node bifurcations of the period n . For example, in the bifurcation diagram shown in Fig. 4.14, the laser parameters are chosen so that for $\mu > 2.308$ the period-2 (P2) and period-3 (P3) orbits coexist in the absence of the resonant perturbation. The addition of the resonant perturbation at $f_d/3$ splits the primary period-3 attractor into three different P3 attractors, which appear in saddle-node bifurcations at $\mu_1 = 2.236$, $\mu_2 = 2.310$, and $\mu_3 = 2.388$.

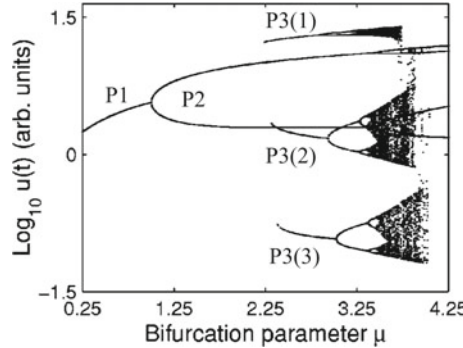


Fig. 4.14 Bifurcation diagram of log of the peak intensity of the loss-driven CO₂ laser under resonant perturbation at $f_d/3$ versus control parameter μ showing the splitting of the primary period-3 attractor into three period-3 attractors denoted by P3(1), P3(2), and P3(3). Reprinted figure with permission from [66] ©2001 by the American Physical Society

The splitting of attractors was experimentally confirmed using the experimental setup similar to that presented in Fig. 4.12, which allowed switching between the attractors [66].

4.3.4 Bistability Induced by a Delayed Feedback

A CO₂ laser with feedback is a complex system extensively studied both experimentally and numerically. As distinct from a loss-modulated CO₂ laser which can be described by the simplest two-level model in Eq. 4.3 (see Sect. 4.3.1), the CO₂ laser with feedback is modeled by either three [67] or six rate equations given as [68, 69]

$$\begin{aligned} \dot{x}_1 &= k_0 x_1 \left\{ x_2 - 1 - k_1 \sin^2 [\epsilon x_6 (\theta - T_0) + (1 - \epsilon) x_6] \right\}, \\ \dot{x}_2 &= -\Gamma_1 x_2 - 2k_0 x_1 x_2 + \gamma x_3 + x_4 + P, \\ \dot{x}_3 &= -\Gamma_1 x_3 + x_5 + \gamma x_2 + P, \\ \dot{x}_4 &= -\Gamma_2 x_4 + \gamma x_5 + z x_2 + z P, \\ \dot{x}_5 &= -\Gamma_2 x_5 + z x_3 + \gamma x_4 + z P, \\ \dot{x}_6 &= \beta \left(B - x_6 - \frac{R x_1}{1 + \alpha x_1} \right), \end{aligned} \quad (4.5)$$

where x_1 is the normalized photon number proportional to the laser intensity, x_2 is proportional to the population inversion, x_3 is proportional to the sum of populations on the two resonant lasing levels, x_4 and x_5 are proportional, respectively, to the difference and sum of populations of the rotational manifolds coupled to the lasing levels, and x_6 is proportional to the feedback voltage that affects cavity

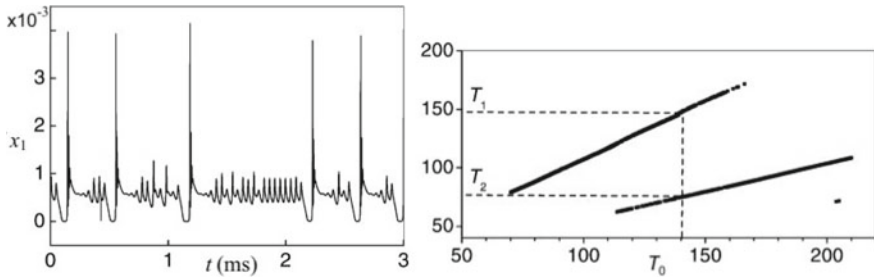


Fig. 4.15 (Left) Chaos in a CO₂ laser without delay. (Right) Periodicity of periodic orbits as a function of feedback delay T_0 . The horizontal dashed lines indicate periods of coexisting orbits $T_1 = 147.3$ and $T_2 = 74.7$ at delay time $T_0 = 140$ shown by the vertical dashed line. The parameters are $\Gamma_1 = 10.0643$, $\Gamma_2 = 1.0643$, $\alpha = 32.8767$, $\beta = 0.4286$, $k_0 = 28.5714$, $k_1 = 4.5556$, $z = 10$, $\gamma = 0.05$, $R = 160$, $B = 0.10315$, and $P = 0.016$, $\epsilon = 0.25$

losses. The parameter k_0 is related to the unperturbed cavity loss, k_1 determines the modulation strength, γ is a constant regulated the coupling between the variables (x_2, x_3, x_4, x_5) and (x_3, x_2, x_5, x_4) , Γ_1 and Γ_2 are decay rates of the lasing levels, P is the pump parameter, z is the effective number of rotational levels, α , β , B , and R are proportional to the saturation factor, bandwidth, bias voltage, and feedback gain, respectively. The delay term $\epsilon x_6(\theta - T_0)$ in Eq. 4.5 contains strength ϵ of the delay signal, delay time T_0 , and time $\theta = t\gamma_r$ (t being the real time) rescaled to collision relaxation rate $\gamma_r = 7 \times 10^5$ s⁻¹.

Martínez-Zérega et al. [70] have found that feedback with certain delay times T_0 converts chaos in a CO₂ laser (Fig. 4.15 (left)) into coexisting periodic orbits (Fig. 4.15 (right)), whose periodicity is a linear function of the delay time T_0 . As seen from the figure, bistability exists in the range of delay times $T_0 \in (110, 170)$ (in normalized units of γ_r). Note, that the periods of the two coexisting orbits are close to T_0 and $T_0/2$.

4.4 Multistability in Semiconductor Lasers

Semiconductor lasers, due to their relatively small size, low cost, and ease of operation, have a wide range of applications, from optical communication to high-speed modulation and detection. They are essentially stable devices which belong to class-B lasers and described by a set of differential equations for the complex field and the carrier density. However, it is only true for narrow-stripe edge-emitting lasers which can easily be destabilized by external perturbations, such as optical self-feedback or optical injection. Similar to other class-B lasers, semiconductor lasers can also exhibit the coexistence of multiple attractors, so that their dynamics strongly depends on initial conditions. This was demonstrated in many theoretical and experimental studies [9, 71–73].

It should be noted that some semiconductor lasers have an additional degree of freedom in the device structure. For example, vertical-cavity surface-emitting semiconductor lasers (VCSEL) have a disk structure of the laser cavity larger than the optical wavelength, and therefore exhibit instabilities even in their solitary oscillations. The spatial dependence of the device structure is an additional degree of freedom beside of the structure of narrow-stripe edge-emitting semiconductor lasers. This additional degree of freedom makes possible a special type of multistability called *polarization multistability* (see Sect. 4.2.3).

Below, we will present two examples which demonstrate how the coexistence of fixed points and periodic orbits arise in semiconductor lasers. In the first example, we will describe a semiconductor laser with an external cavity, and in the second example we will consider a semiconductor laser with modulated pump current.

4.4.1 Semiconductor Laser with Delayed Feedback

In Sect. 2.2.5 we have shown that feedback can induce multistability in a dynamical system. Here, we will show that with appropriate optical feedback and certain parameters a semiconductor laser exhibits the coexistence of several fixed points. Such a behavior was first demonstrated by Masoller and Abraham [71] by numerical simulations of the Lang–Kobayashi model [74] for a single-mode semiconductor laser with weak optical feedback, given by

$$\begin{aligned}\dot{E} &= k(1 + i\alpha) \left(\frac{N}{1 + \epsilon|E|^2} - 1 \right) E + \gamma E(t - \tau) e^{-i\omega_0\tau}, \\ \dot{N} &= \frac{1}{\tau_n} \left(j - N - \frac{N|E|^2}{1 + \epsilon|E|^2} \right),\end{aligned}\tag{4.6}$$

where E is the varying complex field, N is the normalized carrier density, k is the cavity losses, α is the linewidth enhancement factor, ϵ is the gain saturation coefficient, γ is the feedback light intensity, ω_0 is the optical frequency without feedback, j is the normalized injection current, τ is the round-trip time in the external cavity, and τ_n is the carrier lifetime.

While without feedback ($\gamma = 0$) the laser operates in a monostable continuous wave regime, a weak feedback induces an additional fixed point attractor, and as the feedback strength is increased, each of the coexisting states undergoes a quasiperiodic route to chaos. Two frequencies appear on this route. One of them is the relaxation oscillation frequency of the laser itself, and another one is the frequency of the external cavity (around $1/\tau$). As γ is further increased, several chaotic attractors appear for the same parameter values.

The coexistence of five chaotic attractors is shown in Fig. 4.16a in the $(\Delta\phi, |E|^2)$ plane, where $\Delta\phi = \phi(t) - \phi(t - \tau)$. The time series of variables $\Delta\phi(t)$ and $|E(t)|^2$ in one of the coexisting chaotic regimes are illustrated in Fig. 4.16b,c.

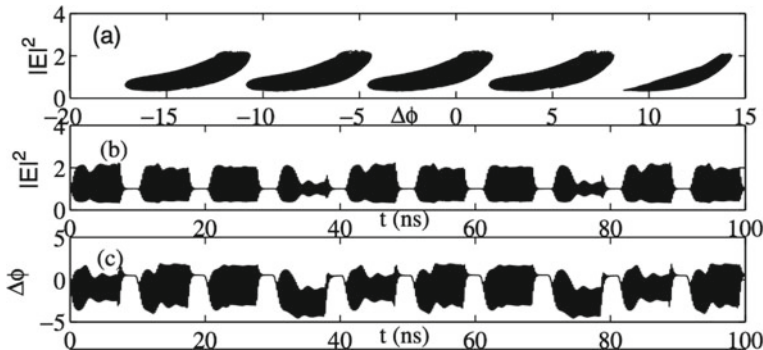


Fig. 4.16 **a** Five chaotic attractors in a semiconductor laser with delayed feedback in the $(\Delta\phi, |E|^2)$ space. **b,c** Time series of variables $\Delta\phi(t)$ and $|E(t)|^2$ in the middle chaotic attractor in **(a)**. Numerical simulations were performed using Eq. 4.6 with $k = 500 \text{ ns}^{-1}$, $\epsilon = 0.003$, $\tau_n = 1 \text{ ns}$, $\alpha = 3$, $j = 2$, $\omega_0\tau = 6 \text{ rad}$, $\gamma = 2 \text{ ns}^{-1}$, and $\tau = 10 \text{ ns}$. Reprinted figure with permission from [75] ©2002 by the American Physical Society

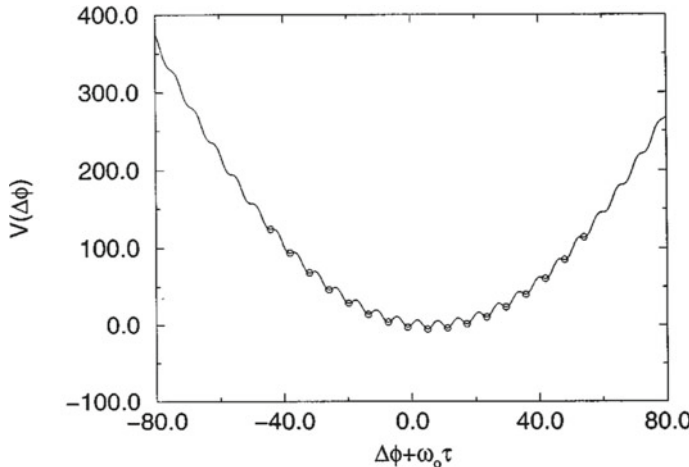


Fig. 4.17 Potential given by Eq. 4.7 of a semiconductor laser with external cavity $\gamma = 1.2 \times 10^9 \text{ s}^{-1}$, $\tau = 10 \text{ ns}$, $\alpha = 4.4$, and $\omega_0\tau = 6$. The circles indicate fixed point positions. Reprinted figure with permission from [71] ©1998 by the American Physical Society

Dynamics of the semiconductor laser with external cavity is governed by the potential given by

$$V(\Delta\phi) = \Delta^2\phi/2\tau - \gamma\sqrt{1+\alpha^2}\cos(\Delta\phi + \omega_0\tau + \arctan\alpha) \quad (4.7)$$

and depicted in Fig. 4.17. For the selected parameter values the potential displays 17 coexisting fixed points.

4.4.2 Directly Modulated Semiconductor Laser

A unique feature of semiconductor lasers is that, unlike other externally modulated lasers, a laser diode can be directly modulated by changing the injection current. This is especially important in view of the possibility of monolithic laser integration and modulation of electronic circuits. High-speed direct modulation in these lasers opens up great opportunities for the development of high-capacity information transfer and ultrafast optical processing systems.

It is now widely accepted that a single-mode semiconductor laser can evolve to chaos through a cascade of period-doubling bifurcations under the action of a modulation current. However, systematic experimental studies, in particular, long time series analysis, are not available because the time scale of the laser pulses is in a picosecond range. Much progress in understanding the origin of bifurcations was achieved through numerical simulations with simple models.

The dynamics of a single-mode semiconductor laser with direct pump current modulation [76] can be described by two evolution equations, one for the photon density of the electric field inside the laser cavity (S) and the other for the carrier density (N) or the number of electron-hole pairs) [77], as follows

$$\begin{aligned}\dot{S} &= G_N(N - N_0)(1 - \epsilon S)S - \frac{S}{\tau_p} + \frac{BN}{\tau_c}, \\ \dot{N} &= j - \frac{N}{\tau_c} - G_N(N - N_0)(1 - \epsilon S)S,\end{aligned}\tag{4.8}$$

where τ_c and τ_p are the carrier and photon lifetimes, respectively, B is the spontaneous emission factor, G_N is the modal gain coefficient, N_0 is the carrier density required for the transparency of the active region, ϵ is the gain saturation coefficient, and j is the injection current density.

Under periodic modulation of the injection current

$$j = j_b + j_m \sin(2\pi\nu_m t),\tag{4.9}$$

with certain parameters of bias current density j_b , driving current density j_m , and driving frequency ν_m , the laser exhibits the coexistence of three attractors: period 1 (P1), period 3 (P3), and period 4 (P4).

The time series of three coexisting periodic orbits are presented in Fig. 4.18 for the following set of the system parameters: $\tau_p = 6 \times 10^{-12}$ s, $\tau_s = 10^{-9}$ s, $N_0 = 10^{24}$ m⁻³, $B = 10^{-5}$, $G_N = 10^{-12}$ m³s⁻¹, $\epsilon = 8 \times 10^{-24}$ m³, $x_m = j_m/j_b = 0.6$, and $\nu_m = 2.9$ GHz.

Figure 4.19 shows the bifurcation diagrams of the peak photon density with respect to the driving frequency (left panel) and amplitude (right panel) calculated for randomly chosen initial conditions. One can see the coexistence of three periodic orbits (P1, P3, and P4) in a certain range of the control parameters.

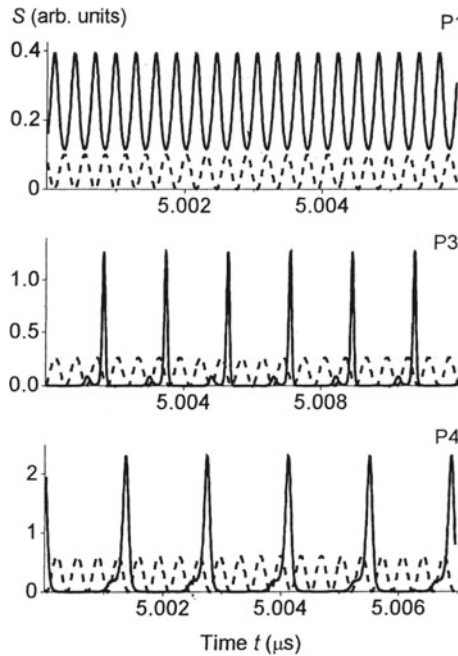


Fig. 4.18 Coexisting period-1 (P1), period-3 (P3), and period-4 (P4) regimes in a semiconductor laser model (Eq. 4.8) with direct current modulation (Eq. 4.9). The dashed lines show the driving signal

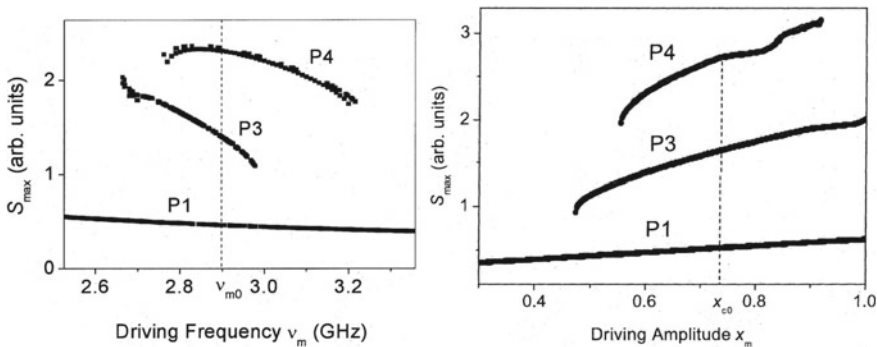


Fig. 4.19 Bifurcation diagrams of peak photon density S_{max} as a function of (left) driving frequency ν_m for the fixed driving amplitude $x_m = x_{c0} = 0.6$ and (right) driving amplitude x_m for the fixed driving frequency $\nu_m = \nu_{m0} = 2.9$ GHz

Knowing how multistability arises, one can begin to manage it. In particular, coexisting attractors can be selectively destroyed by adding harmonic parametric modulation with a frequency an order of magnitude lower than the excitation frequency [76]. Such control provides more flexibility in manipulating the laser dynamics to select the desired behavior, and this technique works well even when both driving and control are applied to the same laser parameter. Optimal control conditions are achieved when the control frequency is close to the relaxation oscillation frequency of the attractor we want to annihilate.

4.5 Multistability in Fiber Lasers

Multistability in fiber lasers has perhaps been studied more extensively than in other types of lasers, particularly, in an erbium-doped fiber laser (EDFL). The interest in studying the dynamics of these lasers is due to their applications in communications, reflectometry, sensing, and medicine [78]. From the viewpoint of nonlinear dynamics, fiber lasers doped with rare earth elements belong to class-B lasers. These are nonautonomous systems in which polarization is adiabatically eliminated and the dynamics can be described by two rate equations for field and population inversion. However, under loss or pump modulation these lasers can exhibit complex dynamical behavior including the coexistence of various attractors.

The dynamics of a single-mode EDFL is described by the following rate equation model [79]

$$\begin{aligned}\dot{P} &= \frac{2L}{T_r} P \{ \tau_w \alpha_0 [N(\xi_1 - \xi_2) - 1] - \alpha_{th} \} + P_{sp}, \\ \dot{N} &= -\frac{\sigma_{12} r_w P}{\pi r_0^2} (N \xi_1 - 1) - \frac{1}{\tau} + P_{pump},\end{aligned}\tag{4.10}$$

where P is the intracavity laser power, $N = (1/n_0 L) \int_0^L N_2(z) dz$ is the averaged (over the active fiber length L) population of the upper lasing level, N_2 is the upper level population at the z coordinate, n_0 is the refractive index of a “cold” erbium-doped fiber core, ξ_1 and ξ_2 are parameters defined by the relationship between cross-section of ground state absorption σ_{12} , return stimulated transition σ_{21} , and excited state absorption σ_{23} , T_r is the photon intracavity round-trip time, α_0 is the small-signal absorption of the erbium fiber at the laser wavelength, α_{th} is the intracavity loss on the threshold, τ is the lifetime of erbium ions in the excited state, r_0 is the fiber core radius, w_0 is the radius of the fundamental fiber mode, and r_w is the factor addressing a match between the laser fundamental mode and erbium-doped core volumes inside the active fiber. The spontaneous emission into the fundamental laser mode P_{sp} and pump power P_{pump} are given as

$$\begin{aligned} P_{sp} &= N \frac{10^{-3}}{\tau T_r} \left(\frac{\lambda_g}{w_0} \right)^2 \frac{r_0^2 \alpha_0 L}{4\pi^2 \sigma_{12}}, \\ P_{pump} &= P_p \frac{1 - \exp[-\alpha_0 \beta L(1 - N)]}{N_0 \pi r_0^2 L}, \end{aligned} \quad (4.11)$$

where λ_g is the laser wavelength, P_p is the pump power at the fiber entrance and β is a dimensionless coefficient. The parameters are chosen so to correspond to real experimental conditions: $L = 0.88$ m, $T_r = 8.7$ ns, $r_w = 0.308$, $\alpha_0 = 40$ m $^{-1}$, $\xi_1 = 2$, $\xi_2 = 0.4$, $\alpha_{th} = 3.92 \times 10^{-2}$, $\sigma_{12} = 2.3 \times 10^{-17}$ m 2 , $r_0 = 2.7 \times 10^{-6}$ m, $\tau = 10^{-2}$ s, $\lambda_g = 1.65 \times 10^{-6}$ m, $w_0 = 3.5 \times 10^{-6}$ m, $\beta = 0.5$, and $N_0 = 5.4 \times 10^{25}$ m $^{-3}$.

For simplicity, the system given by Eq. 4.10 can be transformed into the simple normalized form

$$\begin{aligned} \frac{dx}{d\theta} &= xy - a_1 x + a_2 y + a_3, \\ \frac{dy}{d\theta} &= c - xy - b_1 y - b_2 + P_0(1 - b_3 e^y), \end{aligned} \quad (4.12)$$

where x and y are the normalized laser power density and inversion population, respectively, θ , a_1 , and P_0 are proportional to time, cavity loss, and pump power.

Below, we will describe the EDFL dynamics under periodic modulation of the cavity losses L and pump parameter P .

4.5.1 Loss-Modulated Fiber Laser

We consider first the EDFL in Eq. 4.10 under cavity loss modulation given by

$$L = L_0 [1 + L_m \sin(2\pi f t)], \quad (4.13)$$

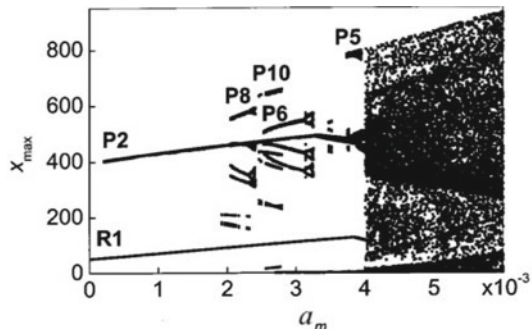
where L_m and f are the modulation depth and frequency, respectively, and L_0 is the constant loss without modulation (at $L_m = 0$). In the normalized form, Eq. 4.13 is equivalent to the modulation of the parameter a_1 in the normalized Eq. 4.12 as follows

$$a_1 = a_0 + a_m \sin(2\pi\nu\theta), \quad (4.14)$$

where a_0 , a_m , and ν are proportional to the constant cavity loss, modulation depth and frequency, respectively.

The loss-modulated EDFL exhibits the coexistence of periodic orbits for a certain parameter range, as shown in the bifurcation diagram in Fig. 4.20 obtained using random initial conditions. When the modulation amplitude is small, the regular period-1 attractor (R1) coexists with the period-2 attractor (P2) which is born in a saddle-node bifurcation. An increase in the modulation depth enriches the laser

Fig. 4.20 Bifurcation diagram of local maxima of normalized photon density versus loss-modulation depth a_m in EDFL with frequency $\nu = 2.2 \times 10^3$. The letters and numbers indicate orbit periods corresponding to different attractors obtained using random initial conditions



dynamics by inducing various bifurcations (periods 8, 10, 6, etc.) which give rise to other periodic attractors that appear in corresponding primary saddle-node bifurcations. All these periodic orbits undergo a cascades of period-doubling bifurcations and finally are simultaneously destroyed with their basins of attraction in boundary crisis.¹

A similar behavior was observed in a driven CO₂ laser [81]. Regular saddles emanating from primary saddle-node bifurcations play a significant role in the emergence of this kind of crisis.

Another type of crisis arises at $a_m \approx 4 \times 10^{-3}$, where a sudden expansion of the chaotic attractor occurs between all branches developing from the primary saddle-node bifurcation giving rise to a period 5 (P5) attractor. Then, the trajectory visits phase space regions which were previously outside the attractor. Such a sudden increase of the chaotic attractor in size occurs when the periodic orbit with which the chaotic attractor collides, is inside its basin, and called *interior crisis* [82]. This kind of crisis was also observed in a loss-modulated CO₂ laser (see Fig. 4.11).

An increase in the modulation amplitude a_m enriches the dynamics of the loss-modulated EDFL, as seen from Fig. 4.21. When a_m is very small, the laser behaves as a harmonic oscillator and responds linearly to external modulation with a resonance at the relaxation oscillation frequency ν_r (Fig. 4.21a). For larger modulation amplitudes, nonlinearity becomes relevant that gives rise to bistability which can be revealed through a hysteresis. R1 and P1 branches of attractors are born and dead in saddle-node bifurcations S_1 and S_2 , respectively, and coexist in the range of $\nu \in (1.1, 1.5) \times 10^3$, as well as P1 and P2 branches coexist in the range of $\nu \in (2.50, 3.05) \times 10^3$. The latter range is located around the second harmonic of ν_r . Due to nonlinearity, the maxima of two stable period-1 branches (P1 and R1) are not located anymore at the relaxation oscillation frequency ν_r , but shifted towards smaller frequencies $\nu(S_1) \approx 1.1 \times 10^3$ and $\nu(S_2) \approx 1.5 \times 10^3$. These stable branches are connected by the unstable period-1 branch (shown by crosses). Such saddle-node bifurcations are interesting, but difficult to find, since the maximum response in both branches

¹ A crisis is a sudden change in the attractor behavior due to a collision of an unstable periodic orbit with a chaotic attractor. When the orbit is just at the boundary of the basin of attraction of the chaotic attractor, the crisis is called *boundary crisis* [80].

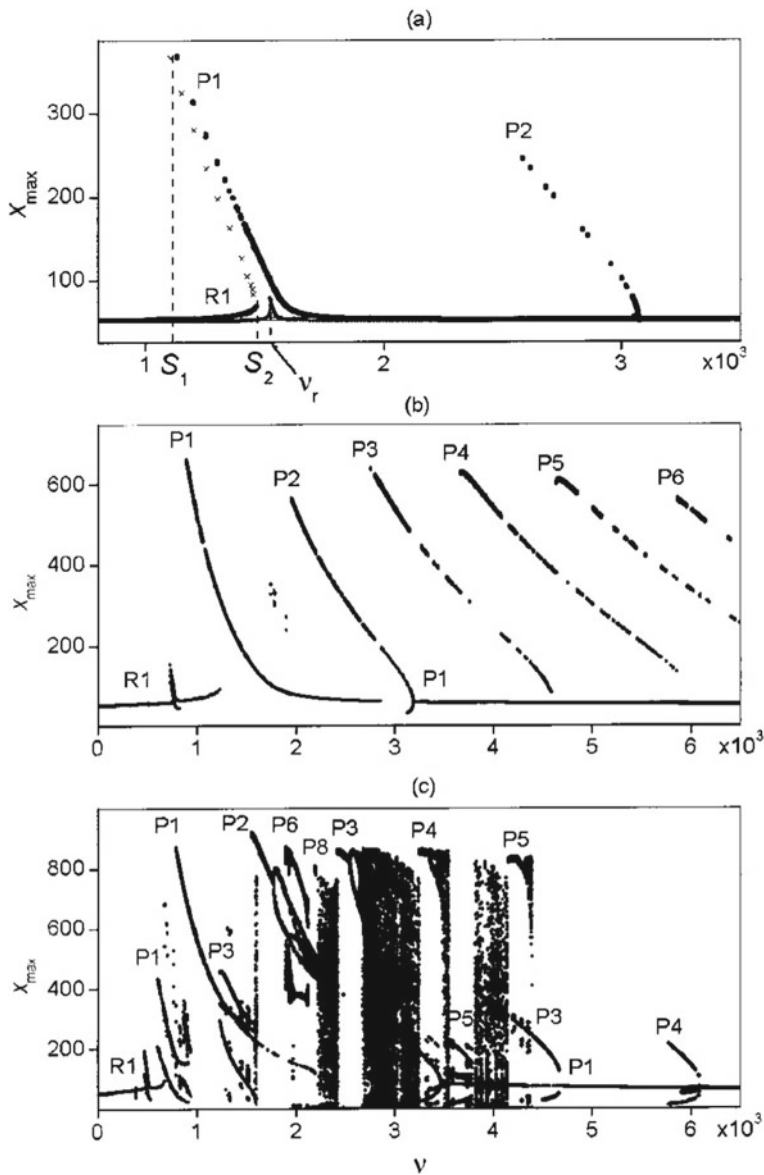


Fig. 4.21 Bifurcation diagrams of EDFL peak density versus modulation frequency at different modulation depths: **a** $a_m = 10^{-5}, 10^{-4}$, **b** 10^{-3} , and **c** 4×10^{-3} . The crosses mark unstable period-1 solutions, S_1 and S_2 indicate supercritical and subcritical period-1 saddle-node bifurcations, and ν_r is the relaxation oscillation frequency. Reprinted with permission from [11] ©2003 The Optical Society

appears just before the solutions become unstable. Similar hysteresis behavior was also observed in pump-modulated [72] and loss-modulated semiconductor lasers (see Sect. 4.4), as well as in a pump-modulated ring EDFL [83].

At high modulation amplitudes (see Fig. 4.21b, c), the laser dynamics becomes more complicated and multistability arises. In addition, primary attractors (P_2 , P_3 , P_4 , P_5) undergo period-doubling bifurcations, as the control parameter ν is increased, followed by the Feigenbaum transition to chaos and ending with crisis.

4.5.2 Pump-Modulated Fiber Laser

Next, we will show how multistability arises in an EDFL under diode pumped current modulation. It should be noted that the experimental implementation of pump modulation is much easier than that of the loss modulation because the former can be achieved by the direct modulation of a diode pump laser current as follows

$$P_p = p [1 - m \sin(2\pi f_d t)], \quad (4.15)$$

where m and f_d are the modulation depth and frequency, respectively, and p is the constant pump power without modulation.

The EDFL under pump modulation displays very rich dynamics. The coexistence of up to four periodic orbits (P_1 , P_3 , P_4 , P_5) is observed, as seen in the bifurcation diagrams of the peak laser power with respect to the modulation frequency and amplitude in Fig. 4.22. Similarly to the loss modulation case (see Sect. 4.5.1), stable

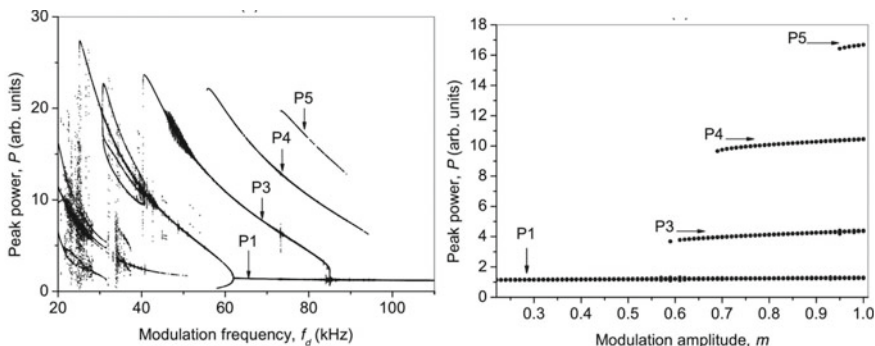


Fig. 4.22 Bifurcation diagrams of EDFL peak power versus (left) driving frequency f_d for $m = 1$ and (right) driving amplitude m with frequency $f_d = 80$ kHz. The diagrams are calculated by random varying initial conditions and using the continuation method. The arrows indicate branches of the coexisting P_1 , P_3 , P_4 , and P_5 orbits. Reprinted figure with permission from [84] ©2012 by the American Physical Society

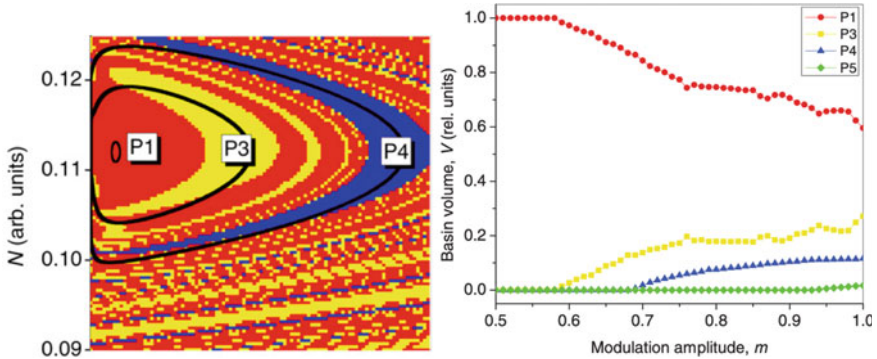


Fig. 4.23 (Left) Basins of attraction of four coexisting periodic orbits in the EDFL under pump modulation with $f_d = 70.2$ kHz and $m = 0.8$. P1, P3, and P4 are shown, respectively, by red, yellow, and blue dots. The corresponding periodic orbits are marked by black lines. (Right) Relative basin volumes of coexisting periodic orbits versus driving amplitude with frequency $f_d = 80$ kHz

periodic orbits on subharmonic frequencies (P3, P4, and P5) are born in saddle-node bifurcations when the control parameter is increased (compare with Figs. 4.20 and 4.21).

In the left panel in Fig. 4.23 we plot the basins of attraction of the coexisting stable periodic orbits. One can see that the basins have Wada properties (see Sect. 1.2.4). The basin volumes shown in the right panel in Fig. 4.23 depend on the modulation amplitude. Note that for low modulation amplitudes ($m < 0.57$) the laser is monostable with a single P1. However, as m is increased, the subharmonic attractors of P3 and P4 emerge, and their basins of attraction enlarge, while the P1 basin volume decreases. Finally, at $m = 0.93$ the P5 attractor arises, so that five attractors coexist.

Laser experiments confirm the coexistence of various attractors in the EDFL. The experimentally obtained bifurcation diagrams with respect to the modulation frequency and amplitude are presented in Fig. 4.24. Due to experimental noise, the attractor branches are broadened.

The comparison of Figs. 4.22 and 4.24 displays a very good agreement between the numerical and experimental results that indicates the adequacy of the used theoretical model in Eq. 4.10. In addition, the model demonstrates a fundamental understanding of the laser dynamics and gives us an idea of the origin of non-trivial experimentally observable effects such as extreme events (see Sect. 5.5.3) and noise-induced preference for certain states (see Sect. 5.5). Due to the uncontrollability of internal laser noise, extreme pulses in the experiment appear at lower amplitudes of external noise than in numerical simulations.

Finally, the preference for certain states in multistate intermittency depends non-monotonically on the noise amplitude. This means that there is a certain level of noise for which a certain state is more likely than for other noise amplitudes. This result agrees with the previously observed effect of nonmonotonic preference of attractors observed in the multistable Hénon map [85].

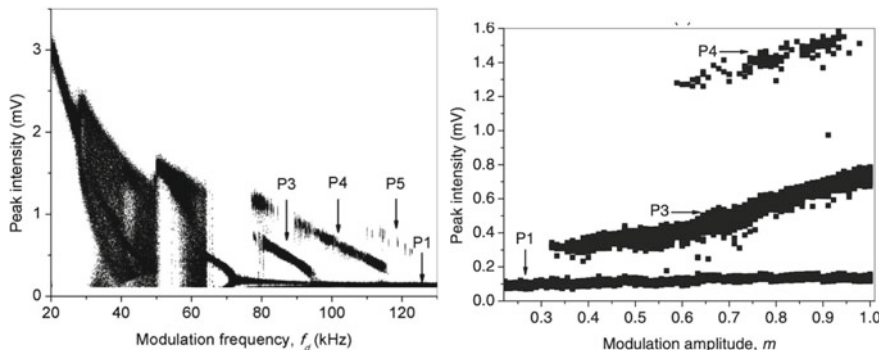


Fig. 4.24 Experimental bifurcation diagrams of laser peak intensity versus (left) driving frequency for $m = 0.8$ and (right) driving amplitude for $f_d = 90$ kHz. The diagrams are calculated by switching on and off the signal generator. The arrows indicate the branches of the coexisting P1, P3, P4, and P5 periodic orbits. Reprinted figure with permission from [84] ©2012 by the American Physical Society

References

1. Szöke A, Daneu V, Goldhar S, Kurnit NA (1969) Bistable optical element and its applications. *Appl Phys Lett* 15(11):376–379
2. Gibbs HM, Mo Call SL, Venkatesan TNC (1976) Differential gain and bistability using a sodium-filled Fabry-Perot interferometry. *Phys Rev Lett* 36(11):1135–1138
3. Grazyuk AZ, Oraevsky AN (1964) Transient processes in a molecular generator. *Radiotekhnika i Elektronika* 9(3):524–532
4. Arechi FT, Meucci R, Puccioni G, Tredicce J (1982) Experimental evidence of subharmonic bifurcations, multistability, and turbulence in a Q-switched gas laser. *Phys Rev Lett* 49:1217–1220
5. Weiss CO, Godone A, Olafsson A (1983) Routes to chaotic emission in a cw He-Ne laser. *Phys Rev A* 28(2):892–895
6. Brun E, Derighetti B, Meier D, Holzner R, Ravani M (1985) Observation of order and chaos in a nuclear spin-flip laser. *J Opt Soc Am B* 2:156–167
7. Baer T (1986) Large-amplitude fluctuations due to longitudinal mode coupling in diode-laser pumped intracavity-doubled Nd:YAG lasers. *J Opt Soc Am B* 3:1175–1180
8. de Jagher PC, van der Graaf WA, Lenstra D (1996) Relaxation-oscillation phenomena in an injection-locked semiconductor laser. *Quant Semiclass Opt* 8:805–822
9. Gavrielides A, Kovanis V, Varangis PM, Erneux T, Lythe G (1997) Coexisting periodic attractors in injection-locked diode lasers. *Quant Semiclass Opt* 9:785–796
10. Pisarchik AN, Barmenkov YO, Kir'yanov AV (2003) Experimental characterization of bifurcation structure in an erbium-doped fiber laser with pump modulation. *IEEE J Quantum Electron* 39:1567–1571
11. Saucedo-Solorio JM, Pisarchik AN, Kir'yanov AV, Aboites V (2003) Generalized multistability in a fiber laser with modulated losses. *J Opt Soc Am B* 20:490–496
12. Pisarchik AN, Feudel U (2014) Control of multistability. *Phys Rep* 540:167–218
13. Brambilla M, Lugiato LA, Penna V, Prati F, Tamm C, Weiss C (1991) Transverse laser patterns. II. Variational principle for pattern selection, spatial multistability and laser hydrodynamics. *Phys Rev A* 43:5114–5120
14. Pampaloni E, Residor S, Soria S, Arechi F (1997) Phase-locking in nonlinear optical patterns. *Phys Rev Lett* 78:1042–1045

15. Brambilla M, Lugiato LA, Pinna M, Prati F, Pagani P, Vanotti V, Li M, Weiss C (1992) The laser as nonlinear element for an optical associative memory. *Opt Commun* 92:145–164
16. Arechi FT, Lippi GL, Puccioni GP, Tredicce JR (1984) Deterministic chaos in laser with injected signal. *Opt Commun* 51(5):308–314
17. Abraham E, Smith SD (1982) Optical bistability and related devices. *Rep Prog Phys* 45(8):815–885
18. Lugiato LA (1983) Optical bistability. *Contemp Phys* 24:333–371
19. Gibbs HM (1985) Optical bistability: controlling light with light. Academic
20. Born M, Wolf E (1999) Principles of optics, 7th edn. Cambridge University Press, Cambridge
21. Miller DAB, Smith SD, Johnston AM (1979) Optical bistability and signal amplification in a semiconductor crystal: applications of new low-power nonlinear effects in InSb. *Appl Phys Lett* 35:658–660
22. Lee WM, El-Ganainy R, Christodoulides DN, Dholakia K, Wright EM (2009) Nonlinear optical response of colloidal suspensions. *Opt Exp* 17:10277
23. Pobegalov G, Agruzov P, Illichev I, Shamray A (2014) Low-power optical bistability and hysteresis in the laser system with absorbing nanosuspension. *Opt Lett* 39(9):2819–2822
24. Psaltis D, Quake SR, Yang C (2006) Developing optofluidic technology through the fusion of microfluidics and optics. *Nature* 442:381–386
25. Monat C, Domachuk P, Eggleton J (2007) Integrated optofluidics: a new river of light. *Nat Photonics* 1:106–114
26. Tamm C, Weiss CO (1990) Bistability and optical switching of spatial patterns in a laser. *J Opt Soc Am B* 7(6):1034–1038
27. Crabb R, Mackey MC, Rey AD (1996) Propagating fronts, chaos and multistability in a cell replication model. *Chaos* 6(3):477–492
28. Bachir M, Borckmans P, Dewel G (1999) Spatial multistability and nonvariational effects. *Phys Rev E* 59(6):R6223–R6226
29. Wang YC, Ferguson E (2005) Spatial bistability of Dpp-receptor interactions during *Drosophila* dorsal-ventral patterning. *Nature* 434(6):229–234
30. Boissonade J, De Kepper P, Gauffre F, Szalai I (2006) Spatial bistability: a source of complex dynamics. From spatiotemporal reaction-diffusion patterns to chemomechanical structures. *Chaos* 16:037110
31. Szalaib I, De Kepper P (2006) Spatial bistability, oscillations and excitability in the Landolt reaction. *Phys Chem Chem Phys* 8:1105–1110
32. Kéfi S, Eppinga MB, de Ruiter PC, Rietkerk M (2010) Bistability and regular spatial patterns in arid ecosystems. *Theor Ecol* 3:257–269
33. Bastiaansen R, Jaibi O, Deblauwe V, Eppinga MB, Siteur K, Siero E, Mermoz S, Bouvet A, Doelman A, Rietkerk M (2018) Multistability of model and real dryland ecosystems through spatial self-organization. *Proc Natl Acad Sci USA* 115:44
34. Andrade-Restrepo M, Champagnat N, Ferrière R (2019) Spatial eco-evolutionary dynamics along environmental gradients: multi-stability and cluster dynamics. *Ecol Lett* 22(5):767–777
35. Tan EZ, Sigurdsson H, Liew TCH (2018) Parity bifurcations in trapped multistable phase locked exciton-polariton condensates. *Phys Rev B* 97:075305
36. Karuseichik SA, Chizhevsky VN, Zhang WL (2020) Experimental study of multistability in a mulimode vertical-cavity laser. *J Appl Spectrosc* 87(1):121–127
37. Zhao X, Xu B, Kong X, Zhong D, Fang M, Zhao D (2020) Tunable optical bistability, tristability and multistability in arrays of graphene. *Appl Sci* 10(17):5766
38. Larger L, Penkovsky B, Maistrenko Y (2015) Laser chimeras as a paradigm for multistable patterns in complex systems. *Nat Commun* 6:7752
39. Ujjwal SR, Punetha N, Prasad A, Ramaswamy R (2017) Emergence of chimeras through induced multistability. *Phys Rev E* 95(3):032203
40. Lugiato LA, Milani H (1983) Disappearance of laser instabilities in a Gaussian cavity. *Opt Commun* 46(1):57–60
41. Chen YC, Liu JM (1985) Polarization bistability in semiconductor lasers. *Appl Phys Lett* 46(1):16–18

42. Martín-Regalado J, Balle S, San Miguel M (1997) Polarization and transverse-mode dynamics of gain-guided vertical-cavity surface-emitting lasers. *Opt Lett* 22(7):460–462
43. Liu A, Wolf P, Lott JA, Bimberg D (2019) Vertical-cavity surface-emitting lasers for data communication and sensing. *Photonics Res* 7(2):121–136
44. Barbay S, Giacomelli G, Lepri S, Marin F, Rabbiosi I, Zavatta A (2003) Experimental investigation of stochastic processes in vertical-cavity lasers. *Physica A* 327(6):120–123
45. Chizhevsky VN (2014) Experimental evidence of vibrational resonance in a multistable system. *Phys Rev E* 89(6):062914
46. Chizhevsky VN, Kovalenko SA (2018) Experimental evidence of spatial multistability in a multimode VCSEL. In: International conference laser optics (ICLO), St. Petersburg, p 151
47. Yu SF (1997) Analysis of polarization bistability in vertical cavity surface emitting semiconductor lasers. *J Light Technol* 15(6):1032–1041
48. Lloyd AD (1985) Polarisation optical bistability in nematic liquid crystals. *Opt Commun* 64(3):302–306
49. Petykiewicz J, Strojewski D (1990) Optical dispersive bistability in media with forced gyrotropy. *Opt Quant Electron* 22(3):131–142
50. Pura B, Wierzbicki M, Petykiewicz J, Ratusznik G (2001) Polarization bistability in a smectic-A liquid crystal. *Opt Appl* 31(3):619–624
51. Gauthier DJ, Malcuit MS, Gaeta AL, Boyd RW (1990) Polarization bistability of counterpropagating laser beams. *Phys Rev Lett* 64(15):1721–1724
52. Tabarin VA, Habibullin RS (2001) The polarization bistability in the $\lambda = 3.39 \mu\text{m}$ He-Ne laser with saturating absorbent. In: Proceedings of the 2nd annual Siberian Russian student workshop on electron devices and materials
53. Dangoisse D, Glorieux P, Hennequin D (1987) Chaos in a CO₂ laser with modulated parameter: Experiments and numerical simulations. *Phys Rev A* 36(10):4775–4791
54. Hohl A, Van der Linden HJC, Roy R (1996) Scaling laws for dynamical hysteresis in a multidimensional laser system. *Phys Rev Lett* 74:2220–2223
55. Wieczorek SM, Krauskopf B, Lenstra D (2002) Multipulse excitability in a semiconductor laser with optical injection. *Phys Rev Lett* 88:063901
56. Junges L, Gallas JAC (2016) Impact of delayed feedback of arbitrary duration in self-pulsations of a CO₂ laser. *J Opt Soc Am B* 33:373–381
57. Pisarchik AN, Kuntsevich BF (2001) Nonlinear dynamics of a CO₂ laser with current modulation and cavity detuning. *J Opt B Quantum Semiclass Opt* 3:363–371
58. Weiss CO, Vilaseca R (1991) Dynamics of lasers. VCH, Weihaim
59. Chizhevsky VN, Corbalán R, R, Pisarchik AN, (1997) Attractor splitting induced by resonant perturbations. *Phys Rev E* 56(2):1580–1584
60. Gallas JAC (2016) Spiking systematics in some CO₂ laser models. In: Arimondo E, C Lin CC, Yelin SF (eds) Advances in atomic, molecular, and optical physics, vol 65, Academic, Burlington, pp 127–191
61. Pisarchik AN, Corbalán R (1998) Stochastic resonance in a chaotic laser. *Phys Rev E* 58(3):R2697–R2700
62. Chizhevsky VN, Turoverts SI (1994) Periodically loss-modulated CO₂ laser as an optical amplitude and phase multitrigger. *Phys Rev A* 50(2):1840–1843
63. Kuntsevich BF, Pisarchik AN, Chizhevsky VN, Churakov VV (1983) Amplitude modulation of the radiation of a CO₂ laser by optically controlled absorption in semiconductors. *J Appl Spectr* 38(2):107–112, translated from *Zhurnal Prikladnoi Spektroskopii* 38 (1983) 126–133
64. Chizhevsky VN (2000) Coexisting attractors in a CO₂ laser with modulated losses. *J Opt B: Quantum Semiclass Opt* 2:711–717
65. Chizhevsky VN, Glorieux P (1995) Targeting unstable periodic orbits. *Phys Rev E* 51(4):R2701–R2704
66. Chizhevsky VN (2001) Multistability in dynamical systems induced by weak periodic perturbations. *Phys Rev E* 64:036223
67. Arecchi FT, Gadomski W, Meucci R (1986) Generation of chaotic dynamics by feedback on a laser. *Phys Rev A* 34:1617–1620

68. Ciofini M, Labate A, Meucci R, Galanti M (1999) Stabilization of unstable fixed points in the dynamics of a laser with feedback. *Phys Rev E* 60:398–402
69. Pisarchik AN, Meucci R, Arechi FT (2001) Theoretical and experimental study of discrete behavior of Shilnikov chaos in a CO₂ laser. *Eur Phys J D* 13:385–391
70. Martínez-Zérega BE, Pisarchik AN, Tsimring L (2003) Using periodic modulation to control coexisting attractors induced by delayed feedback. *Phys Lett A* 318:102–111
71. Masoller C, Abraham NB (1998) Stability and dynamical properties of the coexisting attractors of an external-cavity semiconductor laser. *Phys Rev A* 57(2):1313–1322
72. Mayol C, Turovets SI, Toral R, Mirasso CR, Pesquera L (2001) Main resonances in directly modulated semiconductor lasers: effect of spontaneous emission and gain saturation. *Inst Elect Eng Proc Optoelectron* 148:41–45
73. Mayol C, Toral R, Mirasso CR, Turovets SI, Pesquera L (2002) Theory of main resonances in directly modulated diode lasers. *IEEE J Quantum Electron* 38:260–268
74. Lang R, Kobayashi K (1980) External optical feedback effects on semiconductor injection laser properties. *IEEE J Quantum Electron* 16(3):347–355
75. Masoller C (2002) Noise-induced resonance in delayed feedback systems. *Phys Rev Lett* 88:034102
76. Pisarchik AN, Kuntsevich BK (2002) Control of multistability in a directly modulated diode laser. *IEEE J Quantum Electron* 38:1594–1598
77. Hori Y, Serizawa H, Sato H (1988) Chaos in a directly modulated semiconductor laser. *J Opt Soc Am B* 5:1128–1132
78. Digonnet M (ed) (1993) Rare earth doped fiber lasers and amplifiers. Marcel Dekker, New York
79. Pisarchik AN, Kir'yanov AV, Barmenkov YO, Jaimes-Reátegui R (2005) Dynamics of an erbium-doped fiber laser with pump modulation: theory and experiment. *J Opt Soc Am B* 22(10):2107–2114
80. Grebogi G, Ott E, Yorke JA (1982) Chaotic attractors in crisis. *Phys Rev Lett* 48:1507–1510
81. Schwartz IB (1988) Infinite primary saddle-node bifurcation in periodically forced systems. *Phys Lett A* 126:411–418
82. Ott E (1993) Chaos in dynamical systems. Cambridge University Press, New York
83. Luo LG, Chu PL (1998) Optical secure communications with chaotic erbium-doped fiber lasers. *J Opt Soc Am B* 15:2524–2530
84. Pisarchik AN, Jaimes-Reátegui R, Sevilla-Escoboza R, Huerta-Cuellar G (2012) Multistate intermittency and extreme pulses in a fiber laser. *Phys Rev E* 86:056219
85. Martínez-Zérega BE, Pisarchik AN (2012) Stochastic control of attractor preference in multi-stable systems. *Commun Nonlinear Sci Numer Simul* 17:4023–4028

Chapter 5

Multistate Intermittency



Abstract Irregular switches between two different dynamical regimes, when all system parameters are fixed, is known as *intermittency*. The concept of intermittency was extended to systems with coexisting states and referred to as *multistate intermittency*. Such intermittency reveals itself as alternation of equilibrium, periodic or chaotic regimes. The irregular switching between coexisting states can be caused either by random, chaotic, or periodic perturbations. In the former case, we deal with so-called *noise-induced intermittency* or *attractor hopping*. Although both names are widely used in the literature, in our opinion, the term “multistate intermittency” more accurately reflects the intermittent nature of this kind of dynamics in systems with coexisting attractors. Intermittency in a multistable system can also be caused by an external force that can be either random or periodic in a chaotic system. Since random fluctuations (or noise) are inevitable in real systems, the interaction between nonlinearity and stochasticity has attracted much attention of various researchers. It was found that adding noise to a multistable system causes many interesting effects, such as noise-induced escapes from equilibria [1, 2], stochastic resonance [3, 4], self-organization [5], multistate intermittency [6], noise-induced preference of attractors [7], extreme events [8], etc. Some of these effects are considered in this section.

5.1 Noise-Induced Escapes from Equilibria

Noise can capture a trajectory in order to leave the attractor, or form around it a “blurry” state, which is called a *stochastic attractor* [9], that is a quasi-invariant set [10]. The examples of deterministic and stochastic attractors are illustrated in Fig. 5.1.

In general, when discussing the effect of bounded noise in a dynamical system with coexisting attractors, we can distinguish three different ranges of noise intensity: low, medium, and high. At a low noise level, the phase trajectory remains practically in the vicinity of the stochastic attractor, which leads to small deviations from deterministic dynamics, the intermediate noise level leads to switching between already metastable states, which without noise were deterministic attractors. Due to the

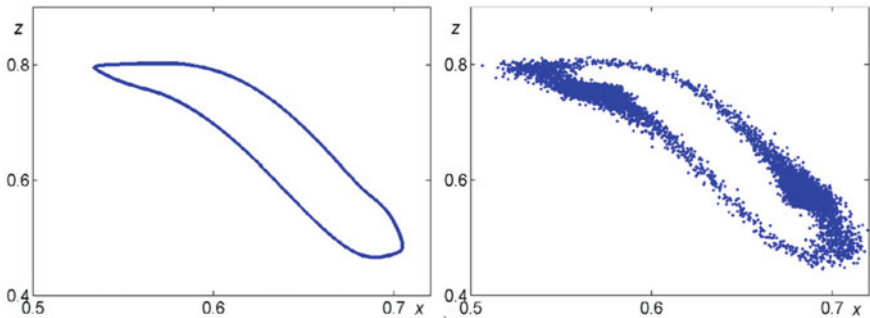


Fig. 5.1 (Left) Deterministic and (right) stochastic attractors of a ring of three unidirectionally coupled nonidentical logistic maps

nontrivial connection between the coexisting states and their basins of attraction, the final state substantially depends on the initial conditions. Under the influence of Gaussian noise, all deterministic attractors in a multistable system become metastable states.

Since any noise, regardless of its amplitude, makes the system dynamics probabilistic, it is necessary to solve stochastic equations. For each initial state, the system will follow the trajectory and reach one of the coexisting states with a certain probability depending on the noise intensity. Generally speaking, the trajectory will remain only for a certain period of time in the vicinity of the attractor, before it is ejected and approaches another one, or returns again to the same attractor. Taking into account this hopping dynamics, the important concept of an attraction domain belonging to one of the attractors now needs a different interpretation. Although the basin of attraction does not exist in a stochastic dynamical system in the strict mathematical sense, it is still possible to consider the basin of attraction in the statistical sense. As a first approach, one can search for each initial condition which of the attractors will be reached first after the start of the iteration, regardless of when it is thrown out of this attractor. As a second approach, you can always start with the same initial condition and vary the noise intensity to find the probability with which each state is reached. This probability again gives some measure of the size of the region of attraction under the influence of noise. Consequently, in both cases, the stability of attractors can only be measured statistically.

Thus, the dynamics of a noisy system is a combination of stochastic attractors and jumps between them. When the noise is weak, the lifetime of the metastable state is very long, although over time this metastable state will change to another. Therefore, if we choose the initial conditions near the deterministic attractor, a very long transient probability density distribution will be formed, which can be considered as the steady state probability density distribution for a finite observation time.

The stability of nonlinear multistable systems in the presence of noise is of great importance for a number of practical applications and is of obvious interdisciplinary interest. As we already mentioned above, noise makes a multistable system metastable, whose trajectory from time to time leaves the open neighborhood of

a metastable state. In the other words, a noise-induced escape over a barrier of a metastable potential occurs with *escape rate* W which obeys the Kramers' law

$$W = k \exp(-\Delta U/\eta^2), \quad (5.1)$$

where $\exp(-\Delta U/\eta^2)$ is the Arrhenius factor with coefficient k (η being the noise intensity) and $\eta^2 \ll \Delta U$. The inverse value of W is the *mean first passage time* given as

$$\langle \tau \rangle = k^{-1} \exp(\Delta U/\eta^2). \quad (5.2)$$

Although a noisy system does not have a potential, we can still estimate the most probable escape path with the help of the theory of *quasipotentials* or *nonequilibrium potentials* introduced by Freidlin and Wentzell [11] for continuous systems and adapted by Kifer [12] for discrete systems. Later, this approach was extended to systems with multiple quasipotentials [1, 13].

5.1.1 Multiple Quasipotential

Multiple quasipotential is introduced in a dynamical system

$$\dot{\mathbf{x}} = \mathbf{F}(\mathbf{x}) + \varepsilon, \xi(t) \quad (5.3)$$

with M coexisting metastable states $\mathbf{x}_1^*, \mathbf{x}_2^*, \dots, \mathbf{x}_M^*$ and $\xi(t)$ is noise with intensity ε . If we want to estimate the stability of each metastable state with the help of some energy function U_1, U_2, \dots, U_M , we have to evaluate a quasipotential function $U^{qp}(\mathbf{x})$ for any system state \mathbf{x} which will inform us about the probability and the direction of a transition between the metastable states. Such a quasipotential function can be obtained by integration of Eq. 5.3.

Figure 2.31 shows a hypothetic quasipotential function of a one-dimensional dynamical system with three coexisting quasistable equilibrium points (A , B , and C) and transitions between them.

In a one-dimensional dynamical system with two coexisting attractors x_A and x_B , the quasipotential in the vicinity of the potential barrier (saddle point S_1) is defined as

$$U_{AB}^{qp}(x) = \int_{x_A}^{x_B} \mathbf{F}(x) dx. \quad (5.4)$$

Correspondingly, the function \mathbf{F} is proportional to the gradient of the quasipotential:

$$\mathbf{F}(x) = -\frac{dU^{qp}}{dx} + \text{const.} \quad (5.5)$$

Now, we can derive the probability of switching from A to B through the potential barrier under the influence of noise. This probability obeys the Arrhenius equation:

$$P_{x_A \rightarrow x_B} = \exp\left(-\frac{U_{AB}^{qp}}{\varepsilon^2}\right). \quad (5.6)$$

In an N -dimensional open system with external forcing, the quasipotential function has the following property:

$$\frac{\partial U^{qp}}{\partial x_1} = -\mathbf{F}_1(\mathbf{x}), \dots, \frac{\partial U^{qp}}{\partial x_N} = -\mathbf{F}_N(\mathbf{x}). \quad (5.7)$$

Finally, the quasipotential function can be found as

$$U^{qp}(\mathbf{x}) = - \int \mathbf{F}_1(\mathbf{x}) dx_1 + \dots + \int \mathbf{F}_i(\mathbf{x}) dx_i + \dots + \int \mathbf{F}_N(\mathbf{x}) dx_N. \quad (5.8)$$

The transition from one quasistable state to another follows the *least action path* or *most probable escape path* in the case of fractal basin boundaries (see Sect. 5.1.3).

To overcome the potential barrier between A and B , the external energy must be higher than the action function

$$V_{AB} = \frac{1}{2} \min \left[\int_{t_A}^{t_B} \left(\sum_{i=1}^N \|\dot{\mathbf{x}}_i - \mathbf{F}_i(\mathbf{x})\|^2 \right) dt \right]. \quad (5.9)$$

Here, the action function V_{AB} is defined as the time integral of the square of the “remainder” of the dynamic equations (deviation from the deterministic trajectory) over the entire trajectory from A to B . On the basis of the variational principle, there is a single minimum action V_{AB} , which is an objective measure of the difficulty of the transition between states in nonequilibrium dynamical systems.

5.1.2 Escape From a Fixed Point with Smooth Basin Boundaries

Graham and Tél [1] have shown that the quasipotential $\Phi(\mathbf{x})$ (\mathbf{x} being the vector of n state variables) can be derived for a dynamical system subject to Gaussian noise ξ_i with infinitesimal intensity ($\eta \rightarrow 0$), if there exists a unique time-independent

probability distribution $P(\mathbf{x}, \eta)$ as the system approaches its steady state, i.e.

$$\Phi(\mathbf{x}) = -\lim_{\eta \rightarrow 0} [\eta \ln P(\mathbf{x}, \eta)], \quad \mathbf{x} = (x_1, x_2, \dots, x_n). \quad (5.10)$$

We suppose that the system deterministic dynamics ($\eta = 0$) is described by a drift vector $\mathbf{K}_\nu(\mathbf{x})$ ($\nu = 1, 2, \dots, n$) as

$$\dot{x}_\nu = \mathbf{K}_\nu(\mathbf{x}), \quad (5.11)$$

while the probability density obeys the Fokker–Planck equation:

$$-\frac{\partial}{\partial x_\nu} P + \frac{\eta}{2} \frac{\partial^2}{\partial x_\nu \partial x_\mu} Q_{\nu\mu}(\mathbf{x}) P = 0, \quad (5.12)$$

where $Q_{\nu\mu}(\mathbf{x}) = \sum_i g_{\nu i} g_{\mu i}$ ($\mu = 1, 2, \dots, n$) is the symmetric diffusion matrix which describes the noise properties.

We also suppose that a stochastic dynamical system is described by a set of differential equations

$$\dot{x}_\nu = \mathbf{K}_\nu(\mathbf{x}) + g_{\nu i} \xi_i(t), \quad (5.13)$$

where ξ_i is Gaussian white noise with no temporal correlations, i.e., its autocorrelation function $\langle \xi_i(t) \xi_j(0) \rangle = \sigma^2 \delta_j(t)$ (σ^2 and δ being the variance and delta function, respectively).

There are two important quantities of quasipotential: the probability density $W(\mathbf{x})$ in the steady state and the mean first passage time $\langle \tau \rangle$.

The probability density

$$W(\mathbf{x}) \sim \exp\left(-\frac{\Phi(\mathbf{x})}{\sigma^2}\right) \quad (5.14)$$

is a time-independent solution of the Fokker–Planck Eq. 5.12

$$\frac{\partial W}{\partial t} = \frac{\partial}{\partial x_\nu} \left[-\mathbf{K}_\nu(\mathbf{x}) + \frac{1}{2} \frac{\partial}{\partial x_\mu} Q_{\nu\mu}(\mathbf{x}) W \right] = 0, \quad (5.15)$$

that leads to the solutions of the Hamilton–Jacobi equation

$$\mathbf{K}_\nu(\mathbf{x}) \partial_\nu \Phi + \frac{1}{2} Q_{\nu\mu}(\mathbf{x}) \partial_\nu \phi \partial_\mu \Phi = 0. \quad (5.16)$$

The mean first passage time out of the basin of attraction B of an attractor \mathcal{A} with basin boundary ∂B is defined as

$$\langle \tau \rangle \sim \exp\left(\frac{\Delta \Phi(\mathbf{x})}{\sigma^2}\right), \quad (5.17)$$

where the minimal quasipotential difference

$$\Delta\Phi := \min\{\Phi(y) - \Phi(a) : a \in \mathcal{A}, y \in \partial\mathcal{B}\}. \quad (5.18)$$

The quasipotential for a system with two coexisting states can be derived as a combination of two local quasipotentials. However, the construction of global quasipotential for a system with multiple coexisting states is a very sophisticated task since the number of combinations grows exponentially as the number of coexisting states is increased.

Let us now illustrate the above concepts on the example of a discrete system, namely, the Ikeda map with additive Gaussian noise (δ_x and δ_y):

$$\begin{aligned} x_{n+1} &= a + b(x_n \cos \omega - y_n \sin \omega) + \delta_x, \\ y_{n+1} &= b(x_n \sin \omega + y_n \cos \omega) + \delta_y, \end{aligned} \quad (5.19)$$

where $\omega = \kappa - \eta/(1 + x_n^2 + y_n^2)$.

The map in Eq. 5.19 was introduced by Hammel et al. [14], who used the Ikeda's plane-wave model used by Ikeda [15] to describe dynamics of the light transmitted through a ring cavity containing a saturable absorber. Without noise, the system in Eq. 5.19 exhibits the coexistence of a stable equilibria and chaos for the parameter values $a = 0.85$, $b = 0.9$, $\kappa = 0.4$, and $\eta = 4.1$. The basins of attraction of these fixed points and corresponding quasipotential are present in Fig. 5.2.

To calculate the noise-induced mean first escape time from the fixed point \diamond , one has to derive quasipotentials which can be obtained using the minimization procedure of the action of escape trajectories from a Hamilton–Jacobi in Eq. 5.16. The minimal quasipotential difference is derived by Eq. 5.18 and the main first escape time by Eq. 5.17.

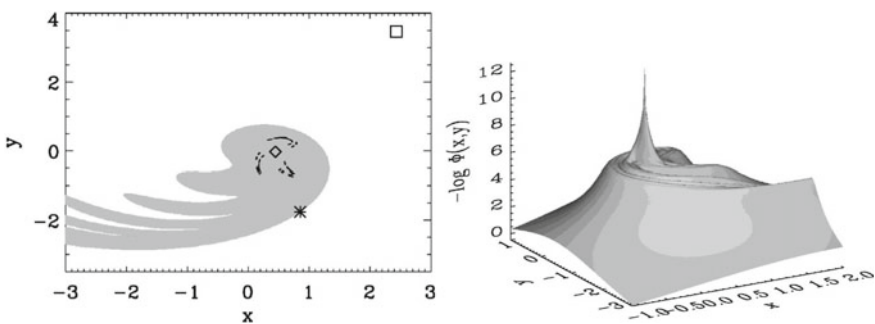


Fig. 5.2 (Left) Basins of attraction of two stable equilibria marked by \square and \diamond of the noiseless system in Eq. 5.19. The basins are shown in grey and white. Black dots and $*$ mark the chaotic saddle and the saddle point on the basin boundary, respectively. (Right) Quasipotential. The sharp peak corresponds to the fixed point \diamond . The plateau at $-\log_{10} \Phi(x, y) \approx 5$ is caused by the chaotic saddle. Reprinted figure with permission from [16] ©2003 by the American Physical Society

The minimum of quasipotential $\Phi(x, y)$ should be determined at the point where it touches the basin boundary. This means that at this point the escape energy takes the minimum value $\Delta\Phi(x, y)$, because the quasipotential at a stable solution is zero. This usually occurs at a saddle point. The escape can be incomplete so that the trajectory comes back to the fixed point from the chaotic saddle and then escape again, thus resulting in multistate intermittency.

It is important to note that the described approach based on the minimum escape energy can only be applied to systems with smooth basin boundaries. In the case of fractal boundaries, for example, in periodically driven systems, the noise-induced transitions occur easier since the effective distance between two states is smaller. Let us now consider how quasipotentials can be evaluated in systems with fractal attractors.

5.1.3 *Escape From a Chaotic Attractor with a Fractal Basin Boundary*

Understanding the mechanism of noise-induced escape from a chaotic attractor though a fractal basin boundary is one of the most difficult unsolved problems in the theory of fluctuations [2, 17]. Silchenko et al. [18] suggested that there exists a generic mechanism of stochastic transitions between coexisting chaotic attractors separated by fractal basin boundaries. This mechanism is determined by a hierarchy of homoclinic initial saddles. In this context, the role of the so-called *most probable* or *optimal escape path* [19], along which the system leaves the given zone of attraction, is especially important.

The optimal escape path of moving away from a chaotic attractor across the fractal boundary can be derived using both the statistical analysis of stochastic trajectories and the Hamiltonian theory of fluctuations. To solve this problem, one has to perform the following tasks:

- To determine boundary conditions for both the chaotic attractor and its fractal basin boundary.
- To determine a unique escape path from the chaotic attractor to the fractal basin boundary using the Hamiltonian theory of fluctuations.
- To determine whether the transition through the fractal boundary contains any deterministic structure.
- To determine the effect of noise intensity.

One of the possible ways to find the most probable escape path is based on the analysis of fluctuations at a very low noise intensity. In this case, the stochastic dynamical system fluctuates to distant states along most probable deterministic trajectories [19] determined by the asymptotic solution of the Wentzel–Kramers–Brillouin type of the Fokker–Planck equation [11]. It was also shown that homoclinic tangencies (see Sect. 2.2.1), which cause the basin fractalization, decrease the activation energy [20].

Let us now demonstrate the existence of the escape mechanism using the example of the two-dimensional Holmes map [21]:

$$\begin{aligned}x_{n+1} &= y_n, \\y_{n+1} &= -bx_n + dy_n - y_n^3 + \xi_n,\end{aligned}\quad (5.20)$$

where ξ_n is zero-mean white Gaussian noise. In the deterministic case ($\xi_n = 0$), the system Eq. 5.20 is bistable for $b = 0.2$ and $d \in [2.0, 2.745]$. The boundary between the basins of attraction of the coexisting symmetric attractors can be either smooth or fractal depending on the parameters.

Let us fix the parameters to $b = 0.2$ and $d = 2.7$ for which two coexisting chaotic attractors are separated by a fractal basin boundary, as shown in Fig. 5.3.

In the presence of weak noise, the system Eq. 5.20 escapes from one of the coexisting basins. If we collect a large number of escape paths from both chaotic states under various noise realisations and average all trajectories, we can calculate the most probable (optimal) escape path which connects two chaotic states. In particular, one

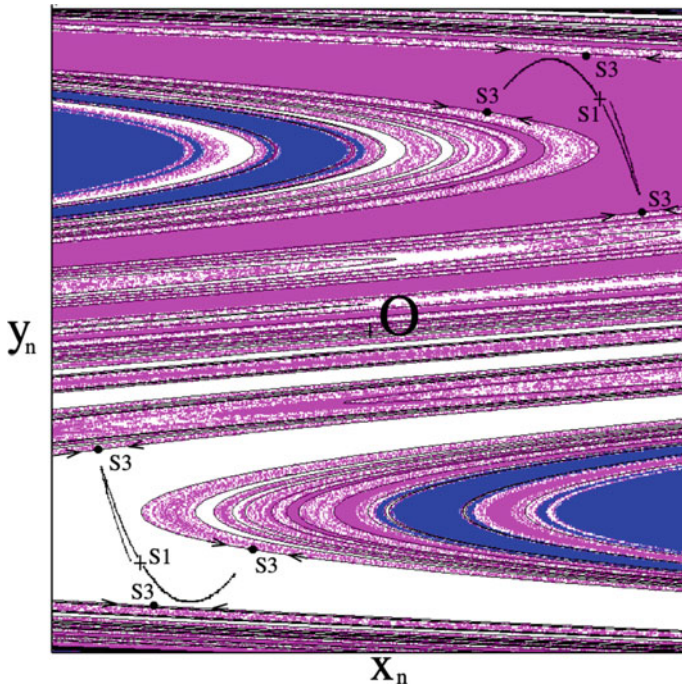
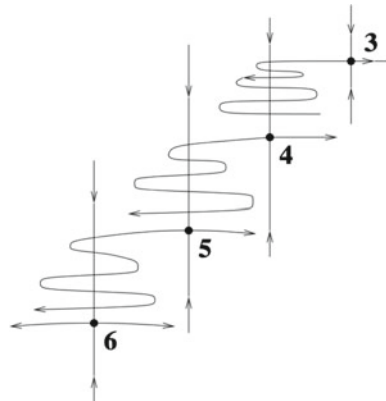


Fig. 5.3 Coexisting chaotic attractors (black curves) and their basins of attraction (blue and white dots). The accessible boundary saddle points of period 3 are shown by filled black circles and labelled S3. Their stable manifolds are indicated by symmetric solid black lines. The saddle points of period 1 are shown by crosses and labelled S1. The central circle is the saddle point at origin. From [18]

Fig. 5.4 Intersections of stable and unstable manifolds of original saddles which form the hierarchical homoclinic structure and play a key role in the formation of escape paths on the fractal basin boundary



can see that the system leaving the escape trajectory falls into a small neighbourhood of the saddle point of period 1 (S_1) located between its two disconnected parts. The stable manifolds separate the parts of the chaotic state, while the unstable manifolds belong to the chaotic state. A period-3 saddle point (S_3) lies on the fractal basin boundary, while the stable manifold (the black curve in Fig. 5.3) detaches the open neighborhood, including the attractor, from the basin boundary, therefore, this is an accessible boundary point.

The homoclinic saddle points play a key role in the formation of the escape path structure on the fractal boundary. In particular, the system Eq. 5.20 displays an infinite sequence of saddle-node bifurcations of periods 3, 4, 5, 6, 7, ..., caused by sequent tangencies of the stable and unstable manifolds of the saddle point \mathbf{O} at origin. The homoclinic orbits resulting from these bifurcations are called *original saddles*, whose stable and unstable manifolds intersect with each other in a hierarchical sequence shown in Fig. 5.4.

According to the Hamiltonian theory of fluctuations, the optimal escape path is the path that consumes minimum energy, that is

$$S = \frac{1}{2} \sum_{n=1}^N \xi_n^\top \xi_n, \quad (5.21)$$

where ξ_n is the n th realisation of noise that induces a transition from S_1 to S_3 through the fractal basin boundary and N is the total number of realisations.

The easiest way to solve the problem of extrema in a discrete stochastic dynamical system is to minimize the Lagrangian

$$\Lambda = \frac{1}{2} \sum_{n=1}^N \xi_n^\top \xi_n + \sum_{n=1}^N \lambda_n^\top (\mathbf{x}_{n+1} + \mathbf{f}(\mathbf{x}_n) - \xi_n), \quad (5.22)$$

where λ_n is the Lagrange multiplier.

The described escape mechanism is common for a wide class of discrete and continuous systems that exhibit the same type of fractal basin boundaries.

Based on the theory of quasipotential, Bashkirtseva and Ryashko [22] proposed a method of stochastic sensitivity function (SSF) for describing the transverse dispersion of stochastic attractors. In this method, the distribution of a stochastic attractor is expressed by a confidence ellipse or confidence band around a deterministic attractor. The original deterministic attractor is calculated numerically, so the nonlinearity problem is eliminated. The SSF method allows constructing probability distribution of stochastic attractors.

5.2 Coherence Resonance in Multistable Systems

In this section, it is worth mentioning resonance effects caused by noise or chaos in multistable systems, since they are somehow connected with multistate intermittency. In coherence resonance, the regularity of a noisy or a chaotic system maximizes at a certain intensity of random or chaotic perturbations. In a noisy system, the resonance is called *stochastic*, while in a chaotic system it is referred to as *deterministic coherence resonance*.

Coherence resonance can occur either in bistable or excitable systems close to the excitation threshold. It should be noted that stochastic resonance is a particular case of coherence resonance in the presence of an external periodic forcing. Stochastic resonance can be revealed as a maximum in the signal-to-noise ratio (SNR) versus the noise intensity.

Coherence resonance can be quantified by the following measures:

- correlation time,
- normalized autocorrelation function,
- normalized standard deviation of peak amplitude (amplitude coherence),
- normalized standard deviation of inter-peak interval (time coherence),
- dominant spectral component (spectral coherence),
- signal-to-noise ratio (SNR),
- similarity function,
- entropy,
- connectivity (topological coherence).

To characterize deterministic coherence resonance, in addition to the above measure, one can use the signal-to-chaos ratio (SCR) and Lyapunov exponents.

The extrema in the dependences of the above measures on the noise intensity or chaos amplitude indicates the existence of coherence or anti-coherence resonance phenomena.

Let us consider how stochastic and deterministic coherence resonances appear in systems with coexisting attractors.

5.2.1 Stochastic Resonance in Multistable Systems

The term *stochastic resonance* was introduced by Benzi and colleagues [23], who investigated the periodicity of the onset of ice ages and found a weak signal amplification when superimposed by noise. Two years later, this phenomenon was studied in detail in the Schmitt trigger,¹ and then discovered in many other systems.

Stochastic resonance in a bistable dissipative system reveals itself as follows. Under the influence of sufficiently strong noise, the system passes from one state to another. If an external periodic force with a sufficiently large amplitude is additionally applied, the system will periodically switch from one state to another, as shown in Fig. 5.5.

In stochastic resonance, the signal-to-noise ratio (SNR) maximizes with respect to the noise intensity because the stochastic oscillations become more coherent, that is more regular. Therefore, stochastic resonance is a particular case of coherence resonance, although the latter can occur not only in bistable systems [24], but also in excitable systems near the excitation threshold [9, 25, 26].

Similar resonance phenomena occur in deterministic multistable chaotic systems without noise [27–30], where a chaotic forcing acts in the same manner as noise, i.e. the trajectory switches between coexisting metastable states.

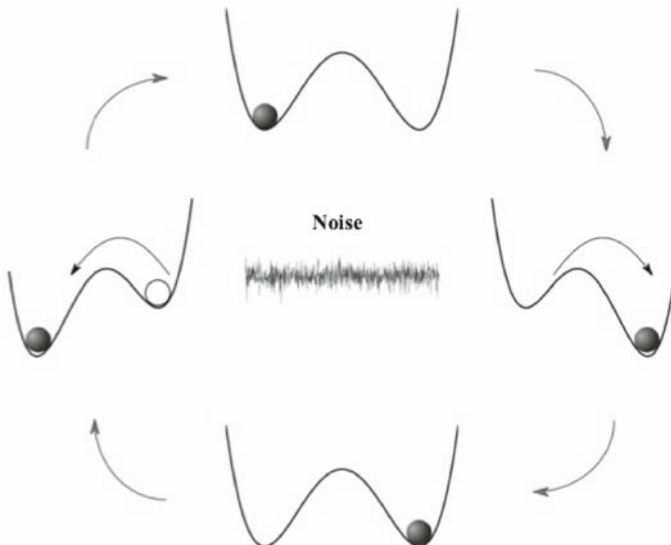


Fig. 5.5 Mechanism of stochastic resonance in a bistable system. External periodic forcing modulates the height of the potential barrier, raising and lowering potential wells. Adding appropriate noise allows the particle to reach a globally stable state

¹ The Schmitt trigger is a bistable two-position relay (switching) element, the static characteristic of which displays a hysteresis loop.

The optimal noise intensity resulting in the maximum SNR is the noise intensity at which the characteristic lifetime of the system in one state is equal to half the period of the periodic modulation. Too strong or too weak noise will make the system less susceptible to light intermittent failures. The optimal noise level is quantitatively determined by matching two time scales: the period of external modulation and the Kramers rate. This means that the average switching rate is caused by noise only, given as [31]

$$\omega_e = \sqrt{2}e^{-\frac{\Delta V}{\sigma^2}}, \quad (5.23)$$

where σ^2 is the variance of Gaussian noise and ΔV is the barrier separating symmetric potential wells.

SNR is defined as the ratio of the spectral component S to the spectral intensity S_N of background noise at the modulation frequency Ω [3]

$$\text{SNR} = \frac{2}{S_N(\Omega)} \lim_{\Delta\omega \rightarrow 0} \int_{\Omega - \Delta\omega}^{\Omega + \Delta\omega} S(\omega) d\omega. \quad (5.24)$$

The factor of 2 appears because of power spectral density symmetry $S(\omega) = S(-\omega)$.

Besides the SNR, stochastic resonance can be characterized by other measures. One of such measures is residence time distribution and the first excursion probability. The time the system spends in one of the basins and then jumps into another basin can be viewed as a problem of the time of the first excursion probability [32]. The assessment of the periods of stay in the same basin can serve as an indicator of the stability and quality of stochastic resonance. This indicator is usually more reliable than SNR, but the procedure of calculating the probability is much more time consuming.

Another measure of stochastic resonance is information entropy-based indication widely used in communication theories. This indicator is based on the Boltzmann information entropy defined as [33]

$$I(\phi) = \int_X p(x, t) \lg p(x, t) dx, \quad (5.25)$$

where $p(x, t)$ is the cross-probability density of the system response. This approach is usually based on maximizing this entropy with additional constraints imposed by the system itself. In particular, the probability distribution function is written as a multidimensional exponent, most often a polynomial in homogeneous form, with free coefficients determined by an extreme search using an appropriate procedure such as Fletcher-Powell, artificial neural network, etc.

The most efficient quantitative parameter for estimating suprathreshold stochastic resonance is mutual information [34]. For instance, if we denote by $p_{\phi\psi}(\phi, \psi)$ the joint probability distribution function (PDF) of input and output processes ($\phi(t)$ and $\psi(t)$), then based on the Shannon's theorem [35], the mutual information between

the processes $\phi(t)$ and $\psi(t)$ is defined as the relative entropy between the joint PDF and the product of partial PDFs [33]

$$I(\phi, \psi) = \int_{\phi, \psi} p_{\phi, \psi}(\phi, \psi) \lg \frac{p_{\phi, \psi}(\phi, \psi)}{p_\phi(\phi)p_\psi(\psi)} d\phi d\psi. \quad (5.26)$$

Note that Eq. 5.26 is basically a significant generalization of the Boltzmann entropy procedure (Eq. 5.25) with respect to the conditional probability related to some intermediate state, similar to Bayesian update.

Finally, stochastic resonance can be estimated using statistics of local random processes in individual basins, surrounding the mean value when residing in a basin. Then, a random mean square root is calculated and compared to the amplitude of the mean of the jump. When applied, this approach is more or less organically integrated into the analytical process. Its application can be seen more in areas related to more general stochastic resonance definitions regarding operator structure and driving noise type.

The theory of stochastic resonance extended to multistable systems [4, 5] has shown that there exists an optimal number of intermediate stable states for which the system response is maximized. The role of stochastic resonance in the destruction of attractors was demonstrated with Duffing oscillators [36, 37].

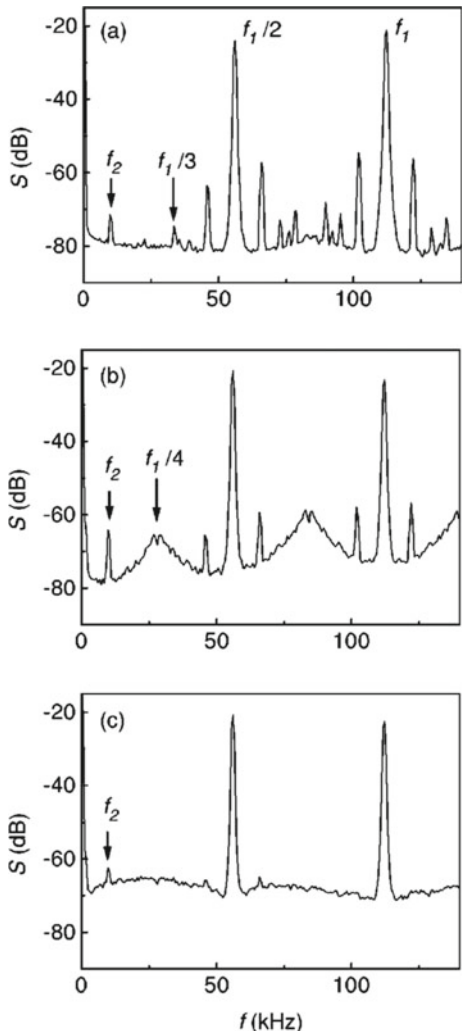
Let us now discuss the main mechanisms of noise-induced escapes of the system from a coexisting metastable state with smooth and fractal boundaries.

5.2.2 Deterministic Coherence Resonance in a Chaotic Bistable System

The phenomenon analogous to stochastic resonance was observed in deterministic chaotic systems without noise, since a pseudorandom chaotic motion in a bistable system acts in a similar way as noise. Thus, the stochastic resonance approach was extended to chaotic systems by maintaining a fixed noise intensity and adding deterministic excitation, rather than increasing noise. Since a chaotic behavior is associated with a broadband spectrum, on the basis of which the signal-to-noise ratio is determined, for a certain region of the parameter space, the system switches between coexisting chaotic states under the influence of a periodic driving. These pseudorandom switches amplify the external signal in much the same way as in the classical stochastic resonance. This phenomenon called *noise-free stochastic resonance* was experimentally observed in the ferromagnetic material [38] and in a CO₂ laser [28].

We will now show how deterministic resonance appears in a loss-driven CO₂ laser described in Sect. 4.3.1. In the experiment, the cavity losses were periodically modulated by an acousto-optical generator. By increasing the driving amplitude, the laser displays a period-doubling route to chaos and exhibits multistability, that can

Fig. 5.6 Experimental averaged power spectra of a CO₂ laser under loss modulation Eq. 5.27 with $f_1 = 112$ kHz, $f_2 = 10$ kHz, $A_2 = 10$ V and driving amplitudes **a** $A_1 = 2.8$ V, **b** 3.2 V, and **c** 3.8 V



be revealed with time series and power spectra. The numerical bifurcation diagram of this laser is present in Fig. 4.11.

The switches between the coexisting attractors are realized when a signal with frequency f_2 is applied to the cavity losses in the additive

$$G(t) = A_1 \cos(2\pi f_1 t) + A_2 \cos(2\pi f_2 t) \quad (5.27)$$

or multiplicative way

$$G(t) = A_1 [1 + m \cos(2\pi f_2 t)] \cos(2\pi f_1 t) \quad (5.28)$$

where A_1 is the driving amplitude, A_2 and m are the signal amplitude in the additive and multiplicative cases, respectively, and f_1 and f_2 ($f_2 \ll f_1$) are the driving and multiplicative frequencies, respectively.

Figure 5.6 displays the averaged power spectra of the laser output for three different values of the driving amplitude A_1 in the case of the additive signal.

For small A_1 the laser alternates between period-2 ($f_1/2$) and period-3 ($f_1/3$) regimes (Fig. 5.6a). For larger A_1 the laser alternates between period-2 and chaotic ($f_1/4$) regimes (Fig. 5.6b). Finally, for high A_1 the laser operates in a chaotic regime (Fig. 5.6c). One can see that the spectral component $S(f_2)$ at the signal frequency f_2 is composed of a broadband background S_b and a signal peak S_s , so that the total power is

$$S(f_2) = S_b(f_2) + S_s(f_2). \quad (5.29)$$

Comparing the spectra for different driving amplitudes A_1 , one can see that the peak $S_s(f_2)$ at the signal frequency $f_2 = 10$ kHz is more pronounced in Fig. 5.6b when the laser alternates between the period 2 and chaos. This resonant effect is caused by intrinsic chaotic dynamics [39].

Now, we can find the signal-to-noise ratio (SNR) derived as

$$\text{SNR} = 10 \log \frac{S_b(f_2) + S_s(f_2)}{S_s(f_2)}. \quad (5.30)$$

Figure 5.7 represents the SNR versus the driving amplitude A_1 for the additive (Fig. 5.7a) and multiplicative (Fig. 5.7b) signals. In both cases, the coherence resonance is observed in the chaotic regime.

Numerical simulations on the base of the two-level laser model in Eq. 4.3 describe well the experimental results.

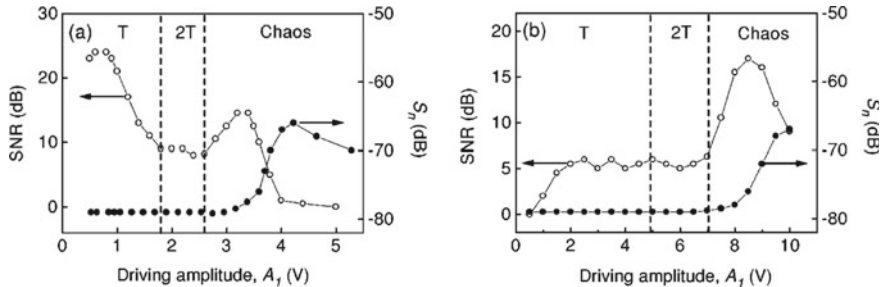


Fig. 5.7 Experimental signal-to-noise ratio (open dots) and power density at $f_2 = 10$ Hz of the broadband background (closed dots) versus the driving amplitude A_1 for **a** additive and **b** multiplicative signals. The vertical dashed lines indicate bifurcations without the signal

5.2.3 Logical Stochastic Resonance

One of the important areas of using stochastic resonance in bistable systems is logical operations. This kind of stochastic resonance is known as *logical stochastic resonance* (LSR). It was discovered by Murali et al. [40] in a bistable system driven by a subthreshold input stream. The logic gate system generates responses corresponding to a desired logical operation for an optimal noise window.

The general principle of LSR is similar to a conventional stochastic resonance. If an input signal $\mathbf{I} = \{I_1, I_2, \dots, I_N\}$ and noise $\mathbf{H} = \mathbf{D}\xi(t)$ ($\mathbf{H} = \{\eta_1, \eta_2, \dots, \eta_N\}$, $(\mathbf{D} = \{D_1, D_2, \dots, D_N\}$ being the noise intensity and $\xi(t)$ is an independent random variable) simultaneously enter to a dynamical system, its dynamics can be described as

$$\dot{\mathbf{x}} = \mathbf{F}(\mathbf{x}) + \mathbf{I} + \mathbf{H}, \quad (5.31)$$

where $\mathbf{F}(\mathbf{x})$ is a vector nonlinear function obtained via the negative gradient of a multistable potential. A logical input/output matching can be implemented by encoding N inputs into N square waves.

The output signal of a bistable system under two square-wave inputs is converted into a logical NOR/OR operation with probability which has a resonant character with respect to the noise intensity. In addition, the NAND and AND logic operations are realized by changing the shape of the potential function.

For further development of the LSR-based logic gate, Aravind et al. [41] put forward the idea to combine LSR and synchronization of bistable systems. For its implementation, they designed a scheme where a logic gate was implemented in a collective state of the coupled system rather than in the state of one system only. Such an improved logic gate was designed on the base of two coupled bistable systems controlled by two independent noise sources [41]. The scheme of this logic gate is present in Fig. 5.8.

In this system, two bistable systems are coupled either attractive (positive) or repulsive (negative). The use of two coupling types provides additional possibility for the system control to obtain all six fundamental, logic operations. Independent Gaussian noise is added to each subsystem. A constant bias b acts as the tether which morphs the bistable potential to reconfigure the system. The input signals I_1 and I_2 encode a binary input data stream for further processing by a logic gate, where a negative value of I_1 or I_2 corresponds to 0 (OFF state), whereas its positive value corresponds to 1 (ON state). It is important to note that these inputs are subthreshold and therefore they cannot cause a transition through the potential wells by themselves, and only noise can induce this transition resembling logical stochastic resonance. The synchronization state of the two subsystems embeds outputs corresponding to logical operations on input streams. By convention, when both systems are in the same potential well (synchronized state) the encoding is 0, otherwise (the systems in different potential wells) the encoding is 1.

The examples of all six basic logic operations performed by electronic circuits constructed on the base of the above consideration are shown in Fig. 5.9. The attraction

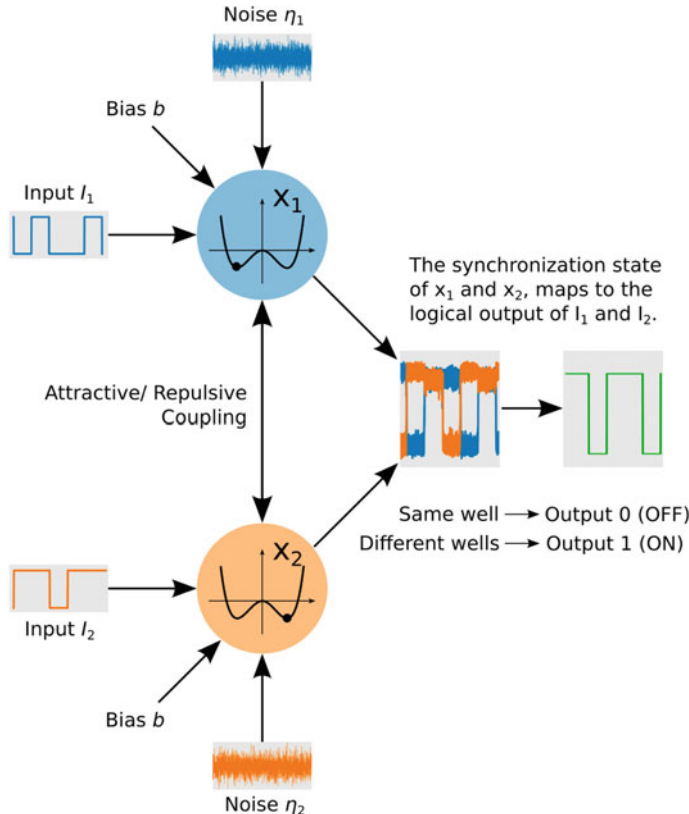


Fig. 5.8 Schematic of the logic gate based on synchronization of two bistable systems. Reprinted figure with permission from [41] ©2021 by the American Physical Society

circuit gives the AND, NOR and XNOR gates, while the repulsion circuit gives the NAND, OR and XOR gates. Note that the two circuits provide additional logical operations for the same set of parameter values, assuming that the two communication circuits are symmetrical analogs of each other.

Figure 5.9 displays the oscilloscope traces V1 (yellow) and V2 (blue) obtained from the attraction circuit (left) and the repulsion circuit (right). The top panel shows the input streams (I_1 and I_2) and the other six panels clearly exhibit robust logic responses. The synchronized segments are accurately mapped to output 0, while anti-synchronized segments to 1, for all six logical operations. The probability of obtaining each logic operation calculated as the ratio of successful runs to the total number of runs exhibits a resonance behavior with respect to noise, i.e. LSR takes place.

The logical stochastic resonance differs from an ordinary stochastic resonance. While in the ordinary stochastic resonance a signal-to-noise ratio has a maximum at a certain noise intensity, in the LSR the performance of each logic operation has

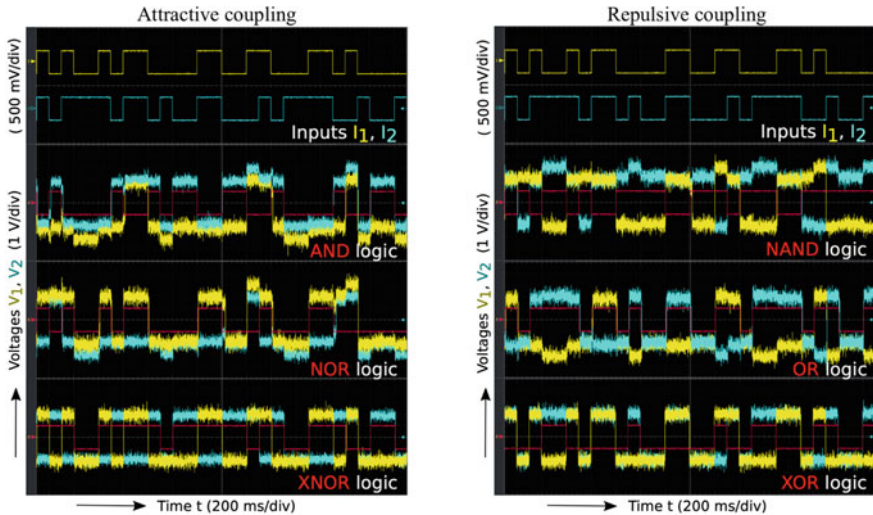


Fig. 5.9 Experimentally realized logic operations. Oscilloscope traces of voltages V_1 (yellow) and V_2 (blue) of (left) attractive and (right) repulsive circuits. Top panels on both sides represent the waveforms of the logic input signals used to drive the circuits. The expected logical output for each logic gate is painted in red. The other panels shows (left) AND, NOR, XNOR and (right) NAND, OR, XOR logic operations, obtained for different bias, coupling, and noise parameters. Reprinted figure with permission from [41] ©2021 by the American Physical Society

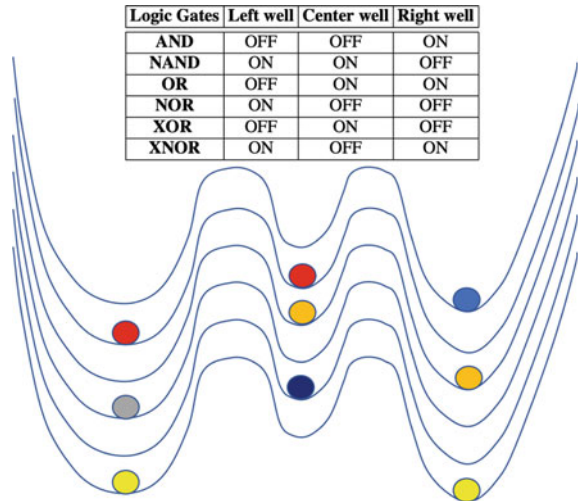
a certain probability defined as the ratio of the successful run to the total number of sampled runs. As was mentioned above, the probability has a resonant character with respect to the noise intensity exhibiting LSR, in which the probability reach 100%. This mean that there is a certain noise strength at which the logic operation is correctly performed.

LSR was found in different systems, including chemical reactions [42], synthetic gene networks [43, 44], and polarization bistable laser [45, 46], Coulomb-coupled quantum dots [47], quasiperiodically driven double-well Duffing oscillator [48]. Logistic systems were also realized on the base of switching between chaotic attractors [49, 50].

Finally, LSR was generalized to multi-well potential systems [51]. In particular, the combination of states in a triple-well potential system can provide with all six logic operations, as illustrated in Fig. 5.10.

The logic gates based on a triple-well potential were experimentally realized in electronic [52] and cavity madnomic systems [53]. In addition, LSR was also found in a fractional-order system with an asymmetric bistable potential function [54].

Fig. 5.10 Definitions of logic gate outputs in a triple-well potential system



5.3 Characterization of Noise-Induced Multistate Intermittency

The term *intermittency* was introduced by Pomeau and Manneville [55], who studied the Lorentz model where the alternation of periodic and chaotic regimes was observed. Later, such a behavior was observed in many dynamical systems, including electrical circuits [56], lasers [57], and living systems [58]. The same term is also used to designate the irregular alternation of two different chaotic regimes, referred to as *crisis-induced intermittency* [59]. Different types of intermittency are distinguished according to the mechanisms leading to switching dynamics and statistical properties of two coexisting regimes called *laminar and turbulent phases*. The most investigated types of intermittency are type I–III intermittency [60], eyelet intermittency [61], ring intermittency [62], and on-off intermittency [63]. Each type of intermittency is characterized by its own scaling law for the average length of the laminar phase versus a criticality parameter and a specific type of distribution of the laminar phase length at fixed parameters.

Gaussian noise or noise of a finite but sufficiently large intensity applied to a multistable system induces switchings among coexisting states, thus making the system metastable. Such a behavior was first observed by Arecchi and Califano [64] in the Duffing oscillator and called *attractor hopping*. Later, similar stochastic dynamics was found in many other nonlinear systems with coexisting attractors in the deterministic case. Here, we will call such switchings among the coexisting metastates *noise-induced multistate intermittency* in analogy to similar phenomena observed in monostable systems where a regular behavior (laminar phase) is interrupted by irregular bursts (turbulent phase). Accordingly, instead of laminar phases, the concept of residence times is used, i.e. time intervals when the system is in the vicinity

of one of the coexisting states without switching between them. As a consequence, for noise-induced multistate intermittency, the residence time distribution and the dependence of the mean residence time on the criticality parameter is considered as statistical characteristics of this type of intermittency.

Among various types of intermittency, one can distinguish type-I, type-II, type-III, Pomeau–Manneville intermittency [55], one-state [63] and two-state on-off intermittency [65], crisis-induced intermittency [66], eyelet intermittency [61], and ring intermittency [62]. The type of intermittency depends on the type of bifurcation at the critical point. For example, type-I and on-off intermittency are associated with saddle-node bifurcations, type-II and type-III with Hopf and reverse period-doubling bifurcations, respectively, crisis-induced intermittency with crisis of chaotic attractors when two or more chaotic attractors collide with a periodic orbits or orbits [67], and two-state on-off intermittency with the coexistence of two fixed points. The simplest case of multistate intermittency, so-called *two-state on-off intermittency* was predicted by Lai and Grebogi [65] and experimentally observed in laser experiments [68]. Each type of intermittency obeys specific statistical properties and a particular scaling law with respect to the noise intensity.

Noise in a multistable system leads to such complex behavior that the overall dynamics can be divided into two different phases: a fairly regular motion near attractors (ordered phase) and noise-induced jumps between coexisting metastable states (random or chaotic phase). The dynamics in this case is characterized by a large number of periodic states embedded in a transient chaos sea [69]. Too strong noise does not allow the system to turn into any ordered phase so that most of the former attractors cannot be identified anymore. Instead, a diffusion process over the state space takes place.

One of the specific applications of noise-induced multistate intermittency is information processing [70] because at the appropriate noise level, the system can easily get quick access to various ordered states. In this case, metastable behavior can be used to process and store information, i.e. different ordered states can be identified using different stored pieces of information, while an external trigger can be used to stabilize the selected ordered state associated with a given input.

5.3.1 Mean Residence Times

A general theory of noise-induced intermittency in a system with two coexisting states was developed by Moskalenko and colleagues [71]. They tested their theory on several systems and compared the statistical characteristics of these systems with theoretical predictions.

Let us consider a dynamical system

$$\dot{x} = -U'(x) + \xi(t), \quad (5.32)$$

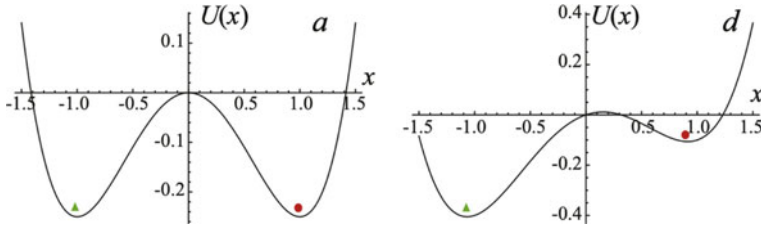


Fig. 5.11 (Left) Symmetric and (right) asymmetric double-well potential function for (left) $b = 0$ and (right) $b = 0.15$

where $U'(x) = dU(x)/dx$ and $\xi(t)$ is zero mean δ -correlated Gaussian noise so that $\langle \xi(t) \rangle = 0$ and $\langle \xi(t)\xi(\tau) \rangle = D\delta(t - \tau)$ (D being the noise intensity). The double-well potential energy function shown in Fig. 5.11 is given as

$$U(x) = \frac{x^4}{4} - \frac{x^2}{2} + bx. \quad (5.33)$$

Equation 5.34 can be rewritten in terms of stochastic process $X(t)$ and one-dimensional Wiener process dW as

$$dX = -U'(x)dt + dW, \quad (5.34)$$

that is equivalent to the Fokker–Planck equation for probability density $\rho_x(x, t)$ of the stochastic process $X(t)$:

$$\frac{\partial_x(x, t)}{\partial t} = \frac{\partial}{\partial x} \left[\frac{dU(x)}{dx} \rho_x(x, t) \right] + \frac{D}{2} \frac{\partial^2 \rho_x(x, t)}{\partial x^2}. \quad (5.35)$$

In the intermittency mode the system can stay in the vicinity of one of the local minima for a relatively long time. This means that the probability densities $\rho_{1,2}(x, t)$ of these states obey a metastable distribution slowly decaying over time, that is

$$\rho_{1,2}(x, t) = A_{1,2}(t)r(x), \quad (5.36)$$

where $A_{1,2}(t)$ are the coefficients which slowly decrease in time and $r(x)$ is the stationary probability density (stationary solution of Eq. 5.35) given as

$$r(x) = \exp \left(-\frac{2U(x)}{D} \right) \left[C_1 + C_2 \int_0^x \exp \left(\frac{2U(\xi)}{D} \right) d\xi \right]. \quad (5.37)$$

Since in the extrema $r'(x_{1,2}) = C_2 = 0$ and finding C_1 from the normalization condition

$$\int_{-\infty}^{+\infty} r(x)dx = 1,$$

we can rewrite Eq. 5.37 as follows

$$r(x) = C_1 \exp\left(-\frac{2U(x)}{D}\right) = C_1 g(x) = \frac{g(x)}{\int_{-\infty}^{+\infty} g(\xi)d\xi}. \quad (5.38)$$

The coefficients $A_{1,2}(t)$ can be found from the equation

$$\dot{A}_{1,2} = -\frac{k}{P_{1,2}} A_{1,2}(t) r(x^*), \quad (5.39)$$

where x^* is the critical point (unstable fixed point) separating two coexisting basins (see Fig. 5.11), k is a scaling factor, and $P_{1,2}$ are the probabilities for the system to be in the vicinity of the first or the second local minimum, derived as

$$P_1 = \int_{-\infty}^{x^*} r(\xi)d\xi = \frac{\int_{-\infty}^{x^*} g(\xi)d\xi}{\int_{-\infty}^{+\infty} g(\xi)d\xi}, \quad P_2 = \int_{x^*}^{+\infty} r(\xi)d\xi = \frac{\int_{x^*}^{+\infty} g(\xi)d\xi}{\int_{-\infty}^{+\infty} g(\xi)d\xi}. \quad (5.40)$$

The solution of Eq. 5.39 can be found as an exponential decay in the form

$$A_{1,2} = -A_{1,2}(0) \exp\left(-\frac{kr(x^*)}{P_{1,2}}t\right). \quad (5.41)$$

Different exponents for each of the two local minima result in the exponential character of the residence time distributions for each of the two coexisting states given as

$$p_1 = - \int_{-\infty}^{x^*} \frac{\partial \rho_1(x, t)}{\partial t} dx, \quad p_2 = - \int_{x^*}^{+\infty} \frac{\partial \rho_2(x, t)}{\partial t} dx. \quad (5.42)$$

Taking into account the normalization conditions

$$\begin{aligned} \int_{-\infty}^{x^*} \rho_1(\xi, 0)d\xi &= \int_{-\infty}^{x^*} A_1(0)r(\xi)d\xi = 1, \\ \int_{x^*}^{+\infty} \rho_2(\xi, 0)d\xi &= \int_{x^*}^{+\infty} A_2(0)r(\xi)d\xi = 1, \end{aligned} \quad (5.43)$$

the residence time distributions become

$$p_{1,2}(t) = k_{1,2} e^{-k_{1,2} t}, \quad (5.44)$$

where $k_{1,2} = kr(x^*)/P_{1,2}$. One can see that in the regime of noise-induced intermittency the residence time distributions exponentially decays.

Now, we can find the mean residence times for the coexisting states as

$$T_{1,2} = \int_0^{+\infty} p_{1,2}(t) dt = \frac{1}{k_{1,2}} \frac{P_{1,2}}{kr(x^*)}. \quad (5.45)$$

Finally, Eq. 5.44 takes the following form

$$p_{1,2}(t) = \frac{1}{T_{1,2}} e^{-t/T_{1,2}}. \quad (5.46)$$

Substituting Eqs. 5.40 and 5.38 for x^* into Eq. 5.45 and considering $x^* \approx b$ for small b , we can write the expressions for the mean residence times for two coexisting states as

$$T_{1,2} = \frac{L_{1,2}}{k} \exp \left[\frac{2}{D} \left(\frac{b^4}{4} + \frac{b^2}{2} \right) \right], \quad (5.47)$$

where

$$L_1 = \int_{-\infty}^{x^*} g(\xi) d\xi, \quad L_2 = \int_{x^*}^{+\infty} g(\xi) d\xi, \quad (5.48)$$

that can be calculated numerically.

In the case of symmetric potential ($b = 0$), the mean residence times of the two fixed points coincide, i.e. $T_1 = T_2 = T$, and equal to the mean first passage time Eq. 5.17 across the point of symmetry x^* . Moreover, the integrals Eq. 5.48 can explicitly be found allowing the analytical expression for the mean residence time

$$T = \frac{\pi}{4k} \exp \left(\frac{1}{4D} \right) \left(\frac{I_{-1/4}}{4D} + \frac{I_{1/4}}{4D} \right), \quad (5.49)$$

where $I_\alpha(x)$ is the modified Bessel function.

A clear evidence of multistate intermittency was found in coupled logistic maps [71, 72]. As shown in Sect. 2.2.4, phase multistability appears in coupled logistic maps (see Eq. 2.18), i.e., for the same parameter values the maps stay either in-phase or anti-phase synchronization depending on the initial conditions. The coupled logistic maps with additive noise are given by

$$\begin{aligned} x_{n+1} &= \lambda - x_n^2 + k(x_n^2 - y_n^2) + D\xi_x, \\ y_{n+1} &= \lambda - y_n^2 + k(y_n^2 - x_n^2) + D\xi_y, \end{aligned} \quad (5.50)$$

where ξ_x and ξ_y are Gaussian zero mean noise of intensity D applied to x and y variables, respectively. For $D > 0$ the system switches between in-phase and anti-phase states.

The distributions of the residence times for in-phase and anti-phase regimes and the mean residence times obey the exponential laws given by Eqs. 5.46 and 5.47, respectively.

5.3.2 Structural Properties of Noise-Induced Multistate Intermittency

Let us now consider topological properties of multistate intermittency on the example of a kicked mechanical rotor. As was shown in Sect. 2.2.2, due to low dissipation the kicked rotor map in Eq. 2.10 exhibits the coexistence a large number of stable periodic orbits. Therefore, it is interesting to see what happen if we add a small amount of noise to this system. This was first done by Kraus, Feudel, and Grebogi [7], who studied noise-induced switching among coexisting states in the model with additive Gaussian noise, given as

$$\begin{aligned} x_{n+1} &= x_n + y_n + \delta_x \mod 2\pi, \\ y_{n+1} &= (1 - \nu)y_n + f_0 \sin(x_n + y_n) + \delta_y, \end{aligned} \quad (5.51)$$

where δ_x and δ_y ($\sqrt{\delta_x + \delta_y} \leq \delta$) are intensities of uniformly distributed noncorrelated noise. Under the influence of noise, the trajectory intermittently visits various coexisting states, as illustrated in Fig. 5.12, and referred this noise-induced multistate intermittency to as *attractor hopping*.

As seen from Fig. 5.12, relatively long laminar phases alternate with short turbulent phases, so that the trajectory $x_{i=0}^n$ is a certain sequence of $n = 5$ metastable states (1–2–1–1–2–3–3–2–5–1–1–3–4–3–1–1–1–3) or partition elements of the phase space $X \in \mathbb{R}^d$. Such symbolic dynamics, if controlled, may be used as a specific information code.

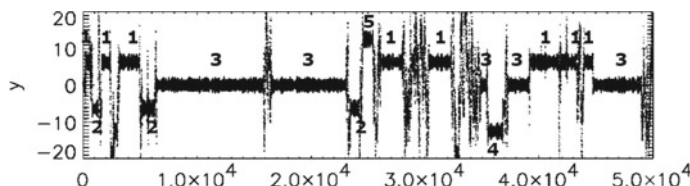


Fig. 5.12 Noise-induced switchings among five coexisting metastable states (1–5) in a periodically kicked mechanical rotor in the presence of noise with $\delta = 0.1$. Modified figure with permission from [7] ©1999 by the American Physical Society

Dividing the phase space into a finite set of b disjoint subsets ($B = B_0, \dots, B_{b-1}$), i.e. $\bigcup_{j=0}^{b-1} B_j = X$ and $B_j \cap B_k (j \neq k)$, we obtain a set of labels $A = 0, \dots, b - 1$ of partition elements, referred to as *alphabet*. Thus, the phase space every trajectory x_n can be mapped into symbolic sequence $S = s_0, s_1, \dots, s_n$, where the symbol $s_i \in A$ indicates the domain $B_{s_i} \in B$ which the trajectory visits at time i .

In the above example of multistate intermittency in the kicked mechanical rotor (Fig. 5.12), a symbol is attributed to every fixed point the trajectory visits, i.e. in fact we construct an alphabet of five elements. This approach allows us to only consider the structural properties of multistate intermittency or its *topology* and ignore the complete temporal evolution.

5.3.3 Entropy Measures of Multistate Intermittency

Entropy is known to be a measure of the system complexity. In Sect. 1.5.1 we introduced the notion of basin entropy to characterize complexity of the basin of attraction. Similarly, using entropy we can characterize the complexity of multistate intermittency. Among various types of entropy, the most convenient ones are Shannon entropy and topological entropy. The former is used to characterize the complexity of symbolic dynamics, while the latter for characterization of topological complexity. Consider these types of the entropy in more detail.

Shannon entropy. The Shannon entropy, also called *informational entropy*, is a measure of the uncertainty of a certain system, in particular, the unpredictability of the appearance of any symbol of the primary alphabet. In the absence of information loss, the entropy is numerically equal to the amount of information per symbol of the transmitted message.

Claude Shannon [73] assumed that an increase in information is equal to the lost uncertainty, and established requirements for its measurement: (i) the measure must be continuous, i.e. a small change in the probability value should cause a small net change in the function, (ii) in the case when all options (visiting states in our example) are equally probable, an increase in the number of options (attractors) should always increase the value of the function, and (iii) it should be possible to make a choice (attractors) in two stages, in which the value of the final result function should be the sum of the functions of intermediate results.

The complexity of the symbol string in multistate intermittency can be measured by the Shannon entropy given as

$$h_S = \lim_{n \rightarrow \infty} \frac{H_n}{n} = \lim_{n \rightarrow \infty} (H_{n+1} - H_n) = \lim_{n \rightarrow \infty} \frac{1}{n} \left(- \sum_{|S|=n} p(S) \ln p(S) \right), \quad (5.52)$$

where $S = s_1 s_2 \dots, s_n$ is a finite symbol sequence of n elements, $p(S)$ is the probability of its occurrence, and H_n is the block entropy of block length n . For the case shown in Fig. 5.12, we have $s_i = 1, 2, 3, 4, 5$. If the symbol sequence corresponds to

the generating partition, the Shannon entropy h_n is identical to the Kolmogorov–Sinai or metric entropy [74, 75].

The difference $h_n = H_{n+1} - H_n$ between block entropies can be interpreted as information needed to specify the symbol $n + 1$ knowing the previous n symbols. For Markovian process² of order k , i.e. if the memory does extend only to the previous k iterations, $h_{k+l} = h_k$ for all $l \in \mathbb{N}$; otherwise $h_l > h_k$ for all $l < k$. In the latter case, the system dynamics is long-range correlated.

To determine what type the multistate intermittency belongs to, it is necessary to calculate $h_n = H_{n+1} - H_n$ depending on the nonlinearity parameter. It was found that multistate intermittency is a first-order Markov process. This means that its dynamics is regulated by the last state only, because higher correlations are suppressed by the long laminar phase.

Topological entropy. Another entropy type which allows characterizing topological properties of multistate intermittency is *topological entropy* introduced by Adler, Konheim and McAndrew [76]. Namely, topological entropy is derived as an exponential growth rate of the number $N(n)$ of allowed sequences versus their length n :

$$h_T = \lim_{n \rightarrow \infty} \frac{\log N(n)}{n}. \quad (5.53)$$

This is the complexity measure of the system dynamics mapped to the symbol sequence

$$\lim_{n \rightarrow \infty} N(n) \sim e^{nh_T}. \quad (5.54)$$

In practice, we construct a 5×5 transition matrix, whose elements are either 1 or 0, depending on whether the transition has occurred or not, respectively. The logarithm of the largest eigenvalue of this matrix yields the topological entropy [77].

5.3.4 Wavelet Transform Method for Detection of Coexisting Regimes

The combination of different types of intermittency in the same system can lead to very complex dynamics. It is noteworthy that the difference in dynamical regimes can be so large that, under certain circumstances, the same type of intermittency can be classified into completely different types [78]. Moreover, two or more different types of intermittency can be interleaved with each other, leading to a very sophisticated behavior called *intermittency of intermittencies* [79]. To distinguish different dynamical regimes in highly intermittent dynamics, especially under strong noise,

² A random process is called *Markovian* (after Russian mathematician Andrey Andreyevich Markov) if at any time t the conditional probability of an arbitrary future event taking into account the entire past process, i.e. given $X(s)$ for all $s \leq t$, equals the conditional probability of this future event in the presence of only $X(t)$.

one needs special approaches. One of the powerful technique to find regularities in the residence time distributions, as well as to separate time intervals belonging to particular dynamical regimes, is the method based on the continuous wavelet transformation [80].

Usually, when the switching occurs between two dynamical regimes only, they can be simply distinguished in time series by their amplitudes, for example, when a peak value of variable x in regime A is much larger than its value in regime B. This difference can be used to separate time windows associated with these regimes. This way, a threshold Δ is introduced such that when $x > \Delta$, we suppose that the system stay in the regime A, otherwise it stays in the regime B. This is so-called *amplitude criterion*. The amplitude criterion can be used to analyze time series of very complex systems, such as the brain, while looking at the system behavior on some predetermined time scales.

The direct application of the amplitude criterion gives acceptable results for a wide range of dynamical systems exhibiting two-state intermittency. However, in systems with multiple coexisting attractors this criterion does not always work. In this case, specific operations are required before applying the amplitude criterion. To study the dynamical behavior of the variable $x(t)$ in the time-scale range $s \in [s_l, s_h]$ (s_l and s_h being the low and high limits), the integral energy $w(t)$ of the wavelet spectrum associated with this range can be given in the terms of complex wavelet surface $W(s, t)$ as

$$w(t) = \int_{s_l}^{s_h} |W(s, t)|^2 ds, \quad (5.55)$$

where is

$$W(s, t_0) = \frac{1}{\sqrt{s}} \int_{-\infty}^{+\infty} x(t) \psi^* \left(\frac{t - t_0}{s} \right) dt \quad (5.56)$$

the complex wavelet transform with complex Morlet mother wavelet

$$\psi(\eta) = \frac{1}{\sqrt[4]{\pi}} \exp(j2\pi\eta) \exp \left(\frac{-\eta^2}{2} \right). \quad (5.57)$$

Here, the symbol “ $*$ ” denotes complex conjugation, and the value of 2π is used to ensure the ratio $s \approx 1/f$ (f being the Fourier transform frequency). After calculating the temporal evolution of the wavelet energy spectrum using Eq. 5.55, the amplitude criterion $w(t) > \Delta_s$ is applied again to separate the time windows associated with alternating states.

This method was used to study intermittency in brain dynamics, where various types of intermittency arise, for example, impulse wave discharges in the form of electroencephalographic signs of absence epilepsy, sleep spindles, brain waves, and background activity [81].

Now, we will show how the wavelet method can be applied in practice to detect and localize different regimes in noise-induced multistate intermittency. As an example, consider a multistable erbium-doped fiber laser (EDFL) with pump modulation described by Eqs. 4.10, 4.11, and 4.15 given in Sect. 4.5, and whose experimentally observed intermittent dynamics is present in Sect. 5.5.2. We remind that this laser can exhibit the coexistence of $i = 1, 3, 4, 5$ periodic orbits, each of which characterized by its own frequency f_i . The maximum energy $|W(s, t_0)|^2$ of the wavelet spectrum $W(s, t_0)$ is observed in the time scale $s_i \approx 1/f_i$ in the dynamical regime which occurs at time t_0 .

The main idea of the method is illustrated in Fig. 5.13, where we show the time series of the EDFL subject to external noise with intensity $\eta = 0.23$. For this level of noise, the laser alternates between period-1 and period-3 regimes with characteristic frequencies f_1 and f_3 , respectively.

The time series of x and $|W(s, t)|$ in Figs. 5.13a, b display the time intervals in which the dynamical regimes with frequencies f_1 and f_3 take place (I and III). The wavelet surface $|W(s, t)|$ in Fig. 5.13b shows sudden switchings between two oscillatory regimes, which can easily be controlled by tracking the wavelet spectrum energy at certain time scales s_i corresponding to characteristic frequencies $f_{1,3}$ of the alternating regimes. One can see that the wavelet energy in the corresponding time scale can serve as the regime marker. By comparing the wavelet spectrum energy $|W(s_i, t_0)|^2$ for each regime, we can distinguish which regime type occurs at time t_0 .

The continuous wavelet transform can neutralize the effect of noise at the characteristic frequencies, that makes possible to use this method for filtering noisy signals. Nevertheless, the frequencies of alternating regimes can still fluctuate, as seen from Fig. 5.13b. Therefore, similar to Eq. 5.55 the energy of the integral wavelet spectrum should be considered in a narrow time-scale interval $s_i - \Delta \leq s \leq s_i + \Delta s$, that is

$$w_i(t) = \frac{1}{2\Delta s} \int_{s_i - \Delta s}^{s_i + \Delta s} \frac{|W(s, t)|^2}{s} ds. \quad (5.58)$$

The $1/s$ coefficient allows direct comparison of the energies of competing regimes, since it is known that for the same harmonic signal amplitude $A \sin(2\pi t/s)$ the wavelet spectrum energy as known [81] to grow quadratically as the time scale s is increased. Thus, the dynamical regime which occurs at a certain moment of time t_0 is distinguished using the highest energy of the wavelet spectrum $w_i(t_0)$.

Using the described approach the period-1 and period-3 dynamical regimes can be distinguished and separated using their wavelet spectral energies $w_{1,3}$, as illustrated in Fig. 5.13c. One can see that the wavelet spectrum energy $w_1(t)$ prevails over $w_3(t)$ in time intervals where the oscillation frequency is close to f_1 , whereas in other windows $w_1(t)$ is smaller than $w_3(t)$.

The method for separation of coexisting regimes based on wavelet spectrum energies can also be used in other dynamical systems exhibiting multistate intermittency with switchings between different oscillatory regimes.

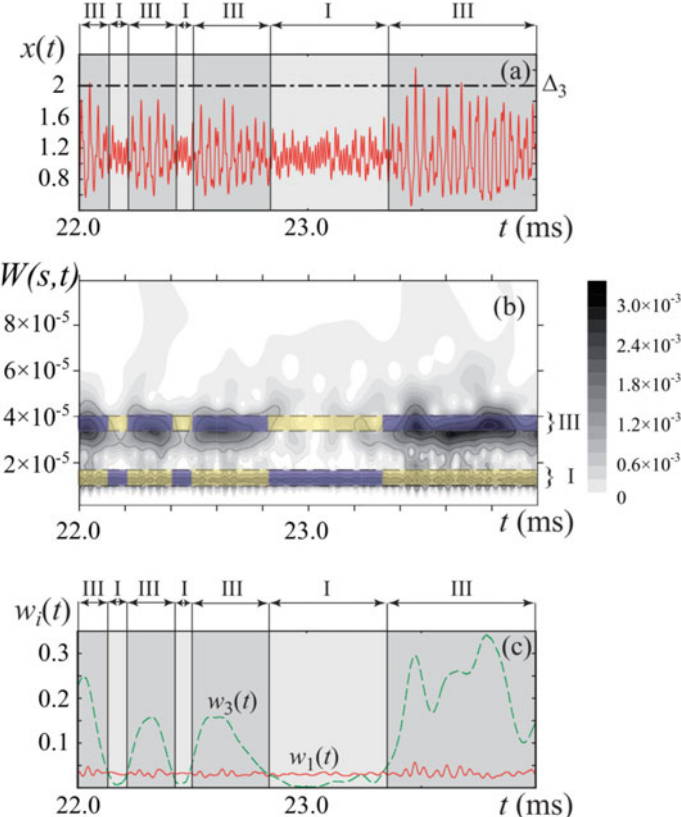


Fig. 5.13 Time series of (upper) state variable x , (middle) wavelet surface $|W(s,t)|$, and (lower) wavelet spectrum energies $w_{1,3}$ of the EDFL in the regime of noise-induced two-state intermittency where the laser switches between period-1 and period-3 regimes. The time windows with different oscillation periods are separated by vertical lines and marked with I and III. The horizontal dot-dashed line shows the threshold value Δ_3 used for the amplitude criterion. The dashed lines in (middle) mark the characteristic time scales for the separated regimes $s_{1,3} \pm \Delta s$. Reprinted figure with permission from [80] ©2016 by the American Physical Society

5.4 Manifestation of Noise-Induced Multistate Intermittency

Multistate intermittency was found in various discrete and continuous systems. Some examples in discrete systems, such as a mechanical rotor and coupled logistic maps, have been already described above. Below, we will consider some realizations of multistate intermittency in continuous systems.

5.4.1 Stochastic Bistable Chua System

Let us consider the double-scroll noisy Chua oscillator defined as [82]

$$\begin{aligned}\dot{x} &= y - x - h(x) + D\xi, \\ \dot{y} &= \alpha^{-1}(x - y + z), \\ \dot{z} &= -\delta(y + \rho z),\end{aligned}\quad (5.59)$$

where $\alpha = 9$, $\delta = 9$, and $\rho = 0.01$ are coefficients, ξ is zero-mean Gaussian noise with unit variance and intensity D , and $h(x)$ is the third degree polynomial given by

$$h(x) = -1.25x - 0.1x^3. \quad (5.60)$$

The deterministic Chua oscillator exhibits the coexistence of two chaotic attractors depending on the initial condition. The time series and phase portrait of one of them are illustrated in Fig. 5.14a, b, respectively.

When the system is affected by noise, random transitions from one quasi-stable state to another occur, i.e. noise-induced two-state intermittency is observed. This situation is illustrated in Fig. 5.14c, where it is clearly seen that the system alternately switches from one state to another. The corresponding double-scroll attractor is present in Fig. 5.14d.

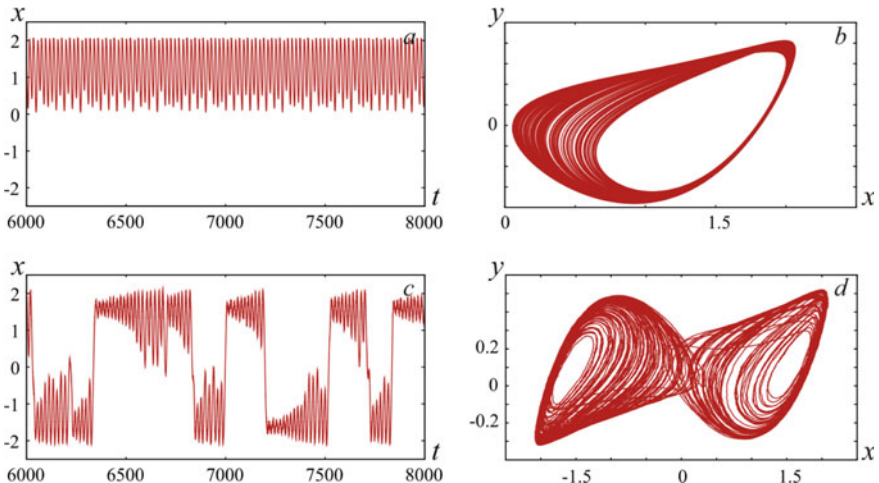


Fig. 5.14 a, c Time series and b, d phase portraits of the Chua oscillator in Eq. 5.59 a, b in the deterministic system ($D = 0$) and c, d in the presence of noise ($D = 1$). Reprinted from [71] ©2018 with permission from Elsevier

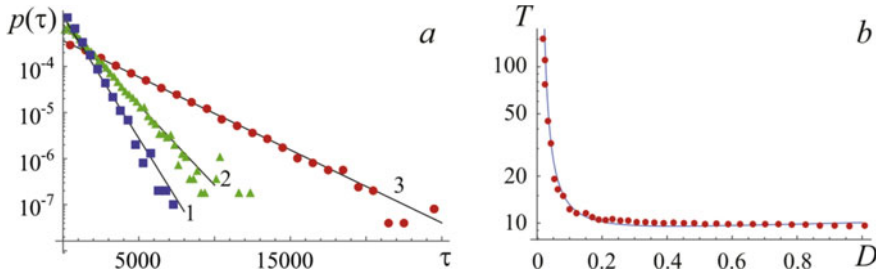


Fig. 5.15 **a** Residence time distributions versus noise intensity and **b** mean residence time in one of the quasi-stable states of the Chua system Eq. 5.59 and their theoretical approximations (solid lines) calculated by Eqs. 5.46 and 5.49 for noise intensities $D = 0.26$ (1), $D = 0.32$ (2), and $D = 0.37$ (3), and $k = 0.318$. Reprinted from [71] ©2018 with permission from Elsevier

Statistical analysis of this noise-induced intermittency shows that the probability distribution $p(\tau)$ of the residence time τ in one of the quasi-stable states exponentially decays with the residence time (laminar phase), as seen from Fig. 5.15a.

Figure 5.15b displays the exponential decay of the average residence time the Chua system spent in one of the quasi-stable state versus the noise intensity. The solid line shows its theoretical approximation by regularity Eq. 5.49 for the symmetric system. One can see that the numerically obtained data are in good agreement with theoretical predictions.

5.4.2 Anti-coherence Resonance in a Bistable Neural Network

As we already discussed in Sect. 3.4, the coexistence of attractors is an important property of neural cells, neural networks, and other biological objects. Multistability in neuronal networks can mark either a normal or a pathological state of a neuronal network, while noise-induced switches between coexisting states play an important role in cell signaling and neuronal interactions [83–85]. Noise caused by random vibrations at the molecular level is a fundamental part of intracellular and other biological processes. Moreover, using noise, one can control the state of the cell [86].

Each neural cell typically receives signals from thousands of other cells mediated by different neurotransmitters and consequently modifying the postsynaptic potential by excitation or inhibition [87]. Communication between cells occurs through synaptic contacts, where an action potential of a presynaptic neuron releases a neurotransmitter and affects a postsynaptic potential of the target cell. Specifically, the coexisting states mimic different brain states representing particular objects of perception which can be selected by giving the neural network an input corresponding to an initial condition [88].

Since noise is always present in real neural networks, its effect on the dynamics of the network is of great importance. For example, in two bistable neurons noise causes synchronous episodic discharges [89], and in bistable neural networks stabilizes neuron clusters [90].

Esir and colleagues [91] suggested that spiking dynamics of synaptically connected bistable neuronal oscillators is regulated by inherent noise. In particular, they found that delays in axonal conductions result in the emergence of coexisting states with high and low activity levels, so-called *up and down states*. In this system, neural noise induces spontaneous transitions between up and down states, characterized by high and low firing rates in cortex and striatum. Such a behavior was observed in various experiments [92–94].

The formation of up and down states can be explained as follows. A noise of a sufficiently high intensity can cause a switch in the dynamics of a neuron from a stationary steady state to an oscillatory state or vice versa. The activation of some neurons in the neural network can also cause a transition to the up state. This process develops like an avalanche, because the more neurons are active, the easier it is for new neurons to enter the active phase. Conversely, the inhibition of some neurons can cause a transition to the down state. Since each neuron is stimulated by a Poisson pulse train of intensity w_p , this random process depends on the phases the Poisson noise spikes.

Thus, in the presence of sufficiently strong noise, the states of the network with intermediate firing rates become unstable, so that the network dynamics becomes metastable exhibiting two-state intermittency, as illustrated in Fig. 5.16. Note that the histograms of firing rate have two apparent peaks that correspond to the duration

Fig. 5.16 Switching between up and down states in the neural network of bistable Hodgkin–Huxley neurons (Eq. 3.28) subject to Poisson noise of different intensities w_p . (Right) Firing rate traces and (left) their histograms. Reprinted figure with permission from [91] ©2018 by the American Physical Society

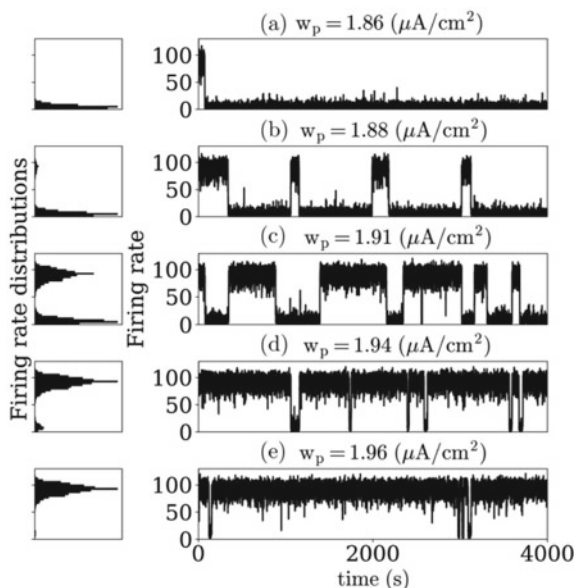
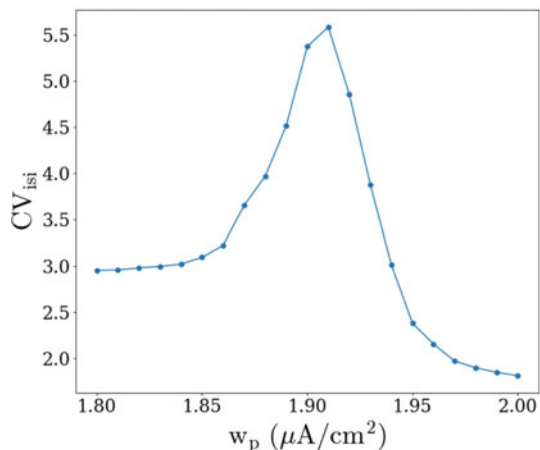


Fig. 5.17 Noise-induced anti-coherence resonance in the neural network of bistable Hodgkin–Huxley neurons. Dependence of standard deviation of ISI variation on noise amplitude w_p . Reprinted figure with permission from [91] ©2018 by the American Physical Society



of windows when the system stays near the up and down states, which depend of the noise intensity.

The statistics of this two-state intermittency can be characterized by the interspike intervals (ISI) of the network neurons. The coefficient of ISI variation is calculated as the standard deviation of the mean ratio. Figure 5.17 shows that the ISI variation coefficient has a visible maximum with respect to the noise intensity w_p that can be interpreted as *anti-coherence resonance*. This resonance appears for the w_p value, at which the histogram of firing rate distribution contains two peaks with approximately the same amplitudes. This means that the system spends approximately the same amount of time near each metastable state.

5.4.3 Multistate Intermittency in Semiconductor Lasers

Here, we present two examples of multistate intermittency in semiconductor lasers. In the first example, we demonstrate two-state intermittency in the experiment with two mutually coupled semiconductor lasers, while the second example we illustrate multistate intermittency with numerical simulations of a semiconductor laser with delayed feedback.

Coupled semiconductor lasers. The experimental evidence of two-state intermittency was found in two mutually coupled semiconductor lasers [95]. For moderate couplings and pumping currents near the lasing threshold, the optical emission of a laser subject to optical feedback presents power drops in the scale of micro- to nano-seconds, so-called *low-frequency fluctuations* (LFF). For a relatively strong coupling, the lasers operate in the LFF regime and when common noise is applied to the laser pump currents, windows of a steady-state (SS) emission appear in the time series. A probable mechanism for such noise-induced two-state intermittency

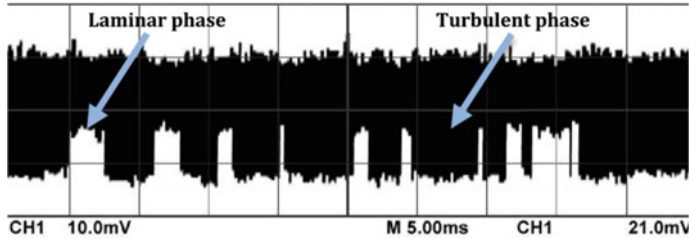


Fig. 5.18 Noise-induced two-state intermittency in coupled semiconductor lasers. The regime of low-frequency fluctuations (LFF) alternates with noisy steady state (SS). The shortest SS length is about 0.12 ms that equivalent approximately to 40000 power drops during all measurements, while the longest SS length is almost 50 ms. Adapted from [95] ©2013 with permission from Elsevier

is the influence of noise on the fixed point stability. The switches appear when the external noise intensity exceeds a threshold value N_{th} . The experimental time series is present in Fig. 5.18.

Time series analysis revealed a power-law scaling typical for on-off intermittency near its onset, with critical exponents of -1 for the mean LFF length versus noise intensity and $-3/2$ for SS phase probability distribution versus the SS length. The same -1 power-law scaling was found by analyzing the power spectrum for the signal-to-noise ratio (SNR) versus the noise intensity.

We will now show that the observed intermittency can also be characterized by a power-law scale for the SNR obtained from the analysis of the frequency spectrum. Figure 5.19 shows a typical power spectrum (averaged over 100 runs) of laser intensity in the regime of intermittency. The spectral component S_{LFF} with a center

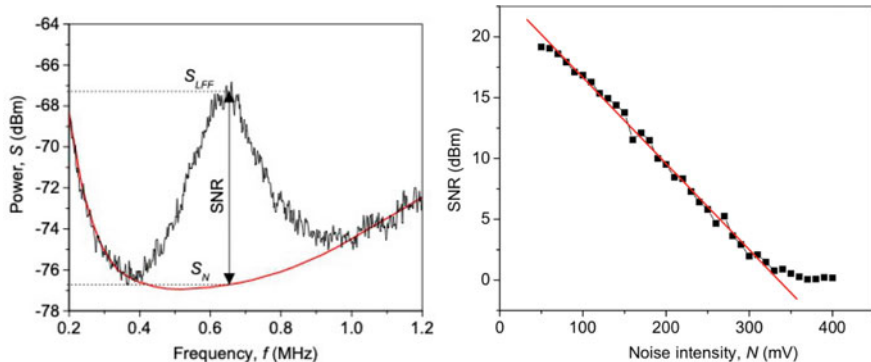


Fig. 5.19 (Left) Laser power spectrum in intermittency regime (upper trace) and interpolated background noise (lower line). Signal-to-noise ratio (SNR) is measured as an excess of the LFF spectral component S_{LFF} over background noise S_N at the central frequency of LFF (about 0.65 MHz). (Right) Signal-to-noise ratio versus noise intensity. The straight line is a linear fit. Adapted from [95] ©2013 with permission from Elsevier

frequency of approximately 0.65 MHz represents the contribution of the LFF phase, while the noise mainly contributes to the background spectral component S_N .

As the noise intensity is increased, the spectral component S_{LFF} decreases while S_N increases, leading to the complete disappearance of the LFF spectral component, which means that the SS phase prevails over the LFF phase. The scaling law can be obtained from the power spectrum by measuring the signal-to-noise ratio as $\text{SNR} = S_{LFF} - S_N$ (dBm) at the center frequency (0.65 MHz) of the LFF mode as a function of the noise intensity. For strong noise, the LFF windows almost disappear in the time series and hence the SNR approaches zero, while the noisy steady state tendency becomes apparent. Near the onset of intermittency, the SNR versus the normalized noise intensity obeys a power law with a critical exponent of about -1 (right panel in Fig. 5.19) that coincides with the scaling ratio obtained from time series analysis. This good agreement reflects the fact that the averaged S_{LFF} is related to the mean duration of the LFF phase.

Semiconductor laser with delayed feedback. Multistability in this laser was demonstrated In Sect. 4.4.1 (see Fig. 4.16). Here, we will show that additive Gaussian white noise induces switching between the coexisting stochastic attractors. This multistate intermittency is observed in the time evolution of the phase delay, as illustrated in the left column of Fig. 5.20.

The middle and right columns show the probability density $P(I)$ of the residence times I the trajectory spends near the stochastic attractors in the log and linear scales, respectively. One can see that for weak noise (Fig. 5.20a), the trajectory spends a large time in the vicinity of each metastable state before it jumps to another state. For stronger noise, the jumps occur more frequently (Fig. 5.20b, c), so that the mean residence time in the stochastic attractors decreases. Finally, for strong noise (Fig. 5.20d, e), all coexisting states are completely mixed, so that they are indistinguishable. As seen from the right column in Fig. 5.20, the probability density exhibits a series of equidistant peaks.

The analysis of the standard deviation of the normalized residence time reveals the existence of two resonances with respect to the noise intensity shown in Fig. 5.21. In particular, for weak noise ($D \approx 0.02 \text{ ns}^{-1}$) sharp coherence resonance (CR) is observed, whereas for stronger noise ($D \approx 0.12 \text{ ns}^{-1}$) wide anti-coherence resonance (ACR) occurs. The coherence is measured using the standard deviation of the normalized residence time on the attractor, $R = \text{std}(I/\langle I \rangle)$. The ACR is also characterized through the $P(I)$ peak strength measured as the area under the peaks. Since an increase in the peak's width means the deterioration of coherence, the maxima in the dependences in the right panel of Fig. 5.21 are anti-coherence resonance.

The appearance of the coherence resonance can be explained by the fact that weak noise induces switches between two states only, which get in resonance with the Kramers times at these states. Whereas, stronger noise involves a larger number of states in the intermittency, thus disordering it leading to anti-coherence resonance. A similar anti-coherence resonance behavior was observed in the network of bistable neurons (see Fig. 5.17).

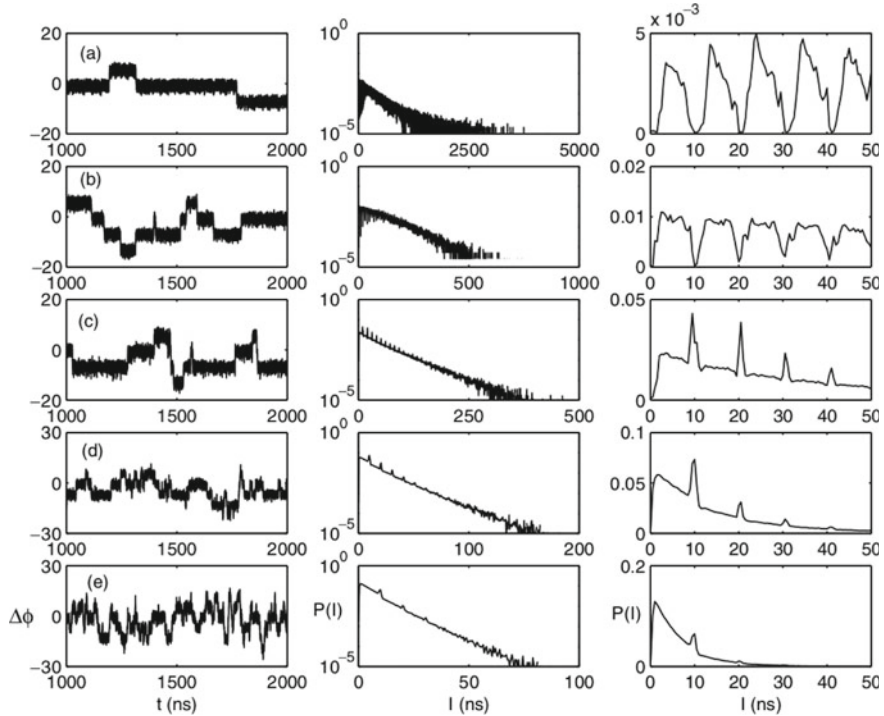


Fig. 5.20 (Left column) Multistate intermittency in a semiconductor laser with delayed feedback for different noise intensities D and (middle and right columns) corresponding probability density of the residence times in the stochastic attractors in log and linear scales. **a** $D = 0.0025 \text{ ns}^{-1}$, **b** $D = 0.0225 \text{ ns}^{-1}$, **c** $D = 0.09 \text{ ns}^{-1}$, **d** $D = 0.16 \text{ ns}^{-1}$, and **e** $D = 0.25 \text{ ns}^{-1}$. Reprinted figure with permission from [96] ©2002 by the American Physical Society

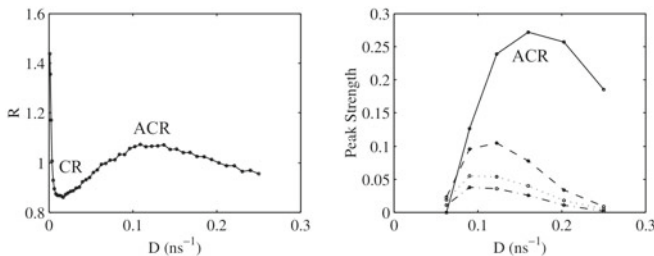


Fig. 5.21 (Left) Standard deviation R of the normalized residence time on an attractor and (right) strengths of the first four peaks of $P(I)$ versus noise intensity D . CR and ACR are coherence and anti-coherence resonances. Reprinted figure with permission from [96] ©2002 by the American Physical Society

5.5 Noise-Induced Preference of Attractors

One of the most interesting effects of noise on a multistable system is noise-induced preference of attractors predicted by Kaneko [72] in coupled logistic maps and observed by Kraut et al. [7] in the model of a periodically kicked mechanical rotor without gravity. Later, a similar behavior was found in coupled logistic maps [72], the Hénon map [97], an erbium-doped fiber laser (EDFL) [8], and a network of coupled FitzHungr–Nagumo oscillators [98].

It was observed that noise changes the size of the basins of attraction of coexisting states, so that some attractors appear more often than others. An interesting feature of this phenomenon is that the size of some of the basins of attraction has a maximum with respect to the noise amplitude. Although this phenomenon is somewhat similar to coherent resonance, it is globally different, because it involves not only the attractors themselves, but also their basins of attraction.

Consider now how noise-induced preference of attractors reveals itself in different dynamical systems.

5.5.1 Attractor Probability Density and Optimal Basin Size

As we mentioned above, any noise, no matter how weak, makes the behavior of a dynamical system probabilistic, that requires a statistical analysis of the final state destination. In this regards, *attractor probability density* and *optimal basin size* are two important quantitative measures of noise-induce preference of attractors in systems with bounded noise. Let us consider how these characteristics can be used on the example of the multistable Hénon map.

In Sect. 3.1.1, we already demonstrated that the deterministic Hénon map given by Eq. 1.11 can exhibit the coexistence of three attractors, period 1 (P1), period 3 (P3), and period 9 (P9), for certain parameters. parameters $J = 0.9$ and $\mu = 1.083$. Figure 5.22 shows the part of the phase space diagram of the deterministic map in the vicinity of one of three P3 points. It is seen that in one region of the phase space the boundary of the basins is smooth, and in the other it is fractal.

Consider now the Hénon map with stochastic terms added to each variable:

$$\begin{aligned} x_{n+1} &= 1 - \mu x_n^2 + y_n + D\xi_n, \\ y_{n+1} &= -Jx_n + D\rho_n, \end{aligned} \tag{5.61}$$

where ξ_n and ρ_n are white zero-mean noise uniformly distributed in the interval $[-1, 1]$ and D is the noise amplitude.

To estimate the probability with which a trajectory starting at a certain initial point ends in one of the coexisting states, we need to calculate the number of initial conditions which lead to each of the coexisting stochastic attractors.

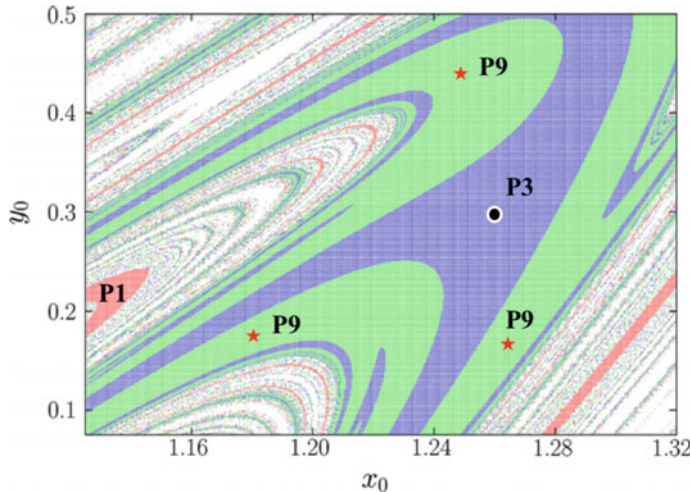


Fig. 5.22 Basins of attraction of three coexisting attractors, period 1 (P1), period 3 (P3), and period 9 (P9), in the deterministic Hénon map Eq. 1.11 for $J = 0.9$ and $\mu = 1.083$. The white region corresponds to the infinity solution. The black dot and three stars indicate the positions of the P3 and P9 fixed points

The examples of probability distributions for two different noise amplitudes are shown in Fig. 5.23. Each basin volume was calculated 1000 times for every fixed value of noise intensity D .

One can note the existence of a maximum probability in the basin size for every coexisting attractor and each noise amplitude, for example, 1.3×10^4 points of P1 for $D = 1.5 \times 10^3$. Since the attractor probability density has a maximum value for a certain basin size, this basin size is optimal for the particular noise amplitude. The optimal basin size N_{max} , which corresponds to the maximum probability, depends on the noise amplitude, as illustrated in Fig. 5.24a. This means that noise of a certain amplitude stabilizes certain attractors, in particular, the period-3 orbit.

As seen from Fig. 5.24a, additive noise has only a weak effect on the probability of the period-1 attractor, while the probabilities of the period 3, period 9, and infinity solutions do vary greatly. Note that very weak noise ($D < 10^{-3}$) does not influence on the statistical properties of the basins in the sense that the number of initial conditions, most likely leading to a particular attractor, is independent of D , but medium noise has a strong effect on the basin volume of attractors P3 and P9, increasing the preference for P3 and decreasing it for P9. Strong noise shrinks the P3 basin's size.

A notable feature of Fig. 5.24a is that the most probable sizes of the basins of attraction P3 and P9 have a non-monotonic character in terms of the noise amplitude. In this sense, the specific noise amplitude ($D_3^{max} \approx 0.0045$ for P3 and $D_9^{max} \approx 0.0085$ for P9) is more preferable for some coexisting attractors than other noise values. The mechanism of this behavior can lie in the interaction between fundamental frequencies (eigenfrequencies) and the Kramers time, which depends on the noise

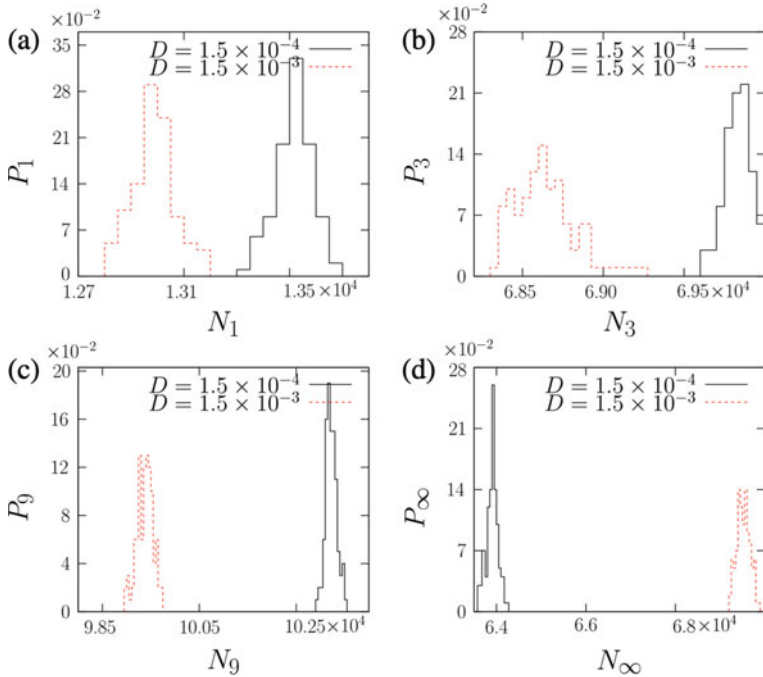


Fig. 5.23 Probability distribution (in %) of the number of points of basins of attraction of **a** P_1 , **b** P_3 , **c** P_9 , and **d** infinity solution P_∞ , for two different noise amplitudes D by exploring 2.5×10^5 initial conditions of the Hénon map in the range of $x_0, y_0 \in [1.125, 1.325], [0.075, 0.5]$. Reprinted from [97] ©2012 with permission from Elsevier

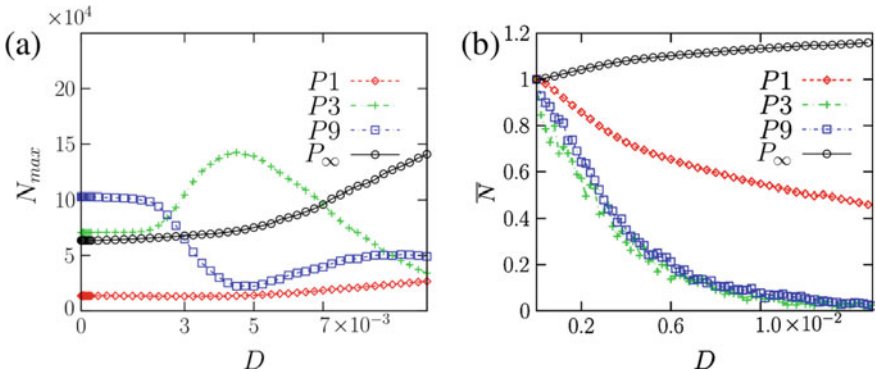


Fig. 5.24 **a** Optimal basin size N_{max} of P_1 (diamonds), P_3 (crosses), P_9 (squares), and P_∞ solutions and **b** normalized average size \bar{N} , as a function of noise amplitude D . Reprinted from [97] ©2012 with permission from Elsevier

amplitude. It is important to note that such a non-monotonic dependence is relevant only for the most probable basin size (attractor preference), but not for the average size \bar{N} , as seen from Fig. 5.24b, where we plot the arithmetic mean of all measurements for the same noise amplitude of each coexisting attractor, normalized to the basin size of the corresponding deterministic attractor, as a function of D . As seen from the figure, for all coexisting attractors, this function decreases monotonically with increasing noise amplitude, with a noticeable preference for the infinity solution.

The statistical analysis is the best way to demonstrate how bounded noise affects attractors and their basins of attraction and modifies the global phase-space structure.

5.5.2 Experimental Evidence of Noise-Induced Preference of Attractors

Among numerous experiments on noise-induced attractor preference, we will focus on the attractor preference on the example of the erbium-doped fiber laser (EDFL) with optical pumping from a laser diode, whose current was modulated by the sum of harmonic and random signals $A_m \sin(2\pi f_m t) + N_{in} G(\xi, f_n)$ from signal and noise generators. Here, A_m and f_m are the amplitude and frequency of the external harmonic modulation, respectively, N_{in} is the input noise intensity, and $G(\xi, f_n)$ is the zero-mean noise function in terms of a random number $\xi \in [-1, 1]$ and noise cutoff frequency f_n .

The EDFL under pump modulation displays very rich dynamics exhibiting the coexistence of different periodic orbits (see Sect. 4.5.2). The experimental bifurcation diagram the EDFL peak intensity with additional noise ($N_n = 0$) versus driving frequency f_m is present in Fig. 5.25.

Adding noise shifts the positions of the branches of attractors in the bifurcation diagram, and sufficiently strong noise makes the laser metastable and results in multistate intermittency. As the noise intensity is increased, more and more periodic orbits are involved in the hopping dynamics over a wider range of the parameters, for example, P1, P3, P4, and P5. Moreover, higher-periodic orbits, not existed in the noiseless laser, appear. In addition, basins of some attractors become larger in the presence of noise.

For relatively weak noise, the laser operates in a periodic state determined by the initial conditions. For instance, if the laser starts with initial conditions corresponding to P3, it will remain in this state for an infinitely long time showing noisy oscillations with frequency $f_m/3$. When the noise intensity is increased, the laser starts jumping back and forth from P3 to P1 (Fig. 5.26a). For stronger noise, the trajectory visits three periodic states (P1, P3, and P4) (Fig. 5.26b). A further increase in the noise intensity induces jumps between five periodic orbits (P1, P3, P4, and P5) (Fig. 5.26c). Finally, for very strong input noise all periodic states are completely mixed and cannot be distinguished.

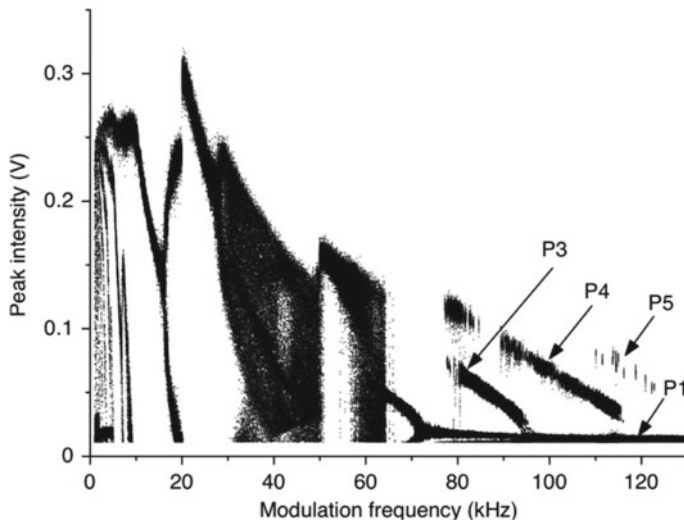
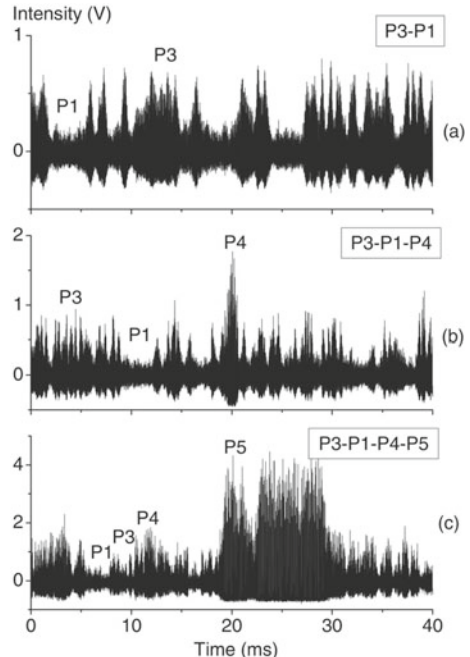


Fig. 5.25 Experimental bifurcation diagram of the fiber laser peak intensity versus the modulation frequency f_m at the fixed driving amplitude $m_d = 0.8$ V. P1, P3, P4, and P5 indicate branches of period-1, period-3, period-4, and period-5 attractors found by switching on and off the signal generator that is equivalent to a random change of the initial conditions. The diagram is obtained by recording the laser output after transients. Reprinted figure with permission from [8] ©2011 by the American Physical Society

Fig. 5.26 Multistate intermittency involving **a** two periodic orbits at $N_{in} = 0.5$ V, **b** three periodic orbits $N_{in} = 0.9$ V, and **c** four periodic orbits at $N_{in} = 1.5$ V. Note the difference in the intensity scales. Reprinted figure with permission from [99] ©2008 by the American Physical Society



One can see that the time series in Fig. 5.26 are very noisy. This is evident because input noise N_{in} is amplified by the system resulting in output noise N_{out} that can be estimated from the power spectra as a background spectral energy at the modulation frequency f_m , as was explained in Sect. 5.4.3 (see Fig. 5.19).

The experiments with the multistable EDFL have shown that noise-induced multistate intermittency can be characterized by the following measures:

- Output noise versus input noise.
- Probability of visiting coexisting metastable states versus input noise.
- Mean escape time versus input noise.
- Probability distribution of residence time.

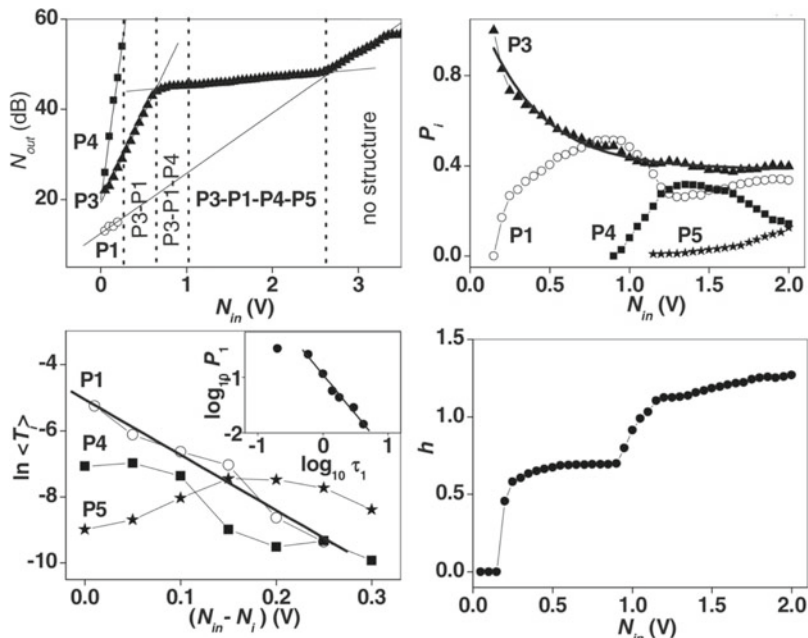


Fig. 5.27 (Left upper panel) Average output versus output noise intensity in coexisting states in periodic (\circ P1, \blacktriangle P3, \blacksquare P4) and intermittency regimes. The dotted lines show the onsets of different intermittency regimes. The solid lines are linear fits of the slopes. The coexistence of three stochastic attractors is observed only for very weak input $N_{in} < 0.2$ V. The noise saturation effect is clearly seen in the middle part of the figure. (Right upper panel) Probability of visiting different attracting sets calculated by summing the duration of periodic windows in ten time series for every noise level. The bold line is the exponential decay fit for the period-3 orbit. (Left down panel) Mean escape times T_i for different attracting sets as a function of the noise intensity excess over critical noise value N_i at the onset of intermittency for the period- i state ($N_{1,4,5} = 190, 800, 1150$ mV). The inset shows the scaling of the probability distribution for the residence time in the period-1 windows inside the intermittent P3-P1 regime showing the $-3/2$ power law (straight line) for $N_{in} = 200$ mV. (Right down panel) Shannon entropy of the symbol sequence versus input noise intensity. Reprinted figure with permission from [99] ©2008 by the American Physical Society

- Shannon entropy of symbolic sequence versus input noise.

All these properties of noise-induced intermittency in the EDFL are displayed in Fig. 5.27. In particular, Fig. 5.27 (left upper panel) shows the dependence of the average spectral energy of output noise N_{out} at the modulation frequency f_m on the input noise intensity N_{in} . Within the time window corresponding to each state (P1, P3, P4), the average output noise obeys a linear dependence on the input noise amplitude (solid lines) whose slope increases with the orbit's period, i.e., the larger the period, the higher the slope. The linear dependence in the semilog scale corresponds to the exponential dependence $N_{out} \sim \exp(\lambda_i N_{in})$, where λ_i is the scaling exponent of the i -periodic orbit ($\lambda_1 = 1.54$, $\lambda_3 = 4.52$, $\lambda_4 = 15.89$, $\lambda_{3-1-4} = 0.20$).

Similar to other types of intermittency, noise-induced multistate intermittency can be characterized by specific scaling laws. To determine the physical mechanisms responsible for the scaling relationships, a statistical approach can be used. To be more specific, we are interested in the nonzero probability of the transition of each periodic orbit to any other periodic orbit through a transient process on a chaotic saddle, i.e. the probability P_i of which the trajectory will visit the i -periodic orbit. Figure 5.27 (right upper panel) shows the dependence of P_i on the input noise intensity N_{in} . In the intermittency dynamics, the probability P_3 of visiting the P3 orbit exponentially decreases as N_{in} is increased (bold line). At the same time, the probability P_1 of visiting P1 increases with increasing N_{in} until the P4 windows appear, that results in decreasing P_1 .

The bifurcation responsible for switching between different noisy periodic states can be regarded as a kind of crisis, and, therefore, the process can be characterized by scaling law for characteristic lifetimes. While for two-state intermittency only two attracting sets are involved in the switching dynamics, and hence only one critical parameter (usually noise intensity) is responsible for the onset of intermittency, in multistate intermittency there is a critical noise amplitude N_i for each i -periodic orbit. In the other words, the trajectory visits the period- i orbit only when $N_{in} > N_i$. Therefore, it is important to estimate the average escape time $\langle T_i \rangle$ from the period- i state, as a function of the excess of the noise intensity over its critical value, i.e. $N_{in} - N_i$. These dependences for every coexisting state are present in Fig. 5.27 (left down panel). For P1, the mean residence time $\langle T_i \rangle$ obeys by the exponential decay shown by the straight line. However, for other periods the dynamics is very different, for example, the mean residence time in P5 increases with noise and has a maximum.

Another characteristic of multistate intermittency is the probability distribution $P(\tau)$ of the residence time τ near a certain coexisting regime. Such a dependence for the period-1 orbit (P_1) in the P1–P3 intermittency is present in the inset of Fig. 5.27 (left down panel). One can see this probability obeys the universal scaling law $P(\tau_1) \sim \tau_1^{-3/2}$, the same as for one-state and two-state on-off intermittency [95] (see Sect. 5.4.3).

As was shown in Sect. 5.3.3, multistate intermittency can be quantified into symbolic sequences of n elements in which the trajectory visits different attracting sets, crossing chaotic sets at the boundaries. By assigning a symbol $s_i = 1, 2, 3, 4$ to each periodic orbit i that arises in multistate intermittency, it is possible to estimate the complexity of the symbolic string among the attracting sets using the Shannon entropy given by Eq. 5.52. The dependence of the entropy h on the input noise is present in Fig. 5.27 (right down panel). For weak noise, each periodic sequence gives $h = 0$. The entropy increases rapidly at the bifurcation point when a new regime appears in the jumping dynamics, and then it is almost constant. The emergence of nontrivial time scaling in a noisy laser is a consequence of a complex interaction between coherent and random structures. The existence of a certain coherent structure in the set of all possible symbol sequences results in almost horizontal plateaus.

5.5.3 Extreme Events in Multistable Systems

Extreme events are events characterized by a large amplitude (more than twice that of the average amplitude of normal events) which rarely and unpredictably happen in dynamical systems. A specific property of such events is the L -shaped probability distribution of the amplitudes in a semilog scale.

Extreme events were observed in both stochastic and deterministic system. The examples are rogue waves in the ocean [100], plasma [101], optical system [102], finance [103], multistable laser [8], as well as in brain diseases, such as epilepsy [104, 105]. One of the mechanisms underlying the formation of extreme events is noise-induced multistate intermittency.

Let us demonstrate how extreme events appear in a multistable erbium-doped fiber laser (EDFL) with pump modulation. As was shown in Sects. 4.5.2 and 5.5.2, this laser exhibits the coexisting of several periodic orbits, in particular, period 1, period 3, period 4, and period 5. Under external noise applied to the diode-pumped current, the laser switches among these state representing multistate intermittency.

Here, we analyze the conditions for the occurrence of extreme events and show how their probability can be controlled using the noise amplitude and the cutoff frequency of a low-pass filter. The probability of visiting different states is defined by the noise amplitude and low-pass filtering frequency. At certain parameter values, rare laser pulses with extremely large amplitude are observed. The example of the extreme event in the EDFL is illustrated in Fig. 5.28.

As seen from Fig. 5.28 the laser being in the period-1 state switches to the period-4 metastable state for a very short time and then come back. The probability density of the laser peak intensity for different noise amplitudes is shown in Fig. 5.29.

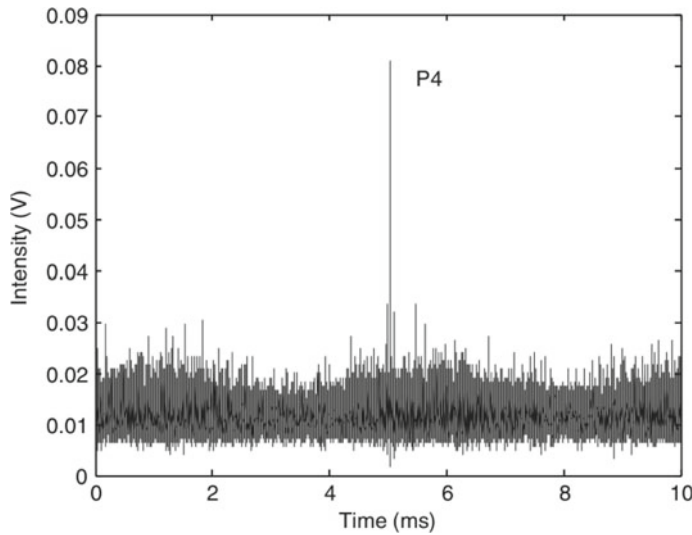


Fig. 5.28 Extreme event in a multistable erbium-doped fiber laser. Oscilloscope recording of laser oscillations demonstrating a rare visiting of the period-4 state induced by loss-pass filtered noise with amplitude $\nu = 0.5$ V and cutting frequency $f_n = 7$ kHz, $f_d = 90$ kHz, $m_d = 0.8$ V

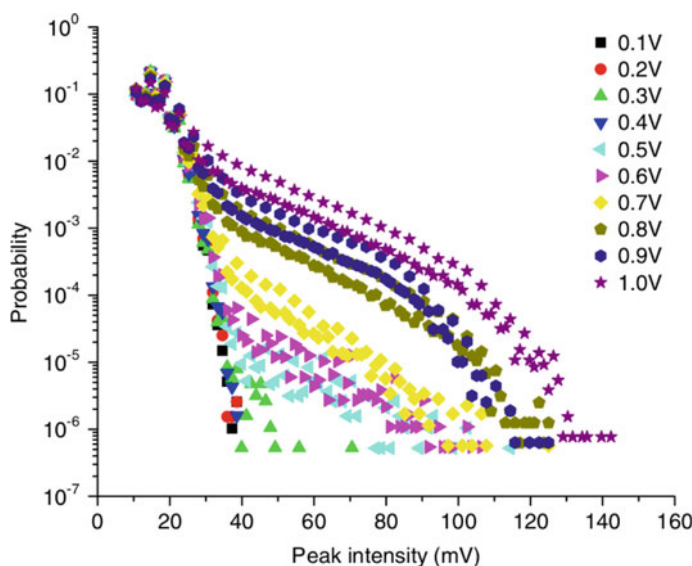


Fig. 5.29 Probability density functions of laser peak intensity for different noise amplitudes filtered at 7 kHz

As can be seen from Fig. 5.29, very high intensity pulses appear much more often than according to Gaussian statistics; this confirms the nature of extreme events. Since noise converts the multistable system into a metastable system, the peak intensity is not the same as in the deterministic system. One sees that for weak noise the probability density function has a *L* shape, that is a particular feature of extreme events.

Thus, the preference of some states in multistate intermittency is defined by the nonmonotonically on the noise amplitude, i.e. there is a certain noise level for which a particular state appears more frequently likely than at other noise amplitudes. This result is consistent with the preference for nonmonotonic attractors observed in the multistable Hénon map (see Sect. 5.5.1).

5.5.4 Preference of Attractors in a Network of Coupled Oscillators

Finally, consider how noise can induce preference for some attractors in a network of coupled oscillators.

In locally coupled excitable systems, noise can strongly affect patterning by inducing, amplifying or controlling wave propagation, spiral dynamics, and stimulation [106]. However, the deterministic dynamics of non-locally connected arrays has an additional feature, namely, the coexistence of multiple attractors, such that the main effect of noise is qualitatively different. In such systems, noise reduces the number of coexisting attractors, suppressing solitary states and thus inducing preference for individual attractors [37].

This process can be understood as follows. In systems with many attractors, noise smears the attractor boundaries so that only those attractors remain that have sufficiently large basins of attraction. When noise is relatively weak, unbalanced frequency clustering is still preserved, but the preferred spatial distribution of minority units is localized rather than random. This results in 1:2 subharmonic frequency-locking synchronization patterns, as shown in Fig. 5.30 which illustrates how noise transforms the initial configuration into a synchronous state.

Thus, in complex networks noise can suppress multistability by promoting certain types of cluster states as well as patched patterns at the expense of solitary states.

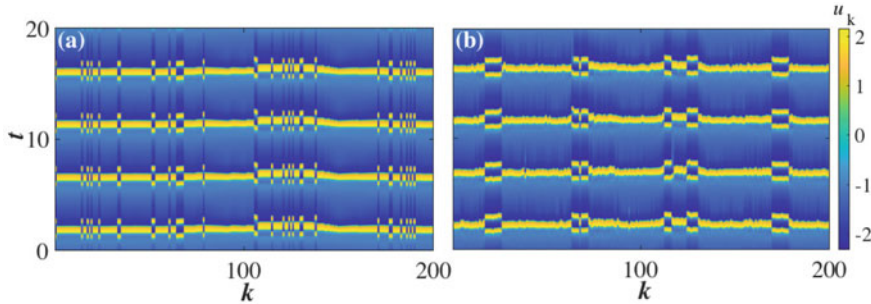


Fig. 5.30 Noise-improved coherence in the network of FitzHunger–Nagumo oscillators. Transformation of solitary states into patched states under noise. **a** Typical spatio-temporal dynamics without noise. **b** Transformation of solitary states into patched states under weak noise. Reproduced from [98] with permission of AIP Publishing

5.6 Multistate Intermittency in Deterministic Systems

Apart from random perturbations, multistate intermittency can also be induced by periodic forcing in chaotic systems with coexisting attractors. We will show how multistate intermittency can arise in periodically modulated deterministic systems on the examples of the Duffing oscillator and a semiconductor laser with external cavities.

5.6.1 Multistate Intermittency Induced by Periodic Forcing

Two-state on-off intermittency induced by periodic forcing was investigated by Lai and colleagues [65, 107] in the system with two symmetric invariant subspaces when their basins of attraction are intermingled. In particular, they considered the two-dimensional Duffing oscillator

$$\ddot{\mathbf{x}} = -\alpha \dot{\mathbf{x}} - \nabla(\mathbf{x}) + f_0 \sin(\omega t) \mathbf{x}_0, \quad (5.62)$$

where $\mathbf{x} \equiv (x, y)$, α is the friction coefficient, \mathbf{x}_0 and $f_0 \sin(\omega t)$ (f_0 and ω being the amplitude and frequency) are respectively the unit vector and periodic forcing in the x direction. The oscillator moves in the double-well potential

$$V(\mathbf{x}) = (1 - x^2)^2 + (y^2 - a^2)^2(x - d) + b(y^2 - a^2)^4. \quad (5.63)$$

For parameter values $a = 0.8$, $b = 0.008$, $d = -1.8$, $f_0 = 2.3$, $\alpha = 0.05$, and $\omega = 3.5$, the oscillator in Eq. 5.62 exhibits two-state intermittency in the double-well potential Eq. 5.63, as illustrated in Fig. 5.31.

The system state, after departing from a given state, stays in the vicinity of another state, and the transient behavior in between these states is governed by a chaotic saddle (see Sect. 5.1.1). The two-state intermittency arises due to the fact that the perpendicular Lyapunov exponents with respect to both invariant subspaces are weakly positive ($\lambda_{\perp} \approx 0.0006$). Therefore, the trajectory stays for a long time in the vicinity of one invariant subspace, then repels from this subspace, and possibly is attracted to another invariant subspace or to the same subspace, and so on. The two metastable states correspond to two holes in the potential $V(x, y)$ in the y direction. The perpendicular (or transverse) Lyapunov exponents are defined as [107]

$$\lambda_{\perp}^i = \lim_{N \rightarrow \infty} \frac{1}{N} \sum_{n=1}^N \ln |\mathbf{DG}(\mathbf{x}_n, \mathbf{y}_n)|_{\mathbf{y}_n=\mathbf{b}} \cdot \mathbf{u}_i | \quad (5.64)$$

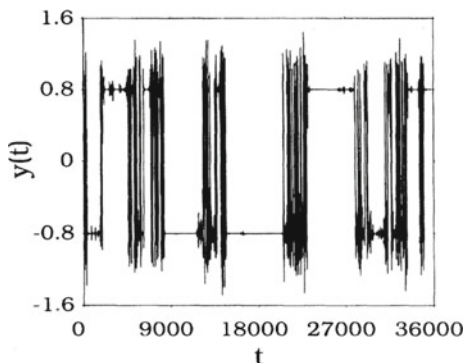
in the perpendicular subspace

$$\mathbf{y}_{n+1} = \mathbf{G}(\mathbf{x}_n, \mathbf{y}_n), \quad (5.65)$$

where $\mathbf{x}_n \in \mathbb{R}^{N_{\parallel}}$ are dynamical variables in the N_{\parallel} -dimensional invariant subspace defined by $\mathbf{y}_n = \mathbf{b}$, $\mathbf{y}_n \in \mathbb{R}^{N_{\perp}}$ are dynamical variables in the N_{\perp} -dimensional invariant subspace perpendicular to $\mathbb{R}^{N_{\parallel}}$ ($N_{\parallel} + N_{\perp} = N$), $\mathbf{DG}(\mathbf{x}_n, \mathbf{y}_n)_{\mathbf{y}_n=\mathbf{b}}$ is the Jacobian matrix of the map \mathbf{G} evaluated at $\mathbf{y}_n = \mathbf{b}$, and \mathbf{u}_i is one of the eigenvectors in the eigenspace of $\Pi_{n=1}^{\infty} \mathbf{DG}((\mathbf{x}_n, \mathbf{y}_n))$. For a randomly chosen unit vector \mathbf{u} , Eq. 5.64 gives the largest perpendicular Lyapunov exponent denoted by λ_{\perp} . Since λ_{\perp} is slightly positive, most of the trajectories go away from the invariant subspace $\mathbf{y}_n = \mathbf{b}$. However, a few trajectories are attracted and stay near the invariant subspace.

It was found that time intervals when the trajectory stays in the vicinity of the metastable states, or the length of the laminar phase defined as time T between successive switches, obeys certain probability distribution $P(T) \sim T^{-3/2}$. This scaling relation is typical for on-off intermittency.

Fig. 5.31 Two-state intermittency induced by a periodic forcing in the Duffing oscillator given by Eq. 5.62. Reprinted figure with permission from [65] ©1995 by the American Physical Society



It should be noted that the $-3/2$ scaling relation is universal. As we demonstrated in Sect. 5.4.3, this scaling exponent was found for noise-induced two-state intermittency between SS and LFF states in the coupled semiconductor lasers. In addition, the same scaling relation was found experimentally between two states with different polarization in a VCSEL with optical injection [108].

5.6.2 Modulational Intermittency in a Semiconductor Laser

Another typical scaling relation for two-state on-off intermittency is the -1 power law of the mean laminar phase (the time the system spends in the vicinity of one state) versus the control parameter near the onset of intermittency. This scaling exponent was experimentally verified in a semiconductor laser with two external cavities [68].

With a single external cavity, the laser generates a steady state emission of radiation at $\lambda_1 = 631.505 \mu\text{m}$ wavelength, whereas with two external cavities, another

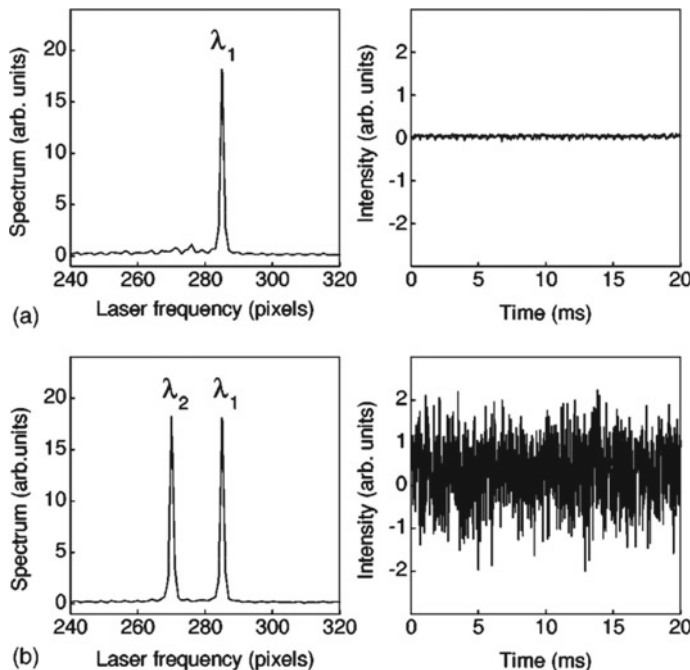
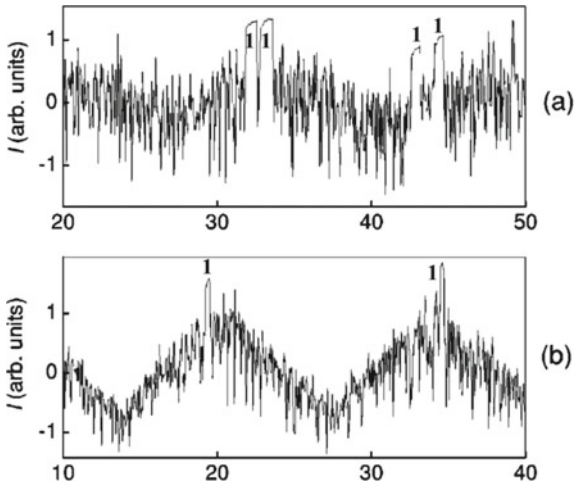


Fig. 5.32 (Left column) Optical spectrum and (right column) corresponding time series of the semiconductor laser radiation with **a** single external cavity and **b** two external cavities. By tuning the grating with a piezo actuator, the gain factors of the two laser modes is adjusted to have approximately the same values. From [68]

Fig. 5.33 Time series of the laser output representing two-state intermittency in the presence of cavity detuning modulation for
a $A = 100$ mV and
b 250 mV at $f = 73$ Hz. The laminar phases are marked with **1**



wavelength $\lambda_1 = 630.866 \mu\text{m}$ appears, that leads to chaotic oscillations. The optical spectrum and time series for both cases are shown in Fig. 5.32.

To observe two-state intermittency, a periodic voltage is applied to the piezo actuator which tunes the grating in order to align and disalign the second cavity during the modulation period. The short temporal traces of the laser output are shown in Fig. 5.33 for two amplitudes A of a periodic signal applied to the piezo actuator and fixed modulation frequency f .

When the second cavity is cut off, the laser operates in a single-mode regime at λ_1 (**1**) with a stable steady state emission, otherwise the chaotic two-mode regime occurs and the laser operates in the chaotic two-mode regime at λ_1 and λ_2 .

Thus, there are two temporally attractive states: the two-mode chaotic state and the single-mode laser emission. The two-state intermittency arises when the cavity detuning passes through the onset of intermittency. One can see from Fig. 5.33 that the mean duration of the laminar phase (single-mode steady state) decreases as the modulation A is increased.

Both the amplitude and frequency variations are equivalent to a change in the velocity v at which the control parameter (cavity detuning) crosses the onset of intermittency. It was found that the scaling relations between the mean duration of the laminar phase τ and the velocity v is

$$\tau \sim v^{-1}. \quad (5.66)$$

This critical exponent coincides with the power law theoretically predicted for on-off intermittency in the case of random driving, that confirms its universality.

References

1. Graham R, Tél T (1986) Nonequilibrium potential for coexisting attractors. *Phys Rev A* 33:1322–1337
2. Grassberger P (1989) Noise-induced escape from attractors. *J Phys A* 22:3283–3290
3. Gammaitoni L, Hänggi P, Jung P, Marchesoni F (1998) Stochastic resonance. *Rev Mod Phys* 70:223–287
4. Nicolis C (2012) Stochastic resonance in multistable systems: the role of dimensionality. *Phys Rev E* 86:011133
5. Nicolis G, Nicolis C (2016) Stochastic resonance, self-organization and information dynamics in multistable systems. *Entropy* 18(5):172
6. Pisarchik AN, Jaimes-Reátegui R, Sevilla-Escoboza R, Huerta-Cuellar G (2012) Multistate intermittency and extreme pulses in a fiber laser. *Phys Rev E* 86:056219
7. Kraut S, Feudel U, Grebogi C (1999) Preference of attractors in noisy multistable systems. *Phys Rev E* 59:5253–5260
8. Pisarchik AN, Jaimes-Reátegui R, Sevilla-Escoboza R, Huerta-Cuellar G, Taki M (2011) Rogue waves in a multistable fiber laser. *Phys Rev Lett* 107:274101
9. Pisarchik AN, Maksimenko VA, Andreev AV, Makarov VV, Zhuravlev MO, Frolov NS, Runnova AE, Hramov AE (2019) Coherent resonance in the distributed cortical network during sensory information. *Sci Rep* 9:18325
10. Billings L, Schwartz IB (2008) Identifying almost invariant sets in stochastic dynamical systems. *Chaos* 18:023122
11. Freidlin MI, Wentzell AD (1984) Random perturbations of dynamical systems. Springer, Berlin
12. Kifer Y (1988) Random perturbations of dynamical systems. Birkhäuser, Boston
13. Zhou JX, Aliyu MDS, Aurell E, Huang S (2012) Quasi-potential landscape in complex multi-stable systems. *J R Soc Interface* 9:3539–3553
14. Hammel SM, Jones CKRT, Moloney JV (1985) Global dynamical behavior of the optical field in a ring cavity. *J Opt Soc Am B* 2(4):552–564
15. Ikeda K (1979) Multiple-valued stationary state and its instability of the transmitted light by a ring cavity system. *Opt Commun* 30:257–261
16. Kraut S, Feudel U (2003) Enhancement of noise-induced escape through the existence of a chaotic saddle. *Phys Rev E* 67:015204(R)
17. Khovanov IA, Luchinsky DG, McClintock PVE, Silchenko AN (2008) Fluctuational escape from chaotic attractors in multistable systems. *Int J Bifurc Chaos* 18:1727–1739
18. Silchenko AN, Beri S, Luchinsky DG, McClintock PVE (2003) Escape from a chaotic attractor with fractal basin boundaries. *Proc SPIE* 5114(4):102–107
19. Dykman MI, Krivoglaz MA (1979) Theory of the fluctuational transitions between the stable states of a nonlinear oscillator. *Sov Phys—JETP* 50:30–37
20. Soskin SM, Arrays M, Mannella R, Silchenko AN (2001) Strong enhancement of the noise-induced escape by non-adiabatic periodic driving due to transient chaos. *Phys Rev E* 63:051111
21. Holmes P (1979) A nonlinear oscillator with a strange attractor. *Philos Trans R Soc A* 292:419–448
22. Bashkirtseva IA, Ryashko LB (2000) Sensitivity analysis of the stochastically and periodically forced Brusselator. *Phys A Stat Mech Appl* 278:126–139
23. Benzi R, Sutera A, Vulpiani A (1981) The mechanism of stochastic resonance. *J Phys A* 14:L453–L457
24. McNamara B, Wiesenfeld K (1989) Theory of stochastic resonance. *Phys Rev A* 39:4854–4869
25. Pikovsky AS, Kurths J (1997) Coherence resonance in a noise-driven excitable system. *Phys Rev Lett* 78:775–778
26. Andreev AV, Makarov VV, Runnova AE, Pisarchik AN, Hramov AE (2018) Coherence resonance in stimulated neuronal network. *Chaos Soliton Fractals* 106:80–85

27. Franaszek M, Simiu E (1996) Stochastic resonance: a chaotic dynamics approach. *Phys Rev E* 54:1298–1304
28. Pisarchik AN, Corbalán R (1998) Stochastic resonance in a chaotic laser. *Phys Rev E* 58(3):R2697–R2700
29. Pisarchik AN, Jaimes-Reátegui R (2015) Deterministic coherence resonance in coupled chaotic oscillators with frequency mismatch. *Phys Rev E* 92:050901
30. García-Vellisca MA, Pisarchik AN, Jaimes-Reátegui R (2016) Experimental evidence of deterministic coherence resonance in coupled chaotic oscillators with frequency mismatch. *Phys Rev E* 94:012218
31. Kramers HA (1940) Brownian motion in a field of force and the diffusion model of chemical reactions. *Physica (Utrecht)* 7:284–304
32. Lin YK, Cai GQ (1995) Probabilistic structural dynamics—advanced theory and applications. McGraw-Hill, New York
33. Cover TM, Thomas JA (1991) Elements of information theory. Wiley, New York
34. McDonnell MD, Stock NG, Pearce CEM, Abbott D (2008) Stochastic resonance: from suprathreshold stochastic resonance to stochastic signal quantization. Cambridge University Press, New York
35. Shannon CE (1949) Communication in the presence of noise. *Proc IRE* 37:10–21
36. Yang W, Ding M, Gang H (1995) Trajectory (phase) selection in multistable systems: Stochastic resonance, signal bias, and the effect of signal phase. *Phys Rev Lett* 74:3955–3958
37. Pisarchik AN, Feudel U (2014) Control of multistability. *Phys Rep* 540:167–218
38. Reibold E, Just W, Becker J, Benner H (1997) Stochastic resonance in chaotic spin-wave dynamics. *Phys Rev Lett* 78:3101–3104
39. Pisarchik AN (1998) Dynamical tracking of unstable periodic orbits. *Phys Lett A* 242:152–162
40. Murali K, Sinha S, Ditto WL, Bulsara AR (2009) Reliable logic circuit elements that exploit nonlinearity in the presence of a noise-floor. *Phys Rev Lett* 102:104101
41. Aravind M, Parmananda P, Sinha S (2021) Emergent noise-aided logic through synchronization. *Phys Rev E* 104:064207
42. Sinha S, Cruz J, Buhse T, Parmananda P (2009) Exploiting the effect of noise on a chemical system to obtain logic gates. *Europhys Lett* 86(6):60003
43. Ando H, Sinha S, Storni R, Aihara K (2011) Synthetic gene networks as potential flexible parallel logic gates. *Europhys Lett* 93(3):50001
44. Zhang L, Zheng W, Song A (2018) Adaptive logical stochastic resonance in time-delayed synthetic genetic networks. *Chaos* 28(3):043117
45. Zamora-Munt J, Masoller C (2010) Numerical implementation of a VCSEL-based stochastic logic gate via polarization bistability. *Opt Exp* 18(16):16418
46. Singh KP, Sinha S (2011) Enhancement of “logical” responses by noise in a bistable optical system. *Phys Rev E* 83:046219
47. Pfeffer P, Hartmann F, Hoing S, Kamp M, Worschech L (2015) Logical stochastic resonance with a Coulomb-coupled quantum-dot rectifier. *Phys Rev Appl* 4:014011
48. Aravindh MS, Venkatesan A, A, Lakshmanan M, (2018) Strange nonchaotic attractors for computation. *Phys Rev E* 97:052212
49. Murali K, Sinha S, Kohar V, Kia B, Ditto WL (2018) Chaotic attractor hopping yields logic operations. *Plos One* 13:e0209037
50. Murali K, Sinha S, Kohar V, Ditto WL (2021) Harnessing tipping points for logic operations. *Eur Phys J Spec Top*
51. Zhang H, Xu Y, Xu W, Li X (2012) Logical stochastic resonance in triple-well potential systems driven by colored noise. *Chaos* 22:043130
52. Ashokkumar P, Aravindh MS, Venkatesan A, Lakshmanan M (2021) Realization of all logic gates and memory latch in the SC-CNN cell of the simple nonlinear MLC circuit. *Chaos* 31:063119
53. Shen RC, Wang YP, Li J, Zhu SY, Agarwal GS, You JQ (2021) Long-time memory and ternary logic gate using a multistable cavity magnonic system. *Phys Rev Lett* 127:183202

54. Hou M, Yang J, Shi S, Liu H (2020) Logical stochastic resonance in a nonlinear fractional-order system. *Eur Phys J Plus* 135:747
55. Pomeau Y, Manneville P (1979) Intermittent and the Lorenz model. *Phys Lett A* 75(1,2):1–2
56. Kyprianidis IM, Petrani ML, Kalomiros JA, Anagnostopoulos AN (1995) Crisis-induced intermittency in a third-order electrical circuit. *Phys Rev E* 52(2):2268–2273
57. Pisarchik AN, Kir'yanov AV, Barmenkov YO, Jaimes-Reátegui R (2005) Dynamics of an erbium-doped fiber laser with pump modulation: Theory and experiment. *J Opt Soc Am B* 22(10):2107–2114
58. Perez Velazquez JL, Khosravani H, Lozano A, Bardakjian BL, Carlen PL, Wennberg R (1999) Type III intermittency in human partial epilepsy. *Eur J Neurosci* 51(7):2571–2576
59. Grebogi C, Ott E, Romeiras J, Yorke JA (1987) Critical exponents for crisis-induced intermittency. *Phys Rev A* 36:5365–5380
60. Bergé P, Pomeau Y, Vidal C (1988) *L'Ordre Dans Le Chaos*. Hermann, Paris
61. Pikovsky AS, Osipov GV, Rosenblum MG, Zaks M, Kurths J (1997) Attractor-repeller collision and eyelet intermittency at the transition to phase synchronization. *Phys Rev Lett* 79:47–50
62. Hramov AE, Koronovskii AA, Kurovskaya MK, Boccaletti S (2006) Ring intermittency in coupled chaotic oscillators at the boundary of phase synchronization. *Phys Rev Lett* 97:114101
63. Platt EA, Spiegel EA, Tresser C (1993) On-off intermittency: a mechanism for bursting. *Phys Rev Lett* 70(3):279–282
64. Arechi FT, Califano A (1984) Low-frequency hopping phenomena in a nonlinear system with many attractors. *Phys Lett* 101A(9):443–446
65. Lai YC, Grebogi C (1995) Itermingled basins and two-state on-off intermittency. *Phys Rev E* 52(4):R3313–R3316
66. Fujisaka H, Kamifukumoto H, Inoue M (1982) Intermittency associated with the breakdown of the chaos symmetry. *Prog Theor Phys* 69(1):333–337
67. Ott E (1993) *Chaos in dynamical systems*. Cambridge University Press, New York
68. Pisarchik AN, Pinto-Robledo VJ (2002) Experimental observation of two-state on-off intermittency. *Phys Rev E* 66(2):027203
69. Poon L, Grebogi C (1995) Controlling complexity. *Phys Rev Lett* 75:4023–4026
70. Foss J, Longtin A, Mensour B, Milton J (1996) Multistability and delayed recurrent loops. *Phys Rev Lett* 76(4):708–711
71. Moskalenko OI, Koronovskii AA, Zhuravlev MO, Hramov AE (2018) Characteristics of noise-induced intermittency. *Chaos Solitons Fractals* 117(1):269–275
72. Kaneko K (1997) Dominance of milnor attractors and noise-induced selection in a multiafftractor system. *Phys Rev Lett* 78:2736–2739
73. Shannon CE (1948) The mathematical theory of communication. *Bell Syst Tech J* 27:379–423
74. Kolmogorov AN (1958) A new metric invariant of transitive dynamical systems and automorphisms in Lebesgue space. *Dokl Acad Nauk SSSR* 119:861–864
75. Sinai YG (1959) On the concept of entropy of a dynamical system. *Dokl Acad Nauk SSSR* 124:768–771
76. Alder RL, Konheim AG, McAndrew MH (1965) Topological entropy. *Trans Am Math Soc* 114:309–319
77. Hao BL (1989) *Elementary symbolic dynamics and Chaos in dissipative systems*. World Scientific, Singapore
78. Hramov AE, Koronovskii AA, Kurovskaya MK, Moskalenko OI (2011) Type-i intermittency with noise versus eyelet intermittency. *Phys Lett A* 375:1646–1652
79. Hramov AE, Koronovskii AA, Moskalenko OI, Zhuravlev MO, Ponomarenko VI, Prokhorov MD (2013) Intermittency of intermittencies. *Chaos* 23(3):033129
80. Hramov AE, Koronovskii AA, Moskalenko OI, Zhuravlev MO, Jaimes-Reátegui R, Pisarchik AN (2016) Separation of coexisting dynamical regimes in multistate intermittency based on wavelet spectrum energies in an erbium-doped fiber laser. *Phys Rev E* 93:052218
81. Hramov AE, Koronovskii AA, Makarov VA, Pavlov AN, Sitnikova E (2015) *Wavelets in neuroscience*. Springer, Heidelberg

82. Chua LO, Komuro M, Matsumoto T (1986) The double scroll family. *IEEE Trans Circuits Syst* 33(11):1073–1118
83. Laurent M, Kellershohn N (1999) Multistability: A major means of differentiation and evolution in biological systems. *Trends Biochem Sci* 24:418–422
84. Angeli D, Ferrell JJE, Sontag ED (2004) Detection of multistability, bifurcations, and hysteresis in a large class of biological positive-feedback systems. *Proc Natl Acad Sci USA* 101(7):1822–1827
85. Newman JP, Butera RJ (2010) Mechanism, dynamics, and biological existence of multistability in a large class of bursting neurons. *Chaos* 20(2):023118
86. Wells DK, Kath WL, Motter AE (2015) Control of stochastic and induced switching in biophysical networks. *Phys Rev X* 5:031036
87. Slepchenko BM, Terasaki M (2003) Bio-switches: what makes them robust? *Curr Opin Genet Dev* 14:428–434
88. Canavier CC, Baxter DA, Clark JW, Byrne JH (1994) Multiple modes of activity in a model neuron suggest a novel mechanism for the effects of neuromodulators. *J Neurophysiol* 72(2):872–882
89. Kazantsev VB, Asatryan S (2011) Bistability induces episodic spike communication by inhibitory neurons in neuronal networks. *Phys Rev E* 84:031913
90. Litwin-Kumar A, Doiron B (2012) Slow dynamics and high variability in balanced cortical networks with clustered connections. *Nat Neurosci* 15:1498–1505
91. Esir PM, Gordleeva SY, Simonov AY, Pisarchik AM, Kazantsev VB (2018) Coupling delays can enhance formation of Up and Down states in spiking neuronal networks. *Phys Rev E* 98:052401
92. Cowan RL, Wilson CJ (1994) Spontaneous firing patterns and axonal projections of single corticostriatal neurons in the rat medial agranular cortex. *J Neurophysiol* 71:17–32
93. Steriade M, Nuñez A, Amzica F (1993) Intracellular analysis of relations between the slow (< 1 Hz) neocortical oscillation and other sleep rhythms of the electroencephalogram. *J Neurosci* 13(8):3266–3283
94. Lampl I, Reichova I, Ferster D (1999) Synchronous membrane potential fluctuations in neurons of the cat visual cortex. *Neuron* 22(2):361–374
95. Campos-Mejia A, Pisarchik AN, Arroyo-Almanza DA (2013) Noise-induced on-off intermittency in mutually coupled semiconductor lasers. *Chaos Solitons Fractals* 54:96–100
96. Masoller C (2002) Noise-induced resonance in delayed feedback systems. *Phys Rev Lett* 88:034102
97. Martínez-Zérega BE, Pisarchik AN (2012) Stochastic control of attractor preference in multistable systems. *Commun Nonlinear Sci Numer Simul* 17:4023–4028
98. Franović I, Eydam S, Semenova N, Zakharyova A (2022) Unbalanced clustering and solitary states in coupled excitable systems. *Chaos* 32:011104
99. Huerta-Cuellar G, Pisarchik AN, Barmenkov YO (2008) Experimental characterization of hopping dynamics in a multistable fiber laser. *Phys Rev E* 78:035202(R)
100. Garrett C, Gemmrich J (2009) Rogue waves. *Phys Today* 62(6):57–59
101. Stenflo L, Shukla PK, (2009) Simulations of two-dimensional magnetic electron drift vortex mode turbulence in plasmas. *J Plasma Phys* 75:133–144
102. Solli DR, Ropers C, Koonath P, Jalali B (2007) Optical rogue waves. *Nature (London)* 450:1054–1057
103. Yan ZY (2010) Financial rogue waves. *Commun Theor Phys* 54:947
104. Pisarchik AN, Grubov VV, Maksimenko VA, Lüttjohann A, Frolov NS, Marqués-Pascual C, Gonzalez-Nieto D, Khramova MV, Hramov AE (2018) Extreme events in epileptic EEG of rodents after ischemic stroke. *Eur Phys J Spec Top* 227:921–932
105. Frolov NS, Grubov VV, Maksimenko VA, Pavlov AN, Sitnikova S, Pisarchik AN, Kurths J, Hramov AE (2018) Statistical properties and predictability of extreme epileptic events. *Sci Rep* 9(1):7243
106. Lindner B, Garcá-Ojalvo J, Neiman A, Schimansky-Geier L (2004) Effects of noise in excitable systems. *Phys Rep* 392:321–424

107. Nagai Y, Hua XD, Lai YC (1996) Controlling on-off intermittent dynamics. *Phys Rev E* 54:1190–1199
108. Denis-le Coarer F, Quirce A, Valle A, Pesquera L, Rodríguez MA, Panajotov K, Sciamanna M (2018) Attractor hopping between polarization dynamical states in a vertical-cavity surface-emitting laser subject to parallel optical injection. *Phys Rev E* 97(3):032201

Chapter 6

Multistability in Complex Networks



Abstract Many systems are composed by a large set of dynamical units that interact with each other forming complex networks demonstrating multistability. We refer the readers interested in the theory of complex networks to the following excellent articles [1–3]. The units can be either simple phase oscillators, like Kuramoto oscillators [4], or dynamical systems modeled by difference or differential equations. The simplest class of such systems is a coupled map lattice with coexisting clusters (see Sect. 2.2.3). Other examples are coupled weakly dissipative systems, logistic maps, Hénon maps, genetic elements, and interconnected semiconductor lasers. The coexistence of synchronous and asynchronous states (so-called “chimeras”) is a particular case of bistability in complex networks. Multistable networks have been receiving much attention since their importance in many areas of natural sciences, including neuroscience [5–7], ecosystems [8], condensed matter physics [9, 10], genetics [11, 12], and power grids [13]. In this section, we first explain how one can characterize the stability of a complex network with coexisting attractors, and then describe multistability in complex networks of different types, including neural networks.

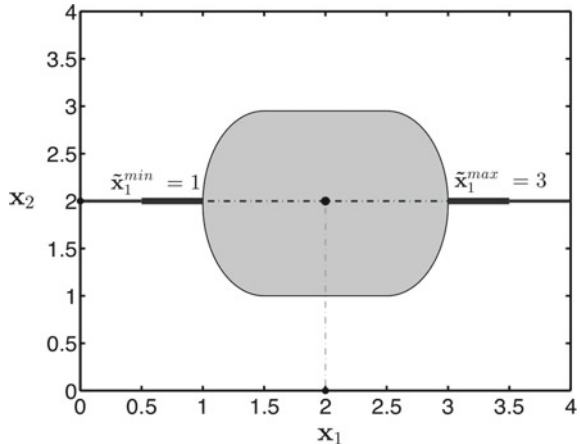
6.1 Stability of Multistable Complex Networks

The stability of a desired network regime, for example, synchronized state, is very important for the correct operation of many real networks, such as neural networks, power grids, ecosystems, etc. Here, we will show how network stability can be characterized.

6.1.1 Single-Node Basin Stability

Single-node basin stability (SNBS) is the probability of the multistable complex network, operating in a desired stable state, to return to this stable state after a non-infinitesimal perturbation is applied to one of its nodes [14]. To define SNBS, let us consider a network of N oscillators (nodes), in which the dynamics of the i th node

Fig. 6.1 Schematic illustration of the concept of single-node basin stability. The grey region is the basin of attraction of the synchronized state, and the white region around is the entire state space of two coupled oscillators. Reprinted figure with permission from [15] ©2017 by the American Physical Society



is modelled by

$$\dot{\mathbf{x}}_i = \mathbf{F}_i(\mathbf{x}_i) + \varepsilon \sum_{j=1}^N A_{ij} \mathbf{H}_{ij}(\mathbf{x}_i, \mathbf{x}_j), \quad (6.1)$$

where the first term describes the intrinsic dynamics and the second term refers to the interaction with other nodes. Here, $\mathbf{x}_i = (x_i^1, \dots, x_i^d)^\top \in \mathbb{R}^d$ is the d -dimensional state vector, $\mathbf{F}_i : \mathbb{R}^d \rightarrow \mathbb{R}^d$, $\mathbf{F}_i = (F_i^1(\mathbf{x}), F_i^2(\mathbf{x}), \dots, F_i^d(\mathbf{x}))^\top$ is a function for node $i = 1, 2, \dots, N$, ε is the overall coupling strength, A_{ij} the matrix element of the adjacency matrix \mathbf{A} such that $A_{ij} \neq 0$ if node j is connected with node i , and $\mathbf{H}_{ij} : \mathbb{R}^d \times \mathbb{R}^d \rightarrow \mathbb{R}^d$ is an arbitrary function described the coupling strength from node j to node i .

We suppose that a disturbance of one node of a synchronized network desynchronizes the entire network. SNBS of the i -th oscillator is defined as a fraction of the d -dimensional volume of the oscillator state space belonging to the $(d \times N)$ -dimensional basin of attraction of the synchronized state.

As an example, we consider now the simplest case of two oscillators, $x_1(t)$ and $x_2(t)$, whose synchronized state is described by the fixed point $\tilde{\mathbf{x}} = (\tilde{x}_1, \tilde{x}_2) = (2, 2)$ depicted in Fig. 6.1.

Let the subspace of the first oscillator be confined between $x_1^{\min} = 0$ and $x_1^{\max} = 4$, and the basin of attraction of the fixed point attractor is located between $\tilde{x}_1^{\min} = 1$ and $\tilde{x}_1^{\max} = 3$. If the coupled system is initiated inside the basin of attraction of the synchronized state (grey region), it will return back to this state. The SNBS of the oscillator x_1 is a part of the one-dimensional volume of the state space of this oscillator, which belongs to the region of attraction of the synchronized state. In other words, it is the ratio between the length of the basin (dotted line) and the length of the subspace, that is

$$\text{SNBS}_1 = \frac{\tilde{\mathbf{x}}_1^{\max} - \tilde{\mathbf{x}}_1^{\min}}{\mathbf{x}_1^{\max} - \mathbf{x}_1^{\min}} = \frac{1}{2}. \quad (6.2)$$

In the example presented in Fig. 6.1, the phase space dimension is $d = 1$ and the number of nodes is $N = 2$. Thus, the SNBS of any particular node is the probability that the system will remain in the basin of attraction of the synchronized state when random disturbances affect only that specific node.

The general algorithm for calculating SNBS includes the following steps:

- (1) Calculate synchronization manifold $\tilde{\mathbf{x}}(t) = (\tilde{\mathbf{x}}_1, \tilde{\mathbf{x}}_2, \dots, \tilde{\mathbf{x}}_N)^T$.
- (2) If the attractor corresponding to the synchronized state is a fixed point, choose one point on the synchronization manifold, otherwise choose $P > 1$ different points so that they sufficiently trace all parts of the attractor.
- (3) For a specific value of $p = 1, 2, \dots, P$ perturb the i -th oscillator by uniformly selecting I_C random initial conditions, each time initiating the system from the synchronized state using the p th point on the synchronization manifold.
- (4) Calculate the number of initial conditions F_C leading to a synchronized state and estimate SNBS_i for the p th point on the synchronization manifold as

$$\text{SNBS}_i(p) = \frac{F_C}{I_C}. \quad (6.3)$$

- (5) Calculate the mean SNBS of node i by averaging SNBS over p as

$$\langle \text{SNBS}_i \rangle = \frac{1}{P} \sum_{p=1}^P \text{SNBS}_i(p). \quad (6.4)$$

- (6) Calculate the mean SNBS of the whole network by averaging SNBS over all N nodes as

$$\langle \text{SNBS} \rangle = \frac{1}{N} \sum_{i=1}^N \langle \text{SNBS}_i \rangle. \quad (6.5)$$

The knowledge of SNBS is useful for determining the contribution of individual nodes to the overall stability of a synchronized state, as well as to identify the most vulnerable and the most stable nodes. The practical importance of SNBS is demonstrated in Fig. 6.2 which illustrates SNBS in the power transmission grid of the United Kingdom modelled with second-order Kuramoto equations.

The network diagram in Fig. 6.2 is helpful for revealing the most vulnerable nodes and links in the power grid.

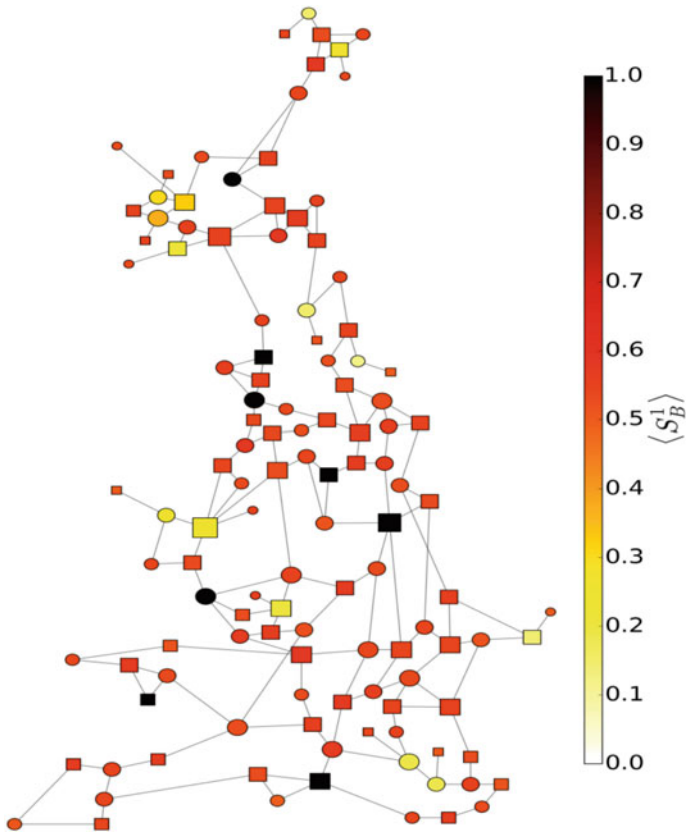


Fig. 6.2 Single-node basin stability of the power transmission grid (120 nodes and 165 links) of the United Kingdom modelled by second-order Kuramoto equations. Net generators and net consumers are shown by dots and squares, respectively. The size is proportional to the node degree and color shows the SNBS value. Based on data from [15]

6.1.2 Multiple-Node Basin Stability

If several nodes are simultaneously perturbed, the concept of SNBS is extended to the framework of *multiple-node basin stability* (MNBS) which measures the global stability and resilience of networked dynamical systems in response to small perturbations simultaneously affecting multiple nodes. MNBS estimates the critical number of disrupted network nodes at which the system ability to return to the desired stable state is significantly reduced. In addition, MNBS can be used to estimate the minimum number of network nodes that must be protected from outside tampering in order to ensure correct system operation, as well as to investigate the impact of spatially localized disruptions or targeted attacks on specific parts of the network.

Let us suppose now that $m > 1$ nodes are simultaneously independently disturbed. The algorithm for calculating MNBS (or m -node basin stability) is given as follows [15].

- (1) For any number of nodes m , generate an ensemble $\{E_j^m\}$ of m -node sets, each containing m nodes, to be perturbed simultaneously. There exists a possible maximum of $\binom{N}{m}$ of such m -node sets. For any particular value of m , randomly choose M or $\binom{N}{m}$ m -node sets.
- (2) For a given j -th set of m -node set E_j^m of the ensemble and for any particular value of p , m nodes are collectively perturbed by uniformly choosing I_C random initial conditions, each time initiating the system from the p -th point on the synchronization manifold.
- (3) Calculate again the number of initial conditions F_C leading to the synchronized state and estimate the m -node basin stability MSBS(E_j, p) of the j th m -node set of the ensemble for the p th point on the synchronization manifold as

$$\text{MNBS}(E_j, p) = \frac{F_C}{I_C}. \quad (6.6)$$

- (4) Average over p and over all m -node sets of the ensemble to obtain the mean basin stability of the network as

$$\langle \text{MNBS} \rangle = \frac{1}{\min \left[M, \binom{N}{m} \right]} \sum_j \frac{1}{P} \sum_p \text{MNBS}(E_j, p) \quad (6.7)$$

for $m = 1$ and $\text{MNBS} = \text{SNBS}$.

The knowledge of MNBS is very important for assessing global stability and fault tolerance of dynamical networks in response to non-infinitesimal disturbances affecting several nodes simultaneously. It is important to note that MNBS allows the estimation of the critical number of nodes, which, when disrupted simultaneously, significantly reduce the system ability to return to the desired stable state.

6.1.3 Resilience of Multistable Networks

In dynamical networks, the issue of paramount importance is the ability of the system to recover from severe failures. Therefore, it is very important to find out how strongly an individual node affects the collective network dynamics. It is expected that the impact of a node on global network dynamics will depend on the node importance to distribute information in the network. Identifying vulnerable nodes will help protect the network from targeted attacks to preserve the collective state.

Now we will show how the stability of a multistable network of various topologies can be characterized. Let us consider a complex network of N interacting two-dimensional oscillators (x, y) given as

$$\begin{aligned}\dot{x}_i &= f_x(x_i, y_i) + C \frac{1}{k_i} \sum_j A_{ij}(x_j - x_i), \\ \dot{y}_i &= f_y(x_i, y_i),\end{aligned}\tag{6.8}$$

where $i = 1, \dots, N$ is a node index, f_x and f_y are nonlinear functions governing the node dynamics, C is the coupling strength, k_i is the degree of i th node, and A_{ij} is the connectivity matrix which defines the network topology. We assume that the individual dynamics of each i th oscillator is regulated by the local mean field created by its neighbors j , that is $\langle x_i^{nn} \rangle = \frac{1}{k_i} \sum_j x_j$ (the super-index nn means “nearest neighbors” of node i),

Supposing that several attractors coexist in the complex network, in order to find the stability of a collective state in which all nodes are in the basin of attraction of the same attractor, we have to quantify the stability of each node. For this purpose, we will define the basic concepts which determine the efficiency of information transmission emanating from a node or through a node that affects the propagation of disturbances arising in the node. The most significant characteristics of the nodes which affect the global stability of the network are the following.

- *Node degree.* The degree of node i , denoted by k_i , is defined as the number of neighbours that are directly connected to the node in an undirected network. A high degree of a node indicates that the node is in direct contact with a large set of nodes.
- *Betweenness centrality.* Normalized betweenness centrality of a node i is given by

$$b_i = \frac{2}{(N-1)(N-2)} \sum_{s,t} \in N \frac{\sigma(s, t|i)}{\sigma(s, t)},\tag{6.9}$$

where N is the total number of nodes in the network, $\sigma(s, t)$ is the number of shortest paths between node s and node t , and $\sigma(s, t|i)$ is the number of shortest paths passing through node i . A high betweenness centrality of node i means that this node lies on many shortest paths, and therefore there is a high probability that the connection between any two nodes goes through it.

- *Closeness centrality.* Normalized closeness centrality is defined as

$$c_i = \frac{N-1}{\sum_j d(j, i)},\tag{6.10}$$

where $d(j, i)$ is the shortest path between node i and node j . In fact, the closeness centrality is the inverse of the average length of the shortest path between the node

and all other nodes in the network. Thus, high closeness centrality means that the number of steps to reach other nodes is small.

To measure global stability and state reliability, one can use the multiple-node basin stability concept described in Sect. 6.1.2. In general, the basin stability of a particular attractor of a multistable dynamical system is determined by the fraction of disturbed states that return to the original basin of attraction after a large disturbance (see Sect. 6.1.2). This measure allows one to assess the global resilience of a dynamical network in response to large disruptions affecting certain nodes.

The resilience depends on the network topology [16]. In particular, when random nodes are perturbed in a *ring network* of multistable oscillators, the network restores its original dynamics faster than when the perturbation is applied to a cluster of neighbouring nodes. Since all nodes in the ring network have the same centrality, the resilience allows understanding how the number of perturbed nodes affects the network stability.

Another situation occurs in a *star network*, where the degree, closeness, and betweenness centrality of the central hub node are very different from the peripheral nodes. Therefore, such networks allow evaluating the correlation between node centrality and network resilience to large localized disturbances. Interestingly, the perturbation of the hub node is only sufficient to destroy the network ability to recover its original state, regardless of the nature of the node dynamics. At the same time, the network dynamics remains resilient to failures of a very large number of peripheral nodes. This means that the hub node can repair the majority of damaged peripheral nodes by turning them to their original state. In addition, it is obvious that ring and star networks of multistable *periodic* oscillators is more stable than networks of multistable *chaotic* oscillators.

It was also found that the interaction of nodal dynamics and the type of disturbance play an important role in determining the global stability of collective dynamics of heterogeneous networks of multistable oscillators, for example, *scale-free networks*, widespread in nature and engineering systems. In such networks, the disturbing nodes with the highest centrality lead to an extreme decrease in basin stability, whereas the basin stability decreases slowly when the nodes with low centrality are disturbed. The scale-free networks of multistable limit cycles are surprisingly less stable than networks of multistable chaotic oscillators when the nodes with the least centrality are perturbed and the perturbation transfers the node state to a random phase point in a small or large volume of phase space. In such networks, the influence of betweenness centrality of the disturbed nodes on the resilience of the collective state prevails over the effect of the degree or closeness centrality of the disturbed nodes.

6.1.4 Minimal Fatal Shock

One of the characteristics of basin stability is the shortest distance between a stable state and its basin boundary. Using the optimization technique to determine the

smallest disturbance or shock, capable of moving the dynamical network from its current stable state to a basin of another state, Halekotte and Feudel [17] introduced the concept of *minimal fatal shock*. A single sharp shock can result in a critical transition called *shock-tipping* or *S-tipping*. The minimal fatal shock is a vector which quantifies global stability in terms of shock magnitude and direction in the state space. In complex networks, this vector can be interpreted using vertices of the basic network topology. This provides us with a promising tool both for identifying weaknesses created by certain network substructures and for understanding their topological and dynamical origins.

The minimal fatal shock is defined as follows. Let us suppose that the system before perturbations was in a desired state \mathbf{x}_0 , and that a shock $\mathbf{x}(0) = \mathbf{X}(0) - \mathbf{X}_0$ applied at the moment $t = 0$ instantly transfers the system to $\mathbf{X}(0)$. The shock is considered fatal if $\mathbf{X}(0)$ is outside the \mathbf{X}_0 basin, and non-fatal if $\mathbf{X}(0)$ is in the \mathbf{X}_0 basin. Thus, the minimal fatal shock is a vector that represents the shortest distance between the desired state \mathbf{x}_0 and the boundary of its basin, and the corresponding direction in the state space, as illustrated in the left panel in Fig. 6.3.

An important question arises: How can we determine a perturbation magnitude d required to reach the basin boundary from the desired state \mathbf{X}_0 ? The simplest way is the use of the Euclidean distance to the desired state \mathbf{X}_0 in phase space, defined as

$$d = \|\mathbf{X}(0) - \mathbf{X}_0\|. \quad (6.11)$$

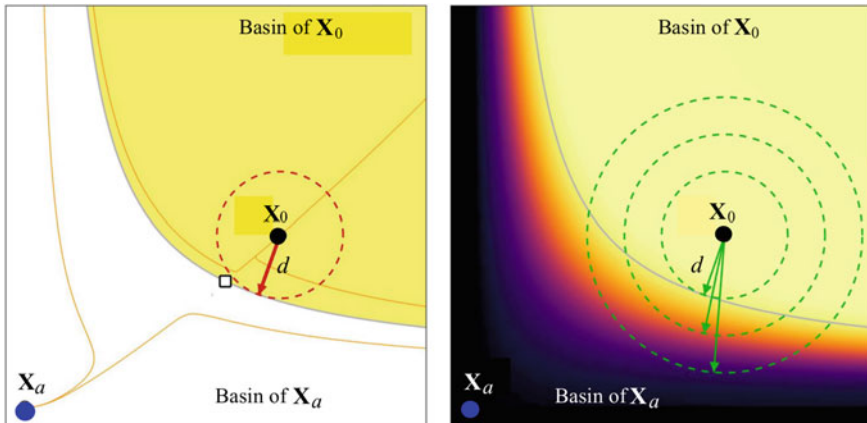


Fig. 6.3 (Left) Minimal fatal shock (arrow) or smallest perturbation applied to the desired state \mathbf{X}_0 which kicks the system outside the basin of attractor \mathbf{X}_0 into the basin of attractor \mathbf{X}_a . (Right) Corresponding search algorithm which starts with a relatively large perturbation magnitude (largest dashed circle) and the direction of maximum amplification (longest arrow). The magnitude of allowed perturbations is reduced and the direction of maximum amplification converges towards the minimal fatal shock. The colors mark the objective function, that is the distance to the desired state after a short integration time. Modified from [17]

For finding the value of minimal fatal shock, we can use the minimum seed approach that includes two stages: global random initialization (stage I) and local non-random optimization (stage II). In stage I, initial conditions are randomly inferred from a shrinking subspace in the state space to find a fatal shock with a preferably small d value. After completing stage I, stage II begins with the smallest fatal shock obtained in stage I. Now, we will consider these two steps in more detail.

Stage I: random global initialization. First, random initial conditions are chosen from a uniform distribution in a subspace centered around \mathbf{X}_0 and bounded by the maximum disturbance d_{max} . For each initial condition, one has to calculate whether it is fatal or non-fatal. When the shock is fatal, it is declared as the current best guess for minimum fatal shock. Then, d_{max} is considered as the best guess, and the random search continues in the now reduced subspace. After a certain number of attempts, one can proceed to stage II.

Stage II: nonrandom local search. First, the perturbation amplitude d is reduced and then its perturbation direction is adapted so that it remains fatal. Starting with the last best guess from stage I, an optimization procedure is applied to d as a constraint, that is the optimization on an $(n - 1)$ -dimensional sphere in n -dimensional phase space, as seen in the right panel in Fig. 6.3. The optimization procedure aims at adapting the perturbation direction to receive the system state $\mathbf{X}(0)$ as far as possible from the basin boundary \mathbf{X}_0 .

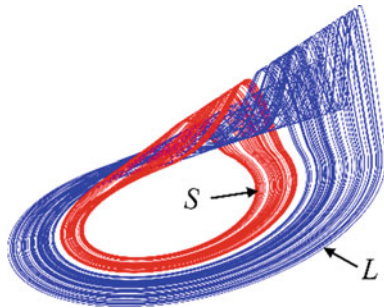
Thus, the optimization procedure allows obtaining the value of the smallest distance to the basin boundary, which can be used as a quantitative measure of global stability and the perturbation direction in the multidimensional phase space with coexisting attractors.

6.1.5 Master Stability Function of Multistable Systems

We have already shown how complex the basins of attraction are even in a single multistable system. Therefore, it is natural to assume that the dynamics of a network of interacting multistable systems will be even more complex. To measure the stability of the synchronous behavior of an ensemble of coupled multistable oscillators, the method of the *master stability function* (MSF) can be used. The MSF allows a quantitative measure of synchronizability of a complex network [18]. In other words, MSF is an extension of the linear stability concept to assess stability of a completely synchronized state in a complex network. The MSF is determined by the maximum Lyapunov exponents transverse to the synchronization manifold and found important applications in studying networks of monostable systems (see, for example, [19]).

Here, we will show how MSF can be applied to measure stability of a synchronization manifold of N coupled multistable systems. In short, the MSF is first estimated for each coexisting chaotic attractor separately, and then it is studied how the coupling parameter affects the system to enter and exit a certain attractor-related synchronization mode without losing synchronization in the entire dynamical system, even in the presence of intermittency.

Fig. 6.4 Coexisting small S (red) and larger L (blue) chaotic attractors in the solitary Rössler-like oscillator



Let us consider, as an example, two bistable bidirectionally coupled Rössler-like oscillators given by

$$\begin{aligned}\dot{x}_{1,2} &= -\alpha_1 \left[x_{1,2} + \beta y_{1,2} + \Gamma z_{1,2} - \sigma \psi(x_{2,1} - x_{1,2}) \right], \\ \dot{y}_{1,2} &= -\alpha_2 \left[-\gamma x_{1,2} - (1 - \delta) y_{1,2} \right], \\ \dot{z}_{1,2} &= -\alpha_3 \left[-g(x_{1,2}) + z_{1,2} \right],\end{aligned}\quad (6.12)$$

where σ is the coupling strength and $\psi = 20$ is the scaling factor. The dynamics of the solitary oscillator is described in Sect. 3.2.2. For parameter values $\alpha_1 = 500$, $\alpha_2 = 200$, $\alpha_3 = 10000$, $\beta = 10$, $\Gamma = 20$, $\gamma = 50$, $\delta = 15.625$, and $\mu = 15$, the single oscillator exhibits the coexistence of two chaotic attractors depicted in Fig. 6.4.

The system in Eq. 6.12 asymptotes to four possible solutions.

LL state: Both oscillators end up in an attractor indistinguishable from L .

SS state: Both oscillators end up in an attractor indistinguishable from S .

SL state: One oscillator asymptotes to L and another to S .

I state: Intermittency attractor when the system exhibits irregular switches back and forth between L and S .

All these regimes depend on the coupling strength σ . Figure 6.5 shows the basins of attraction of these four regimes for four different values of σ .

Figure 6.6 displays MSF for S (dashed line) and L (solid line) attractors versus parameter $v = \sigma \lambda$ (λ being a specific eigenvalue of the network Laplacian matrix that corresponds to the considered eigenmode). The MSF measures stability of a synchronous state and is determined by the maximum Lyapunov exponents transverse to the synchronization manifold. A negative MSF indicates that synchronization is stable. In a multistable system, the MSF should be considered separately for each attractor.

For each eigenmode transverse to the synchronization manifold, there is one such eigenvalue, and there are $N - 1$ eigenvalues for a fully connected network of size N . The parameter v denotes the product of a given coupling strength and a graph Laplacian eigenvalue, and therefore it implicitly takes into account an infinite set of network topologies and coupling strengths.

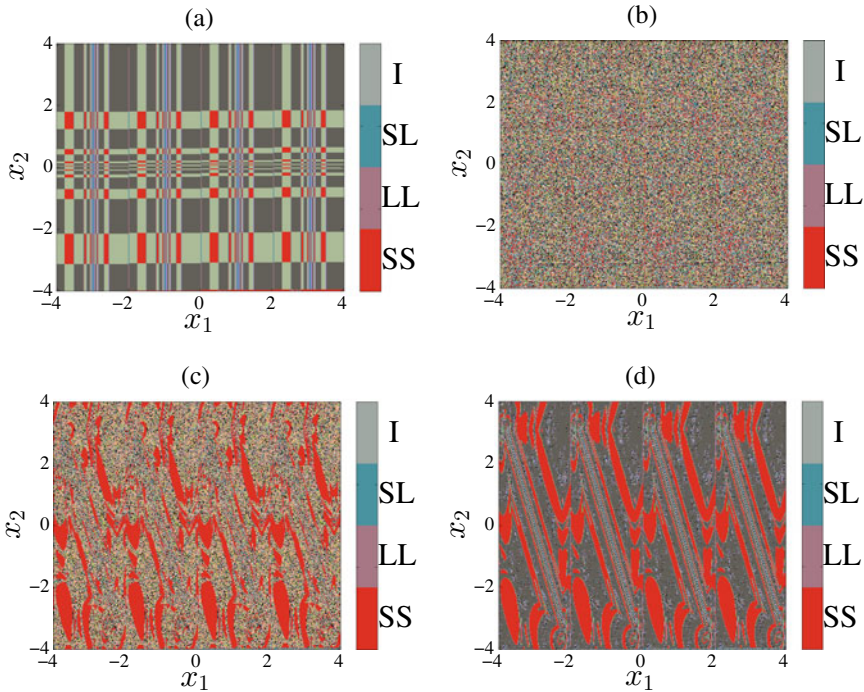
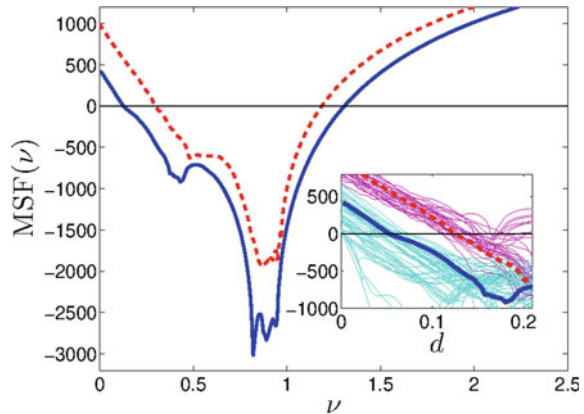


Fig. 6.5 Basins of attraction of four coexisting states of the system in Eq. 6.12 for coupling strengths **a** $\sigma = 0$ (uncoupled systems), **b** $\sigma = 0.06$, **c** $\sigma = 0.14$, and **d** $\sigma = 0.20$. Reprinted figure with permission from [20] ©2015 by the American Physical Society

Fig. 6.6 Master stability functions for S (dashed line) and L (solid line) coexisting attractors of the system in Eq. 6.12 with respect to uncertainty parameter $v = \sigma \lambda$. Inset: variability of the first zero crossing as the parameters are affected by uncertainties. Reprinted figure with permission from [20] ©2015 by the American Physical Society



As seen from Fig. 6.6, the stability region of L is contained in that of S . The interplay between the two stability regions (S and L) explains how the synchronous state is maintained (or lost) in one of the three possible scenarios: SS, LL, and I.

In the multistable system given by Eq. 6.12, we can distinguish three possible synchronization states with respect to the uncertainty parameter $\nu\sigma\lambda$:

- (i) both S and L are asynchronous; MSFs for both S and L are positive,
- (ii) S synchronizes, but L not; MSF for S is negative, while for L is positive,
- (iii) both S and L synchronize; both MSFs are negative.

Only case (ii) guarantees synchronization stability in the SS regime, whereas case (iii) means that synchronization is always stable no matter how complex the dynamics is, even in the presence of intermittency. Therefore, if the product of each eigenmode for a given topology and the coupling σ are within the region described by case (iii), synchronization is stable. Similar arguments can be used in systems with an arbitrarily large number of attractors, provided stability regions of different attractors are not disjoint.

The described methodology is of particular interest for the analysis of synchronization stability in multistate intermittency, since any monostable approach to synchronization is doomed to failure in this mode. Knowing the coupling strengths and the network topology required to maintain complete synchronization in any possible attractor, one can effectively control the network dynamics. The MSF arguments in the context of multistable systems provide a versatile tool for understanding complete synchronization in real multistable networks.

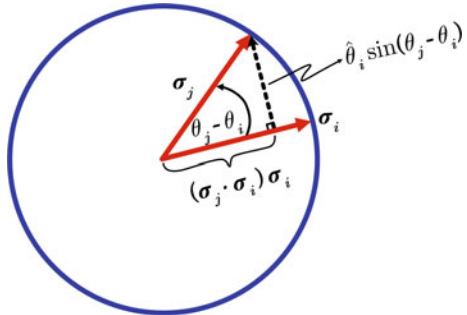
6.2 Manifestation of Multistability in Different Networks

Multistability is a widespread phenomenon observed in various complex networks formed by discrete or continuous systems. Below, we will present some paradigmatic examples of this exciting phenomenon in the popular networks of Kuramoto, Duffing, and Chua oscillators, as well as in Boolean networks.

6.2.1 Network of Networks of Kuramoto Oscillators

We start with the simplest case of coupled phase oscillators, namely, the network of *Kuramoto oscillators* coupled through the sinus of their phase differences [21]. The phase of each uncoupled oscillator grows linearly in time, meaning that its angular frequency is constant. When the oscillators are coupled, the coupling strength between each pair of oscillators is usually described by a 2π -periodic function of their phase difference. In the original Kuramoto model, each i -th oscillator is represented by a D -dimensional vector σ_i of norm one. Therefore, the trajectories of all σ_i are wandering on the hyper-surface of a $(D - 1)$ -dimensional unit sphere.

Fig. 6.7 Vector representation of the Kuramoto model for $D = 2$. σ_i and σ_j are vectors of two interacting oscillators and $\hat{\theta}_i$ is a unit vector along the direction of the black dashed arrow



The example of a one-dimensional sphere ($D = 2$) is illustrated in Fig. 6.7, where each oscillator i is simply described by its phase θ_i , that is $\sigma_i = (\cos \theta_i, \sin \theta_i)$.

Each oscillator rotates on a unit circle with a different natural frequency and connects to all other oscillators through a sinusoidal phase difference function. In other words, units are described using a single scalar variable, i.e. phases on a two-dimensional circle. This model and its generalizations are often used to study various problems in biology, physics, and technology [22].

The model proposed by Frolov and Hramov [23] takes into account the time-varying nature of the excitability of N individual units due to their connection to the resource baths λ_i through a diffusion connection shown in Fig. 6.8. The model is given by

$$\begin{aligned} \dot{\theta}_i &= \omega_i + \lambda_i \sum_{j=1}^N A_{ij} \sin(\theta_j - \theta_i), \\ \dot{\lambda}_i &= \alpha(\lambda_i - \lambda_0) - \beta r_i, \end{aligned} \quad (6.13)$$

where θ_i and $\dot{\theta}_i$ are the phase and angular velocity of the i -th oscillator ($i \in [1, N]$), ω_i is its natural frequency, λ_i is the coupling strength, α and β are the excitability recovery and resource constraints rates, respectively, λ_0 is the excitability unperturbed level in the absence of resource constraints, r_i is the order parameter, and A is the adjacency matrix which determines connections between the oscillators. In particular, $A_{ij} = 1$ means the presence of a link between the i -th and j th nodes, and $A_{ij} = 0$ means that a link is absent.

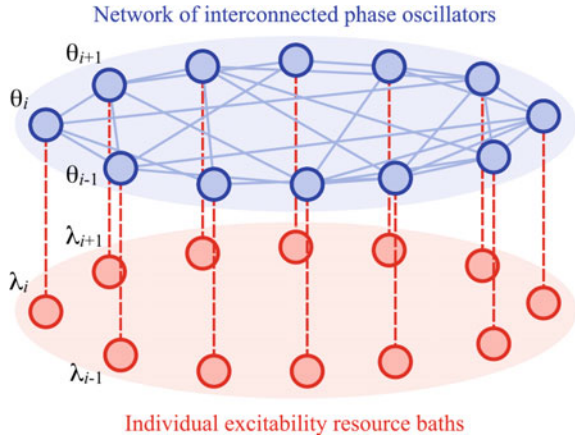
Local synchrony in the neighborhood of the i -th oscillator is estimated by the local order parameter

$$r_i = \frac{1}{k_i} \left| \sum_{j=1}^N A_{ij} e^{\theta_j} \right|, \quad (6.14)$$

where $k_i = \sum_{j=1}^N A_{ij}$ defines the i -th node degree.

Global coherence is quantified by the global order parameter defined as

Fig. 6.8 Illustration of a conventional Kuramoto model under resource constraints. Oscillators in the upper layer defined by phase θ_i ($i \in [1, N]$) interact through connections shown by solid blue lines. Each node is diffusively coupled (dashed red lines) to an individual resource bath (red nodes in the lower layer) defined by the oscillator's excitability λ_i . Reproduced from [23] with permission of AIP Publishing



$$R = \frac{1}{N} \left| \sum_{j=1}^N e^{\theta_j} \right|, \quad (6.15)$$

where $0 \leq R \leq 1$. In the uniformly distributed network $R = 0$ meaning that all oscillators are completely asynchronous, whereas $R = 1$ corresponds to the case when all oscillators have the same phase.

It is assumed that the natural frequencies is equal to the node degree, i.e. $\omega_i = k_i$. This assumption is relevant for a class of real networked systems, including power grids and neural networks.

It was found that the hierarchical scale-free graph exhibits bistability, while the small-world network does not. The coexistence of the high-order and low-order states in the scale-free network of the Kuramoto oscillators was revealed by increasing and decreasing the excitability unperturbed level in the absence of resource constraints (λ_0), i.e. when $\beta = 0$. Bistable behavior in the global order parameter can be seen in the bifurcation diagrams in Fig. 6.9. In the left panel, we plot the diagram for the conventional Kuramotoc model ($\beta = 0$) and in the right panel with a resource constraint for $\beta = 0.002$. One can see that this network displays the first-order explosive transition to coherence resulting in the hysteresis area.

The resource constraints induce two-state intermittency. The switching between globally coherent and incoherent states is shown in Fig. 6.10 for two values of λ_0 . While in the middle of the bistability range (right panel), the time the system spends in the vicinity of each state is approximately the same, close to the bistability boundary (left panel), the coherent states appear abruptly for a very short time, giving rise to *extreme coherence events*. The system occasionally leaves the basin of attraction of the global coherent attractor under a sudden shortage of resources and switches between coherent and incoherent states, consuming and restoring its resource.

The intermittent behavior shown in the left panel in Fig. 6.10 is similar to extreme events observed in a multistable fiber laser (see Sect. 5.5.3). The existence of such

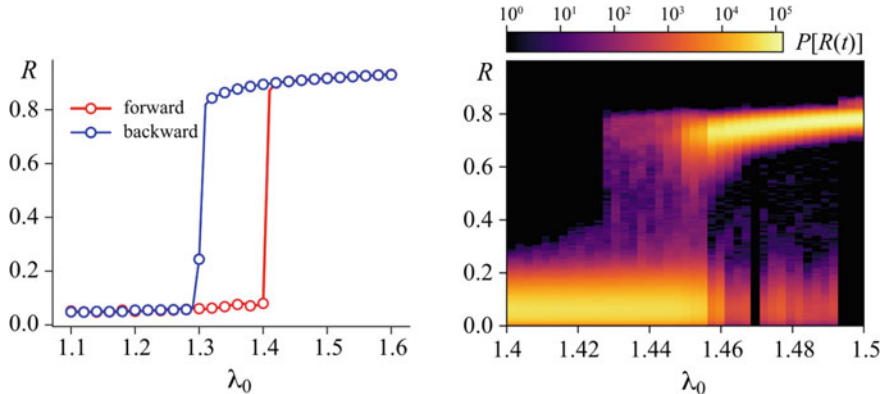


Fig. 6.9 Bistability in global coherence in the scale-free network of (left) conventional Kuramoto model ($\beta = 0$) and (right) resource constraint model ($\beta = 0.002$). The grey scale shows the probability distributions for specific λ_0 values. $N = 1000$, $\alpha = 0.01$. Reproduced from [23] with permission of AIP Publishing

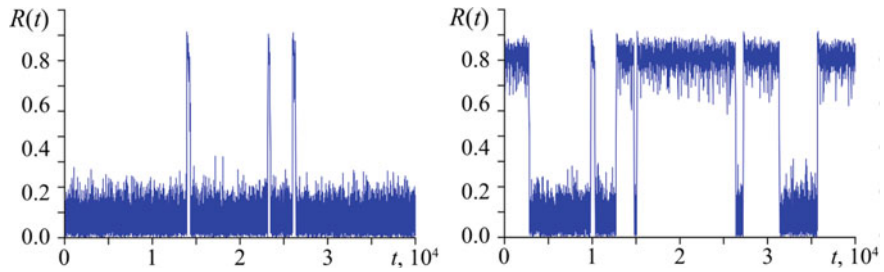


Fig. 6.10 Two-state intermittency between global coherent and incoherent states in the scale-free network of Kuramoto oscillators with resource constraints for (left) $\lambda_0 = 1.4425$ and (right) $\lambda_0 = 1.4525$. Reproduced from [23] with permission of AIP Publishing

events in complex networks can shed light on understanding complex dynamics of real networks, such as, for example, abnormal synchronization of neural ensembles that causes epilepsy. Some researchers believe that the formation of epileptic seizures has features of extreme events [24, 25] observed in both animal [26, 27] and human [28] models. Further research aimed at improving the existing model and approximating its properties to real neural ensembles may improve our understanding of the extreme network activity.

6.2.2 Potential Landscape of a Network of Networks

Dynamical structure of coexisting states in a networked system can be characterized with potential landscape $L(z)$ (z being the state variable) derived from inverted Gaussian functions of M states [29]

$$\dot{L}(z) = \sum_{n=1}^M \frac{z - \mu_n^G}{(\sigma_n^G)^2} \frac{a_n^G}{\sqrt{2\pi(\sigma_n^G)^2}} \exp\left(-\frac{(z - \mu_n^G)^2}{2(\sigma_n^G)^2}\right), \quad (6.16)$$

where a_n^G , μ_n^G , and σ_n^G are amplitude, mean, and standard deviation of the n -th Gaussian function.

The state variable or position $z(t)$ is regulated by the equation of motion:

$$\dot{z}(t) = \dot{L}(z)|_{z(t)} + \zeta(t)\bar{x}(t), \quad (6.17)$$

where $\zeta(t) = (0.6 - 0.01z(t))$ is a scaling factor and $\bar{x}(t)$ is the mean field of the system variable x .

The advantage of the potential landscape approach based on a sequence of inverted Gaussian functions over other ways for constructing multiple quasipotentials, for example, those based on an n -th order polynomial [30], is an easy way to add additional potential wells, thereby preserving the order of the wells.

One of the drawbacks of the potential landscape is smooth barriers between potential wells. This can result in a too fast escape from the well and therefore in a too short transition. This disadvantage can be overcome by adding the barrier fragmentation, for example, using a classic Cantor fractal construction process [31]. Fragmented barriers can also be used to mimic riddled basins of attractions (see Sect. 1.2.5).

Figure 6.11 shows the example of the potential landscape with fragmented barriers for a dynamical system with four coexisting states.

The applicability of the potential landscape for the analysis of switching dynamics between coexisting states was demonstrated by Fischer et al. [29] with a network of N_n networks of diffusively coupled FitzHugh–Nagumo (FHN) oscillators. The equations of motion of the i -th oscillator ($i \in \{1, \dots, N_o\}$) in the k -th sub-network ($k \in \{1, \dots, N_n\}$) are given by

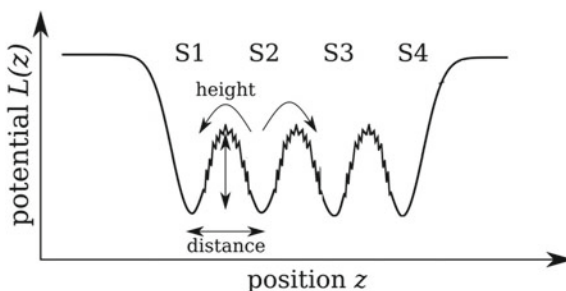


Fig. 6.11 Potential landscape of a dynamical system with four coexisting attractors (S1, S2, S3, S4) with fragmented barriers generated by using the classic Cantor fractal construction process. Enabling a fragmented barrier can be thought of as adding intermediate states that temporarily delay the dynamics. Adapted from [29]

$$\begin{aligned}\dot{x}_i^{(k)} &= x_i^{(k)} \left(a_i - x_i^{(k)} \right) \left(x_i^{(k)} - 1 \right) - y_i^{(k)} + \\ &+ \frac{C_w^{(k)}}{N_o - 1} \sum_{j=1}^{N_o} A_{ij} \left(x_j^{(k)} - x_i^{(k)} \right) + \frac{C_b}{N} \sum_{l=1}^{N_n} B_{kl} \sum_{j=1}^{N_o} \left(x_j^{(l)} - x_i^{(k)} \right), \\ \dot{y}_i^{(k)} &= b_i x_i^{(k)} - c_i y_i^{(k)},\end{aligned}\quad (6.18)$$

where x and y are fast (excitatory) and slow (inhibitory) state variables, a , b , and c are parameters, and I is an external current. Here, $C_w^{(k)}$ and C_b are global coupling strengths within and between sub-networks, A_{ij} are matrix elements of symmetric adjacency matrix $\mathbf{A} \in \{0, 1\}^{N_o \times N_o}$ ($A_{ij} = A_{ji} = 1$, if oscillators i and j are coupled), and B_{ij} are matrix elements of adjacency matrix $\mathbf{B} \in \{0, 1\}^{N_o \times N_n}$ that characterizes the coupling structure between sub-networks.

For example, the mean field of a two-layer network ($N_n = 2$), each of N_o diffusively coupled non-identical oscillators can be calculated as

$$M(t) = \frac{1}{N_o} \sum_{i=1}^{N_o} x_i^{(1)}(C_w^{(1)}, C_b, t) + x_i^{(2)}(C_w^{(2)}, k_b, t). \quad (6.19)$$

The first term in Eq. 6.17 enables switching to different potential wells dependent on the mean field $M(t)$ generated by the system.

The self-switching among different states depends on the mean field $M(t)$ of the network. To provide discernible dynamics for different potential wells, the coupling strengths $C_w^{(k)}$ and C_b are changed as soon as the mean field $M(t)$ forces $z(t)$ to cross the local barrier between the respective wells.

Figure 6.12 shows the time series of the average value of the variable $\bar{x}^{(1)}(t) = \sum_{i=1}^{N_o} x_i^{(k)}(t)$ of sub-network 1 of $N_o = 25$ FHN oscillators and the corresponding state variable $z(t)$, obtained by random variation of initial conditions for $x_i^{(k)} \times y_i^{(k)} \in$

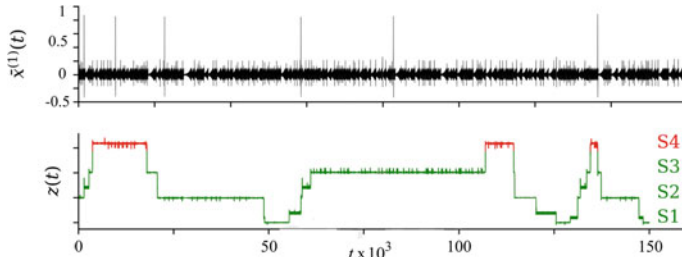


Fig. 6.12 Time series of the average dynamical variable $\bar{x}^{(1)}(t)$ of the FHN network and the corresponding state variable $z(t)$ for the following parameters: $a^G = [5.5, 5.5, 5.5, 5.5]$, $\mu^G = [-5.75, -2.25, 2.25, 5.75]$, $(\sigma^G)^2 = [2.9, 2.9, 2.9, 2.9]$, $C_w^{(1)} = 0.115$ (for all states), $C_w^{(2)} = 0.116$ and $C_B = 1.045 \times 10^{-5}$ (for state S1), $C_w^{(2)} = 0.116$ and $C_b = 1.425 \times 10^{-5}$ (for state S2), $C_w^{(2)} = 0.125$ and $C_b = 1.045 \times 10^{-5}$ (for state S3), $C_w^{(2)} = 0.125$ and $C_b = 1.5 \times 10^{-5}$ (for state S4). Based on data from [29]

$[0, 1]$ and $z \in [-5, 5]$, and parameters $a_i = -0.0276$ and $c_i = -0.02$ for all i , and b_i is linearly distributed on $[0.006, 0.014]$ to prevent immediate synchronization among oscillators for non-zero coupling strengths.

The fragmented barrier acts as intermediate states that introduce a delay into the network dynamics. It should be noted that the dynamics in these intermediate states is different from the potential wells.

6.2.3 Ring-Coupled Oscillators

Ring-coupled discrete and continuous systems as known [32, 33] to display very rich dynamics. Even three unidirectionally ring-coupled oscillators can exhibit multistability [34].

Since large-scale dynamical properties of networks are determined by their much smaller constituent elements called network motifs [35, 36], the understanding of the dynamics of such motifs can help us to shed light into mechanisms underlying multistability in larger network. From a technical point of view, Milo et al. [37] defined *network motifs* as patterns of relationships (or subgraphs) that occur in complex networks in numbers significantly greater than in randomized networks. The presence of network motifs indicates the operation of underlying non-random structural or evolutionary design principles that may have been involved in building the network. Therefore, knowledge of the dynamics of network motifs can help us understand the self-organization of large networks.

Here, we will show how multistability arises in a simple network motif formed by three unidirectionally coupled Duffing oscillators. We remind the reader that the emergence of multistability in a single Duffing oscillator and in two coupled Duffing oscillators was discussed in Sects. 3.2.1 and 3.3.3, respectively.

We should note that unidirectionally ring-coupled configuration of Duffing oscillators exhibits richer dynamics (including multistability) than bidirectional. This system of three coupled oscillators is modelled by the following equations [34]

$$\begin{aligned}\ddot{x}_1 &= -\gamma \dot{x}_1 - ax_1 - bx_1^3 + \sigma(x_3 - x_1), \\ \ddot{x}_2 &= -\gamma \dot{x}_2 - ax_2 - bx_2^3 + \sigma(x_1 - x_2), \\ \ddot{x}_3 &= -\gamma \dot{x}_3 - ax_3 - bx_3^3 + \sigma(x_2 - x_3).\end{aligned}\tag{6.20}$$

The bifurcation diagrams of three coupled oscillators are shown in Fig. 6.13. The branches CI-1, CI-2, CI-3, CI-4, CI-5, and CI-6 are found using different initial conditions. There are two Hopf bifurcation points, where the oscillators begin to oscillate with the same frequency (HB at $\sigma = 0.36$) and where the second frequency appears (HP at $\sigma = 0.48$).

It is important to note that multistability was only found in unidirectional ring-coupled oscillators, but not in other configurations which three oscillators can form (bidirectional or combined).

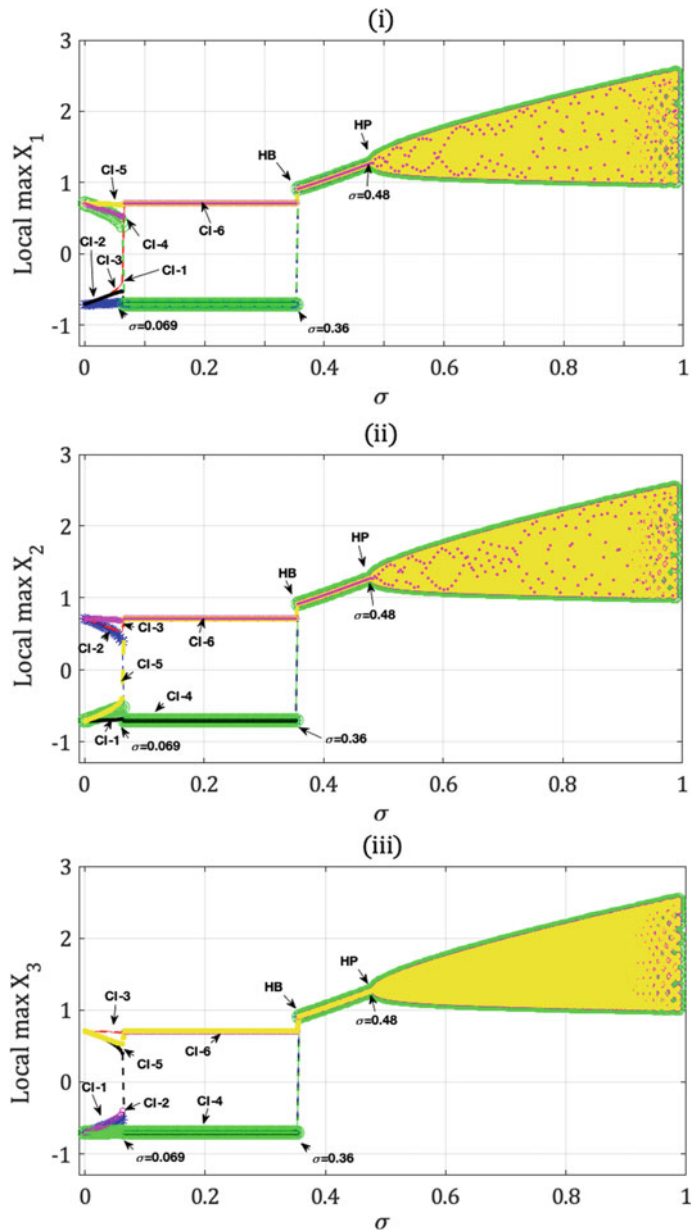


Fig. 6.13 Bifurcation diagrams of the local maxima of three unidirectionally ring-coupled Duffing oscillators with respect to the coupling strength σ , obtained for random initial conditions. HB and HP are Hopf bifurcations where periodic and quasiperiodic orbits are born

6.2.4 Structural Multistability in Boolean Networks

In complex networks, multistability can be associated with network structure. This interesting type of multistability known as *structural multistability* should not be confused with multistability in the structure of metamaterials (see Sect. 2.2.9), although it has the same name. The concept of structural network bistability is useful in situations when the information about individual node dynamics is absent, while the information about the whole network structure is available. We often face such a situation, because, in general, a mathematical model of individual nodes is unknown, for instance, in biological networks.

As an example, consider a class of networks known as *Boolean networks*. These are discrete systems whose nodes are represented by binary numbers (1 or 0). Such networks are often used to model the gene expression in genetic networks [38]. Bistability in the Boolean network arises as either the coexistence of two stable equilibria, when the node values are fixed to different values depending on the initial condition, or the coexistence of a stable equilibrium and an oscillatory state, when the node values periodically change in time.

The regulatory Boolean network with n nodes is modelled by the following expression [39]

$$x_i(t+1) = f_i \left((x_j(t))_{j \in N_i}, (\bar{x}_j(t))_{j \in \bar{N}_i} \right), \quad i = 1, 2, \dots, n, \quad (6.21)$$

where $x_i(t) \in \{0, 1\}$ is the state of i -th node. The sets $N_i \subseteq \{1, 2, \dots, n\}$ and $\bar{N}_i \subseteq \{1, 2, \dots, n\} \setminus N_i$ are composed of the neighbors of node i . The nodes in N_i are connected to node i without changing the state, while the nodes in \bar{N}_i are connected to node i with inverting the state and so the negated states affect the update of the state of node i . The Boolean function $f_i : \{0, 1\}^{|N_i|} \times \{0, 1\}^{|N_i|} \rightarrow \{0, 1\}$ is

- independent of $x_j(t)$ and its negation $\bar{x}_j(t)$ at the same time, i.e. $N_i \cap \bar{N}_i = \emptyset$,
- composed of logical AND and OR operators,
- identical to 0 or 1 if $N_i = \bar{N}_i = \emptyset$, and
- minimally represented.

Thus, the Boolean network contains sets $(N_1, \bar{N}_1, N_2, \bar{N}_2, \dots, N_n, \bar{N}_n)$ and function set $F = (f_1, f_2, \dots, f_n)$. The former provides with information about the network structure, while the latter about the node dynamics. Therefore, the Boolean network is defined by $\Sigma(G, F)$, where $G = (V, E, L)$ denotes the network structure modeled as the edge-labeled directed graph with the node set $V := \{1, 2, \dots, n\}$, the edge set $E := \{(j, i) \in \{1, 2, \dots, n\}^2 \mid j \in N_i \cup \bar{N}_i\}$, and the labeling function $L : E \rightarrow \{-1, 1\}$ such that $L(j, i) = 1$ for $j \in N_i$. There are two kinds of links: activating (\rightarrow) and inhibiting (\dashv).

The Boolean network topology is characterized by the number of simple cycles k , their lengths (l_0, l_1, \dots, l_k) , and the number of inhibiting links in each simple cycle.

Azumal et al. [40] have proven the theorems which derive necessary and sufficient conditions for structural bistability in Boolean networks of flower-shaped and

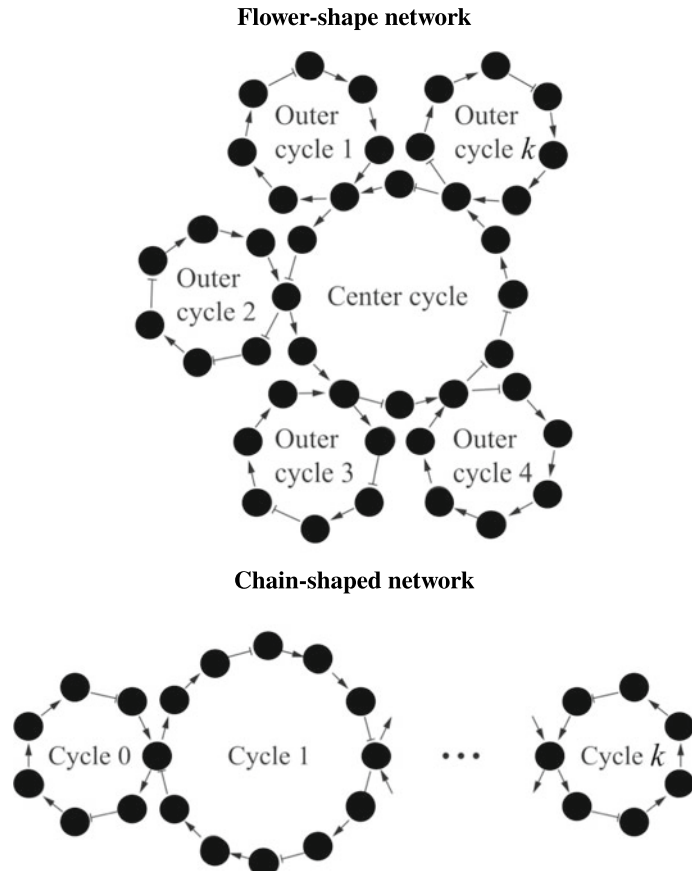
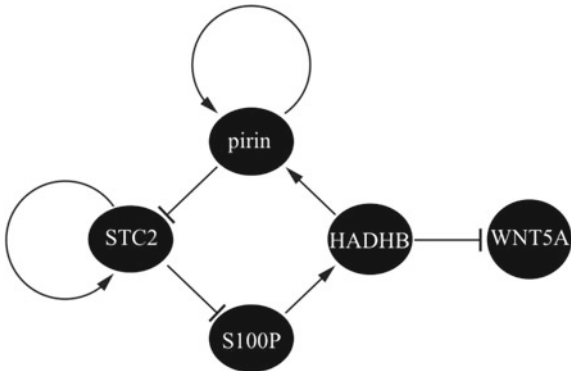


Fig. 6.14 Flower-shaped and chain-shaped Boolean networks

chain-shaped structures illustrated in Fig. 6.14. The theorems state that such Boolean networks are *structurally bistable* if and only if either one of the following conditions holds for G :

- $k = 0$ (cyclic network), $l_0 = 1$, and the simple cycle contains no inhibiting edge;
- $k = 1$ (8-shaped network), l_0 and l_1 are coprime, and both the two simple cycles contain an even number of inhibiting edges;
- $k = 2$ and for flower-shaped networks $l_1 = l_2 = 1$, the center cycle contains an odd number of inhibiting edges, and the outer cycles contain an even number of those (more precisely, contain none of those because $l_1 = l_2 = 1$);
- $k = 2$ and for chain-shaped networks $l_0 = l_2 = 1$, the simple cycle of length l_1 contains an odd number of inhibiting edges, and the other simple cycles contain an even number of those (more precisely, contain none of those because $l_0 = l_2 = 1$).

Fig. 6.15 Schematic of the melanoma network of genes PIR, STC2, S100P, HADHB, and WNT5A. Based on data from [40]



Let us illustrate how non-structural and structural bistability appears in Boolean networks. First, we consider the genetic network related to melanoma onset [41] and shown in Fig. 6.15. This network is modeled by the following equations:

$$\begin{aligned} x_1(t+1) &= x_1(t) \wedge x_4(t), \\ x_2(t+1) &= \bar{x}_1(t) \vee x_2(t), \\ x_3(t+1) &= \bar{x}_2(t), \\ x_4(t+1) &= x_3(t), \\ x_5(t+1) &= \bar{x}_4(t), \end{aligned} \quad (6.22)$$

where $x_i \in \{1, 2, 3, 4, 5\}$ are the expression levels of the genes: PIR, STC2, S100P, HADHB, and WNT5A, respectively.

The system in Eq. 6.21 is a cascade connection of the upper subsystem with PIR, S100P, HADHB and STC2, and the lower subsystem with WNT5A. This system exhibits the coexistence of stable fixed-point attractors $[0\ 1\ 0\ 0]^T$ and $[1\ 0\ 1\ 1]^T$. The network structure of the upper subsystem is flower-shaped with $k = 2$, $l_0 = 4$, and $l_2 = 1$, and contains two inhibiting edges in the simple cycle of length 4 and no inhibiting edge in the other simple cycles. Therefore, the subsystem is not structurally bistable. However, if a new gene is inserted to the center cycle and the gene is activated by the predecessor and inhibits the successor, then the resulting system becomes structurally bistable.

The examples of structurally bistable networks are presented in Fig. 6.16.

It would be interesting to extend the theory of structural bistability to structural multistability not only in Boolean networks but also for a more general class of networked systems [42, 43].

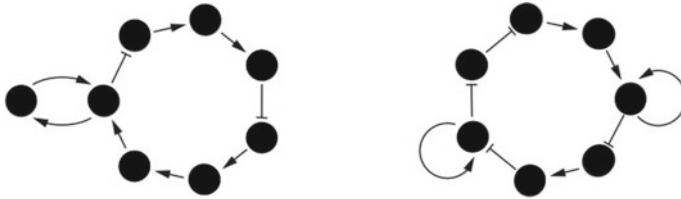


Fig. 6.16 Examples of structurally bistable Boolean networks with (left) $s = 1, l_0 = 2, l_1 = 7$ and (right) $k = 2, l_0 = 7, l_1 = l_2 = 1$

6.2.5 Multistate Chimeras

Chimeras are coexisting collective states in a network of coupled oscillators, when one part of the oscillators synchronize, while another part desynchronize [44, 45]. Such chimeric states exist in many physical and biological networks [46]. While in low-dimensional dynamics of cluster states, units within each group exhibit identical dynamics (see Sect. 2.2.3), chimeras are patterns of coexisting coherent and incoherent states. In addition, solitary states display *spatial chaos* [47] demonstrating a sensitive dependence on spatial coordinates, that leads to *spatial multistability* when the number of states grows exponentially with the system size.

It is important to note that inhomogeneity in the network is the necessary condition for the appearance of chimeras [48]. The inhomogeneity can arise in the coupling, topology, or parameters, as well as be caused by delays in the coupling between oscillators. In addition, we should emphasize that the presence of multistability is also the necessary condition for the emergence of chimeras [49, 50].

Here, we will show how multistate chimeras emerge in a network of globally coupled chaotic oscillators with the example of Lorenz oscillators with linear diffusive coupling, given by [51]

$$\begin{aligned}\dot{x}_i &= \sigma(y_i - x_i), \\ \dot{y}_i &= r x_i - y_i - x_i z_i, \\ \dot{z}_i &= x_i y_i - \beta z_i + \frac{K}{N-1} \sum_{j \neq i} (z_j - z_i),\end{aligned}\tag{6.23}$$

where $i, j = 1, \dots, N$ is the oscillator number, K is the coupling strength, and $\sigma = 10$ and $\beta = 8/3$ are parameters. The system in Eq. 6.23 is symmetric, that is $(x, y, z) \rightarrow (-x, -y, z)$. For $r \in [24.06, 24.76]$ three attractors coexist, two symmetric fixed points (A_{\pm}) given by $(\pm\sqrt{\beta(r-1)}, \pm\sqrt{\beta(r-1)}, (r-1))$ and a chaotic attractor A_0 . The basins of attraction of these states are shown in Fig. 6.17. One can see that the basins are intertwined, which makes the existence of the chimera inevitable.

Figure 6.18 illustrates a chimera state in the network of $N = 100$ globally coupled oscillators given by Eq. 6.23 which has several coexisting attractors with different dynamics.

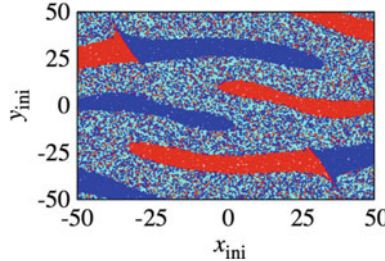


Fig. 6.17 Basins of attraction of the system in Eq. 6.23 for parameters $r = 24.4$, $\sigma = 10$, $\beta = 8/3$, and $K = 0.05$. The blue and red regions are basins of small attractors A_{\pm} , and the cyan region is the basin of the large attractor A_0 . Reprinted figure with permission from [51] ©2017 by the American Physical Society

This chimera consists of three distinct subpopulations corresponding to three attractors (B_- , B_+ , and B_0) shown in left panel in Fig. 6.18. In the first two groups, the oscillators synchronize, while in the last group, they desynchronize. In the chimera state, about 40 oscillators are in the groups B_- and B_+ synchronized in-phase or anti-phase, and 60 oscillators are in the desynchronized group B_0 .

A similar chimeric behavior is observed in the network of globally coupled Chua oscillators with three coexisting scroll attractors. The network dynamics is given by

$$\begin{aligned}\dot{x}_i &= \alpha [y_i - h_a(x_i, z_i)], \\ \dot{y}_i &= x_i - \rho y_i + z_i + \frac{K}{N-1} \sum_{j \neq i} (y_j - y_i), \\ \dot{z}_i &= -\delta y_i,\end{aligned}\quad (6.24)$$

where

$$h_a(x, z) = \begin{cases} g(x), & |z| \geq c, \\ -g(x), & |z| \leq c, \end{cases}\quad (6.25)$$

with $c > 0$ and $g(x) = m_1 x + 0.5(m_0 - m_1)(|x + 1| - |x - 1|)$.

The coexisting scroll attractors and chimeras in $N = 100$ globally coupled Chua oscillators are illustrated in Fig. 6.19.

The coupling affects the parameter ρ , and for the corresponding value of K the system is involved into a mode in which a synchronized attractor coexists with two asynchronous attractors. This system evolves into a chimera, where a synchronized group (B_1) coexists with two asynchronous groups (B_2 and B_3), as seen from the right panel in Fig. 6.19. The dynamics of the oscillators in the synchronized group is located on attractor S_0 , whereas the asynchronous oscillators can be installed either on the attractor D_- or D_+ shown in the left panel in Fig. 6.19.

Thus, the appearance of dynamical chimeras in ensembles of coupled chaotic oscillators in the absence of inhomogeneity in coupling occurs due to multistability.

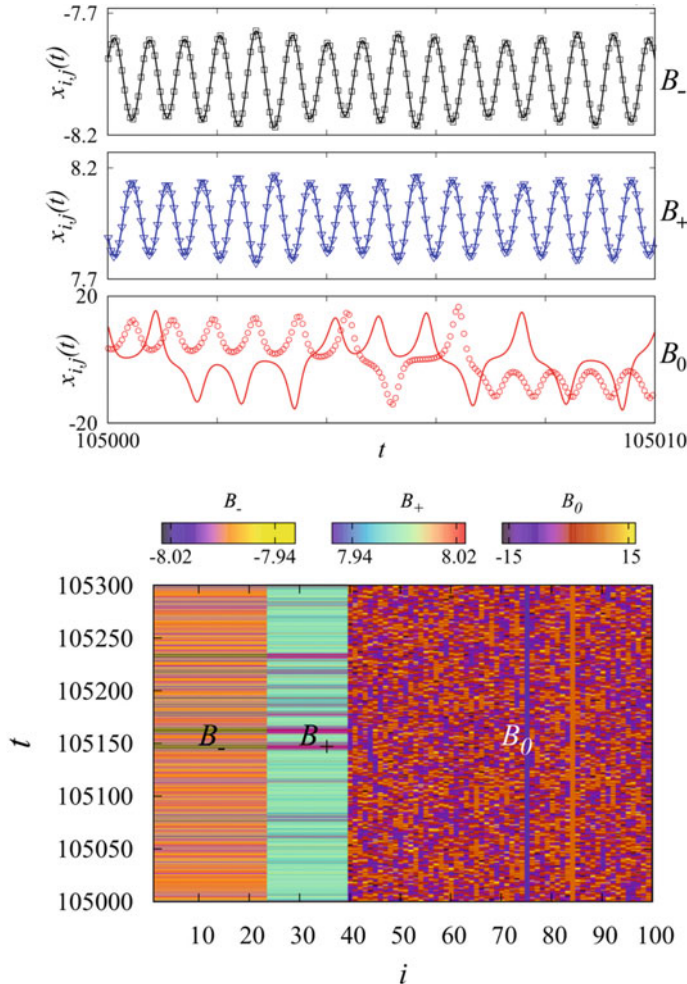


Fig. 6.18 Chimeras in globally coupled Lorenz oscillators Eq. 6.23. (Upper) Time series of $x_{i,j}$ for two arbitrarily chosen oscillators i (solid lines) and j (symbols) belonging to group B_- , B_+ , and B_0 . (Lower) Time evolution of x variable for $N = 100$ oscillators for parameters $r = 24.8$, $\sigma = 10$, $\beta = 8/3$, and $K = 0.07$, starting from random initial conditions $x_0, y_0, z_0 \in [-100, 100]$. Reprinted figure with permission from [51] ©2017 by the American Physical Society

At the same time, symmetry breaking, which leads to stable chimeric dynamics, results from multistability induced by the coupling, and because basins of coexisting attractors are intertwined into a complex structure. It should be noted that chimera states can be observed even when basins of coexisting attractors do not mix, but when multistability and intertwined basins are present together. Nevertheless, the system inevitably demonstrates stable chimeras that can exist even for small networks.

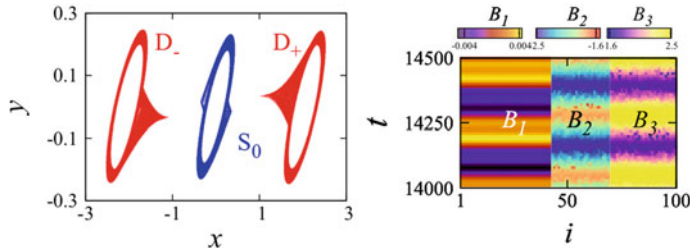


Fig. 6.19 (Left) Coexisting scroll attractors in the coupled Chua oscillators (Eq. 6.24) and (right) chimeric behavior in the ensemble of 100 globally coupled Chua oscillators. S_0 is the synchronized attractor and D_- and D_+ are asynchronous attractors. B_1 , B_2 , and B_3 denote a synchronized group and two asynchronous, respectively. The parameters are $K = 0.03$, $\rho = 1.47$, $\alpha = 10$, $\delta = 14$, $c = 1$, $m_0 = -0.43$, and $m_1 = 0.41$. Adapted from [51]

6.3 Multistability in Neural Networks

The human central nervous system contains a complex large-scale interconnected neural network that includes feedforward and feedback (or recurrent) subnetworks, where the brain is a central element of this complex networked system. The brain is connected to the senses, which transmit sensory information to the brain, which transmits action commands to the executive elements. The brain neural network consists of approximately 86 billion nerve cells connected by 10^4 to 10^5 synapses. All neural cells in the human body maintain an electrochemical potential gradient between the cell membrane and the environment, that is the most basic neuron characteristic. Since neurons can be excited if the stimulation exceeds the threshold value, they fire by producing an action potential (large voltage spike) before returning to the resting potential. The brain neurons are connected in a complex network so that the excitation of one neuron can be a stimulus for the excitation of other neurons.

Many experimental neuroimaging results can be interpreted in terms of complex high level networks. This requires the developments of mathematical models on the base of nonlinear differential equations. Therefore, nonlinear dynamics is the basis for a rigorous description of the behavior of large-scale neural networks. An interesting application of the theory of nonlinear dynamical systems to neuroscience is the study of the phenomena of the central nervous system, which exhibits almost discontinuous transitions between metastable brain states.

Neural networks are characterized by high dimensionality and multiple nonlinear interactions between neurons, often with delays and feedbacks. Although in neuronal systems the coexistence of multiple stable and metastable states is expected, a single synchronous state can exist, when the global coupling is too strong. Thus, neural networks must have destabilizing factors that allow switching among different states. When examining factors that can cause such itinerancy, one has to focus on connectivity. Numerical simulations of biologically plausible excitable systems have shown that synaptic delays are important for the appearance of partially synchronized subnetwork states, as well as slowly fluctuating synchronization patterns. It was also

shown that multiple attractors can only be detected in the range of global coupling strengths. Another important factor is the connectivity pattern or network topology.

There are two possible sources of intermittent dynamics, chaos and noise. Deterministic trajectories and stochastic switching between basins of attraction of stochastic attractors are by no means mutually exclusive, but this does not mean that their results are the same. Xu et al. [52] showed that a neural network composed of chaotic oscillators has a higher tendency to exhibit multistability than when composed of nonchaotic neural oscillators. It is also known that chaos can occur in large neural networks [53].

At the same time, neural activity is inherently irregular during the generation of action potentials, their propagation along axons and subsequent synaptic transmission [54], constant bombardment of synaptic inputs [55], and synaptic unreliability. Consequently, both deterministic and stochastic mechanisms regulate the neural network dynamics, but they differently affect functional connectivity [56].

When studying dynamics of multistable neural networks, some researchers considered deterministic models of coupled chaotic oscillators [57], others used simple oscillatory or non-oscillatory nodes that were displaced from their attractors due to noise [58]. In addition, many studies are based on models with relatively complex dynamics at the node level, but still some stochastic term is introduced to control multistability [59]. Finally, Orio et al. [7] investigated how a heterogeneous network of oscillatory neurons can display different patterns of multistability when triggered by chaos, channel noise, or both.

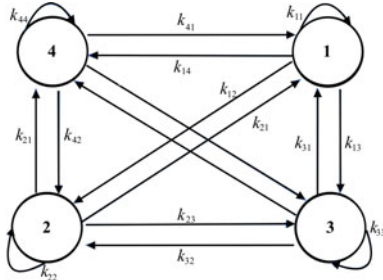
Below, we will first show how multistability appears in small neural circuits, and then how multistability arises in artificial neural networks. Finally, we will describe how multistability can be revealed by analysing functional connectivity.

6.3.1 *Multistability in Small Neural Circuits*

The groups of cortical neurons are often described by *neural-mass models* [60] of such models, so-called *Jansen–Rit model* [61] which describes local cortical circuits representing excitatory pyramidal cells with inhibitory and excitatory feedback from local interneurons and excitatory signals from other regions such as the thalamus. This class of models is studied using *mean field theory* [62] that approximates the behavior of large networks. This approximation is adequate in the case of an infinite number of neurons, i.e. at the *thermodynamic limit*. However, for networks of finite size, the mean field theory allows only an approximation of the actual behavior and hence may ignore some dynamical phenomena, for example, chaos and multistability.

Several mathematical methods were developed to characterize the behavior of finite-size neural circuits. Among many approaches, we have to mention the linear noise approximation [63], the density functional approach [64], large-deviations theory [65], and path-integral methods [66]. These methods typically can only be applied to mesoscopic circuits composed of a finite but large number of neurons.

Fig. 6.20 Topological connection of the hyperchaotic Hopfield neural network with four neurons



On the other hand, it is very important to understand the behavior of small neural networks composed of 2–4 neurons.

The dynamics of small neural networks was first analyzed by Beer, who studied bifurcations of arbitrary-size networks with highly symmetric assumptions about the strength of synaptic weights [67], and using asymptotic approximations of the bifurcation manifolds [68].

As an example, we will consider a Hopfield neural network [69], often used to describe some brain process related to learning and memory. The dynamics of the Hopfield circuit composed by n neurons is described as

$$\dot{x}_i = -c_i x_i + \sum_{j=1}^n k_{ij} \tanh x_j + I_i, \quad (6.26)$$

where c_i is the membrane resistance of the i th neuron, I_i is the input bias current, and k_{ij} is the matrix element of a $n \times n$ synaptic weight matrix representing the strength of connections between neurons. The $\tanh x_j$ function indicates the activating input voltage from the j th neuron.

For simplicity, let us consider a small network composed by four neurons without any input ($n = 4$, $I_i = 0$), which topology is illustrated in Fig. 6.20.

This small neural network exhibits the coexistence of periodic, quasiperiodic, chaotic, and hyperchaotic attractors for a certain set of parameters. For example, when $c = [1, 1, 1, 100]^T$ and the synaptic weight matrix is chosen as

$$W = \begin{bmatrix} k_{11} & k_{12} & k_{13} & k_{14} \\ k_{21} & k_{22} & k_{23} & k_{24} \\ k_{31} & k_{32} & k_{33} & k_{34} \\ k_{41} & k_{42} & k_{43} & k_{44} \end{bmatrix} = \begin{bmatrix} 1 & 0.5 & -3 & -1 \\ 0 & 1.58 & 3 & 0 \\ 3 & -3 & 1 & 0 \\ 100 & 0 & 0 & 190 \end{bmatrix}, \quad (6.27)$$

the system in Eq. 6.26 has three attractors. The phase portraits of symmetric periodic (A_1) and two quasiperiodic (A_2 and A_3) orbits and the section of their basins of attraction are presented in Fig. 6.21.

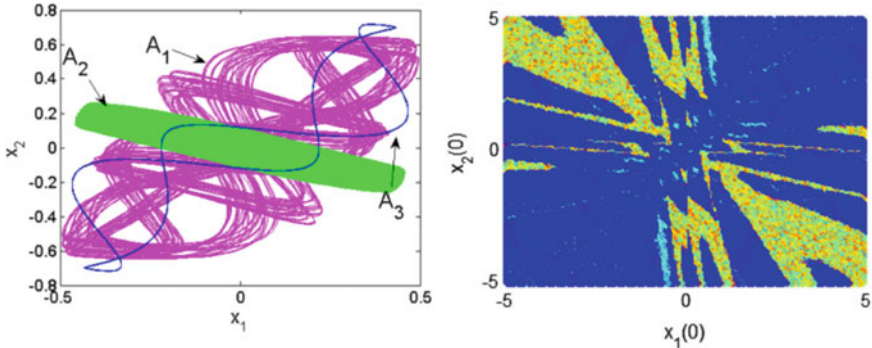


Fig. 6.21 (Left) Phase portraits of three coexisting symmetric attractors with different shape. (Right) Section of basins of attraction of periodic (blue) and quasiperiodic (green) attractors. Adapted from [70]

6.3.2 Spatial Phase Multistability

Multiplex complex networks have attracted a lot of attention due to their rich synchronization dynamics which displays coexisting chimeras. A particular type of multistability referred to as *spatial phase multistability* was observed in these multiplex networks by Makovkin et al. [71], who studied synchronization in the two-layer network of Kuramoto oscillators. Using this system, the authors intended to simulate a glial-neural network.

In the considered multiplex network, the both layers contain the same number of nodes. It is supposed that the frequency of oscillators in one layer is slow, and the frequency of oscillators in another layer is fast. Each node in the “glial” layer (G) is connected bidirectionally with eight neighboring nodes, while the coupling in the “neural” layer (N) is modelled by the Watts–Strogatz approach, so that the nodes are connected with probability p varying from $p = 0$ (regular network) to $p = 1$ (random network) [72]. At the same time, each node in the neural layer is coupled with the corresponding node in the glial layer. Thus, the dynamics of such a network can be described as

$$\dot{\theta}_n = \omega_n + \sum_{m=1}^{M^2} \sigma_{nm} A_{nm} \sin(\theta_m - \theta_n), \quad (6.28)$$

where θ_n and ω_n are, respectively, the phase and natural frequency of the n -th oscillator and $A_{nm} = 0, 1$ are adjacency matrix elements, and $\sigma_{nm} = \{\sigma_G, \sigma_N, \sigma_{GN}\}$ are coupling strengths for interglial, interneuronal and glial-neuronal interactions, respectively. The natural frequencies are uniformly distributed from $\omega \in [\omega(G, N) - 1/2; \omega(G, N) + 1/2]$, where $\omega(G) = 1$ and $\omega(N) = 10$.

The spatial phase patterns in the neural layer found using different initial conditions are shown in Fig. 6.22.

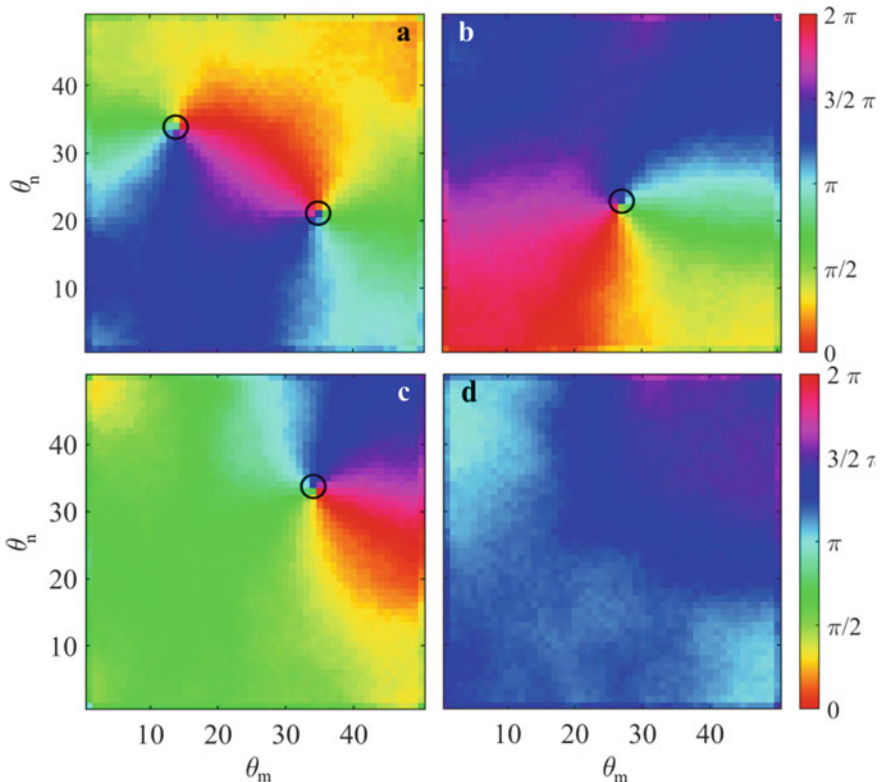


Fig. 6.22 Coexisting phase synchronization states in the neural layer of Kuramoto oscillators with $\sigma_N = 6$ and $\sigma_G = 16$, characterized by different values of order parameter $R \approx 0.12$ (a), 0.33 (b), 0.59 (c), and 0.9 (d). The black circles mark asynchronous phase oscillators. Reproduced from [71] with permission of AIP Publishing

The regular neural layer exhibits multistability which manifests itself as the coexistence of different synchronization regimes, where all oscillators have the same frequency but distinct phases. The network of N oscillators with different phase synchronization states is characterized by different values of the Kuramoto order parameter R which can be calculated by Eq. 6.15.

Interestingly, in the frequency synchronized network there are oscillators whose frequencies differ from other (synchronized) oscillators. These oscillators marked by circles in Fig. 6.22a–c are located at the border between different phase synchronous regions.

6.3.3 *Multistability in Inhibitory Neural Networks*

A surprising fact in neuroscience is the large number of synchronized oscillations in small neural networks compared to a few oscillation waves in the brain (alpha, beta, gamma, delta, theta). A possible reason for this discrepancy may lie in the background noise of biological networks [73], which destabilizes some states more than others through a multitude of synchronized oscillations. In this contexts, an interesting question arises: What is the maximum number of synchronized oscillations that a neural network can support?

To answer this question, Nagaret and King [74] studied inhibitory neural networks of interconnecting Hodgkin–Huxley neurons. Inhibitory neurons as known to take part in the genesis of biological rhythms and encode a large amount of information through delayed inhibition [75]. Moreover, inhibitory interneurons participate in the involvement of cortical circuits and demonstrate the importance of synaptic kinetics in triggering synchronized oscillations. To determine the maximum network capacity and predict the formation of locally coherent modes associated with pathological cortical oscillations, we have to know how the number of attractors depends on the number of coupled neurons, and how they are interconnected.

Using *in-silico* neuromorphic models, Zhao et al. [76] found that a network of N inhibitory mutually connected neurons can host up to $(N - 1)!/\ln^N 2$ stable oscillatory states. The phases of neuron oscillations define the dynamical state of the network. The number of attractors can be calculated according to the Stirling transform operation [77]. For instance, a 3-neuron network exhibits from 2 to 6 coexisting synchronous states, while a 4-neuron network shown in Fig. 6.23 displays from 6 to 26 coexisting attractors.

Later, Chauhan and colleagues [78] investigated oscillation patterns of 2-neuron, 3-neuron, and 4-neuron inhibitory networks in a neuromorphic device based on the Hodgkin–Huxley model, and found that the maximum number of limit cycles depends on the delay of the inhibitory postsynaptic potential relative to the presynaptic action potential. Each neuron in the network was stimulated by currents with the same amplitude, but supplied with a different time delay δt , which set the initial condition of the network.

In the 4-neuron network presented in Fig. 6.23, the current steps apply to neurons $n = 2, \dots, N$ are delayed by δt_n with respect to the step applied to neuron 1 and varied in the interval $0 \leq \delta t_n \leq T$. The system state is constructed in the state vector of the phase differences (ϕ_2, \dots, ϕ_N) of the network by measuring the AP dephasings (ϕ_2, ϕ_3, ϕ_4) of neurons 2, 3, and 4 relative to the action potential of neuron 1. The state trajectory is built by tracking the action potential dephasings in each period of oscillation starting from the first ($i = 1$) to further ($i > 50$). The trajectory of the state vector $[\phi_2(i), \phi_3(i), \phi_4(i)]$ is then constructed in the phase space for $i = 1, 2, \dots, 50$ periods and orthogonally projected onto the (ϕ_2, ϕ_3, ϕ_4) plane. The trajectories drawn from all epochs represent the entire phase space and hence the overall network dynamics.

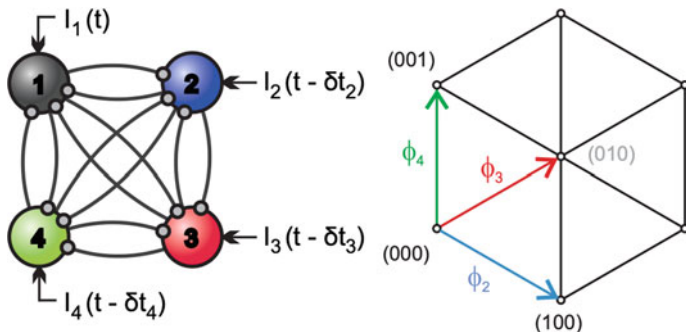


Fig. 6.23 Inhibitory mutually coupled neurons stimulated by currents I_1 , I_2 , I_3 , and I_4 applied with delays. The network state is represented by orthographic projection of the three-dimensional space mapping of the time evolution of the state vector (ϕ_2, ϕ_3, ϕ_4) of neuron dephasings relative to neuron 1. Reprinted from [78]; licensed under a Creative Commons Attribution 4.0 International license

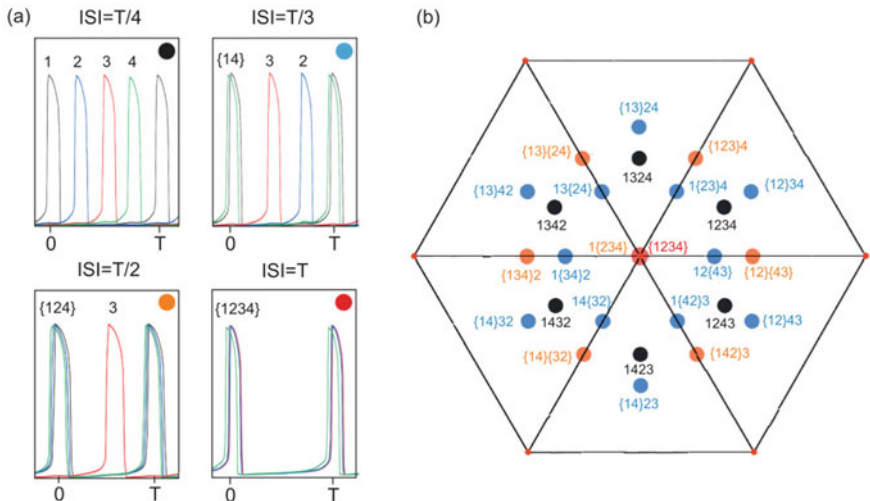


Fig. 6.24 Coexisting synchronized oscillation patterns in the 4-neuron inhibitory network shown in Fig. 6.23. **a** Synchronized modes of spatio-temporal oscillations ranging of sequentially discharging neurons ($ISI = T/4$), partially coherent oscillations ($ISI = T/3$, $T/2$), and fully coherent state when all neurons fire in phase ($ISI = T$). **b** Phase-space coordinates of stable modes of synchronized oscillations. Each node is labeled with its own action potential sequence. Curly braces indicate simultaneously firing neurons. Colored dots correspond to oscillation modes in (a). Reprinted from [78]; licensed under a Creative Commons Attribution 4.0 International license

The steady-state oscillations are classified according to their inter-spike interval (ISI). Four modes of synchronized oscillations in the 4-neuron network are labeled as $ISI = T/4$, $T/3$, $T/2$, T (see Fig. 6.24).

The $ISI = T/4$ mode is denoted as the 1234 action potential sequence and its five cyclically ordered permutations. The coordinates of the phase map of the corresponding attractor are $(1/4, 2/4, 3/4) + 5$ permutations (black dots). The $ISI = T/3$ mode has one coincident and three consecutive action potentials that form 12 following patterns: {12}34 at coordinates $(0, 1/3, 2/3) + 5$ permutations, 1{23}4 at $(1/3, 1/3, 2/3) + 2$ permutations, and 12{34} at $(1/3, 2/3, 2/3) + 2$ permutations (blue dots). Next, the $ISI = T/2$ mode has two coincident and two sequential action potentials distributed as {12}{34} and 1{234} with attractors located at $(0, 1/2, 1/2) + 2$ permutations, $(0, 0, 1/2) + 2$ permutations, and $(1/2, 1/2, 1/2)$, respectively, giving seven attractors in total (orange dots). Finally, the $ISI = T/1$ mode has all four neurons firing in phase giving a single attractor at $(0,0,0)$. Thus, the maximum number of oscillations is $T4 = 6 + 12 + 7 + 1 = 26$.

6.3.4 *Multistability in Artificial Neural Networks*

Artificial neural networks (ANNs) are widely used in various fields of science and technology [79]. Applications of ANNs include classification, associative memory, image processing, pattern recognition, parallel computing, optimization. They are also successfully applied to the analysis of neurophysiological data [80–83]. On one hand, the ANN applications to parallel computing and signal processing require finding the best solution of an optimization problem, and hence the ANN must have a unique equilibrium for all possible initial conditions. This means that the system should be monostable. On the other hand, when an ANN is used as a store of associative memory or for pattern recognition, the presence of multiple equilibria is beneficial.

The existence of multistability in ANNs was discovered by Cheng et al. [84] in Hopfield-type recurrent neural networks¹ with and without delays. Then, multistability was found in ANNs of other types, such as Cohen–Grossberg neural networks [85], delayed neural networks with unsaturating piecewise linear transfer functions [86], neural networks with discontinuous activation functions [87, 88], competitive neural networks with time-varying and distributed delays [89], neural networks with piecewise linear nondecreasing activation functions [90], neural networks with time-varying delays and the piecewise linear activation function [91], second-order competitive neural networks with nondecreasing saturated activation functions [92], impulsive hybrid discrete-time Hopfield neural networks with delays [93], cellular neural networks [94], neural networks with time-varying delays and concave-convex characteristics [95], neural networks with Mexican-hat-type activation functions [96], cooperative neural networks with delays [97], high-order competitive neural networks with a general class of activation functions [98], delayed competitive neural networks with nondecreasing piecewise linear activation functions

¹ A recurrent neural network is a class of ANNs where connections between nodes form a directed graph along a temporal sequence.

[99], neural networks with activation functions symmetrical about the origin on the phase plane [100], neural networks with unbounded time-varying delays [101], delayed hybrid impulsive neural networks [102], discrete-time neural networks with nonmonotonic piecewise linear activation functions [103], delayed fractional-order competitive neural networks [104], etc.

It should be noted that most of the multistable ANN have delays in neuron connections because delays always exist due to the finite switching speed of the amplifiers and the distances between neurons. An important issue in modeling ANN is the choice of a nonlinear activation function. In early studies, the typical choice was a sigmoid function. However, researchers soon realized that a piecewise linear function has important advantages to approximate the sigmoid function, because it allows one to find exact equilibria.

The dynamic scenario for a multistable ANN system is more complex than for a monostable system. Indeed, the theoretical substantiation of the complete stability of delayed neural networks or other systems with delay and multiple equilibrium states is a very nontrivial task.

To illustrate multistability in ANNs, let us consider a general class of competitive neural networks of n nodes given by

$$\begin{aligned}\dot{x}_i(t) &= -d_i x_i(t) + \sum_{j=1}^n a_{ij} f_j(x_j(t)) + B_i S_i(t) + I_i, \\ \dot{m}_{ij}(t) &= -\alpha_i M_i(t) + y_j \beta_i f_i(x_i(t)),\end{aligned}\tag{6.29}$$

where $x_i(t)$ is the state of the i th neuron ($i = 1, \dots, n$), $d_i > 0$ is the rate with which the i th neuron will reset its potential to the resting state in isolation when disconnected from the network and external inputs, $a_{i,j}$ are the coupling weight between i th and j th ($j = 1, \dots, P$) neurons, I_i is the external input, y_j is the constant external stimulus with strength B_i , I_i is the constant input, $\alpha_i > 0$ and $\beta_i \geq 0$ are scaling coefficients, and the activation function $f_j(x_j(t))$ is the Mexican-hat-type discontinuous activation function. The value of $M_i(t)$ in Eq. 6.29 is defined as

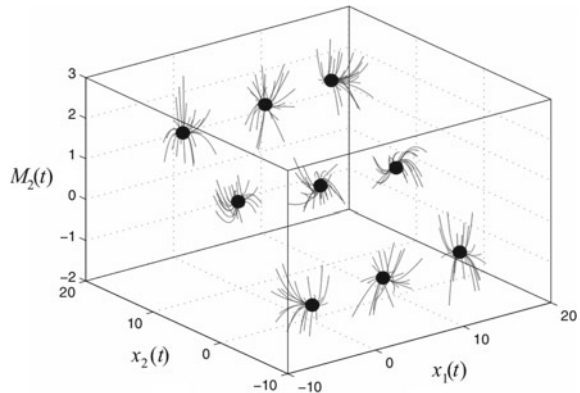
$$M_i(t) = \sum_{j=1}^P m_{ij} y_j,\tag{6.30}$$

where m_{ij} denotes the synaptic efficiency.

Nie et al. [105] have proved that the competitive neural networks with n neurons, activated by a discontinuous function, have 4^n equilibrium points and 3^n of them are locally stable.

As an example, let us consider the competitive neural network formed by two neurons ($n = 2$, $i = 1, 2$) with the following parameters: $d_1 = d_2 = 1$, $a_{11} = a_{22} = 2$, $a_{12} = -0.2$, $a_{21} = 1/3$, $B_1 = 0.2$, $B_2 = -0.2$, $I_1 = 2$, $I_2 = 1$, $\alpha_1 = \alpha_2 = 3$, and $\beta_1 = \beta_2 = 1$. The discontinuous piecewise linear activation function is

Fig. 6.25 Nine stable equilibria (dots) in the competitive neural network of two neurons with discontinuous piecewise linear activation function modelled by Eqs. 6.29–6.31. Based on data from [106]



$$f_i(x) = \begin{cases} -1, & -\infty < x < -2, \\ 2x + 1, & -2 \leq x \leq 1, \\ -x + 7, & 2 < x \leq 10, \\ 6, & 10 < x < +\infty. \end{cases} \quad (6.31)$$

Therefore, the ANN modelled by Eqs. 6.29–6.31 has $4^2 = 16$ equilibria and $3^2 = 9$ of them are locally stable. These stable fixed points are visualized in Fig. 6.25 in the (x_1, x_2, M_2) phase space.

6.3.5 Functional Connectivity in Neural Networks

Neural systems are characterized by high dimensionality and multiple nonlinear interactions between neuronal cells, often with delays and feedbacks. In such systems, the coexistence of multiple stable and metastable states is expected. However, if the global connection between neurons is too strong, only one completely synchronized state should arise. To avoid this situation, neural networks must have destabilizing factors that allow itinerancy between different states. One of such factors is *functional connectivity* [107–110].

Functional connectivity patterns can be found by analyzing time series of brain activity obtained with electroencephalography (EEG), magnetoencephalography (MEG), or functional magnetic resonance imaging (fMRI). Inherent neuronal brain noise induces switching among different coexisting states, whereas in a deterministic system would stabilize in one of the attractors, depending on the initial conditions. On the other hand, not only noise, but also chaos can induce switching between coexisting states.

It is also known that neural activity is inherently irregular during the generation of action potentials, their propagation along axons, and subsequent synaptic transmission. This is due to the random opening and closing of ion channels, constant

bombardment of synaptic inputs, and synaptic inreliability. Consequently, both deterministic and stochastic switching mechanisms should be taken into account, although they have different effects on functional connectivity dynamics.

To evaluate functional connectivity, different measures are used. Among them, we have to mention the order parameter, time variance of the order parameter, pair-wise phase synchrony matrix, comparison and clustering of the functional connectivity matrices.

Next, we will show how these measures can be extracted from neurophysiological time series data.

Order parameter. The order parameter quantifies global synchrony of the neural network and is defined as follows

$$R(t) = \left| \langle e^{i\phi_k(t)} \rangle_N \right|, \quad (6.32)$$

where ϕ is the phase of slow oscillations that can be extracted using a Hilbert transform applied to the band-pass filtered voltage of the k -th neuron, typically in the alpha band of $(8-10)\pm3$ Hz, and $\langle \cdot \rangle_N$ denotes the signal averaged over all neurons.

Time variance of the order parameter. The time variance of the order parameter is a measure of metastability defined as

$$\chi = \frac{1}{n} \sum^n \left(\langle R \rangle_T - R \right)^2, \quad (6.33)$$

where n is the number of time points in the time series and $\langle \cdot \rangle_T$ denotes the average over time for the whole time series or for time windows.

Pair-wise phase synchrony matrix. The pair-wise phase synchrony matrix is a measure of functional connectivity usually performed over a given time window as follows

$$R_{k,l} = \left\langle \left| \frac{1}{2} (e^{i\phi_k(t)} + e^{i\phi_l(t)}) \right| \right\rangle_T, \quad (6.34)$$

where indices k, l refer to the network nodes.

Examples of functional connectivity matrices constructed for selected time windows are presented in Fig. 6.26. The time series shown in the figure is obtained in a small-world network of fifty Huber–Braun neurons with additional hyperpolarization activated current, coupled by electrical synapses [7].

When the network is not synchronized, functional connectivity is not completely determined by structural connectivity and, moreover, it evolves over time, alternating between different (and usually repetitive) synchronization patterns in the network.

Comparison of functional connectivity matrices. The comparison of functional connectivity matrices obtained at different time windows allows revealing functional connectivity dynamics. To do this, the time series is divided into overlapping time windows with 50% overlap. The functional connectivity comparison allows the construction of the functional connectivity dynamics matrix as follows

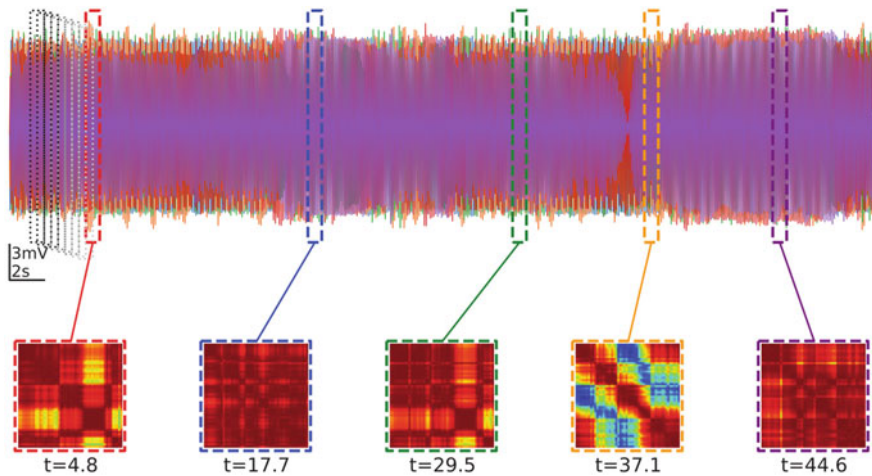


Fig. 6.26 Time series of low-pass filtered voltage traces of a small-world network of Huber-Braun neurons and functional connectivity matrices constructed for the selected time windows, by measuring the pair-wise phase synchrony. Reproduced from [7] with permission of AIP Publishing

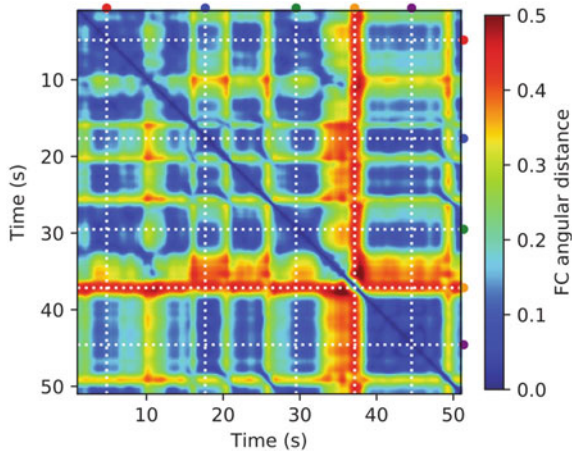


Fig. 6.27 Functional connectivity dynamics matrix, where all functional connectivities are compared with each other by the angular distance between the corresponding vectors. Blue spots denote functional connectivity patterns that repeat over time (if they are outside the diagonal) or remain for some time (if they are in the diagonal). Reproduced from [7] with permission of AIP Publishing

$$D_{i,j} = \left\| \frac{R_i}{\|R_i\|} - \frac{R_j}{\|R_j\|} \right\|, \quad (6.35)$$

where indices i, j refer to functional connectivity matrices at different times. The example of the functional connectivity dynamics matrix is shown in Fig. 6.27.

A histogram of functional connectivity values and their variance yields an approximate estimate of multistability. The blue color of the entire matrix means that there is a single functional connectivity or synchronization pattern. On the other hand, if yellow or red spots appear simultaneously, this means that different functional connectivity patterns coexist, i.e. multistability takes place.

Clustering of functional connectivity. Some researchers use an *unsupervised clustering algorithm* that automatically determines the number of clusters by embedding data at a suitable distance. For this purpose, *principal component analysis* is usually performed on a matrix containing all functional connectivities in their vector form. Then, the Euclidean distance is calculated between all functional connectivities projected onto main components.

Each data point, i.e. each functional connectivity, is characterized by two parameters, namely, density ρ and distance δ to the nearest higher density data point. The density ρ of functional connectivity i is determined by the expression $\rho = 1/\langle d_{ic} \rangle$, where $\langle d_{ic} \rangle$ is the average distance from point i to its $c = d_c n_{win}$ nearest neighbors (n_{win} being the total number of functional connectivities considered for clustering), and d_c determines the share of neighbors that need to be considered. Then, the cluster centroids can be found by fitting a power-law to the $\delta(\rho)$ curve, using the 99.8% upper confidence bound as a threshold. All points falling above this bound can be selected as centroids, and no centroid points can be assigned to their closest centroids, building up the clusters.

References

1. Newman MEJ (2003) The structure and function of complex networks. SIAM Rev 45:167–256
2. Strogatz SH (2001) Exploring complex networks. Nature 410(6825):268–276
3. Boccaletti S, Latora V, Moreno Y, Chavez M, Hwang DU (2006) Complex networks: structure and dynamics. Phys Rep 424:175–308
4. Rodrigues FA, Peron TKD, Ji P, Kurths J (2016) The Kuramoto model in complex networks. Phys Rep 610:1–98
5. Wassim MH, Hui Q, Bailey JM (2014) Human brain networks: spiking neuron models, multistability, synchronization, thermodynamics, maximum entropy production, and anesthetic cascade mechanisms. Entropy 16:3939–4003
6. Chen YA, Huang TR (2014) Multistability of the brain network for self-other processing. Sci Rep 7:43313
7. Orio P, Gatica M, Herzog R, Maidana JP, Castro S, Xu K (2018) Chaos versus noise as drivers of multistability in neural networks. Chaos 28:106321
8. May R (1977) Thresholds and breakpoints in ecosystems with a multiplicity of stable states. Nature 269:471–477
9. Prengel F, Wacker A, Schöll E (1994) Simple model for multistability and domain formation in semiconductor superlattices. Phys Rev B 50:1705–1712
10. Bonilla LL, Escobedo R, Dell'Acqua G (2006) Voltage switching and domain relocation in semiconductor superlattices. Phys Rev B 73:115341–115353
11. Koseska A, Volkov E, Zaikin A, Kurths J (2007) Inherent multistability in arrays of autoinducer coupled genetic oscillators. Phys Rev E 75:031916
12. Ullner E, Koseska A, Kurths J, Volkov E, Kantz H, Garcia-Ojalvo J (2008) Multistability of synthetic genetic networks with repressive cell-to-cell communication. Phys Rev E 78:031904

13. Hellmann F, Schultz P, Jaros P, Levchenko R, Kapitaniak T, Kurths J, Maistrenko Y (2020) Network-induced multistability through lossy coupling and exotic solitary states. *Nat Commun* 11:592
14. Menck PJ, Heitzig J, Kurths J, Schellnhuber HJ (2014) How dead ends undermine power grid stability. *Nat Commun* 5:3969
15. Mitra C, Choudhary A, Sinha S, Kurths J, Donner RV (2017) Multi-node basin stability in complex dynamical networks. *Phys Rev E* 95:032317
16. Meena C, Rungra PD, Sinha S (2020) Resilience of networks of multi-stable chaotic systems to targeted attacks. *Eur Phys J B* 93:210
17. Halekotte L, Feudel U (2020) Minimal fatal shocks in multistable complex networks. *Sci Rep* 10:11783
18. Pecora LM, Carroll TL (1998) Master stability functions for synchronized coupled systems. *Phys Rev Lett* 80:2109–2112
19. Boccaletti S, Hwang DU, Chavez M, Amann A, Kurths J, Pecora LM (2006) Synchronization in dynamical networks: evolution along commutative graphs. *Phys Rev E* 74:016102
20. Sevilla-Escoboza R, Buldú JM, Pisarchik AN, Boccaletti S, Gutiérrez R (2015) Synchronization of intermittent behavior in ensembles of multistable dynamical systems. *Phys Rev E* 91:032902
21. Kuramoto Y (1984) Chemical oscillations, waves, and turbulence. Springer, Berlin
22. Dai X, Kovalenko K, Molodyk M, Wang Z, Li X, Musatov D, Raigorodskii AM, Alfaro-Bittner K, Cooper GD, Bianconi G, Boccaletti S (2021) D-dimensional oscillators in simplicial structures: odd and even dimensions display different synchronization scenarios. *Chaos Soliton Fractals* 146:110888
23. Frolov N, Hramov A (2021) Extreme synchronization events in a Kuramoto model: the interplay between resource constraints and explosive transitions. *Chaos* 31:063103
24. Lehnertz K (2006) Epilepsy: extreme events in the human brain, Springer, Berlin, pp 1123–143
25. Pisarchik AN, Jaimes-Reátegui R, Sevilla-Escoboza R, Huerta-Cuillar G, Taki M (2011) Rogue waves in a multistable fiber laser. *Phys Rev Lett* 107:274101
26. Pisarchik AN, Grubov VV, Maksimenko VA, Lüttjohann A, Frolov NS, Marqués-Pascual C, Gonzalez-Nieto D, Khranova MV, Hramov AE (2018) Extreme events in epileptic EEG of rodents after ischemic stroke. *Eur Phys J Spec Top* 227:921–932
27. Frolov NS, Grubov VV, Maksimenko VA, Pavlov AN, Sitnikova S, Pisarchik AN, Kurths J, Hramov AE (2018) Statistical properties and predictability of extreme epileptic events. *Sci Rep* 9(1):7243
28. Karpov OE, Grubov VV, Maksimenko VA, Utashev N, Semerikov VE, Andrikov DA, Hramov AE (2018) Noise amplification precedes extreme epileptic events on human EEG. *Phys Rev E* 103:022310
29. Fischer T, Rings T, Reza Rahimi Tabar M, Lehnertz K (2022) Towards a data-driven estimation of resilience in networked dynamical systems: designing a versatile testbed. *Front Netw Physiol*
30. Hänggi P, Talkner P, Borkovec M (1990) Reaction-rate theory: fifty years after Kramers. *Rev Mod Phys* 62:251–342
31. Mandelbrot BB (1982) The fractal geometry of nature. Freeman, San Francisco
32. Poria S, Srimali MD, Sinha S (2008) Enhancement of spatiotemporal regularity in an optimal window of random coupling. *Phys Rev E* 78:035201(R)
33. Nag M, Poria S (2015) Synchronized states and multistability in a random network of coupled discontinuous maps. *Chaos* 25:083114
34. Jaimes-Reátegui R, Castillo-Cruz JM, García-López JH, Huerta-Cuellar G, Gallegos-Infante LA, Pisarchik AN (2020) Self-organization in network motifs of three bistable Duffing oscillators. *Cybern Phys* 9(1):31–40
35. Alon U (2007) Network motifs: Theory and experimental approaches. *Nat Rev Genetics* 8(6):450–461
36. Stone L, Simberloff D, Artzy-Randrup Y (2019) Network motifs and their origins. *PLoS Comput Biol* 15(4):2623–2634

37. Milo R, Shen-Orr S, Itzkovitz S, Kashtan N, Chklovskii D, Alon U (2002) Network motifs: simple building blocks of complex networks. *Science* 298(5594):824–827
38. Harris SE, B K Sawhill BK, A Wuensche A, S Kauffman S, (2002) A model of transcriptional regulatory networks based on biases in the observed regulation rules. *Complexity* 7(4):23–40
39. Aracena J (2008) Maximum number of fixed points in regulatory Boolean networks. *Bull Math Biol* 70(5):1398–1409
40. Azuma SI, Kure T, Sugie T (2020) Structural bistability analysis of flower-shaped and chain-shaped Boolean networks. *IEEE/ACM Trans Comput Biol Bioinform* 17(6):2098–2106
41. Kobayashi K, Hiraishi K (2014) ILP/SMT-based method for design of Boolean networks based on singleton attractors. *IEEE/ ACM Comput Biol Bioinf* 11(6):1253–1259
42. Huang B, Xia Y, Liu F, Wang W (2016) Realization of tristability in a multiplicatively coupled dual-loop genetic network. *Sci Rep* 6:28096
43. Lai Q, Zhao XW, Huang JN, Pham VT (2018) Monostability, bistability, periodicity and chaos in gene regulatory network. *Eur Phys J: Spec Top* 227:719–730
44. Kuramoto Y, Battogtokh D (2002) Coexistence of coherence and incoherence in nonlocally coupled phase oscillators. *Nonlin Phenom Compl Syst* 5:380–385
45. Abrams DM, Strogatz SH (2004) Chimera states for coupled oscillators. *Phys Rev Lett* 93:174102
46. Zaharova A (2020) Chimera patterns in networks: interplay between dynamics, structure, noise, and delay. Springer, Berlin
47. Omelchenko I, Maistrenko Y, Hövel P, Schöll E, E, (2011) Loss of coherence in dynamical networks: spatial chaos and chimera states. *Phys Rev Lett* 106:234102
48. Panaggio MJ, Abrams DM (2015) Chimera states: coexistence of coherence and incoherence in networks of coupled oscillators. *Nonlinearity* 28(3):R67–R87
49. Yeldesbay A, Pikovsky A, Rosenblum M (2014) Chimera-like states in an ensemble of globally coupled oscillators. *Phys Rev Lett* 112:144103
50. Chandrasekar VK, Suresh R, R, D V Senthilkumar DV, M Lakshmanan M, (2015) Coexisting coherent and incoherent domains near saddle-node bifurcation. *Europhys Lett* 111(6):60008
51. Ujjwal SR, Punetha N, Prasad A, Ramaswamy R (2017) Emergence of chimeras through induced multistability. *Phys Rev E* 95(3):032203
52. Xu K, Maidana JP, Castro S, Orio P (2018) Synchronization transition in neuronal networks composed of chaotic or non-chaotic oscillators. *Sci Rep* 8:8370
53. Sprott JC (2008) Chaotic dynamics on large networks. *Chaos* 18:023135
54. O'Donnell C, van Rossum MCW (2014) Systematic analysis of the contributions of stochastic voltage gated channels to neuronal noise. *Front Comput Neurosci* 8(4):105
55. Destexhe A, Rudolph M, Fellous JM, Sejnowski TJ (2001) Fluctuating synaptic conductances recreate in vivo-like activity in neocortical neurons. *Neuroscience* 107(1):13–24
56. Freeman WJ (2000) A proposed name for aperiodic brain activity: stochastic chaos. *Neural Netw* 13(1):11–13
57. Gollo LL, Zalesky A, Hutchison RM, van den Heuvel M, Breakspear M (2015) Dwelling quietly in the rich club: brain network determinants of slow cortical fluctuations. *Philos Trans R Soc B Biol Sci* 370(1668):20140165
58. Deco G, Cabral J, Woolrich MW, Stevner ABA, van Harteveld TJ, Kringsbach ML (2017) Single or multiple frequency generators in on-going brain activity: a mechanistic whole-brain model of empirical MEG data. *Neuroimage* 152:538–550
59. Deco G, Ponce-Alvarez A, Mantini D, Romani GL, Hagmann P, Corbetta M (2013) Resting-state functional connectivity emerges from structurally and dynamically shaped slow linear fluctuations. *J Neurosci* 33(27):11239–11252
60. Deco G, Jirsa VK, Robinson PA, Breakspear M, Friston K (2008) The dynamic brain: From spiking neurons to neural masses and cortical fields. *PLoS Comput Biol* 4:e1000092
61. Jansen B, Rit V (1995) Electroencephalogram and visual evoked potential generation in a mathematical model of coupled cortical columns. *Biol Cybern* 73:357–366
62. Faugeras O, Touboul J, Cessac B (2009) A constructive mean-field analysis of multi-population neural networks with random synaptic weights and stochastic inputs. *Front Comput Neurosci* 3:1

63. Bressloff P (2010) Stochastic neural field theory and the system-size expansion. *SIAM J Appl Math* 70(5):1488–1521
64. Buice MA, Chow CC (2013) Dynamic finite size effects in spiking neural networks. *PLoS Comput Biol* 9(1):e1002872
65. Faugeras O, MacLaurin J (2015) Asymptotic description of neural networks with correlated synaptic weights. *Entropy* 17:4701–4743
66. Bressloff P (2015) Path-integral methods for analyzing the effects of fluctuations in stochastic hybrid neural networks. *J Math Neurosci* 5:4
67. Beer RD (1995) On the dynamics of small continuous-time recurrent neural networks. *Adapt Behav* 3(4):469–509
68. Beer RD (1995) Parameter space structure of continuous-time recurrent neural networks. *Neural Comput* 18:3009–3051
69. Hopfield JJ (1984) Neurons with graded response have collective computational properties like those of two-state neurons. *Proc Natl Acad Sci USA* 16(81):3088–3092
70. Njitacke ZT, Isaac SD, Kengne J, Negou NA, Leutcho GD (2020) Extremely rich dynamics from hyperchaotic Hopfield neural network: hysteretic dynamics, parallel bifurcation branches, coexistence of multiple stable states and its analog circuit implementation. *Eur Phys J Spec Top* 229:1133–1154
71. Makovkin S, Laptyeva T, Jalan S, Ivanchenko M (2021) Synchronization in multiplex models of neuron-glial systems: Small-world topology and inhibitory coupling. *Chaos* 31:113111
72. Albert R, Barabási AL (2002) Statistical mechanics of complex networks. *Rev Mod Phys* 74:47–97
73. Faisal AA, Selen LPJ, Wolpert DM (2008) Noise in the nervous system. *Nat Neurosci* 9:292
74. Nogaret A, King A (2018) Inhibition delay increases neural network capacity through Stirling transform. *Phys Rev E* 97(3):030301(R)
75. Bartos M, Vida I, Jonas P (2007) Synaptic mechanisms of synchronized gamma oscillations in inhibitory interneuron networks. *Nat Rev Neurosci* 8:45
76. Zhao L, Nogaret A (2015) Experimental observation of multistability and dynamic attractors in silicon central pattern generators. *Phys Rev E* 92:052910
77. Bernstein M, Sloane NJA (1995) Some canonical sequences of integers. Linear algebra and its applications, vol 226–228. Elsevier Science Inc., New York, pp 57–72
78. Chauhan A, Taylor J, Nogaret A (2021) Local inhibitory networks support up to $(N - 1)!/(ln^N 2)$ limit cycles in the presence of electronic noise and heterogeneity. *Phys Rev Res* 3:043097
79. (2011) Artificial neural networks: methods and applications. In: Livingstone DJ (ed) Methods in molecular biology, vol 458, Humana Press
80. Hramov AE, Maksimenko VA, Pchelintseva SV, Runnova AE, Grubov VV, Musatov VY, Zhuravlev MO, Koronovskii AA, Pisarchik AN (2017) Classifying the perceptual interpretations of a bistable image using EEG and artificial neural networks. *Front Neurosci* 11:674
81. Hramov AE, Frolov NS, Maksimenko VA, Makarov VV, Koronovskii AA, García-Prieto J, Antón-Toro LF, Maestú F, Pisarchik AN (2018) Artificial neural network detects human uncertainty. *Chaos* 28(3):033607
82. Frolov NS, Pisarchik AN (2018) Diagnostics of the brain neural-ensemble states using MEG records and artificial neural-network concepts. *Tech Phys Lett* 44(5):441–444
83. Maksimenko VA, Kurkin SA, Pitsik EN, Musatov VY, Runnova AE, Efremova TY, Hramov AE, Pisarchik AN (2018) Artificial neural network classification of motor-related EEG: an increase in classification accuracy by reducing signal complexity. *Complexity* 2018:9385947
84. Cheng C, Lin K, Shih C (2006) Multistability in recurrent neural networks. *SIAM J Appl Math* 66(4):1301–1320
85. Cao JD, Feng G, Wang YY (2008) Multistability and multiperiodicity of delayed Cohen-Grossberg neural networks with a general class of activation functions. *Phys D* 237(13):1734–1749
86. Zhang L, Yi Z, Yu J (2008) Multiperiodicity and attractivity of delayed recurrent neural networks with unsaturating piecewise linear transfer functions. *IEEE Trans Neural Netw* 19(1):158–167

87. Huang G, Cao JD (2008) Multistability of neural networks with discontinuous activation function. *Commun Nonlinear Sci Numer Simul* 13(10):2279–2289
88. Huang YJ, Zhang HG, Wang ZS (2012) Multistability and multiperiodicity of delayed bidirectional associative memory neural networks with discontinuous activation functions. *Appl Math Comput* 219(3):928–942
89. Nie X, Cao J (2009) Multistability of competitive neural networks with time-varying and distributed delays. *Nonlinear Anal Real World Appl* 20(10):928–942
90. Wang L, Lu W, Chen T (2010) Coexistence and local stability of multiple equilibria in neural networks with piecewise linear nondecreasing activation functions. *Neural Netw* 23(2):189–200
91. Zeng Z, Huang T, Zheng WX (2010) Multistability of recurrent neural networks with time-varying delays and the piecewise linear activation function. *IEEE Trans Neural Netw* 21(8):1371–1377
92. Nie X, Cao J (2011) Multistability of second-order competitive neural networks with nondecreasing saturated activation functions. *IEEE Trans Neural Netw* 22(11):1694–1708
93. Kaslik E, Sivasundaram S (2011) Impulsive hybrid discrete-time Hopfield neural networks with delays and multistability analysis. *Neural Netw* 24(4):370–377
94. Lu W, Wang L, Chen T (2011) On attracting basins of multiple equilibria of a class of cellular neural networks. *IEEE Trans Neural Netw* 22(3):381–394
95. Zeng ZG, Zheng WX (2012) Multistability of neural networks with time-varying delays and concave-convex characteristics. *IEEE Trans Neural Netw Learn Syst* 23(2):293–305
96. Wang LL, Chen TP (2012) Multistability of neural networks with Mexican-hat-type activation functions. *IEEE Trans Neural Netw Learn Syst* 23(11):1816–1826
97. Marco MD, Forti M, Grazzini M, Pancioni L (2012) Limit set dichotomy and multistability for a class of cooperative neural networks with delays. *IEEE Trans Neural Netw Learn Syst* 23(9):1473–1485
98. Nie X, Huang Z (2012) Multistability and multiperiodicity of high-order competitive neural networks with a general class of activation functions. *Neurocomputing* 82:1–13
99. Nie XB, Cao JD, Fei SM (2013) Multistability and instability of delayed competitive neural networks with nondecreasing piecewise linear activation functions. *Neurocomputing* 119:281–291
100. Zeng ZG, Zheng WX (2013) Multistability of two kinds of recurrent neural networks with activation functions symmetrical about the origin on the phase plane. *IEEE Trans Neural Netw Learn Syst* 24(11):1749–1762
101. Wang LL, Chen TP (2014) Multiple μ -stability of neural networks with unbounded time-varying delays. *Neural Netw* 53:109–118
102. Hu B, Guan ZH, Chen G, Lewis FL (2019) Multistability of delayed hybrid impulsive neural networks with application to associative memories. *IEEE Trans Neural Netw Learn Syst* 30:1537–1551
103. Wan P, Sun D, Zhao M, Wan L, Jin S (2020) Multistability and attraction basins of discrete-time neural networks with nonmonotonic piecewise linear activation functions. *Neural Netw* 122:231–238
104. Zhang F, Huang T, Wu Q, Zeng Z (2021) Multistability of delayed fractional-order competitive neural networks. *Neural Netw* 140:323–335
105. Nie X, Cao J, Fei S (2014) Multistability and instability of competitive neural networks with Mexican-hat-type activation functions. *Abstr Appl Anal* 2014:901519
106. Nie X, Zheng WX (2014) On multistability of competitive neural networks with discontinuous activation functions. In: Australian control conference. Canberra, pp 245–250
107. Cabral J, Kringelbach ML, Deco G (2018) Functional connectivity dynamically evolves on multiple time-scales over a static structural connectome: Models and mechanisms. *Euroimage* 160:84–96
108. Frolov NS, Maksimenko VA, Khramova MV, Pisarchik AN, Hramov AE (2019) Dynamics of functional connectivity in multilayer cortical brain network during sensory information processing. *Eur Phys J: Spec Top* 228(11):2381–2389

109. Hramov AE, Maksimenko VA, Koronovskii AA, Runnova AE, Zhuravlev MO, Pisarchik AN, Kurths J (2019) Percept-related EEG classification using machine learning approach and features of functional brain connectivity. *Chaos* 29:093110
110. Hramov AE, Frolov NS, Maksimenko VA, Kurkin SA, Kazantsev VB, Pisarchik AN (2021) Functional networks of the brain: from connectivity restoration to dynamic integration. *Phys Usp* 191(6):614–650

Chapter 7

Extreme Multistability



Abstract Extreme multistability or the coexistence of an infinite number of coexisting attractors is an intriguing phenomenon which appears in forced, coupled, and self-reproducing systems. At the first glance, extreme multistability in a dissipative system seems rather strange because the coexistence of infinite number of states is usually attributed to a conservative system. However, as we will show below, the existence of infinitely many attractors is possible at certain conditions. Historically, Newhouse [1] was the first who predicted the coexistence of infinitely many periodic attractors back in 1974. This surprisingly complex phenomenon was found in connection with a two-dimensional diffeomorphism (see Sect. 2.2.1). Just over 20 years later, Chawanya [2] reported the coexistence of infinitely many periodic and chaotic attractors in a class of dynamical systems with networks of heteroclinic orbits. In particular, he has shown that the phase-space structure in such systems is generic, i.e. robust against small parameter changes. We recall that attractors can be classified into two groups, self-excited and hidden [3] (see Sect. 2.4). If the basin of attraction includes (even at its boundary) at least one equilibrium, this attractor is self-excited, otherwise the attractor is hidden. Infinitely many hidden attractors were discovered in both mathematical models and real dynamical systems, for instance, in memristors. When the coexisting attractors have a similar structure but different location in phase space, extreme multistability is called “homogeneous”, otherwise it is called “inhomogeneous” [4]. In this chapter, we will show how extreme multistability emerges in different dynamical systems. Special attention will be given to memristive systems due to their widespread implementation in electronic circuits. Finally, we will describe important applications of extreme multistability in cryptography and secure communication.

7.1 Extreme Multistability in Continuous-Time Systems

Extreme multistability theoretically predicted in discrete and continuous dynamical systems, was then evidenced in experiments with electronic circuits. Here, we consider some classes of systems where extreme multistability occurs.

7.1.1 Game Dynamical Systems

We start with the game system because it was one of the first dynamical systems where the coexistence of infinitely many attractors was reported [2]. Game dynamics is usually described by the Lotka–Volterra model, also known as predator-prey equations. This is one of the simplest models of ecological systems [5] given by [6]

$$\begin{aligned} \dot{x}_i &= x_i \left(\sum_{j=1}^n g_{ij} x_j - \sum_{j=1}^n \sum_{k=1}^n g_{ij} x_j x_k \right), \\ \sum_{i=1}^n x_i &= 1, \quad 0 \leq x_i \leq 1, \end{aligned} \tag{7.1}$$

where g_{ij} is an $(n \times n)$ matrix.

The important feature of Eq. 7.1 is the existence of a hierarchical recurrent network of heteroclinic orbits which contains

- (i) partially stable saddles and elemental heteroclinic orbits connecting the saddles,
- (ii) one of the saddles is child cycle, i.e. a partially stable heteroclinic cycle, and the remain saddles are fixed point,
- (iii) an elemental heteroclinic orbit starting from a fixed point saddle and asymptotic to the child cycle,
- (iv) every component takes a non-zero value at one or more of the fixed points in the network [7]. Although the structure of the basins of attraction has a fractal character, it is structurally stable.

7.1.2 Hamiltonian-Driven Dissipative Systems

As we already mentioned in Sect. 2.2.2, one of the methods to obtain multistability is to take a conservative system and add a weak dissipation. Note that conservative and dissipative systems can admit the Hamilton function, although in dissipative cases the energy is not conserved. The particle motion in a potential field occurs in a group of potential hills. There is a region where the scattering particles interact with the potential, while outside this region the potential can be neglected, so that

the particle practically moves free. This area is often called *scattering area*, as stated in Sect. 5.1. For many potential functions of physical interest, the corresponding classical Hamiltonian functions and equations of motion are nonlinear. This makes possible chaotic dynamics in the scattering region. In open systems, there must be “channels” in this area for particles to enter or escape. This means that particles from afar can enter the scattering region through one of the channels. They experience chaotic dynamics in the region due to the interaction with the potential and then leave the region along the same or another channel.

For particles falling into the scattering region from afar, their lifetime in this region should be finite. As a result, they demonstrate chaotic dynamics, but only for a finite period of time, so-called *transient chaos* [8] emerging due to the existence of non-attracting chaotic invariant sets (chaotic saddles) in phase space, that can be revealed via unstable periodic orbits. For example, in symmetric potential hills used to study various bifurcations of chaotic scattering, there are trajectories that are reflected back and forth along line segments connecting the hills centers. Because particles move exactly along these lines, they stay on the same paths, resulting in unstable periodic orbits. The main property of a chaotic saddle is that it includes an infinite number of unstable periodic orbits. These orbits become stable if a weak dissipation is added, and thus the particles never leave the scattering region.

In Hamiltonian systems, regular motions are fundamental and chaotic scattering can either be hyperbolic or nonhyperbolic. If all periodic orbits are unstable, there are no Kolmogorov–Arnold–Moser (KAM) tori¹ in phase space. In this case, all particles escape from the potential and the number of particles randomly distributed in the scattering region decay exponentially. Instead, in nonhyperbolic chaotic scattering, KAM tori coexist with chaotic saddles, which usually lead to a decrease in the probability of particle survival in the scattering region. It seems that the movements on the KAM tori are neither stable nor unstable, and therefore the corresponding Lyapunov exponents are equal to zero. In Hamiltonian systems, it is assumed that the motions transverse to the KAM tori also have zero Lyapunov exponents. This means that particles approaching KAM tori can stay there for an arbitrarily long time.

Thus, for hyperbolic chaotic scattering, the exponential decay law remains unchanged in the presence of weak dissipation, but for nonhyperbolic chaotic scattering the decay law is structurally unstable in the sense that it immediately becomes exponential in the presence of any dissipation. This can be explained by the fact that hyperbolic dynamics in the Hamiltonian systems is usually structurally stable instead of nonhyperbolic dynamics.

The possibility of obtaining an infinite set of coexisting attractors was first predicted by Lai and Grebogi [9], who considered oblique product dynamical systems in which a conservative (Hamiltonian) system acts as a driver for a dissipative system. They called such systems *Hamiltonian-driven dissipative dynamical systems* and showed that an infinite number of different attractors coexist in this class of systems. Attractors can be quasiperiodic, strange not-chaotic, or chaotic with different

¹ The KAM theorem asserts the preservation in a certain sense of the majority of invariant tori in phase space under a small perturbation of a completely integrable Hamiltonian system.

positive Lyapunov exponents. In particular, they studied the following general class of N -dimensional discrete mappings in \mathbb{R}^N :

$$\begin{aligned}\mathbf{x}_{n+1} &= \mathbf{f}(\mathbf{x}_n), \\ \mathbf{y}_{n+1} &= \mathbf{F}(\mathbf{x}_n, p)\mathbf{G}(\mathbf{y}_n),\end{aligned}\tag{7.2}$$

where $\mathbf{x} \in \mathbf{S} \subset \mathbb{R}^{N_S}$, $\mathbf{y} \in \mathbf{T} \subset \mathbb{R}^{N_T}$, $N_S \leq 1$, $N_T \leq 1$, $N_S + N_T = N$, and p is a parameter. The conservative dynamics of the area-preserving map \mathbf{x} takes place in the invariant subspace \mathbf{S} . Therefore, every trajectory starting from the initial conditions in \mathbf{S} remains in \mathbf{S} forever.

The \mathbf{y} trajectory occurs in the subspace \mathbf{T} transverse to \mathbf{S} . The functions $\mathbf{F}(\mathbf{x}_n, p)$ and $\mathbf{G}(\mathbf{y})$ are chosen so that the modulus of the Jacobi matrix determinant $|D\mathbf{J}_y| \equiv |\partial\mathbf{y}_{n+1}/\partial\mathbf{y}_n|$ is less than unity in some regions of the phase space. The function $\mathbf{G}(-\mathbf{y}) = -\mathbf{G}(\mathbf{y})$ is symmetric and $\mathbf{G}(\mathbf{0}) = \mathbf{0}$. Thus, the dynamics in the transverse subspace is dissipative and, therefore, the entire system is also dissipative. The control variable \mathbf{x} demonstrates different types of dynamics, for example, quasi-periodic motion on KAM tori or chaotic motion, so that each initial condition in \mathbf{x} causes a different effect and, due to the structure of the asymmetric product, a different attractor throughout the phase space. This is a way to obtain the coexistence of an infinite number of attractors.

The observed complexity of the Hamiltonian system is a direct consequence of the Hamiltonian structure of phase space, which usually contains chaotic components and a hierarchy of KAM islands; the introduction of transverse dissipation leads to much richer dynamics. Quasiperiodic motion on KAM surfaces in an invariant subspace can lead to quasiperiodic, strange non-chaotic, and chaotic attractors in the complete phase space. Moreover, chaotic motion in an invariant subspace can induce chaotic attractors with different positive Lyapunov exponents.

7.1.3 Complex-Coupled Systems

Another class of systems exhibiting extreme multistability was discovered by Sun et al. [10], who observed that identical systems, for example, two Lorenz oscillators, coupled in a certain way, exhibit an infinite number of coexisting attractors. The coupling was arranged as follows

$$\begin{aligned}\dot{x}_1 &= \sigma(y_1 - x_2), & \dot{x}_2 &= \sigma(y_2 - x_2), \\ \dot{y}_1 &= rx_1 - y_1 - x_1 z_1, & \dot{y}_2 &= rx_2 - y_2 - x_2 z_2, \\ \dot{z}_1 &= x_1 y_1 - bz_1, & \dot{z}_2 &= x_2 y_2 - bz_2.\end{aligned}\tag{7.3}$$

One can see that the variable x_2 of the second oscillator is included in the first equation of the first oscillator, while the variable x_1 of the first oscillator is included in both

the second and third equations of the second oscillator. Such cross-coupling enriches the system dynamics and leads to extreme multistability.

The two coupled oscillators demonstrate generalized synchronization so that their y and z variables completely synchronize, while the x variables maintain a certain distance c determined by the initial conditions. The error dynamics can be analyzed by introducing the error variables which measure the distance from the synchronization manifold: $e_1 \equiv x_1 - x_2$, $e_2 \equiv y_1 - y_2$, and $e_3 \equiv z_1 - z_2$. Then the error dynamics is written as

$$\begin{aligned}\dot{e}_1 &= \sigma e_1, \\ \dot{e}_2 &= -x_1 e_3 - e_2, \\ \dot{e}_3 &= x_1 e_2 - b e_3.\end{aligned}\tag{7.4}$$

The phase trajectory of the system in Eq. 7.4 converges to the fixed point $(e_1^*, e_2^*, e_3^*) = (c, 0, 0)$. The Lyapunov function $\Lambda = e_2^2 + e_3^2$ describes a continuous set of fixed points depending on the real value of the distance c which defines the synchronization manifold when $t \rightarrow \infty$. In fact, the state space splits into an infinite set of synchronizing manifolds, each of which has at least one attractor. The dynamics of such a system in many ways resembles the dynamics of a conservative system, where for each value of a stored quantity (for example, energy) a different state is realized. However, the considered system completely differs from a conservative system because the stored quantity is not set at the very beginning, but changes over time, since the two oscillators synchronize.

The coexistence of an infinite number of attractors is illustrated in Fig. 7.1 with the leading Lyapunov exponent and bifurcation diagram of peak x_6 with respect to initial condition x_{05} . One can see that any change in the initial condition leads to a different attractor.

A similar extremely multistable behavior was observed in chemical models [11, 12]. Using two coupled Rössler oscillators, Hens et al. [13] developed a general approach allowing infinitely many attractors. The authors demonstrate how multiple scroll attractors can be obtained in any identical chaotic systems coupled in a specific configuration. The coexistence of multiple attractors was evidenced in experiments with two coupled Rössler electronic circuits [14] which confirm the robustness of extreme multistability to a small parameter mismatch and experimental noise.

Commenting on this type of extreme multistability, Sprott and Li [15] state that extreme multistability of the type described above can be achieved in almost any dynamical system by adding extraneous variables and using their initial conditions instead of existing parameters or as additional parameters. They conclude that any dynamical system can be transformed in such a way that it exhibits extreme multistability by replacing one of its bifurcation parameters with an additional variable whose value is constant or approaches a constant in the asymptotic limit $t \rightarrow \infty$, the value of which is determined by the initial conditions.

However, the dimension of most systems cannot be reduced so that the parameters are specified by the initial conditions. The examples given in some of the articles are exceptions where the coupling between two identical systems is carefully chosen.

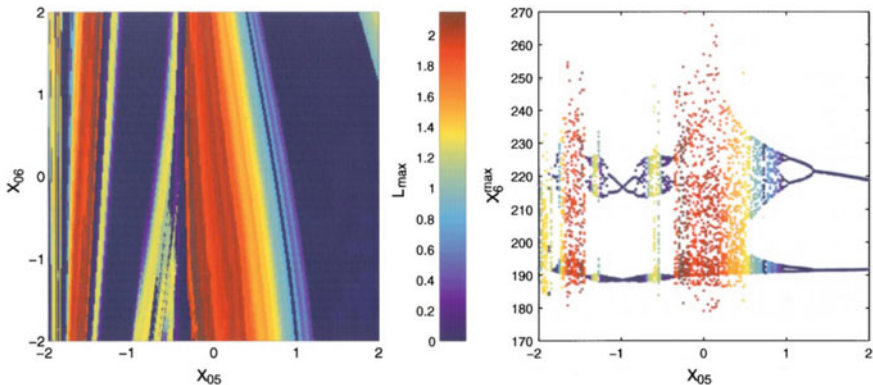


Fig. 7.1 Extreme multistability in the coupled Lorenz oscillators given by Eq. 7.3 in terms of (left) leading Lyapunov exponent in the space of initial conditions (x_{05}, x_{06}) and fixed initial conditions for other variables, and (right) the bifurcation diagram of local maxima x_6 versus initial condition x_{05} for $\sigma = 10$, $r = 160$, and $b = 8/3$. Reprinted figure with permission from [10] ©1999 by the American Physical Society

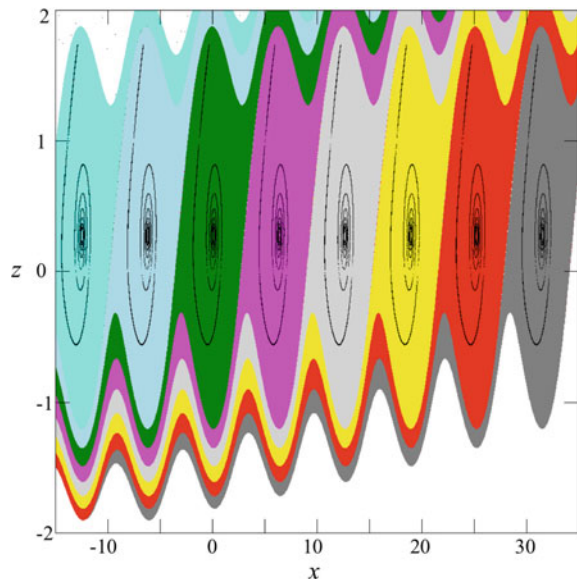
When studying attractors in dynamical systems, it is important to make sure that all equations are independent and affect the system dynamics. The presence of extraneous equations and their obvious extra dimensions can lead to false conclusions, such as the assertion that the initial conditions are bifurcation parameters or that the system has infinitely many equilibrium positions. Nevertheless, the construction of bifurcation diagrams depending on the initial conditions, similar to that shown in Fig. 7.1, is a useful tool for identifying extraneous equations in dynamical models.

7.1.4 Variable-Boostable Systems

Extreme multistability can be obtained in variable-boostable systems (see Sect. 2.2.8) with periodic functions applied either to one or several system variable. A self-reproducing system can be generated from an offset-boostable dynamical system, where the offset boosting provides a direct entrance for attractor hatching. To make a variable-boostable system self-reproducible with an infinite number of coexisting attractors, two internal operations are required: the displacement of the attractor in a desired direction and periodic modulation applied to the system variables. As a result, extreme multistability arises in corresponding phase-space directions. Let us consider how this approach works with the concrete examples.

Li et al. [16] propose a simple method for constructing variable-boostable chaotic systems with infinitely many attractors which reside in phase space along a specific coordinate axis. As an example, they consider a 3D dissipative self-reproducing dynamical system

Fig. 7.2 Self-excited chaotic attractors (black spirals) and their basins of attraction (color area) on the (x, z) plane for $y = 1$. Based on data from [16]



$$\begin{aligned}\dot{x} &= 1 - ayz, \\ \dot{y} &= z^2 - z, \\ \dot{z} &= F(x) - bz\end{aligned}\tag{7.5}$$

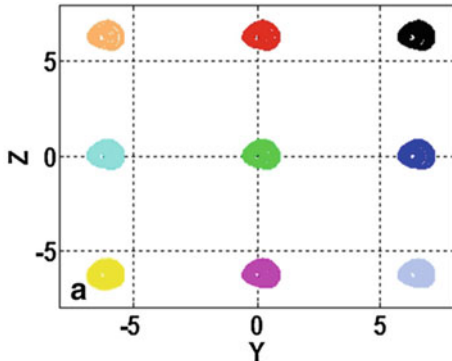
with periodic function $F(x) = \sin(\epsilon x)/\epsilon \rightarrow x$ for $\epsilon \rightarrow 0$, which preserves chaos. To obtain infinitely many attractors in this system, they set $F(x) = A \sin(x)$ (A being a constant amplitude) and change the variables as $x = u + 2\pi k$ ($2\pi k$ being the offset boosting), $y = v$, and $z = w$, that results to $F(x) = F(u + 2\pi k) = A \sin(u) = F(u)$. Since the system with new variables u , v , and w is identical to Eq. 7.5, we say that it is self-reproducing along the x -axis.

With parameters $a = 3.55$, $b = 0.5$, and $A = 2$, the system in Eq. 7.5 exhibits infinitely many coexisting attractors, as illustrated in Fig. 7.2.

The system displays homogeneous extreme multistability, and all coexisting attractors have approximately the same Lyapunov exponents. The sinusoidal nonlinearity exhibiting extreme multistability was successfully implemented in electronic circuits [17].

It should be noted that extreme multistability can be obtained not only in one phase-space direction, but also in several directions. The procedure for such a behavior was proposed by Li, Sprott, and Mei [18] in 2D offset-boostable chaotic systems. To be more concrete, they developed a general method for constructing two-dimensional chaotic flows with the possibility for increasing a bias, after which the method is extended to create an infinite two-dimensional lattice of strange attractors by modulating the offset-boostable variables.

Fig. 7.3 2D lattice of chaotic attractors of the system in Eq. 7.6 found using initial conditions $(0, 0.1 + 2k\pi, 0 + 2l\pi)$ for $-1 \leq k, l \in z \leq 1$. Reprinted by permission from the Springer Nature [18] ©2017



In the following example, a 2D lattice of coexisting attractors is obtained if two variables are periodically modulated. Namely, the system

$$\begin{aligned}\dot{x} &= \sin(y), \\ \dot{y} &= 1.05 \sin(z), \\ \dot{z} &= -\dot{x} - 0.5\dot{y} - x + x^2\end{aligned}\tag{7.6}$$

exhibits an infinite 2D lattice of strange attractors illustrated in Fig. 7.3. Instead of a sinusoidal function, other trigonometric periodical functions can be used, for instance, tangential.

Accordingly, periodic modulation of three variables leads to the coexistence of an infinite number of attractors in three dimensions. The simplest variant of such a system has the form

$$\begin{aligned}\dot{x} &= \sin(y), \\ \dot{y} &= \sin(z), \\ \dot{z} &= 0.442x - \sin(z).\end{aligned}\tag{7.7}$$

This system has an infinite 3D lattice of chaotic and limit cycle attractors. However, for most parameter values the attractors are combined into one attractor, which extends to infinity, despite the zero measure in the 3D state space.

Correspondingly, an n D hyperjerk system can be transformed into an $(n - 1)$ D self-reproducing system by the periodic offset boosting [19]. Thus, an effective way for transforming a dynamical system into a self-reproducing system with infinitely many attractors is the introduction of trigonometric functions into variables. For example, infinite 1D, 2D, 3D lattices of hyperchaotic attractors can be created from a 4D hyperchaotic snap system, and so on. This method can be generalized to create multidimensional lattices with an infinite number of homogeneously distributed chaotic attractors.

7.1.5 Systems with Hyperbolic Cosine Nonlinearity

In addition to sinusoidal modulation, extreme multistability can also be generated by hyperbolic cosine nonlinearity in a 4D chaotic system. Let us consider the example of such a system modeled by the following equations [20]

$$\begin{aligned}\dot{x}_1 &= -x_2 - x_3 - x_4, \\ \dot{x}_2 &= x_1, \\ \dot{x}_3 &= 0.5(x_2 - 0.5 \cosh(x_2) - x_3 + 1), \\ \dot{x}_4 &= x_1.\end{aligned}\tag{7.8}$$

The system in Eq. 7.8 exhibits the coexistence of infinitely many periodic and chaotic attractors revealed by varying initial conditions. This phenomenon is illustrated in Fig. 7.4 with the leading Lyapunov exponent (left panel) and the bifurcation diagram (right panel) with respect to the initial conditions.

Interestingly, the dynamics of this system is very similar to the dynamics of the six-dimensional system of coupled oscillators (compare with Fig. 7.1). However, there is an important advantage of the system with cosine nonlinearity over the high dimensional systems. Namely, the former can be more easily implemented in electronic circuits with standard electronic components such as two semiconductor diodes, instead of an analog multiplier in the case of quadratic nonlinearity [20].

7.1.6 Systems with Time-Periodic Forcing

One of the simplest ways to obtain an infinite number of hidden and self-extracting attractors is adding a time-periodic forcing to a variable. This converts an autonomous

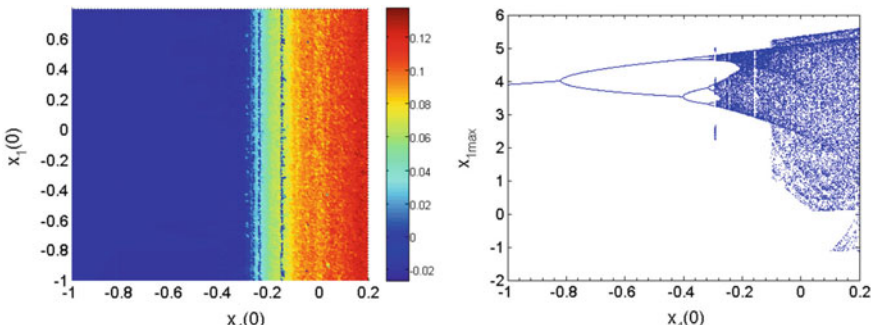


Fig. 7.4 (Left) Leading Lyapunov exponent (color scale) in the space of initial conditions $(x_4(0), x_1(0))$ for fixed $x_2(0) = x_3(0) = 0$. (Right) Bifurcation diagram of x_1 local maxima versus initial condition $x_4(0)$. Reprinted by permission from the Springer Nature [20] ©2019

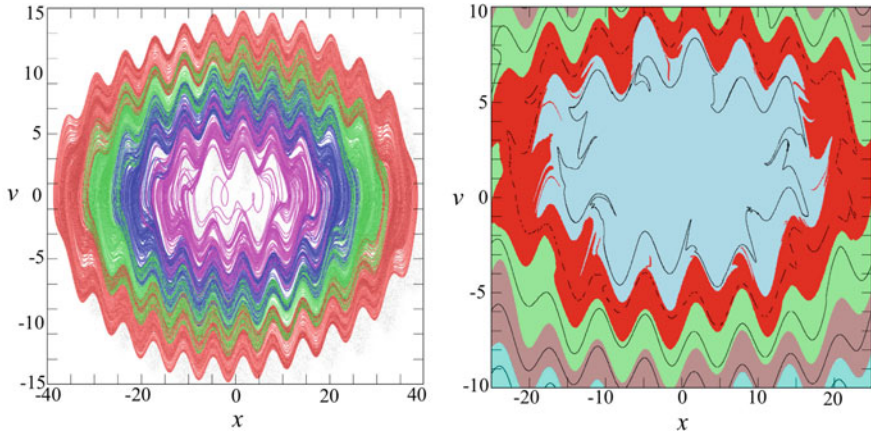


Fig. 7.5 (Left) First four coexisting attractors of Eq. 7.9 for initial conditions $(x_0, v_0) = (n\pi, 0)$ with $n = 5, 7, 9, 11$. (Right) Poincaré section of the first five coexisting attractors (black lines) in the plane $t \bmod 2\pi = \pi$ with their respective basins of attraction (colors). Based on data from [21]

system to a nonautonomous one. In this regard, Sprott et al. [21] have shown that the periodic forcing can induce infinitely many nested hidden attractors of different types, including limit cycles, attracting tori, and strange attractors, which form a layered structure similar to cabbage. Such systems are called *megastable*.

Based on the example of the van der Pol equation with time-periodic forcing $F(t) = A \sin(\Omega t)$, we will show how an infinite number of hidden attractors can be obtained. The system is given by

$$\begin{aligned}\dot{x} &= v, \\ \dot{v} &= -\omega^2 x + v \cos x + F(t).\end{aligned}\tag{7.9}$$

For parameters $\omega = 0.33$, $A = 1$, and $\Omega = 0.73$, the system in Eq. 7.9 exhibits an infinite number of hidden attractors. Some of these attractors and their basins of attraction are illustrated in Fig. 7.5.

It is important to note that the coexisting attractors form a cabbage structure. The innermost attractor is chaotic, the next one is weakly chaotic, and the rest attractors are attracting tori with two zero Lyapunov exponents and one negative exponent. One can see that the basin boundaries for the tori are relatively smooth, while the basin structures of the two inner strange attractors are fractal.

7.2 Extreme Multistability in Discrete-Time Systems

Discrete-time dynamical systems are characterized by homoclinic connections given by intersections between stable and unstable manifolds of invariant sets. If the intersections are transverse, they are not destroyed by small perturbations. Therefore, transverse homoclinic connections are robust structures which imply the presence of Smale horseshoes, infinitely many unstable periodic orbits, and chaos [22]. When the map parameters are varied, transverse homoclinic connections can be created or broken in homoclinic tangencies. Since stable and unstable manifolds intersect tangentially, a homoclinic tangency is codimensional-one. Thus, the dynamics associated with the tangency as the system is perturbed, can be understood by varying a single parameter.

7.2.1 Two-Dimensional Chaotic Map

Similar to the variable-boostable method for continuous-time chaotic systems described in the previous section, a sinusoidal parameter modulation is introduced to a two-dimensional chaotic map. Under this modulation, the map can exhibit infinitely many coexisting attractors, despite the fact that the phase-space dimension of discrete systems is lower than that of continuous systems.

In order to demonstrate the generation of infinitely many attractors in two-dimensional chaotic maps, Zhang et al. [23] consider the following map

$$\begin{aligned} x_{n+1} &= x_n + ax_n \sin y_n, \\ y_{n+1} &= y_n + bx_n + c. \end{aligned} \tag{7.10}$$

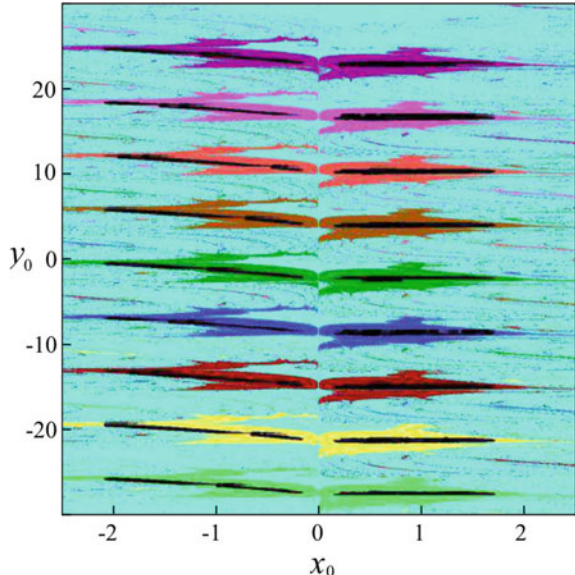
Due to the translation symmetry, i.e. $F(x, y + 2m\pi) = F(x, y)$, where $F(x, y) = (ax \sin y, bx + c)$ ($m = 0, \pm 1, \pm 2, \dots$), the map Eq. 7.10 exhibits homogeneous extreme multistability for parameters $(a, b, c) = (\pm 2.7, \pm 1, \pm 0.1)$.

Figure 7.6 shows the fractal basins of attraction of uniformly distributed chaotic attractors in the phase space. One can see that the attractors have the same shape but shifted in the phase space.

7.2.2 Area-Preserving Lozi Map

The Lozi map is a two-dimensional piecewise-linear map which at some parameters exhibits a hyperbolic chaotic attractor [24]. In addition, under certain parameter values the Lozi map is converted into a specific area-preserving map and can generate an infinite number of coexisting stable orbits [25].

Fig. 7.6 Basins of attraction of chaotic attractors of Eq. 7.10 illustrating homogeneous extreme multistability. Black dots show the coexisting chaotic attractors. The unbounded basin of attraction is shown in cyan, indicating initial conditions which bring the trajectory to the area $(x, y) | |x| + |y| > 100$. The basins of chaotic attractors are shown in red, light red, blue, light blue, green, light green, brown, magenta, and light megenta, respectively. Based on data from [23]



The Lozi map is obtained by substituting quadratic nonlinearity in the Hénon map (see Eq. 1.11) with absolute value nonlinearity, so that

$$\begin{aligned} x_{n+1} &= 1 - a|x_n| + y_n, \\ y_{n+1} &= bx_n, \end{aligned} \tag{7.11}$$

where a and $b \neq 0$ are real values. For $b = -1$ the Lozi map is area-preserving.

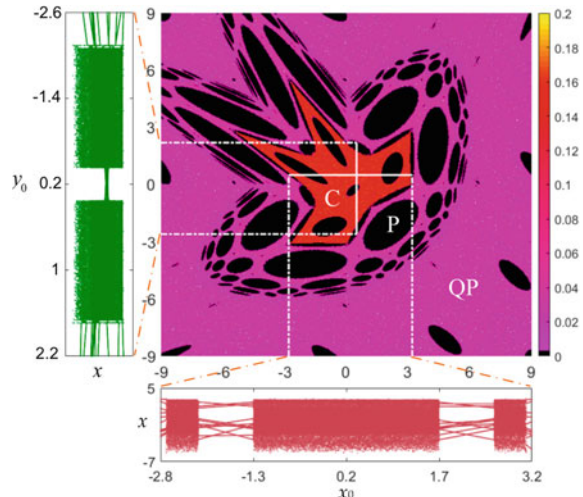
Extreme multistability can be revealed by calculating the largest Lyapunov exponent as a function of initial conditions. Such bifurcation diagrams and basins of attraction of chaotic, quasiperiodic, and periodic orbits in the Lozi map in Eq. 7.11 are illustrated in Fig. 7.7. The coexistence of infinitely many attractors is clearly seen in the bifurcation diagrams with respect to the initial conditions. A similar extremely multistable behavior also occurs for other values of the parameter b .

The complexity of systems with infinitely many attractors can be characterized by spectral (Sect. 1.5.2) and sample entropy (Sect. 1.5.3).

7.3 Extreme Multistability in Memristive Systems

A memristor is a nonlinear resistor with memory invented by Chua [26] in 1971. It is the fourth basic electronic element in addition to three conventional elements, namely, resistor, capacitor, and inductor. Later, a memristive device was fabricated by William and his colleagues at the Hewlett Packard laboratory [27]. In 2009, the concept of the

Fig. 7.7 Largest Lyapunov exponent of the Lozi map in Eq. 7.11 with $a = 1.2$ and $b = -1$ in the (x_0, y_0) space, representing the coexistence of infinitely many chaotic C (red), quasiperiodic QP (blue), and periodic P (black) orbits. The bottom and left panels display the bifurcation diagrams of x with respect to the initial conditions x_0 and y_0 for fixed $y_0 = 0.5$ and $x_0 = 0.5$, respectively. Based on data from [25]



memristor was extended to other basic elements, giving rise to a meminductor and a memcapacitor [28]. The relation between the main circuit elements is illustrated in Fig. 7.8.

The memristor connects two main variables of the electronic circuit: charge and flux [29]. Due to the memory effect, a memristive device plays important role in the self-organization of complex systems capable of learning and remembering. The interest to memristors was stimulated by their applications in chaotic circuits, flash memory, neural networks, etc. [30].

A memristive system is described by the following generic equations [31].

$$V = M(q)I, \quad M(q) = \frac{d\phi(q)}{dq}, \quad (7.12)$$

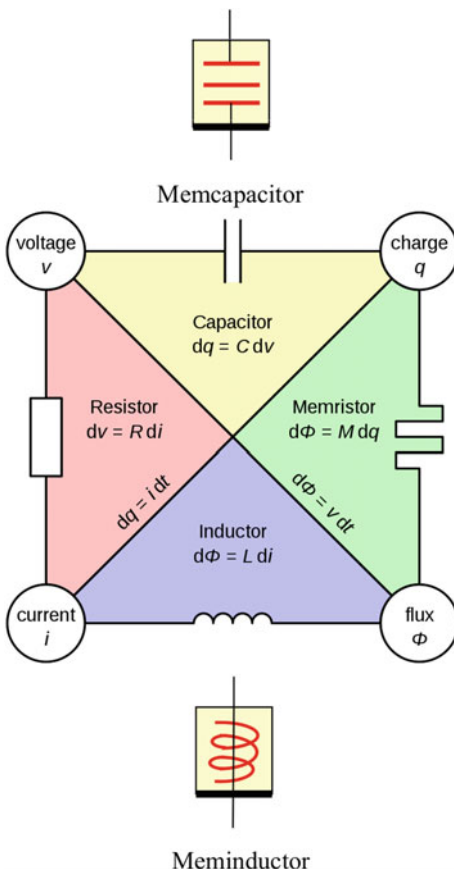
$$I = W(\phi)V, \quad W(\phi) = \frac{dq(\phi)}{d\phi}, \quad (7.13)$$

where V and I are the voltage and current, respectively, $M(q)$ and $W(\phi)$ are the memristance and memductance,² and q and ϕ are the charge and flux across the memristor, respectively. These functions indicate how many electric charges and magnetic fluxes pass through the memristor in a particular direction.

The memristor models are conventionally divided into charge-controlled and flux-controlled. Next, we will consider these types of memristive systems separately.

² Memristance and memductance are respectively electrical resistance and inductance that varies according to the history of the electric charge that has flowed through a device.

Fig. 7.8 Relation between main circuit elements



7.3.1 Charge-Controlled Memristive Model

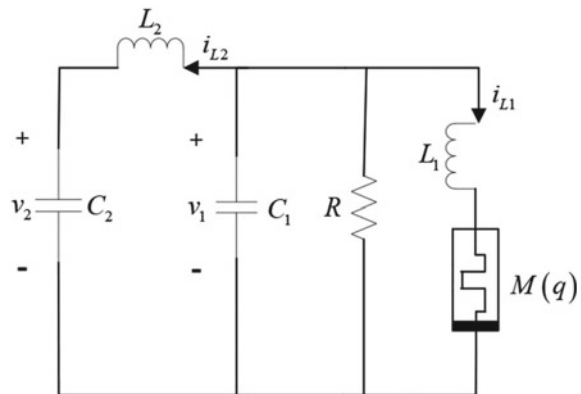
In the charge-controlled memristive device, the memristance is expressed as

$$M(q) = \frac{d\phi(q)}{dq} = m + nq^2, \quad (7.14)$$

where m and n are parameters. The electronic scheme of the charge-controlled memristive circuit is presented in Fig. 7.9.

Using the Kirchhoff law, the circuit in Fig. 7.9 can be modelled as

Fig. 7.9 Electronic scheme of a charge-controlled memristive circuit. i_{L1} and i_{L2} are currents, v_1 and v_2 are voltages, C_1 and C_2 are capacitors, and R is a resistor. Reprinted from [32]; licensed under a Creative Commons Attribution (CC BY) license



$$\begin{aligned}\frac{di_{L1}}{dt} &= \frac{V_1 - I_{L1}M(Q)}{L_1}, \\ \frac{di_{L2}}{dt} &= \frac{v_1 - v_2}{L_2}, \\ \frac{dv_1}{dt} &= -\frac{i_{L1} + i_{L2} + v_1/R}{C_1}, \\ \frac{dv_2}{dt} &= \frac{i_{L2}}{C_2}, \\ \frac{dq}{dt} &= i_{L1}.\end{aligned}\tag{7.15}$$

Using the following substitutions: $x = i_{L1}$, $y = i_{L2}$, $z = v_1$, $u = v_2$, $v = q$, $a = 1/L_1$, $b = 1/C_1$, $c = 1/C_2$, $L_2 = 1$, and $R = 1$, the system in Eq. 7.15 is transformed into

$$\begin{aligned}\dot{x} &= a(z - xM(v)), \\ \dot{y} &= -z - u, \\ \dot{z} &= -b(y + x + z), \\ \dot{u} &= cy, \\ \dot{v} &= x.\end{aligned}\tag{7.16}$$

Numerical simulations of Eq. 7.16 shows that the system exhibits infinitely many coexisting attractors for a certain set of the parameters. The bifurcation diagram of the charge-controlled memristive system is depicted in Fig. 7.10. The diagram displays the peak values of x with respect to the initial condition $v(0)$ for fixed initial conditions of other variables to $[x(0), y(0), z(0), u(0)] = [\pm 10^{-6}, 0, 0, 0]$.

Figure 7.11 shows the phase portraits of some coexisting attractors in the (x, y) phase space. The coexistence of a single-scroll chaotic spiral, periodic orbit, asymmetric chaotic attractor, and other attractors is revealed for different initial conditions $v(0)$.

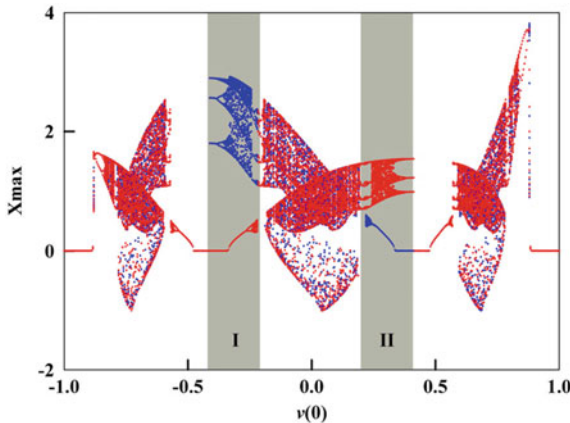


Fig. 7.10 Bifurcation diagrams of the peak memristive current as a function of the initial condition $v(0)$ at $x(0) = \pm 10^{-6}$ for $a = 9$, $b = 30$, $c = 17$, $m = -1.2$, and $n = 1.2$. Reprinted from [32]; licensed under a Creative Commons Attribution (CC BY) license

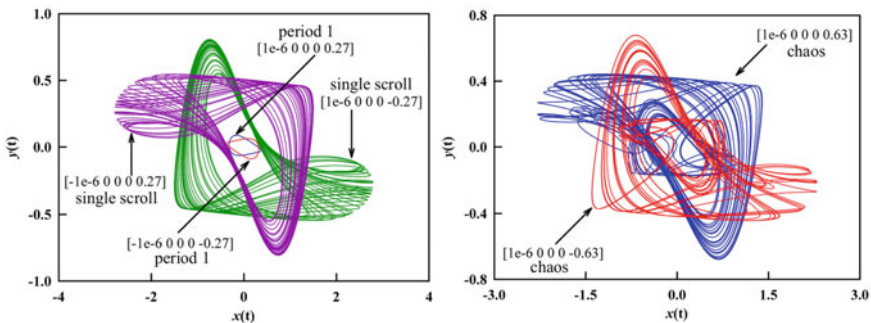


Fig. 7.11 Coexisting attractors in the memristive model in Eq. 7.16 for different initial conditions $v(0)$. (Left) Symmetric period-1 and single-scroll chaotic attractors. (Right) Asymmetric chaotic attractors. Reprinted from [32]; licensed under a Creative Commons Attribution (CC BY) license

7.3.2 Flux-Controlled Memristive Model

A similar multistable behavior is observed in the flux-controlled memristive system with the memductance given by

$$W(\phi) = \frac{dq(\phi)}{d\phi} = \alpha + \beta\phi^2, \quad (7.17)$$

where α is a parameter indicating the memristor polarity and β is a constant. The memristor is passive if $\alpha > 0$, whereas it is active if $\alpha < 0$. The electronic scheme of a flux-controlled memristive system is presented in Fig. 7.12.

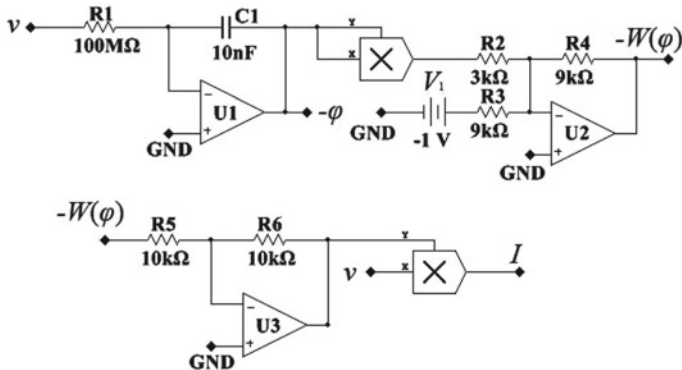


Fig. 7.12 Electronic scheme of a flux-controlled memristive circuit. R_1 – R_6 are resistors, C_1 is a capacitor, and U_1 – U_3 are operational amplifiers. Reproduced from [33] with permission of AIP Publishing

The input voltage v is applied to the integral circuit to obtain the flux $-\phi$ which transforms to ϕ^2 by the multiplier, and then sent to the inverting adder constructed by U_2 , whose output is described as

$$W(\phi) = -\left(\frac{R_4}{R_3}V_1 + \frac{R_4}{R_2}\phi^2\right). \quad (7.18)$$

The equivalent equations are written as

$$\begin{aligned} \dot{x} &= ax - yz, \\ \dot{y} &= -by + xz + W(\phi), \\ \dot{z} &= -cz + xy, \\ \dot{\phi} &= -kyW(\phi). \end{aligned} \quad (7.19)$$

This system exhibits infinitely many coexisting attractors. Depending on the parameters and initial conditions, different kind of attractors are observed, including single scroll, twin-scroll, strange attractors with one, two, three, and four impact waves, and with no impact wave, as well as hidden attractors. Some of the impact wave attractors are depicted in Fig. 7.13.

The observed extremely multistable dynamics was confirmed with Multisim experiments [33].

Many other memristor models also display extreme multistability [34–37], including those with sinusoidal or tangent function [38] and with two [39–41] and multiple memristors [42]. In addition, homogeneous extreme multistability was discovered in a hyperchaotic meminductive circuit [43]. Infinitely many coexisting attractors were also found in a Josephson-junction circuit [44].

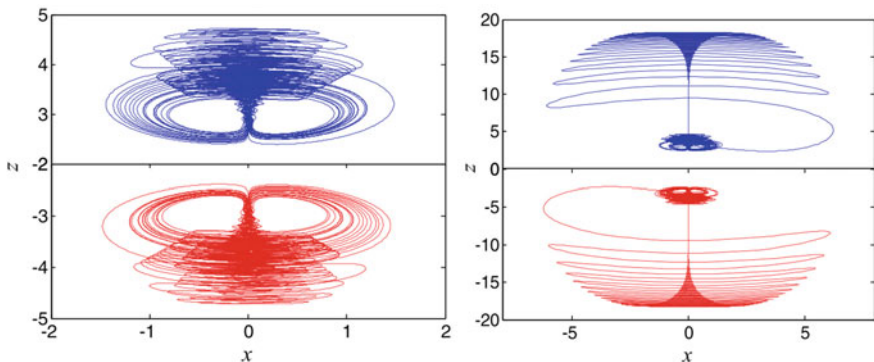


Fig. 7.13 Phase portraits of strange attractors in the flux-controlled memristive system given by Eq. 7.19 with $a = 2.6$, $b = 3$, $c = 0.02$, $k = 12$, $\alpha = -9$, and $\beta = 0.01$. Symmetric pairs of coexisting attractors with (left) no impact wave for initial conditions $(\pm 0.1, 0, \mp 4, 0)$ and (right) one impact wave for $(\pm 0.1, 0, \mp 4, 1)$. Reproduced from [33] with permission of AIP Publishing

7.4 Application of Extreme Multistability in Cryptography and Secure Communication

The continuous and dizzying development of new technologies requires increased information security, although absolute security can ever be achieved. The term “security” means that under certain assumptions, no cyberattack should compromise the system performance. Nowadays, many companies in all sectors sell their products over Internet, and the number of Internet users is constantly growing. At the same time, the threat of cyberattacks increases. The growth of the network as sales, management or distribution channel for companies also coincides with an increase in illegal activities such as cyberattacks to undermine a company image, seize data and user keys or confidential information, and compromise data management systems. Traditional encryption algorithms such as Data Encryption Standard (DES), International Data Encryption Algorithm (IDEA), Advanced Encryption Standard (AES), Linear Feedback Shift Register (LFSR), etc. are vulnerable to cyberattacks. Therefore, unconventional encryption ciphers such as chaotic cryptography have become a good alternative to improve security. Since the late 80s—early 90s of the last century, chaotic cryptography [45–48] and communication based on synchronization of chaotic systems [49, 50] have been increasingly developed (see the comprehensive review on this topic in [51]), and secure chaotic communication schemes were implemented using laser systems [52, 53].

In terms of security, multistable systems have an undeniable advantage over monostable systems since they can hide information in different coexisting attractors and hence improve secure communication performance, where a special choice of initial conditions plays the role of a “secret key”.

7.4.1 Chaotic Cryptography Based on Extreme Multistability

It is quite natural that the systems with infinitely many coexisting chaotic attractors motivate scientists to use extreme multistability for secure communication. In particular, a pseudorandom numbers generator can be created on the basis of such systems. However, in order to use this generator in cryptography, it should pass special tests.

The National Institute of Standards and Technology (NIST) has established 15 tests to determine statistical characteristics of a random or pseudorandom number generator (SP800-22 standard). They are (1) frequency, (2) block frequency, (3) cumulative sums, (4) runs, (5) longest run, (6) rank, (7) FFT, (8) non-overlapping template, (9) overlapping template, (10) universal, (11) approximate entropy, (12) random excursions, (13) random excursions variant, (14) serial, and (15) linear complexity.

One of the most important components of the encryption algorithm is an S-Box that provides data confusion. Several S-box generation algorithms were created on the base of multistable three-dimensional [54] and four-dimensional [55] chaotic systems, as well as using a plasma perturbation model [56].

In order to use extreme multistability for image encryption, Liu et al. [57] discretized the continuous-time system

$$\begin{aligned}\dot{x} &= y - \cos(2x), \\ \dot{y} &= a \cos(2x) \cos(2z), \\ \dot{z} &= b - y \cos(2x),\end{aligned}\tag{7.20}$$

as follows

$$\begin{aligned}\dot{x}_{n+1} &= x_n + h[y_n - \cos(2x_n n)], \\ \dot{y}_{n+a} &= y_n + h[a \cos(2x_n n) \cos(2z_n n)], \\ \dot{z}_{n+1} &= z_n + h[b - y_n \cos(2x_n n)],\end{aligned}\tag{7.21}$$

where a and b are control parameters, $h = 0.01$ is the step size, and n is the number of cycles.

The idea is that an extremely multistable system generates infinitely many secret keys of initial conditions that highly increases the security of the encryption algorithm. Using pseudorandom numbers generated by Eq. 7.21, the diffusion algorithm is designed as the scrambling operation between three first pixels and three last pixels, as follows

$$\begin{aligned}E_{n+2}^{(1)} &= \left(E_{n+1}^{(1)} + 10^5 \left\lfloor (a E_n^{(1)} / 255) \right\rfloor (1 - E_n^{(1)} / 255) + P_n + \left\lfloor x_n 10^{12} \right\rfloor \right) \mod 256, \\ E_{n+1}^{(2)} &= E_{n+1}^{(2)} \oplus E_n^{(1)} \oplus \mod \left(\left\lfloor (x_n 10^{12}) \right\rfloor, 256 \right), \\ E_1^{(2)} &= E_N^{(2)}, E_2^2 = E_{N-1}^2, E_3^2 = E_{N-2}^2,\end{aligned}\tag{7.22}$$

where P_n is the n -th pixel value of the plaintext formed by N pixels, x_n is the value generated by the proposed discrete chaos system, $E_n^{(1)}$ is the pixel value of the first diffusion algorithm, and E_n^2 is the pixel value of the XOR diffusion algorithm. Each pixel value depends on the values of two adjacent pixels. Equations 7.22 imply the XOR (\oplus) diffusion operation between each pixel value and the floor ($\lfloor \dots \rfloor$) operation.³

To further improve the algorithm, the second and third diffusion and scrambling operations are applied. The tests confirm that the algorithm can effectively hide the key information of the original image.

7.4.2 Secure Communication Based on Extreme Multistability

Despite good statistical properties of chaotic systems, they have not found real applications in communications for a long time due to their vulnerability to synchronization attacks [58]. Unlike traditional encryption methods, which require digitizing information for further encryption, chaotic communication ciphers allow signal encryption without having to digitize it. This important property greatly simplifies and speeds up the computational process. The temporal behavior of a chaotic system is demonstrated by a sequence of pseudorandom numbers that strongly depend on the initial conditions. Nevertheless, since the system is deterministic, the forecast of its development in time is possible if all parameters and initial conditions are known.

One of the methods to encrypt information consists in the parameter modulation with a signal carrying information, or adding the information signal to a chaotic carrier. Typically, a message is digitally encoded into a chaotic carrier, and the combined signal is transmitted to a chaotic receiver that generates the same pseudorandom number sequence. The resulting chaotic signal is transmitted using conventional transmission technologies from a transmitter containing an encoder to a receiver containing a decoder. The decoder synchronizes the chaotic signal generated in the transmitter with the transmitted chaotic signal without the need for key exchange. This comparison allows extracting the original information.

Thus, the recipient can easily obtain information using a secret key passed to him. The disadvantage of this method is its low security due to the possibility of stealing the secret key, because the transmission can be intercepted, and therefore the basic dynamics of the encoder can be recovered. This facilitates information extraction using synchronization attacks by means of a virtual system [59] based on the parametric optimization of the virtual receiver to achieve the best synchronization by minimizing the synchronization error after a certain transient time required for synchronization, referred to as *synchronization time* t_s .

³ The floor function takes a real number x as an input, and gives the greatest integer less than or equal to x .

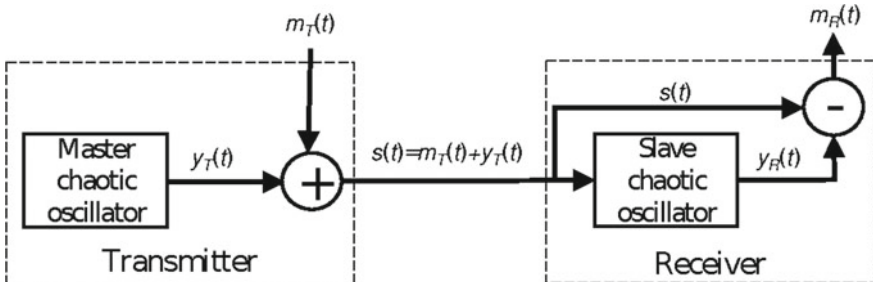


Fig. 7.14 Simple chaotic-masking communication scheme in a single-channel master-slave configuration

Most chaotic communication schemes are implemented in a master-slave configuration using a single channel, where the master and slave generators are identical chaotic systems, as illustrated in Fig. 7.14.

The information is often encoded using a *chaotic masking* approach. This method consists in adding the information message $m_T(t)$ to one of the chaotic variables (say, $y_T(t)$) of the master oscillator, that acts as a chaotic carrier. The complete signal $s(t) = m_T(t) + y_T(t)$ is then transmitted to the receiver. This signal is usually used to synchronize the transmitter with the receiver and to recover the information in the receiver. However, the chaotic signal $y_R(t)$ generated by the receiver cannot be completely synchronized with the transmitted signal $s(t)$ because the latter contains a message signal. This causes a synchronization error $\epsilon(t) = m_R(t) - m_T(t)$ in the resting signal $m_R(t) = s(t) - y_R(t)$ restored in the receiver. This is the main drawback of this scheme because the error reduces the communication quality and security. Moreover, the transmitted signal should be strong enough to provide synchronization, that also reduces the security.

Chaotic communication, on one hand, requires synchronization of interconnected chaotic systems, but on the other hand, it must be resistant to synchronization attacks, i.e. synchronization should be avoided. To resolve this contradiction, a hybrid communication system based on extreme multistability was created [60]. Both the transmitter and the receiver of this system contain identical continuous-time systems with an infinite number of chaotic attractors chosen by varying initial conditions of the transmitter which can be generated by a chaotic system, for example, the logistic map. Since complete synchronization between the transmitter and the receiver is only possible if they stay in the same attractor, relatively fast switching between coexisting attractors provides reliable protection against synchronization attacks if the time interval between subsequent switches is shorter than the synchronization time.

In the communication system based on extreme multistability both the transmitter and the receiver contain a pair of coupled Rössler-like oscillators which exhibit infinitely many chaotic attractors due to a special nonlinear coupling (see Sect. 7.1.3).

In other words, the transmitter and the receiver are formed by six-dimensional dynamical systems given by

$$\begin{aligned}\dot{x}_T &= -y_T - z_T, & \dot{x}_R &= -y_R - z_R + k(x_T - x_R), \\ \dot{y}_T &= x_T + av_T, & \dot{y}_R &= x_R + av_R, \\ \dot{z}_T &= b - cz_T + u_T w_T, & \dot{z}_R &= b - cz_R + u_R w_R, \\ \dot{u}_T &= x_T - y_T - z_T - u_T, & \dot{u}_R &= x_R - y_R - z_R - u_R, \\ \dot{v}_T &= u_T + av_T, & \dot{v}_R &= u_R + av_R, \\ \dot{w}_T &= b + w_T(u_T - c), & \dot{w}_R &= b + w_R(u_R - c),\end{aligned}\tag{7.23}$$

where the subindices T and R refer to the transmitter and receiver, respectively, and k is the coupling strength.

The main idea behind communication based on extreme multistability can be formulated as follows. The information is encrypted into chaotic attractors, which are changed using a dynamic key generated by a discrete chaotic system. Since the number of coexisting attractors is infinite and each attractor is chaotic, the information confusion is very high. If the coupling k is strong enough, the chaotic oscillator in the receiver is synchronized with the chaotic oscillator in the transmitter, even if they started with different initial conditions. However, any change in the initial state of the transmitter switches it to another attractor and, therefore, interrupts synchronization. After that, a certain time is required to restore synchronization. During this synchronization time, the information cannot be retrieved at the recipient and therefore is not sent. As soon as synchronization is established again, the information encoded in another chaotic attractor is sent to the recipient. The time interval during which information is transmitted should not be too long to avoid synchronization attacks, that is, the time it takes for a hacker to configure the parameters of a virtual system. Thus, switching between chaotic attractors ensures high communication security.

The communication scheme contains two channels; private and public, as shown in Fig. 7.15. The private channel is used to synchronize the receiver R with the transmitter T , and the public channel is used to transmit information. This two-channel communication scheme provides not only a higher level of security, but also a much better communication quality [61] because different state variables are used to synchronize and transfer information. In particular, the variables x_T and x_R act to synchronize the variables u_T and u_R in order to encode and decode information, respectively. Switching between coexisting attractors is achieved by changing the initial condition for the variable u_T in the range where the attractors are chaotic.

The attractor is chosen by varying initial condition generated by a chaotic map, for example, a logistic map, although other chaotic maps can also be used. The variation of the initial condition of the variable u_T in Eq. 7.23 leads the system to different dynamical regimes, as shown in the bifurcation diagram in Fig. 7.16.

The communication algorithm includes the following steps.

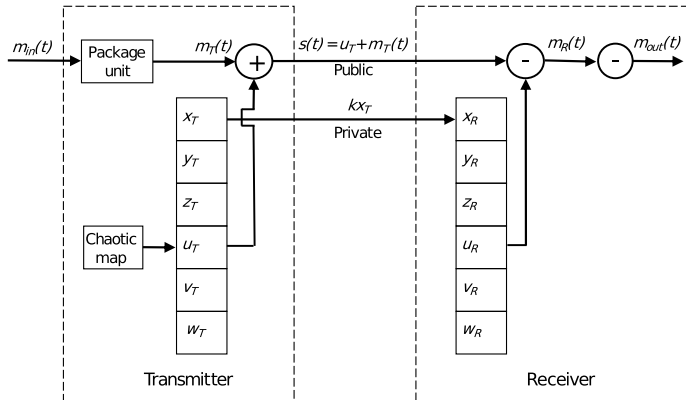
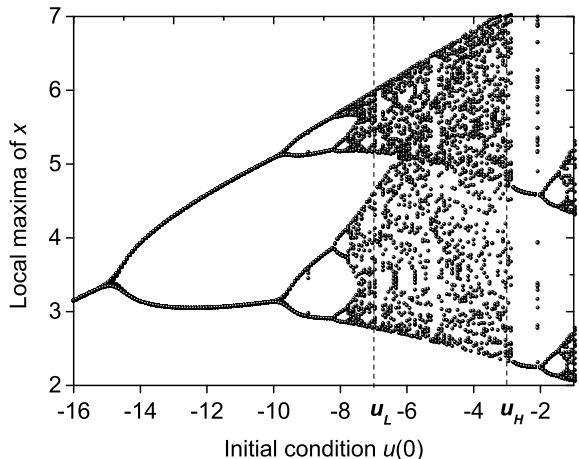


Fig. 7.15 Two-channel communication scheme containing private and public channels. The private channel serves to synchronize the receiver with the transmitter using x_T variable, while the public channel is used to transfer information. $m_{in}(t)$ is the input message, $m_T(t)$ is the information packages, $s(t)$ is the encrypted signal, $m_R(t)$ is the decoded signal in the receiver containing the synchronization error, and $m_{out}(t)$ is the recovered message

Fig. 7.16 Bifurcation diagram of local maxima of x versus initial condition $u(0)$ showing the Feigenbaum cascade of period-doubling bifurcations to chaos. The system parameters are $a = 0.2$, $b = 0.2$, and $c = 5.7$. The initial condition is varied between $u_L = -7$ and $u_H = -3$ to be inside the chaotic range



- (1) A plain digitalized message $m_{in}(t)$ is divided into d packages, i.e. $m_{in}(t) = \{m_1(t), m_2(t), \dots, m_i(t), \dots, m_d(t)\}$.
- (2) A sequence of values generated by a discrete chaotic system in the transmitter serves as a dynamic secret key used as initial conditions for variable u_T . For every subsequent package, the initial condition is different and defined by the chaotic map.
- (3) An i th package is encoded into an i th coexisting chaotic attractor using the chaotic masking method to obtain the encrypted signal $s(t) = u_T(t) + m_T(t)$ to be sent to the receiver via a public channel. At the same time, the variable $x_T(t)$ is sent to the receiver through a private channel to synchronize the receiver

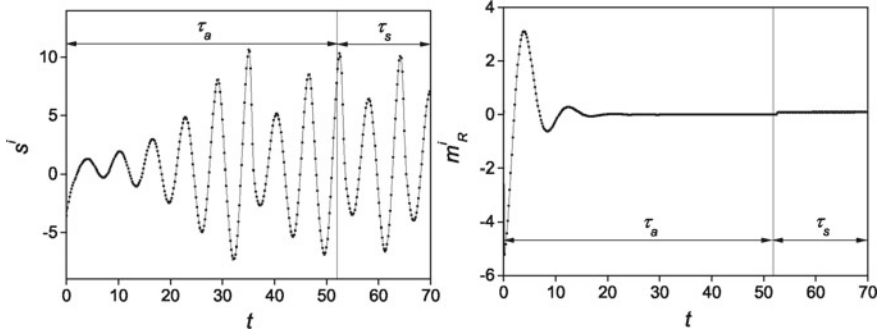


Fig. 7.17 Examples of time series of (left) transmitted single package with signal s^1 carrying the information $0.1m_T^1$ encrypted in one of the coexisting chaotic attractors during interval τ_s after transient time τ_a and (right) synchronization error obtained in the receiver. During τ_a the oscillators are asynchronous, whereas during τ_s they completely synchronize

with the transmitter by adding the term $k(x_T - x_R)$ to the first equation of the receiver (see Eq. 7.23).

- (4) The information is decrypted in the receiver by resting the variable u_R from the received signal as $m_R(t) = s(t) - u_R(t)$. The decoded signal $m_R(t)$ in each i th package includes two time intervals, asynchronous ($0 < t_s < \tau_a$) and synchronous ($\tau_a < t_s < \tau_s$), as illustrated in Fig. 7.17.
- (5) The synchronization error is eliminated by removing asynchronous transient windows (τ_a) and leaving only time intervals (τ_s) of synchronous dynamics to obtain output signal $m_{out} = m_{in}$.

Each package consists of two phases, $\tau^i = \tau_a + \tau_s$. The first phase τ_a should be larger than the mean synchronization time ($\tau_a > \tau_s$) needed for synchronization of the receiver with the transmitter. During this time interval, the chaotic systems in the transmitter and in the receiver oscillate asynchronously, as seen from the right panel in Fig. 7.17. The useful information is only added to the second phase τ_s when the oscillators completely synchronize. However, the duration of this phase should be shorter than the synchronization time ($\tau_s < \tau_s$).

The information package m_T^i is added to the chaotic carrier $u_T^i(t)$ using the chaotic masking, so that the transmitted signal in each package is $s_i(t) = u_T^i(t) + 0.1m_T^i(t)$, as illustrated in the left panel in Fig. 7.17. The coefficient 0.1 is introduced to hide the information in the chaotic carrier, i.e. to make it indistinguishable. The signal $s(t)$ is transmitted to the receiver via the public channel, while the variable x_T is sent to the receiver via the private channel to synchronize the oscillator in the receiver with that in the transmitter. After the transient time τ_a has passed, complete synchronization is achieved, as demonstrated in the right panel in Fig. 7.17.

A significant advantage of the communication system based on extreme multistability in comparison with traditional monostable chaotic communication is a much

higher communication security provided by switching between coexisting chaotic attractors. After each switch, a certain amount of time is required to synchronize the receiver with the transmitter. Once complete synchronization is achieved, the information is transmitted in a relatively short time (shorter than the synchronization time), so that the hacker does not have time to synchronize his virtual system with the transmitter. This makes the synchronization attack completely useless.

References

1. Newhouse S (1974) Diffeomorphism with infinitely many sinks. *Topology* 13:9–18
2. Chawanya T (1996) Infinitely many attractors in game dynamics system. *Prog Theor Phys* 95(3):679–684
3. Leonov GA, Kuznetsov NV (2013) Hidden attractors in dynamical systems: From hidden oscillations in Hilbert-Kolmogorov, Aizerman, and Kalman problems to hidden chaotic attractor in Chua circuits. *Int J Bifurc Chaos* 23:1330002
4. Li C, Thio JCW, Iu HHC, Lu TA (2018) A memristive chaotic oscillator with increasing amplitude and frequency. *IEEE Access* 6:12945–12950
5. Hofbauer J, Sigmund K (1988) The theory of evolution and dynamical systems. Cambridge University Press
6. Taylor PD, Jonker LB (1978) Evolutionary stable strategies and game dynamics. *Math Biosci* 40:145–156
7. Chawanya T (1997) Coexistence of infinitely many attractors in a simple flow. *Physica D* 109:201–241
8. Grebogi C, Ott E, Yorke JA (1983) Crises, sudden changes in chaotic attractors, and transient chaos. *Physica D* 7:181–200
9. Lai YC, Grebogi C (1996) Complexity in Hamiltonian-driven dissipative chaotic dynamical systems. *Phys Rev E* 54:4667–4675
10. Sun H, Scott S, Showalter K (1999) Uncertain destination dynamics. *Phys Rev E* 60:3876–3880
11. Wang J, Sun H, Scott SK, Showalter K (2003) Uncertain dynamics in nonlinear chemical reactions. *Phys Chem Chem Phys* 5:5444–5447
12. Ngonghala CN, Feudel U, Showalter K (2011) Extreme multistability in a chemical model system. *Phys Rev E* 83:056206
13. Hens CR, Banerjee R, Feudel U, Dana SK (2012) How to obtain extreme multistability in coupled dynamical systems. *Phys Rev E* 85:035202(R)
14. Patel MS, Patel U, Sen A, Sethia GC, Hens C, Dana SK, Feudel U, Showalter K, Ngonghala CN, Amritkar RE (2014) Experimental observation of extreme multistability in an electronic system of two coupled Rössler oscillators. *Phys Rev E* 89:022918
15. Sprott JC, Li C (2014) How to obtain extreme multistability in coupled dynamical systems. *Phys Rev E* 89:066901
16. Li C, Sprott JC, Hu W, Xu Y (2017) Infinite multistability in a self-reproducing chaotic system. *Int J Bifurc Chaos* 27(10):1750160
17. Lai Q, Kuang PD, Liu F, Iu H (2019) An extremely simple chaotic system with infinitely many coexisting attractors. *IEEE Trans Circuits Syst II Exp Briefs* 67(6):1129–1133
18. Li C, Sprott J, Mei Y (2017) An infinite 2-D lattice of strange attractors. *Nonlinear Dyn* 89(4):2629–2639
19. Li C, Sprott J, Kapitaniak T, Lu T (2018) Infinite lattice of hyperchaotic strange attractors. *Chaos Soliton Fractals* 109:76–82
20. Singwi VF, Kengne J (2019) Reversal of period-doubling and extreme multistability in a novel 4D chaotic system with hyperbolic cosine nonlinearity. *Int J Dyn Control* 7:439–451

21. Sprott JC, Jafari S, Khalaf AJM, Kapitaniak T (2017) Megastability: coexistence of a countable infinity of nested attractors in a periodically-forced oscillator with spatially-periodic damping. *Eur Phys J Spec Top* 226(9):1979–1985
22. Palis J, Taken F (1993) Hyperbolicity and sensitive chaotic dynamics at homoclinic bifurcations. Cambridge University Press, New York
23. Zhang LP, Liu Y, Wei ZC, Jiang HB, Bi QS (2020) A novel class of two-dimensional chaotic maps with infinitely many coexisting attractors. *Chin Phys B* 29(6):060501
24. Rybalova E, Semenova N, Strelkova G, Anishchenko V (2017) Transition from complete synchronization to spatio-temporal chaos in coupled chaotic systems with nonhyperbolic and hyperbolic attractors. *Eur Phys J Spec Top* 226:1857–1866
25. Li H, Li K, Chen M, Bao B (2020) Coexisting infinite orbits in an area-preserving Lozi map. *Entropy* 22:1119
26. Chua LO (1971) Memristor—the missing circuit element. *IEEE Trans Circuit Theory* 18:507–519
27. Strukov DB, Snider GS, Stewart DR, Williams RS (2008) The missing memristor found. *Nature* 453:80–83
28. Ventra MD, Pershin YV, Chua LO (2017) Circuit elements with memory: memristors, mem-capacitors and meminductors. *Proc IEEE* 97:1715
29. Tetzlaff R (2014) Memristors and memristive systems. Springer, New York
30. Itoh M, Chua LO (2008) Memristor oscillators. *Int J Bifurc Chaos* 18:3183–3206
31. Di VM, Pershin YV, Chua LO (2009) Circuit elements with memory: memristors, memcapacitors, and meminductors. *Proc IEEE* 97:1717–1724
32. Li C, Min F, Me H (2017) Extreme multistability analysis of memristor-based chaotic system and its application in image decryption. *AIP Adv* 7:125204
33. Yuan F, Wang G, Wang X (2016) Extreme multistability in a memristor-based multi-scroll hyper-chaotic system. *Chaos* 26:073107
34. Bao B, Chen M, Bao H, Quan X (2016) Extreme multistability in a memristive circuit. *Electron Lett* 52:1008–1010
35. Bao B, Bao H, Wang N, Chen M, Quan X (2017) Hidden extreme multistability in memristive hyperchaotic system. *Chaos Solitons Fractals* 94:102–111
36. Njitacke ZT, Kengne J, Tapche RW, Pelap FB (2018) Uncertain destination dynamics of a novel memristive 4D autonomous system. *Chaos Solitons Fractals* 107:177–185
37. Chang H, Li Y, Yuan F, Chen G (2019) Extreme multistability with hidden attractors in a simplest memristor-based circuit. *Int J Bifurc Chaos* 29:1950086
38. Sun J, Zhao X, Fang J, Wang Y (2018) Autonomous memristor chaotic systems of infinite chaotic attractors and circuitry realization. *Nonlinear Dyn* 94:2879–2887
39. Bao B, Jiang T, Wang G, Jin P, Bao H, Chen M (2017) Two-memristor-based Chua's hyper-chaotic circuit with plane equilibrium and its extreme multistability. *Nonlinear Dyn* 89:1157–1171
40. Zhang YZ, Liu Z, Wu HG, Chen SY, Bao BC (2019) Two-memristor-based chaotic system and its extreme multistability reconstitution via dimensionality reduction analysis. *Chaos Solitons Fractals* 127:354–363
41. Chen M, Sun M, Bao H, Hu Y, Bao B (2020) Flux-charge analysis of two-memristor-based Chua's circuit: dimensionality decreasing model for detecting extreme multistability. *IEEE Trans Ind Electron* 67(3):2197–2206
42. Ye X, Wang X, Gao S, Mou J, Wang Z, Yang F (2020) A new chaotic circuit with multiple memristors and its application in image encryption. *Nonlinear Dyn* 99:1489–1506
43. Ye X, Wang X, Gao S, Zhang M (2020) Extreme multistability in a new hyperchaotic meminductive circuit and its circuit implementation. *Eur Phys J Plus* 134(5):1489–1506
44. Louodop P, Tchitnga R, Fagundes FF, Kountchou M, Kamdoun Tamba V, Pando LCL, Cerdeira HA (2019) Extreme multistability in a Josephson-junction-based circuit. *Phys Rev E* 99:042208
45. Matthews R (1989) On the derivation of a chaotic encryption algorithm. *Cryptologia* XIII:29–42

46. Pisarchik AN, Flores-Carmona NJ, Carpio-Valadez M (2006) Encryption and decryption of images with chaotic map lattices. *Chaos* 16:033118
47. Pisarchik AN, Zanin M (2008) Image encryption with chaotically coupled chaotic maps. *Physica D* 237:2638
48. Zanin M, Pisarchik AN (2014) Gray code permutation algorithm for high-dimensional data encryption. *Inform Sci* 270:288–297
49. Hayes S, Grebogi C, Ott E, Mark A (1993) Communicating with chaos. *Phys Rev Lett* 70:3031–3034
50. Boccaletti S, Pisarchik AN, del Genio I, Amann A (2018) Synchronization: from coupled systems to complex networks. Cambridge University Press, Cambridge
51. Pisarchik AN, Zanin M (2012) Chaotic map cryptography and security. In: Clary TS (ed) Horizons in computer science, vol 4. NOVA, pp 301–332
52. Pisarchik AN, Ruiz-Oliveras FR (2010) Optical chaotic communication using generalized and complete synchronization. *IEEE J Quantum Electron* 46(3):299a–299f
53. Pisarchik AN, Jaimes-Reátegui R, Sevilla-Escoboza JR, Ruiz-Oliveras FR, García-López JH (2012) Two-channel opto-electronic chaotic communication system. *J Franklin Inst* 349:3194–3202
54. Wang X, Akgul A, Cavusoglu U, Pham VT, Hoang DV, Nguyen XQ (2018) A chaotic system with infinite equilibria and its S-box constructing application. *Appl Sci* 8:2132
55. Dong E, Yuan M, Du S, Chen Z (2019) A new class of Hamiltonian conservative chaotic systems with multistability and design of pseudo-random number generator. *Appl Math Mod* 73:40–71
56. Farhan AK, Ali RS, Natiq H, Al-Saidi NMG (2019) A new S-box generation algorithm based on multistability behavior of a plasma perturbation model. *IEEE Access* 7:124914–124924
57. Liu B, Ye X, Chen Q (2021) Generating infinitely many via a new 3D cosine system and Its application in image encryption. *IEEE Access* 9:136292–136301
58. Zanin M, Sevilla-Escoboza R, Jaimes-Reátegui R, García-Lopez JH, Pisarchik AN (2013) Synchronization attack of chaotic communication systems. *Discontinuity, Nonlinearity, Complex* 2:333–343
59. García-López JH, Jaimes-Reátegui R, Chiu-Zarate R, Lopez-Mancilla D, Ramirez-Jiménez R, Pisarchik AN (2008) Secure computer communication based on chaotic Rössler oscillators. *Open Electr Electron Eng J* 2:41–44
60. Pisarchik AN, Jaimes-Reátegui R, Rodríguez-Flores C, García-López JH, Huerta-Cuellar G, G, Martín-Pasquín FJ, (2021) Secure chaotic communication based on extreme multistability. *J Franklin Inst* 358(4):2561–2575
61. García-López JH, Jaimes-Reátegui R, Pisarchik AN, Medina-Gutiérrez C, Jiménez-Godínez JC, Murguía-Hernandez AU, Valdivia R, (2005) Novel communication scheme based on chaotic Rössler circuits. *J Phys: Conf Ser* 23:175–184

Chapter 8

Multistability in Perception



Abstract Multistability exists not only in mathematical models, but also in complex biological systems, such as the brain. We can easily confirm that our psyche is multistable under certain conditions. For example, ambiguous visual stimuli provide the brain with sensory information that contains conflicting evidence for multiple mutually exclusive interpretations. In this regard, perceptual multistability was one of the first issues discussed in terms of coexisting states, which was introduced to perform information processing of biological neural systems. Even the term “multistability” itself was first used in relation to visual perception. The thinking process in the brain, as a multistable dynamical system, can be considered as alternative switching between coexisting mental states. These switches can be either spontaneous or initiated by external stimulation, but in both cases they are triggered by neuronal brain noise. In this chapter, we first demonstrate how multistability reveals itself in different sensory modalities. Then, we describe popular models of bistable perception and the most important results of psychological and physiological experiments using electroencephalography (EEG) and magnetoencephalography (MEG). We also show how artificial intelligence can help in the recognition of perceptual states. Finally, we explain the operation principle of brain-computer interfaces based on bistable perception.

8.1 Multistability in Different Sensory Modalities

Multistability in perception occurs when a single physical stimulus produces alternations between different subjective percepts. For example, the human brain, while renowned for its amazing computing power, falls into deep confusion when it receives conflicting views of the visual world. In everyday life, we usually manage to avoid ambiguity of perception due to our previous experience or by introducing additional information. However, during prolonged viewing of ambiguous images, their interpretation switches spontaneously, changing every few seconds. This alternation was attributed to neural adaptation or satiety.

8.1.1 Perceptual Decision-Making

Why is the study of multistable perception interesting? In modern neuroscience it is well-known that perception and sensory information processing are the most important functions of the brain that ensure our interaction with the environment (see Fig. 8.1a) [1]. Humans and animals receive information from sensory inputs of various modalities (tactile, visual, auditory, etc.), process them and use them in a decision-making process known as perceptual decision making, which can be assessed by a number of characteristics, for example, response speed or reaction time, decision correctness, etc. [1]. When performing cognitive decision-making tasks, the brain dynamically adjusts its functional network structure to maintain optimal behavioral characteristics in a situation of changing cognitive demands [2–4].

Modern neurophysiological research emphasizes the leading role of brain functional connectivity in human cognition and behavior [5]. The entire brain network activity is generated through the interaction of several functional subnetworks, either during a rest-state or during the execution of the perceptual or cognitive tasks [6]. These brain functional subnetworks include the dorsal network of attention, the fronto-parietal network, the executive control network, the default mode network, etc. [7]. Although brain functional networks have different anatomical locations, they interact with each other and overlap during perceptual or cognitive tasks [8].

Performance and neural activity during sensory processing depend on a person's inner state, alertness, and fatigue. In particular, resting functional connectivity can predict a subject's ability to maintain sustained attention during complex cognitive tasks [9]. Fatigue causes changes in the structure of the brain functional network, making the brain regions more isolated and their interaction less efficient [10]. Increased cognitive load leads to a decrease in the modularity of the functional network; the default mode network increases connectivity with other networks, while the connectivity within the network itself decreases [11].

Multistability provides a window into consciousness, as it gives a natural and unique dissociation between the objective properties of the stimulus and the subjective sensations: the stimulus features are constant, while the sensations change

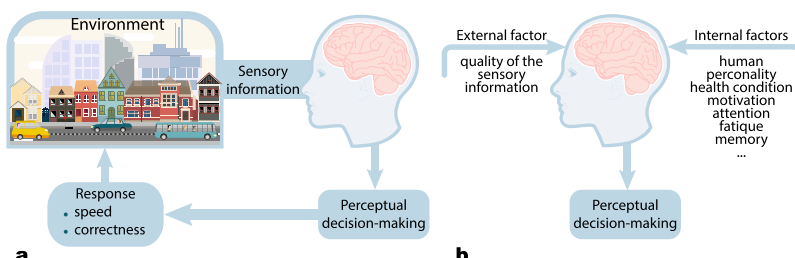


Fig. 8.1 **a** Perceptual decision-making as a process of choosing an action course by a living organism based on the available sensory information from the environment. **b** Perceptual decision-making depends on external and internal factors

dynamically. As a consequence, we can consider the situation of perceptual decision-making in conditions of insufficient sensory information. The traditional concept of multistable visual perception suggests that spontaneous perceptual reversals are a consequence of the brain lower-level processes based on antagonistic neural activity in the visual system [12, 13].

Currently, we can conclude that perceptual decision-making is largely determined by the high-level brain mechanisms that actively select and interpret sensory information, and their interactions with lower-level processes that are more directly related to the processing of sensory stimulus properties [14]. Interest in ambiguous image studies is determined by the unique possibility of analyzing the bottom-up and top-down processes of sensory information processing in the brain. The ambiguous stimuli can split external and internal factors which influence their processing and perception (see Fig. 8.1b). Bottom-up brain information flows are responsible for processing sensory data, which can be interpreted unambiguously, while top-down information flows in the brain arise when it is necessary to involve the sensory data interpretation, our experience, memory, etc., i.e. endogenous factors.

As a consequence, the interest in studying multistable perception has increased with the advent of modern non-invasive high-resolution brain imaging techniques such as functional magnetic resonance imaging (fMRI) and magnetoencephalography (MEG) because multistable stimuli allow neural activity related to conscious perception to be distinguished from that related to physical stimulus features. Moreover, multistable perception can help us understand the constructive neural processes that generate a unified and coherent subjective experience of the world even though the information available is often fragmentary, conflicting or even ambiguous. Based on these experimental results, Leopold and Logothetis [15] proposed that “*reorganizations of activity throughout the visual cortex, concurrent with perceptual reversals, are initiated by higher, largely non-sensory brain centers*”. Since then, hybrid theoretical proposals have emerged, on the basis of behavioural evidence, which conceptualise multistable perception as arising from interactions between low-level (sensory) and high-level (cognitive) processes [14]. In other words, multistable perception can be considered as the product of continuous interactions between “low-level” (sensory) and “high-level” (frontal and parietal) brain regions.

Returning to the above-mentioned brain functional networks, we can find a reflection of these processes using EEG/MEG recordings characterized by a high temporal resolution. Traditionally, several rhythms of nervous activity are distinguished: δ -range (1–5 Hz), θ -range (5–8 Hz), α -range (8–12 Hz), β -range (15–30 Hz) and γ -range (> 30 Hz). According to neurophysiological studies, these rhythms facilitate the coordination of neuronal activity in distant brain regions [16, 17]. The low-frequency θ -rhythm modulates the high-frequency electrical activity of the brain in the γ -range of the electrocorticograms [18].

In addition to the θ -range, according to Fries [16], low-frequency α - and β -rhythms in the visual cortex control neural activity in the γ -range. The functional connections between neural ensembles cause a correlation or synchronization between recorded EEG signals in different frequency ranges [16, 17]. As pointed out by

Maksimenko et al. [19], neuronal populations in distant brain regions interact differently at different frequency ranges.

During the perception of visual stimuli, neural populations in the visual cortex interact at frequencies in the combined α/β (8–30 Hz) and γ (50–70 Hz) ranges [20, 21]. Moreover, the analysis of the functional connectivity in the parieto-occipital cortex shows a different structure of communication in the separated α - and β -ranges [22–24]. In contrast, functional connectivity in the β range is affected by the complexity of the visual information [25]. Along with the neural connection in the visual cortex, the interpretation of visual stimulus also requires communication between distant cortical regions [26].

So, during the processing of visual information, δ -activity in the frontal region and α -activity in the parieto-occipital region are functionally connected and jointly direct visual perception to integrate sensory data with the current requirements of the task [27]. During the task of sustained attention, functional communication at a great distance between different parts of the fronto-parietal network is characterized by fluctuations in the θ -range, and communication within these areas is provided by high-frequency γ -activity [28]. Attention-related functional connectivity is also present in the fronto-parietal cortex in different frequency ranges [29, 30].

This means that there is some evidence that fluctuations in neuronal population activity at both anatomically early and later stages of visual processing are strongly correlated with perception. Such neuronal activity fluctuations can arise from different sources, including top-down modulation, mnemonic processes, adaptation, and spontaneous fluctuations. At the same time, high-level fronto-parietal processes continuously re-evaluate the current interpretation of the sensory input and initiate changes in subjective perception leading to the formation of multistable perception. The same or similar mechanisms involved in visual multistable perception might also have a role in other sensory modalities (e.g. auditory and tactile multistability). Let us start our consideration with examples of multistability in different sensory domains following a review article by Schwartz et al. [31].

Information from the outside world that we receive through our senses (sight, smell, touch, hearing and taste) can be ambiguous, which, in turn, affects our decision-making. Therefore, research in the field of multistability perception is of paramount importance for the correct interpretation of the information received.

8.1.2 Visual Perception

Multistability was first described for vision, where it occurs, for example, when different stimuli are presented to the two eyes or for certain ambiguous figures. For more than two centuries, it has been a major conceptual and experimental tool for investigating perceptual awareness in vision. Following Schwartz et al. [31], the first report on visual multistability belongs to Dutoit [32]. This report describes what is now called *binocular rivalry* (Fig. 8.3). Dutoit noticed that when he held the blue taffeta disc to one eye and the yellow taffeta disc to the other eye, he did not see the

mixture of blue and yellow. Rather, he “could not detect even the smallest shade of green”. His conscious experience alternated with blue and yellow. In perception, it seemed that at any moment of time the signal from one of the two eyes dominated, and the dominant eye alternated in a clearly random manner. This illustrates the main characteristic of multistable perception: a static physical stimulus can induce a subjective experience of perception that is stable for a short time, but changes from time to time.

The sensory information input to vision remains unchanged, and yet the resulting perceptual interpretation fluctuates over time between alternative views. These fluctuations are presumably due to the fact that the brain receives ambiguous information about the nature of the object at a given location in visual space. Faced with ambiguity, the brain oscillates between different neuronal states over time.

Bistability in visual perception can result from different mechanisms. We can distinguish at least six types of visual perception bistability. These are

- perspective reversal (Necker cube, Schroeder stairs),
- pattern reversal (Rubin vase–face, rabbit–duck),
- monocular rivalry,
- binocular rivalry,
- rotating objects (sphere, spinning dancer),
- apparent motion (moving plaid, motion quartet).

In Fig. 8.2 we present some examples of ambiguous images, such as the Rubin vase–face illusion, duck–rabbit illusion, Schroeder stairs, and monocular rivalry. Multistability was described for ambiguous figures involving depth interpretation, like the figure/ground organization, for example, the Rubin vase which is an example of bistable (i.e. reversing) two-dimensional images (developed by the Danish psychologist Edgar Rubin in 1915 [33]); see Fig. 8.2a or the classical illustration of perspective reversal in psychology of perception—the 2D stair outline, which is a two-dimensional drawing which may be perceived either as a drawing of a staircase leading downwards from left to right or the same staircase only turned upside down, first described by the German natural scientist Heinrich G. F. Schroeder in 1858 [34] (see Fig. 8.2b). Another very famous example of perspective reversal image is the 2D outline of a cube—the Necker cube (first suggested by the Swiss crystallographer Louis Albert Necker in 1832 [35]) shown in the left panel in Fig. 1.1 in Sect. 1.1.

The difference is that multistability in binocular rivalry (Fig. 8.3) involves perceptual competition between two images, while the multistable perception of ambiguous figures involves competition between interpretations of a single image. For a long time, these two types of bistable visual perception were considered as different effects, but later Walker [38], and Leopold and Logothetis [15] assumed that both types of bistable perception have similarities [31].

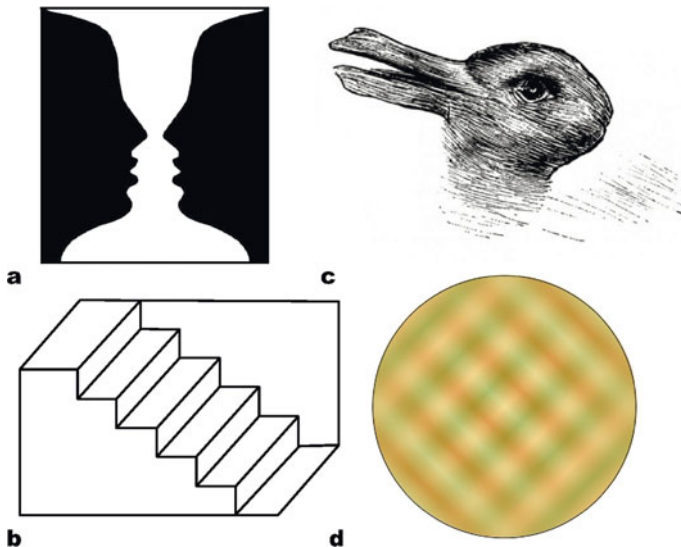


Fig. 8.2 Well-known ambiguous images: **a** Rubin vase–face figure, **b** Schroeder stairs, **c** duck–rabbit illusion, and **d** monocular rivalry where two physically superimposed patterns that are dissimilar in colour and orientation compete for perceptual dominance. The perceptual appearance fluctuates over time despite unchanging physical stimulation [36, 37]

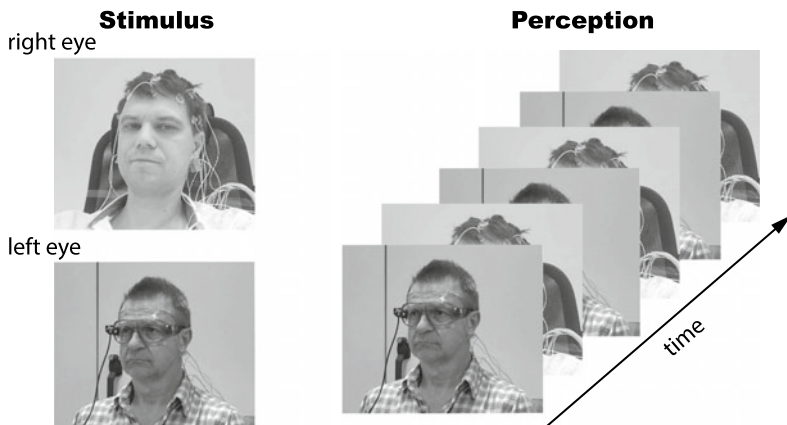


Fig. 8.3 Binocular rivalry example. Different images with pictures of the authors of this book (visual stimuli) presented to the left and right eyes

8.1.3 Auditory Perception

In addition to visual multistable perception, there also exists multistability in other types of sensory information. Let us now consider multistability in auditory perception, in particular, the effect of *verbal transformation* [39], which consists of the following. When a word is presented repeatedly (for example, ‘life, life, life, …’), the words or phonemes that are perceived change over time; in our case, ‘fly, fly, fly’ might be perceived after a while (Fig. 8.4a). Also, when a rapid sequence of tones with two different frequencies, f_1 and f_2 ($f_1 > f_2$), is presented, the subject may perceive either a single stream with a ‘gallop’ rhythm ($f_1 f_2 f_1 f_1 f_2 f_1 f_1 f_2 f_1$), or as two regular audio streams ($f_1 f_1$ and $f_2 f_2$ simultaneously), and the percept may ‘flip’ between the two interpretations (Fig. 8.4b).

It should be noted that auditory streaming was studied in many works where detailed comparisons of the phenomenology of multistability across visual and auditory modalities are provided [40–43]. These studies reported that the distributions of the random durations of switches in auditory perceptual organization were very similar to those observed for visual multistability. In fact, when measured using the same observers, the dynamics of auditory and visual switching revealed almost identical patterns [40]. Interestingly, bistability for streaming seemed to be the rule rather than the exception, as it could be observed over a surprisingly broad range of stimulus parameters [41, 42]. Similar dynamical properties were observed for the

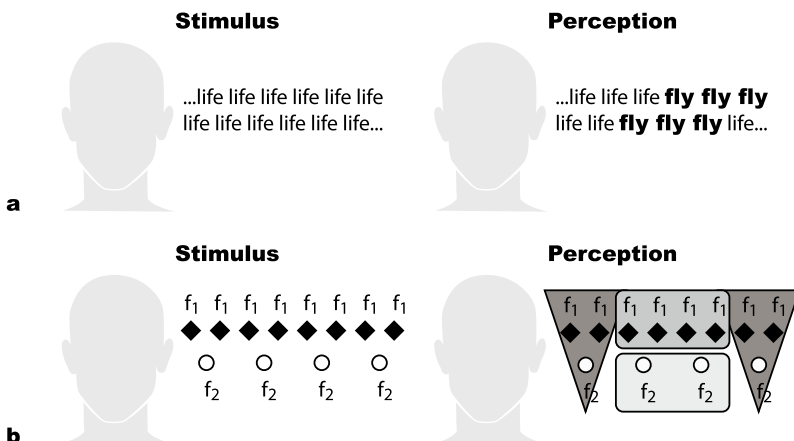


Fig. 8.4 Examples of bistable auditory perception. **a** Illustration of verbal transformation effect. The audio stimulus is a sequence of words presented repeatedly (here “life, life, life, …”). After some time, the percept may change reflecting a different perceptual organization of the sound segments (e.g. “fly, fly, fly, …”), and then may alternate between the two organizations. **b** The bistable auditory streaming illustration. Stimulus is the regular sequence of tones with frequencies $f_1 > f_2$. The percept can alternate between the two interpretations—a single stream with the “gallop” rhythm (triangles) and two regular streams (ellipses). Based on data from [31]

verbal transformation effect [43, 44]. Auditory multistability was also reported with very different stimuli, using rhythmic cues [45, 46].

In particular, a possible instance of musical multistability is the scale illusion melody [48] which is analogous to a visual ambiguous figure [49, 50]. The scale illusion melodies are based on dichotic tonal sequences. Such musical illusions occur because subjects stream not just by ear of presentation but also by pitch. Deutsch [48] presented subjects dichotic repetitions of C major scales in which successive notes of ascending and descending versions of the scale alternated between ears. Figure 8.5a shows how these ascending and descending C major scales switch from ear to ear.

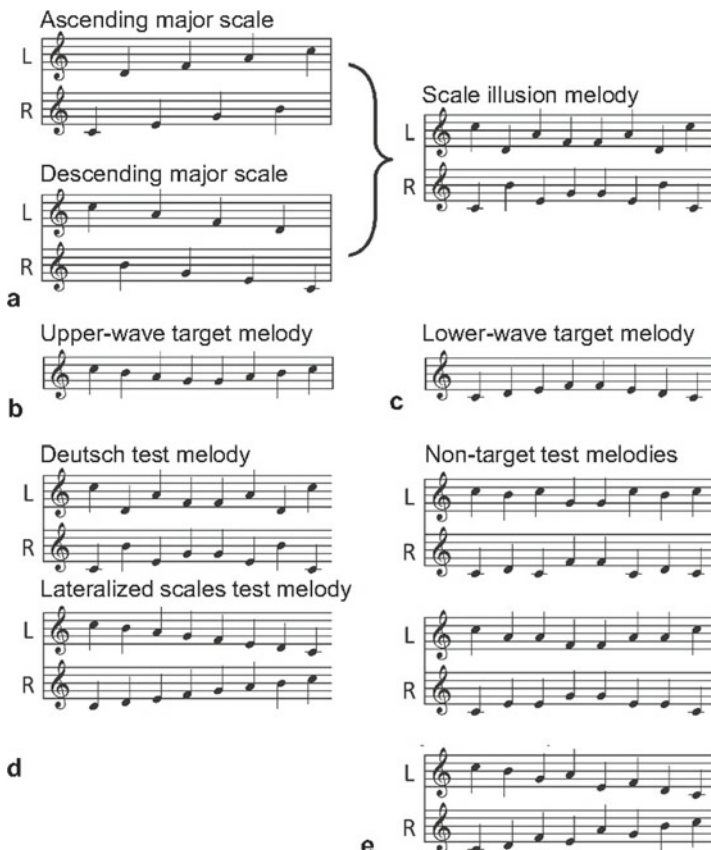


Fig. 8.5 a Arrangement of stimulus presentation for the scale illusion melody based on the C major scale. The scale illusion melody is the dichotic presentation of an ascending and descending major scale alternating between ears on each successive note. The ascending and descending major scales are presented in isolation on the left, the combination of which produces the scale illusion melody (on the right). b, c Target bistable sequences: upper- and lower-wave target melodies. d The Deutsch test melody (top) and the lateralized scale test melody (bottom). e Three non-target test melodies. L and R mark the sequence presented to the left and right ears, respectively. Based on data from [47]

In classic studies of musical *scale illusion*, ascending and descending major scales are presented dichotically with successive notes from each scale alternating between ears. The stimulus sequence involves presenting the first, third, fifth, seventh, ninth, etc., notes of an ascending or descending pattern to one ear, and the second, fourth, sixth, eighth, etc., notes to another ear. Importantly, listeners typically fail to report hearing the ascending and descending scales or patterns based on ear of input. Instead, the majority of listeners report classical situation of bistable perception—two wave-like patterns separated by frequency range with each pattern localized to one ear (Fig. 8.5b, c).

In the study of Diana Deutsch [48, 51] about 70% of participants reported hearing both an upper and lower wave-like melody while the remaining 30% reported hearing only one wave-like melody. Additionally, right-handed listeners misperceived the locations of the melodies reporting the upper wave-like melody entirely in the right ear and the lower wave-like melody entirely in the left ear. Deutsch suggested that the complex sound sequence caused perceptual confusion and to reconcile the ambiguity the notes were organized in the simplest possible manner, which in this case is by pitch [47].

It should be noted that the scale illusion can be described in a similar way as an ambiguous figure [49, 50]. From this perspective, spatial and pitch cues provide conflicting organizational information, and because pitch appears to be the dominant cue, spatial cues are ignored resulting in undulating melodies. However, the defining characteristic of an ambiguous figure is the availability of multiple perceptual interpretations [12]. At the same time, many studies of bistable perception of musical illusions have used the methodologies in which participants were presented with a stimulus and required to report their perception either verbally or with a forced-choice questionnaire. The use of these techniques is based on the assumption that an individual will only hear a single, clearly defined response option. This approach, of course, does not take into account the possibility that multiple perceptions are not only competing, but may all be available simultaneously to an individual in a given instance.

Brosowsky and Mondor [47] addressed this problem to determine whether simultaneously presented melodies, such as underlined scale musical illusion, can elicit multiple mutually exclusive percepts. In their study, participants were presented with target sequences derived from possible perceptual organizations of patterns typically used in studying the scale illusion (see, for example, Fig. 8.5a, b) and required to report the presence or absence of these targets in subsequent complex melodies, hereafter referred to as test melodies illustrated in Fig. 8.5c, d.

Two different test melodies containing target sequences were tested to determine if multistability would be unique to the scale illusion or, more generally, a characteristic of simultaneously presented melodies, overlapping in pitch and space. The first was the original scale illusion melody, here called Deutsch test melody (Fig. 8.5c, top panel), and the second was a similar melody known to elicit spatially defined perceptual organizations, here called lateralized test scales melody (Fig. 8.5c, bottom panel) [49]. Target sequences were created such that they would only be heard if the listener interpreted the test melody according to various perceptual cues. Critically

and in contrast with previous examinations of the scale illusion, an objective measure of target detection was obtained by including non-target test melodies (Fig. 8.5d). As a result, listeners could reliably identify target sequences from different perceptual organizations when presented with the same test melody on different trials. This result demonstrates the ability to alternate between mutually exclusive percepts of an unchanged musical stimulus.

8.1.4 Tactile Perception

Bistable tactile perception can be observed in experiments with an ambiguous apparent-motion quartets as shown in Fig. 8.6 [52]. Initially, such a paradigm was developed as a dynamic dots visualization for visual multistability study. When a subject is presented with two successive visual images (“visual loop”) with two black dots moving from one configuration (on one diagonal) to the other (on the inverse diagonal), the subject may perceive either a horizontal or a vertical displacement of the two black dots, and switch from one percept to the other. The same bistability illusion may be obtained also with tactile stimuli (“tactile loop”), using motion touch zones on the thumb. In this case, the subject experiences the same illusion, but now with tactile perception.

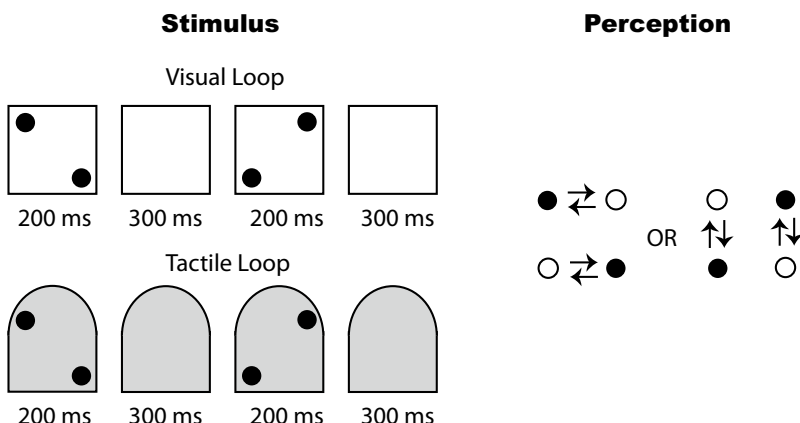


Fig. 8.6 Ambiguous apparent-motion quartets (visual and tactile) examples. When a subject is presented with two successive visual images (“Visual Loop”) with two black dots moving from one configuration (on one diagonal) to another (on the inverse diagonal), the subject may perceive either a horizontal or a vertical movement of the two black dots, and switch from one percept to the other. The same bistability illusion may be obtained with tactile stimuli (“Tactile Loop”), using motion touch zones on the thumb. Based on data from [31]

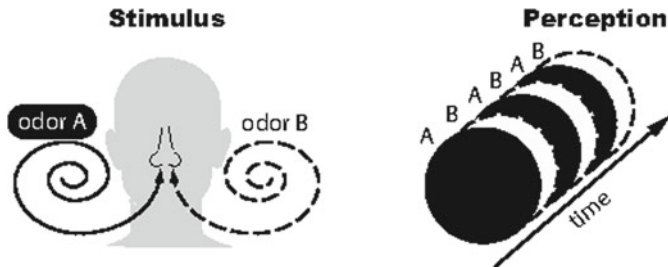


Fig. 8.7 Examples of bistable olfactory perception. When a subject is presented with two different odors A and B, one in each nostril, perception may switch from one odor to the other. Based on data from [31]

8.1.5 Olfactory Perception

Early described paradigm of binocular rivalry can be extended to olfaction. Zhou et al. [53] reported alternating olfactory percepts when different odors were presented to the two nostrils. As in the case of the two images, in olfactory paradigm as shown in Fig. 8.7, the subject's perception may switch from one odor to the other.

In this case we have an almost complete analogy with binocular rivalry example (see Fig. 8.3), when the subject does not see a mixture of pictures shown to the left and right eye, but an interchangeability between the perception of these images. The situation with the perception of different odors is the same: when presented with two odors, we alternately feel one odor and then the other, but not their mixture.

8.2 Bistable Perception Models

Multistable perception characterizes fluctuating perceptions that can be caused by certain visually ambiguous patterns, such as the Necker cube shown in the left panel in Fig. 1.1. When this drawing is viewed for a long time, the two perceptions spontaneously alternate, changing every few seconds. This alternation has been attributed to neural adaptation or satiation [54, 55]. Random switches between the two percepts were confirmed by neurophysiological experiments, where the underlying electrical membrane potential was measured [56]. Although these switches are known to be induced by inherent brain noise, the exact microscopic mechanism of these oscillations remains unknown [14].

There are various approaches to explain the mechanisms underlying the switching between different perceptions. The majority of models suggest that the biological origin of perceptual switching lies in noise inherent in the activity of nerve cells in the brain, which is the result of relatively random bursts of individual neurons [57]. In addition, occasional external stimuli can also induce perceptual changes [58].

It is widely accepted that no object-oriented neurons (or engrams) exist inside the brain; rather, there is a particular neural network with a finite number of neurons that can be activated appropriately to form a unique representation of each object or thought. However, neural clusters representing each feature can compete internally for the manifestation of the degree of excitation of a subgroup of features as a whole. This means that the same ambiguous image can excite or inhibit different sets of neurons, depending on its interpretation.

Some models suppose that different percepts are associated with coexisting attractors and brain noise results in switching between them. These models are called *attractor models*. Another approach to model bistable perception is based on neural adaptation or satiation [54, 55], since the time the subject fixates on a particular percept is approximately the same for every subject [59]. These so-called *oscillatory models* imply that the perceptual states are unstable and the neural network switches between them. While in the oscillatory models the switching occurs even without noise mainly due to adaptation, in the attractor models, noise is the only reason for the switching between coexisting attractors. In both models, brain noise is crucial for understanding the mechanisms for random switching between perceptual states. Therefore, it is important to consider how brain noise can be measured.

8.2.1 Brain Noise Estimation

Electroencephalographic (EEG) and magnetoencephalographic (MEG) measurements of the cerebral cortex neural activity demonstrate a good correlation with periodic switching between different perceptions of an ambiguous image. It is assumed that the biological reason for switching perception lies in the inherent noise in the activity of neuronal cells in the brain. Since without the brain noise concept it is impossible to explain the irregularity in switching between different percepts, we will first describe where the noise comes from and how it can be estimated.

First of all, it should be noted that all natural systems are noisy, and the brain is no exception. Moreover, noise is ubiquitous in the brain at various levels, from the release of vesicular substances and surges in variability to fluctuations in the global level of neurotransmitters. Sources of endogenous brain noise lie in the quasi-random release of neurotransmitters by synapses, random synaptic input from other neurons, random switching of ion channels, stochasticity of receptors activated by N-methyl-D-aspartate, which affect the stability of the short-term memory and attention, an accidental change in the gamma-aminobutyric acid receptor, which activates the conductivity of synaptic ion channels and determines the probability of the system's transition to a pathological state [57]. Today, the presence of noise in neural perception is recognized by many researchers, and this issue is widely covered in scientific literature (see, for example, [60–64]).

Endogenous brain noise is essential for the normal functioning of the brain at all levels of its organization, from neural cells to the neural network. Indeed, spontaneous neuronal activity plays an important role in the thinking process and perception. For

example, noise of certain intensity helps to detect weak stimuli due to the coherence resonance phenomenon (see Sect. 5.2). In addition, brain noise avoids deadlocks and allows switching between different perceptual states [62, 65], underlying important mechanisms of the brain functionality and self-organization [66, 67]. In other words, without noise it would be difficult or impossible to make a decision, i.e. noise allows one to make a probabilistic choice between different decisions. Random switching between two percepts were also detected in neurophysiological experiments, where the underlying electrical membrane potential was measured [56].

One of the methods for estimating brain noise is based on frequency locking of the brain response to a periodically modulated stimulus [68]. As is known from the theory of coupled oscillators [69], the frequency locking occurs in a stochastic or chaotic system, which is acted upon by a periodic external force. Frequency locking can be either permanent or intermittent depending on both the strength of the external force and noise intensity. In the intermittency mode, the frequency-locking windows are interrupted by unlocking periods when the phase is slipped by $2\pi n$ radians ($n = \pm 1, \pm 2, \dots$). At the same time, in the frequency-locking regime, the oscillation phase is not completely locked, but fluctuates around the mean value due to noise. Therefore, the phase fluctuation amplitude is associated with internal brain noise. The stronger the noise, the larger the fluctuation amplitude.

The experimental procedure for assessing brain noise was as follows. A visual stimulus flickering with a frequency of $f_s = 6.67$ Hz was presented to the participants, and simultaneously their magnetoencephalograms (MEG) were being recorded. Since the flicker frequency is high enough to prevent the evoked neural activity from returning to a baseline state, the elicited response is continuous. In the case of MEG, this response is called *steady-state visual evoked field* (SSVEF). A typical SSVEF evaluated in the occipital cortex is presented in Fig. 8.8.

Spectral analysis shows (Fig. 8.9) that the largest SSVEF brain response occurs at the second harmonic of the flicker frequency, i.e. at $2f_s = 13.34$ Hz.

As known from the synchronization theory [70], noise in a system of coupled stochastic or chaotic oscillators results in their desynchronization, which can be detected from fluctuations of the phase difference of coupled variables. Since the strongest brain response is observed at the second harmonic of the flicker frequency, the phase difference is measured between SSVEF and the second harmonic of the stimulation signal as

$$\Phi = (t_n^b - t_n^s)2f_s, \quad (8.1)$$

where t_n^b and t_n^s are the positions in time of the n -th maxima of the brain response (SSVEF) and the second harmonic of the flicker signal, respectively.

Figure 8.10 shows intermittent phase locking of the SSVEF phase fluctuation Φ in units of periods (cycles) of the second harmonic of the flicker frequency. One can see that although the phase is locked for a certain time, there are phase slips on one or more cycles.

The SSVEF phase fluctuations within time windows where the phase is locked are used for statistical analysis. Examples of the probability distribution for two subjects are illustrated in Fig. 8.11.

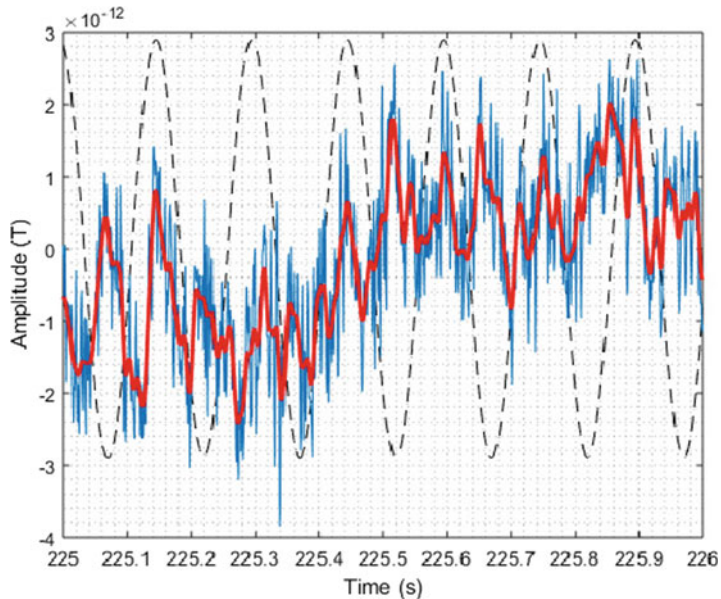


Fig. 8.8 SSVEF brain response to visual stimulation with 6.67 Hz frequency. The dashed line shows the signal at the flicker frequency. The red line is the averaged brain response in the occipital area

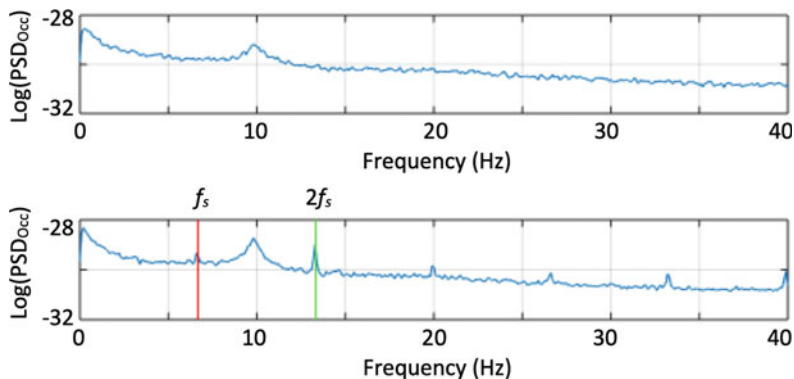


Fig. 8.9 Power spectrum density (PSD) of SSVEF for (upper) stationary (unmodulated) image and for (lower) image flicked at 6.67 Hz. The vertical red and green lines indicate tags at the flicker frequency f_s and its second harmonic $2f_s$, respectively

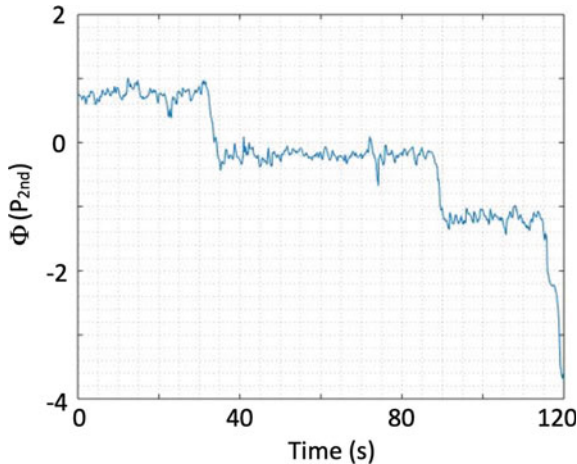


Fig. 8.10 Intermittent phase locking of brain response to the flickering image. The phase difference Φ fluctuates in time near a certain mean value within frequency-locking windows and sometimes drops one or more cycles

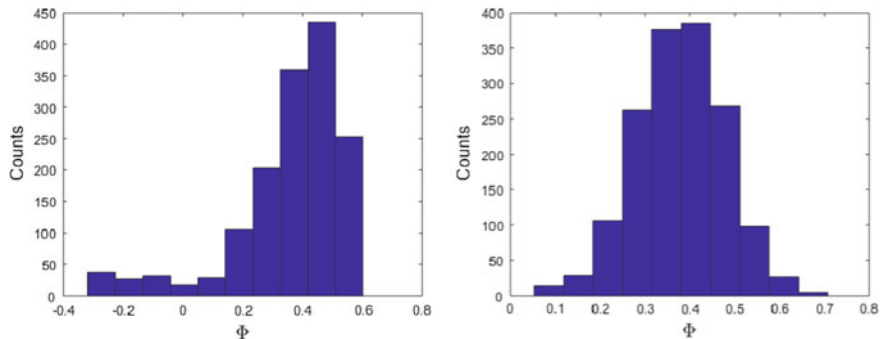


Fig. 8.11 Probability distributions of SSVEF phase fluctuations for two subjects exhibiting (left) weak and (right) strong brain noise

The sharpness of the distributions presented in Fig. 8.11 can be characterized by kurtosis defined as

$$K = \frac{E(\Phi - \langle \Phi \rangle)^4}{\sigma^4}, \quad (8.2)$$

where $\langle \Phi \rangle$ is the average phase difference, σ is the standard deviation, and E is the function of the expected value. The kurtosis for normal distribution is equal to 3.¹

It is assumed that brain noise leads to a widening of the phase probability distribution and, therefore, can be associated with an inverse kurtosis. This means that

¹ In some definitions of kurtosis, 3 is subtracted from the computed value in order to get a kurtosis value of 0 for normal distribution.

stronger noise is associated with a wider probability distribution and therefore with smaller kurtosis.

Thus, brain noise can experimentally be evaluated by measuring quasi-stationary fluctuations of the phase of brain response to flickering stimulation. The method is based on the assumption that the SSVEF phase fluctuation probability distribution depends on brain noise. We suppose that this type of noise is mainly associated with neural noise resulting from random neurophysiological activity of the neural network, while attentional noise leads to intermittent phase desynchronization. Since the neural network is unique for every person, assessing brain noise can be helpful in developing effective brain-computer interfaces that can be adapted to each individual according to his/her brain noise level.

8.2.2 Simple Energy Model

In attractor models, two different percepts of a bistable stimulus such as the Necker cube, are associated with two stable steady states (attractors). A change in the control parameter (for example, the contrast of the cube wires) leads to the deformation of their basins of attraction and, finally, to a change in their stability, which occurs at the critical point.

Let us first consider the simplest attractor model with third-order nonlinearity given by

$$\dot{x} = -4x(x^2 - 1) - 2c_A(x - 1) - 2c_B(x + 1) + \alpha\xi(t), \quad (8.3)$$

which exhibits the coexistence of two fixed points, i.e., this is a double-well potential model based on the assumption that each of the two neural populations (say, A and B) represents different interpretations (c_A and c_B) of the same ambiguous stimulus [62]. Here, x is a state variable proportional to the difference between the dimensionless firing rates of two competing neural populations, $\xi(t)$ is Gaussian white noise with zero mean and intensity α . Equation 8.3 is derived from the energy function $dE/dx = -\tau\dot{x}$, which describes the perception of the alternation dynamics, where the minima are located near $x = \pm 1$.

In the case of the Necker cube, $\tau = 1$ and c_A and c_B are associated to wire contrasts responsible for different interpretations of the cube orientation. If the contrasts of two cube frameworks change simultaneously in opposite directions (while one increases, the other decreases), then only one control parameter can be used $c = c_A = -c_B$, that simplifies Eq. 8.3 to

$$\dot{x} = -4x(x^2 - 1) + 4c + \alpha\xi(t). \quad (8.4)$$

The advantage of theoretical consideration over experimental one is that theoretically we can study the behavior of a noiseless bistable system ($\alpha = 0$), but in an experiment this is impossible, since the internal brain noise is not only inevitable, but also very strong, because instead of bistability we deal with metastability.

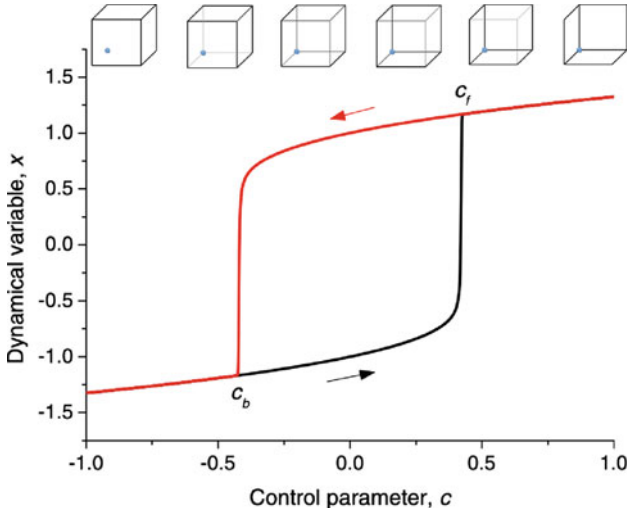


Fig. 8.12 Bifurcation diagram of a deterministic attractor model ($\alpha = 0$) showing hysteresis when the control parameter c is varied with velocity $v = 1$. The arrows indicate the directions of the control parameter change, and c_f and c_b are forward and backward saddle-node bifurcations, respectively. The upper panel shows the Necker cube images with different wire contrasts

Starting from a random initial condition, the system in Eq. 8.4 without noise ($\alpha = 0$) is attracted to one of the stable states and remains on it forever. If the control parameter linearly changes as $c = c_0 \pm vt$ with velocity v , the system passes through two saddle-node bifurcation points c_f and c_b forward and backward, as seen in the bifurcation diagram in Fig. 8.12.

The system state depends both on the initial conditions c_0 and the direction of the parameter change. A change in the control parameter c leads to the deformation of the energy potential and hence the volumes of the basins of attraction. This in turn leads to a change in the stability of fixed points that occurs at critical points c_f and c_b . For certain values of the parameter c , there is bistability which can be characterized by hysteresis $h = c_f - c_b$. Due to the critical slowing down, the position of the bifurcation points also depends on the velocity v , i.e. h becomes larger as v is increased. On the other hand, the hysteresis decreases and even disappears in the presence of noise, as illustrated in Fig. 8.13. One can see that for strong noise the hysteresis becomes negative $h < 0$, i.e. instead of hysteresis we deal with noise-induced two-state intermittency (see Sect. 5).

Based on the attractor model in Eq. 8.4, the following psychological experiment was performed [71]. The Necker cube with varied contrast of the inner wires was displayed on the computer monitor in front of a subject. The contrast was changed in two directions (first increasing and then decreasing). The participants were instructed to press a key on the computer keyboard the first time they distinguished a change in the cube orientation from left-oriented to right-oriented and vice versa. The difference

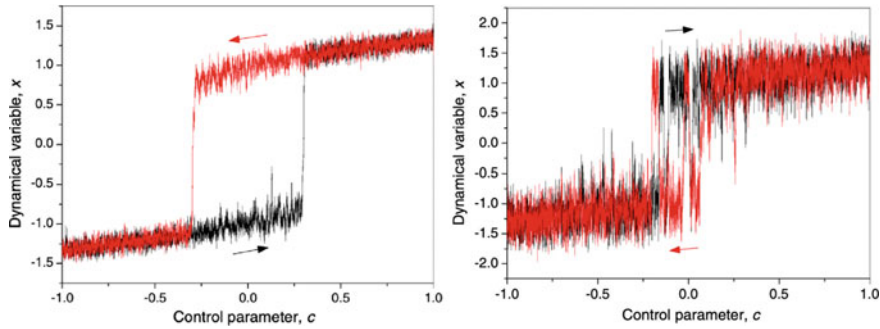


Fig. 8.13 Bifurcation diagrams of the attractor model in Eq. 8.4 demonstrating a change in the hysteresis value when the noise intensity increased from (left) $\alpha = 18$ to (right) $\alpha = 60$ at fixed velocity $v = 0.01$

between the times of the key pressing in the two directions was treated as the hysteresis, which depended on both the velocity of the contrast change and brain noise. Since the velocity was the same for all subjects, the difference in the hysteresis was only caused by the difference in their brain noise.

The experimental results confirmed the numerical results obtained with the energy model. In particular, the experimental evidence of negative hysteresis allowed us to conclude that brain noise is so strong that perceptual bistability does not exist. In a real situation, instead of bistability we deal with intermittent switching between two metastable perceptual states. Moreover, the experiments based on the attractor model allow a relative measurement of the brain noise level among different subjects.

8.2.3 Fokker–Plank Equation Attractor Model

We now consider a more complex attractor model based on the Fokker–Plank equation [67]. The main idea of this model implies that the alternation between two possible interpretations of an ambiguous stimulus indicates that the system is close to the cusp catastrophe [72] (see Sect. 1.4.5), in which absolutely all systems are described by the dimensionless potential energy function with two local minima $x_{l,r}$:

$$U(x) = \frac{a_4 x^4}{4} + \frac{a_3 x^3}{3} + \frac{a_2 x^2}{2} + a_1 x, \quad (8.5)$$

while the dimensionless firing rate x of the neuronal population can be given by

$$\dot{x} = -U'(x) + \xi(t), \quad (8.6)$$

where $\xi(t)$ is zero-mean δ -correlated Gaussian noise with $\langle \xi_n \rangle = 0$ and $\langle \xi_n \xi_m \rangle = D\delta(n - m)$ (D being the noise intensity).

It is assumed that the perception potential function $U(x)$ is individual for each person. In addition, it is not fixed and can change its shape from time to time depending on many factors, such as health, mood, tiredness, adaptability, etc. Therefore, the coefficients a_i ($i = 1, 2, 3, 4$) in Eq. 8.5 may vary from person to person.

Taking for definite the following parameter values $a_1 = b$, $a_2 = -1$, $a_3 = 0$, and $a_4 = 1$, Eq. 8.5 is simplified to [72]

$$U(x) = \frac{x^4}{4} - \frac{x^2}{2} + bx. \quad (8.7)$$

to be used in Eq. 8.6. For example, the perception of the Necker cube can be governed by the stochastic Eq. 8.6 with the potential function given by Eq. 8.7 with $b = \Delta I/\alpha$, where α is the scaling factor determined by individual features of the double-well potential function and $\Delta a = a - a_0$ is the deviation of the Necker cube parameter from the symmetric case $a = a_0$ (see Sect. 8.3.1 for detail). In the simplest case we can vary the intensity of different edges of the 2D outline of cube as shown in Fig. 8.21a, b).

Noise in Eq. 8.6 results in the stochastic differential equation

$$dX = -U'(x) dt + dW, \quad (8.8)$$

where $X(t)$ and $W(t)$ describe stochastic and one-dimensional Wiener processes, respectively. The probability density $\rho(x, t)$ of the stochastic process $X(t)$ can be modeled using the Fokker–Plank equation

$$\frac{\partial \rho_X(x, t)}{\partial t} = \frac{\partial}{\partial x} [U'(x)\rho_X(x, t)] + \frac{D}{2} \frac{\partial^2 \rho_X(x, t)}{\partial x^2}. \quad (8.9)$$

Since stationary probability density $\rho(x)$ being the solution of Eq. 8.9 is time independent, Eq. 8.9 can be reduced to the following ordinary differential equation

$$\frac{d}{dx} [U'(x)\rho(x)] + \frac{D}{2} \frac{d^2 \rho(x)}{dx^2} = 0, \quad (8.10)$$

which is equivalent to

$$\rho'(x) + \frac{2}{D} U'(x)\rho(x) - C = 0, \quad (8.11)$$

where C is an unknown constant.

To solve the inhomogeneous first-order ordinary differential Eq. 8.11 we first consider the homogeneous ordinary differential equation

$$\rho'(x) + \frac{2}{D} U'(x) \rho(x) = 0. \quad (8.12)$$

The solution of the inhomogeneous ordinary differential equation Eq. 8.11 is known to have the following form

$$\rho(x) = B(x) \exp\left(-\frac{2}{D} U(x)\right), \quad (8.13)$$

where B is a constant. Having substituted Eq. 8.13 for $\rho(x)$ in Eq. 8.11, we obtain the differential equation for the unknown function $B(x)$ as

$$B'(x) = C \exp\left(\frac{2}{D} U(x)\right), \quad (8.14)$$

whose solution can be found in the form

$$B(x) = C \int_0^x \exp\left(\frac{2}{D} U(z)\right) dz + A, \quad (8.15)$$

where A is a constant. Finally, from Eqs. 8.13 and 8.15 we obtain the general form of the stationary probability density $\rho(x)$ being the solution of the Fokker–Plank Eq. 8.9 as

$$\rho(x) = \exp\left(-\frac{2U(x)}{D}\right) \left[A + C \int_0^x \exp\left(\frac{2U(z)}{D}\right) dz \right]. \quad (8.16)$$

Having found the constant C from the extremum condition

$$\rho'(x_{l,r}) = C = 0, \quad (8.17)$$

we obtain the final form for the stationary probability density function as

$$\rho(x) = A \exp\left(-\frac{2U(x)}{D}\right), \quad (8.18)$$

where A is determined by the normalization condition

$$\int_{-\infty}^{+\infty} \rho(x) dx = 1. \quad (8.19)$$

In the case of a symmetric ambiguous stimulus, such as the Necker cube, the probability for the person to perceive one of two possible interpretations, for example,

left-cube orientation, can be found as

$$\hat{P}_l = \int_{-\infty}^0 \rho(x) dx, \quad (8.20)$$

where $\hat{P}_l = \hat{P}_l(\Delta I, \alpha, D)$ is determined by the parameters ΔI , α , and D . Fixing α and D and using ΔI as a control parameter, one can calculate the probability $\hat{P}_l(\Delta I, \alpha, D)$ to perceive the left-oriented cube and compare it with experimental data which, in turn, may also be considered as dependent on the deviation of the Necker cube parameter from the symmetrical case, that is $P_l = P_l(\Delta I)$.

Practically, the dependence (Eq. 8.20) of the probability of a subject to perceive the left-oriented image of the Necker cube on the parameter Δa of image bistability is, in fact, a psychometric function actively studied in psychophysics [73]. It is well-known that a psychometric function is an inferential psychometric model applied in detection and discrimination tasks. It reflects the relationship between a given feature of a physical stimulus. In our case of the Necker cube, this is the brightness of edges and forced-choice responses of a subject. In Sect. 8.3.1 we will consider how this theoretical approach can be applied to estimate the brain noise intensity of a subject under the Necker cube classification task.

8.2.4 Oscillatory Model

Another approach to model bistable perception is based on competition and self-inhibition of representative populations of neurons or engrams² [74–76]. This so-called *oscillatory models* were proposed to describe the random learning process where competition between perceptual neural populations takes place through reciprocal inhibition accompanied by slow adaptation of the dominant population. In particular, Huguet et al. [77] suggest that adaptation plays a crucial role in determining perceptual choice, while brain noise provides the randomness in switching between different engrams [78].

To be more specific, consider the Haken synergetic model [79], which consists of two mutually coupled subsystems given as

$$\dot{x}(t) = x [z - Ax^2 + g(x, y)], \quad (8.21)$$

$$\dot{z}(t) = \gamma (1 - z - x^2) + F(t), \quad (8.22)$$

$$\dot{y}(t) = y [\nu - Ay^2 - h(x, y)], \quad (8.23)$$

$$\dot{\nu}(t) = \gamma (1 - \nu - y^2) + F(t), \quad (8.24)$$

² An engram is a hypothetical memory trace or cognitive information that represents a particular stimulus.

where (x, z) and (y, ν) are state variables of two coupled subsystems, and functions g and h are described as

$$g(x, y) = -By^2 + 4(B - A)\alpha y^2 \left[1 - \frac{2y^4}{(x^2 + y^2)^2} \right], \quad (8.25)$$

$$h(x, y) = Bx^2 + 4(B - A)\alpha x^2 \left[1 - \frac{2x^4}{(x^2 + y^2)^2} \right]. \quad (8.26)$$

This model is a straightforward extension of a general algorithm for pattern recognition of ambiguous images and on the other hand, it reflects the saturation of attention. This oscillatory model was used to simulate visual perception of ambiguous images, such as the Necker cube. The pair of variables (x, y) is associated with perception of ambiguous patterns corresponding to two different cube orientations, while the other pair (z, ν) corresponds to saturation attention. The functions $g(x, y)$ and $h(x, y)$ describe asymmetric nonlinear mutual coupling in the corresponding subsystems. In the model, attention is subjected to a damping mechanism mimicking the effect of saturation and synaptic connections. Finally, α is a bias parameter which refers to the perception state preference and $F(t) = \nu\xi(t)$ is a random variable with amplitude ν and bounded at $\xi(t) \in [-1, 1]$.

Taking parameter values $A = 1.5$, $B = 2$, $\gamma = 0.1$ and using bias α as a control parameter, we construct the bifurcation diagram for the deterministic system ($F(t) = 0$), which is shown in Fig. 8.14.

As the bias parameter α is increased from 0 to 0.17, the system is in a periodic regime (region I). Then, a stable equilibrium (region III) arises at $\alpha \approx 0.17$. This attractor coexists with a periodic orbit (region II). When α is further increased, the periodic orbit disappears and only the stable equilibrium remains (region IV). The blue line represents the preferential attractor where only one percept is possible, obtained for initial conditions $x = 0$, $y = 0.6325$, $z = 1$, and $v = 0.6$ in the interval $0 < \alpha < 0.35$.

In the presence of noise, the dynamics becomes probabilistic. For $\alpha = 0.2$, weak noise with $\eta < 0.012$ does not induce intermittency in variables x and y , but only changes statistical properties of the system providing preference of one of dynamical regime over the others, as seen from the time series in Fig. 8.15a. In this case, x and y exhibit almost coherent behaviors rarely interrupted by disturbances during short time intervals. For stronger noise ($0.012 < \eta < 0.094$), intermittent switches between different regimes arise, as clearly seen in Fig. 8.15b.

During relatively large time windows, x takes zero (partial amplitude death), while y exhibits noisy oscillations around 0.6325 marked by a blue line in the bifurcation diagram in Fig. 8.14. In terms of perception, these intervals can be interpreted as preferential perception of one face of the Necker cube only. For stronger noise ($\eta < 0.12$), the duration of the dead states becomes larger as the noise intensity is increased (see Fig. 8.15c).

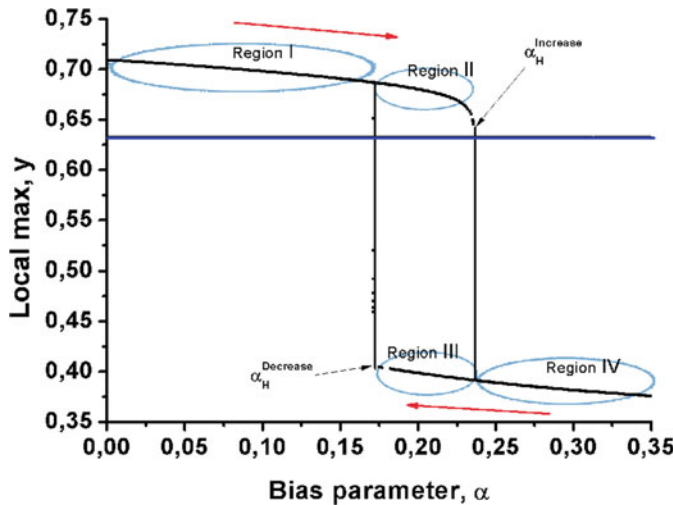


Fig. 8.14 Bifurcation diagram of local maxima of percept y as a function of bias parameter α . The red arrows indicate the direction of the control parameter change. Regions I-IV marked by blue ellipses represent different perception states, while the horizontal blue line shows the preferential state

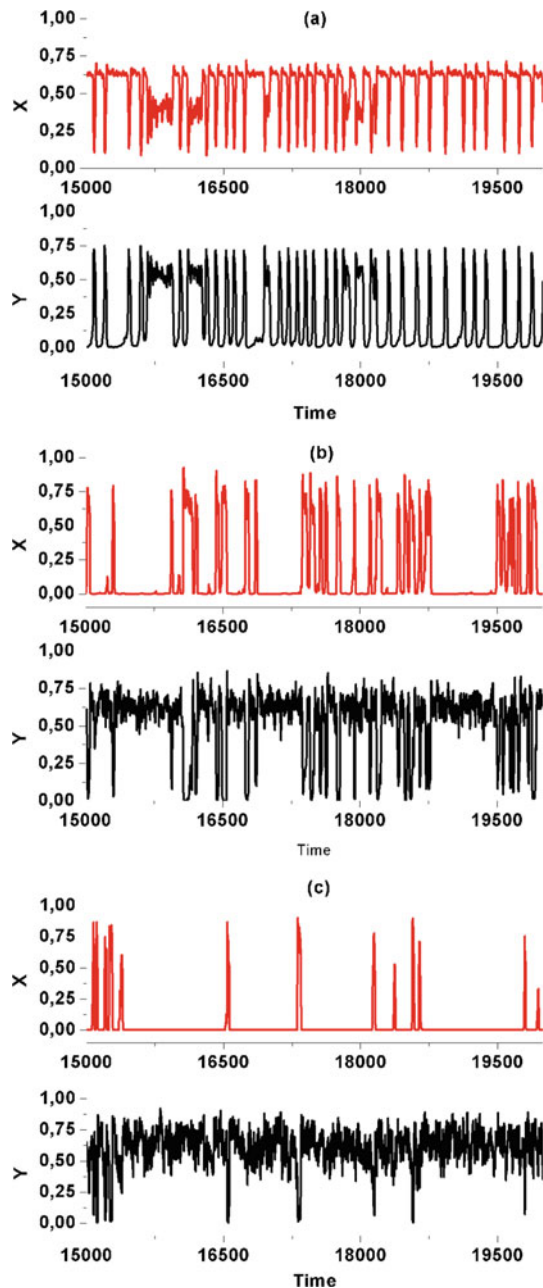
Thus, the oscillation demonstrates that additional noise can cause a preference for one of the states. When the noise amplitude exceeds a certain threshold, one of the perceptual states disappears at regular intervals, resulting in the interruption of perception. At the same time, the duration of one of the perceptions prevails over the other and increases together with the noise amplitude [80].

8.2.5 Advanced Perception Model with Adaptation and Noise

Bistable perception in general is determined by both adaptation and noise. Adaptation provides an innate tendency for the brain to eventually switch between two states of perception, destabilizing the current state. This deterministic mechanism is critical for switching between alternating perceptual decisions about comparable energy potentials and avoiding the first deep decision that might be encountered. At the same time, the stochastic mechanism allows the system to easily navigate the energy landscape, avoiding small energy holes that can be overcome solely with the help of noise.

The disadvantage of the pure attractor and pure oscillatory models is that they cannot simulate real experimental data such as histograms of rest times and correlations between the durations of consecutive engrams. However, a combination of these models makes it possible to measure the relative effects of noise and adaptation. Empirically defined arbitrary parameters, such as stimulus amplitude, noise

Fig. 8.15 Time series of x and y at $\alpha = 0.2$ for noise amplitudes **a** $\eta = 0.01$, **b** $\eta = 0.09$, and **c** $\eta = 0.1$. The windows of the preferential state at $x = 0$ and $y \approx 0.6$ intermittently appears and their duration increases as η is increased



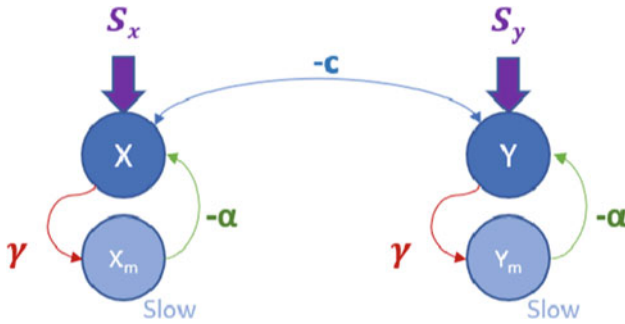


Fig. 8.16 Schematic illustration of the advanced perception adaptation model. X_m and Y_m are memory neuron states, inhibitory coupled with perceptual states X and Y , which in turn are inhibitory coupled with each other, α and γ are the corresponding coupling strengths, and h and h_m are the resting potential for perceptual states and working memory, respectively. The big arrows indicate the inputs of stimuli S_x and S_y

intensity, and strength of mutual inhibition and adaptation, are significant in relation to each other, and the qualitative behavior of perception in the context of the model, in turn, reflects the real cognitive process.

Therefore, a good perception model should take into account the following processes.

- **Self-stabilization:** The ability to maintain stable perception in the presence of random fluctuations of physiological variables (endogenous noise), such as body temperature, blood pressure, spontaneous neuronal activity, all of which result in physiological tremor.
- **Competitive inhibition:** A person is capable to interpret an ambiguous stimulus in only one of the possible ways at a time, and can never make two interpretations simultaneously, so the other solutions are suppressed. The neuron fires only if the input signal is sufficiently strong (otherwise, the neuron is silent), therefore a sigmoidal function $\sigma(X) = 1/(1 + e^{-\beta X})$ is used to model synaptic connections for competitive inhibition.
- **Adaptation:** Self-destabilization or involuntary transitions between perceptual states X and Y from memory states X_m and Y_m which are also self-destabilized. A sigmoidal function is also used to capture the memory effect on the perceptual state.

Keeping in mind the above requirements, the model is schematically illustrated in Fig. 8.16 and given by the following equations [81].

$$\tau \dot{X} = S_x + h - X - c\sigma(Y) - \alpha\sigma(X_m) + \eta\xi_X(t), \quad (8.27a)$$

$$\tau_m \dot{X}_m = h_m - X_m + \gamma\sigma(X) + \eta_m\xi_{X_m}(t), \quad (8.27b)$$

$$\tau \dot{Y} = S_y + h - Y - c\sigma(X) - \alpha\sigma(Y_m) + \eta\xi_Y(t), \quad (8.27c)$$

$$\tau_m \dot{Y}_m = h_m - Y_m + \gamma\sigma(Y) + \eta_m\xi_{Y_m}(t), \quad (8.27d)$$

where X and Y are perceptual neuronal states, X_m and Y_m are memory states, S_X and S_Y are input signals, α is a coefficient related to the adaptation strength, γ is the strength of memory which determines how much the choice of the current state affects memory, τ and τ_m are time-scaling coefficients, h and h_m are resting potentials for perceptual states and working memory, respectively, without external stimulation, and c is a competitiveness coefficient which represents the strength of suppression the winner state has on the losing state. The competitiveness coefficients for both perceptual states are taken to be the same because any state can win the competition initially and suppress the losing neuron with equal strength. The ratio between S_X and S_Y is determined by the stimulus ambiguity. When the stimulus is completely ambiguous (as the bistable Necker cube), we deal with an unbiased signal, i.e. $S_X = S_Y$.

Endogenous brain noise is added to the perception and memory variables as independent zero-mean Gaussian noise ξ of intensities η and $\eta_m = \sqrt{\tau/\tau_m}\eta$, respectively. The probability density function of a random variable z is determined by the expression

$$p(z) = \frac{1}{\sigma\sqrt{2\pi}} \exp\left[-\frac{(z-\mu)^2}{2\sigma^2}\right], \quad (8.28)$$

where $\mu = 0$ is the mean and $\sigma = 1$ is the standard deviation. Since the same set of perceiving neurons is involved in processing both input signals, the time constant remains the same for both states.

Noise-induced drifts along the path of the activation variable affect the relative values of X and Y , which in turn determine the amount of competitive inhibition between the two perceptual states. This results in early or late switching between these states, deterministically induced by adaptation. Thus, the trajectory alternates randomly between two perceptual states, as shown in Fig. 8.17.

The recognition of the moments of switching between two noisy states is not a trivial task. Among different criteria to do this, a 3η test gives very good statistical results. This criterion states that a switch is recognized when the difference between X and Y crosses a threshold defined as $|X - Y| = 3\eta$. When noise is very strong, it is difficult or even impossible to recognize the moments of switching (lower panel in Fig. 8.17).

The stochastic dynamics of the bistable perception can be characterized by the following measures.

- Number of switches between perceptual states X and Y versus noise intensity.
- Probability distribution of residence times in each state.
- Mean residence time versus noise intensity.
- Correlation time versus noise intensity.

The number of switches as a function of the noise intensity is present in Fig. 8.18. One can see that it can be well fitted by a linear dependence for relatively strong noise ($\eta > 0.3$).

Another important characteristic is the residence time, i.e. the time that the system spends in one of the perceptual states. The notion of residence times was introduced in

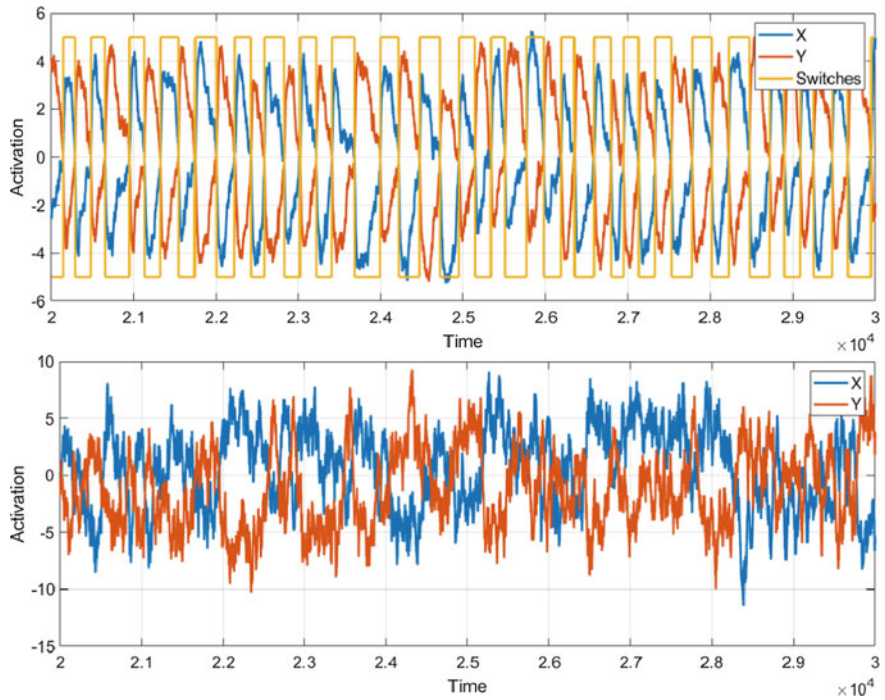
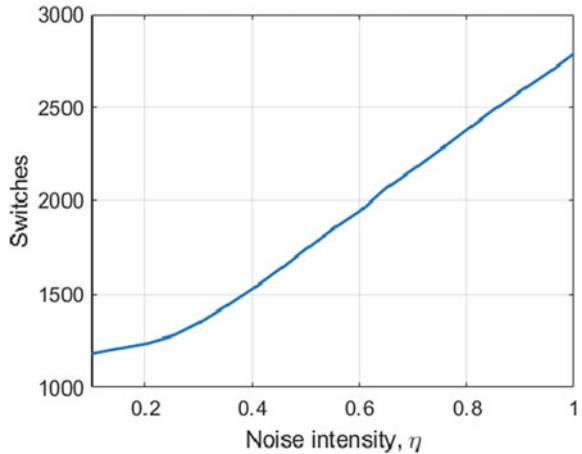


Fig. 8.17 Time series of activation ($X - Y$) at noise intensities (upper) $\eta = 0.1$ and (lower) $\eta = 0.5$. The rectangular line shows switching between two states recognized with a 3η criterion

Fig. 8.18 Number of switches versus noise intensity



Sect. 5.3.1. Given that we recognize time instants corresponding to perceptual switchings using the 3η -criterion discussed above, the intervals between these switches indicate the time the system spends in each perceptual state, as shown in Fig. 8.17.

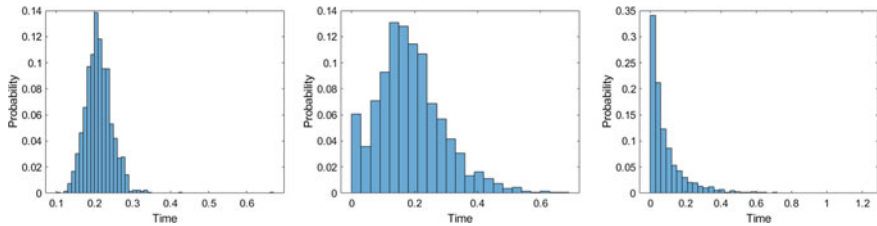


Fig. 8.19 Probability distributions of residence times for noise intensities (left) $\eta = 0.1$, (middle) $\eta = 0.3$, and (right) $\eta = 1$

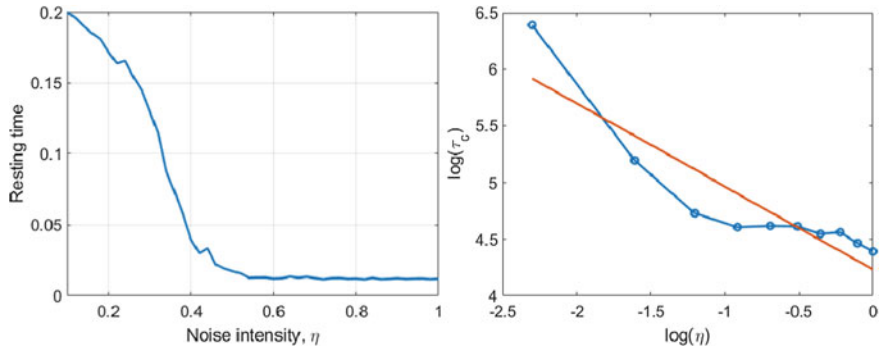


Fig. 8.20 (Left) Mode residence time versus noise intensity. (Right) Correlation time versus noise intensity. The straight red line is a power-law approximation with a -0.73 scaling exponent

When the system resides in the positive area (i.e. $X > Y$), the X -state is dominant, otherwise the Y -state dominates.

Figure 8.19 shows the probability distributions of residence times for three different values of the noise intensity. When noise is weak, the distribution is almost Gaussian (left panel in Fig. 8.19), whereas for intermediate values of the noise intensity the distribution is close to a gamma distribution (middle panel in Fig. 8.19) which is typical for biological systems. Finally, for strong noise the distribution is exponential (right panel in Fig. 8.19).

The simulations also show that the most probable (mode) residence time decreases as the noise intensity is increased. Such a behavior is illustrated in the left panel in Fig. 8.20. This result is in a good agreement with experiments on bistable perception [82, 83].

Finally, stochastic dynamics can also be characterized by coherence (see Sect. 5.2) as a measure of order using correlation time defined as

$$\tau_c = \int_0^\infty C^2(t) dt, \quad (8.29)$$

where C is the normalized autocorrelation function given as

$$C(\tau) = \frac{\langle (X(t) - \langle X(t) \rangle)(X(t + \tau) - \langle X(t) \rangle) \rangle}{\langle (X(t) - \langle X(t) \rangle)^2 \rangle}, \quad (8.30)$$

where $\langle \dots \rangle$ means averaging and τ is the lag time. The larger the correlation time τ_c , the higher the coherence.

The correlation time Eq. 8.29 versus noise intensity well characterizes the random switching between the perceptual states with an approximately $-3/4$ scaling exponent, as shown in the right panel of Fig. 8.20.

In experiments on bistable perception, Meilikhov et al. [64] found that brain noise provides only 15–40% of the energy gap among the participants of the experiment described in Sect. 8.2.2 [71]. This is an additional argument in favour of the advanced model showing that the adaptation effect prevails over the effect of noise.

Thus, the advanced perception model combines the activity of all neurons representing a feature in each hemisphere and neglects spatial variations across the surface. Despite a rough approximation, this model is suitable for qualitative modeling of many neurophysiological experiments. For example, the most popular neuroimaging technique, electroencephalography (EEG), often records the activity of neurons in the visual cortex of both hemispheres using only two channels (O_1 and O_2) in the simplest settings. Other techniques, such as magnetoencephalography (MEG) and functional magnetic resonance imaging (fMRI), do not have very high spatial resolution either.

8.3 Physiological Experiments with Ambiguous Stimuli

8.3.1 Behavioral Experiment with Ambiguous Stimuli for Brain Noise Estimation

The bistable perception mathematical model described in the previous section can be used for measuring brain noise intensity related to the perception of ambiguous bistable images. For this measurement, Runnova et al. [67] proposed an experimental technique based on the peculiarities of a person's activity related to the interpretation of ambiguous images. Let us consider this psychophysical approach.

The main idea of the experiment was to present bistable images with varying degrees of ambiguity to the subject. Obviously, images with a weak degree of ambiguity will be interpreted almost always in the same way. On the other hand, bistable images with a high degree of ambiguity will be interpreted in either of the two possible ways with approximately equal probability. We can measure the experimental psychometric curve by presenting the subject with many images with varying degrees

of ambiguity and measuring the probability of choosing either interpretation of the bistable image.

In the behavioral experiments with the Necker cube [67], non-perceptually impaired volunteers interpreted this two-dimensional (2D) image as a three-dimensional (3D) object oriented either left or right. The balance between the brightness of the three inner lines (1, 2, 3) located in the left bottom corner and the three inner lines (4, 5, 6) in the right upper corner determines the ambiguity and orientation of the 3D cube (Fig. 8.21a). The contrast parameter $a \in [0, 1]$ is the normalized brightness of the inner lines (1, 2, 3) in the greyscale palette. In turn, the normalized brightness of the other inner lines (4, 5, 6) is defined as $1 - a$. Thus, the limiting cases $a = 0$ and $a = 1$ correspond to unambiguous 2D projections of the cube oriented to the left or to the right, respectively, whereas $a = 0.5$ implies a completely ambiguous spatial orientation of the 3D cube.

During the experiment $N = 16$ Necker cube images with different frame contrasts, i.e. with different values of the contrast parameter a (Fig. 8.21b), were repeatedly presented to a subject in a random sequence. The Necker cubes (22.55×22.55 cm) were shown on a white background using a 24" monitor (52.1×29.3 cm) with a 1920×1080 pixels resolution and a 60-Hz refresh rate. The distance between the participant and the monitor was 0.79–0.8 m, and the visual angle was approximately 0.39 rad.

The mean duration of a visual percept is known to vary from one second to several minutes depending on each observer and the stimulus conditions (see, for example, [84]), whereas the mean response times are rather consistent and vary only by a few hundred milliseconds (see, for example, [85]). At the same time, the most common experimental length for each percept of the Necker cube was found to be approximately 1 s [83]. Therefore, to fix the first impression of the person and avoid switches between two possible percepts the image exhibition was limited to $\tau \approx 0.5\text{--}0.7$ s. Between subsequent demonstrations of different Necker cube images other abstract pictures were exhibited for about $\gamma \approx 1.5\text{--}2.0$ s to draw away the observer's attention and make the perception of the next Necker cube image independent of the previous one. A schematic representation of the experimental paradigm is given in Fig. 8.21c.

All participants were well aware of the two possible orientations of the Necker cube, and both orientations were seen by all of them. The subjects were also instructed to press either the left or the right key on the control panel according to their first visual impression (left-oriented cube or right-oriented cube) as shown in a detailed illustration of a single stimulus presentation (Fig. 8.21d).

For each value a_j of the contrast parameter a the probability $P_l(a_j)$ of the left-oriented cube (the left key choice) was calculated as

$$P_l(a_j) = \frac{l(a_j)}{l(a_j) + r(a_j)}, \quad (8.31)$$

where $l(a_j)$ and $r(a_j)$ are the numbers of clicks on the left and right keys, respectively, for the j -th Necker cube with the value a_j of the contrast parameter.

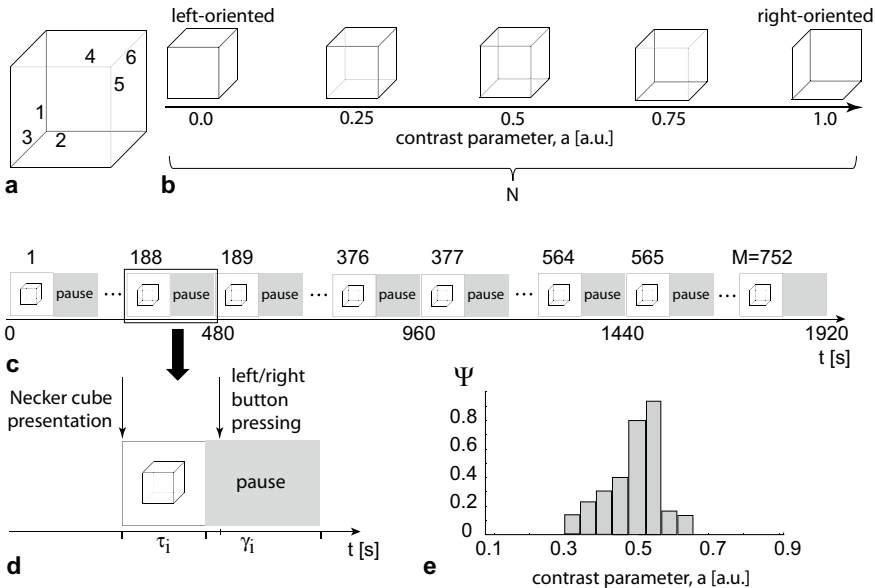


Fig. 8.21 Experimental paradigm for psychometric curve measurement: **a** An example of the Necker cube image with the labeled inner edges. **b** Visual stimuli (Necker cubes) with different values of the contrast parameter a , which determines orientation and ambiguity. **c** Experimental protocol including the presentation of 400 stimuli alternating with pauses. The total length of the experiment is 32 min in which Necker cube images are presented $M = 752$ times to the subject, with each of the $N = 16$ Necker cubes (with the fixed contrast parameter a_j) being shown exactly $K = 47$ times. **d** Detailed illustration of a single stimulus presentation. During the pause an abstract picture was demonstrated. The cube presentation starts at the presentation time and lasts $\tau_i \in [0.5, 0.7]$ s. The pause time γ_i varies from 1.5 to 2 s. **e** Typical level of uncertainty (8.44) in the Necker cube interpretation by a subject

To estimate brain noise intensity we can compare theoretical prediction (Eq. 8.20) with experimental dependence (Eq. 8.31). The values of α and D in Eq. 8.20 can be found using the least square technique [86] for the minimum error value

$$E(\alpha, D) = \sum_{j=1}^N \left[P_l(\Delta a_j) - \hat{P}_l(\Delta a_j, \alpha, D) \right]^2. \quad (8.32)$$

A typical surface of the error E in the (α, D) parameter space, calculated with the least square method, is shown in Fig. 8.22a for a single subject. Figure 8.22b represents the contour plot corresponding to this surface.

The minimal error E_{\min} corresponds to the best coincidence of theoretical and experimental results. This curve found empirically can be approximated by

$$\alpha D = D_p = \text{const.} \quad (8.33)$$

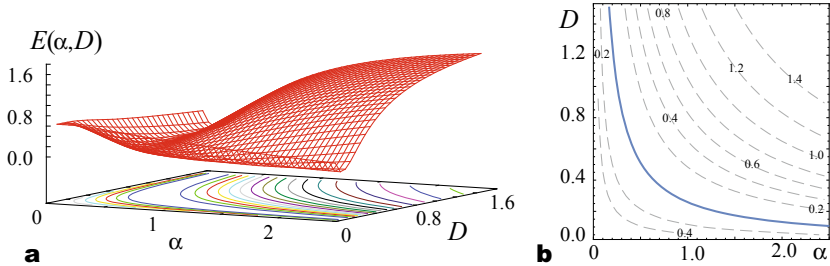


Fig. 8.22 **a** Error surface $E(\alpha, D)$ calculated using the least square method and **b** contour plot corresponding to this surface. The bold solid curve $\alpha D = D_p = 0.31$ represents the minimum error $E_{\min} = 0.026$

Table 8.1 The values of the noise intensity D_p measured experimentally and the minimum error E_{\min} characterizing the deviation of the experimentally obtained P_l from the theoretical predicted \hat{P}_l for twenty subjects

#	D_p	E_{\min}	#	D_p	E_{\min}	#	D_p	E_{\min}
1	0.310	0.026	8	0.205	0.085	15	0.370	0.021
2	0.175	0.021	9	0.925	0.027	16	0.245	0.024
3	0.250	0.024	10	0.085	0.003	17	0.250	0.034
4	0.245	0.056	11	0.300	0.035	18	0.155	0.041
5	0.445	0.075	12	0.240	0.053	19	0.745	0.060
6	0.310	0.076	13	0.255	0.010	20	0.455	0.093
7	0.195	0.049	14	0.175	0.035		Mean	0.317
								0.042

Noticeably, exactly the same regularity was observed for absolutely all subjects in the experiments [67].

In other words, the parameter D_p is actually a universal invariant that ensures the minimum E_{\min} of the error value surface $E(\alpha, D)$. Accordingly, the value of D_p can be interpreted as the intensity of the effective noise associated with the individual double-well potential function $U(x)$ in Eq. 8.7. Most importantly, although it is impossible to find quantitative characteristics of $U(x)$, it is possible to accurately measure the intensity D_p of noise involved in bistable visual perception. This effective noise intensity D_p can easily be detected from experimental data using the least square method and should be considered as closely related to the individual characteristics of bistable human perception.

On the base of the model described above, perceptual noise intensity was experimentally estimated using the Necker cube images [67]. The results of the experimental studies are illustrated in Fig. 8.23 and summarized in Table 8.1, where the subject number, the obtained value of effective noise intensity D_p , and the minimum error E_{\min} for Eq. 8.32 are given. It should be noted that an excellent agreement of the theoretical prediction with the experimentally obtained data is observed.

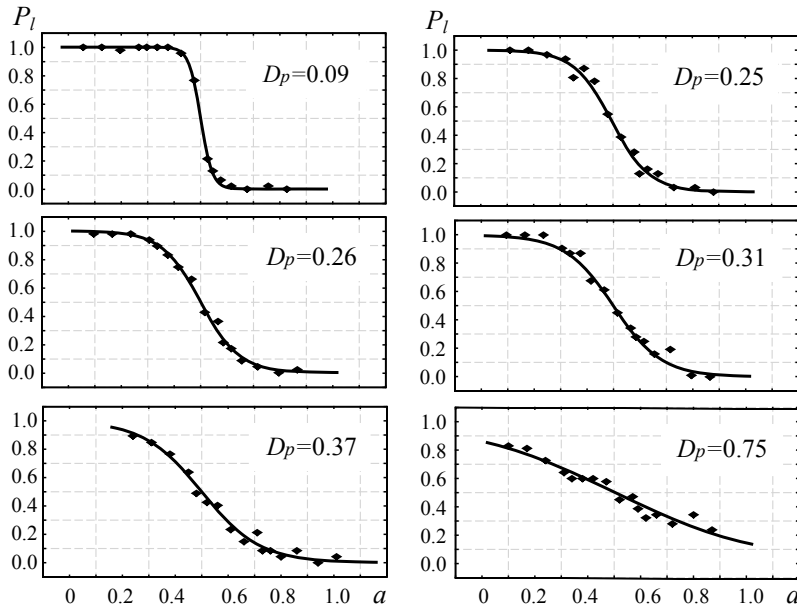


Fig. 8.23 Experimentally measured dependencies of the probability to perceive the left-oriented image of the Necker cube $P_l(a)$ on the contrasts parameter a obtained for six typical subjects (dots) and their corresponding theoretical approximations $\hat{P}_l(a)$ shown by the solid lines. The values of the effective noise intensity D_p related to the individual bistable perception energy function are determined with the help of the least square technique. All panels are ordered by increasing effective noise intensity D_p

This fact can be considered as irrefutable proof of the correctness of the proposed approach aimed at quantitatively characterizing the brain noise associated with the visual perception of ambiguous images. Revealed regularity Eq. 8.33 is extremely important in terms of understanding brain function and measuring brain noise intensity. The empirical nature of this regularity equation in no way diminishes the discovery value, because absolutely all theories accepted today (whether in astronomy, physics, biology or elsewhere) are based on previous empirical observations. It is noteworthy that the studied type of brain activity can be quantitatively characterized by the effective noise intensity D_p , despite the individual characteristics of the human perception mechanism and the lack of information about the numerical parameters responsible for visual stimuli recognition.

8.3.2 EEG Experiments

In the previous section, we discussed a method for estimating brain noise by measuring a psychometric curve in a simple psychological experiment. Much more information about brain dynamics can be obtained by analyzing not only behavioral characteristics but also brain activity using various neuroimaging techniques. Neurophysiologists have accumulated extensive experience in studying visual perception of bistable images and analyzing brain activity in the course of such experiments. The works of the Kornmeier and Bach groups on the study of activity of brain processing of images such as Necker cubes and Necker cube lattices are worthy of mention [87–89].

The use of not one, but a combination of several Necker cubes was motivated by the hypothesis, based on texture-segregation experiments [90], that a stronger brain response measured by event related potential (ERP) amplitude could be obtained by combining several Necker cubes into a “Necker lattice” [87]. There are a number of papers on EEG studies and other bistable imaging, including Boring’s old/young female stimulus [91], ambiguous stimuli in the Rorschach cards [92], series of inkblots [93], etc. Here we will briefly discuss the experimental paradigms of Necker cube research using electrophysiological measurements.

Obviously, the experimental paradigm depends on the hypothesis that the corresponding experiment is designed to verify. One of the important questions that recent research on bistable images with varying degrees of ambiguity has focused on is the question of how the brain adapts to the need to classify images with high and low degrees of ambiguity during prolonged cognitive load. In this case, the experimental paradigm is based on the experiment described in the previous section. However, unlike the brain noise experiment, where subjects were asked to classify their first impression on the orientation of a cube, in this experiment subjects were asked to evaluate a bistable image to correctly classify the cube orientation based on the contrast of the inner edges 1–2–3 and 4–5–6 (see Fig. 8.21a). During the classification task the EEG signals were recorded using the monopolar registration method and the 10–10 electrode scheme [94] that corresponds to 31 signals with two reference electrodes, A1 and A2, on the earlobes and a ground electrode N just above the forehead.

As in the previous case, the whole experiment lasted 40 minutes, including 150-second recordings of the resting-state EEG before and after the main part of the session. During the main part, 400 Necker cube images with predefined values for the degree of ambiguity a are presented in a random order. We used Necker cube images with eight different values of the control parameter (Fig. 8.21b). Half of them ($a = \{0.15, 0.25, 0.4, 0.45\}$) were considered left-oriented and another half ($a = \{0.55, 0.6, 0.75, 0.85\}$) were right-oriented. Each stimulus with a particular ambiguity was presented 50 times. The i -th stimulus was presented during a time interval τ_i , followed by abstract image presentation for a time interval of γ_i (Fig. 8.21d).

The participants were instructed to identify stimulus orientation as accurately as possible. Subjects reported their decisions by pressing either the left (for a left orientation) or the right (for a right orientation) key with their left or right hand, respectively. The duration of the stimulus exhibition varied in the range of 1–1.5 s. We also applied random variation in the stimulus ambiguity. Lastly, to draw away the observer's attention and make the perception of the next stimulus independent of the previous one, different abstract pictures were exhibited for 3–5 s between subsequent demonstrations of the Necker cube images. For each stimulus, the behavioral response by measuring the response time (RT) as the time interval between the stimulus onset and key pressing (time interval between two arrows in Fig. 8.21d) was estimated.

In the described experimental design, all participants were instructed to press either the left or the right key on the two-button keypad by the left or right hand according to their first visual impression on the cube orientation (left-oriented or right-oriented), as shown in Fig. 8.21d. However, if further classification of bistable brain states corresponding to the perception of left or right cube orientation is necessary, the fact of motor reaction can lead to a false classification of brain activity corresponding to left- or right-handed motor acts. As a consequence, other experimental designs were developed. In the first design to further classify bistable brain state in order to exclude the effect of motor reaction after the image presentation, the experimenter asked the participant to interpret the cube orientation as either "left" or "right" and then voice her/his interpretation [95]. The disadvantage of such an experiment is a significant load on the experimenter, who has to interactively participate in the experiment, as well as the increasing duration of the measurement.

To automatize the experimental procedure, the following second experimental design was proposed [96]. Before the experiment, every subject was instructed on how they should indicate their decision on the cube's orientation. There were two possible ways to do this. In the first series of experiments, they had to press either the left or the right key on the control panel according to their first visual impression for an uncertainty level determination (see details in Sect. 8.4.2, Eq. 8.44, and Fig. 8.21e), whereas in the second series, they had to answer one of the two following questions randomly appearing on the screen:

- (1) Do you interpret this cube as left-oriented? If YES, then press the right key, otherwise press the left key.
- (2) Do you interpret the cube as right-oriented? If YES, then press the right key, otherwise press the left key.

The right key was associated with a positive answer, while the left key with a negative answer. Thus, the subject did not know in advance which key (left or right) he/she will press until the question (1) or (2) appears on the screen. This fact made his/her reaction independent of the imaginary movement associated with the preparation to press either left or right key during perception.

The results described in Sect. 8.4.1 are obtained using the first experimental design. The classification algorithm was optimized using a classifier based on the machine learning [96]. The authors reconstructed functional brain networks on the

base of the results of the experimental study using the second design described here. The developed classifier allows the classification of single EEG traces related to different interpretations of the Necker cube images. The classification algorithm was optimized by reducing 90% of the number of analyzed EEG channels. The analysis of a 25-subject group revealed that the highest accuracy (up to 95%) was reached using only two EEG channels for particular sets of EEG channels, namely, for a pair of occipital channels (O1 and O2), and a pair of channels in the parietal and central lobe (Cz and Pz). The significance of such channel combinations is explained by the differences in the structure of brain neuronal network interactions corresponding to different interpretations of the bistable Necker cube.

To detect the functional brain network during bistable image interpretation, the source-level synchronization improvement was measured, and a strong interaction between EEG channels in the occipital lobe after the Necker cube presentation and a further interpretation of its orientation as left- or right-oriented was detected. Analyzing the strength of interaction between occipital EEG channels for the typical frequency bands (delta, theta, alpha, beta, and gamma.) showed that the pair of channels Cz and Pz demonstrated the strongest connections in the delta-, theta-, alpha-, and gamma-ranges, and the pair of channels O1 and O2 only in the delta-range.

The set and configuration of the connections were significantly different in the case of left- and right-oriented Necker cube interpretations. The left-oriented cube perception was characterized by connections with the channels Cz and C4 in the right hemisphere in all frequency bands. The right-oriented cube interpretation led to the formation of a connection between the pair of channels Pz and P3 in the left hemisphere. The trained classifier employs features of the EEG signals typical for different cube interpretations and well-pronounced for the most significant pairs of channels (O1, O2) and (Cz, Pz) from the viewpoint of brain connectivity during the Necker cube visual perception.

Other experiments were related to the investigation of the perceptual decision-making process related to the interpretation of the bistable Necker cube image. The degree of ambiguity a indicates how difficult it is to determine a correct cube orientation. While for $a \approx 1$ and $a \approx 0$ the Necker cubes can easily be classified as a left- or right-oriented, for $a \approx 0.5$ the classification task is more complex since we deal with a highly ambiguous image. We can divide conventionally the set of all cubes into two subsets: $a = \{0.4, 0.45, 0.55, 0.6\}$ (high-ambiguous images) and $a = \{0.15, 0.25, 0.75, 0.85\}$ (low-ambiguous images). It is clear that the classification of the cubes belonging to the former subset is a simpler task and therefore it is considered a low-complexity (LC) task, whereas the classification of the cubes from the latter subset requires a higher cognitive effort and hence it is referred to as a high-complexity (HC) task.

In a series of papers [26, 97–100], a study of these questions was conducted under conditions of prolonged exposure of the subject to the task, which was to correctly classify Necker cubes with different degrees of ambiguity a . It should be noted that in this case we always have a correct interpretation of the presented image, because a completely symmetric cube with $a = 0.5$ is not used as visual stimulus here.

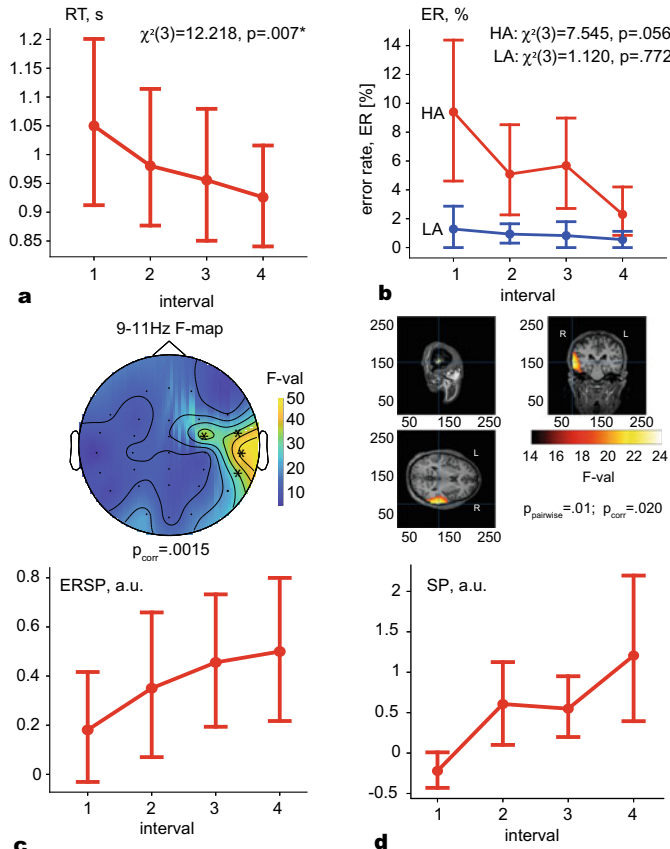


Fig. 8.24 **a, b** Results of the behavioral data analysis: median RT (group mean $\pm 95\%$ CI) on four intervals (* $p = 0.007$ via Friedman test, uncorrected) and percentage of ER to the HA and LA stimuli (* $p = 0.001$ via Wilcoxon test, uncorrected), respectively. **c** Results of the EEG analysis on the sensor level: (top) a scalp topogram illustrates F-value and EEG channels cluster, demonstrating the significant change of ERSP between four intervals (* $p = 0.0015$ via F-test and cluster-based correction for multiple comparisons) and (bottom) changing ERSP in this cluster with the time with the interval number. **d** Results of the EEG data analysis in the source space: (top) source plot shows F-value, reflecting the significant change of the SP between four intervals on the prestimulus interval (F-test, permutation-based correction); (bottom) SP in this cluster on four intervals

Some of the results of these studies are shown in Fig. 8.24. It is worth noting that the presented data is based on the comparison of EEG power and behavioral estimates between four time segments, each of which lasted 10 min with a 40 min total experiment duration. Therefore, we have associated the described effects with slow changes that lasted 10 minutes. By observing behavioral responses in Fig. 8.24a, we found that RT decreased with time spent on the task for both HA and LA stimuli.

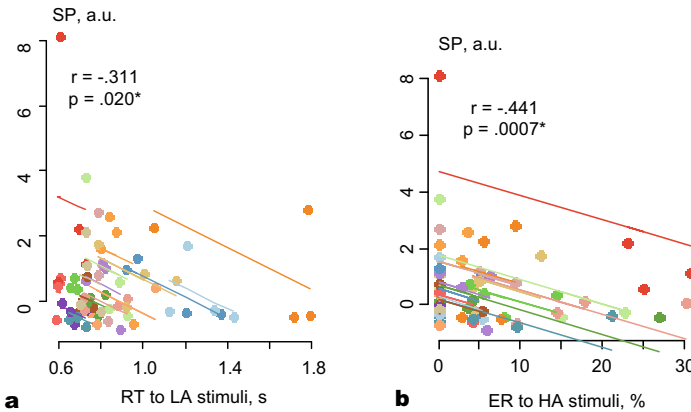


Fig. 8.25 Results of the correlation analysis: **a** regression plots illustrate the relationship between SP and RT to LA stimuli; **b** SP and ER for HA stimuli. The colored dots correspond to each participant's data; the lines have the same slope estimated for these participants via correlation analysis with repeated measures

At the same time, the subjects improved the correctness of the interpretation of the HA stimuli, but not the LA stimuli (see Fig. 8.24b).

The interpretation correctness is monitored using error rate (ER) by comparing the actual stimulus orientation with the subject's response. We can suggest that the prestimulus EEG power reflects changes in a person's condition. The condition, in turn, affected the performance of processing the ongoing visual stimulus. To prove this hypothesis, the prestimulus EEG power will be calculated as both the event-related spectral perturbation (ERSP) on sensor-level and the power SP of brain activity source on source level. In the last case a low-resolution precision electromagnetic brain tomography (eLORETA) is used to solve the inverse problem and localize the sources of neuronal activity according to EEG data at each of the predetermined points (voxels) in the brain volume. As a result, you can see in Fig. 8.24c, d, the high prestimulus (9–11 Hz EEG power predicted faster decision times and greater accuracy. At the same time, the prestimulus EEG power negatively correlated with the decision time to LA stimuli (Fig. 8.25a) and the number of erroneous responses to HA (Fig. 8.25b) stimuli.

The RT decreases due to neural adaptation (NA) which occurs when the same visual stimulus is repeatedly presented within a short interval and causes a decrease in neural response to repetitive versus non-repeated stimulus [101]. The NA is thought to arise from at least two types of neural activity. One explanation is that only the part belonging to the neuronal ensemble is sensitive to stimulus recognition. Thus, the neurons that are not critical for stimulus recognition decrease their responses when the stimulus reappears, while on the contrary, neuronal populations carrying essential information continue to give a robust response. As a result, the mean firing rate decreases due to stimulus repetition [102].

An alternative explanation is that stimulus repetition reduces response in the time domain [101]. According to this theory, a neural network that processes sensory information responds faster to a repetitive stimulus than to a new stimulus, i.e. a stable response. The network connections involved in the response creation were reinforced by the previous presentation of the same stimulus [103]. An increase in the prestimulus EEG power (Fig. 8.24) reflects the preactivation of sensory neurons, and the neural ensemble exhibits less activation in response to the stimulus in this preparatory state.

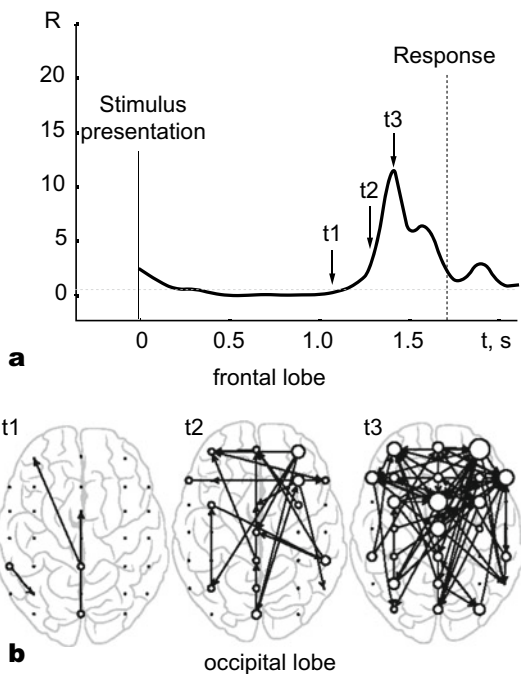
Simultaneously, an increase in the (9–11) Hz band power correlates with enhancing processing performance. It should be noted that the role of alpha-band oscillations depends largely on their incident brain region. For example, right temporal alpha oscillations play a crucial role in inhibiting habitual thinking modes, thereby developing creative cognition [104]. The authors of Ref. [105] show that observing a Necker cube can improve subsequent creative problem-solving. According to these works, the increasing (9–11) Hz power in the right temporal region results in a developing ability to inhibit obvious associations. The latter may be a biomarker of neural processes facilitating creative problem-solving.

Taken into account the above-described results, there is a possibility to propose an application of the findings in passive brain-computer interfaces to monitor human condition and predict decision speed and errors for the visual multistable decision-making tasks [106, 107]. The first step on this road is illustrated in Sect. 8.5, where we discuss the results of development of brain-computer interfaces based on bistable perception. In the future, we can expect to see neurointerfaces that could not only monitor human conditions during a routine task, but also correct them, taking into account relevant brain activity biomarkers of interpretation error detected during the perception of the Necker cube.

Simultaneously with the previously discussed formation of a pre-activated zone in the brain cortex during the perception of a bistable image, a reconfiguration of brain functional networks and involvement of additional brain regions is observed as a result of integration of sensory processing with other cognitive processes, primarily with decision-making [26]. Thus, visual stimulus processing begins with synchronization of neural activity between the parietal and occipital areas of the brain. The decision-making process, namely, the classification of the Necker cubes, begins later and is characterized by the activation of the frontal and prefrontal cortex with establishment of powerful functional connections between them [108].

To describe this process, Maksimenko et al. [26] considered the formation of functional connectivity during perception and interpretation of a bistable Necker cube. In order to reconstruct functional connections, EEG power changes in the beta range were calculated. Functional connections were then reconstructed from the values obtained using a recurrence measure of conditional dependence [109]. Changes in the intensity of connections between brain regions compared to the prestimulus period in the EEG were considered, so that functional network reconfiguration can be described by the relationship R between the number of increasing and decreasing links in the obtained brain functional network.

Fig. 8.26 **a** The fraction of functional links R , which are increased during perception of a visual stimulus. The vertical dashed line corresponds to the subject's response time (button pressing); **b** The structure of brain functional network at characteristic times $t_{1,2,3}$ of reconfiguration of the functional network. The size of a network node characterizes its degree k_i^{out} by outgoing links. Based on data from [26]



Analysis of the functional connectivity structure revealed a number of features associated with decision-making. In particular, it was found that 0.3 s before pressing the button, there was a strengthening of neural connections in the beta range, characterized by increasing fraction of functional links R during the perception of the visual stimulus (Fig. 8.26a). A detailed analysis of the network structure was carried out by calculating the degrees of nodes by outgoing connections k_i^{out} . It was shown that at the time interval preceding the decision, there is an increase in the value of k_i^{out} over time (Fig. 8.26b), with the highest value of node degrees being reached in the frontal cortex.

In addition, the analysis of the structure of functional connections showed that the increase in the value of k_i^{out} is associated with both an increase in the density of connections within the frontal cortex and a greater number of outgoing connections directed toward the occipital region (Fig. 8.26b) at time t_3 . This means that the high-level processes associated with the processing of sensory information, its interpretation, and subsequent decision-making are realized through the activation of the fronto-parietal functional network of the brain. The leading role in this formed functional network is assigned to frontal areas.

8.3.3 MEG Experiments

Along with electroencephalography (EEG), magnetoencephalography (MEG) neuroimaging technique is widely used in brain activity measurements in medicine and neuroscience [107, 110, 111]. Such a method measures weak magnetic fields generated by neurocortical ionic currents. This is a safe noninvasive method of brain imaging that provides important information about neuronal activity in the living human brain with high temporal (about 1 ms) and spatial (about 1–2 mm) resolution. While the EEG modality benefits from the simplicity of the measurement equipment, it suffers from a relatively low (around 2 cm) spatial resolution. At the same time, MEG requires more sophisticated instrumentation and measurement methods due to the extremely low magnetic fields generated by the brain tissue. The magnetic field is detected with a magnetometer known as superconducting quantum interference device (SQUID) [112] placed close to the scalp. SQUID can detect tiny magnetic signals, much less than one-billionth the strength of the Earth's magnetic field, and then convert these signals into electric voltages. The SQUID array is mounted in a close-fitting helmet and is cooled with liquid helium. The SQUID array is used in combination with superconducting pickup coils acting like antennas. When a magnetic signal from the brain traverses the coil, it induces a current measured by the SQUID.

A MEG scanner, for example, the widely used Vectorview MEG system (Elekta AB, Stockholm, Sweden) used in the MEG experiments presented in this chapter [68, 82, 113, 114], contains 306 sensors covering the entirety of the scalp. These sensors include magnetometers which measure magnetic fields directly, and gradiometers which are pairs of magnetometers placed at a small distance from each other, measuring the difference in the magnetic field between their two locations. This difference measure subtracts out large and distant sources of magnetic noise (such as the Earth's magnetic field), while remaining sensitive to local sources of magnetic fields (such as those emanating from the brain). Due to their positioning, the magnetometers and gradiometers provide complementary information about the direction and amplitude of brain magnetic fields.

The first MEG-based experiments with Necker cube perception practically copied the EEG studies described in the previous section. The structure of the experimental session for each subject was as follows. A set of Necker cubes with different wireframe contrasts were presented during approximately 20 minutes. In this experiment, we used 15 Necker cubes with randomly chosen contrast parameters from the set $a \in \{0.1, 0.15, 0.3, 0.4, 0.47, 0.48, 0.49, 0.5, 0.51, 0.52, 0.53, 0.6, 0.7, 0.85, 0.9\}$. Each contrast was presented 15 times. In order to fix the first impression of the person and avoid switches between two possible percepts, the image exhibition in our experiments was limited to $\tau \in (0.8, 1.2)$ s (see Fig. 8.21d). The short duration of stimulus presentation is also needed to reduce the stabilization effect [115]. Indeed, the probability of the configuration persisting until the subsequent presentation is known to be highly dependent on how long it was seen before the stimulus was removed [115]. Only when the perceptual configuration was consistently seen for a

relatively long time before the stimulus disappeared, there was a high probability of it persisting onto the next stimulus presentation. Since the required time for consistent observation of the Necker cube is about 1 s [115], the stimulus exhibition for a shorter time diminished the “memory” effect. The random sequence of Necker cubes with different values of the control parameter a also prevented the appearance of perception stabilization. Finally, to draw away the observer’s attention and make the perception of the next Necker cube independent of the previous one, different abstract pictures were randomly exhibited for about $\gamma \in (4.2, 5.25)$ s between demonstrations of the different Necker cube images.

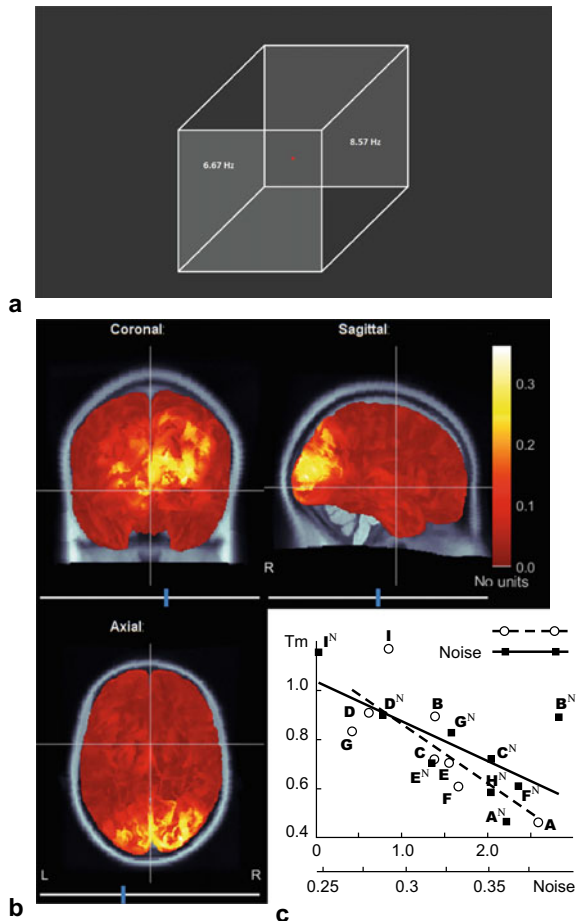
The MEG data recorded in the experiment were not associated with the motor-related brain activity and therefore suitable for the analysis of the cognitive activity involved in the decision-making process [114]. Based on this experimental MEG data (see Sect. 8.4.2), the efficiency of machine learning methods for classification of human MEG trials corresponding to the perception of bistable visual stimuli with different degrees of ambiguity is demonstrated. Along with classification of brain states associated with multistable image interpretations, in the case of significant ambiguity, the artificial neuronal network can detect an uncertain state when the observer doubts about the image interpretation. So, there is the possibility of using MEG data and artificial intelligence for detection of bistable brain activity associated with difficulties in the decision-making process.

Several papers [68, 82, 113] were devoted to a study of the perception of flickering bistable Necker cube in order to analyze the corresponding visual evoked potentials (VEP) or visual evoked fields (VEF). These are electrical or magnetic neural responses recorded from the surface of the scalp using EEG or MEG, respectively. These responses are locked to repeated presentations of a visual stimulus. If the stimulus frequency is fast enough to prevent the evoked neural activity from returning to a base line state, the elicited response is continuous and called steady-state visual evoked potential (SSVEP) or steady-state visual evoked field (SSVEF).

In the simple experiment, brain noise was estimated from the MEG response to flickering visual stimulation [68]. A brief summary of the results of this experiment is described above (see Sect. 8.2.1). The visual stimulus was a gray square image on a black background generated by a personal computer on a computer monitor with a 60-Hz frame rate and projected by a digital light processing projector onto a translucent screen in the MEG chamber. The pixel brightness of the Necker cube image was modulated with either 6.67 Hz (60/9) or 8.57 Hz (60/7) frequency by a sinusoidal or a rectangular signal. The modulation depth was 100% with respect to the medium grayscale level of the pixels’ brightness (128 in an 8-bit format). This means that the image brightness varied from completely black (0) to completely white (255). These particular modulation frequencies were chosen in preliminary experiments with other possible flicker frequencies, integer fractions of the 60 Hz frame rate (i.e. 60/2, 60/3, 60/4, 60/5, 60/6, ...), as frequencies which produce the best tagging response in the brain at the same frequencies and their second harmonics.

Another more complex experiment was designed to study voluntary and involuntary visual attention focused on different interpretations of bistable images [82]. In this experiment, as shown in Fig. 8.27a, the visual stimulus was a Necker cube with

Fig. 8.27 **a** Necker cube with flickering left and right faces at 6.67 and 8.57 Hz, respectively. The subjects were asked to fix their gaze on the central red dot. **b** Typical source localization map using average event-related coherence which are calculated and averaged for both stimulation frequencies to reveal brain sources active during the spontaneous switching between the visual perceptual states. The sources are localized in the visual cortex in the right hemisphere. **c** Relation of dominance time T_m with attention performance μ and brain noise: (dotted line with circles) T_m versus μ with a linear fit (root mean squared error: 0.168; F-statistics: 5.7; p-value: 0.0484) (solid line with black boxes) T_m versus brain noise with a linear fit (root mean squared error: 0.147; F-statistics: 8.95; p-value: 0.0242). Based on data from [82]



sinusoidally modulated pixels' intensity in the front and rear faces with frequencies $f_1 = 6.67$ Hz (60/9) and $f_2 = 8.57$ Hz (60/7), respectively. The experiment contained two parts. In the first part the subjects were asked to voluntarily control their attention by interpreting the cube orientation as either being left or right. Accordingly, we observed the dominance of the corresponding spectral component at 6.67 or 8.57 Hz, and voluntary attention performance was measured. In the second part, the subjects were asked to focus their gaze on a red marker at the center of the cube image (see Fig. 8.27a), without putting any effort in its interpretation. The alternation of the dominant spectral energies at the second harmonics of the stimulation frequencies was treated as changes in the cube orientation. Based on the results of the first experimental stage and using a wavelet analysis for the dominant spectral components recognition, methods to identify the currently perceived cube orientation and to calculate the attention performance were developed [82].

The wavelet power spectrum $E^n(f, t) = \sqrt{W_n(f, t)^2}$ was calculated for each MEG channel $X_n(t)$ in the $f \in [1, 30]$ -Hz frequency range. Here, $W_n(f, t)$ is the complex-valued wavelet coefficients calculated as [116]

$$W_n(f, t) = \sqrt{f} \int_{t-4/f}^{t+4/f} X_n(t) \psi^*(f, t) dt, \quad (8.34)$$

where $n = 1, \dots, N$ is the MEG channel number and “*” defines the complex conjugation. The mother wavelet function $\psi(f, t)$ is the Morlet wavelet often used for the analysis of neurophysiological data $\psi(f, t) = \sqrt{f} \pi^{1/4} e^{j\omega_0 f(t-t_0)} e^{f(t-t_0)^2/2}$, where $\omega_0 = 2\pi$ is the central frequency of the Morlet mother wavelet [117].

The wavelet powers $E(f_1, t)$ and $E(f_2, t)$ given by Eq. (8.34) were evaluated at the tagging frequencies $f_1^2 = 13.33$ Hz and $f_2^2 = 17.14$ Hz (second harmonics of the flicker frequencies), respectively. Since the frequency response decays with increasing frequency as a $1/f$ -rule, the wavelet energy is normalized to the corresponding modulation period ($1/f_{1,2}^2$). Hence, the wavelet time series are multiplied to their defining frequencies to get

$$\bar{E}_1(f_1^2, t) = f_1 E(f_1^2, t), \quad \text{and} \quad \bar{E}_2(f_2^2, t) = f_2 E(f_2^2, t) \quad (8.35)$$

and the difference between the spectral energies at f_1^2 and f_2^2 is then calculated as

$$\Delta \bar{E} = \bar{E}_1(f_1^2, t) - \bar{E}_2(f_2^2, t). \quad (8.36)$$

and normalized to its maximum absolute value as

$$\overline{\Delta E} = \Delta \bar{E} / \max |\Delta \bar{E}|. \quad (8.37)$$

To determine the moment of switching between two different cube orientations, $\overline{\Delta E}$ is screened for significant changes above a threshold equal to its standard deviation δ : $|\overline{\Delta E}| > \delta$. The active state is determined as left-oriented if $\overline{\Delta E} > \delta$ and as right-oriented if $\overline{\Delta E} < -\delta$. The algorithm is resilient to insignificant perturbations and sticks to the previous state for $-\delta < \overline{\Delta E} < \delta$. The efficiency of the algorithm is shown [82].

To estimate attention performance, the values \bar{E}_1 and \bar{E}_2 over time and over all trials separately for the left-oriented (\bar{E}_1^L and \bar{E}_2^L) and for the right-oriented (\bar{E}_1^R and \bar{E}_2^R) cube interpretations are used. The differences between the wavelet energies at f_1 and f_2 corresponding to the left-oriented and right-oriented cube perceptions ($D_{1,2} = \bar{E}_{1,2}^L - \bar{E}_{1,2}^R$) signify the bias in spectral reflection of left orientation in comparison to right orientation so that D_1 should be higher and D_2 should be lower. The difference between D_1 and D_2 defines the performance index μ as

$$\mu = D_1 - D_2. \quad (8.38)$$

The performance μ characterizes the ability of the subject to attend to the foretold cube orientation.

Based on the results of the second experimental stage, when the subjects spontaneously switch their attention to either of the cube orientations, the authors [82] showed that the most probable or modal dominance time for the left orientation ($T_m^L = 2.275$ s) is much higher than for the right orientation ($T_m^R = 0.424$ s). This seems to suggest a bias in the perception of the two cube orientations, i.e. the same stimulation excites the left orientation more easily and frequently than the right orientation. The possible reason for the preference of the left-cube orientation can be that in our everyday lives, we see the left-oriented cube more often and hence the perceptual stability of the left-cube orientation is higher [81]. This form of attention in perceptual selection that does not depend upon ocular, spatial, or feature-based mechanisms but solely on the representational object it corresponds to, is called object-based attention and has shown to determine dominance in bistable perception [118]. This is confirmed by the analysis of brain source activity localization using event-related coherence (ERC) calculation [113].

The ERC was computed over all 15,004 brain sources to generate heat maps for source localization. The ERC heat maps were evaluated at both tagging frequencies, (f_1 and f_2) and then averaged to give the final source localization map. Fig. 8.27b shows the localized brain activity in the visual cortex of one of the subjects under study. Interestingly, we observed a comparatively stronger activation in the right hemisphere, which corresponds to the left visual field. These results fall in line with the preference of the left-cube orientation.

Figure 8.27b demonstrates the average modal dominance time $T_m = (T_m^L + T_m^R)/2$ versus attention performance μ . One can see, that higher attention performance leads to shorter dominance time. This is in accordance with the hypothesis that higher attention requires a larger neuronal network to process information and make a decision, this in turn increases neural noise since a larger number of synapses and neurons are involved [23]. At the same time, stronger brain noise causes more frequent switching between perceptual states or more frequent response selection and hence shorter dominance times.

To check this hypothesis, the brain noise is estimated using the methodology based on phase synchronization [68, 69] as described in Sect. 8.2.1. In a separate set of experiments with only a single face of the cube flickering, we measured kurtosis of the probability distributions of the phase difference between the second harmonic of the flickering signal with frequency f_1 and brain response in the occipital cortex. In Fig. 8.27c, we show the average modal dominance time vs. brain noise (in units of inverse kurtosis). Not only do the two curves follow a similar downward trend, but subjects with higher voluntary attention also have a roughly higher noise. It is important to note that brain noise was measured in a different way. Nonetheless, a subject with higher (Subject-A) or lower voluntary attention capabilities (Subject-I) can be assumed to have paid a similar level of attention during the subsequent brain noise measurement experiment. As expected, these values anticorrelate, which confirms our hypothesis that higher attention performance is associated with stronger brain noise because a larger neural network is involved in information processing.

This result is consistent with the Bialek and DeWeese theory [119], who predicted that “*the brain always finds the statistically optimal interpretation of the incoming sense data.*”

8.4 Artificial Intelligence for Classification of Multistable Perceptual States

While observing an ambiguous object for a long enough time, the subject demonstrates individual features of alternative switching between different percepts, for example, the Rubin vase is alternately perceived as two faces and a vase; the Necker cube can be interpreted as a left-oriented or a right-oriented cube. According to existing hypothesis, the switches in perception are caused by stochastic processes in the brain’s neural network due to spontaneous neural activity, random generation of membrane potentials and random synaptic connections [62, 65, 77, 83]. These random neural background activity plays a crucial role in the interpretation of ambiguous images and other decision-making tasks. Following this hypothesis, perception of ambiguous objects has been described mathematically by simple stochastic models, discussed in Sect. 8.2. It is clear that the description and classification of brain states during the decision-making process opens wide perspectives for deeper understanding of mechanisms responsible for visual spatial perception in the human brain with a strong stochastic component, as well as the possibility for perception control.

One of the most appropriate techniques for studying brain states is based on the analysis of multichannel electroencephalographic (EEG) or magnetoencephalographic (MEG) signals [120]. In the context of bistable perception, the analysis of the EEG data allows one to reveal specific features of the perceptive process. In particular, Kornmeier et al. [88] discovered two types of EEG signatures, stimulus-related (low-level) and percept-related (high-level) during perception of the Necker cube. The percept-related features associated with the Necker cube reversals were found in gamma [121] and delta [122] frequency bands. Thus, different brain states manifest themselves as specific oscillatory patterns in EEG signals characterized by a particular time-frequency structure. This gives us the possibility to detect and classify the brain states by processing the EEG data [123].

Among various approaches proposed for the classification of oscillatory patterns observed in the EEG recordings [124, 125], it is worth to mention discriminant analysis methods, independent component analysis, often used for finding and eliminating biased artifacts in EEG signals, short-time Fourier transform, and wavelet-based methods, and methods based on estimation of event-related synchronization/desynchronization (for a comprehensive review see [107]). Nowadays, another machine learning based classification technique known as artificial neural network (ANN) [126] is widely used in computer science, biophysics, deep learning, econometrics, etc. This method inspired by biological interconnected neurons is based on nonlinear models of neural units (artificial neurons).

The ANNs can be either hardware-based (neurons represented by physical components) or software-based (computer models), and can use a variety of topologies and learning algorithms. Hardware ANNs are more accurate in mimicking the performance of real neural networks and have a higher performance speed than software-based ANNs. Due to these features hardware ANNs have a better prospective for real-time implementation, but they heavily rely on a specific hardware configuration. In contrast, software ANNs have a more simple and therefore a more flexible structure and can be easily implemented in practice [127].

Many types of architectures of software-based ANNs were developed to solve different relevant tasks (for details you can see the review of machine learning techniques in neuroscience applications in Refs. [107, 128]. In particular, convolutional neural networks (CNN) were applied for the recognition of different types of images, including patterns in EEG signals [129]. The CNNs are very efficient in revealing specific features in unstructured data, like images, audio and video. However, in spite of their excellent properties in pattern recognition and classification, the CNNs require a precise tuning for each task because the number of varied parameters is quite large and most of them can only be determined empirically. Therefore, in such a specific task as the classification of undetermined types of EEG patterns, it is more convenient to use simpler and hence more flexible ANNs, such as multilayer perceptron (MLP) [130].

In this section we will discuss the problems artificial intelligence has for the classification of multistable perceptual states. In Sect. 8.4.1 we consider the ANN based technique that makes it possible to distinguish with high precision particular EEG features inherent to different cube orientations. Moreover, we apply ANN in a cross-subject mode and discover the existence of universal patterns in EEG, common for all subjects. In Sect. 8.4.2 we show that along with the classification of brain states associated with multistable image interpretations, in the case of significant ambiguity, the ANN can detect an uncertain state when the observer doubts about the image interpretation. We also describe the possible application of ANNs for the detection of bistable brain activity associated with difficulties in the decision-making process.

8.4.1 Recognition and Classification of Multistable Brain States Using Artificial Neuronal Networks

Every subject completed a single recording session to avoid possible adaptation and habituation of the person to solving the task. During the experiment, seven Necker cube images ($N = 7$) with different wireframe contrasts, i.e. with seven different values of the control parameter $a_i = 0.15, 0.3, 0.4, 0.5, 0.6, 0.7, 0.85$, were randomly presented to each subject. All participants were aware about the two possible cube interpretations and were able to see both of them.

Figure 8.28a shows the block diagram illustrating the main steps for the M/EEG data analysis by means of artificial intelligence techniques. First of all, we collected an

entire M/EEG dataset obtained during the experiments described in Sects. 8.3.2 and 8.3.3. Afterwards, the M/EEG signals were pre-processed via filtration and artifact removal techniques. Finally, the pre-processed M/EEG recordings were normalized and fed to the trained ANN.

The ANN consists of a number of artificial neurons interconnected with each other by synaptic weights to form a net. There are many possible ANN architectures to be used for pattern recognition. One of them, a spiking neural network (SNN) is aimed at realistically simulating neurons because it takes into account their advanced properties, such as spike-timing-dependent plasticity. This type of ANN has proved to be an effective tool for pattern recognition [131, 132], but it is usually hardware-based and requires specific software/hardware platforms. To classify bistable images based on M/EEG data modalities in Refs. [95, 96, 114, 133], a class of ANN known as a multilayer perceptron (MLP) was employed. An important characteristic feature of the MLP is that signals propagate only in a forward direction (feedforward network), from left to right on a layer-by-layer basis [126].

In our case, the classification problem consists in the recognition of two different brain states corresponding to the perception of the bistable Necker cube as left-oriented or right-oriented. Figure 8.28b shows the ANN architecture of MLP used in our analysis for EEG signal classification. The used ANN has input layer IL , two hidden layers, $HL1$ and $HL2$, and output layer OL . The input layer IL contained $P = 19$ inputs, one for each of 19 EEG channels. For every p th ($p = 1, 2, \dots, 19$) input we used the functional EEG signal $s_p(t)$ with 1 s duration (250 samples) from p -th channel registered for the case of left- or right-oriented cube interpretation. The signal from each input was fed to all computational nodes in the first hidden layer $HL1$ with H_1 artificial neurons. The resulting output signal from $HL1$ entered the second hidden layer $HL2$ with H_2 neurons of the same type. Finally, the output signal from $HL2$ entered to a single neuron in the output layer OL . Since our classification problem was the recognition of two brain states using the 19-channel EEG data set, the ANN contained only one output neuron, which output value should classify the current brain state to either left- or right-oriented cube interpretation.

The ANN evolution is described by the following mathematical model

$$u_i^l(t) = F^l \left(\sum_{p=1}^{H^{l-1}} w_{pi}^l u_p^{l-1}(t) - \theta_i^l \right), \quad (8.39)$$

where H^l is the number of neurons in the l -th layer (a layer with $l = 0$ is supposed to be the input layer), $u_i^l(t)$ is the output signal of the i -th neuron belonging to the l -th layer ($u_i^0(t)$ being the signals from analyzed EEG channels), $\mathbf{W}^l = \{w_{pi}^l\}$ is the weight matrix of the l th layer of dimension $(H^{l-1} \times H^l)$, and w_{pi}^l ($p = 1, \dots, H^{l-1}$, $i = 1, \dots, H^l$) are the synaptic weights of input signals for the i -th neuron in the l th layer, $\Theta^l = \{\theta_i^l\}$ is the threshold vector for neurons in the l -th layer, and

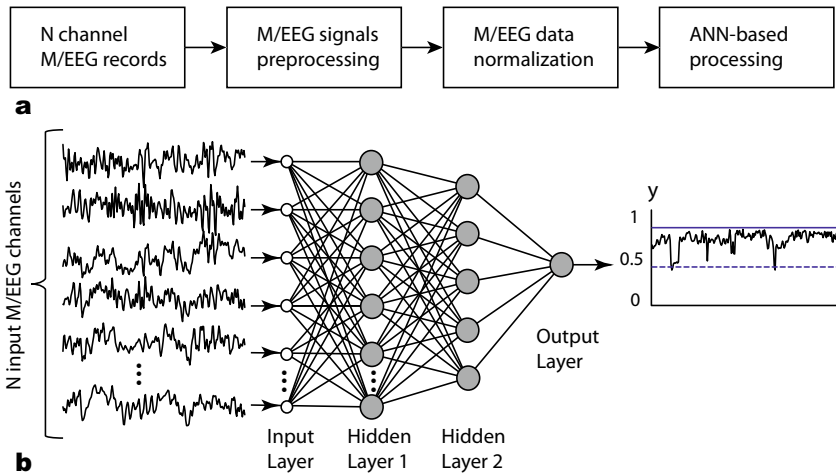


Fig. 8.28 **a** Block diagram illustrating the main procedures carried out to prepare multivariate M/EEG signals for ANN processing. **b** MLP architecture with two hidden layers in M/EEG signal classification. IL ($l = 0$) is the input layer, $HL1$ and $HL2$ are the first ($l = 1$) and second ($l = 2$) hidden layers, respectively, which nodes (artificial neurons) are characterized by nonlinear activation function given by Eq. 8.40, and OL is the output layer ($l = 3$) consisting of one artificial neuron with the same activation function

$$F^l(\eta) = f(\eta) = \frac{1}{1 + \exp(-\eta)} \quad (8.40)$$

is the nonlinear logistic activation function for neurons in the hidden and output layers $l = 1, 2, 3$.

A class of recognized objects can be characterized by the mean squared value of output signal $u(t) = u_1^3(t)$, as follows

$$y = \sqrt{\frac{1}{N} \sum_{i=1}^N (u(t_i))^2}. \quad (8.41)$$

For the left-oriented Necker cube perception, the mean squared value of the output signal is supposed to be $y \geq 0.5$ and for the right-oriented cube $y < 0.5$.

The unknown matrices \mathbf{W}^l and vectors Θ^l can be obtained during the learning process by minimizing the mean squared error (MSE):

$$\text{MSE} = \sqrt{\frac{1}{K} \sum_{k=1}^K (d_k - y_k)^2}, \quad (8.42)$$

where K is the total number of objects in the training set, y_k is the mean squared value of the output calculated for the k -th object using Eq. 8.41, d_k is a desired output value of y_k which we wish the MLP learns ($d_k = 1$ corresponds to the left-oriented cube perception and $d_k = 0$ to the right-oriented one). To find unknown parameters of ANN, we used the Levenberg–Marquardt algorithm (LMA) [134]. By differentiating the error criterion Eq. 8.42 with respect to the unknown parameters, the LMA method yields better results in comparison with other optimization methods, but requires more computational time to determine the unknown parameters. For the learning process, we created a data set consisting of 70 single trials with 1 s duration (250 samples) randomly selected from EEG records obtained from one volunteer. This data set consisted of 35 trials for each orientation of the Necker cube images with different contract parameters a . For a more reliable assessment of the results of ANN learning, we repeated the training procedure many times (1000 learning cycles in total). As a consequence, we obtained 1000 ANNs with different parameters and different values of classification error μ .

We also introduced another characteristic for estimation of classification precision, called recognition accuracy ρ of ambiguous images defined as

$$\rho = \frac{N_p}{N} \times 100\%, \quad (8.43)$$

where N_p is the number of true classified cubes and N is the total number of analyzed Necker cube images.

Finally, for further analysis we chose the ANN with the smallest MSE characterized by the highest accuracy ρ , to be the best ANN for classification. The procedure of ANN learning was implemented to each volunteer in order to find his/her optimal ANN topology with the highest recognition accuracy.

The development of our classification algorithm started with the training of ANNs for each subject who participated in the experiments. The training data set was formed individually for every participant and the optimal set of ANN parameters $\Gamma_r = (\mathbf{W}_r^1, \mathbf{W}_r^2, \mathbf{W}_r^3, \Theta_r^1, \Theta_r^2, \Theta_r^3)$ was obtained for classification of brain states of subject $r = 1, \dots, 12$.

Now, we will analyze the experimental data obtained in the first set of experiments (with key pressing) (Fig. 8.21a). The recognition accuracy of the brain states classification during visual perception of ambiguous images (left-/right-oriented perception) for each of the 12 subjects, used for training ANN, is shown in Fig. 8.29a. To analyze the classification accuracy we took the part of the EEG which was not used for training, i.e. about 330 EEG trials of the registered brain states after image demonstration. In this case, the mean classification accuracy for all of the 12 subjects was close to $82.6 \pm 10.7\%$ (mean \pm S.D.) (left column in the right panel of Fig. 8.29a). The recognition accuracy for every subject, shown in the left columns in the left panel of Fig. 8.29a, varied between 68% and 98% for different subjects.

Practically the same recognition accuracy was calculated by analyzing experimental data obtained in the second set of experiments (without key pressing). The recognition accuracy of the brain states classification for each of the 12 subjects is

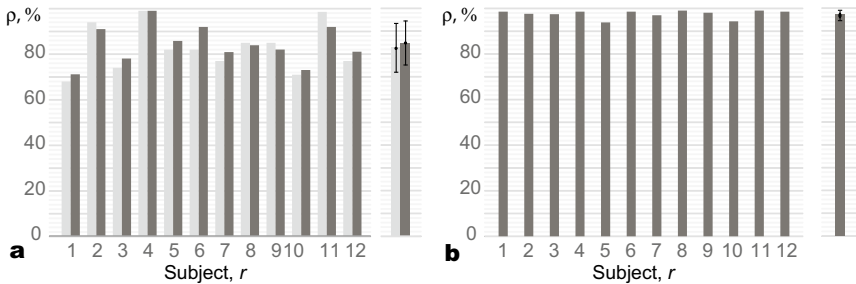


Fig. 8.29 **a** Recognition accuracy for all of the 12 subjects. The left-hand light grey columns represent accuracy for each subject, using ANN trained on his/her own EEG ($h = r$) obtained in the first set of experiments (with key pressing). The right-hand black columns show accuracy for the second set of experiments (without key pressing). The right panel represents the data averaged over all subjects under study. **b** Recognition accuracy using ANN trained on subject 4 ($h = 4$) for all of the 12 subjects. The right panel represents the data averaged over all subjects under study. Based on data from [95]

shown in Fig. 8.29a the experimenter asked the subject about how he/she interpreted the Necker cube, and then made the corresponding note in the presentation software according to the answer. As in the previous case, to analyze recognition accuracy we took the part of the EEG which was not used for training, i.e. about 130 EEG trials of the registered brain states after image demonstration. The mean classification accuracy for all of the 12 subjects was close to 87% (right column in the right panel in Fig. 8.29a), while the recognition accuracy for every subject, shown in the right columns in the left panel of Fig. 8.29a, varied between 71% and 98% for different subjects.

Thus, the comparison of the results for classification of the brain states obtained in the two different sets of experiments (with and without key pressing) demonstrated almost identical results for the same subject. The quality of recognition of the brain states in the group of 12 subjects was around 82–84% in both sets of experiments. Therefore, we can conclude that motor reaction had no effect on classification quality.

It is remarkable that one of the subjects ($r = 4$) demonstrated very high recognition accuracy in classification of image perception, which reached 98%. When we applied the ANN trained on this subject to the analysis of the EEG data of other subjects, we obtained a much higher accuracy than when we used the ANNs trained on their own data. These results are shown in Fig. 8.29b. Using ANN with parameters Γ_4 evaluated for subject $r = 4$ the accuracy of classification was close to 95–98% for almost all subjects, except for subjects $r = 5$ and $r = 10$, who demonstrated $\rho < 95\%$. Thus, we can conclude that the features of EEG patterns corresponding to the perception of left- or right-oriented cubes were typical for all subjects, which means that even a single ANN trained on the EEG data set of one person can classify with high accuracy the corresponding brain states of a large group of people.

8.4.2 Detecting Human Uncertainty in Perception of Bistable Visual Stimuli Using Artificial Neural Networks

The ANN approach to the analysis of neurophysiological data can be described as follows. The ANN receives, as an input, a set of EEG or MEG signals and converts them to a binary output. The ANN trained on some known data set in order to learn features of the input data associated with a certain brain state, becomes able to extract similar states from a large amount of unknown input data. This is the advantage of the ANN in the detection of highly reproducible events in the human brain, for example, motor-related activity, epileptic seizures, etc.

On the other hand, the application of ANNs in cases when the brain is not able to select any stable long-term state and exhibits multiple abrupt switches between different states is much more challenging. This situation is common in decision-making processes where a person lacks information and, as a consequence, doubts about the decision [135]. In this case, two interesting questions arise: (i) How does the ANN, being trained to identify brain states associated with firmly adopted decisions, find a state of uncertainty in decision-making? and (ii) How can the ANN be applied for detecting human uncertainty in decision-making via EEG and MEG signals? The answers to these questions are important for understanding fundamental aspects of the brain's cognitive activity and practical use of artificial intelligence and deep learning tools aimed at the development of BCIs for improving human performance in decision-making. Moreover, this ANN application for decision-making in uncertain conditions is very promising for intelligent robotics and information systems.

To answer these problems we can consider the human MEG trials corresponding to the perception of ambiguous visual stimuli. As an example of a bistable image, we will again use the familiar Necker cube. The perception of such stimuli is associated with a multistable decision-making process, since the same object can be interpreted in different ways. While the interpretation of most bistable visual objects is random, there are some bistable stimuli for which the degree of ambiguity can be easily controlled, and this allows the selection of one or another interpretation. The Necker cubes with $a \approx 0.1$ and $a \approx 0.9$ can easily be interpreted as left-oriented and right-oriented, respectively (see Fig. 8.21b). However, the Necker cubes with $a \approx 0.5$ cannot be unambiguously interpreted, especially if the decision time is too short.

Several experiments demonstrated that the level of uncertainty in the Necker cube interpretation significantly increased for $a \approx 0.5$ due to strong image ambiguity. Figure 8.21e shows the level of uncertainty, $\Psi(a)$, in the interpretation of the bistable image, defined as

$$\Psi(a) = \begin{cases} 2P_l(a), & a \geq 0.5, \\ 2(1 - P_l(a)), & a < 0.5, \end{cases} \quad (8.44)$$

where $P_l(a)$ is the probability (Eq. 8.31) for the left-oriented cube perception. As expected, a high degree of uncertainty ($\Psi(a) > 0.8$) is observed for $a \approx 0.5$. We suppose that an ANN trained to identify brain states associated with left-oriented and right-oriented interpretations is able to describe the decision-making process

and detect the degree of uncertainty, which would allow to find any doubts during this process.

The experimental procedure is described in Sect. 8.3.3. The experimental MEG data processing scheme is shown in Fig. 8.28a.

At the first stage of the analyses, the MLP was trained and validated individually for each of the five subjects who participated in the MEG experiment. The mean accuracy in MLP classification obtained during the validation procedure for all subjects was close to 86%. The application of well trained MLP allowed us to assess important features of the human decision-making process.

The time series in Fig. 8.30a–c show typical MLP responses $y(t)$ to individual MEG trials when cubes with different ambiguity were presented. One can see in Fig. 8.30a, b, that in the case of low-ambiguous left- or right-oriented cubes, the MLP response curve, after short transient fluctuations, converges to a stable state “0” or “1”, respectively. We refer to such behavior of the ANN trace as a decision-making certainty since ANN handles identification of well-established and temporally stable brain states associated with left- or right-oriented cube interpretations. Contrary to this, the observation of a highly-ambiguous image is characterized by multiple irregular switches between “0” and “1” values, as seen in Fig. 8.30c. The latter is interpreted as uncertainty of ANN, consequence of human decision-making uncertainty.

In order to find trends and general features of the decision-making process and highlight the most significant brain areas, we carried out the MLP response analysis over experimental sessions individually for each participant. Let $y_n^a(t)$ be the MLP response to the MEG signals taken during the observation of the Necker cube image with edge intensity a during the n th experimental session. Then,

$$\langle y^a \rangle(t) = \frac{1}{N} \sum_{n=1}^N y_n^a(t) \quad (8.45)$$

is the averaged MLP response to the MEG signals taken during the observation of a Necker cube image with edge intensity a over N experimental sessions, and

$$\sigma^a(t) = \sqrt{\frac{1}{N} \sum_{n=1}^N (y_n^a(t) - \langle y^a \rangle(t))^2} \quad (8.46)$$

is the standard deviation of the MLP responses over N sessions, presented in Fig. 8.30d–f. While in the former case the standard deviation is distributed in a wide range from 0 to 0.5, in the latter case the standard deviation is localized in a narrow range above the threshold σ_{tr} to 0.5 indicating decision-making uncertainty. As a consequence we can suggest standard deviation σ to be a measure of decision-making uncertainty.

We suppose that the interpretation process of identical images should proceed in approximately the same way. Thus, the MEG traces corresponding to certain

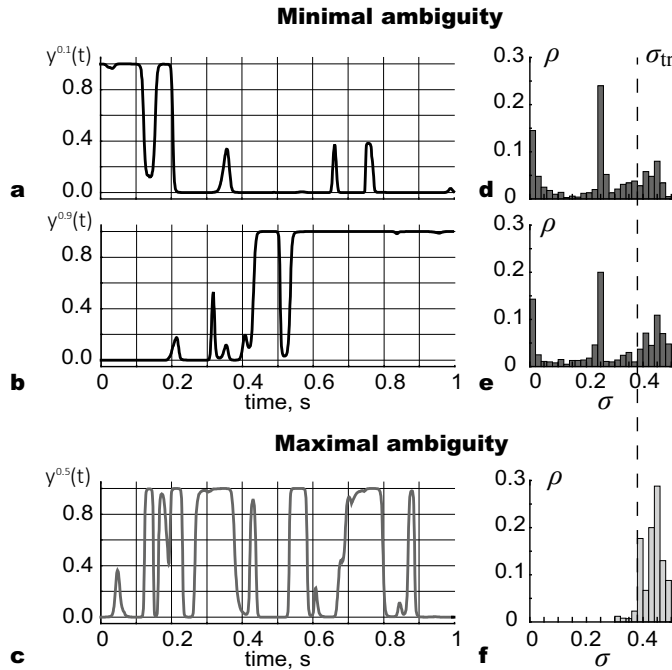


Fig. 8.30 **a–c** Individual MLP response traces $y(t)$ and **d–f** probability distribution of standard deviation $\rho(\sigma)$ calculated over MEG experimental sessions. Panels (**a**, **d**) and (**b**, **e**) show MLP responses to the interpretation of low ambiguous left- and right-oriented Necker cubes with $a = 0.1$ and 0.9 , respectively. Panels (**c**, **f**) illustrate MLP response to the interpretation of a highly-ambiguous cube with $a = 0.5$. The dashed line denotes standard deviation threshold σ_{tr} . Based on data from [114]

decisions about observed image interpretation should be characterized by a small variation of the MLP response over different trials. In contrast, a large variation of instantaneous MLP responses over different trials should be inherent to traces corresponding to high decision-making uncertainty. So, one can introduce the threshold value σ_{tr} above which one can assume that the brain is typically uncertain about the decision-making at time t_i of the considered 1 s interval.

To define the threshold σ_{tr} and distinguish between decision-making uncertainty and certain brain states, we calculate the MLP output standard deviation during observation of the ambiguous Necker cube with $a = 0.5$. The observation of this image cannot provide any certain decision on the cube orientation because all edges have the same contrast. Indeed, a typical MLP response trace, corresponding to the perception of this image is characterized by multiple irregular switches between “0” and “1” (see Fig. 8.30c). The standard deviation calculated using Eq. 8.46 and its distribution $\rho(\sigma)$ exhibit the values of $\sigma^{0.5} \geq 0.3$. Based on this result, we define the threshold value σ_{tr} as the 5% percentile of the $\sigma^{0.5}$ distribution. Values of $\sigma^a(t)$ with $a \neq 0.5$ are compared with the threshold σ_{tr} . If $\sigma^a(t) < \sigma_{tr}$, we state that the

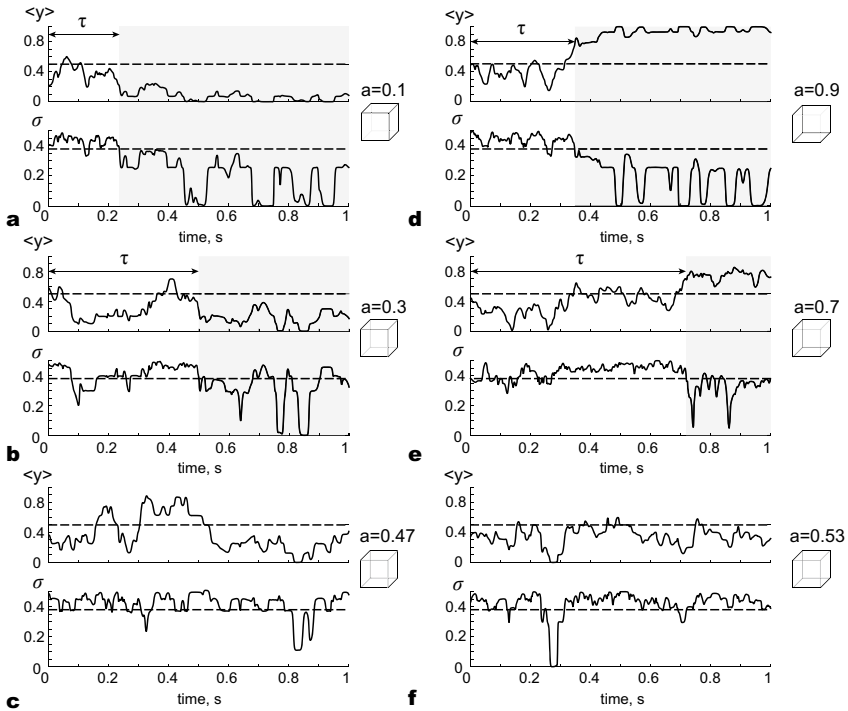


Fig. 8.31 Sequence of MLP responses averaged over experimental sessions ($\langle Y \rangle$) (upper traces) and standard deviation σ (lower traces). Decision-making process in interpretation of **a, d** low-ambiguous, **b, e** medium-ambiguous, and **c, f** high-ambiguous images is shown. The corresponding Necker cube images with specified edge intensities a are shown in the right-hand side of each panel. Gray areas highlight the regions of 1-second trials, which are significant in terms of decision-making certainty. Based on data from [114]

participant is typically certain about the cube interpretation, whereas $\sigma^a(t) \geq \sigma_{tr}$ indicates a decision-making uncertainty state.

Figure 8.31 shows the sequence of averaged MLP outputs along with traces of standard deviation corresponding to MEG recordings taken during 1 s after demonstration of the Necker cube with different edge intensities a . The left and right columns represent the MLP outputs and standard deviations obtained from MEG signals corresponding to the left- and right-oriented cubes with the same value of relative edge intensity $\Delta a = |a - 0.5|$ or ambiguity degree. The lower Δa , the higher the ambiguity. Figures 8.31a, d show that the subject clearly interpreted the orientation of the presented Necker cubes while observing images with evident orientations ($\Delta a = 0.4$); the MLP outputs converge to either 0 or 1 in the case of left- or right-oriented cubes, respectively. We can see in Figs. 8.31a, d that the standard deviation is below the threshold ($\sigma < \sigma_{tr}$) during a major part of the 1 s interval. It should be noted, that the convergence of $\langle y \rangle$ to 0 and 1 is accompanied by the drop of σ .

The analysis of the MLP output curves together with the standard deviation allowed us to conclude that the subjects made a decision on the cube orientation after a short transient time τ during which he/she was uncertain about the image interpretation. Thus, we can divide the perception process into two stages: stage I (the decision is in process, which can be considered as the time of decision-making uncertainty) and stage II (the decision is already made, which can be considered as a stable well-recognized brain state). Therefore, the value of τ characterizes the time interval required for visual stimulus processing and decision-making on image interpretation.

Figures 8.31b, e show the curves of the averaged MLP output and standard deviation corresponding to the observation of images with a medium degree of ambiguity. One can see that an increase in ambiguity leads to an increase in the duration τ of the transient stage I required for visual stimulus processing via higher-nervous activity, because high-ambiguity images are more complex for visual perception and further interpretation. The interpretation process of the Necker cube with small Δa qualitatively differs from the interpretation of low-ambiguity images. Figures 8.31c, f illustrate the subject's uncertainty on the cube orientation during the observation of high-ambiguity Necker cubes with $\Delta a = 0.03$.

The features of the human brain behavior detected via MLP allow one to distinguish different stages of the decision-making process and decide whether a subject (in average) handles the interpretation successfully or not, as well as to estimate how difficult it was for him to interpret the observed image. Thus, looking at the averaged MLP output and standard deviation one can realize whether the participant has already interpreted the observed Necker cube or still remains uncertain about its orientation.

On the base of the above discussion, we can introduce the uncertainty measure $U(a)$ characterized by the individual level of decision-making uncertainty during the observation of the bistable image with parameter a , as follows

$$U(a) = \frac{1}{T} \sum_{i=1}^T \Theta(\sigma^a(t_i) - \sigma_{tr}), \quad (8.47)$$

where T is a number of MEG trial samples and $\Theta(\bullet)$ is a Heaviside step-function. The uncertainty measure $U(a)$ is a portion of the 1 s time interval during which the brain is uncertain in the decision-making.

Figure 8.32 illustrates the values of uncertainty $U(a)$ calculated according to Eq. 8.47 and above-introduced time lag $\tau(a)$ in decision-making. The data was averaged over the group of participants. One can see from Fig. 8.32a that $U(a)$ grows up as ambiguity increases, and has a well-pronounced peak at $a = 0.5$ (highest ambiguity). Figure 8.32b also shows the explicit tendency in increasing time τ needed for the brain to perceive and interpret the demonstrated image. It should be noted that both dependencies $U(a)$ and $\tau(a)$ are asymmetric with respect to $a = 0.5$, that indicates a lower level of decision-making uncertainty while observing left-oriented Necker cube images. Such left-oriented perceptual bias observed in the data of all

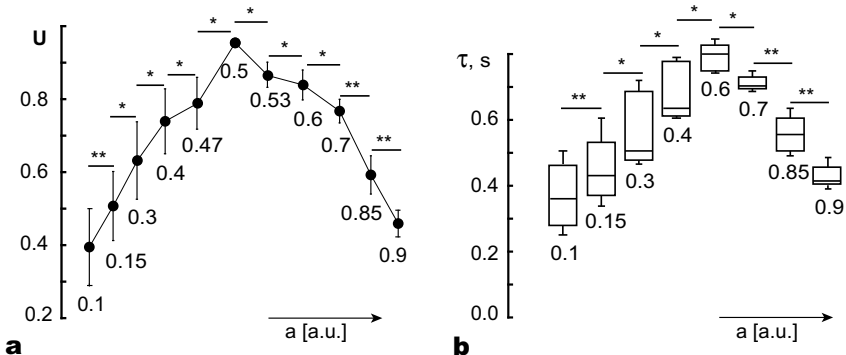


Fig. 8.32 Statistical characteristics of Necker cube interpretation for the group of subjects, calculated on the base of MLP processing of experimental MEG signals. **a** Uncertainty measure U (a) in Eq. 8.47 averaged over the group of subjects. Error-bars show the standard deviation. **b** Boxes and whiskers indicate time lags τ (a) for different edge intensities a . The stars “**” and “***” indicate the statistical significance of $p < 0.05$ and $p < 0.001$, respectively. The p -values were calculated via paired t-test. Based on data from [114]

participants may be caused by different reasons, for example, the influence of the leading eye [136], features of visual information interpretation conditioned by left-to-right reading or left hemispherical attentional bias [137, 138].

The experimental data was analyzed using paired t-test. According to the obtained p -values, significant changes in U and τ are marked by “**” for $p < 0.05$ and “***” for $p < 0.001$. It can be seen that both U (a) and τ (a) exhibit significant changes as the edge intensity varies, more pronounced for high and low a associated with unambiguous cases ($p < 0.001$). On the contrary, for $a \approx 0.5$ the changes are less significant ($p < 0.05$).

Thus, summarizing these results, we can say that an increase of uncertainty in decision-making was observed not only in one participant, but was common to the whole group. The features of the decision-making process, detected via artificial intelligence tools, namely, the duration of image perception τ and uncertainty measure U helped us to distinguish between clear interpretation of the visual stimuli and the state of uncertainty, without the analysis of direct answers from the subject, but solely from his/her brain activity. While studying mechanisms of perceptual decision-making, Heekeren et al. [1] noted that “*During a rainstorm, however, the sensory input is noisier, and thus you have to look longer to gather more sensory data to make a decision about the person at the light and the appropriate behavioural response*”. Using the described approach it is possible to estimate how long the decision-making process will take. Finally, it should be noted that the provided measures are able to indicate the difference in interpretation between left- and right-oriented Necker cube images, and that the latter induces a higher level of decision-making uncertainty [136–138].

8.5 Brain-Computer Interfaces Based on Bistable Perception

8.5.1 Brain-Computer Interface for Monitoring and Controlling Alertness

Alertness is known as a state of active attention with high sensory awareness, such as being watchful and prepared to meet danger or an emergency, or being quick to perceive and act. Drowsiness is a state of strong desire for sleep. It can be dangerous when performing tasks that require sustained attention, such as driving a vehicle, piloting an aircraft, monitoring air traffic, etc.

It has been known for more than 50 years, that in tasks requiring sustained attention, people cannot maintain alertness at a certain constant level [139]. It is also known that changes in the alertness degree reflect features of brain activity signals. Currently, a number of approaches for real-time monitoring and control of different types of attention are proposed based on selected features of electrical neuronal activity using EEG [140–145] and hemodynamic response of the brain using functional near infrared spectroscopy [146–149]. The first attempt to detect these brain hallmarks in real time was made in 1994 by the researchers from the Naval Health Research Center (USA) who demonstrated a system for monitoring human alertness based on online EEG spectral properties detection using ANN [140],

It should be noted, that human alertness can be estimated in real time during the task accomplishing. In this context, the most effective way to assess an attention state is to use visual stimuli and analyse the stimulus-related response of the neuronal brain network in attention-related brain areas. Maksimenko et al. [145] have proposed an experimental paradigm to monitor human alertness in real time during the accomplishment of a prolonged task of bistable visual stimuli classification. In order to focus the subject's attention on the stimuli, the authors used the Necker cube.

During the experimental session, Necker cubes with different values of the control parameter were presented to the subject for short time intervals, each lasting between 1 and 1.5 s. In order to draw away the subject's attention and make the perception of the next stimulus independent of the previous one, different abstract pictures were shown for about (5–5.5) s between subsequent demonstrations of Necker cube images. The subjects were instructed to press either the left or right key depending on the first impression of the cube orientation at each presentation.

The EEGs were recorded using five electrodes (O1, O2, P3, P4, Pz) in accordance with the 10–20 international system [94] located in the occipital and parietal areas as shown in Fig. 8.33a. It is known that the perception of an ambiguous image is associated with an increase in the electrical activity of neurons in the occipital lobe [150, 151]. This effect is explained by the existence of visual areas in the occipital lobe and attentional areas in the parietal lobe [152]. We have estimated the corresponding activity of different frequency bands by means of continuous wavelet transform [116].

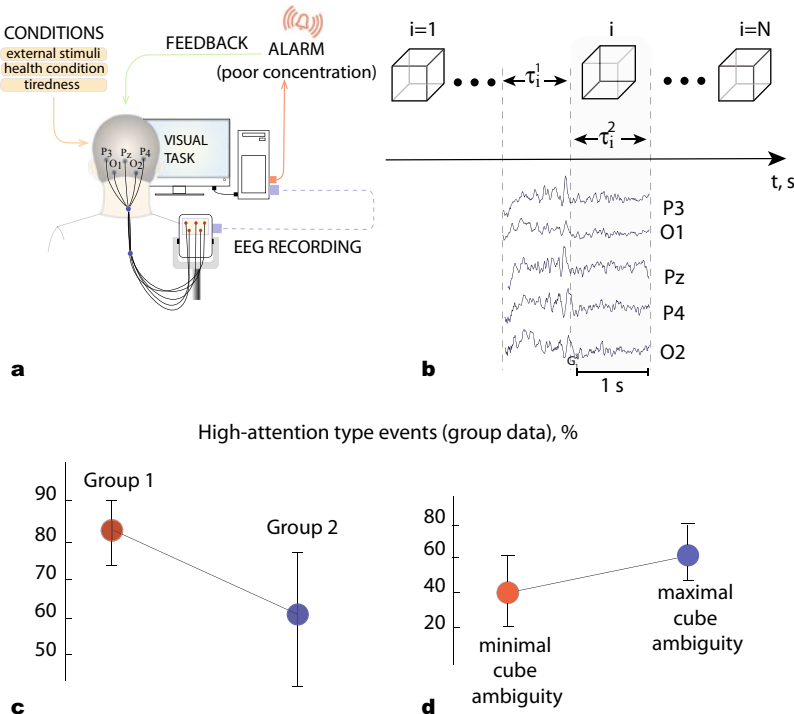


Fig. 8.33 **a** BCI for monitoring and controlling human alertness in real time during the accomplishment of a prolonged task of visual stimuli classification [145]. **b** Temporal scheme of presentation of i -th visual stimuli divided into two time intervals $\tau_i^1 = 1$ s and $\tau_i^2 = 1$ s preceded the presentation of the stimuli and was immediately followed by the stimulus appearance, and typical EEG traces registered in the occipital area during intervals τ_i^1 and τ_i^2 . **c** Illustration of the effect of motivation. Percentage of high-attention events averaged over participants belonging to Group 1 (high motivation; left circle) and Group 2 (low-motivation; right circle). The error bars show the standard deviation for each group. **d** Illustration of the effect of cube ambiguity. Percentage of high-attention events observed in sessions with low (left red circle) and high (right blue circle) ambiguity, averaged over all participants. The error bars indicate the deviation of these values among all participants. Based on data from [145]

The wavelet energy spectra given in (Eq. 8.34) were calculated for each EEG channel $X_n(t)$ in the $f \in [1, 30]$ Hz frequency range. Each event associated with the presentation of a single visual stimulus was analyzed separately in the alpha and beta frequency bands during a 1 s interval preceding the presentation, and followed by the moment of the stimulus appearance (see Fig. 8.33b). A special digital trigger was sent by the software together with the presentation of the stimuli that initiated the calculation.

As a result, the set of values $A_i^1, A_i^2, B_i^1, B_i^2$ were calculated for i th presentation as

$$A_i^{1,2} = \sum_{n=1}^N \int_{t \in \tau_i^{1,2}} \xi^n(t') dt', \text{ where} \quad (8.48)$$

$$\xi^n(t) = \begin{cases} 1, & \text{if } f_{max}^n \in \Delta f_\alpha, \\ 0, & \text{if } f_{max}^n \notin \Delta f_\alpha. \end{cases} \quad (8.49)$$

$$B_i^{1,2} = \sum_{n=1}^N \int_{t \in \tau_i^{1,2}} \xi^n(t') dt', \quad (8.50)$$

$$\text{where } \xi^n(t) = \begin{cases} 1, & \text{if } f_{max}^n \in \Delta f_\beta, \\ 0, & \text{if } f_{max}^n \notin \Delta f_\beta, \end{cases} \quad (8.51)$$

where $N = 5$ is the number of EEG channels and f_{max}^n is the location of the maximal spectral component.

The obtained values quantify neural activity in alpha- and beta-frequency bands which are known to be associated with visual perception [25]. In particular, changes in alpha-activity are associated with visual [153] or auditory attention [154] and changes in beta-activity, with stimuli processing [155] and shifts of the brain to an attention state [156].

The obtained values were averaged over six presentations and the degree of visual attention (DVA) $I(i)$ was calculated as

$$I(i) = \frac{1}{2} ((\alpha_i^1 - \alpha_i^2) + (\beta_i^2 - \beta_i^1)), \quad (8.52)$$

where $\alpha_i^{1,2}$ and $\beta_i^{1,2}$ were obtained as

$$\alpha_i^{1,2} = \frac{1}{6} \sum_{n=i-6}^i A_n^{1,2}, \quad \beta_i^{1,2} = \frac{1}{6} \sum_{n=i-6}^i B_n^{1,2} \quad (8.53)$$

by averaging $A_i^{1,2}$ and $B_i^{1,2}$ values over six presentations.

The value of $I(i)$ calculated using Eqs. 8.48–8.53 in real time reflects the intensity of the brain response on the appearing visual stimuli. Large $I(i)$ is associated with a high response due to more careful image processing by the subject, whereas small $I(i)$ is associated with a low response, which takes place when the subject does not pay much attention on the classification task.

During the experimental sessions the authors observed that the characteristic feature of the state of alertness was a decrease in alpha-energy with a simultaneous increase in beta-energy during the stimulus presentation. To prove that such features of brain activity constitute high attention events, two auxiliary experiments were conducted.

In the first experiment, the authors analysed the effect of motivation. For this purpose, they considered two groups of 10 participants in each. Group 1 consisted of financially motivated subjects, while group 2 was formed by non-motivated subjects. The members of Group 1 had a concrete task, namely, they were asked to identify all Necker cubes as correctly as possible. The members of Group 2 participated in experimental sessions daily at random hours. The solid circles in Fig. 8.33c show the percentage of type-1 events averaged over the participants belonging to Group 1 (left circle) and Group 2 (right circle). One can see that the percentage of high-attention type events varied from 73% to 87% in Group 1 and from 47% to 77% in Group 2, and the averaged percentages were 81% and 62%, respectively. Having compared the mean values of the degree of alertness, the authors found that additional motivation in the first group increased alertness.

In the second experiment, the effect of task complexity on alertness was considered. The participants took part in two sessions. The design of these sessions was practically the same, but the contrast parameter a of the Necker cubes was different. In one session only cubes with low ambiguity ($a = 0.15$ and $a = 0.85$) were presented, whereas in the other session only cubes with high ambiguity ($a = 0.4, 0.5, 0.6$) were shown. As you can see in Fig. 8.33d, an increase in subject alertness estimated by the number of high-attention type events was observed during the second session.

Thus, we estimate the subject's attention span not by counting the number of high-attention events, but by using the DVA, $I(t)$ (Eq. 8.52), which is more convenient for creating an automatic system which operates in real time.

Finally, the authors demonstrated the possibility to estimate human alertness in real time via a BCI (Fig. 8.33a). The experiment lasted 12 min and was divided into three sessions (4 min each). The experimental results are illustrated in Fig. 8.34a, b. The left and right arrows indicate, respectively, the moments of time, t_{EP} and t_{FB} , when the external influence and the feedback control were switched on. These moments divided the experiment into three sections. During the first session, stimuli were presented to each subject seated in comfortable conditions in the absence of any additional tasks. In the first part ($t < t_{EP}$), the subjects performed the task in the absence of external influence. One can see that $I(t)$ fluctuated near a certain mean value of $I_{1,2,3}^1$, individual for each subject. The second session ($t_{EP} < t < t_{FB}$) included external influence on the subject in the form of an additional cognitive task. It is easy to see that when external influence took place, the value of $I(t)$ sharply decreased for all subjects and oscillated near the mean value $I_{1,2,3}^2$, significantly lower than the mean in the first section.

Finally, the third section that started at ($t = t_{FB}$) showed the effect of feedback control, when the subject received a short audio stimulus, sent each time the value of $I(t)$ fell below the threshold level which was estimated for each subject based on the values of $I_{1,2,3}^1$. One can see that in the presence of feedback control, $I(t)$ significantly increased for all subjects and oscillated near the mean values $I_{1,2,3}^3$. It is important to note that a significant change in $I(t)$ was observed within a relatively short time interval (less than 30 s) during which the visual stimulus was presented

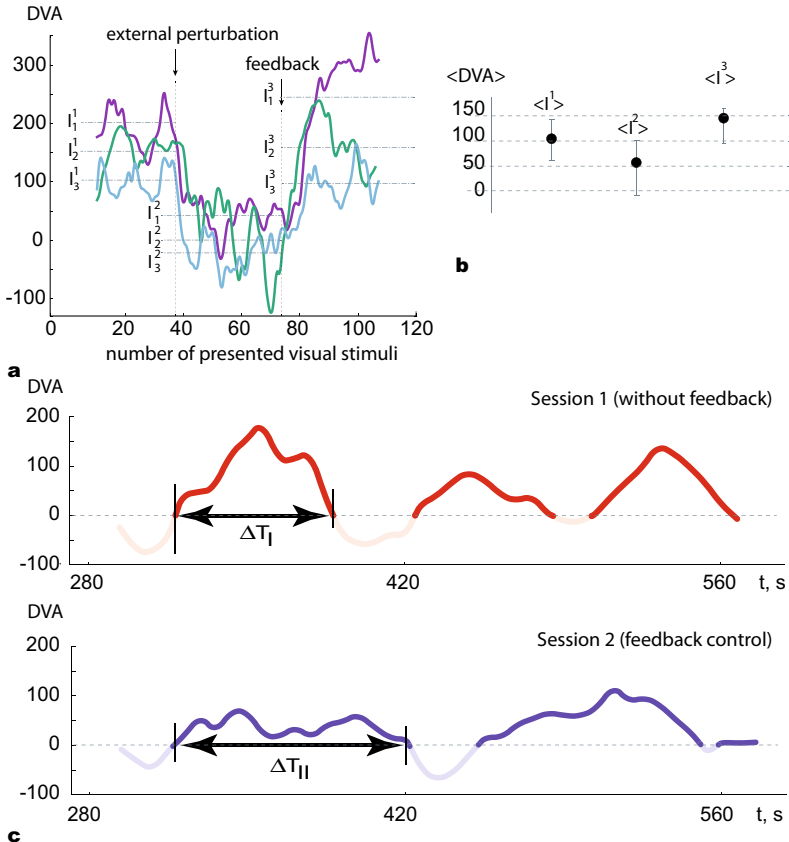


Fig. 8.34 a Control characteristics $I_{1,2,3}(t)$ describing the DVA during the processing of visual stimuli, obtained from three subjects of the group. The vertical dashed lines indicate the moments of time when the external disturbance (t_{EP}) was applied and the feedback message about the attention decrease (t_{FB}) was sent. The horizontal dash-dotted lines indicate the values of DVA $I_{1,2,3}^1$, $I_{1,2,3}^2$, $I_{1,2,3}^3$ calculated by averaging $I_{1,2,3}(t)$ over time intervals $t < t_{EP}$, $t_{EP} > t > t_{FB}$ and $t > t_{FB}$. b DVA $\langle I_{1,2,3}^1 \rangle$, $\langle I_{1,2,3}^2 \rangle$ and $\langle I_{1,2,3}^3 \rangle$ averaged over the group of eight subjects. The error bars indicate the standard deviation of these values among all participants. Based on data from [145]. c DVA temporal evolution estimated for a session without feedback (upper panel) and with feedback (lower panel). Based on data from [97]

about 5 times. This means that significant loss of attention can be promptly detected and controlled in real time.

Having considered the evolution of alertness, the authors found that the alertness degree fluctuates in time. Time intervals of high alertness ($I > 0$) alternate with intervals of low alertness ($I < 0$) with an average period of $T = 150$ s (Fig. 8.34c, upper panel). In order to control the degree of alertness, the authors implemented biological feedback [97]. As soon as the subject was starting to fall asleep, an audio

alarm woke him/her up, which resulted in an increase of attention. Having compared the experimental results with and without feedback control, the authors concluded that feedback enlarged intervals of high alertness, but did not affect the mean degree of alertness during the session. Typical dependencies of the alertness degree on time are shown in Fig. 8.34c for sessions without feedback (upper panel) and with feedback (lower panel). One can see that while the duration of the intervals with $I > 0$ increases in the presence of feedback $\Delta T_{II} > \Delta T_I$, the mean value of I is lower than without feedback. According to this, we can conclude that the brain's cognitive resource is limited, and therefore, to maintain high performance for a prolonged time the brain needs, from time to time, to switch to a “safe-mode” regime of low-energy activity.

8.5.2 *Brain-to-Brain Interface for Enhancing Human Performance by Sharing Cognitive Load*

In the previous section we considered the possibility of alertness monitoring and controlling through DVA estimations by mathematically processing Eqs. 8.48–8.53 EEG recordings in real time. Based on these results there exists a promising way to increase the cognitive performance of healthy humans via a direct interaction between their brains. While a traditional BCI described in the previous section is aimed at increasing human performance with the assistance of a computer, a brain-to-brain interface (B2BI) can use the cognitive resource of one human to increase the performance of another human in solving cognitive tasks. This is of particular importance for people performing together a common working task requiring sustained attention and alertness. The first attempt to implement B2BI for increasing human cognitive performance was made in 2018 [157]. A schematic illustration of the proposed B2BI is shown in Fig. 8.35.

Two participants were subjected to a prolonged (approximately 40 min) task on classification of ambiguous visual stimuli with different degrees of ambiguity. The whole set of ambiguous stimuli was divided into two subsets: images with low ambiguity and images with high ambiguity. The classification of weakly ambiguous images was judged as a low complexity task (LCT), whereas the classification of highly ambiguous images was considered a high complexity task (HCT).

During the session, the DVA was estimated for each participant based on the mathematical procedure described by Eqs. 8.48–8.53. DVA was considered a factor which characterises human performance during this classification task. The task was distributed between two partners depending on individual DVA scores; the subject with a higher DVA received a higher complexity part, while his/her partner received a lower complexity part.

With the proposed B2BI, two experiments were conducted for six pairs. In the first experiment, the task was distributed based on the instantaneous DVA of the participants. In the second experiment, there was a delay in the coupling between

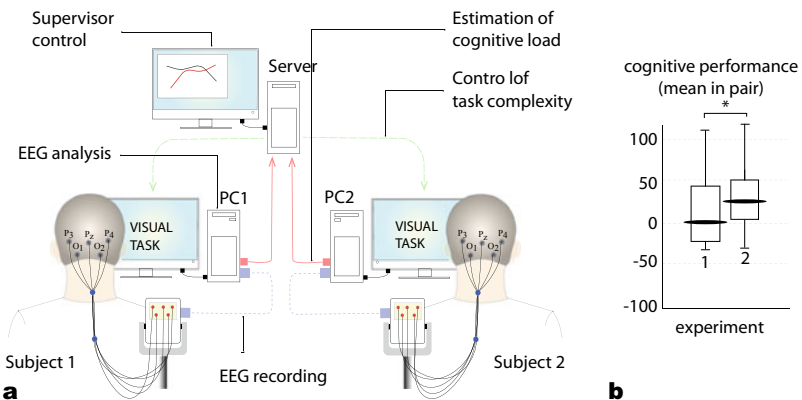


Fig. 8.35 B2BI for sharing cognitive load between two subjects in accordance with their current levels of cognitive performance estimated from EEG signals. Based on data from [157]

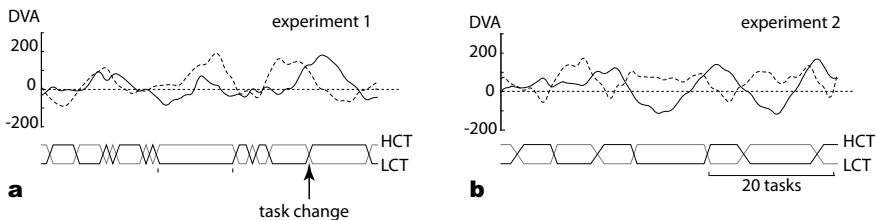


Fig. 8.36 Results of **a** experiment 1 and **b** experiment 2. (Upper traces) Evolution of DVA of each subject in pair. (Lower traces) Switches between two sets of visual stimuli (HCT and LCT). The arrow shows the single switch between HCT and LCT. Reprinted from [107] ©2021 with permission from Elsevier

the subjects, if the difference in DVA between subject 1 and subject 2 became higher than 10%, the partner with higher DVA received the higher complexity part.

In order to evaluate the effect of cognitive load distribution on cognitive performance, the mean DVA was calculated by averaging the whole experimental session. Figure 8.35b demonstrates the comparison between the mean DVA in the pair of two experiments. During experiment 1, the mean DVA was close to zero, while during experiment 2 the mean DVA was significantly increased for all pairs. To understand the changes in the DVA, the authors considered the evolution of DVA in time for both experiments. The time series illustrating the evolution of DVA are presented in Fig. 8.36 for both experiments. One can see that DVA evolves periodically. The intervals with high DVA are replaced by intervals with low DVA. The latter is associated with stages of cognitive fatigue, which require some time for restoring cognitive resource. In experiment 2 (Fig. 8.36b), where the mean DVA is increased, the DVA of the two participants are anti-phase synchronized. The DVA of one of the subjects achieves high values while the other subject exhibits cognitive fatigue and vice versa. In experiment 1, DVA are not synchronized (Fig. 8.36a). Thus, a delay in

experiment 2 led to an optimal mode of the task redistribution. The authors concluded that DVA oscillated with a certain period, which was determined by entire cognitive processes. Therefore, the performance of a common task by a working team can be improved if the task is distributed among the team members according to their brain rhythms. Otherwise, it caused a lot of extra switching interfering with synchronisation between DVAs.

References

1. Heekeren HR, Marrett S, Bandettini PA, Ungerleider LG (2004) A general mechanism for perceptual decision-making in the human brain. *Nature* 431(7010):859
2. Davison EN, Schlesinger KJ, Bassett DS, Lynall ME, Miller MB, Grafton ST, Carlson JM (2015) Brain network adaptability across task states. *PLoS Comput Biol* 11(1):e1004029
3. Parks EL, Madden DJ (2013) Brain connectivity and visual attention. *Brain Connect* 3(4):317–338
4. Shine JM, Poldrack RA (2018) Principles of dynamic network reconfiguration across diverse brain states. *NeuroImage* 180:396–405
5. Smith S (2016) Linking cognition to brain connectivity. *Nat Neurosci* 19(1):7
6. Hramov AE, Frolov NS, Maksimenko VA, Kurkin SA, Kazantsev VB, Pisarchik AN (2021) Functional networks of the brain: From connectivity restoration to dynamic integration. *Phys-Uspekhi* 64(6):584
7. Van Den Heuvel MP, Pol HEH (2010) Exploring the brain network: a review on resting-state fMRI functional connectivity. *Eur Neuropsychopharmacol* 20(8):519–534
8. Xu J, Potenza MN, Calhoun VD (2013) Spatial ICA reveals functional activity hidden from traditional fMRI GLM-based analyses. *Front Neurosci* 7:154
9. Rosenberg MD, Finn ES, Scheinost D, Papademetris X, Shen X, Constable RT, Chun MM (2016) A neuromarker of sustained attention from whole-brain functional connectivity. *Nat Neurosci* 19(1):165
10. Li J, Lim J, Chen Y, Wong K, Thakor N, Bezerianos A, Sun Y (2016) Mid-task break improves global integration of functional connectivity in lower alpha band. *Front Hum Neurosci* 10:304
11. Finc K, Bonna K, Lewandowska M, Wolak T, Nikadon J, Dreszer J, Duch W, Kühn S (2017) Transition of the functional brain network related to increasing cognitive demands. *Hum Brain Mapp* 38(7):3659–3674
12. Atteneave F (1971) Multistability in perception. *Sci Am* 225:63–71
13. Blake R (1989) A neural theory of binocular rivalry. *Psychol Rev* 96(1):145
14. Sterzer P, Kleinschmidt A, Rees G (2009) The neural bases of multistable perception. *Trends Cogn Sci* 13(7):310–318
15. Leopold DA, Logothetis NK (1999) Multistable phenomena: changing views in perception. *Trends Cogn Sci* 3(7):254–264
16. Fries P (2015) Rhythms for cognition: communication through coherence. *Neuron* 88(1):220–235
17. Lisman JE, Jensen O (2013) The theta-gamma neural code. *Neuron* 77(6):1002–1016
18. Canolty RT, Edwards E, Dalal SS, Soltani M, Nagarajan SS, Kirsch HE, Berger MS, Barbaro NM, Knight RT (2006) High gamma power is phase-locked to theta oscillations in human neocortex. *Science* 313(5793):1626–1628
19. Maksimenko VA, Lütjohann A, Makarov VV, Goremyko MV, Koronovskii AA, Nedai佐 V, Runnova AE, van Luijtelaar G, Hramov AE, Boccaletti S (2017) Macroscopic and microscopic spectral properties of brain networks during local and global synchronization. *Phys Rev E* 96(1):012316

20. Michalareas G, Vezoli J, Van Pelt S, Schoffelen JM, Kennedy H, Fries P (2016) Alpha-beta and gamma rhythms subserve feedback and feedforward influences among human visual cortical areas. *Neuron* 89(2):384–397
21. Buffalo EA, Fries P, Landman R, Buschman TJ, Desimone R (2011) Laminar differences in gamma and alpha coherence in the ventral stream. *Proc Nat Acad Sci* 108(27):11262–11267
22. Frolov N, Maksimenko V, Hramov A (2020) Revealing a multiplex brain network through the analysis of recurrences. *Chaos* 30(12):121108
23. Pisarchik AN, Maksimenko VA, Andreev AV, Makarov VV, Zhuravlev MO, Frolov NS, Runnova AE, Hramov AE (2019) Coherent resonance in the distributed cortical network during sensory information. *Sci Rep* 9:18325
24. Frolov NS, Maksimenko VA, Khramova MV, Pisarchik AN, Hramov AE (2019) Dynamics of functional connectivity in multilayer cortical brain network during sensory information processing. *Eur Phys J: Spec Top* 228(11):2381–2389
25. Maksimenko VA, Runnova AE, Frolov NS, Makarov VV, Nedaivozov V, Koronovskii AA, Pisarchik A, Hramov AE (2018) Multiscale neural connectivity during human sensory processing in the brain. *Phys Rev E* 97(5):052405
26. Maksimenko VA, Frolov NS, Hramov AE, Runnova AE, Grubov VV, Kurths J, Pisarchik AN (2019) Neural interactions in a spatially-distributed cortical network during perceptual decision-making. *Front Behav Neurosci* 13:220
27. Helfrich RF, Huang M, Wilson G, Knight RT (2017) Prefrontal cortex modulates posterior alpha oscillations during top-down guided visual perception. *Proc Nat Acad Sci* 114(35):9457–9462
28. Sellers KK, Yu C, Zhou ZC, Stitt I, Li Y, Radtke-Schuller S, Alagapan S, Fröhlich F (2016) Oscillatory dynamics in the frontoparietal attention network during sustained attention in the ferret. *Cell Rep* 16(11):2864–2874
29. Scolari M, Seidl-Rathkopf KN, Kastner S (2015) Functions of the human frontoparietal attention network: Evidence from neuroimaging. *Curr Opin Behav Sci* 1:32–39
30. Clayton MS, Yeung N, Kadosh RC (2015) The roles of cortical oscillations in sustained attention. *Trends Cogn Sci* 19(4):188–195
31. Schwartz JL, Grimault N, Hupé JM, B C J Moore CJ, Pressnitzer D, (2012) Multistability in perception: sensory modalities, an overview. *Philos Trans R Soc B* 367:896–905
32. Dutour É (1760) Discussion d'une question d'optique. l'académie des sciences. Mémoires de mathématique et de physique présentés par divers Savants 3:514–530
33. Rubin E (1915) Synsoplevede Figurer: Studier i Psykologisk Analyse. Gyldendal, Nordisk forlag
34. Scott A (1999) Stairway to the mind: the controversial new science of consciousness. Springer Science & Business Media
35. Necker LA (1832) Lxi. observations on some remarkable optical phænomena seen in switzerland; and on an optical phænomenon which occurs on viewing a figure of a crystal or geometrical solid. London, Edinburgh Dublin Philos Mag J Sci 1(5):329–337
36. Campbell F, Gilinsky A, Howell E, Riggs L, Atkinson J (1973) The dependence of monocular rivalry on orientation. *Perception* 2(2):123–125
37. Blake R, Logothetis NK (2002) Visual competition. *Nat Rev Neurosci* 3(1):13–21
38. Walker P (1975) Stochastic properties of binocular rivalry alternations. *Percept Psychophys* 18(6):467–473
39. Warren RM, Gregory RL (1958) An auditory analogue of the visual reversible figure. *Am J Psychol*
40. Pressnitzer D, Hupé JM (2006) Temporal dynamics of auditory and visual bistability reveal common principles of perceptual organization. *Curr Biol* 16(13):1351–1357
41. Denham SL, Winkler I (2006) The role of predictive models in the formation of auditory streams. *J Physiol Paris* 100(1–3):154–170
42. Kashino M, Okada M, Mizutani S, Davis P, Kondo HM (2007) The dynamics of auditory streaming: psychophysics, neuroimaging, and modeling. In: Hearing—from sensory processing to perception. Springer, Berlin, pp 275–283

43. Sato M, Schwartz JL, Abry C, Cathiard MA, Loevenbruck H (2006) Multistable syllables as enacted percepts: a source of an asymmetric bias in the verbal transformation effect. *Percept Psychophys* 68(3):458–474
44. Yu C, Li J, Liu Y, Qin W, Li Y, Shu N, Jiang T, Li K (2008) White matter tract integrity and intelligence in patients with mental retardation and healthy adults. *Neuroimage* 40(4):1533–1541
45. Repp BH (2007) Hearing a melody in different ways: Multistability of metrical interpretation, reflected in rate limits of sensorimotor synchronization. *Cognition* 102:434–454
46. Repp BH, Iversen JR, Patel AD (2008) Tracking an imposed beat. *Music Percept* 26:1–18
47. Brosowsky NP, Mondor TA (2016) Multistable perception of ambiguous melodies and the role of musical expertise. *J Acoust Soc Am* 140(2):866–877
48. Deutsch D (1974) An illusion with musical scales. *J Acoust Soc Am* 56(S1):S25–S25
49. Radvansky GA, Hartmann WM, Rakcer B (1992) Structural alterations of an ambiguous musical figure: the scale illusion revisited. *Percept Psychophys* 52(3):256–262
50. Smith J, Hausfeld S, Power RP, Gortat A (1982) Ambiguous musical figures and auditory streaming. *Percept Psychophys* 32(5):454–464
51. Deutsch D (1975) Two-channel listening to musical scales. *J Acoust Soc Am* 57(5):1156–1160
52. Carter O, Konkle T, Wang Q, Hayward V, Moore C (2008) Tactile rivalry demonstrated with an ambiguous apparent-motion quartet. *Curr Biol* 18(14):1050–1054
53. Zhou W, Chen D (2009) Binalar rivalry between the nostrils and in the cortex. *Curr Biol* 19(18):1561–1565
54. Hebb DO (1949) The organization of behavior. Wiley, New York
55. Köhler W, Wallach H (1944) Figural after-effects, an investigation of visual processes. *Proc Am Phil Soc* 88:269–357
56. Burns BD (1968) The uncertain nervous system. Edward Arnold, London
57. Deco G, Jirsa VK, McIntosh AR, Sporns O, Kötter R (2009) Key role of coupling, delay, and noise in resting brain fluctuatiions. *Proc Natl Acad Sci USA* 106(25):10302–10307
58. Kanai R, Moradi F, Shimojo S, Verstraten FAJ (2005) Perceptual alternation induced by visual transients. *Perception* 34:803–822
59. Carter OL, Pettigrew JD (2003) A common oscillator for perceptual rivalries? *Perception* 32(3):295–305
60. Brascamp JW, van Ee R, Noest AJ, Jacobs RHAH, van den Berg AV (2006) The time course of binocular rivalry reveals a fundamental role of noise. *J Vis* 6(11):8
61. Dotov DG, Turvey MT, Frank TD (2019) Embodied gestalts: Unstable visual phenomena become stable when they are stimuli for competitive action selection. *Atten Percept Psychophys* 81:2330–2342
62. Moreno-Bote R, Rinzel J, Rubin N (2007) Noise-induced alternations in an attractor network model of perceptual bistability. *J Neurophysiol* 98:1125–1139
63. Shpiro A, Moreno-Bote R, Rubin N, Rinzel J (2009) Balance between noise and adaptation in competition models of perceptual bistability. *J Comput Neurosci* 27(1):37–54
64. Meilikhov EZ, Farzettinova RM (2019) Bistable perception of ambiguous images: simple Arrhenius model. *Cogn Neurodyn* 13:613–621
65. Gigante G, Mattia M, Braun J, Del Giudice P (2009) Bistable perception modeled as competing stochastic integrations at two levels. *PLoS Comput Biol* 5:e1000430
66. Kelso JAS (1997) Dynamic patterns: the self-organization of brain and behavior. A Bradford Book
67. Runnova AE, Hramov AE, Grubov VV, Koronovskii AA, Kurovskaya MK, Pisarchik AN (2016) Theoretical background and experimental measurements of human brain noise intensity in perception of ambiguous images. *Chaos Solitons Fractals* 93:201–206
68. Pisarchik AN, Chholak P, Hramov AE (2019) Brain noise estimation from MEG response to flickering visual stimulation. *Chaos Solit Fractals: X* 1:100005
69. Boccaletti S, Pisarchik AN, del Genio I, Amann A (2018) Synchronization: from coupled systems to complex networks. Cambridge University Press, Cambridge

70. Boccaletti S, Bianconi G, Criado R, del Genio CI, Gómez-Gardeñes J, Romance M, Sendiña Nadal I, Wang Z, Zanin M (2014) The structure and dynamics of multilayer networks. *Phys Rep* 544:1–122
71. Pisarchik AN, Jaimes-Reátegui R, Magallón-García CDA, Castillo-Morales CO (2014) Critical slowing down and noise-induced intermittency in bistable perception: bifurcation analysis. *Biol Cybern* 108(4):397–404
72. Poston T, Stewart I (1978) Catastrophe theory and its applications. Pitman
73. Wixted JT, Thompson-Schill SL (2018) Stevens' handbook of experimental psychology and cognitive neuroscience, language and thought, vol 3. Wiley, New York
74. Lago-Fernández LF, Deco G (2002) A model of binocular rivalry based on competition in IT. *Neurocomputing* 44–46:503–507
75. Laing CR, Chow CC (2002) A spiking neuron model based for binocular rivalry. *J Comput Neurosci* 12:39–53
76. Wilson HR, Blake R, Lee SH (2001) Dynamics of travelling waves in visual perception. *Nature* 412(6850):907–910
77. Huguet G, Rinzel J, Hupe JM (2014) Noise and adaptation in multistable perception: Noise drives when to switch, adaptation determines percept choice. *J Vis* 14(3):19
78. Urakawa T, Bunya M, Araki O (2017) Involvement of the visual change detection process in facilitating perceptual alternation in the bistable image. *Cogn Neurodyn* 11(4):307–318
79. Haken H (2004) Synergetic computers and cognition a top-down approach to neural nets. Springer, Berlin
80. Jaimes-Reátegui R, Magallán-García DA, Gallegos A, Huerta-Cuellar G, García-López JH, Pisarchik AN (2020) Noise-induced intermittent oscillation death in a synergetic model. *Discontinuity Nonlinearity Complex* 9(1):167–172
81. Chholak P, Hramov AE, Pisarchik AN (2020) An advanced perception model based on brain noise and adaptation. *Nonlinear Dyn* 100:3695–3709
82. Chholak P, Maksimenko VA, Andreev AA, Hramov AE, Pisarchik AN (2020) Voluntary and involuntary attention in bistable visual perception: a MEG study. *Front Hum Neurosci* 14:555
83. Merk I, Schnakenberg J (2002) A stochastic model of multistable visual perception. *Biol Cybern* 86:111–116
84. Pastukhov A, Garcia-Rodriguez PE, Haenicek J, Guillamon A, Deco G, Braun J (2013) Multistable perception balances stability and sensitivity. *Front Comput Neurosci* 7:17
85. Carpenter RHS (2012) Analysing the detail of saccadic reaction time distributions. *Biocybern Biomed Eng* 32(2):49–63
86. Wolberg J (2005) Data analysis using the method of least squares: extracting the most information from experiments. Springer, Berlin
87. Kornmeier J, Bach M (2004) Early neural activity in Necker-cube reversal: evidence for low-level processing of a gestalt phenomenon. *Psychophysiol* 41(1):1–8
88. Kornmeier J, Pfäffle M, Bach M (2011) Necker cube: Stimulus-related (low-level) and percept-related (high-level) EEG signatures early in occipital cortex. *J Vis* 11(9):12–12
89. Joos E, Giersch A, Hecker L, Schipp J, Heinrich SP, Tebartz van Elst L, Kornmeier J (2020) Large EEG amplitude effects are highly similar across Necker cube, smiley, and abstract stimuli. *PloS One* 15(5):e0232928
90. Bach M, Meigen T (1992) Electrophysiological correlates of texture segregation in the human visual evoked potential. *Vis Res* 32(3):417–424
91. Kornmeier J, Bach M (2014) EEG correlates of perceptual reversals in Boring's ambiguous old/young woman stimulus. *Perception* 43(9):950–962
92. Giromini L, Porcelli P, Viglione DJ, Parolin L, Pineda JA (2010) The feeling of movement: EEG evidence for mirroring activity during the observations of static, ambiguous stimuli in the Rorschach cards. *Biol Psychol* 85(2):233–241
93. Gill HS, O'Boyle MW (2003) Generating an image from an ambiguous visual input: An electroencephalographic (EEG) investigation. *Brain Cogn* 51(3):287–293
94. Campbell IG (2009) EEG recording and analysis for sleep research. *Curr Protoc Neurosci* 10

95. Hramov AE, Maksimenko VA, Pchelintseva SV, Runnova AE, Grubov VV, Musatov VY, Zhuravlev MO, Koronovskii AA, Pisarchik AN (2017) Classifying the perceptual interpretations of a bistable image using EEG and artificial neural networks. *Front Neurosci* 11:674
96. Hramov AE, Maksimenko VA, Koronovskii AA, Runnova AE, Zhuravlev MO, Pisarchik AN, Kurths J (2019) Percept-related EEG classification using machine learning approach and features of functional brain connectivity. *Chaos* 29:093110
97. Maksimenko VA, Hramov AE, Grubov VV, Nedaivozov VO, Makarov VV, Pisarchik AN (2019) Nonlinear effect of biological feedback on brain attentional state. *Nonlinear Dyn* 95(3):1923–1939
98. Maksimenko VA, Kuc A, Frolov NS, Kramova MV, Pisarchik AN, Hramov AE (2020) Dissociating cognitive processes during ambiguous information processing in perceptual decision-making. *Front Behav Neurosci* 14:95
99. Maksimenko V, Kuc A, Frolov N, Kurkin S, Hramov A (2021) Effect of repetition on the behavioral and neuronal responses to ambiguous necker cube images. *Sci Rep* 11(1):1–13
100. Kuc AK, Kurkin SA, Maksimenko VA, Pisarchik AN, Hramov AE (2021) Monitoring brain state and behavioral performance during repetitive visual stimulation. *Appl Sci* 11(23):11544
101. Henson R, Rugg M (2003) Neural response suppression, haemodynamic repetition effects, and behavioural priming. *Neuropsychologia* 41(3):263–270
102. Wiggs CL, Martin A (1998) Properties and mechanisms of perceptual priming. *Curr Opin Neurobiol* 8(2):227–233
103. Henson RN, Price CJ, Rugg MD, Turner R, Friston KJ (2002) Detecting latency differences in event-related BOLD responses: application to words versus nonwords and initial versus repeated face presentations. *Neuroimage* 15(1):83–97
104. Luft CDB, Zioga I, Thompson NM, Banissy MJ, Bhattacharya J (2018) Right temporal alpha oscillations as a neural mechanism for inhibiting obvious associations. *Proc Nat Acad Sci* 115(52):E12144–E12152
105. Laukkonen RE, Tangen JM (2017) Can observing a Necker cube make you more insightful? *Conscious Cogn* 48:198–211
106. Zander TO, Kothe C (2011) Towards passive brain-computer interfaces: applying brain-computer interface technology to human-machine systems in general. *J Neural Eng* 8(2):025005
107. Hramov AE, Maksimenko VA, Pisarchik AN (2021) Physical principles of brain-computer interfaces and their applications for rehabilitation, robotics and control of human brain states. *Phys Rep* 918:1–133
108. Mostert P, Kok P, de Lange FP (2015) Dissociating sensory from decision processes in human perceptual decision making. *Sci Rep* 5(1):1–13
109. Ramos AM, Builes-Jaramillo A, Poveda G, Goswami B, Macau EE, Kurths J, Marwan N (2017) Recurrence measure of conditional dependence and applications. *Phys Rev E* 95(5):052206
110. Stefan H, Trinka E (2017) Magnetoencephalography (MEG): past, current and future perspectives for improved differentiation and treatment of epilepsies. *Seizure* 44:121–124
111. Supek S, Aine CJ (2016) Magnetoencephalography. Springer, Berlin
112. Zimmerman JE, Thiene P, Harding JT (1993) Design and operation of stable rf-biased superconducting point-contact quantum devices, and a note on the properties of perfectly clean metal contacts. *J Appl Phys* 41(4):1572–1580
113. Chholak P, Kurkin SA, Hramov AE, Pisarchik AN (2021) Event-related coherence in visual cortex and brain noise: an MEG study. *Appl Sci* 11(1):375
114. Hramov AE, Frolov NS, Maksimenko VA, Makarov VV, Koronovskii AA, García-Prieto J, Antón-Toro LF, Maestú F, Pisarchik AN (2018) Artificial neural network detects human uncertainty. *Chaos* 28(3):033607
115. Leopold DA, Wilke M, Maier A, Logothetis NK (2002) Stable perception of visually ambiguous patterns. *Nat Neurosci* 5:605–609
116. Hramov AE, Koronovskii AA, Makarov VA, Pavlov AN, Sitnikova E (2015) Wavelets in neuroscience. Springer, Heidelberg

117. Sitnikova E, Hramov AE, Grubov V, Koronovsky AA (2014) Time-frequency characteristics and dynamics of sleep spindles in WAG/Rij rats with absence epilepsy. *Brain Res* 1543:290–299
118. Mitchell JF, Stoner GR, Reynolds JH (2004) Object-based attention determines dominance in binocular rivalry. *Nature* 429(6990):410–413
119. Bialek W, DeWeese M (1995) Random switching and optimal processing in the perception of ambiguous signals. *Phys Rev Lett* 74(15):3077
120. Niso G, Krol L, Combrisson E, Dubarry AS, Elliott M, François C, Héjja-Brichard Y, Herbst S, Jerbi K, Kovac V, et al (2021) Good scientific practice in MEEG research: progress and perspectives. *OSF Preprints* <https://doi.org/10.31219/osf.io/n2ryp>
121. Strüber D, Baar-Eroglu C, Miener M, Stadler M (2001) EEG gamma-band response during the perception of Necker cube reversals. *Vis Cogn* 8(3–5):609–621
122. Mathes B, Strüber D, Stadler MA, Basar-Eroglu C (2006) Voluntary control of Necker cube reversals modulates the EEG delta-and gamma-band response. *Neurosci Lett* 402(1–2):145–149
123. Donner TH, Siegel M, Fries P, Engel AK (2009) Buildup of choice-predictive activity in human motor cortex during perceptual decision making. *Curr Biol* 19(18):1581–1585
124. Lotte F, Bougrain L, Cichocki A, Clerc M, Congedo M, Rakotomamonjy A, Yger F (2018) A review of classification algorithms for EEG-based brain-computer interfaces: a 10 year update. *J Neural Eng* 15(3):031005
125. Lotte F, Congedo M, Lécuyer A, Lamarche F, Arnaldi B (2007) A review of classification algorithms for EEG-based brain-computer interfaces. *J Neural Eng* 4(2):R1
126. Haykin S (2008) Neural networks: a comprehensive foundation, 3rd edn. Pearson
127. Baptista D, Abreu S, Freitas F, Vasconcelos R, Morgado-Dias F (2013) A survey of software and hardware use in artificial neural networks. *Neural Comput Appl* 23(3):591–599
128. Helmstaedter M (2015) The mutual inspirations of machine learning and neuroscience. *Neuron* 86(1):25–28
129. Kuc A, Korchagin S, Maksimenko VA, Shusharina N, Hramov AE (2021a) Combining statistical analysis and machine learning for EEG scalp topograms classification. *Front Syst Neurosci* 15
130. Haselsteiner E, Pfurtscheller G (2000) Using time-dependent neural networks for EEG classification. *IEEE Trans Rehabil Eng* 8(4):457–463
131. Masquelier T, Guyonneau R, Thorpe SJ (2009) Competitive STDP-based spike pattern learning. *Neural Comput* 21(5):1259–1276
132. Grassia F, Levi T, Doukkali E, Kohno T (2018) Spike pattern recognition using artificial neuron and spike-timing-dependent plasticity implemented on a multi-core embedded platform. *Artif Life Robot* 23(2):200–204
133. Frolov NS, Pisarchik AN (2018) Diagnostics of the brain neural-ensemble states using MEG records and artificial neural-network concepts. *Tech Phys Lett* 44(5):441–444
134. Strutz T (2016) Data fitting and uncertainty (A practical introduction to weighted least squares and beyond), 2nd edn. Springer, Berlin
135. Zhang Z, Vanderhaegen F, Millot P (2006) Prediction of human behaviour using artificial neural networks. In: Advances in machine learning and cybernetics, Springer, Berlin, pp 770–779
136. Mapp AP, Ono H, Barbeito R (2003) What does the dominant eye dominate? a brief and somewhat contentious review. *Atten Percept Psychophys* 65(2):310–317
137. Chokron S, De Agostini M (1995) Reading habits and line bisection: A developmental approach. *Brain Res Cogn Brain Res* 3(1):51–58
138. Nicholls ME, Roberts GR (2002) Can free-viewing perceptual asymmetries be explained by scanning, pre-motor or attentional biases? *Cortex* 38(2):113–136
139. Mackworth NH (1948) The breakdown of vigilance during prolonged visual search. *Q J Exp Psychol* 1(1):6–21
140. Makeig S, Elliott FS, Postal M (1994) First demonstration of an alertness monitoring management system. Naval Health Research Center (Report No. 93–36):21

141. Vuckovic A, Radivojevic V, Chen AC, Popovic D (2002) Automatic recognition of alertness and drowsiness from EEG by an artificial neural network. *Med Eng Phys* 24(5):349–360
142. Pal NR, Chuang CY, Ko LW, Chao CF, Jung TP, Liang SF, Lin CT (2008) EEG-based subject- and session-independent drowsiness detection: an unsupervised approach. *EURASIP J Adv Signal Process* 2008:519480
143. Hsu SH, Jung TP (2017) Monitoring alert and drowsy states by modeling EEG source non-stationarity. *J Neural Eng* 14(5):056012
144. Ko LW, Komarov O, Hairston WD, Jung TP, Lin CT (2017) Sustained attention in real classroom settings: an EEG study. *Front Hum Neurosci* 11:388
145. Maksimenko VA, Runnova AE, Zhuravlev MO, Nedaivozov V, Grubov VV, Pchelintseva SV, Hramov AE, Pisarchik AN (2017) Visual perception affected by motivation and alertness controlled by a noninvasive brain-computer interface. *PloS One* 12(12):1–20
146. Fazli S, Mehnert J, Steinbrink J, Curio G, Villringer A, Müller KR, Blankertz B (2012) Enhanced performance by a hybrid NIRS-EEG brain computer interface. *Neuroimage* 59(1):519–529
147. Khan MJ, Hong MJ, Hong KS (2014) Decoding of four movement directions using hybrid NIRS-EEG brain-computer interface. *Front Hum Neurosci* 8:244
148. Khan MJ, Hong KS (2015) Passive BCI based on drowsiness detection: an fNIRS study. *Biomed Opt Exp* 6(10):4063–4078
149. von Lüthmann A, Wabnitz H, Sander T, Müller KR (2017) M3BA: a mobile, modular, multi-modal biosignal acquisition architecture for miniaturized EEG-NIRS-based hybrid BCI and monitoring. *IEEE Trans Biomed Eng* 64(6):1199–1210
150. Mulckhuyse M, Kelley TA, Theeuwes J, Walsh V, Lavie N (2011) Enhanced visual perception with occipital transcranial magnetic stimulation. *Eur J Neurosci* 34(8):1320–1325
151. Gleiss S, Kayser C (2014) Acoustic noise improves visual perception and modulates occipital oscillatory states. *J Cogn Neurosci* 26(4):699–711
152. Laufs H, Holt JL, Elfond R, Krams M, Paul JS, Krakow K, Kleinschmidt A (2006) Where the BOLD signal goes when alpha EEG leaves. *Neuroimage* 31(4):1408–1418
153. Sauseng P, Klimesch W, Stadler W, Schabus M, Doppelmayr M, Hanslmayr S, Gruber WR, Birbaumer N (2005) A shift of visual spatial attention is selectively associated with human eeg alpha activity. *Eur J Neurosci* 22(11):2917–2926
154. Foxe JJ, Snyder AC (2011) The role of alpha-band brain oscillations as a sensory suppression mechanism during selective attention. *Front Psychol* 2:154
155. Sehatpour P, Molholm S, Schwartz TH, Mahoney JR, Mehta AD, Javitt DC, Stanton PK, Foxe JJ (2008) A human intracranial study of long-range oscillatory coherence across a frontal-occipital-hippocampal brain network during visual object processing. *Proc Nat Acad Sci* 105(11):4399–4404
156. Wróbel A (2000) Beta activity: a carrier for visual attention. *Acta Neurobiol Exp* 60(2):247–260
157. Maksimenko VA, Hramov AE, Frolov NS, Lüttjohann A, Nedaivozov VO, Grubov VV, Runnova AE, Makarov VV, Kurths J, Pisarchik AN (2018a) Increasing human performance by sharing cognitive load using brain-to-brain interface. *Front Neurosci* 12

Chapter 9

Concluding Remarks



Multistability or coexistence of different attractors for a given set of parameters is one of the fundamental properties of nonlinear dynamical systems. Along with the phenomenon of dynamical chaos, multistability is an important source of complexity and unpredictability in the dynamics of complex systems, when even tiny fluctuations or inaccurate parameter settings can lead to a dramatic change in the system dynamics. The final state of a multistable system crucially depends on initial conditions. Noise in a multistable system spontaneously changes the system state, resulting in multistate intermittency. As a consequence, in applied technical problems this phenomenon often causes inconvenience, for example, when designing a commercial device with specific characteristics, when multistability must be avoided or the desired state needs to be stabilized in a noisy environment. On the other hand, multistability can also be a boon when the coexistence of different stable states provides more flexibility in the system operation.

Thus, without significant changes in parameters, using smart strategies to affect a multistable system, it is possible to induce switching between different coexisting states, realizing the desired state at each moment of time. Living systems, apparently, have learned to masterfully control multistability. This is particularly evident in brain dynamics, which exhibits multistable coordination dynamics at many levels, from multifunctional neural circuits in vertebrates and invertebrates to large-scale neural circuits in humans. Moreover, multistability encompasses the areas of perception and decision-making, as detailed in our book. This multistability imposes strong constraints and even dictates the nature of deliberate changes and the learning process. Scott Kelso [1] suggests that multistability, combined with important aspects of coordination dynamics such as instability, self-organization, and the non-equilibrium phase transitions, provide a platform for understanding cognitive and creative dynamics of complex goal-directed systems, including the brain and brain-behavioral relations.

In our book, we have addressed just a few problems related to multistability which are frequently encountered in modern complex systems theory, and mathematical biology and experimental neuroscience. Even this non-exhaustive review demonstrates beneficial ways and promising perspectives for using multistability ideas in modern multidisciplinary research, including living systems analysis. We focused mainly on theoretical and mathematical issues of analysis, diagnostics, and characteristics of multistability in dynamical systems, dwelling more on the multistability phenomenon in real-world objects such as lasers and human sensory perception and decision-making. However, every month many new papers devoted to the study of multistability appear.

There are still many open problems in the field of multistability which need to be understood, only some of them are mentioned here.

Multistability in quantum systems. One crucial issue is connected with the important problem of coherent control over quantum single- and few-body dynamics, which is a perspective approach to improve atomic, optical, and solid-state systems [2–4]. Coherent driving leads to rich dynamics observed in systems with strong light-matter interactions at the interface between quantum optics and condensed matter [5–7]. Systems with a competition between interactions, nonlinearity, coherent external driving and dissipative dynamics include arrays of coupled circuit quantum electrodynamic units, cold atoms, and ions. Critical phenomena and dissipative phase transitions in these open systems often come with new properties and novel dynamic universality classes [8–11]. For example, Haggai Landa et al. [12] considered the dynamics of lattice models of quantum spins, driven by a coherent drive and subject to dissipation. Using a new approach that accounts for the leading-order lattice correlations and their feedback onto the mean magnetization, the authors showed that bistability appears to be possible in driven-dissipative quantum systems already in 2D. The same conclusion about bistable behaviour in 2D is consistent with works done in the context of Rydberg atoms [13]. For example, Andreev et al. [14] observed multistable behaviour in hyperchaotic driven chain of interacting qubits with dissipation.

Multistability in social interaction models on hypergraphs. How individuals interact in groups has motivated research in many different areas ranging from sociology and political sciences [15] to physics and mathematics, including modern paradigms of high-order interactions [16–18]. In this age of social networks and limitations of normal communication due to the COVID-19 pandemic, the understanding of dynamical processes in socio-political systems is extremely important. Many researchers seek to comprehend how societies move towards consensus in the adoption of ideologies, traditions, and attitudes. The dynamics of social networks including small group interactions explains how an individual can adopt a new state in behavior, opinion, or consumption through the influence of others. Since opinions spread through social contacts, competing states are an intrinsic part of society. A simple example of bistability in social competition is the naming game, where two words compete across an intermediate state and agents accept both words [19, 20]. Multistability was introduced in the network model [21], where the agents represented by vertices are allowed to have one of several opinions each. These opinions

are updated by voter dynamics of the network. Moreover, agents accept connections with other agents provided they have equal opinions. When links are removed and disconnected agents are assigned to have new opinions randomly, the model has multiple solutions with a mixed metastable state of the disconnected agents, this corresponds to a dissolved society. In the model introduced by Sneppen and Mitarai [22], states or species compete and exhibit multistability through combinations of antagonistic conversions. In the context of a society with antagonistic political fractions, the mixed metastable state may be associated with a representative democracy with many balanced interest groups, while the extreme states correspond to a one-party system. Recently, models of social interactions on hypergraphs, in which multistability was also found, have been of particular interest [23, 24].

Multistability in genetic oscillators and synthetic circuits. The existence of multiple operating regimes is essential for biological systems, because they provide functional flexibility in responding to external stimuli [25]. This subject was largely investigated in relation to genetic oscillators [26, 27], with strong emphasis on biological mechanisms and topological structures leading to multistability [28–30]. Recently, the task of synthetic biology was of particular interest, which aims to build artificial decision-making circuits that are programmable, predictable and perform a specific function. The most synthetic circuits were governed by protein-based and RNA regulators [31, 32]. It was found that synthetic genetic networks are able to generate various dynamical regimes in relation to the topology of their interactions, including effects of multistability [33]. A detailed analysis of multistability, including multistability control [34] in coupled genetic oscillators could lead to new insights in the interplay between topology and the functioning of genetic networks.

Finally, we would like to mention another field of knowledge, far from the mathematical, physical and biological problems discussed in this book, where also the concept of multistability takes an important and central meaning. We refer to a school of thought in the philosophy of science and technology called postphenomenology, which considers issues of user experience through the prism of the practical use of technologies [35]. The postphenomenological perspective combines ideas from phenomenological and American practical philosophy to develop tools for in-depth analysis and description of the human-technology relations [36–38]. Central to this conceptual scheme is the notion of *multistability*. Based on Don Ihde's ideas [36], the concept of multistability in postphenomenology implies the idea that any technology can be used for a variety of applications and can be interpreted in a variety of ways. Ihde writes [39], “*I have argued that technologies are non-neutral and essentially, but structurally, ambiguous... Further, I have argued that at the complex level of cultural hermeneutics, technologies may be variantly embedded; the ‘same’ technology in another cultural context becomes quite a ‘different’ technology*”.

The following situation, described in [35] is an illustrative example. *Back in 2017, the city of Seattle installed eighteen bicycle racks, tightly spaced, under an overpass. But the purpose of the racks—simple metal arches attached to the ground—was not primarily for providing a place to lock up a bike. As Heidi Groover reports, “The city installed the racks in September after officials conducted a homeless encampment sweep in the area. SDOT considered the racks ‘part of the Homelessness Emergency*

Response effort' and they were meant to discourage camping".... The space under the overpass was being used by people living unhoused. The overpass provided some protection from the environment, and thus served as a good place to put up a tent. In an effort to drive out these unhoused campers from this space, the bike racks were installed in such a way to obstruct the ability to camp there. They were effective in this function.

So, if we look at this situation in terms of the notion of multistability, what is striking is the use of different technologies for different purposes than those for which they were developed. In the illustrative example described above, the Seattle overpass is multistable, this overpass was built as part of the road infrastructure, it was then used by the social stratum as part of a shelter-seeking strategy. Similarly, bike racks also become multistable—being part of the infrastructure for temporary bike storage, they simultaneously prevent homeless people from pitching tents under the overpass. According to postphenomenological philosophers, there are many experientially stable ways in which humans can learn a particular technology or a particular technique. In other words, technology can develop along different trajectories, or in the mathematical language of this book, find itself in basins of attraction of different stable applications. Examples of the multifaceted nature of various modern technologies can easily be traced by analyzing smartphones [40], digital video [41], robotics [42], etc.

The consideration of the philosophical issues of postphenomenological perspectives goes far beyond the scope of this book. However, it may be of interest to anyone who wants to look at such a fundamental nonlinear effect as multistability more broadly and not only from mathematical and biological viewpoints, but also from the perspective of the relationship of people and society with modern technology.

References

1. Kelso JAS (2012) Multistability and metastability: understanding dynamic coordination in the brain. *Phil Trans R Soc B* 367:906–918
2. Haroche S, Raimond JM (2006) Exploring the quantum: atoms, cavities, and photons. Oxford University Press, Oxford
3. Schoelkopf R, Girvin S (2008) Wiring up quantum systems. *Nature* 451(7179):664–669
4. Yamamoto Y, Tassone F, Cao H (2000) Semiconductor cavity quantum electrodynamics. Springer, Berlin
5. Greentree AD, Tahan C, Cole JH, Hollenberg LC (2006) Quantum phase transitions of light. *Nat Phys* 2(12):856–861
6. Noh C, Angelakis DG (2016) Quantum simulations and many-body physics with light. *Rep Prog Phys* 80(1):016401
7. Carusotto I, Ciuti C (2013) Quantum fluids of light. *Rev Mod Phys* 85(1):299
8. Marino J, Diehl S (2016) Driven markovian quantum criticality. *Phys Rev Lett* 116(7):070407
9. Jin J, Rossini D, Fazio R, Leib M, Hartmann MJ (2013) Photon solid phases in driven arrays of nonlinearly coupled cavities. *Phys Rev Lett* 110(16):163605
10. Diehl S, Tomadin A, Micheli A, Fazio R, Zoller P (2010) Dynamical phase transitions and instabilities in open atomic many-body systems. *Phys Rev Lett* 105(1):015702

11. Sieberer L, Huber SD, Altman E, Diehl S (2013) Dynamical critical phenomena in driven-dissipative systems. *Phys Rev Lett* 110(19):195301
12. Landa H, Schiró M, Misguich G (2020) Multistability of driven-dissipative quantum spins. *Phys Rev Lett* 124(4):043601
13. Marcuzzi M, Levi E, Diehl S, Garrahan JP, Lesanovsky I (2014) Universal nonequilibrium properties of dissipative rydberg gases. *Phys Rev Lett* 113(21):210401
14. Andreev A, Balanov A, Fromhold T, Greenaway M, Hramov A, Li W, Makarov V, Zagoskin A (2021) Emergence and control of complex behaviors in driven systems of interacting qubits with dissipation. *Npj Quantum Inf* 7(1):1–7
15. Centola D, Becker J, Brackbill D, Baronchelli A (2018) Experimental evidence for tipping points in social convention. *Science* 360(6393):1116–1119
16. Battiston F, Amico E, Barrat A, Bianconi G, Ferraz de Arruda G, Franceschiello B, Iacopini I, Kéfi S, Latora V, Moreno Y et al (2021) The physics of higher-order interactions in complex systems. *Nat Phys* 17(10):1093–1098
17. Higham DJ, de Kergerlay HL (2021) Mean field analysis of hypergraph contagion model. [arXiv:2108.05451](https://arxiv.org/abs/2108.05451) [math.DS]
18. Alvarez-Rodríguez U, Battiston F, de Arruda GF, Moreno Y, Perc M, Latora V (2021) Evolutionary dynamics of higher-order interactions in social networks. *Nat Hum Behav* 5(5):586–595
19. Xie J, Sreenivasan S, Korniss G, Zhang W, Lim C, Szymanski BK (2011) Social consensus through the influence of committed minorities. *Phys Rev E* 71:011130
20. Niu X, Doyle C, Korniss G, Szymanski BK (2017) The impact of variable commitment in the naming game on consensus formation. *Sci Rep* 7(1):1–11
21. Ehrhardt GCMA, Marsili M, Vega-Redondo F (2006) Phenomenological models of socioeconomic network dynamics. *Phys Rev E* 74:036106
22. Sneppen K, Mitarai N (2012) Multistability with a metastable mixed state. *Phys Rev Lett* 109:100602
23. de Arruda GF, Petri G, Moreno Y (2020) Social contagion models on hypergraphs. *Phys Rev Res* 2(2):023032
24. de Arruda GF, Petri G, Rodriguez PM, Moreno Y (2021) Multistability, intermittency and hybrid transitions in social contagion models on hypergraphs. [arXiv:2112.04273](https://arxiv.org/abs/2112.04273) [physics.soc-ph]
25. Angeli D, Ferrell JJE, Sontag ED (2004) Detection of multistability, bifurcations, and hysteresis in a large class of biological positive-feedback systems. *Proc Natl Acad Sci USA* 101(7):1822–1827
26. Ullner E, Zaikin A, Volkov EI, García-Ojalvo J (2007) Multistability and clustering in a population of synthetic genetic oscillators via phase-repulsive cell-to-cell communication. *Phys Rev Lett* 99:148103
27. Yuan Z, Zhang J, Zhou T (2008) Coherence, collective rhythm, and phase difference distribution in populations of stochastic genetic oscillators with cellular communication. *Phys Rev E* 78:031901
28. Koseska A, Kurths J (2010) Topological structures enhance the presence of dynamical regimes in synthetic networks. *Chaos* 20(4):045111
29. Ullner E, Koseska A, Kurths J, Volkov E, Kantz H, Garcia-Ojalvo J (2008) Multistability of synthetic genetic networks with repressive cell-to-cell communication. *Phys Rev E* 78:031904
30. Hellen EH, Volkov E (2018) How to couple identical ring oscillators to get quasiperiodicity, extended chaos, multistability, and the loss of symmetry. *Commun Nonlinear Sci Numer Simul* 62:462–479
31. Xie M, Fussenegger M (2018) Designing cell function: assembly of synthetic gene circuits for cell biology applications. *Nat Rev Mol Cell Biol* 19(8):507–525
32. Chappell J, Watters KE, Takahashi MK, Lucks JB (2015) A renaissance in RNA synthetic biology: new mechanisms, applications and tools for the future. *Curr Opin Chem Biol* 28:47–56
33. Santos-Moreno J, Tasiudi E, Stelling J, Schaerli Y (2020) Multistable and dynamic CRISPRi-based synthetic circuits. *Nat Commun* 11(1):1–8

34. Li T, Dong Y, Zhang X, Ji X, Luo C, Lou C, Zhang HM, Ouyang Q (2018) Engineering of a genetic circuit with regulatable multistability. *Integr Biol* 10(8):474–482
35. Rosenberger R (2020) On variational cross-examination: a method for postphenomenological multistability. *AI Soc* pp 1–14
36. Ihde D (2009) Postphenomenology and technoscience: the peking university lectures. Suny Press
37. Verbeek PP (2011) Moralizing technology. University of Chicago Press
38. Hasse C (2015) Social designation of cultural markers. In: An anthropology of learning. Springer, Berlin, pp 133–175
39. Hauser S, Oogjes D, Wakkary R, Verbeek PP (2018) An annotated portfolio on doing postphenomenology through research products. In: Proceedings of designing interactive systems conference, pp 459–471
40. Wellner G (2015) A postphenomenological inquiry of cell phones: Genealogies, meanings, and becoming. In: Postphenomenology and the philosophy of technology. Rowman & Littlefield
41. Irwin S (2017) Multimedia stabilities: exploring the gopro experience. In: Van Den Eede Y, Irwin S, Wellner G (eds) Postphenomenology and media. Lexington Books, Lanham, pp 103–121
42. Blond L (2019) Studying robots outside the lab: Hri as ethnography. *Paladyn* 10(1):117–127

Index

A

- Ambiguous image, 2, 331
- Necker cube, 1, 331, 356, 360, 373, 378, 384, 387
- Andronov–Hopf bifurcation, 45, 49–51, 71–73
- Anti-coherence resonance, 229, 230
- Artificial neural network, 287, 372, 374, 378
- Asymptotic stability, 18
- Attractor, 1

B

- Basin boundary dimension, 13
- Basin boundary metamorphosis, 30
- Basin catastrophe, 30
- Basin entropy, 35
 - boundary, 37, 38
- Basin integrity, 32
- Basin of attraction, 6, 10, 16, 23
- Basin of death, 29
- Basin of infinity attractor, 10
- Basin of survival, 28
- Basin reversal, 31
- Basin stability, 23, 24, 27, 30
- Biochemical oscillator, 70
- Biological feedback, 388
- Bistability, 2, 6, 48, 71, 125, 155, 184, 255, 274, 331
 - phase, 117
- Bistable perception, 2
 - auditory, 333
 - olfactory, 337
 - olvisual, 330
 - tactile, 336

Boolean network, 274

- Boosting, 96
- Boundary fractality, 38
- Box-counting dimension, 36, 38
- Brain-computer interface, 387
- Brain noise, 338, 358
- Brain-to-brain interface, 389

C

- Capacity dimension, 13
- Chaotic attractor, 10, 15, 55, 69
- Chemical oscillator, 71
- Chimera, 17, 255, 277
- Chua oscillator, 120, 278
- Chua system, 11, 93, 120, 228, 229
- Clustering, 61, 62
- Coherence resonance, 208–214, 233, 235
- Coherent control, 400
- Cold atom, 400
- Complexity, 35, 37, 38
- Complex network, 255, 274, 283
- Conditionally symmetric structures, 73
- Conditionally symmetric system, 74
- Conservative system, 8
- Continuation method, 80, 91
- Convolutional neural network, 373
- CO₂ laser, 3, 70, 71, 169, 170, 178, 180, 181, 183, 184, 191, 211, 212
- Coupled chaotic oscillator, 17
- Cryptography, 317

D

- Damped pendulum, 14, 87

- Dark region, 29
 Delay-coupled system, 17
 Delayed feedback, 69, 70, 233, 234
 Diffeomorphic manifolds, 57
 Diffeomorphic subsets of manifolds, 57
 Diffeomorphism, 57
 Dissipation, 58, 59
 Dissipative system, 8, 59, 60
 Duffing oscillator, 14, 114–116, 127, 128, 245, 272
 Dynamical system, 1, 6
- E**
 Ecological resilience, 25
 Ecological system, 14, 300
 Electroencephalogram, 289, 327, 329, 338, 360, 372, 384
 Engineering resilience, 25
 Entropy, 35, 37, 223, 224
 Epilepsy, 242
 Equilibrium point, 5
 Erosion profile, 34
 Evolution operator, 6
 Extreme event, 242
 Extreme multistability, 4, 10, 300, 302, 318, 320
- F**
 Fabry–Pérot resonator, 168
 Fiber laser, 3, 169, 170, 189–194, 242, 243
 Final state sensitivity, 28
 Finite-state machine, 101
 FinzHung–Nagumo neuron, 135
 FitzHung–Nagumo oscillator, 71
 Fractal basin, 11
 Fractal-fractal metamorphosis, 31
 Fractional-order Lorenz system, 123
 Fractional-order system, 122
 Functional connectivity, 289, 292, 328, 330, 365
 Functional magnetic resonance imaging, 289
- G**
 Game dynamical system, 300
 Genetic network, 276
 Genetic oscillator, 401
 Gibbs entropy, 35
 Global bifurcation, 45
 Global integrity measure, 33
 Gluing bifurcation, 54, 55
- Group of diffeomorphisms, 57
- H**
 Hamiltonian, 300
 Hamiltonian-driven dissipative dynamical system, 301
 He–Ne laser, 169
 Hénon map, 11, 31, 59, 66, 79, 111, 112, 124–126, 235, 236, 255, 310
 Heteroclinic bifurcation, 31, 45
 Hidden attractor, 3, 78, 86, 90, 91, 94–96, 98–100
 Hidden multistability, 10
 Hindmarsh–Rose neuron, 135, 136
 Hodgkin–Huxley neuron, 134, 135, 285
 Homoclinic, 58
 behavior, 2
 orbit, 51, 54, 55, 71
 tangency, 57, 58
 Homoclinic bifurcation, 31, 45
 Homotopy, 91
 Hopfield neural network, 282
 Hydrodynamical flow, 14
 Hypergraph, 400
- I**
 Infinite-period bifurcation, 53
 Insulator
 ferromagnetic, 141
 topological, 141
 Integral stability, 24
 Integrity factor, 33
 Interacting qubits, 400
 Intermittency, 199, 217, 218, 268
 Inter-spike interval, 286
 Invariant set, 8, 17, 45
 Inverse gluing bifurcation, 54
 Inversion symmetric system, 73
- J**
 Jansen–Rit model, 281
 Jerk system, 121, 122
- K**
 Kuramoto oscillator, 266, 268, 283
- L**
 Lactose utilization network, 3
 Lebesgue measure, 9, 16

- Limit cycle, 10, 45
Local bifurcation, 45
Local integrity measure, 33
Local Lyapunov exponent, 22
Logistic map, 55, 66, 69
Lorenz system, 118, 119, 131
Lotka–Volterra model, 300
Lozi map, 309, 310
Lyapunov criterion, 20, 22
Lyapunov exponent, 16, 22, 25, 26, 131
Lyapunov function, 20, 21, 303
Lyapunov stability, 17
- M**
Mackey–Glass model, 70
Magnetoencephalogram, 289, 327, 329, 338, 339, 367
Master stability function, 263
Memristor, 310, 311
Metamaterial, 75
Milnor attractor, 9, 15
Monte Carlo procedure, 24
Morris–Lecar neuron, 135
Multilayer perceptron, 373
Multiple limit cycles bifurcation, 45, 51
Multiple-node basin stability, 258
- N**
Necker cube, 367
Neimark–Sacker bifurcation, 45, 51, 52, 73
Nested double-scroll attractor, 98, 99
Neural-mass model, 281
Neural network, 3, 280, 282, 285, 311
Neuron, 70, 71, 132, 133, 136, 280, 281, 285
Newhouse phenomenon, 57
Nonlinear dynamics, 4, 23, 46, 189, 280
Nontwist map, 113
Nuclear spin-flip laser, 169
- O**
Optical bistability, 3, 167, 169, 171
Optoelectronic ring-coupled oscillator, 70
Orbital stability, 19
 asymptotic, 19
- P**
Parkinson’s disease, 132
Perceptional multistability, 2
 musical, 334
Perceptual decision-making, 328, 383
Period-doubling bifurcation, 31, 45, 70
Period-doubling system, 65
Periodic orbit, 10, 45, 57, 59, 69
Phase bistability, 139
Phase oscillator, 71
Phase space, 5, 6
Phosphorylation system, 3
Pitchfork bifurcation, 45, 46
Poincaré recurrence theorem, 101
Poisson’s ratio, 76
Polarization, 175
Postphenomenology, 401
Predator–prey equations, 300
Psychometric curve, 355, 360
- Q**
Quantum system, 400
- R**
Recurrent neural network, 287
Reflectional symmetric system, 73
Repeller, 4
Resilience, 24, 259
Riddled basin, 9, 15, 28, 102, 270
Rogue wave, 242
Rössler oscillator, 56, 70, 117, 130, 264, 303
Rotational symmetric system, 73
Rotor map, 59
Rydberg atom, 400
- S**
Saddle-node bifurcation, 31, 45, 46, 48, 49, 70–72, 191, 192
Saddle-node infinite period bifurcation, 70
Safe basin, 32
Safe motion, 32
Safe operating space, 29
Sample entropy, 38
Scale-free network, 268
Scroll attractor, 278
Secret key, 318
Secure communication, 318
Semiconductor laser, 3, 70, 71, 169, 170, 184, 231, 232, 247
Semiconductor superlattice, 3, 141
Single-node basin stability, 255
Smooth basin, 11
Solid-state laser, 169
Spatial multistability, 170
Spatial phase multistability, 283
Spectral entropy, 37

Steady-state visual evoked field, 339
Stochastic resonance, 199, 208–212
Structural multistability, 75, 274
Structural network bistability, 274
Structural stability, 20
Sudden erosion, 34
Sunny region, 29
Survivability, 28, 30
Symmetric system, 55, 73
Symmetry, 55, 56, 73, 74
Symmetry-increasing bifurcation, 55
Synthetic circuit, 401

T

Tokamak, 14
Transcritical bifurcation, 45
Tremor, 133

U

Uncertain destination dynamics, 4
Uncertainty dimension, 13, 28, 35
Uncertainty exponent, 13
Unsupervised clustering algorithm, 292

V

Van der Pol oscillator, 66, 70
Variable-boostable system, 74

W

Wada basin, 14, 15, 30, 194
Wada property, 14, 28, 38, 157
Watts–Strogatz approach, 283